Alexander Horn

The Physics of Laser Radiation–Matter Interaction

Fundamentals, and Selected Applications in Metrology

Springer

The Physics of Laser Radiation–Matter Interaction

Alexander Horn

The Physics of Laser Radiation–Matter Interaction

Fundamentals, and Selected Applications in Metrology

Springer

Alexander Horn
Mittweida, Sachsen, Germany

ISBN 978-3-031-15861-2 ISBN 978-3-031-15862-9 (eBook)
https://doi.org/10.1007/978-3-031-15862-9

© Springer Nature Switzerland AG 2022
This work is subject to copyright. All rights are reserved by the Publisher, whether the whole or part of the material is concerned, specifically the rights of translation, reprinting, reuse of illustrations, recitation, broadcasting, reproduction on microfilms or in any other physical way, and transmission or information storage and retrieval, electronic adaptation, computer software, or by similar or dissimilar methodology now known or hereafter developed.
The use of general descriptive names, registered names, trademarks, service marks, etc. in this publication does not imply, even in the absence of a specific statement, that such names are exempt from the relevant protective laws and regulations and therefore free for general use.
The publisher, the authors, and the editors are safe to assume that the advice and information in this book are believed to be true and accurate at the date of publication. Neither the publisher nor the authors or the editors give a warranty, expressed or implied, with respect to the material contained herein or for any errors or omissions that may have been made. The publisher remains neutral with regard to jurisdictional claims in published maps and institutional affiliations.

This Springer imprint is published by the registered company Springer Nature Switzerland AG
The registered company address is: Gewerbestrasse 11, 6330 Cham, Switzerland

To my wife, Sylke.
She interacts seriously with me,
making life better.

Preface

This textbook is intended for students of physics, physical or mechanical engineering, or natural sciences. The idea to start to write a book on the interaction of laser radiation with matter began to grow when I moved to Mittweida in 2013, tooling there a new professorship in physics and laser microtechnology. Textbooks on these topic exist for professionals, but my research on comprehensive books didn't get any valuable books on, in my opinion, very important derivations from equations and thoughts, describing such processes. So, I started to collect passages, generated topics, and finally finalized this book.

These years of development were accompanied by numerous discussions with my team members, who in fact cleared my mind and allowed me to determine a red line on which a lecture on laser radiation–matter interaction should follow. My team colleagues were the "seeds and the plants" of most results described in this book. Especially, Markus Olbrich, M.Sc., being our fundamentalist in sense of the physical understanding, pitched this textbook on the right level. He was my first group member, and together we set up our lab at the laser institute in Mittweida. He introduced my group to the numerical techniques and taught all group members, and additionally also our students learning physical technology, to apply these wonderful techniques to many physical problems. The second key player in my group, Dr. rer. nat. Theo Pflug, was the experimenter, who developed many novel ultra-fast metrologies and who published in a very short time many wonderful articles on our group activities. Both supported me during my writing of this textbook with fruitful discussions and in setting up many diagrams and modeling plots. The last member who supported me is Philipp Lungwitz, M.Sc., who developed often very unorthodox physical techniques and opened some new research topics in my group. He is the perfectionist in our lab, who pushed some of our research to new levels. All of them I thank very much for the fruitful years and the friendship. The laser institute in Mittweida is a jewel, as there best-skilled scientists are working on different leading topics in laser technology. I thank all my colleagues for the strong collaboration. One great property is that many of them work together when help is needed, even not being in the same research group. Nothing would work in our labs at the institute without the strong support of Lars Hartwig, Sascha Klötzer, and Alexander Thurm. They were the first setting up

the illumination technology in my lab, making the room cleaner with flow boxes, and allowing us to start to work very quickly.

This textbook is structured into four great parts, starting from the characterization of laser radiation. In my opinion, the most important topics deal little with "laser" radiation, but just on electromagnetic radiation. As this textbook does not deal with ultra-high-energy physics, also the topic laser will just deal with pulse duration down to the femtosecond regime. Just some insight on pulse shaping will enlarge the physics of laser radiation with matter.

The second part of this textbook describes the processes for the generation of electromagnetic radiation, as firstly often radiation is generated during laser radiation/matter interaction, and secondly, every process of interaction features a kind of scattering of charges. Oscillating charges emit radiation, as will be shown by solving the Maxwell equations. In my opinion, even these derivations are somehow very theoretical, also an engineer should be able to follow the idea. This is important to understand physics!

The third and largest part describes the interaction of radiation with matter. As a textbook, I decided to go step-wise from the simplest system, a free electron, to the most complex one, condensed matter, introducing semi-classical models for the interaction. In this textbook, no strong quantum mechanical derivations are given, as this is more adequate for the physicist, not for a user. Even though the semi-classical model is somehow crude, they describe the processes very well. Many examples are given. Getting an understanding of the interaction of simple systems, linear optics dealing with the interaction of radiation with the condensed matter without absorption is described. As ultra-fast laser metrology is in my opinion the metrology being able to investigate very fundamental processes, non-linear optics is then introduced, being the key process for ultra-fast physics. Up to now, no absorption is given, which is why in the following sections the absorption is introduced. To describe this properly in condensed matter, especially in this textbook solid state matter is discussed, and the name model for crystalline matter is introduced. Before that, clearly, the free electron gas is used as the simplest model to describe absorption and as a consequence, their optical properties. As now the inter- and intraband transitions are understood, many examples on the excitation of condensed matter are given, for metals, semiconductors, and as well dielectrics. Especially for dielectrics, as absorption can only take place when non-linear processes are given, a topic on non-linear absorption will describe the different channels enabling radiation to ionize matter.

The fourth and last part deals with applications in metrology using laser radiation. I decided to describe some special metrologies, where ultra-fast laser radiation features the best properties to get some very deep insight. Also, I focused on pump-probe technologies only. I start with reflectometry, being the simplest metrology. There I describe the fundamentals of the pump-probe idea. A very impressive setup is then described allowing to detect space- and time-resolved reflectance change. The next chapter deals with ellipsometry, a fantastic metrology, allowing to determine the complex refractive index. After some fundamentals, I describe space-resolved and in the following space- and time-resolved ellipsometry. A more qualitative metrology, but quick in setting up, is Nomarski microscopy. It allows to determine space- and

time-resolved refractive index changes. Finally, I will describe in this part the white-light interferometry. It is the royal league of interferometry, as using white-light a biunique detection of phase changes is possible, and combined with ultra-fast laser radiation, it becomes a very powerful metrology for the investigation of laser-induced processes.

Many thanks to Prof. Sauerbrey for allowing me to use his very focused lecture notes on non-linear optics. I hope I got his message and could transpose it well. Also, I adopted some notes from the lectures on electrodynamics by S. Brandt and D. Dahmen I listened to as a student in physics at the University of Siegen in the year 1992. Finally, I want to thank many students, like Melwin Göse, B.Sc., Philipp Rebentrost M.Sc., Eric Syrbe M.Sc., Katrin Zerbe M.Sc., giving me a lot of helpful comments and revisions to the textbook.

Oberschöna, Germany Alexander Horn
August 2022

Contents

Part I Electromagnetic Radiation

1 Properties of Electromagnetic Radiation 3
1.1 Fundamental Interactions 4
1.1.1 Nuclear Forces 5
1.1.2 Electromagnetic Force 6
1.1.3 Gravitational Force 6
1.2 Wave and Particle Description of Electromagnetic Radiation 7
1.3 Photon Description 8
1.4 Maxwell Equations 9
1.4.1 Maxwell Equations in Vacuum 9
1.4.2 Continuity Equation 11
1.4.3 Integral Description of Maxwell Equations 12
1.5 Electromagnetic Waves 12
1.5.1 Derivation of Wave Equations 12
1.5.2 Fundamentals on Waves 14
1.5.3 Orthogonality of the Vector Fields 15
1.5.4 Scalar and Vector Potential 17
1.6 Energy Density of Electromagnetic Wave 20
1.6.1 Electrostatic Approach 20
1.6.2 Generalization to Electromagnetic Fields 24
1.6.3 Planar Electromagnetic Waves 28
1.6.4 Phase and Group Velocity 33
1.7 Laser Radiation 35
1.7.1 Spatial and Temporal Properties 35
1.7.2 Coherence 37
1.7.3 Spectral Modulation 39
References 50

2 Generation of Electromagnetic Radiation 51
2.1 Discrete and Continuous Transitions 51
2.2 Spontaneous Emission 52
2.3 Acceleration of a Free Charge 54
2.3.1 General Aspects on the Retardation 56
2.3.2 General Solution of a Retarded Wave Equation 58
2.3.3 Maxwell Equations for a Moving Charge 59
2.4 Emission of Accelerated Charges 65
2.4.1 Collinear Velocity and Acceleration Vectors 65
2.4.2 Acceleration Perpendicular to the Velocity 68
2.4.3 Periodic Oscillation of a Charged Particle 70
2.5 Black-Body Radiation 75
2.5.1 One-Dimensional Hollow Black Body 76
2.5.2 Three-Dimensional Hollow Black Body 79
2.5.3 High- and Low Photon Energy Limits 82
2.5.4 The Stefan–Boltzmann Law 83
2.5.5 Wien's Displacement Law 83
2.5.6 Emitted Radiation Power 84
2.5.7 Real Thermal Emitter 87
2.6 Laser-Generated X-Rays 87
2.7 Concluding Remarks 90
References 91

Part II Interaction of Particles with Electromagnetic Radiation

3 Elastic Scattering at Charged Particles 95
3.1 Free Electron 95
3.1.1 Radiation Force 96
3.1.2 External Field 98
3.1.3 Dipole Moment and Differential Power per Solid Angle 99
3.2 Bounded Electron 101
3.2.1 Equation of Motion of a Weakly-Bounded Electron 102
3.2.2 Radiation Force 105
3.2.3 External Field 106
3.2.4 Dipole Moment and Differential Power per Solid Angle 107
3.3 Cross-Section 109
3.4 Polarization of Scattered Radiation 113
3.5 Photo-Excitation of Atoms 114
3.5.1 Linear Scattering 114
3.5.2 Non-linear Scattering 115

4 Inelastic Scattering and Absorption 117
4.1 Free Carrier Absorption—Inverse Bremsstrahlung 117
4.2 Raman Scattering 119
4.3 Photo-Ionization or Photo-Effect 120
4.4 Ponderomotive Energy and Force 122
4.5 Non-linear Photo-Ionization 124
4.5.1 Tunnel Ionization 124
4.5.2 Multi-photon Ionization 125
4.5.3 Keldysh Parameter for Atoms 126
4.5.4 Above-Threshold Multi-photon Ionization 129
4.6 Compton Scattering 130
4.7 Pair Production 132
References 132

5 Scattering by Many Charges 135
5.1 Attenuation Coefficient 135
5.2 Coherent Scattering 136
References 139

Part III Interaction with Condensed Matter Without Absorption

6 Scattering in Matter 143
6.1 Reversible and Irreversible Interaction 143
6.2 Maxwell Equations in Matter 145
6.3 Lorentz Model 151
6.4 Refractive Index 153
6.5 Many Different Scatterers 156
6.6 Wave Equation in Matter 159
6.7 Straight Propagation in Condensed Matter 160
6.8 Speed of Light in Media 163
References 165

7 Linear Optics 167
7.1 Steadiness of Fields 167
7.2 S-Polarized Radiation 168
7.3 P-Polarized Radiation 174
7.4 Boundary Conditions with Complex Refractive Index 176
7.5 Fresnel Equations for Transparent Dielectrics 177
7.6 Reflectance and Transmittance 178
7.7 Nearly Perpendicular Irradiation 180
7.8 Brewster Angle 181
7.9 Critical Angle for Total Reflection 181
7.10 Internal Reflection and Evanescent Waves 185

8 Non-linear Optics 189
8.1 Principal Equations of Non-linear Optics 189
8.2 Non-linear Repulsive Forces 191
8.3 Second-Order Processes 192
8.3.1 Equation of Motion with Non-centrosymmetric Media 193
8.3.2 Non-linear Polarization Density 197
8.3.3 Differential Equation for the Second Harmonic Field 197
8.3.4 Second Harmonic Generation 200
8.3.5 Three-Wave Mixing 202
8.3.6 Parametric Amplification 206
8.4 Third-Order Processes 209
8.4.1 Equation of Motion with Centrosymmetric Media 210
8.4.2 Four-Wave Mixing 211
8.4.3 Third-Harmonic Generation 212
8.4.4 Kerr Effect 213
8.4.5 Self-focusing 215
8.4.6 Catastrophic Self-focusing 217
8.4.7 Self-phase Modulation 218
References 219

Part IV Interaction with Absorption

9 Electron Gas in Condensed Matter 223
9.1 Periodic Potentials 223
9.2 Electronic Properties at Zero Temperature 224
9.2.1 Quantized Wave Number and Energy 224
9.2.2 Density of States 229
9.2.3 Fermi–Dirac Distribution at $T = 0$ K 233
9.3 Electronic Properties at Higher Temperatures 237
9.3.1 Fermi–Dirac Distribution at Higher Temperatures 237
9.3.2 High Electron Density: Metals 239
9.3.3 Low Electron Density: Semiconductors 242
References 244

10 Optical Properties of an Electron Gas 245
10.1 General Aspects—Lambert–Beer's Law 245
10.2 Electron Gas 246
10.2.1 Free Electron Gas 247
10.2.2 Quasi-free Electron Gas 251

11 Band Theory of Crystals 255
11.1 Electronic Band Formation 255
11.2 Valence and Conduction Bands 259
11.2.1 Crystals at Absolute Zero Temperature 260

11.2.2 Crystals at Higher Temperatures 262
11.2.3 Electrons and Holes in Semiconductors 264
11.2.4 Electrons in the Conduction Band of Metals 268
11.3 Band Structure and Dispersion Relation in Crystals 269
11.4 Non-crystalline Matter 273
References 276

12 Linear Absorption 277
12.1 Absorption in Condensed Matter 277
12.2 Interband Excitation 279
12.2.1 Reduced Band Structure Plot 279
12.2.2 Dielectrics and Semiconductors 281
12.2.3 Transition Metals 282
12.3 Intraband Excitation 283
12.4 Non-crystalline Matter—Disordered Matter 285
12.5 Excited State Transitions 286
12.5.1 Dielectrics and Semiconductors 286
12.5.2 Recombination and Meta-Stable States 289
12.5.3 Excited Transition Metals 289
12.6 Optical Properties of Metals 291
12.6.1 Non-excited Metals 291
12.6.2 Excited Dielectrics 292
References 296

13 Non-linear Absorption 297
13.1 Excitation Pathways 297
13.2 Electron Rate Equation 299
13.3 Non-linear Photo-Excitation 300
13.3.1 Keldysh Parameter for Crystals 300
13.3.2 Tunnel Excitation 301
13.3.3 Multi-photon Excitation 303
13.3.4 Non-linear Photo-Excitation 304
13.3.5 Two-Photon Absorption 306
13.3.6 Three-Photon Absorption 307
13.4 Impact Ionization 308
13.5 Channeling and Filamentation 312
13.5.1 Channeling 312
13.5.2 Filamentation 314
References 315

14 Heating 317
14.1 Process Steps of Heating 317
14.2 Two-Temperature Model 318
14.3 Derivation of the Heat Equation 320
14.4 Heating of Metals 324
14.5 Thermophysical Properties of the Electron System 325

14.5.1 Heat Capacity of the Electron System 325
14.5.2 Thermal Conductivity of the Electron System 330
14.5.3 Electron-Phonon Coupling Parameter 332
14.6 Thermodynamic Properties of the Phonon System 333
14.6.1 Heat Capacity of the Phonon System 334
14.6.2 Thermal Conductivity of the Phonon System 336
14.7 Numerical Approach 337
14.8 Examples for Laser-Heated Metals 339
14.8.1 Nanosecond Laser Radiation 339
14.8.2 Femtosecond Laser Radiation 340
References 342

15 Phase Transitions 343
15.1 Laser-Induced Phase Changes 343
15.1.1 Slow Heat Transfer 343
15.1.2 Fast Heat Transfer 346
15.2 Heating with Phase Transitions—Modeling 347
15.3 Thermo-physical Equations 349
References 355

Part V Selected Applications in Metrology

16 Reflectometry 359
16.1 Measurement Methods 359
16.2 Pump and Probe Metrology 360
16.3 Time-Resolved Reflectometry 361
16.3.1 Principle and Set-Up 362
16.3.2 Examples 363
References 367

17 Ellipsometry 369
17.1 Fundamentals on Polarization States 369
17.2 Principles of Ellipsometry 371
17.3 Experimental Approach 373
17.4 Reflection at One Interface 377
17.5 Reflection at Many Interfaces for Thin Layers 379
17.6 Layer- and Dispersion-Models 381
17.7 Imaging Ellipsometry 383
17.7.1 Principle Set-Up 383
17.7.2 Spatial-Resolved Measurement 384
17.8 Space- and Time-Resolved Ellipsometry 384
17.8.1 Principle Set-Up 385
17.8.2 Examples 388
References 389

18 Nomarski Microscopy 391
18.1 Principle of Nomarski Microscopy 391
18.2 Time-Resolved Nomarski Microscopy 393
18.3 Examples 395
Reference 395

19 White-Light Interferometry 397
19.1 Principle of Mach-Zehnder Interferometry 397
19.2 White-Light Interferometry 397
19.3 Pump-Probe White-Light Interferometry 399
19.4 Super-Continuum Source 400
19.5 Interferogram Analysis 402
19.6 Examples 403
19.7 Conclusion 405
Reference 406

Bibliography 407

Index 409

Acronyms

$\boldsymbol{A}$	Vector potential field
AOM	Acousto-optical modulator
a-SiO_2	Amorphous quartz
A_{21}	Einstein coefficient for spontaneous emission
a	Area
$\boldsymbol{a}$	Acceleration vector
$\boldsymbol{a}$	Area vector
a_B	Bohr acceleration
$\hat{\boldsymbol{a}}$	Unity area vector
α	Angle of reflection
α	Linear absorption coefficient
α_e	Electric polarizability
α_B	Brewster angle
α_F	Fourier coefficient
α_T	Critical angle for total reflection
α_av	Avalanche coefficient
α_th	Thermal diffusivity
$\boldsymbol{B}$	Magnetic induction field strength vector
β	Relativistic factor vector
β	Angle of refraction
β	Two-photon absorption coefficient
β_F	Fourier coefficient
β_i	Complex angle of refraction
CP	Critical point
c	Specific heat capacity
c_e	Specific heat capacity of electron system
c_p	Specific heat capacity of phonon system
c_0	Speed of light in vacuum
c_M	Speed of light in medium
C	Capacity of capacitor
C	Molar heat capacity

$C_{\mathrm{e,V}}$	Molar electron heat capacity at constant volume
$C_{\mathrm{ph},V}$	Molar phonon heat capacity at constant volume
c_v	Specific heat capacity at constant volume
c_p	Specific heat capacity at constant pressure
CB	Conduction band
CCD	Charged-coupled device
χ_{e}	Electric susceptibility
$\widetilde{\chi}_{\mathrm{e}}$	Complex electric susceptibility
$\underset{=\mathrm{e}}{\widetilde{\chi}}$	Complex electric susceptibility tensor of second rank
χ_{m}	Magnetic susceptibility
χ^{NL}	Non-linear susceptibility
$\boldsymbol{D}$	Electric displacement vector
D	Spring constant
$\boldsymbol{d}$	Dipole moment
D_k	Density of states related to wave number vector
D_k	Density of states related to value of wave number
D_ε	Density of states related to energy
D_{b}	Density of states near bottom edge
D_{t}	Density of states near top edge
D_0	Effective density of states
d_ε	Density of states related to energy and volume
δ	Delta function
Δ	Ellipsometric parameter
$\boldsymbol{E}$	Electric field strength vector
$\boldsymbol{E}_{\mathrm{p}}$	Electric polarization vector
$\widetilde{\boldsymbol{E}}$	Complex electric field strength vector
E_γ	Photon energy
E_{res}	Resonance energy
E_{p}	Pulse energy
E_{ext}	Electric field strength of external radiation
E'_e	Energy of scattered electron
$\tilde{E}_{\mathrm{gap}}$	Extended band gap energy
$\tilde{E}^*_{gap}$	Effective band gap energy
$\boldsymbol{E}^{\mathrm{s}}$	Electric field strength of s-polarized radiation
$\boldsymbol{E}^{\mathrm{p}}$	Electric field strength of p-polarized radiation
ES	Excited state
ΔE	Energy band gap
E_{gap}	Energy band gap
e	Elementary charge, Electron charge
$\boldsymbol{e}_x, \boldsymbol{e}_y, \boldsymbol{e}_z$	Unity vectors in $x-$, $y-$, and z-directions
ε_0	Vacuum permittivity
$\varepsilon(T)$	Emissivity
ε	Permittivity (absolute)
ε_n	Energy of a free electron in potential well

$\varepsilon(k)$	Dispersion relation
$\varepsilon(\mathrm{F})$	Fermi energy
ε_r	Relative permittivity
ε_e	Specific internal energy of electron system
ε_ph	Specific internal energy of phonon system
ε_1	Real component of the complex relative permittivity
ε_2	Imaginary component of complex relative permittivity
$\tilde{\varepsilon}_\mathrm{r}$	Complex relative permittivity, dielectric function
$\underset{=\mathrm{r}}{\tilde{\epsilon}}$	Complex relative permittivity tensor of second rank
ε_ITT	Interband transition threshold energy
η	Impact excitation/ionization rate
$\boldsymbol{F}$	Force
$\boldsymbol{F}_\mathrm{rad}$	Radiation force
$\boldsymbol{F}_\mathrm{P}$	Ponderomotive force
$\boldsymbol{F}_\mathrm{L}$	Lorentz force
$F^{1/2}$	Fermi function at index 1/2
$F(\boldsymbol{q})$	Form factor
f_i	Oscillator strength
f_BE	Bose–Einstein distribution function
f_FD	Fermi–Dirac distribution function
G	Generalized Green function
G	Gravitational constant
$G(T_\mathrm{e})$	Electron–phonon coupling factor
$\boldsymbol{G}$	Reciprocal lattice vector
G	Reciprocal lattice distance
GD	Group delay
GDD	Group delay dispersion
GVD	Group velocity dispersion
GS	Ground state
Γ_em	Damping coefficient
Γ_opt	Optical retardation
γ	Keldysh parameter
γ	Three-photon absorption coefficient
$\boldsymbol{H}$	Magnetic field strength
H	Fluence
H	Hamiltonian
H	Directional dose
H_thr	Threshold fluence
h	Planck constant
h	Hole
ΔH_v	Enthalphy of evaporation
ΔH_c	Enthalphy of condensation
ΔH_m	Enthalphy of melting
ITT	Interband transition threshold

I	Intensity
IS	Ionization state
IR	Infrared radiation
I_0	Peak intensity
I^a	Electric current
$\boldsymbol{j}$	Current density
$\boldsymbol{k}$	Wave number vector
k	Wave number value
k_B	Boltzmann constant
$\boldsymbol{k}_\mathrm{Br}$	Brillouin wave number vector
Δk	Phase mismatch
κ	Extinction coefficient
κ	Compensator angle
k_F	Fermi wave number
$\boldsymbol{L}$	Angular momentum
LIPSS	Laser-induced periodical surface structures
L_c	Coherence length
λ	Wavelength
λ_res	Resonant wavelength
λ_ITT	Interband transition threshold wavelength
λ_e	Heat conductivity of electron system
λ_ph	Heat conductivity of phonon system
l_opt	Optical penetration depth
λ_opt	Optical absorption length
l_T	Potential barrier width
MPE	Multi-photon excitation
MPI	Multi-photon ionization
MCP	Multi-channel plate
m	Mass
m^*	Effective mass
m_e	Electron mass
μ_0	Vacuum permeability
$\mu(T)$	Chemical potential
μ_r	Relative permeability
μ	Attenuation coefficient
μ^m	Mass attenuation coefficient
NA	Numerical aperture
N_ε	Number of states per energy
n_ε	Number density of states per energy
N_e	Number of electrons
n_e	Number density of electrons
n_d	Dipole density
n_F	Fermi quantum number
n_2	Kerr coefficient
ν	Frequency

ν_j	Mode frequency
ν_ee	Electron-electron collision frequency
ν_ep	Electron-phonon collision frequency
ν_e	Average collision frequency
n_e	Electron density
n	Refractive index
$n(\nu)$	Mode density
$\tilde{n}$	Complex refractive index
OPA	Optical parametric amplifier
OPG	Optical parametric generator
OPO	Optical parametric oscillator
OTM	One-temperature model
OPL	Optical path length
OPD	Optical path difference
p_e	Pressure of electron system
p_ph	Pressure of phonon system
PMMA	Poly(methyl methacrylate)
P3HT	Poly(3-hexylthiophene-2,5-diyl)
PEDOT:PSS	poly(3,4-ethylenedioxythiophene) polystyrene sulfonate
PE	Photo excitation
PI	Photo ionization
PSAR	Rotating-analyzer ellipsometry
PSCAR	Rotating-analyzer ellipsometry with compensator
PSCRA	Rotating-compensator ellipsometry
P	Power
P	Degree of polarization
P_0	Peak power
P_crit	Critical peak power for self-focusing
$\boldsymbol{p}$	Momentum
$\boldsymbol{P}$	Polarization density
$\boldsymbol{P}^\mathrm{NL}$	Non-linear polarization density
$\boldsymbol{P}^\mathrm{L}$	Linear polarization density
$\boldsymbol{p}_\mathrm{F}$	Fermi momentum
$\boldsymbol{\Psi}^a$	Electric flux
ψ_k	Wave function
$\lvert\psi\rvert^2$	Probability density function
$\boldsymbol{\Phi}^a$	Magnetic flux
ϕ	Analyzer angle
φ	Scalar potential field
φ	Phase
φ_a	Phase function
ϕ_m	Spectral transfer function
$\Phi(t)$	Time-dependent phase
Φ	Ellipsometric parameter
φ_s	Phase for s-polarized radiation

φ_{p}	Phase for p-polarized radiation
Q	Heat
q_V	Heat source
q, Q	Electric charge
q	Electrical charge
q_{e}	Electron charge
r	Radial distance
r_{e}	Classical hydrogen radius
r_{B}	Bohr radius
r_{c}	Classical electron radius
r^{s}	Reflection coefficient for s-polarized radiation
r^{p}	Reflection coefficient for p-polarized radiation
R^{s}	Reflectance for s-polarized radiation
R^{p}	Reflectance for p-polarized radiation
$\boldsymbol{r}$	Radial vector
$\hat{\boldsymbol{r}}$	Radial unity vector
ρ	Density
ρ_0	Charge density
ρ_{rec}	Recombination rate
$\boldsymbol{S}$	Spin angular momentum
$\boldsymbol{S}$	Poynting vector
$\boldsymbol{S}_N$	Normalized Stokes vector
s	Volumetric heat capacity
SHG	Second-harmonic generation
SVEA	Slow varying envelope approximation
STE	Self-trapped exciton
SC	Super-continuum source
S_0, S_1, S_2, S_3	Stokes parameter
σ	Surface charge
σ	Total cross-section
σ_{T}	Overall cross-section
σ_{c}	Total cross-section for Compton scattering
σ_{Th}	Total cross-section for Thomson scattering
σ_{R}	Total cross-section for Rayleigh scattering
σ_{res}	Total cross-section for Resonant scattering
σ_{pe}	Total cross-section for photo-excitation
σ_{pe}^{K}	Total cross-section for K-shell ionization
σ_{PP}^{K}	Total cross-section for pair production
σ_{SB}	Stefan–Boltzmann constant
σ_{N}	Total cross-section for N-Photon ionization
σ_{p}	Polarization surface charge density
σ_{eff}	Effective surface charge density
σ_{3PA}	Three-photon absorption molecular cross-section
σ_{TPA}	Two-photon absorption molecular cross-section

T	Period
T_{crit}	Critical temperature
T_{m}	Melting temperature
T_{v}	Vaporization temperature
T_{D}	Degeneracy temperature
T_{e}	Temperature of electron system
T_{Ph}	Temperature of phonon system
TI	Tunnel ionization
TE	Tunnel excitation
THG	Third-harmonic generation
t_{T}	Tunneling time
TTM	Two-temperature model
TOD	Third-order dispersion
t_{p}	Pulse duration
ta-C	Tetragonal amorphous carbon
T_{g}	Instantaneous group delay
t^{s}	Transmission coefficient for s-polarized radiation
t^{p}	Transmission coefficient for p-polarized radiation
T^{s}	Transmittance for s-polarized radiation
T^{p}	Transmittance for p-polarized radiation
$\hat{t}$	Tangential unity vector
τ_{trap}	Trapping time
τ_{ep}	Electron–phonon collision time
τ_{ee}	Electron–electron collision time
τ_{R}	Electron–phonon coupling time
Θ_{D}	Debye temperature
UV	Ultraviolet radiation
U^{c}	Electric tension
$u(\nu)$	Spectral energy density
U^{m}	Magnetic tension
U_{P}	Ponderomotive energy
V	Volume
VB	Valence band
VIS	Visible radiation
$\boldsymbol{v}$	Velocity vector
$\boldsymbol{v}_{\mathrm{F}}$	Fermi velocity vector
$\boldsymbol{v}_{\mathrm{e}}$	Electron velocity vector
v_{p}	Phase velocity
v_{s}	Sound velocity
v_{g}	Group velocity
v_{B}	Bohr velocity
ω	Angular frequency
$\Delta\omega$	Spectral bandwidth
ω_{em}	Angular frequency of electromagnetic radiation
ω_{p}	Plasma frequency

ω_{T}	Tunneling frequency
ω_{eff}	Effective angular frequency
ω_{D}	Debye frequency
ω_0	Resonance frequency
w_{e}	Electric energy density
w_{m}	Magnetic energy density
w_{em}	Electromagnetic energy density
w_0	Beam waist radius
x	Spatial coordinate
$\dot{x}$	Velocity
$\ddot{x}$	Acceleration
Z	Atomic number
z_{csf}	Focal distance for catastrophic focusing

Part I
Electromagnetic Radiation

This part of the book is dedicated to electromagnetic radiation. We start with its properties, Chap. 1, and clearly, we introduce the Maxwell equations. From there we deviate the wave equations for the electric and the magnetic fields. We will show the orthogonality of these fields as electromagnetic radiation, will talk about the energy density transported by the radiation introducing the Poynting vector, and will show the continuity equation for that.

In this chapter also some more fundamental aspects of the potential field for the electric and the magnetic field strengths are given, so that the wave equations for the electric and magnetic field are now written as the homogeneous d'Alembert equation. Also, some properties of laser radiation are given, becoming important in the second large chapter dealing with the generation of electromagnetic radiation.

Chapter 2 deals with the generation of electromagnetic radiation. There we will distinguish between discrete and continuous emissions of radiation. The first one is purely a quantum mechanical process and is difficult to be treated mathematically in the context of this book. Easier, we will describe the acceleration of electrons in electromagnetic fields using the Newton field theory dealing with forces.

As the locations where we want to determine electromagnetic fields and their generation at the position of the electron are different, a retardation is expected, as the velocity of light is limited. We will deduce the fundamental potential equations describing the generation of electromagnetic radiation by accelerated particles, the Liénard–Wiechert potential, determine the directional radiation characteristics, and show typical applications for accelerated electrons, like the synchrotron or the X-ray tube.

Much more important for us are the periodically accelerated electrons, representing the sources of the electrons in atoms when interacting with electromagnetic radiation. We will introduce therefore the electric dipole and its directional radiation characteristics.

Now, we can start to look at the solid state, discussing its emission of radiation due to the temperature, thermal emission, or black-body radiation. Lastly, we discuss the possibility to generate X-rays using intensive laser radiation, like ultra-fast laser radiation.

Chapter 1
Properties of Electromagnetic Radiation

Abstract Light represents one form of electromagnetic radiation, which can be described by a wave theory. Through the scientific history of the sixteenth to nineteenth century a solid knowledge has been developed on electromagnetic radiation, culminating in the classical theory of James Clerk Maxwell (1864) coupling electric with magnetic fields, and describing together with the equation of continuity the interaction of electromagnetic radiation with matter. We start describing first looking at the principal forces acting during the interaction of laser radiation with matter. Thereby we will describe the common fundamental forces. In the following, the Maxwell equations in the differential and in the integral form will be discussed. These equations are for this book of central importance allowing to describe scattering, reflection, and refraction of radiation. As typical fields, the electric and the magnetic field strengths will be introduced. As shown in classical mechanics, it is convenient to define a potential to a force allowing an easier calculation of the interaction. Also for the two electromagnetic field strengths, a scalar and a vector potential will be introduced. In the following of this chapter, we talk about the energy density given by the electromagnetic field getting at the end an idea of how electromagnetic radiations transports energy, namely by the Poynting vector. Using exemplary planar waves, the orientation of the fields as well as the energy density are defined, and at the end also, the important connection between field strength and intensity of radiation is defined. As laser radiation must not be monochromatic, the velocity of light, the so-called phase velocity, is discussed for temporal limited radiation pulses getting the definition of the group velocity. Up to now we worked only with the wave description of photons. Here we start to have a look at its particle character. Finally, we talk about the special properties of laser radiation delimiting from the conventional radiation. So the property of coherence will be discussed here briefly.

© Springer Nature Switzerland AG 2022

A. Horn, *The Physics of Laser Radiation–Matter Interaction*,
https://doi.org/10.1007/978-3-031-15862-9_1

1.1 Fundamental Interactions

The interaction of electromagnetic radiation with matter implies many processes, starting from the propagation through matter, the reflection at specific boundaries, and the deposition of energy into matter.

Looking at a laser drilling process using conventional commercial infrared (IR) laser radiation quickly (Fig. 1.1), one could release that this process is quite simple: but in fact, just the process time window where radiation interacts with matter contains a lot of complex sub-processes. Apparently, laser radiation propagates nearly undisturbed and without any energy losses through *optical systems*, like lenses, apart from the refraction taking place at the boundaries.

There are different processes induced in the matter by the same radiation, depending on the material class involved: refraction is induced in dielectric materials, and phase transitions after absorption of radiation are taking place, e.g. when metals are heated and possibly melted.

So, in our case during the laser drilling process, the metal absorbs partly the radiation and gets heated. The questions to be answered here are, for example, what is the absorption process for the radiation involved and how is the optical energy converted into heat?

Specifying the laser drilling process one observes the expulsion of melt and the formation of vapor and also plasma. The hydrodynamics of the melt and the vapor will be very complex influencing the ablation process considerably. Also, melt, vapor, and plasma can interact with the incoming laser radiation. Especially the plasma can thereby exhibit mirror-like properties, depending on the process parameters chosen.

So, summarizing, the interaction of laser radiation with matter can be very complex. The following book will give an introduction to the meaning of this interaction, being the keyword and key process throughout this lecture.

Firstly, let us discuss the meaning of *interaction*. Generally in classical physics, the interaction between two systems is described by a force acting between them inducing changes in the states of the interacting systems. So, if we are dealing with the interaction of radiation with matter, we are as well asking about the forces involved.

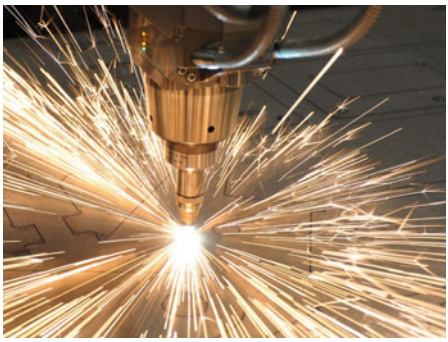

Fig. 1.1 Laser cutting of steel [1]

In physics, we know four fundamental forces, which describe the interaction of particles or systems in the micro and macro cosmos of our world:

1. The strong and the weak nuclear forces,
2. the gravitational force, and
3. the electromagnetic force.

We will now briefly describe these forces, to get an idea about their effect on matter and their need for our topic on laser radiation–matter interaction.

1.1.1 Nuclear Forces

Two forces act on the nuclear size (about 1 fm and less), the strong and the weak nuclear forces. *The strong nuclear force* is responsible for the interaction between the three *quarks* within the neutrons and protons compensating for any repulsive electrostatic forces between the protons [2]. The force acts by an interchange of virtual force carrier particles, called *gluons*. The strong nuclear force is acting only on a very short range of some femtometers and is in this regime much stronger than the electrostatic force (see Fig. 1.2 left).

The weak nuclear force has a much shorter interaction range of $\approx 10^{-2}$ fm and is responsible for the β-decay and for the processes involved in nuclear fission [3]. As virtual force carrier particles *bosons* are exchanged, like a $W^{\pm}$ or Z^0 boson (Fig. 1.2 right).

In principle, an interaction between photons and the particles of the nucleus is possible, as the weak nuclear force handles with bosons, as photons. But, because the probability for an interaction between photons and electrons located in the shell of atoms is very much larger, only at very high photon energies, or laser radiation intensities $I > 10^{20}$ W/cm^2 photon–nucleus interaction becomes probable. In this textbook, these high-energy physics interactions will not be discussed further.

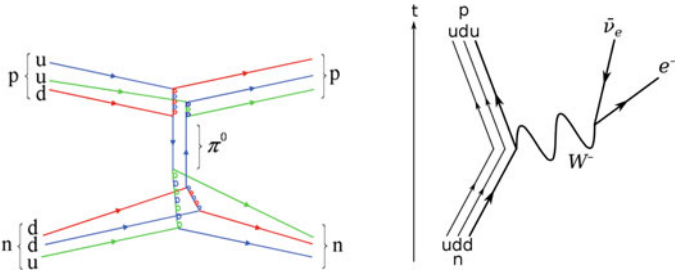

Fig. 1.2 Strong nuclear force acting on a proton and neutron [2] (left), and weak nuclear force acting during the β^- decay [3] (right)

1.1.2 Electromagnetic Force

The Coulomb force

The Coulomb force

$$\boldsymbol{F}(r) = \frac{1}{4\pi \cdot \varepsilon_0} \frac{q_1 \cdot q_2}{r^2} \hat{\boldsymbol{r}} \tag{1.1}$$

represents the fundamental electrostatic force with q_1 and q_2 representing the electric charges being located at $\boldsymbol{r}_1$ and $\boldsymbol{r}_2$, and separated by $\boldsymbol{r} = \boldsymbol{r}_1 - \boldsymbol{r}_2$ using the unity vector $\hat{\boldsymbol{r}} = \boldsymbol{r}/r$. The Lorentz force is a consequence of the Coulomb force using the Maxwell equations of moved charges, applying the theory of special relativity, and getting the force

Generalized Lorentz force

$$\boldsymbol{F}(r) = q\,(\boldsymbol{E} + \boldsymbol{v} \times \boldsymbol{B})\,. \tag{1.2}$$

Here the electric field strength is given by $\boldsymbol{E}$, and the charge of a particle q featuring the velocity $\boldsymbol{v}$ is moving within a magnetic field strength $\boldsymbol{B}$.

The exchange particle for electron–electron interactions is a *virtual photon*: during the interaction, virtual photons are exchanged between the two electrons. The result of the interaction is a scattering of the two electrons, so-called Møller scattering [4], which can be described graphically by the Feynman diagrams; see Fig. 1.3. Virtual photons cannot be detected and only the change of the interacting particles is detectable.

1.1.3 Gravitational Force

Two bodies with the masses m_1 and m_2 interact by the attractive gravitational force, being dependent on the masses and the distance between this bodies. The gravitational force is expressed by the third Newton law

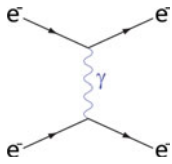

Fig. 1.3 Feynman diagram to the electron–electron scattering with acting electromagnetic force [4]

Gravitational force

$$\boldsymbol{F} = -G\frac{m_1 \cdot m_2}{r^2}\hat{\boldsymbol{r}} \tag{1.3}$$

with the gravitational constant $G = 6.67 \cdot 10^{-11}\frac{m^3}{kg \cdot s^2}$. The separation vector between the masses is given by $\boldsymbol{r} = \boldsymbol{r}_1 - \boldsymbol{r}_2 = r\hat{\boldsymbol{r}}$.

The gravitational force cannot be deduced from the quantum mechanics and is a consequence of the theory of general relativity of Albert Einstein. The exchange particle is the mass-less *graviton*. Its detection has been accomplished in 2017 using very elaborated and extended interferometers.

Taking the ratio between gravitational force and the electromagnetic force emphasizes that in comparison the gravitational force results as a very weak force

$$F_{grav}/F_{em} = \frac{G \cdot m_e \cdot m_\mathrm{p}}{4\pi\varepsilon_0 \cdot e^2} = 4 \cdot 10^{-40}.$$

The electromagnetic force, especially the electrostatic force, resembles all charges in order to get charge neutrality. For most processes in our macroscopic world, the electromagnetic force dictates the most important laws and rules of science, like the quantum mechanics and the following rules in chemistry for the formation of atoms and the periodic table, the chemical reactions with atoms and molecules, and the electrostatic forces between atoms and molecules like the van-der-Waals force striking adhesion, adsorption, and viscosity. Also, phase changes are in combination with newtons laws more significant than the gravitational force. Clearly, the gravitational force is of importance, but for the processes of laser radiation–matter interaction discussed in this textbook, they are ignored.

1.2 Wave and Particle Description of Electromagnetic Radiation

The interaction of radiation with matter is manifold and depends on not only the properties of matter, but also on the radiation property of "wave" or "particle" itself. So, light is easily described by electromagnetic waves, and its propagation direction is described by rays. The effects observed with the wave model allow one to understand reflection, refraction, and diffraction. Therefore, electrodynamics is applied describing the interaction of radiation waves with charged particles. The basic equations on electrodynamics and the interaction of radiation as waves will be treated in the following sections.

At the end of the nineteenth century, discrete absorption and emission lines had been observed in excited gases and atoms by optical spectroscopy, and by the photo-effect the particle nature of the electromagnetic radiation was introduced. Albert Einstein seeded in 1905 the idea of quantized energy portion, the so-called

"Lichtquanten" with discrete energy transitions, and Max Planck as well introduced the quantization of energy of electromagnetic radiation to describe the energy distribution of thermally emitting black bodies.

It should be emphasized that the three processes of excitation by photons on a two-level system are a priori easily described by quantized states. Albert Einstein expressed these processes in 1917 by

- the absorption,
- the spontaneous emission, and
- the stimulated emission.

Even described by the quantum mechanical equations with the Einstein coefficients A_{21} for spontaneous emission, B_{12} for absorption, and B_{21} for the stimulated emission, the spontaneous emission cannot be described by conventional quantum mechanics, even introducing the quantization of the electromagnetic field. For that, a transition to the QED (quantum electrodynamics) has to be fulfilled. This theory started to be developed in 1925 by Max Born, Pascual Jordan, and Werner Heisenberg and was continued by Paul Dirac in 1927. Its final state had been reached in the 1940s.

The interaction with atoms, either being described by the quantum mechanics, is challenging. Aggregation of atoms, so-called condensations, results, e.g. in a liquid or solid state of matter. There the quantum character of the energy states of each individual atom merges into the band structure of the condensed matter. Depending on its properties, like metallic, semiconductor, or dielectric, one can distinguish valence and conduction bands, being populated by electrons. For many purposes, a semiclassical approach is applicable, where the matter is described quantum mechanically and the radiation classically by Maxwell equations. This will be discussed in a later section.

In this textbook, the description of electromagnetic radiation will be varied depending on the questions to be answered. So, some processes need an electrodynamic wave description giving an easier description and also interpretation, and for other processes, the quantum mechanic description using quantized photons will allow a simpler explanation.

1.3 Photon Description

Describing electromagnetic radiation via waves allows to describe many effects in optics. But, some effects, like the photo-effect observed first by Heinrich Hertz in 1886, needed another way to describe electromagnetic radiation. Since antiquity, a particle description was proposed. The corpuscular theory of light, arguably set forward by René Descartes in 1637, states that light is made up of small discrete particles called "corpuscles". Also, Sir Isaac Newton proposed a particle theory of light preparing the modern photon description.

In 1900, Max Planck had to introduce the quantization of the electromagnetic radiation in small energy packets

Photon energy

$$E_\gamma = h\nu = \hbar\omega \tag{1.4}$$

in order to be able to describe the emission spectrum of black bodies.

Albert Einstein explained in 1905 the photo-electric effect introducing "spatially localized" energy quanta. In 1923, Arthur Compton described the inelastic scattering of photons at electrons.

The quantum mechanics built the bridge between the wave and particle description of electromagnetic radiation by the wave–particle duality, first proposed by Louis de Broglie in 1924 for electrons. A full description of photons is possible by QED, developed by Richard P. Feynman, Julian Schwinger, and Shin'ichirō Tomonaga in 1940.

Photons are particles belonging to the bosons; see Sect. 2.5.2. Even not having any mass

$$m_\gamma = 0$$

they feature an momentum

Momentum of a photon

$$\boldsymbol{p} = \hbar\boldsymbol{k}, \tag{1.5}$$

with the wave number vector $\boldsymbol{k}$. Its magnitude is expressed by

$$p = \hbar k = \frac{h\nu}{c_0} = \frac{h}{\lambda}. \tag{1.6}$$

The last equation contains the de Broglie wavelength λ of the photon being equivalent to the wavelength of the electromagnetic wave.

Photons have an integral spin angular momentum S, being independent of the frequency. In propagation direction, one talks about helicity being right-handed for $S = +\hbar$, and left-handed for $S = -\hbar$. It represents the circular polarization states of the electromagnetic radiation in the wave description.

1.4 Maxwell Equations

1.4.1 Maxwell Equations in Vacuum

The Maxwell–Faraday equation is a generalization of Faraday's law stating that a time-varying magnetic field will always accompany a spatially varying, non-

conservative electric field, and vice versa. The Maxwell–Faraday equation is written as

Maxwell–Faraday equation

$$\nabla \times \boldsymbol{E} = -\frac{\partial \boldsymbol{B}}{\partial t} = rot\ \boldsymbol{E}. \tag{1.7}$$

This differential equation of first order combines the curl of the electric field with the time derivative of the magnetic field.

The Gauß law describes the relationship between a static electric field and the electric charges that cause it: The electric flux leaving a volume is proportional to the charge inside the volume:

The Gauß law

$$\nabla \cdot \boldsymbol{E} = \frac{\varrho}{\varepsilon_0} = div\ \boldsymbol{E}. \tag{1.8}$$

Sources and sinks of the electric field are given by charges; here in differential form, the electrical charge density ϱ is written, coupled to the vacuum permittivity ε_0. This equation describes the charge as the source/cause for an electric field in space.

Ampère's circuital law describes the induced magnetic field around a closed loop being proportional to the electric current plus the displacement current (rate of change of electric field) in the loop, and is given by

The Ampère's circuital law

$$\nabla \times \boldsymbol{B} = \mu_0\, \boldsymbol{J} + \frac{1}{c_0^2}\frac{\partial \boldsymbol{E}}{\partial t} = rot\ \boldsymbol{B}. \tag{1.9}$$

Similar to the Maxwell–Faraday equation (1.7), the curl of the magnetic field is represented by the time derivative of the electric field. But, additionally it features also a current density $\boldsymbol{j}$ coupled to the vacuum permeability μ_0.

Here, c_0 represents the velocity of electromagnetic radiation in vacuum, also called the velocity of light in the vacuum, and has the relation

Speed of light in vacuum

$$c_0 = \frac{1}{\sqrt{\varepsilon_0 \cdot \mu_0}}. \tag{1.10}$$

The Maxwell equations combine the two field constants to the vacuum light velocity, as will be shown in Sect. 1.5 deriving the wave equations from the Maxwell equations (Table 1.1).

Table 1.1 Fields, charges, currents, and as well field constants used in the Maxwell equations

Vector fields	Symbol	SI units
Electric field strength	$\boldsymbol{E}$	$\mathrm{V m^{-1}}$
Electric displacement field	$\boldsymbol{D}$	$\mathrm{A\,s\,m^{-2}}$
Magnetic flux density	$\boldsymbol{B}$	$\mathrm{kg(A{\cdot}s^2)^{-1}} = 1\ \mathrm{T}$
Magnetic field strength	$\boldsymbol{H}$	$\mathrm{A\,m^{-1}}$
Charge density	ϱ	$\mathrm{C m^{-1}}$
Current density	$\boldsymbol{J}$	$\mathrm{A m^{-2}}$
Field constants		
Vacuum permittivity	ε_0	$8.8541878128(13) \cdot 10^{-12}\mathrm{A^2 s^4\,kg^{-1}\,m^{-3}}$
Vacuum permeability	μ_0	$1.25663706212(19) \cdot 10^{-6}\mathrm{kg\,m\,(sA)^{-2}}$
Velocity of light in vacuum	c_0	$2.99792458 \cdot 10^8\ \mathrm{m\,s^{-1}}$

The Gauß law for magnetism explains that no magnetic monopoles can exist. The total magnetic flux through a closed surface is zero, and given by

The Gauss law for magnetism

$$\nabla \cdot \boldsymbol{B} = 0 = div\ \boldsymbol{B}. \tag{1.11}$$

1.4.2 Continuity Equation

The continuity equation can be derived from the Maxwell equations by applying the divergence on Ampère's circuital law (1.9)

$$\underbrace{\nabla \cdot (\nabla \times \boldsymbol{B})}_{=0} = \nabla \cdot \left(\mu_0 \boldsymbol{J} + \frac{1}{c_0^2} \frac{\partial \boldsymbol{E}}{\partial t} \right).$$

The left side is per definition zero, and the right-hand side is written to

$$\mu_0\, \nabla \cdot \boldsymbol{J} = -\frac{1}{c_0^2} \frac{\partial (\nabla \cdot \boldsymbol{E})}{\partial t}.$$

With the Gauss law and (1.10), one gets the differential description of the charge conservation law describing the temporal change of the current density ϱ within a volume by a current density $\boldsymbol{J}$ flowing throughout this volume.

Continuity equation—Conservation law for charges

$$\nabla \cdot \boldsymbol{J} = -\frac{\partial \varrho}{\partial t}. \tag{1.12}$$

1.4.3 Integral Description of Maxwell Equations

Applying the Gauss and the Stokes laws for vector fields, the integral descriptions of the Maxwell equations are derived:

electric tension	$U^c = \int_c \boldsymbol{E} \cdot d\boldsymbol{s}$
electric flux	$\psi^a = \int_a \boldsymbol{E} \cdot d\boldsymbol{a}$
magnetic tension	$U_{\mathrm{m}}^c = \int_c \boldsymbol{B} \cdot d\boldsymbol{s}$
magnetic flux	$\Phi^a = \int_a \boldsymbol{B} \cdot d\boldsymbol{a}$
electric charge	$Q^V = \int_V \varphi \, dV$
electric current	$I^a = \int_a \boldsymbol{j} \cdot d\boldsymbol{a}.$

These integral equations are important when quantitative values for all acting physical parameters are needed.

1.5 Electromagnetic Waves

1.5.1 Derivation of Wave Equations

A wave equation results from the Maxwell equations by building the rotation $\nabla\times$ on equation (1.7), getting

$$\nabla \times (\nabla \times \boldsymbol{E}) = -\nabla \times \frac{\partial \boldsymbol{B}}{\partial t}.$$

Consideration of the left equation side

$$\nabla \times (\nabla \times \boldsymbol{E}) = \nabla(\nabla \cdot \boldsymbol{E}) - \nabla \cdot \nabla \boldsymbol{E}.$$

In case of a charge- and current-free space, one calculates

$$\nabla \cdot \boldsymbol{E} = 0$$
$$\nabla \times (\nabla \times \boldsymbol{E}) = -\nabla \cdot \nabla \boldsymbol{E} = -\Delta \boldsymbol{E}$$

with the Laplace operator $\Delta = \frac{\partial^2}{\partial x^2} + \frac{\partial^2}{\partial y^2} + \frac{\partial^2}{\partial z^2}$.

Consideration of the right equation side

$$\begin{aligned} -\nabla \times \frac{\partial \boldsymbol{B}}{\partial t} &= -\frac{\partial}{\partial t} \nabla \times \boldsymbol{B} \\ &= -\frac{\partial}{\partial t} \frac{1}{c^2} \frac{\partial \boldsymbol{E}}{\partial t} \\ &= -\frac{1}{c^2} \frac{\partial \boldsymbol{E}}{\partial t^2}. \end{aligned}$$

Considering both sides, the wave equation results in

Wave equation for the electric field strength

$$\Delta \boldsymbol{E} - \frac{1}{c^2} \frac{\partial^2 \boldsymbol{E}}{\partial t^2} = 0. \tag{1.13}$$

This approach is also applicable for the magnetic field using the rotation on Ampère's circuital law (1.9) in vacuum, getting

Wave equation for the magnetic flux density field

$$\Delta \boldsymbol{B} - \frac{1}{c^2} \frac{\partial^2 \boldsymbol{B}}{\partial t^2} = 0. \tag{1.14}$$

1.5.2 Fundamentals on Waves

Electromagnetic radiation consists of spatial and temporal varying electric and magnetic fields. The propagation of each coupled vector wave is described in vacuum by a homogeneous partial differential equation of second order with constant coefficients; see (1.13) and (1.14).

The wave equation for a general one-dimensional field $U(x, t)$ is given by

$$\frac{\partial^2 U}{\partial x^2} - \frac{1}{c^2}\frac{\partial^2 U}{\partial t^2} = 0. \tag{1.15}$$

The general solution of a wave equation describes the temporal and spatial development of each component of the vector field, here, e.g. the electric and magnetic fields $\boldsymbol{E}$ and $\boldsymbol{B}$. The general solution of a wave equation represents a linear superposition of single wave functions. The Maxwell equations, being linear, result also in a set of linear wave equations.

The differential equation (1.15) is solved by functions coupling the spatial and the temporal variables, like

$$U(x, t) = f(x - c \cdot t),$$

with the velocity c of a disturbance. In fact, this equation is not only applicable for periodic functions, like trigonometric functions, but also for deliberate functions being temporally limited, like pulses or solitons.

Generally, a linear superposition of two deliberately differentiable functions, e.g. trigonometric functions,

$$f(x, t) = \cos(x \cdot k + \omega \cdot t)$$
$$g(x, t) = \sin(x \cdot k - \omega \cdot t)$$

is possible. It results in a linear combination of these functions getting

$$U(t, x) = f(x, t) + g(x, t)$$

being as well a solution of equation (1.15). Also, transferring the trigonometric functions into the complex space results in a complex function

$$\tilde{f} = e^{i(k \cdot x - \omega t)},$$

which also solves the wave equation. Working with complex functions enables easier calculations, but in the end, only the real part of the complex function is of physical interest.

Now expanding the wave equation in the three-dimensional space, one gets

$$\Delta U(\boldsymbol{r},t) - \frac{1}{c^2}\frac{\partial^2 U(\boldsymbol{r},t)}{\partial t^2} = 0$$

and a general solution as a plane wave could be

$$U(\boldsymbol{r},t) = f(\boldsymbol{r}\cdot\boldsymbol{k} - \omega t)$$

with the propagation vector $\boldsymbol{k}$, also called the wave number vector given by

Wave number vector and angular frequency

$$\boldsymbol{k} = \frac{2\pi}{\lambda}\hat{\boldsymbol{k}} \tag{1.16}$$

with the wavelength of the plane wave λ, and the angular frequency

$$\omega = 2\pi\nu = \frac{2\pi}{T} \tag{1.17}$$

using the frequency ν or the period T.

In general, the Fourier development of a field holds

Fourier development of a field

$$U(t,x) = Re\left[\int dk\, U(t,k)e^{i(kx-\omega t)}\right]. \tag{1.18}$$

1.5.3 Orthogonality of the Vector Fields

One approach to prove the orthogonality relations is to assume planar waves for $\boldsymbol{B}$ and $\boldsymbol{E}$:

$$\begin{aligned} \boldsymbol{E} &= \boldsymbol{f}(u) \quad \text{with} \quad u = \boldsymbol{k}\cdot\boldsymbol{r} - \omega\cdot t \\ \boldsymbol{B} &= \boldsymbol{g}(u) \quad \text{and} \quad \boldsymbol{r} = x\boldsymbol{e}_x + y\boldsymbol{e}_y + z\boldsymbol{e}_z. \end{aligned}$$

The vector functions $\boldsymbol{f}$ and $\boldsymbol{g}$ represent multiple differentiable vector functions, with

$$\boldsymbol{k} = \frac{2\pi}{\lambda}\boldsymbol{e}_k \tag{1.19}$$

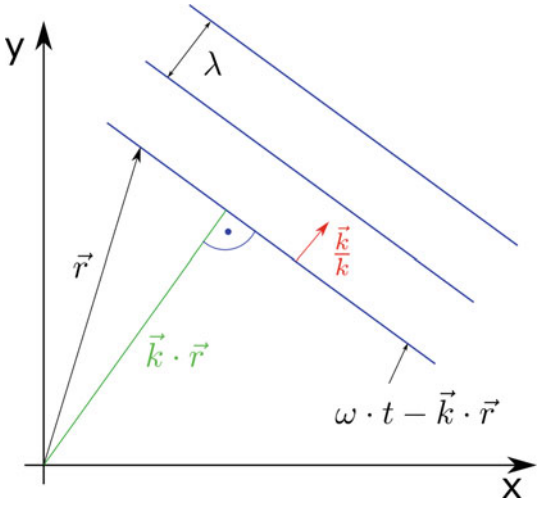

Fig. 1.4 Propagation of a planar wave in space

being the wave number vector describing the propagation direction of the plane wave by its unity vector $\boldsymbol{e}_k = \boldsymbol{k}/k$, and ω represents the angular frequency. u describes the position of the phase front, and the scalar product $\boldsymbol{k} \cdot \boldsymbol{r}$ represents the shortest distance of the planar wave from the coordinate origin at a fixed time t; see Fig. 1.4.

The rotation of the electric and magnetic fields results in

$$\nabla \times \boldsymbol{E} = \boldsymbol{k} \times \frac{\partial \boldsymbol{f}}{\partial u} \propto \boldsymbol{B} \tag{1.20}$$

$$\nabla \times \boldsymbol{B} = \boldsymbol{k} \times \frac{\partial \boldsymbol{g}}{\partial u} \propto \boldsymbol{E} \tag{1.21}$$

expressing the orthogonality of the field vectors $\boldsymbol{E}$ or $\boldsymbol{B}$ to the plane spanned by $\boldsymbol{k}$ with one of the field vectors, $\boldsymbol{B}$ or $\boldsymbol{E}$, resulting in

$$\boldsymbol{E} \perp \boldsymbol{k} \times \boldsymbol{B} \text{ reading to } \boldsymbol{E} \perp \boldsymbol{k} \text{ and } \boldsymbol{E} \perp \boldsymbol{B} \tag{1.22}$$

$$\boldsymbol{B} \perp \boldsymbol{k} \times \boldsymbol{E} \text{ reading to } \boldsymbol{B} \perp \boldsymbol{k} \text{ and } \boldsymbol{B} \perp \boldsymbol{E}. \tag{1.23}$$

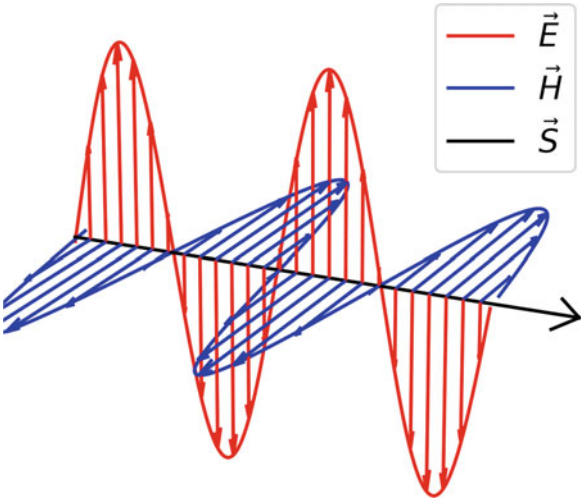

Fig. 1.5 Orthogonal orientation of the $\boldsymbol{E}$ and $\boldsymbol{B}$ fields, being orthogonal also to the propagation direction

Properties of electromagnetic waves in vacuum

$\Longrightarrow$ From the Maxwell equations follows that a temporal dependent electric field induces magnetic fields, and vice versa.

$$B = B(t) \curvearrowright E(t).$$

$\Longrightarrow$ Electromagnetic radiation features E- and B-fields, being to each other orthogonal-oriented, and also being both orthogonal-oriented to the propagation direction $\boldsymbol{k}$ (only in vacuum!); see Fig. 1.5.

$\Longrightarrow$ This wave system is called a transversal wave.

$$(\boldsymbol{E} \perp \boldsymbol{B}) \perp \boldsymbol{k} \qquad \text{only in vacuum.}$$

1.5.4 Scalar and Vector Potential

The Maxwell equations represent a set of *four coupled differential equations of first order*, which have to be solved, to get the electric and magnetic fields. As described in corresponding literature [5, 6], the curl of the electric field spoils for static magnetic fields and can be described by a scalar potential field $\varphi(\boldsymbol{r})$, so that the electric field gets to

$$\boldsymbol{E}(t,\ \boldsymbol{r}) = -\nabla\varphi(t,\ \boldsymbol{r}). \tag{1.24}$$

Also, for the spoiling divergence of the magnetic field, one can determine a vector potential field $\boldsymbol{A}(t,\ \boldsymbol{r})$ that results in

$$\boldsymbol{B}(t,\ \boldsymbol{r}) = \nabla \times \boldsymbol{A}(t,\ \boldsymbol{r}). \tag{1.25}$$

This approach allows to transform the four Maxwell equations into two potential equations, both now being of second order.

In general, the curl of the electric field does not spoil, see (1.7), so that one has to expand the definition of the electric field in order to satisfy this equation. From (1.25), one gets with the Maxwell equation (1.7)

$$\nabla \times \left(\boldsymbol{E} + \frac{\partial}{\partial t} \boldsymbol{A} \right) = 0. \tag{1.26}$$

Using the relation for the electric field equation (1.24), including both potential field, one gets

Electric field strength as function of the potentials

$$\boldsymbol{E}(t,\ \boldsymbol{r}) = -\nabla \varphi(t,\ \boldsymbol{r}) - \frac{\partial}{\partial t} \boldsymbol{A}(t,\ \boldsymbol{r}), \tag{1.27}$$

fulfilling now all Maxwell relations, and results in

$$\nabla \cdot \boldsymbol{E} = \frac{\varrho}{\varepsilon_0} = \nabla \cdot \left(-\nabla \varphi(t,\ \boldsymbol{r}) - \frac{\partial}{\partial t} \boldsymbol{A}(t,\ \boldsymbol{r}) \right).$$

This scalar relation gives rise to the expanded Poisson equation

Poisson equation

$$-\Delta \varphi - \frac{\partial}{\partial t} \nabla \cdot \boldsymbol{A} = \frac{\varrho}{\varepsilon_0}. \tag{1.28}$$

Similarly, one gets from the curl of the magnetic field, see (1.9),

$$\nabla \times \boldsymbol{B} = \nabla \times (\nabla \times \boldsymbol{A}) = \nabla(\nabla \cdot \boldsymbol{A}) - \Delta \boldsymbol{A},$$

and taking the derivative of (1.27) using

$$\frac{\partial \boldsymbol{E}}{\partial t} = -\frac{\partial}{\partial t} \nabla \varphi - \frac{\partial^2}{\partial t^2} \boldsymbol{A},$$

one gets the Maxwell equation, written as

$$\nabla(\nabla \cdot \boldsymbol{A}) - \Delta \boldsymbol{A} = \mu_0 \boldsymbol{J} + \frac{1}{c_0^2}\left(-\frac{\partial}{\partial t}\nabla\varphi - \frac{\partial^2}{\partial t^2}\boldsymbol{A}\right). \tag{1.29}$$

Rewriting this equation, one gets the d'Alembert equation

$$\frac{1}{c_0^2}\frac{\partial^2}{\partial t^2}\boldsymbol{A} - \Delta \boldsymbol{A} = \mu_0 \boldsymbol{J} - \nabla\left(\frac{1}{c_0^2}\frac{\partial}{\partial t}\varphi + \nabla \cdot \boldsymbol{A}\right)$$
$$\Box\, \boldsymbol{A} =$$

where $\Box = \frac{1}{c_0^2}\frac{\partial^2}{\partial t^2} - \Delta$ represents a special operator, the so-called d'Alembert operator, or "Box" operator.

d'Alembert operator

$$\Box = \frac{1}{c_0^2}\frac{\partial^2}{\partial t^2} - \Delta. \tag{1.30}$$

In theoretical electrodynamics [5, 6], it can be shown that the two equations resulting from the Maxwell equations,

$$-\Delta\varphi - \frac{\partial}{\partial t}\nabla \cdot \boldsymbol{A} = \frac{\varrho}{\varepsilon_0}, \text{ and}$$
$$\Box\, \boldsymbol{A} + \nabla\left(\frac{1}{c_0^2}\frac{\partial}{\partial t}\varphi + \nabla \cdot \boldsymbol{A}\right) = \mu_0 \boldsymbol{J}$$

are invariant to gauge transformations. One possible gauge transformation χ, the so-called Lorenz gauge transformation, applies

$$\Box\,\chi = \frac{1}{c_0^2}\frac{\partial}{\partial t}\varphi + \nabla \cdot \boldsymbol{A} = 0,$$

and one gets for the potential fields the relations

Inhomogeneous d'Alembert equations

$$\Box\, \varphi^{(L)} = \frac{\varrho}{\varepsilon_0}, \qquad \Box\, \boldsymbol{A}^{(L)} = \mu_0\, \boldsymbol{J}. \tag{1.31}$$

The *inhomogeneous d'Alembert equations* represent two decoupled differential equations, one for the scalar potential field φ and one for the vector potential field $\boldsymbol{A}$. They are typically solved by Greens functions (see for example Sect. 2.3.2). Solving this equations gets the scalar φ and vector potential $\boldsymbol{A}$, which in turn allows one to calculate the electric and magnetic field strengths; see (1.25) and (1.27).

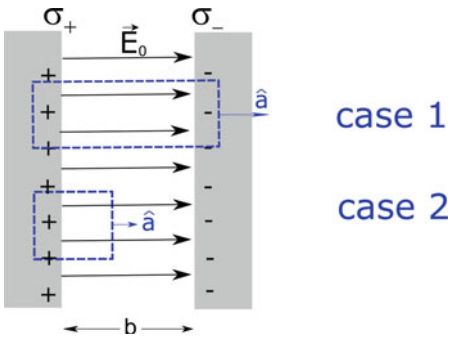

Fig. 1.6 Scheme of a parallel-plate capacitor

1.6 Energy Density of Electromagnetic Wave

In order to determine the energy density of the electromagnetic field, we start firstly looking at the static problem of a capacitor. This approach gives us the first good application of some Maxwell equations without getting too much complexity, like temporal dependencies. As a rule of thumb, a straight generalization from static to dynamic fields is given.

1.6.1 Electrostatic Approach

In principle, we have to get an idea about the energy stored in a capacitor. This can be done by calculating the force needed to separate the two plates when one of them is charged, or thinking about the work necessary to charge it getting the equivalent stored energy.

We apply the first approach and have to calculate the work $W = \boldsymbol{F} \cdot \boldsymbol{s}$. The force is in the static case equal to the Coulomb force, see (1.1), being in the capacitor given by $\boldsymbol{F} = q\,\boldsymbol{E}$. So, we have to think about the charges (positive and negative charges), their locations on the plates, and the electric fields therein. Thereby one charge is placed on the one capacitor plate, e.g. electrons, and by influence, the other plate results with the opposite charging.[1]

Considering the energy density exemplary on a parallel-plate capacitor with a charge q, the plate area a, and a plate distance b, the surface charge σ is defined by

$$\sigma_{\pm} = \frac{\pm q}{a},$$

with q being the overall charge per plate, and a the surface area of the plate (Fig. 1.6). If the volume $V = a \cdot b$ is comprising the left and right plates (see case 1 in Fig. 1.6),

[1] To be correct: during charging the first plate, the second one is grounded. After charging, the second plate is disconnected from ground.

one gets, using the electrical flux and the Gauß theorem,[2]

$$\psi^a = \int_V \nabla \cdot \boldsymbol{E}\, dV = \int_{(V)} \boldsymbol{E} \cdot d\boldsymbol{a}.$$

As no net charges are given between the plates, it holds

$$\nabla \cdot \boldsymbol{E} = \frac{\varrho}{\varepsilon_0} = 0,$$

also because no fields are passing through the the boundaries of the volume V, e.g. through the surfaces of the volume V (no net flux), and the charges on both plates are canceled. So, by applying the electric flux, one gets

$$\int_V \frac{\varrho}{\varepsilon_0}\, dV = \int_{(V)} \frac{\sigma}{\varepsilon_0}\, da = \frac{1}{\varepsilon_0}(\sigma_+ + \sigma_-) \cdot a = 0.$$

For the case 1, this gives us the dependence of the surface charges on both plates

Surface charges on condensator plates

$$\sigma = \sigma_+ = -\sigma_-. \tag{1.32}$$

For the case 2, where only one plate is included in the volume V, see Fig. 1.6, one gets here a non-vanishing electric flux at the surface $\boldsymbol{a}$ of V between the plates

$$\psi^a = \int_{(V)} \boldsymbol{E} \cdot d\boldsymbol{a} = \boldsymbol{E} \cdot \boldsymbol{a} = \frac{\sigma}{\varepsilon_0} a.$$

As the electric field $\boldsymbol{E}$ is parallel oriented to $\boldsymbol{a} = a\hat{\boldsymbol{a}}$, one gets the resulting scalar relation

Electric field strength within a condensator

$$\boldsymbol{E} = \frac{\sigma}{\varepsilon_0}\hat{\boldsymbol{a}} = \frac{q}{a \cdot \varepsilon_0}\hat{\boldsymbol{a}}. \tag{1.33}$$

We have to take a closer look at the charge distribution within the plates itself. A good assumption is that the charges are located close to their surfaces and that they are distributed homogeneously along a skin depth δ; see Fig. 1.7. We consider for the charge density ϱ_0 a constant homogeneous charge density vanishing everywhere except for

[2] For a deliberate vector field $\boldsymbol{F}$ one can write $\int_V \nabla \cdot \boldsymbol{F} dV = \oint_{(V)} \boldsymbol{F} \cdot d\boldsymbol{a}$, with $\boldsymbol{a}$ representing the surface vector of the volume V.

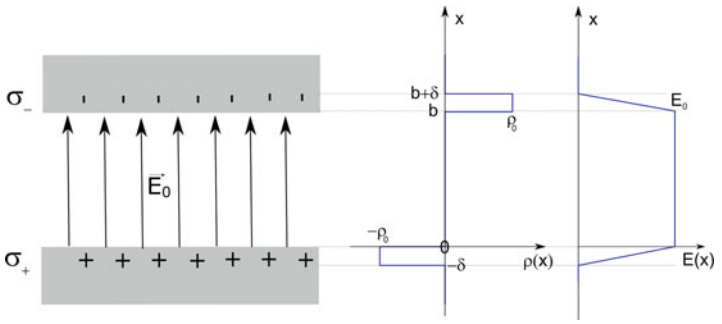

Fig. 1.7 Electric field between the plates (up), charge distribution (middle), and electric field in the plates (bottom)

$$-\delta < x < 0: \quad \varrho_0 = \frac{\sigma}{\delta}$$
$$b < x < b + \delta: \quad -\varrho_0 = -\frac{\sigma}{\delta}.$$

We calculate now the electric field distribution within the plates using the electric field $\boldsymbol{E}(\boldsymbol{r}) = \boldsymbol{E}(x) = E(x)\,\boldsymbol{e}_x$ and the divergence of the electric field; see (1.8). One gets in one dimension for the left plate[3]

$$\nabla \cdot \boldsymbol{E} = \frac{\varrho}{\epsilon_0} \quad \curvearrowright \quad \frac{dE(x)}{dx} = \frac{\varrho}{\epsilon_0}$$
$$\curvearrowright \quad \int \frac{dE}{dx} dx = \int \frac{\varrho(x)}{\epsilon_0} dx.$$

The integral is solved in the defined boundary regime given by (1.33)

$$E = \begin{cases} E_0 = \sigma/\varepsilon_0\,, & \text{for} \quad x = 0 \\ 0 \qquad\qquad\;\; , & \text{for} \quad x = -\delta \end{cases}$$

and leads to a linear dependence of the electric field within the first plate on the x-coordinate, see Fig. 1.7,

$$E(x) = \frac{\varrho_0}{\epsilon_0} x + E_0. \tag{1.34}$$

The acting force can now be rewritten by taking the calculated electric field strength getting

[3] Here we do not consider any edge effects at the boundaries of the plates. The field is within the plates constant.

$$
\begin{aligned}
F(x) = qE(x) &= \int_V \varrho_0 \, dV \; E(x) \\
&= \underbrace{\int_y dy \int_z dz}_{=a} \int_x \varrho_0 \, dx \; E(x) \\
&= a \int_{-\delta}^{0} \varrho_0 \left(\frac{x}{\epsilon_0} \varrho_0 + E_0 \right) dx \\
&= -\frac{a}{2\epsilon_0} \varrho_0^2 \, \delta^2 + \varrho_0 \, a \, \delta \, E_0.
\end{aligned}
$$

Because $\varrho_0 \cdot \delta = \sigma$ holds, the force results in

$$
\begin{aligned}
F &= -\frac{a}{2\epsilon_0} \sigma^2 + a \, \sigma \, E_0 \\
&= -\frac{q}{2\epsilon_0} \sigma + q \, E_0 \\
&= -\frac{q}{2\epsilon_0} \epsilon_0 \, E_0 + q \, E_0 \\
&= \frac{1}{2} \, q \cdot E_0.
\end{aligned}
$$

Acting force between the capacitor plates

The force acting on a charge q is proportional to the charge itself, and the electric field: $\boldsymbol{F} = q\boldsymbol{E}$.
The force F is thereby the electrostatic force on the charge q being induced by the electric field. In the case of the parallel-plate capacitor, the electric field within the parallel plates is homogeneous, and outside zero. From there, one gets the constant force:

$$F = \frac{1}{2} \, q \cdot E_0.$$

Finally, we calculate now the work, and so **the electrostatic energy stored in a capacitor**, by moving the plates from initially a distance b until they get in contact:

$$W = \int \boldsymbol{F} \cdot d\boldsymbol{s} = F \cdot b = \frac{1}{2} \, q \cdot E_0 \cdot b. \tag{1.35}$$

One calculates now for the work, or the potential energy of a capacitor substituting the charge using (1.33)

$$\begin{aligned} W &= \frac{1}{2}\, q \cdot E_0 \cdot b \\ &= \frac{1}{2}\epsilon_0 ab E_0^2 \\ &= \frac{1}{2}\epsilon_0 V E_0^2. \end{aligned}$$

Reintroducing the vector property of the electric field strength, one gets the electric energy density stored in a capacitor

Electric energy density

$$w_e = \frac{W}{V} = \frac{1}{2}\epsilon_0 \boldsymbol{E}_0^2. \tag{1.36}$$

1.6.2 Generalization to Electromagnetic Fields

Without loss of generality, the magnetic energy density derived from the magnetic flux density in a coil reads to

Magnetic energy density

$$w_m = \frac{1}{2\mu_0}\boldsymbol{B}_0^2, \tag{1.37}$$

depicting the equivalent quadratic nature in the field strength [5].

Introducing the electric displacement

The electric displacement field

$$\boldsymbol{D} = \epsilon_0 \boldsymbol{E}, \tag{1.38}$$

one rewrites the electric energy density, (1.36), getting

$$w_\mathrm{e} = \frac{1}{2}\, \boldsymbol{E} \cdot \boldsymbol{D}. \tag{1.39}$$

Analogous, introducing the magnetic field strength

Magnetic field strength

$$\boldsymbol{H} = \frac{1}{\mu_0}\boldsymbol{B}, \tag{1.40}$$

the magnetic energy density, (1.37), results now in

$$w_{\mathrm{m}} = \frac{1}{2}\, \boldsymbol{B} \cdot \boldsymbol{H}. \tag{1.41}$$

With the two new definitions for the electric and magnetic fields, we get the Maxwell equations in absence of matter rewritten to

Maxwell equations in absence of matter

$$\begin{aligned} \nabla \times \boldsymbol{E} &= -\frac{\partial \boldsymbol{B}}{\partial t} \\ \nabla \cdot \boldsymbol{D} &= \varrho \\ \nabla \times \boldsymbol{H} &= \boldsymbol{J} + \frac{\partial \boldsymbol{D}}{\partial t} \\ \nabla \cdot \boldsymbol{B} &= 0. \end{aligned}$$

Let us have a look at the scalar product of the electric field strength and electric displacement field vectors $\boldsymbol{E} \cdot \boldsymbol{D}$. Taking its derivative in time results in

$$\frac{\partial}{\partial t}(\boldsymbol{E} \cdot \boldsymbol{D}) = \frac{\partial \boldsymbol{E}}{\partial t}\boldsymbol{D} + \frac{\partial \boldsymbol{D}}{\partial t}\boldsymbol{E}. \tag{1.42}$$

The second addend can be changed in

$$\begin{aligned} \boldsymbol{E} \cdot \frac{\partial \boldsymbol{D}}{\partial t} &= \boldsymbol{E}\epsilon_0 \frac{\partial \boldsymbol{E}}{\partial t} \\ &= \boldsymbol{D}\frac{\partial \boldsymbol{E}}{\partial t}, \end{aligned}$$

so that one can rewrite (1.42) to

$$\frac{\partial}{\partial t}(\boldsymbol{E} \cdot \boldsymbol{D}) = 2\boldsymbol{E} \cdot \frac{\partial \boldsymbol{D}}{\partial t} \tag{1.43}$$

$$= 2\frac{\partial w_{\mathrm{e}}}{\partial t}. \tag{1.44}$$

In the same way, one gets for the magnetic contribution

$$\frac{\partial}{\partial t}(\boldsymbol{B} \cdot \boldsymbol{H}) = 2\boldsymbol{B} \cdot \frac{\partial \boldsymbol{H}}{\partial t} = 2\frac{\partial w_{\mathrm{m}}}{\partial t}.$$

Now, starting from (1.9), using the definitions (1.38) and (1.40):

$$\nabla \times \boldsymbol{H} = \boldsymbol{\jmath} + \frac{\partial \boldsymbol{D}}{\partial t} \qquad |\boldsymbol{E}\cdot$$

$$\curvearrowright \qquad \boldsymbol{E}\cdot(\nabla \times \boldsymbol{H}) = \boldsymbol{E}\cdot\boldsymbol{\jmath} + \boldsymbol{E}\cdot\frac{\partial \boldsymbol{D}}{\partial t}.$$

And, because the Ohms resistance in vacuum is spoiling due to missing charges and currents, $\boldsymbol{E}\cdot\boldsymbol{\jmath} = 0$, one gets using the relation (1.43)

$$\boldsymbol{E}\cdot(\nabla \times \boldsymbol{H}) = \frac{1}{2}\frac{\partial}{\partial t}(\boldsymbol{E}\cdot\boldsymbol{D}) \tag{1.45}$$

$$= \boldsymbol{E}\cdot\frac{\partial \boldsymbol{D}}{\partial t} = \frac{\partial w_\mathrm{e}}{\partial t}. \tag{1.46}$$

Analogous therefore we get, starting from (1.7) and extending it by the scalar product of the magnetic field strength $\boldsymbol{H}\cdot$,

$$\nabla \times \boldsymbol{E} = -\frac{\partial \boldsymbol{B}}{\partial t} \qquad |\boldsymbol{H}\cdot$$

$$\curvearrowright \qquad \boldsymbol{H}\cdot(\nabla \times \boldsymbol{E}) = -\boldsymbol{H}\cdot\frac{\partial \boldsymbol{B}}{\partial t} \tag{1.47}$$

$$= -\frac{1}{2}\frac{\partial}{\partial t}(\boldsymbol{B}\cdot\boldsymbol{H}) \tag{1.48}$$

$$= -\frac{\partial w_\mathrm{m}}{\partial t}. \tag{1.49}$$

Thereby, one gets the energy density for the electromagnetic fields of a capacitor and a coil, and allowing a temporal dependence of both fields, for the electromagnetic radiation too, one can define the electromagnetic energy density by

The energy density of the electromagnetic field

$$w_\mathrm{em} = w_\mathrm{e} + w_\mathrm{m}. \tag{1.50}$$

As (1.46) and (1.49) describe the change in energy densities, one can deduce, assuming energy conservation, an equation of continuity by calculating first the time derivative of the electromagnetic energy density

$$\frac{\partial w_\mathrm{em}}{\partial t} = \frac{\partial}{\partial t}(w_\mathrm{e} + w_\mathrm{m}) \tag{1.51}$$

$$= \boldsymbol{E}\cdot\nabla \times \boldsymbol{H} - \boldsymbol{H}\cdot\nabla \times \boldsymbol{E}. \tag{1.52}$$

To fulfill the conservation law, the divergence of a vector field is needed describing a energy flux density. It can easily be shown by applying on the ansatz

$$-\nabla \cdot (\boldsymbol{E} \times \boldsymbol{H})$$

the product law for differentiation,[4] and multiple permuting the triple product (each permutation gets one "-"), so that the nabla operator acts only on one vector field each, that is equal to (1.52):

$$\begin{aligned} -\nabla \cdot (\boldsymbol{E} \times \boldsymbol{H}) &= -\nabla \cdot (\dot{\boldsymbol{E}} \times \boldsymbol{H}) - \nabla \cdot (\boldsymbol{E} \times \dot{\boldsymbol{H}}) \\ &= +\nabla \cdot (\boldsymbol{H} \times \dot{\boldsymbol{E}}) + \boldsymbol{E} \cdot (\nabla \times \dot{\boldsymbol{H}}) \\ &= -\boldsymbol{H} \cdot (\nabla \times \dot{\boldsymbol{E}}) + \boldsymbol{E} \cdot (\nabla \times \dot{\boldsymbol{H}}) \\ &= \frac{\partial w_\mathrm{m}}{\partial t} + \frac{\partial w_\mathrm{e}}{\partial t} = \frac{\partial w_\mathrm{em}}{\partial t}. \end{aligned}$$

Rewriting the right-hand side of equation (1.52), one can set up the continuity equation for electromagnetic fields

Continuity equation for electromagnetic fields

$$\frac{\partial w_\mathrm{em}}{\partial t} = -\nabla \cdot (\boldsymbol{E} \times \boldsymbol{H}). \tag{1.53}$$

Introducing a new vector representing the energy flux, the so-called the **Poynting vector**

Poynting vector

$$\boldsymbol{S} = \boldsymbol{E} \times \boldsymbol{H}, \tag{1.54}$$

one gets the Poynting theorem in differential form by

$$\begin{aligned} &\frac{\partial w_\mathrm{em}}{\partial t} + \nabla \cdot (\boldsymbol{E} \times \boldsymbol{H}) = 0 \\ \curvearrowright \quad &\frac{\partial w_\mathrm{em}}{\partial t} + \nabla \cdot \boldsymbol{S} = 0. \end{aligned}$$

Poynting's theorem

Poynting's theorem describes the transport of electromagnetic energy. It describes the energy balance in electrodynamics and reproduces the continuity equation of the energy density w_em and energy flow

$$\frac{\partial w_\mathrm{em}}{\partial t} + \nabla \cdot \boldsymbol{S} = 0. \tag{1.55}$$

[4] In the following emphasized by a dot over the vectors.

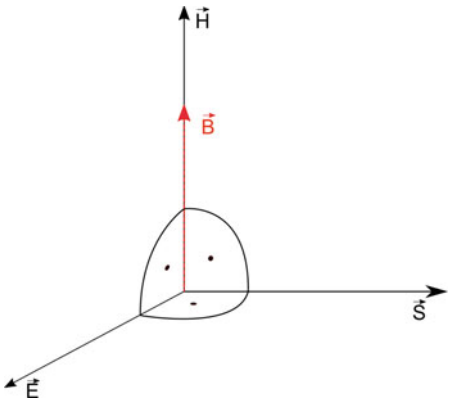

Fig. 1.8 Scheme of the orientation of the electric, magnetic, and Poynting vectors

Obviously, the Poynting theorem is an analogous description of (1.12), describing the density change in a volume by the in-flowing energy flux density, being constant.

The Poynting vector represents the energy flux of the electromagnetic field given in the unity $[|\boldsymbol{S}|] = \mathrm{Wm}^{-2}$. The propagation direction of electromagnetic radiation $\hat{k}$ is identical to the energy flux, being orthogonal to $\boldsymbol{E}$ and $\boldsymbol{H}$ (Fig. 1.8).

In integral form, the Poynting theorem describes the change of energy in time $\dot{W}_{\mathrm{em}}$ in a volume V expressed by the energy flux of the Poynting vector through its surface

$$\int_V \nabla \cdot \boldsymbol{S}\, dV = \int_{(V)} \boldsymbol{S} \cdot d\boldsymbol{a} = \int_V \frac{\partial w_{\mathrm{em}}}{\partial t}\, dV = \dot{W}_{\mathrm{em}}. \tag{1.56}$$

1.6.3 Planar Electromagnetic Waves

Now, we set together all parts describing the vector fields, the energy density, and the energy flux, for a special but very important field function: the planar wave. In fact, many descriptions of processes at boundaries are given using plane waves.

We will get some general expressions and interpretations, being relevant for the later discussed interaction of electromagnetic radiation with matter. Let's assume a planar electromagnetic wave propagating in vacuum described by

$$\boldsymbol{E}(t, \boldsymbol{x}) = \boldsymbol{E}_0\, e^{-i(\omega \cdot t - \boldsymbol{k} \cdot \boldsymbol{r})} \tag{1.57}$$

$$\boldsymbol{B}(t, \boldsymbol{x}) = \boldsymbol{B}_0\, e^{-i(\omega' \cdot t - \boldsymbol{k}' \cdot \boldsymbol{r})}. \tag{1.58}$$

We allow at the moment that the propagation vectors $\boldsymbol{k}$ and $\boldsymbol{k}'$ as well as the angular frequencies ω and ω' are deliberate. $\boldsymbol{E}_0$ and $\boldsymbol{B}_0$ are constant and complex amplitude vectors ($\boldsymbol{E}_0$, $\boldsymbol{B}_0 \in \mathbb{C}$). Just to motivate the complex approach: the mathematics gets easier, as we will see. But hold in mind: physics works only with real values of all physical variables!

In vacuum, the Maxwell equations (1.7)–(1.11) are simplified, because no charges are given and $\varrho = 0$ and $\boldsymbol{J} = 0$ hold, and are written

$$\nabla \cdot \boldsymbol{E} = 0 \tag{1.59}$$

$$\nabla \times \boldsymbol{E} = -\frac{\partial \boldsymbol{B}}{\partial t} \tag{1.60}$$

$$\nabla \cdot \boldsymbol{B} = 0 \tag{1.61}$$

$$\nabla \times \boldsymbol{B} = \frac{1}{c_0^2}\frac{\partial \boldsymbol{E}}{\partial t}. \tag{1.62}$$

Applying the planar electric field on (1.60), one gets

$$\nabla \times \boldsymbol{E} = i\boldsymbol{k} \times \boldsymbol{E} = -\frac{\partial \boldsymbol{B}}{\partial t} = +i\omega' \boldsymbol{B}. \tag{1.63}$$

So, for planar waves, we get the relation

$$\boldsymbol{k} \times \boldsymbol{E} = \omega' \boldsymbol{B}.$$

One sees, looking at the written out relation

$$\boldsymbol{k} \times \boldsymbol{E}_0 \, e^{-i(\omega \cdot t - \boldsymbol{k} \cdot \boldsymbol{r})} = \omega' \, \boldsymbol{B}_0 \, e^{-i(\omega' \cdot t - \boldsymbol{k}' \cdot \boldsymbol{r})}$$

that in order this relation holds, the equalities $\omega = \omega'$ and $\boldsymbol{k} = \boldsymbol{k}'$ have to be fulfilled, explaining that the propagation vectors as well as the angular frequencies are equal. This also gives rise to a description of the coefficient

$$\boldsymbol{B}_0 = \frac{\boldsymbol{k}}{\omega} \times \boldsymbol{E}_0. \tag{1.64}$$

In the same way, we can apply the vector field to the other Maxwell equations getting the relations

$$\begin{aligned} \boldsymbol{k} \cdot \boldsymbol{E}_0 &= 0, && (1.59), \\ \boldsymbol{k} \times \boldsymbol{B}_0 &= -\frac{\omega}{c_0^2}\boldsymbol{E}_0, && (1.62), \text{ and} \\ \boldsymbol{k} \cdot \boldsymbol{B}_0 &= 0, && (1.61). \end{aligned}$$

Planar waves

Planar electromagnetic waves give rise to very simple relations between the constants of each equation:

$$\boldsymbol{B}_0 = \frac{\boldsymbol{k}}{\omega} \times \boldsymbol{E}_0 \tag{1.65}$$

$$\boldsymbol{k} \cdot \boldsymbol{E}_0 = 0 \tag{1.66}$$

$$\boldsymbol{k} \times \boldsymbol{B}_0 = -\frac{\omega}{c_0^2} \boldsymbol{E}_0 \tag{1.67}$$

$$\boldsymbol{k} \cdot \boldsymbol{B}_0 = 0. \tag{1.68}$$

Also, substituting $\boldsymbol{B}_0$ in (1.67), one gets

$$\boldsymbol{k} \times \boldsymbol{B}_0 = \boldsymbol{k} \times \left(\frac{\boldsymbol{k}}{\omega} \times \boldsymbol{E}_0 \right) = -\frac{\omega}{c_0^2} \boldsymbol{E}_0. \tag{1.69}$$

The double vector product gives $\boldsymbol{k}(\boldsymbol{k} \cdot \boldsymbol{E}_0) - \boldsymbol{E}_0 (\boldsymbol{k} \cdot \boldsymbol{k})$. Due to (1.66), the relation simplifies to

$$k^2 \boldsymbol{E}_0 = -\frac{\omega}{c_0^2} \boldsymbol{E}_0. \tag{1.70}$$

The dispersion relation of electromagnetic radiation in vacuum is given $k^2 \cdot c_0^2 = \omega^2$, and taking only the positive square root, one gets

Dispersion relation of radiation

$$\omega(k) = k \cdot c_0. \tag{1.71}$$

Taking as one given field

$$\boldsymbol{E}_0 = E_0 \, \boldsymbol{e}_x, \tag{1.72}$$

the magnetic field as well as the propagation vector are due to the orthogonality relations given by

$$\boldsymbol{B}_0 = B_0 \, \boldsymbol{e}_y, \text{ and} \tag{1.73}$$

$$\boldsymbol{k} = k \, \boldsymbol{e}_z. \tag{1.74}$$

Together with the dispersion relation, (1.71), one gets

$$\boldsymbol{B}_0 = \frac{1}{c_0} E_0 \, \boldsymbol{e}_y. \tag{1.75}$$

Now, getting back to the physical world, one has to determine the real parts of the actually complex electric and magnetic fields. This is achieved by

$$\boldsymbol{E}_R = \frac{1}{2}\,(\boldsymbol{E} + \boldsymbol{E}^*) = E_0\,\cos(\omega \cdot t - \boldsymbol{k} \cdot \boldsymbol{x})\,\boldsymbol{e}_x, \tag{1.76}$$

$$\boldsymbol{B}_R = \frac{1}{2}\,(\boldsymbol{B} + \boldsymbol{B}^*) = \frac{1}{\omega}\,\boldsymbol{k} \times \boldsymbol{E}_R = \frac{1}{c_0}\,\boldsymbol{e}_z \times \boldsymbol{E}_R \tag{1.77}$$

$$= \frac{1}{c_0}\,E_0\,\cos(\omega \cdot t - \boldsymbol{k} \cdot \boldsymbol{r})\,\boldsymbol{e}_y, \quad \text{due to } \boldsymbol{e}_z \times \boldsymbol{e}_x = \boldsymbol{e}_y. \tag{1.78}$$

The energy densities of the electric field can be calculated

$$w_e = \frac{1}{2}\,\boldsymbol{D}_R \cdot \boldsymbol{E}_R = \frac{\varepsilon_0}{2}\,\boldsymbol{E}_R \cdot \boldsymbol{E}_R \tag{1.79}$$

$$= \frac{\varepsilon_0}{2}\,(\frac{1}{2}\,(\boldsymbol{E} + \boldsymbol{E}^*) \cdot \frac{1}{2}\,(\boldsymbol{E} + \boldsymbol{E}^*)) \tag{1.80}$$

$$= \frac{\varepsilon_0}{8}\,(\boldsymbol{E}^2 + \boldsymbol{E}^{*2} + 2\,\boldsymbol{E} \cdot \boldsymbol{E}^*). \tag{1.81}$$

The energy densities of the magnetic field can be calculated

$$w_m = \frac{1}{2}\,\boldsymbol{H}_R \cdot \boldsymbol{B}_R = \frac{1}{2\mu_0}\,\boldsymbol{B}_R \cdot \boldsymbol{B}_R \tag{1.82}$$

$$= \frac{1}{2\mu_0}\frac{1}{\omega^2}(\boldsymbol{k} \times \boldsymbol{E}_R) \cdot (\boldsymbol{k} \times \boldsymbol{E}_R). \tag{1.83}$$

Using the dispersion relation $\omega = kc_0$ and the relation $\boldsymbol{a} \cdot (\boldsymbol{b} \times \boldsymbol{c}) = \boldsymbol{b} \cdot (\boldsymbol{c} \times \boldsymbol{a})$, one gets

$$w_m = \frac{1}{2\mu_0}\frac{1}{k^2 c_0^2}\,\boldsymbol{k} \cdot (\boldsymbol{E}_R \times (\boldsymbol{k} \times \boldsymbol{E}_R)) \tag{1.84}$$

$$= \frac{1}{2\mu_0}\frac{1}{k^2 c_0^2}\,\boldsymbol{k} \cdot (\boldsymbol{k} E_R^2) \tag{1.85}$$

$$= \frac{1}{2\mu_0}\frac{1}{c_0^2}\,E_R^2, \quad \text{with (1.10) one gets} \tag{1.86}$$

$$= \frac{\varepsilon_0}{2}\,\boldsymbol{E}_R \cdot \boldsymbol{E}_R \tag{1.87}$$

$$w_m = w_e. \tag{1.88}$$

Finally, the electromagnetic energy density results to

$$w_{\text{em}} = w_e + w_m \tag{1.89}$$

$$= \varepsilon_0\,\boldsymbol{E}_R \cdot \boldsymbol{E}_R. \tag{1.90}$$

The temporal evolution of the density is given by

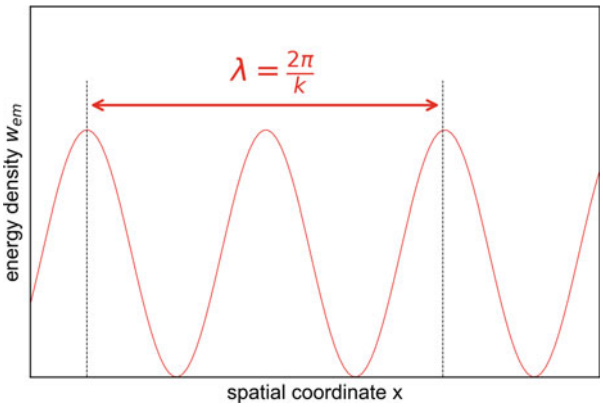

Fig. 1.9 Energy density as function of space

$$\begin{aligned} w_{\text{em}} &= \frac{\varepsilon_0}{4} \left(\boldsymbol{E}^2 + \boldsymbol{E}^{*2} + 2\, \boldsymbol{E} \cdot \boldsymbol{E}^* \right) \\ &= \frac{\varepsilon_0}{2} \left(\Re(\boldsymbol{E}^2) + |\boldsymbol{E}|^2 \right) \\ &= \frac{\varepsilon_0}{2}\, E_0^2 (\cos(2(\omega \cdot t - \boldsymbol{k} \cdot \boldsymbol{r})) + 1) \\ &= \varepsilon_0\, E_0^2\, \cos^2(\omega \cdot t - \boldsymbol{k} \cdot \boldsymbol{r}). \end{aligned}$$

One result is that the energy density of the electromagnetic radiation oscillates double the angular frequency of the electric field with half the wavelength; see Fig. 1.9. The Poynting vector is given by

$$\begin{aligned} \boldsymbol{S} &= \frac{1}{\mu_0}\, \boldsymbol{E} \times \boldsymbol{B} \\ &= \frac{1}{\mu_0 \omega}\, \boldsymbol{E} \times (\boldsymbol{k} \times \boldsymbol{E}) \\ &= \frac{\boldsymbol{E}^2}{\mu_0 \cdot c_0 \cdot k}\, \boldsymbol{k} \\ &= c_0\, \varepsilon_0\, \boldsymbol{E}^2\, \hat{\boldsymbol{k}}. \end{aligned} \tag{1.91}$$

In summary, the Poynting vector represents the energy density propagating in $\hat{\boldsymbol{k}}$-direction

Poynting vector

$$\boldsymbol{S} = c_0\, w_{\text{em}}\, \hat{\boldsymbol{k}}. \tag{1.92}$$

Also, the energy density of the Poynting vector of electromagnetic radiation oscillates double the angular frequency of the electric field with very large angular frequency $\omega \approx 10^{14}$ Hz. This very fast energy(density) fluctuation can not be detected by any electronic system, so to calculate the temporal average of the Poynting vector is favorable.

The temporal average of a function $f(t)$ is calculated by

$$\langle f(t) \rangle = \frac{1}{T} \int_t^{t+T} f(t)\, dt, \tag{1.93}$$

and one calculates the temporal averaged Poynting vector as

$$\begin{aligned} \langle \boldsymbol{S} \rangle &= c_0 \ \langle w_{\text{em}} \rangle \ \hat{\boldsymbol{k}} \\ &= c_0 \, \varepsilon_0 \, \boldsymbol{E}_0^2 \left\langle \cos^2(\omega \cdot t - \boldsymbol{k} \cdot \boldsymbol{r}) \right\rangle \hat{\boldsymbol{k}} \\ &= \frac{1}{2} c_0 \, \varepsilon_0 \, \boldsymbol{E}_0^2 \, \hat{\boldsymbol{k}}. \end{aligned}$$

The magnitude of the Poynting vector gives the definition of the *intensity* of the electromagnetic radiation, i.e. the averaged power per area

Intensity of electromagnetic radiation in vacuum

$$I = \langle |\boldsymbol{S}| \rangle = \frac{1}{2} \, c_0 \, \varepsilon_0 \, |\boldsymbol{E}_0|^2. \tag{1.94}$$

1.6.4 Phase and Group Velocity

As we have seen, the speed of light is given by the solution of the wave equation from the Maxwell equations, and being in vacuum resulting in the inverse square root of the permeability and the permittivity; see (1.10). Also, we have retrieved from solving the wave equation for planar electromagnetic waves that we get a simple relation, a dispersion relation between the speed of light, the wave number, and angular frequency $c_0 = \omega / k$ see (1.71). This velocity is attributed to the velocity of the phase, the so-called phase velocity of an electromagnetic wave v_{p}.

Phase velocity

$$v_{\text{p}} = c_0 = \frac{\omega}{k}. \tag{1.95}$$

Now, in practice, electromagnetic radiation is emitted temporally from any source only for a limited time. So the radiation emitted by spontaneous emission lasts about 1 ns. Typical sources in nature emit similar duration packages of radiation, so-called

pulses. In laser technology, one finds pulsed laser radiation with a pulse duration ranging from the attosecond (as) and femtosecond (fs) to the nearly-cw regime.[5]

Assuming now pulsed electromagnetic radiation, maybe just one pulse proceeding in the x-direction, so we can describe its electric field strength by

$$\boldsymbol{E}(x,t) = \boldsymbol{E}_0 \int_{-\infty}^{\infty} dk A(k) e^{i(k\cdot x - \omega\cdot t)}, \tag{1.96}$$

with $A(\boldsymbol{k})$ being the Fourier transform of the involved wave numbers (i.e. wavelengths) defining the pulse shape.[6]

Now we will further restrict our model, by assuming a nearly monochromatic radiation, e.g. pulsed laser radiation in the nanosecond-regime. In this case, we can describe the angular frequency as a Taylor series around a central angular frequency $\omega_0 = \omega(k_0)$

$$\omega(k) = \omega(k_0) + \left.\frac{\partial\omega}{\partial k}\right|_{k=k_0} (k-k_0) + \frac{1}{2}\left.\frac{\partial^2\omega}{\partial k^2}\right|_{k=k_0} (k-k_0)^2 + \ldots$$

Being the radiation nearly monochromatic, meaning $k - k_0 \ll 1$, allows us to omit the higher orders of the Taylor series:

$$\omega(k) = \omega(k_0) + \left.\frac{\partial\omega}{\partial k}\right|_{k=k_0} (k-k_0).$$

Substituting now $\omega(k)$ in (1.96), we get

$$\boldsymbol{E}(x,t) = \boldsymbol{E}_0 \int_{-\infty}^{\infty} dk A(k) e^{i(k\cdot x - (\omega(k_0) + \left.\frac{\partial\omega}{\partial k}\right|_{k=k_0}(k-k_0))\cdot t)},$$

and expanding the exponential function by $+k_0 \cdot x - k_0 \cdot x$, we get

$$\boldsymbol{E}(x,t) = \boldsymbol{E}_0 e^{i(k_0\cdot x - \omega(k_0)\cdot t)} \int_{-\infty}^{\infty} dk A(k) e^{i(k-k_0)(x - \left.\frac{\partial\omega}{\partial k}\right|_{k=k_0} t)}.$$

The first exponential function represents the plane wave of a fully monochromatic radiation, and the integral represents the amplitude, or so-called envelope of the pulse, moving as a wave in space and time by the relation $x - \left.\frac{\partial\omega}{\partial k}\right|_{k=k_0} t$. We read from there that the velocity of the envelope, the so-called group velocity, is given by

[5] Nearly-cw radiation is given for a very long emission preserving the coherence length. Clearly, every source can be (in theory) turned on and never stopped. But, the emission thereby is not continuous.

[6] Remember that in order to generate any periodic function, not being a harmonic function, needs the linear superposition of the fundamental with the higher harmonics.

Group velocity

$$v_g = \left.\frac{\partial \omega}{\partial k}\right|_{k=k_0}. \tag{1.97}$$

We will see in the later sections that the phase velocity v_p can be larger than the vacuum speed of light, but the group velocity v_g never gets larger than the vacuum speed of light (see Sect. 10.2.1).

1.7 Laser Radiation

Laser radiation is electromagnetic radiation with special properties. In the following, the interaction of laser radiation with matter in conjunction with the special properties is discussed.

1.7.1 Spatial and Temporal Properties

Here, we will talk about the importance of the spatial intensity distribution of the laser radiation for the interaction process. Very often the spatial intensity distribution of laser radiation is of Gaussian shape and so-called a TEM_{00} mode. So, what is important when we talk about a Gaussian intensity profile in the context of interaction of laser radiation with matter? The Gaussian spatial intensity distribution gets predominant in the laser processing, when the process features a threshold behavior. For example, the melting of a metal irradiated with laser radiation starts depending on many laser parameters, like pulse duration, wavelength, and repetition rate, at a specific intensity. Having a spatial Gaussian intensity distribution will, in consequence of the interaction, shape the ablation region, distinguishing regions of the radiation at intensities above some threshold, and resulting in, e.g. melting or evaporation, and in the other regions below this threshold.

In the consequence of radiation with TEM_{00} mode (Gaussian shape), the threshold nature will result in ablation features with diameters being proportional to the intensity of the radiation. Now, the irradiation is temporally limited, and especially using ultra-fast laser radiation, where often the temporal dependence of the pulse is also Gaussian with the pulse duration t_p, the beam radius w_0, and the pulse energy E_p, resulting in a spatial and temporal Gaussian intensity distribution

Intensity of Gaussian pulsed laser radiation

$$I(\boldsymbol{r}, t) = I_0 \exp\left(-\frac{2r^2}{w_0^2}\right) \exp\left(-4 \ln 2 \frac{t^2}{t_\mathrm{p}^2}\right), \tag{1.98}$$

with the peak intensity

$$I_0 = \frac{2E_\mathrm{p}}{1.064 \pi t_\mathrm{p} w_0^2}. \tag{1.99}$$

Integration over the irradiated area results in the power distribution of the laser pulse, being again Gaussian in time

Power distribution for Gaussian pulsed laser radiation

$$P(t) = \int_A I(\boldsymbol{r}, t) dA = P_0 \exp\left(-4 \ln 2 \frac{t^2}{t_\mathrm{p}^2}\right), \tag{1.100}$$

with the peak power

$$P_0 = \frac{E_\mathrm{p}}{1.064\, t_\mathrm{p}}. \tag{1.101}$$

Contrary, integrating the intensity of the Gaussian laser radiation over the time results in the fluence

Fluence of Gaussian pulsed laser radiation

$$H(\boldsymbol{r}) = \int_{-\infty}^{\infty} I(\boldsymbol{r}, t) dt = H_0 \exp\left(-\frac{2r^2}{w_0^2}\right), \tag{1.102}$$

with the peak fluence

$$H_0 = \frac{2E_\mathrm{p}}{\pi w_0^2}. \tag{1.103}$$

Knowing the spatial intensity distribution of the radiation allows on the other hand to assign a specific fluence to a radial coordinate r; see an application in Sect. 16.3.2.

Another consequence of using laser radiation with a spatially Gaussian intensity profile is the possibility to use the ablation threshold H_thr of a material to determine the beam radius w_0. Therefore, the ablation process must be linear, meaning that linear absorption takes place, and no non-linear processes are involved. In this case, the dependence of the ablated diameter D of the structure scales with the peak fluence H_0 given by

$$D^2 = 2w_0^2 \ln \frac{H}{H_\mathrm{thr}}. \tag{1.104}$$

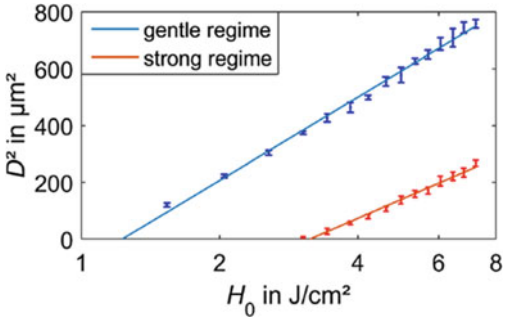

Fig. 1.10 Squared diameter of the structures generated by single-pulsed pump radiation depending on the fluence of the pump radiation for gentle and strong ablation [7]

Plotting the squared diameters as function of the natural logarithm of the fluence results in straight distributions allowing by approximation to determine the threshold fluence H_{thr} and the beam radius w_0, the so-called Liu plot (Fig. 1.10) [8].

Exemplary for a thin gold film irradiated with one ultra-fast laser pulse, two ablation thresholds are detectable due to different involved processes, like spallation and phase explosion, and are visible after irradiation by two distinct diameters; see Fig. 1.11.

1.7.2 Coherence

Coherence is important for many interference processes using laser radiation, like holography and interferometry, but what about the temporal coherence and what about the spatial coherence using laser radiation interacting with the matter with phase transition?

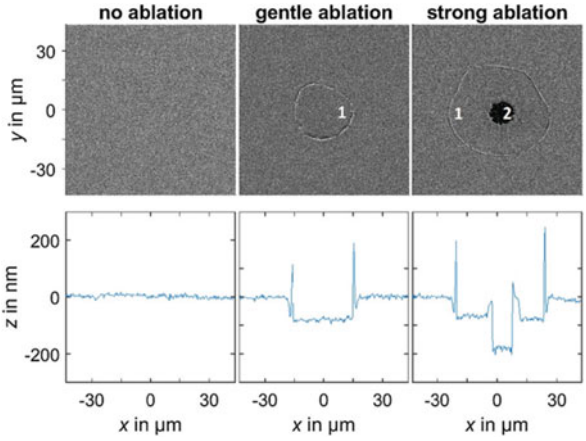

Fig. 1.11 Top: structures generated by single-pulsed irradiation detected by SEM (left: $H_0 < H_{\text{thr,gentle}}$, middle: $H_{\text{thr,gentle}} < H_0 < H_{\text{thr,strong}}$, right: $H_0 > H_{\text{thr,strong}}$); bottom: cross-section of the generated structures detected by confocal microscopy [7]

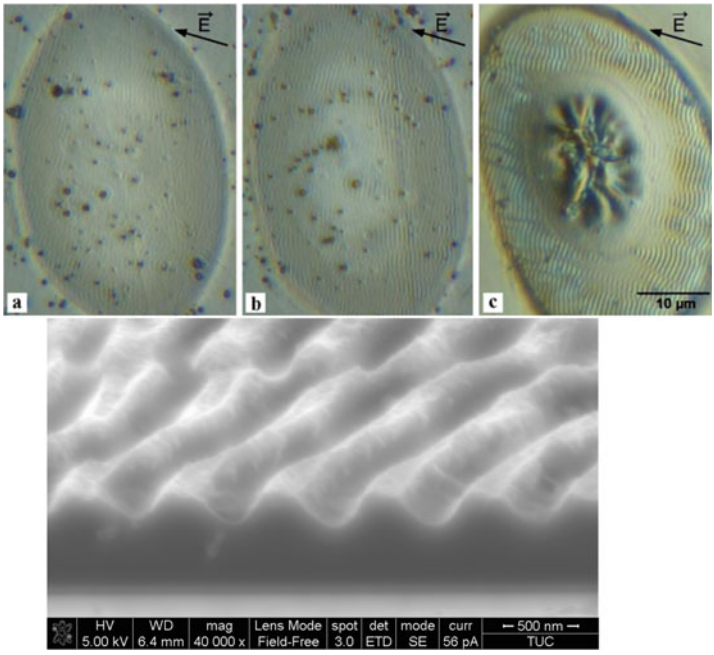

Fig. 1.12 (Top) Ripple structures on a ta-C coated steel sample using ultra-fast laser radiation with different pulse numbers **a** 1 pulse, **b** 2 pulses, and **c** 10 pulses. (Bottom) SEM image of cross-section of ripples on ta-C (peak fluence $H_0 = 3.56$ J/cm^2) [10]

The coherence of radiation can be used to excite matter very specifically. When we talk here about coherence, we need to distinguish between *spatial and temporal coherence*, first. As shown in [9], the temporal coherence results from the spatial homogeneous excitation of the laser medium resulting in photons featuring at one specific place in the axial direction of the radiation beam phase locking along its spatial intensity distribution.

This means that as we are talking about the interaction of radiation with matter, the photons reaching the surface of matter will interact with matter inducing a reaction. As the photons are spatially phase-locked, i.e. **spatial coherent**, the reaction of matter will also be phase-locked. So imagine, at two different locations on the surface, e.g. **surface plasmons** are induced at the same time. As they are all along the surface phase-locked, they will show typical effects of coherence, like interference effects. As a prominent example of spatial coherence are the **ripple** formations; see Fig. 1.12 [10]. With increasing pulse number, the periodical structures generated in ta-C, i.e. tetragonal amorphous carbon, get more pronounced. The periodicity of the ripples is in the range of the applied wavelength of $\lambda = 800$ nm.

Temporal coherence effect during laser radiation–matter interaction is much more delicate, as the coherence time of pulsed laser radiation is mostly limited by its pulse duration. An effect of spatial coherence in material processing is the multi-

photon excitation of matter; see Sect. 13.3.3. As long as the excited matter, i.e. its electronic system is in phase with the photons, a coherent excitation by ulterior photons gets probable. Every quantum mechanical system being excited in such a way will de-phase after a specific de-phasing time. This means a multi-photon excitation is given when the de-phasing time is larger than the excitation probability. The excitation probability itself depends on the photon density of the radiation, and it scales with the intensity.

1.7.3 Spectral Modulation

Ultra-fast laser radiation[7] features apart from a very short pulse duration in the pico- or femtosecond regime, also a broad spectral distribution, as the time-bandwidth product of pulsed radiation is limited and given by

$$t_\mathrm{p} \cdot \Delta\omega \approx 1. \tag{1.105}$$

Depending on the temporal and spectral shape of the pulsed radiation, the value varies and is given for the Gaussian shape of the radiation as 0.315. As a consequence, very short-pulsed radiation, e.g. with a pulse duration of $t_\mathrm{p} = 35$ fs features a spectral bandwidth of about $\Delta\omega = 40$ nm. This means that within ultra-fast laser pulses many different frequencies, i.e. wavelengths, of the electromagnetic radiation are given, all contributing to the final spatial and temporal energy distribution of the laser pulse.

1.7.3.1 Ultra-Fast Laser Pulses

Now, we assume an electrical field strength of the laser radiation given by

$$E(t) = E_0(t) \cos \varphi(t),$$

where the phase ϕ is given by

$$\varphi(t) = \varphi_0 + \omega_0 t + \varphi_a(t),$$

and the envelope function by E_0. The temporal dependence is shown in Fig. 1.13a with the value of the envelope given by the dotted lines. The phase features a constant part, the linear dependence given by the central frequency ω_0, and an additional time-dependent phase term φ_a. The central frequency is coupled to the central wavelength λ_0 of the radiation by

[7] This section is mostly extracted from the master thesis of Philipp Lunwitz, M.Sc. [11].

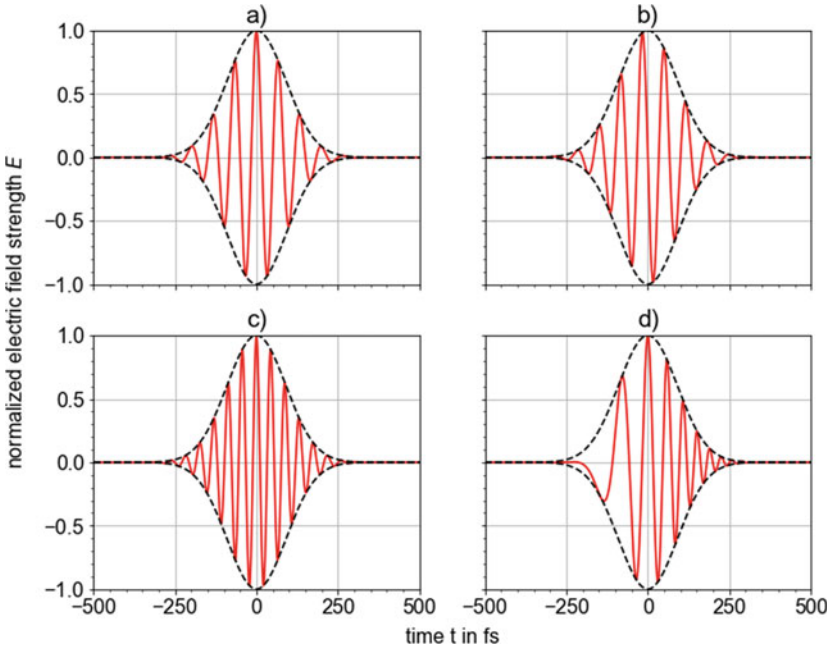

Fig. 1.13 Phase-dependence within an envelope of the electric field strength of an ultra-fast laser pulse with the coefficients **a** $a_m = 0$, **b** $a_{m\neq 0} = 0$ and $a_0 \neq 0$, **c** $a_{m\neq 1} = 0$ and $a_1 \neq 0$, and **d** $a_{m\neq 2} = 0$ and $a_2 > 0$

$$\omega_0 = \frac{2\pi c_0}{\lambda_0 n},$$

with the refractive index of the medium n. One defines the instantaneous angular frequency to

Instantaneous angular frequency

$$\omega(t) = \frac{d\varphi(t)}{dt} = \omega_0 + \frac{d\varphi_a(t)}{dt}, \tag{1.106}$$

with the phase function φ_a, the so-called **chirp** describing variations of the angular frequency in time.

The instantaneous angular frequency can be approximated by a Taylor series, getting

$$\omega(t) = \omega_0 + \frac{d}{dt}\sum_{m=0}^{\infty}\frac{a_m}{m!}(t - t_0)^m, \tag{1.107}$$

where a_m influences the temporal development of the electrical field strength.

One can firstly distinguish four cases for the derivative of φ_a:

- $\varphi_a = \text{const.}$ results in a constant frequency

$$\omega(t) = \omega_0$$

with a defined position of the phase within the envelope of the electric field strength; see Fig. 1.13b.
- $\frac{d\varphi_a}{dt} \neq 0$, but constant ($a_1 \neq 0$, $a_m = 0$ for $m > 1$) with an increase of the central frequency to $\omega_0 + a_1$; see Fig. 1.13c.
- $\frac{d^2\varphi_a}{dt^2} \neq 0$, but constant ($a_2 \neq 0, a_m = 0$ for $m > 2$) with a linear increase (decrease) of the instantaneous frequency $\omega_0 + a_2(t - t_0)$ for $d^2\varphi_a/dt^2 > 0$ (for $d^2\varphi_a/dt^2 < 0$), the so-called positive (negative) chirp; see Fig. 1.13d.

As previously shown in Sect. 1.6.3, (1.94), the temporal dependence of the intensity is proportional to

$$I(t) \propto (E_0(t))^2$$

and is given in Fig. 1.13 by the envelope $\pm|E_0(t)|$ of the laser pulse.

Alternatively, a more mathematical approach [12] using complex numbers allows one to describe the electric field of ultra-fast laser radiation by introducing the Fourier decomposition into individual monochromatic waves

Fourier transformation

$$E(t) = \frac{1}{2\pi}\int_{-\infty}^{\infty} \tilde{E}(\omega)\mathrm{e}^{i\omega t}d\omega, \tag{1.108}$$

with the complex-valued spectrum $\tilde{E}$, which can be determined by the inverse Fourier transformation.

Inverse Fourier transformation

$$\tilde{E}(\omega) = \int_{-\infty}^{\infty} E(t)\mathrm{e}^{-i\omega t}dt. \tag{1.109}$$

The electric field strength $E(t)$ is real-valued, $E(t) \in \mathcal{R}$, what implies that $\tilde{E}(\omega)$ must be Hermitian and obeys

$$\tilde{E}(\omega) = \tilde{E}^*(-\omega).$$

This property implies that the knowledge of the spectrum of the positive frequencies assures a full characterization of the electromagnetic radiation. For the forthcoming calculation it is reasonable to introduce two spectral components of the electric field, one for the positive, the other for the negative angular frequencies,

$$\tilde{E}^{+}(\omega) = \begin{cases} \tilde{E}(\omega) & \text{for } \omega \geq 0 \\ 0 & \text{for } \omega < 0 \end{cases}$$

and

$$\tilde{E}^{-}(\omega) = \begin{cases} \tilde{E}(\omega) & \text{for } \omega \leq 0 \\ 0 & \text{for } \omega > 0, \end{cases}$$

defining also

$$\tilde{E}(\omega) = \tilde{E}^{+}(\omega) + \tilde{E}^{-}(\omega).$$

Applying (1.108) on the two electrical fields $\tilde{E}^{+}(\omega)$ and $\tilde{E}^{-}(\omega)$, we realize that the real-valued electric field strength $E(t)$ in the time domain is given by

$$\begin{aligned} E(t) &= E^{+}(t) + E^{-}(t) \\ &= 2\Re\left\{E^{+}(t)\right\} \\ &= 2\Re\left\{E^{-}(t)\right\}. \end{aligned}$$

So, we have different ways to determine the electrical field strength in the time domain, and we will continue using $\tilde{E}^{+}(t)$. As shown in [12], the envelope function is calculated by

$$E_0(t) = 2\left|E^{+}(t)\right|.$$

One realizes also that $\tilde{E}^{+}(t)$ is a complex function and can be written as

$$\begin{aligned} E^{+}(t) &= \left|E^{+}(t)\right| \exp\left(i\varphi(t)\right), \\ &= \left|E^{+}(t)\right| \exp\left[i\left(\omega_0 t + \varphi_a(t)\right)\right], \end{aligned}$$

or its Fourier transformation

$$\tilde{E}^{+}(\omega) = \left|\tilde{E}^{+}(\omega)\right| \exp\left(-i\phi(\omega)\right),$$

introducing the spectral amplitude $\left|\tilde{E}^{+}(\omega)\right|$ and the spectral phase $\phi(\omega)$. Now, we can determine the instantaneous group delay $T_g(\omega)$ analogous to the instantaneous angular frequency, (1.107), by determining the derivative of the spectral phase on the frequency

Instantaneous group delay

$$T_g(\omega) = \frac{d\phi(\omega)}{d\omega}, \tag{1.110}$$

describing the relative phase delay of each spectral component. Also analogous to the Taylor series of the phase function φ_a, we can expand the spectral phase

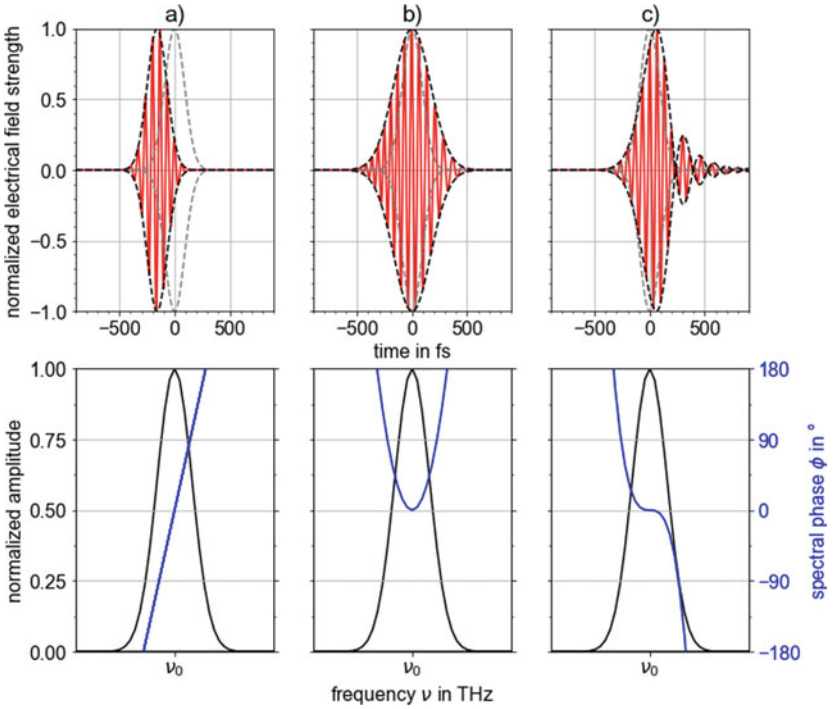

Fig. 1.14 Normalized electric field strength as function of time (upper row) and normalized spectral intensity as function of frequency (lower row) for different dispersion parameters b_m: **a** $b_{m\neq 1} = 0$ and $b_1 \neq 0$, **b** $b_{m\neq 2} = 0$ and $b_2 \neq 0$, and **d** $b_{m\neq 3} = 0$ and $a_3 \neq 0$

$$\phi(\omega) = \sum_{m=0}^{\infty} \frac{b_m}{m!} (\omega - \omega_0)^m, \tag{1.111}$$

with the spectral phase coefficients

$$b_m = \left. \frac{d^m \phi(\omega)}{d\omega^m} \right|_{\omega=\omega_0}.$$

The zeroth order of the spectral phase coefficients ϕ_0 describes the absolute phase $\phi_0 = \phi(\omega_0) = -\varphi_0$.

The first-order term b_1 given by a linear dependence of the spectral phase on the frequency describes a temporal translation of the envelope of the electrical field strength, i.e. its temporal intensity distribution; see Fig. 1.14a.

A quadratic dependence on the frequency is given by a non-vanishing second-order term b_2, which results in the time domain in an increasing width of the electrical field strength, i.e. in an increase in the pulse duration; see Fig. 1.14b.

The third-order term b_3 represents the **third-order dispersion**

$$TOD = \frac{1}{6} b_3 (\omega - \omega_0)^3$$

and induces an asymmetric intensity distribution in time; see Fig. 1.14c. Important to note is the fact that the spectral intensity distribution, i.e. the spectrum of the radiation, remains unchanged for all applied spectral phases; Fig. 1.14 lower row.

1.7.3.2 Spectral Transfer Function

In vacuum ultra-fast laser radiation, like every electromagnetic radiation, features a frequency-independent velocity of all spectral components of the radiation, being equal to the vacuum speed of light c_0. This changes dramatically when the radiation passes matter of the length L. Then, by the interaction of the radiation with matter, an accumulation of the spectral phases takes place, resulting in the spectral transfer function

Spectral transfer function

$$\phi_m(\omega) = k(\omega) L = \frac{\omega}{c_0} n(\omega) L, \tag{1.112}$$

with the wave number k and the frequency-dependent refractive index $n(\omega)$. The propagation of radiation through this medium is calculated by the **complex optical transfer function**

$$\tilde{M}(\omega) = \tilde{R}(\omega) \exp(-i\phi_m),$$

with the spectral amplitude response $\tilde{R}$ depicting the energy gain or losses, e.g. by reflection, as well as a spatial chirp. An incoming electromagnetic field $\tilde{E}^+_{\mathrm{IN}}$ gets to the output field

$$\tilde{E}^+_{\mathrm{OUT}} = \tilde{M}(\omega) \tilde{E}^+_{\mathrm{IN}} = \tilde{R}(\omega) \exp(-i\phi_m) \tilde{E}^+_{\mathrm{IN}}.$$

In the following, we discuss only the phase changes in the complex optical transfer function setting $\tilde{R}(\omega) = 1$. For more details, see [12].

Again, like for the spectral phase of an ultra-fast laser pulse, see (1.111), the spectral transfer function can be Taylor expanded, getting

$$\begin{aligned}\phi_m(\omega) = {} & \phi_m(\omega_0) + \phi'_m(\omega_0)(\omega - \omega_0) + \\ & + \frac{1}{2}\phi''_m(\omega_0)(\omega - \omega_0)^2 + \frac{1}{6}\phi'''_m(\omega_0)(\omega - \omega_0)^3 + \ldots.\end{aligned}$$

The incoming radiation $\tilde{E}_{IN}$ is written by

$$\tilde{E}^+_{IN}(\omega) = \left|\tilde{E}^+_{IN}(\omega)\right| \exp(-i\phi(\omega_0)) \exp(-i\phi'(\omega_0)(\omega - \omega_0)),$$

resulting in an overall spectral phase with constant part and its derivatives.

As described before, the first derivative of the spectral phase induces a temporal shift of the laser pulse, see Fig. 1.14a, the so-called first-order dispersion

$$\phi(\omega)^{(1)} = \phi'(\omega_0)(\omega - \omega_0)$$

which is why it $\phi'(\omega_0)$ is called also **group delay GD**,

$$\begin{aligned} GD = \phi'(\omega_0) &= \frac{d\phi(\omega)}{d\omega} \\ &= \frac{dk(\omega)}{d\omega} L = \left(\frac{d\omega}{dk(\omega)}\right)^{-1} L = \frac{L}{v_g}, \end{aligned}$$

with the group velocity v_g; see (1.97). Applied to the spectral phase function induced in an optical material, (1.111), we get as a group delay,

Group delay

$$GD = \frac{L}{c_0}\left(n(\omega) + \omega\frac{dn(\omega)}{d\omega}\right). \tag{1.113}$$

For sake of simplicity, we omit the group delay GD, because it changes not the pulse shape at all.

Differently, and as shown in Fig. 1.14b, the second-order dispersion

$$\phi(\omega)^{(2)} = \frac{1}{2}\phi''(\omega_0)(\omega - \omega_0)^2$$

changes the width of the pulse in the temporal regime. The second-order derivative of the spectral phase function is called the **group velocity dispersion GVD**

$$GVD = \phi''(\omega_0) = \frac{d^2\phi(\omega)}{d\omega^2}.$$

Applied to the spectral phase function induced in an optical material, (1.111), we get as group velocity dispersion GVD,

Group velocity dispersion

$$GVD = \frac{L}{c_0}\left(2\frac{dn(\omega)}{d\omega} + \omega\frac{d^2n(\omega)}{d\omega^2}\right), \tag{1.114}$$

representing a symmetric change in the temporal pulse shape. Often for given optical systems, the **group delay dispersion** (GDD) is introduced calculating it using the GVD on a characteristic length of the optical system

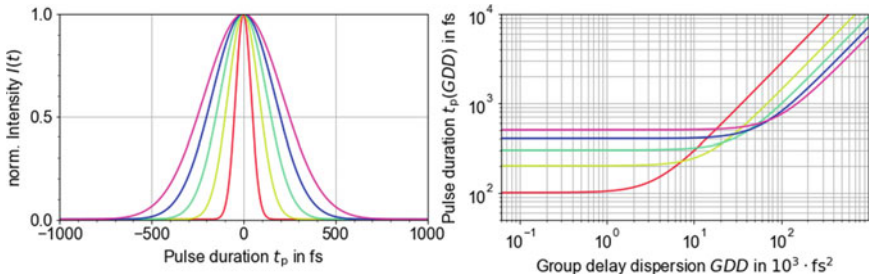

Fig. 1.15 Pulse duration magnification by GDD at different pulse durations [11]

$$GDD = GVD \cdot L.$$

The pulse duration depends on the GDD and is given by

$$t_{\mathrm{p}}(GDD) = \sqrt{t_{p,0}^2 + \left(4\log(2)\frac{GDD}{t_{p,0}}\right)^2},$$

using the minimal pulse duration $t_{p,0}$. As one can see in Fig. 1.15, the relevance of taking GDD into account begins for increasing pulse durations only for larger values of GDD.

An asymmetric pulse shape is induced by the third-order dispersion

$$\phi(\omega)^{(3)} = \frac{1}{6}\phi'''(\omega_0)(\omega - \omega_0)^3.$$

The third-order derivative of the spectral phase function has no additional name and is again called the **third-order dispersion TOD**

$$TOD = \phi'''(\omega_0) = \frac{d^3\phi(\omega)}{d\omega^3}.$$

Applying a TOD on a spectral phase function of an optical material results in

Third-order dispersion

$$TOD = \frac{L}{c_0}\left(3\frac{d^2n(\omega)}{d\omega^2} + \omega\frac{d^3n(\omega)}{d\omega^3}\right). \tag{1.115}$$

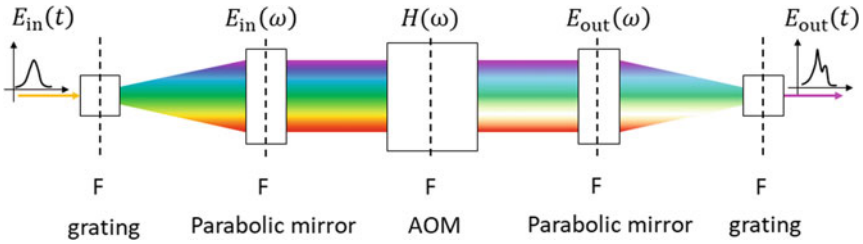

Fig. 1.16 Schematic setup for spectral pulse shaping [11]

1.7.3.3 Spectral Pulse Shaping

Spectral pulse shaping changes the properties of ultrashort pulsed laser radiation by **changing the amplitude and phase** of the individual frequency components contained in the pulse. Variations of the phase of the spectral components are possible in the simplest case by passing through dispersive media. An extension of the method is the use of a Soleil Babinet compensator, in which the dispersion length can be continuously adjusted by changing the geometric path.

Programmable pulse shaping can be realized by phase transfer. In a so-called AOPDF (acousto optic programmable dispersive filters), a shock wave propagates in the beam direction through a birefringent crystal, whereby shaping takes place by selecting suitable parameters [13]. The advantage of the mentioned methods of pulse shaping is that no transformation into the frequency domain is necessary to realize shaping. However, a major disadvantage is the susceptibility to non-linear effects caused by the small interaction volumes resulting in high fluences.

Other possibilities of spectral pulse shaping require the **transformation into frequency space** (see Fig. 1.16). Here, the ultrashort pulsed radiation is decomposed into its spectral components via a grating, whereby the frequencies become location-dependent. The frequencies are mapped into the Fourier plane F via optics. Subsequently, the frequencies are focused on a grating, which removes the spatial dependence of the frequencies, and the ultrashort pulsed laser radiation is characterized by a defined phase relation of the radiation components in the time domain. The

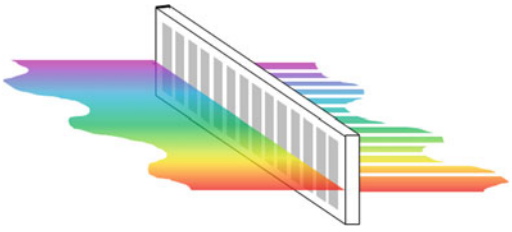

Fig. 1.17 Schematic passage of the frequency components through a liquid crystal mask to form the phase. You can see the expansion of the pixels (gray) themselves, in which area a modulation is generated. Further, you can see the influence of the gaps between the pixels [11]

modulation of the frequencies in their amplitudes and phase positions is performed in the Fourier plane between the two optics via the function $\tilde{H}(\omega)$

$$\tilde{E}_{OUT}(\omega) = \tilde{H}(\omega)\tilde{E}_{IN}(\omega),$$

so that the re-transformed complex field strength has undergone a **spectral shaping** with respect to the input pulse. $\tilde{H}(\omega)$ can thereby be the amplitude, the phase as well as both parameters of the input laser pulse $\tilde{E}_{IN}(\omega)$.

Since the distance between the first grating, first optics, shaping area, second optics, and second grating corresponds to the focal length f in each case, the variants are called $4f$-structures. For shaping itself, different approaches such as **spatial light modulator (SLM)** are also used. E.g. liquid crystal masks are used, with which a shaping of amplitude, phase, and polarization is possible [14]. The disadvantage of this method is that the resolution of the shapable frequencies is limited by the pixels of the mask. Furthermore, due to the design, there are gaps where no modulation can take place, as shown in Fig. 1.17 for a mask for phase modulation. If the amplitude is to be changed additionally, the construction has to be extended by another liquid crystal mask and two polarizers.

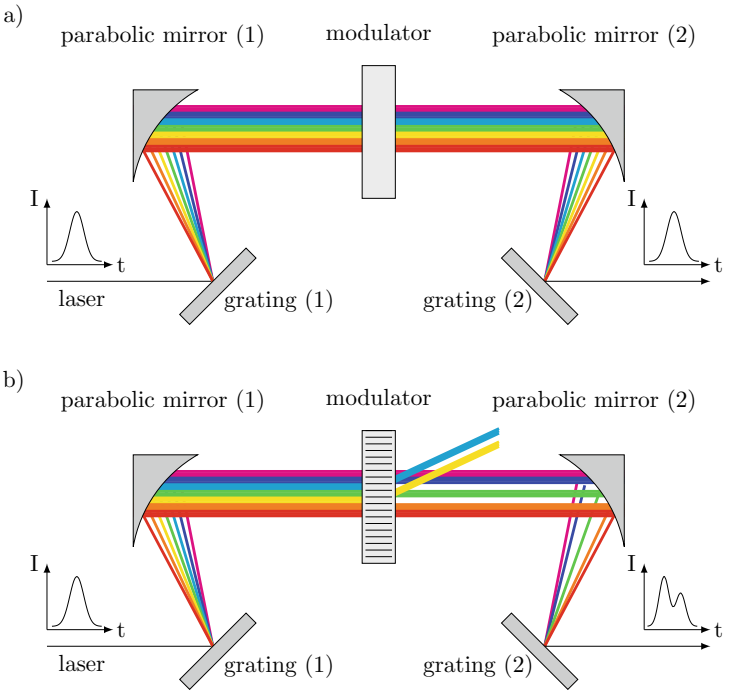

Fig. 1.18 Schematic beam path for pulse shaping using AOM and parabolic mirrors for **a** unshaped and **b** shaped pulse, using zero order [11]

Another possibility to shape the pulse in frequency space is the use of **acousto-optical modulators (AOM)**. In this case, a sound wave is induced in a crystal, which causes local modulations of the refractive index via the photo-elastic effect [15]. As a consequence, the varying refractive index acts as a grating on the frequencies of the laser radiation. By variation of the sound wave frequency and amplitude, the

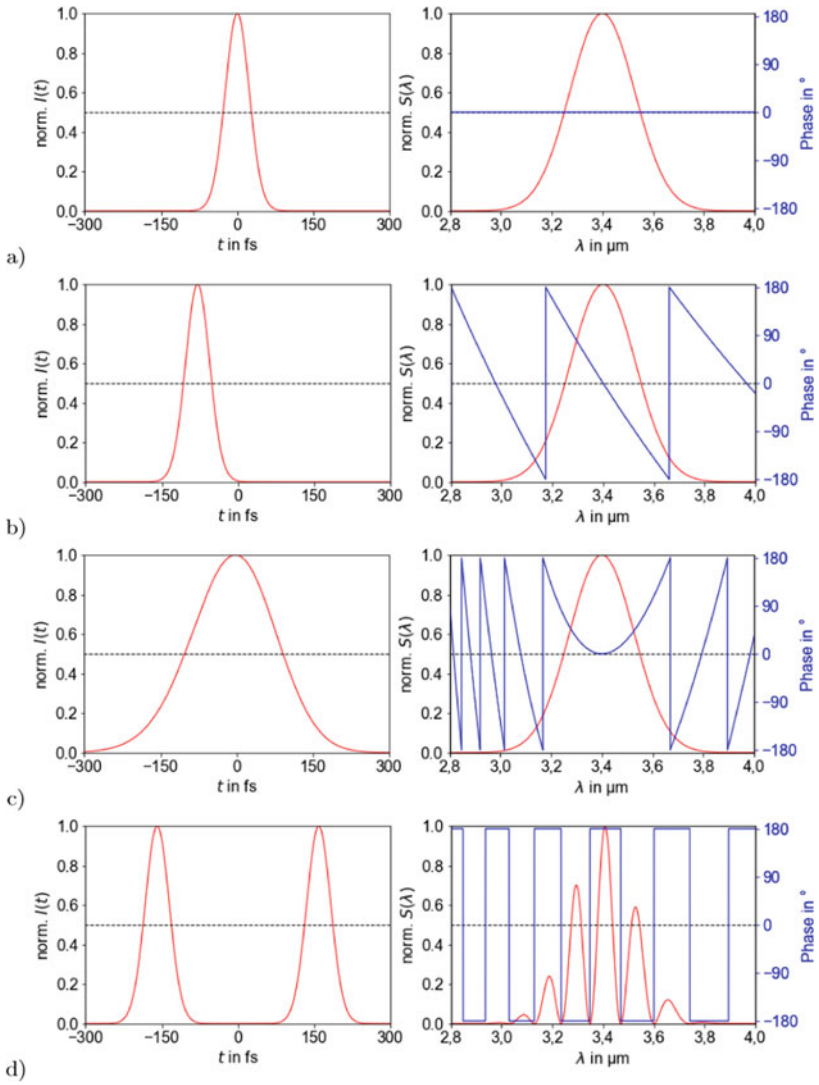

Fig. 1.19 Temporal calculated and spectral intensity distribution is given for different masks: **a** Gaussian mask, **b** Gaussian mask with linear phase, **c** Gaussian mask with quadratic phase, and **d** Cosinus mask with step-like phase [11]

properties of the grating change, and the laser radiation is diffracted to different degrees (Fig. 1.18). In this way, individual frequencies of the laser radiation can be controlled; see Fig. 1.18b. The resolution thereby is limited by the control signal resolution. In shaping, the first-order diffraction of the frequency components in the Bragg regime is usually used, since in this case the selected radiation components in the first order are completely masked out. Another advantage of using an AOM is that the applied mask can arbitrarily be varied between subsequent pulses. The use of an AOM is limited by several parameters. For example, it must be ensured that the grating has been formed over the entire spectrum for each pulse, so the pulse repetition frequency is limited to 100 kHz [14]. Furthermore, the length of the crystal must be taken into account. Due to the material-specific damping of the shock wave in the crystal, the grating is only formed to a limited extent.

Exemplary, the calculated temporal and spectral intensity distribution is given for different masks; see Fig. 1.19.

References

1. Laserinstitut Hochschule Mittweida (2022)
2. https://commons.wikimedia.org/wiki/File:Pn_scatter_quarks.png
3. https://en.wikipedia.org/wiki/Beta_decay
4. https://en.wikipedia.org/wiki/M%C3%B8ller_scattering
5. J. David Jackson, *Classical Electrodynamics*, 3rd edn. (Wiley, 1998)
6. S. Brandt, H.D. Dahmen, *Elektrodynamik* (Springer, Heidelberg, 2005)
7. T. Pflug, J. Wang, M. Olbrich, M. Frank, A. Horn, Case study on the dynamics of ultrafast laser heating and ablation of gold thin films by ultrafast pump-probe reflectometry and ellipsometry. App. Phys. A **124**, 116 (2018)
8. J.M. Liu, Simple technique for measurements of pulsed Gaussian-beam spot sizes. Opt. Lett. **7**, 196 (1982)
9. A.E. Siegman, Lasers, University Science Books, U.S. (1990)
10. M. Pfeiffer, A. Engel, H. Gruettner, K. Guenther, F. Marquardt. G. Reisse, S. Weissmantel, Ripple formation in various metals and super-hard tetrahedral amorphous carbon films in consequence of femtosecond laser irradiation. Appl. Phys. A **110**, 655–659 (2013)
11. P. Lungwitz, *Resonantes Abtragen von Poly(3-hexylthiophen) mit spektral geformter ultrakurz gepulster Laserstrahlung im mittleren Infrarot* (Masterarbeit Hochschule Mittweida, Fakultät Ingenieurwissenschaften, 2020)
12. F. Träger, *Springer Handbook of Lasers and Optics*, 2nd edn. (Springer, Berlin and New York, 2012)
13. https://de.wikipedia.org/wiki/Duane-Hunt-Gesetz
14. A. Monmayrant, S. Weber, B. Chatel, A newcomer's guide to ultrashort pulse shaping and characterization. J. Phys. B: At. Mol. Opt. Phys. **43**(10), 103001 (2010)
15. J.-M. Liu, *Photonic Devices* (Cambridge University Press, Cambridge, 2009)

Chapter 2
Generation of Electromagnetic Radiation

Abstract The generation of electromagnetic radiation is described primarily by the acceleration of charges. Firstly, one has to distinguish between the discrete transition from continuous one, as the one is discussed easily using quantum mechanical descriptions, and the other by classical approaches. Therefore, the Maxwell equations are used and the Liénard–Wiechert potentials are derived. As a consequence of heat, particles gain energy emitting black-body radiation. In this chapter, also the acceleration of particles by high intense radiation is discussed, where X-rays can be generated.

2.1 Discrete and Continuous Transitions

Electromagnetic radiation can be generated in many ways, resulting in specific forms of radiation. Mainly, we distinguish **continuous** versus **discrete** energy transitions.

Continuous energy transitions

- **Bremsstrahlung**: strongly accelerated electric charges emit electromagnetic radiation in the X-ray range with a continuous energy distribution.
- **Thermal radiation:** thermally driven oscillations of atoms consisting also of charges cause emission of radiation.
- **Cherenkov radiation:** ultra-relativistic scattering processes of charged particles in dielectrics emitting visible electromagnetic radiation.

© Springer Nature Switzerland AG 2022

A. Horn, *The Physics of Laser Radiation–Matter Interaction*,
https://doi.org/10.1007/978-3-031-15862-9_2

Discrete Energy Transitions

- **Spontaneous emission:** valence electrons of atoms or molecules transiting from a high energy level to a lower energy level can emit a photon. A photon represents electromagnetic radiation with discrete, quantized energy, given by the energy difference between the two energy levels.
- **Stimulated emission:** a non-natural process can be designed, using at least three energy levels. The laser uses this process, known as the "light amplification by stimulated emission of radiation". From the ground state level, a system (energy level of atoms, molecules, solids, or fluids) is excited to a pump level. From the pump level, the system relaxes to an intermediated level, the so-called upper laser niveau. From the upper laser niveau, the system can relax again to the ground state, if a photon stimulates the system having an energy equivalent to the energy difference between the upper laser level and the ground state.
- **Gamma radiation emission:** atomic nuclei being excited after an α or β decay can relax its excessive energy by emission of γ radiation.
- **Chemical reaction**: Chemically and/or bio-chemical transformation of molecules, reactions, and structural changes resulting in net energy being emitted.

In this textbook, the generation or laser radiation is not of central interest for the interaction of radiation with matter. But to understand, where the interactions of radiation with matter follow the generation of radiation, we will have to look closer on it. Especially, the acceleration of charged particles and the resulting emission of radiation are needed to describe the linear and non-linear optical properties of matter, and also for the generation of X-rays.

2.2 Spontaneous Emission

Generation of electromagnetic radiation by spontaneous emission of radiation is a quantum mechanical process describing an energy state transition of an atom or molecule from an excited state to a ground state. This excitation process will not be discussed further, except for atoms or molecules brought into an excited state and being able to emit electromagnetic radiation. Examples for excitation processes are, atoms ore molecules excited by electric or magnetic fields, or by inelastic scattering with other particles, like electrons or heavy atoms. Also, excitation by chemical reactions is common.

In order to calculate this transition, one has to work with non-equilibrium processes; the quantum electrodynamics (QED) has to be applied, which is not the aim of this book. See for further reading [1, 2].

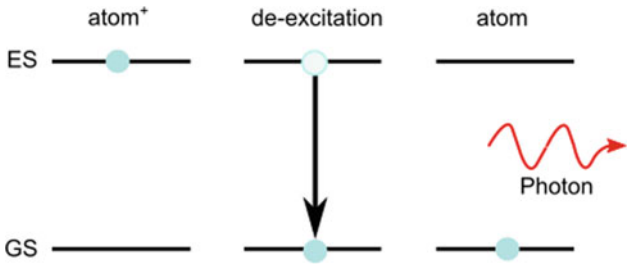

Fig. 2.1 De-excitation of a two-level system consisting of a ground state (GS) and an excited state (ES)

As an atom is excited, it can relax by spontaneous emission of electromagnetic radiation:

$$(\text{atom})^+ \rightarrow \text{atom} + \gamma.$$

The photon energy is quantized, as explained in Sect. 3.5, and the emitted radiation is best described by photons. Using energy levels corresponding to the states of the electrons of the atom, the relaxation process is qualitatively described by a transition of an electron from an excited state to the ground state; see Fig. 2.1.

Here, a two-level system consisting of a ground state (GS) and an excited state (ES) is used as a simplified model for an atom. As known from quantum mechanics, atoms feature many energy levels resulting in manifold excitation channels. See, for example, the excitation series of hydrogen, like (3.40) in Sect. 3.5. Usually, the transition energies of atoms are in the range of some ten eV, so that common laser radiation will not excite any atom or molecule into an excited state. When considering non-linear processes, we will see that excitation becomes probable even if the energy of the photons is below the excitation gap, see Chap. 13.

A rate equation describes the dynamics of the number of atoms from the excited state (2) into the ground state (1) in time

$$\frac{\partial N(t)}{\partial t} = -A_{21} N(t),$$

with A_{21} being an Einstein coefficient describing the rate for spontaneous emission directly related to the radiative decay rate Γ_{rad}

Einstein coefficient for spontaneous emission

$$A_{21} = \Gamma_{rad} = \frac{1}{\tau_{21}}, \tag{2.1}$$

and the lifetime τ_{21}. Applying quantum mechanics and using Fermi's Golden rule, one gets the radiative decay rate for spontaneous emission to

$$\Gamma_{rad} = \frac{n \cdot |\mu_{12}|^2}{3\pi\varepsilon_0 \hbar c_0^3} \omega^3,$$

with the refractive index n, the transition dipole moment μ_{12}, and ω the frequency of the emitted radiation.

2.3 Acceleration of a Free Charge

Assuming a free and static electron having the charge q and the mass m_e in vacuum, the interaction of an incoming planar electromagnetic wave can firstly be described by the Coulomb force, induced by the electric field $\boldsymbol{E} = E_0 \cos(\omega \cdot t)\, \boldsymbol{e}_x$ of the radiation at the location of the electron $F = q \cdot E$ with $q = -e$. This assumption is a good approximation for small accelerations of the electron. At large field strengths, the Lorentz force has to be chosen, too. The equation of motion for the electron is then given by

Equation of motion for the electron

$$m_\mathrm{e} \cdot a = m_\mathrm{e} \cdot \ddot{x} = -e \cdot E_0 \cos(\omega t) \tag{2.2}$$

$$\curvearrowright \quad \ddot{x} = -\frac{e}{m_\mathrm{e}} E_0 \cos(\omega t).$$

By subsequent integration for a quarter of a period T (just describing the maximum amplitude of the electron), one gets the velocity and the location of the electron in the electric field

$$\begin{aligned}
\curvearrowright \quad \dot{x} = v_\mathrm{e} &= -\frac{e\, E_0}{m_\mathrm{e}} \int_0^{T/4} \cos(\omega t) dt \\
&= -\frac{e\, E_0}{m\, \omega} \sin(\omega t) \Big|_0^{T/4} \\
\curvearrowright \quad x &= \frac{e\, E_0}{m_\mathrm{e}\, \omega^2} \cos(\omega t) \Big|_0^{T/4} \\
&= -\frac{e\, E_0}{m_\mathrm{e}\, \omega^2} \\
&= -\frac{e\, E_0}{m_\mathrm{e}\, 4\pi^2 \nu^2}.
\end{aligned}$$

Finally, one can determine the location of the electron using (1.71) and $c_0 = \lambda \cdot \nu$ and $k = \pi/\lambda$ getting

Location of the electron

$$x = -\frac{e\ E_0\ \lambda^2}{m_e\ 4\pi^2 c_0^2.} \tag{2.3}$$

Example

A 100-W light bulb emits with 100 % efficiency electromagnetic radiation (assumptions: monochromatic radiation $\lambda = 500$ nm, collimated completely in one beam). Please calculate

(a) the electric field of the collected radiation with a beam radius $r = 6$ mm;
(b) the maximum elongation of an electron in this electric field.

(a) The intensity of the light bulb is calculated to

$$I = \frac{P}{A} = \frac{100\ W}{\pi(6 \cdot 10^{-3}\ m)^2} = 884\ \mathrm{kW/m^2} \approx 1\ \mathrm{MW/m^2}.$$

From (1.94), one gets from the energy density of the electric field

$$E = \sqrt{\frac{2\ I}{\epsilon_0 \cdot c_0}}$$

$$E = \sqrt{\frac{2 \cdot 1 \cdot 10^3\ Wm^{-2}}{8.85 \cdot 10^{-12}\ As/(V\ m) \cdot 3 \cdot 10^8\ m/s}}$$

$$E = \underline{\underline{25.8\ \mathrm{kV/m}}}.$$

(b) The elongation of the periodic oscillation of the electron is given by

$$x = \frac{e\ E\ \lambda^2}{m_e\ 4\ \pi^2\ c_0^2}$$

$$= \frac{1.602 \cdot 10^{-19}\ A\ s \cdot 25\ 10^3 V/m \cdot 25 \cdot 10^{-14}\ m^2}{9.11 \cdot 10^{-31}\ kg \cdot 40 \cdot 9 \cdot 10^{16}\ m^2/s^2}$$

$$= 3.2 \cdot 10^{-16}\ \mathrm{m}$$

$$x = \underline{\underline{0.3\ \mathrm{fm}}}.$$

The example shows that

- without any damping, the electron follows the electric field with the same frequency and features a maximal elongation of 0.6 fm.

- after irradiation, the electron results again at rest (imagine a temporal limited electric pulse). This means that even though the electron gets energy to be accelerated, at the end the electron has absorbed no energy from the electromagnetic field.
- for intensities of the radiation $\gg \mathrm{MW/m^2}$ to $\mathrm{GW/m^2}$, the elongations of the electrons and their velocities get large enough to make electron–electron collisions probable $\Rightarrow$ Heating of the system by absorption; see Sect. 12.3.

Is this approach correct? First, we can assert that a light bulb emits at the most only 5% of the electrical power as electromagnetic radiation in the visible region. We will talk about it when we will have a look at the thermal emission of solid state matter in Sect. 2.5, the so-called black-body radiation. There we will see that the power and the intensity of the emitted radiation scale with the temperature in the fourth power

$$P = \sigma_{\mathrm{SB}} A T^4 \qquad \curvearrowright \quad I = \frac{P}{A} = \sigma_{\mathrm{SB}} T^4.$$

Also, it is hard to collect all the emitted radiation of a light bulb, because one would need reflective optics to collect all the radiation emitted in 4π. Due to the missing damping, the electromagnetic field will recover its energy completely, representing a perfect process, which is impossible.

2.3.1 General Aspects on the Retardation

But the most important dependence has not been considered. We took the electron as a point-like particle with a charge q, just by looking at the first Maxwell equation

$$\nabla \cdot \boldsymbol{E} = \frac{q}{\varepsilon_0} \delta^3(\boldsymbol{r} - \boldsymbol{r}\,'),$$

with the charge density of an electron given by $\varrho(\boldsymbol{r}) = q_{\mathrm{e}}\ \delta^3(\boldsymbol{r} - \boldsymbol{r}\,')$. The delta distribution $\delta^3(\boldsymbol{r} - \boldsymbol{r}\,')$ describes the position of a point-like charge at $\boldsymbol{r}\,'$; see the Info box on page 58.[1] As the first consequence, if the electric field depends on time, $\boldsymbol{E} = \boldsymbol{E}(t)$, also the charge position gets time-dependent $\curvearrowright\ \boldsymbol{r}\,' = \boldsymbol{r}\,'(t)$. This implies

[1] For more details on delta distributions δ^3 and the distribution theory, see [3].

for the Maxwell equation (1.9) a time dependence of the magnetic field $\curvearrowright \boldsymbol{B} = \boldsymbol{B}(t)$, and in consequence makes the current density of an electron moving at velocity $\boldsymbol{v}_0$, given by

Current density of a moving charge

$$\boldsymbol{J} = q\delta^3(\boldsymbol{r} - \boldsymbol{r}')\,\boldsymbol{v}_0(t)$$

a time-dependent current density $\boldsymbol{J} = \boldsymbol{J}(t)$, too.

A moving electron, accelerated by an electromagnetic field, represents a spatial and temporal dependent electrical charge, which is also given by a time-dependent current density.

The accelerated electron induces time-dependent electric and magnetic fields

$$\varrho(t) \curvearrowright \boldsymbol{J}(t) \curvearrowright \quad \boldsymbol{E} = \boldsymbol{E}(t) \text{ and } \boldsymbol{B} = \boldsymbol{B}(t).$$

As learned, the wave equations deduced by the Maxwell equations can describe the propagation of electromagnetic radiation. In order to get the field distributions of time-dependent electric and magnetic fields, one has to think about the definitions of the locations of the charges and the location of the fields itself.

Imagine a temporal dependent charge at $\boldsymbol{r}'$, maybe by a little spatial oscillation of an electron or a moving charge. An induced electromagnetic field will be generated and propagated through space. Between the position and the time of the charges $\boldsymbol{r}'$ and t' and the position of the generated field at $\boldsymbol{r}$ a temporal separation is given (in vacuum) by the limited and constant velocity of light c_0, resulting in a so-called retarded time

Retarded time

$$t = t' + \frac{|\boldsymbol{r} - \boldsymbol{r}'|}{c_0}. \tag{2.4}$$

The electromagnetic field at $\boldsymbol{r}$ is detected at the time t, being later compared to its generation in $\boldsymbol{r}'$ at the time t'.

Info box: The δ distribution

The delta distribution is a very important tool in physics, especially for describing point-like systems.
Exemplarily, one can apply the Gaussian function $f(x) = \frac{1}{\sqrt{2\pi}\sigma} \exp(-\frac{x^2}{2\sigma^2})$ with the definition for the delta distribution as an infinite small Gaussian function, but with a definite area:

$$\lim_{\sigma \to 0} f(x) = \delta(x).$$

The delta distribution has the following properties:

$$\begin{gathered}
\delta(x) = \delta(-x) \\
\int_{-\infty}^{\infty} \delta(x')dx' = 1 \\
\int_{-\infty}^{\infty} \delta(x - x') f(x')dx' = \int_{-\infty}^{\infty} \delta(x) f(x + x')dx' = f(x) \\
\delta(\alpha x) = \frac{1}{|\alpha|}\delta(x) \\
\delta^3(\boldsymbol{r}) = \delta(x)\delta(y)\delta(z).
\end{gathered}$$

Also interesting is the dependence of the step function, the so-called Heaviside function $\Theta(x)$, defined as

$$\Theta(x) = \begin{cases} 0 \ , & x < 0 \\ 1 \ , & x > 0. \end{cases}$$

One can alternatively construct to the Gaussian function a limited step function, a so-called impulse. The derivative of the Heaviside function results also in

$$\delta(x) = \frac{d\Theta(x)}{dx}.$$

2.3.2 General Solution of a Retarded Wave Equation

Remembering that the electric and magnetic fields can be described by scalar and vector potential fields, see (1.27) and (1.25), the Maxwell's equations can be described by these potential fields resulting in the d'Alembert equations (1.31):

$$\Box \varphi^{(L)} = \frac{\varrho}{\varepsilon_0} \text{ and } \Box \boldsymbol{A}^{(L)} = \mu_0 \, \boldsymbol{j}.$$

These equations can be solved mathematically by taking the generalized d'Alembert equation.

Generalized d'Alembert equation

$$\Box G(t, \boldsymbol{r}, t', \boldsymbol{r}') = 4\pi\delta(c_0 t - c_0 t')\delta^3(\boldsymbol{r} - \boldsymbol{r}'). \tag{2.5}$$

Here, the delta distributions are acting in space and time. The solution of the generalized d'Alembert equation is given by the generalized Green equation

$$G(t, \boldsymbol{r}, t', \boldsymbol{r}') = \frac{\delta(c_0 t - c_0 t' - |\boldsymbol{r} - \boldsymbol{r}'|)}{|\boldsymbol{r} - \boldsymbol{r}'|}. \tag{2.6}$$

The potential fields will now be determined by integration in space and time at the charge coordinates (primed variables!) of the charge distribution density and current density combined with the Green equation getting

Green equations for charge and current distributions

$$\varphi(t, \boldsymbol{r}) = \frac{c_0}{4\pi\varepsilon_0} \int\int \frac{\delta(c_0 t - c_0 t' - |\boldsymbol{r} - \boldsymbol{r}'|)}{|\boldsymbol{r} - \boldsymbol{r}'|} \varrho(t', \boldsymbol{r}')dt'dV' \tag{2.7}$$

$$\boldsymbol{A}(t, \boldsymbol{r}) = \frac{c_0\mu_0}{4\pi} \int\int \frac{\delta(c_0 t - c_0 t' - |\boldsymbol{r} - \boldsymbol{r}'|)}{|\boldsymbol{r} - \boldsymbol{r}'|} \boldsymbol{\jmath}(t', \boldsymbol{r}')dt'dV'. \tag{2.8}$$

So, knowing the charge density ρ and the current density $\jmath$ distributions for a deliberate moving particle, we are able to calculate the potential fields, the so-called *Liénard–Wiechert potentials*, see next section. By applying the Lorenz gauge in the resulting equations, the electric and magnetic fields can be calculated using (1.27) and (1.25).

2.3.3 Maxwell Equations for a Moving Charge

A moving and accelerated point-sourced charge q can be described by a charge distribution density and a current density

$$\varrho(t, \boldsymbol{r}) = q\,\delta^3(\boldsymbol{r} - \boldsymbol{r}'(t))$$
$$\boldsymbol{\jmath}(t, \boldsymbol{r}) = q\,\boldsymbol{v}'(t)\delta^3(\boldsymbol{r} - \boldsymbol{r}'(t)),$$

being located in $\boldsymbol{r}'(t)$ at the time t with the velocity of the particle $\boldsymbol{v}'(t) = d\boldsymbol{r}'(t)/dt$; see Fig. 2.2.

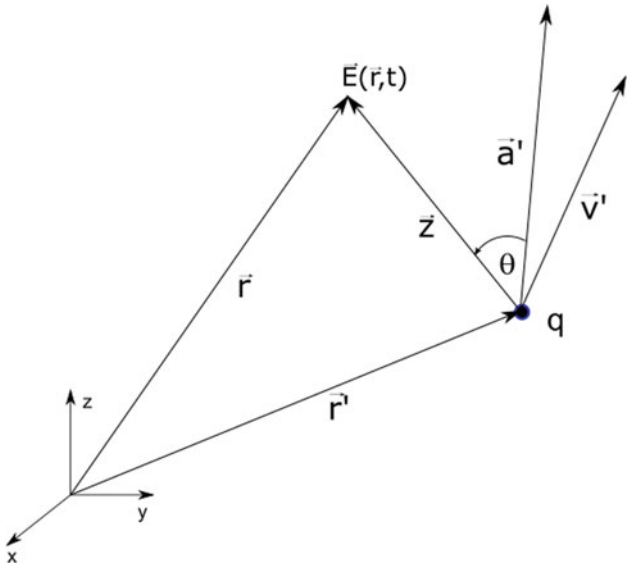

Fig. 2.2 Schematics of a charged particle r at $\boldsymbol{r}'$and location of the electric field at $\boldsymbol{r}$

The potential fields for a moving charge, the so-called **Liénard–Wiechert potentials**, are calculated by integration of the generalized Green equations (see last section and [4]) and result in

Liénard–Wiechert potentials

$$\varphi(t,\boldsymbol{r}) = \frac{q}{4\pi\,\varepsilon_0}\left[\frac{1}{|\boldsymbol{r}-\boldsymbol{r}\,'(t')| - (\boldsymbol{v}\,'(t')/c_0)\cdot(\boldsymbol{r}-\boldsymbol{r}\,'(t'))}\right]_{t'}$$

$$\boldsymbol{A}(t,\boldsymbol{r}) = \frac{q\;\mu_0}{4\pi}\left[\frac{\boldsymbol{v}\,'(t')}{|\boldsymbol{r}-\boldsymbol{r}\,'(t')| - (\boldsymbol{v}\,'(t')/c_0)\cdot(\boldsymbol{r}-\boldsymbol{r}\,'(t'))}\right]_{t'}$$

$$= \frac{\varphi(t,\boldsymbol{r})}{c_0^2}\left[\boldsymbol{v}\,'(t')\right]_{t'}$$

$$\text{with the retarded time } t' = t - \frac{\left|\boldsymbol{r}-\boldsymbol{r}\,'(t')\right|}{c_0}.$$

Using the definitions for the electric and magnetic fields by (1.27) and (1.25) (see the full calculations in [4]) and the following relations

- the relative velocity $\boldsymbol{\beta} = \frac{\boldsymbol{v}'}{c_0}$, also called the relativistic factor,
- the acceleration of the particle $\boldsymbol{a}\,' = \frac{d\boldsymbol{v}'}{dt}$,
- the vector $\boldsymbol{z}(t') = \boldsymbol{r} - \boldsymbol{r}\,'(t')$ oriented starting from location of the particle to the point of the electromagnetic field, and

- the unity vector in this direction $\hat{\boldsymbol{z}} = \boldsymbol{z}/z$,

one gets for the electric and magnetic fields of a moved charged particle

$$\boldsymbol{E}(t,\boldsymbol{r}) = \frac{q}{4\pi\epsilon_0}\left[\overbrace{\frac{(c_0\boldsymbol{z} - z\boldsymbol{v}')c_0^2(1-\beta^2)}{(c_0 z - \boldsymbol{v}'\cdot\boldsymbol{z})^3}}^{\text{Term 1}} + \overbrace{\frac{\boldsymbol{z}\times((c_0\boldsymbol{z} - z\boldsymbol{v}')\times\boldsymbol{a}')}{(c_0 z - \boldsymbol{v}'\cdot\boldsymbol{z})^3}}^{\text{Term 2}}\right]_{t'=t-z/c_0} \tag{2.9}$$

$$\boldsymbol{B}(t,\boldsymbol{r}) = \frac{\mu_0 c_0\, q}{4\pi}\left[\overbrace{\frac{(\boldsymbol{v}'\times\boldsymbol{z})c_0^2(1-\beta^2)}{(c_0 z - \boldsymbol{v}'\cdot\boldsymbol{z})^3}}^{\text{Term 1}} + \overbrace{\frac{\hat{\boldsymbol{z}}\times(\boldsymbol{z}\times(c_0\boldsymbol{z} - z\boldsymbol{v}')\times\boldsymbol{a}')}{(c_0 z - \boldsymbol{v}'\cdot\boldsymbol{z})^3}}^{\text{Term 2}}\right]_{t'=t-z/c_0} \tag{2.10}$$

One sees that the magnetic field rules to

$$\boldsymbol{B} = \frac{1}{c_0}\hat{\boldsymbol{z}}\times\boldsymbol{E} \qquad \curvearrowright \qquad \boldsymbol{B} \perp \text{plane}(\boldsymbol{E},\hat{\boldsymbol{z}}).$$

The magnetic field $\boldsymbol{B}$ is orthogonal to the plane spanned by the vectors of the electric field $\boldsymbol{E}$ and $\hat{\boldsymbol{z}}$. Both (2.9) and (2.10) for the electric and magnetic fields exhibit two addends, here called **Term 1** and **Term 2**. The **Term 1** in both equations depends not on the acceleration $\boldsymbol{a}'$ of the charged particle, and has a spatial dependency

$$\boldsymbol{E}_1 \text{ and } \boldsymbol{B}_1 \sim \frac{1}{z^2}.$$

Term 1 represents the near field description of the electric and magnetic fields. It can also be seen here that for increasing particle velocity $|\boldsymbol{v}'| \to c_0$, the field strengths vanish:

$$\boldsymbol{E}_1 \text{ and } \boldsymbol{B}_1 \ \to 0 \text{ for } \beta \to 1.$$

The **Term 2**, different from Term 1, depends on the acceleration $\boldsymbol{a}_0$ and exhibits a spatial proportionality representing the inverse distance between the charge and the region of the electric field

$$\boldsymbol{E}_2 \text{ and } \boldsymbol{B}_2 \sim \frac{1}{z},$$

featuring electric and magnetic fields of plane waves in the far field.

The Poynting vector for the far field is calculated using $\boldsymbol{B}_2 = \frac{1}{c_0}(\hat{\boldsymbol{z}}\times\boldsymbol{E}_2)$ getting

$$\begin{aligned}\boldsymbol{S}_2 &= \frac{1}{\mu_0}\boldsymbol{E}_2\times\boldsymbol{B}_2 \ \text{ with}\\ &= \frac{1}{c_0\mu_0}\boldsymbol{E}_2\times(\hat{\boldsymbol{z}}\times\boldsymbol{E}_2) = \frac{1}{c_0\mu_0}(\boldsymbol{E}_2\cdot\boldsymbol{E}_2)\hat{\boldsymbol{z}}\end{aligned}$$

as one can prove by recalculation that $\boldsymbol{E}_2 \cdot \hat{\boldsymbol{z}}$ vanishes and gets

$$\boldsymbol{S}_2 = \frac{q^2\mu_0}{16\pi^2 z^2 c_0}\,\hat{\boldsymbol{z}}\frac{\left|\hat{\boldsymbol{z}} \times \left[(\hat{\boldsymbol{z}} - \boldsymbol{\beta}) \times \boldsymbol{a}'\right]\right|^2}{(1 - \boldsymbol{\beta}\cdot\hat{\boldsymbol{z}})^6}. \tag{2.11}$$

The square of the absolute value is then calculated getting

Poynting vector of far field radiation emitted by a charged particle

$$\boldsymbol{S}_2(\boldsymbol{r}, t) = \frac{q^2\mu_0}{16\pi^2 z^2 c_0}\,\hat{\boldsymbol{z}}\left[\frac{|\hat{\boldsymbol{z}} \times \boldsymbol{a}'|^2 - 2(\boldsymbol{\beta} \times \boldsymbol{a}')\cdot(\hat{\boldsymbol{z}} \times \boldsymbol{a}')}{(1 - \boldsymbol{\beta}\cdot\hat{\boldsymbol{z}})^6} + \frac{(\boldsymbol{\beta} \times \boldsymbol{a}')^2 - [\hat{\boldsymbol{z}}\cdot(\boldsymbol{\beta} \times \boldsymbol{a}')]^2}{(1 - \boldsymbol{\beta}\cdot\hat{\boldsymbol{z}})^6}\right]. \tag{2.12}$$

The Poynting vector is oriented along the $\hat{z}$-direction and represents the unity vector oriented from the location of the particle to the point of the electromagnetic field. Obviously, the Poynting vector depends on a small particle velocity $\boldsymbol{v}' \ll c_0$, $\beta \ll 1$ only on the first addend of the fraction, resulting in

Poynting vector for slow charged particle

$$\boldsymbol{S}(\boldsymbol{r}, t) = \hat{\boldsymbol{z}}\frac{q^2\mu_0}{16\pi^2 z^2 c_0}|\hat{\boldsymbol{z}} \times \boldsymbol{a}'|^2. \tag{2.13}$$

The Poynting vector scales with the square of the acceleration value a' and scales reciprocally with the square of the distance of the source to the point of interest z of the electromagnetic field.

The energy $\mathcal{E}$ of the emitted radiation per solid angle $d\Omega$ through the elementary area $d\boldsymbol{a}$ at $\boldsymbol{r}$ over the time dt is calculated using the Poynting vector

$$d\mathcal{E} = \boldsymbol{S}\cdot d\boldsymbol{a}\, dt.$$

In our case, we want to calculate the energy emitted by the particle in the time dt', because we only know the time dependence in t' of the charge. So we have to expand

$$d\mathcal{E} = \boldsymbol{S}\cdot d\boldsymbol{a}\,\frac{dt}{dt'}dt' \tag{2.14}$$

using the retardation equation (2.4) getting the dependence of the retarded time t with the time of the particle frame t' thereby calculating the derivative

$$\frac{dt}{dt'} = 1 - \frac{\boldsymbol{v}_0}{c_0}\cdot\frac{\boldsymbol{r} - \boldsymbol{r}'}{|\boldsymbol{r} - \boldsymbol{r}'|} = 1 - \boldsymbol{\beta}\cdot\hat{\boldsymbol{z}}$$

and using the differential area

$$d\boldsymbol{a} = \hat{\boldsymbol{z}} z^2 d\Omega \qquad (d\Omega = \text{solid angle}). \tag{2.15}$$

One calculates the transmitted energy per time t' and solid angle $d\Omega$, the so-called power or the yield per solid angle, which is defined through

$$dP = d\left(\frac{d\mathcal{E}}{dt'}\right) = (\boldsymbol{S}\cdot\hat{\boldsymbol{z}})(1-\boldsymbol{\beta}\cdot\hat{\boldsymbol{z}})z^2\, d\Omega,$$

getting finally the emitted power per solid angle, the so-called differential power

$$\begin{aligned}\frac{dP}{d\Omega} &= z^2(\boldsymbol{S}\cdot\hat{\boldsymbol{z}})(1-\boldsymbol{\beta}\cdot\hat{\boldsymbol{z}}) \\ &= \frac{q^2\mu_0}{16\pi^2 c_0}\frac{\left|\hat{\boldsymbol{z}}\times\left[(\hat{\boldsymbol{z}}-\boldsymbol{\beta})\times\boldsymbol{a}'\right]\right|^2}{(1-\boldsymbol{\beta}\cdot\hat{\boldsymbol{z}})^5},\end{aligned}$$

Directional radiation characteristics of an accelerated particle

$$\frac{dP}{d\Omega} = \frac{q^2\mu_0\, a'^2}{16\pi^2 c_0}\frac{\left|(\hat{\boldsymbol{z}}\times(\hat{\boldsymbol{z}}\times\hat{\boldsymbol{a}}')+\hat{\boldsymbol{z}}\times(\hat{\boldsymbol{a}}'\times\boldsymbol{\beta})\right|^2}{(1-\boldsymbol{\beta}\cdot\hat{\boldsymbol{z}})^5}. \tag{2.16}$$

One sees from (2.16) that the power emitted per solid angle is proportional to the squared acceleration of the charged particle

$$\frac{dP}{d\Omega} \sim a'^2.$$

The angular dependence of $dP/d\Omega$, also called the *directional radiation characteristics* of an accelerated particle, depends on the relative velocity $\boldsymbol{\beta}$. For small particle velocities, (2.16) simplifies to

Angular dependence of the directional radiation characteristics

$$\frac{dP}{d\Omega} = \frac{q^2\mu_0\,(a')^2}{16\pi^2 c_0}|(\hat{\boldsymbol{z}}\times(\hat{\boldsymbol{z}}\times\hat{\boldsymbol{a}}')|^2 = \frac{q^2\mu_0\,(a')^2}{16\pi^2 c_0}\sin^2\vartheta. \tag{2.17}$$

Here, the angle ϑ is spanned between the unity vectors $\hat{\boldsymbol{a}}'$ and $\hat{\boldsymbol{z}}$; see Fig. 2.2. Integrating the differential power on the solid angle, one gets for the overall emitted power

$$P = \int_0^{2\pi} d\varphi \int_0^{\pi} d\vartheta \sin^3\vartheta \frac{q^2\mu_0 (a')^2}{16\pi^2 c_0}$$
$$= \frac{q^2\mu_0 (a')^2}{6\pi},$$

Emitted power of a constant accelerated charged particle

$$P = \frac{q^2\mu_0}{6\pi c_0} a'^2. \tag{2.18}$$

In case of a periodic oscillating charge, the integration has to be carried out for the differential power over the solid angle. Additionally a temporal average has to be considered for a periodical acceleration $\boldsymbol{a}'$,[2] getting the averaged emitted power

$$\langle P\rangle = \langle \int_0^{2\pi} d\varphi \int_0^{\pi} d\vartheta \sin^3\vartheta \frac{q^2\mu_0 (a')^2}{16\pi^2 c_0}\rangle$$
$$= \langle \frac{q^2\mu_0 (a')^2}{6\pi}\rangle$$
$$= \frac{q^2\mu_0}{6\pi}\langle a'^2\rangle. \tag{2.19}$$

Taking the temporal average on a'^2 with $\langle a'^2\rangle = 1/2\, a'^2$, one gets the averaged emitted power of an oscillating charge

$$\langle P\rangle = \frac{1}{T}\int_t^{t+T} \frac{q^2\mu_0 a'^2}{6\pi} dt = \frac{q^2\mu_0}{12\pi c_0} a'^2$$

resulting in

Averaged emitted power of periodically accelerated charged particle

$$\langle P\rangle = \frac{q^2\mu_0}{12\pi c_0} a'^2. \tag{2.20}$$

[2] For example, a circular motion of the charged particle.

2.4 Emission of Accelerated Charges

In the following, we will have a look at three examples describing the movement of a charged particle with

1. **collinear** velocity and acceleration vectors, with the Brownian X-ray tube as an example,
2. acceleration vector **perpendicular** to the velocity vector represented by a circular movement, and
3. periodic **oscillation** of a charged particle, described by a time-dependent electric dipole.

2.4.1 Collinear Velocity and Acceleration Vectors

Now, we consider a charged particle, e.g. an electron, and accelerating it in a static electric field results in an acceleration vector being collinearly oriented to the velocity vector

$$\boldsymbol{a}' \parallel \boldsymbol{v}'.$$

Since the relative velocity vector $\boldsymbol{\beta}$ influences the direction of the maximum power emission by the second addend in (2.16), we discuss first the dependence on β (Fig. 2.3).

- For $\beta \to 0$, the second term in (2.16) vanishes. Slow particles ($\boldsymbol{v}' \ll \boldsymbol{\beta}$) emit electromagnetic radiation perpendicular to the propagation direction $\hat{z}$ with the maximum power emission at $\vartheta = \pi/2$, to be seen best by looking at the Poynting vector, (2.13).
- For $\beta \approx 1$, the second term gets dominant. A charged particle with a significant large velocity $v' \approx c_0$ is called relativistic, and emits pronounced electromagnetic radiation forward oriented, with ϑ getting smaller with increasing velocity.

The Brownian X-Ray Tube

As an important example, one can mention the Brownian X-ray tube. Electrons generated by thermal emission from a cathode within a vacuum tube are first accelerated in an electrostatic field. Reaching the anode, the electrons are quickly stopped by multiple scattering at the atoms of the cathode (e.g. tungsten). The electrons emit due to this second, very strong deceleration high-energy electromagnetic radiation, called *X-rays* or *Bremsstrahlung*.

The final kinetic energy of the electron is controlled by the potential difference U between anode and cathode. The anode is geometrically designed to allow a free emission of the X-rays by tailoring the anode geometry, e.g. tilting the surfaces. The maximum energy of the X-rays, and so the smallest wavelength representing a complete stopping of the electron at one scattering, is given by the *Duane–Hunt law*.

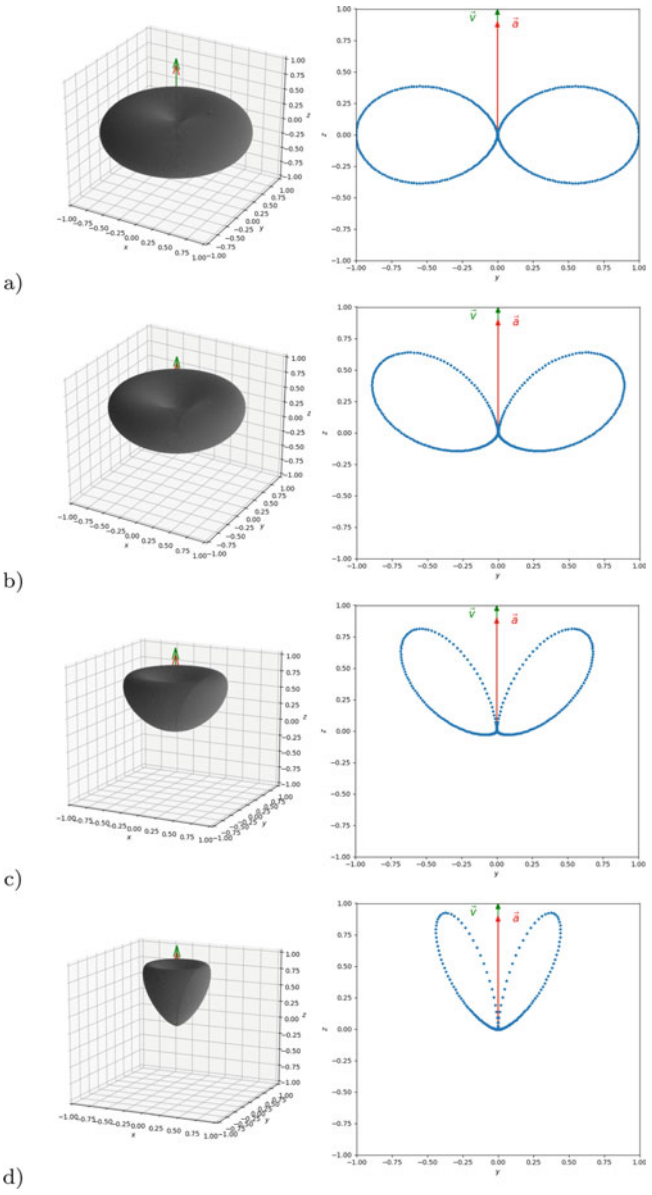

Fig. 2.3 Directional radiation characteristics of a particle accelerated in propagation direction z with parallel unity vectors $\hat{\boldsymbol{a}}' \parallel \hat{\boldsymbol{v}}'$ with relative velocity parameters **a** $\beta = 0$, **b** $\beta = 0.25$, and **c** $\beta = 0.50$, and $\beta = 0.75$

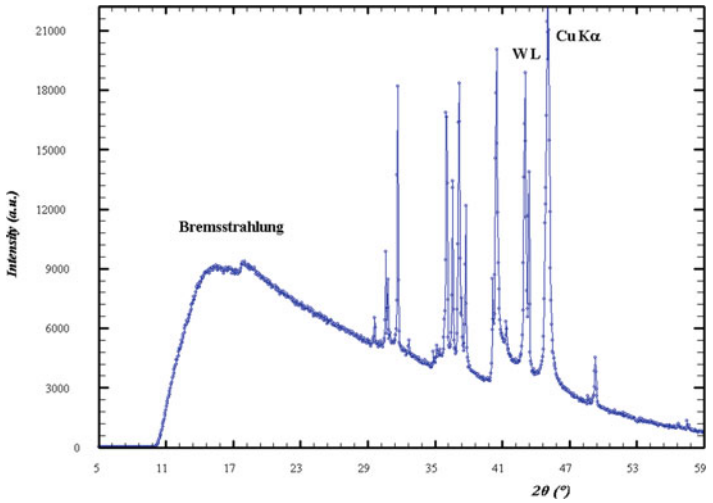

Fig. 2.4 X-ray spectrum emitted by an X-ray tube with a rhodium target, operated at 60 kV acceleration tension [5]

Duane–Hunt law

$$\lambda_{min} = \frac{h \cdot c_0}{e\,U}, \tag{2.21}$$

with U the applied voltage between the cathode and anode. The energy distribution of the X-rays depends on the energy losses during the scattering of the electrons in the solid (anode) and is not easily described (see Fig. 2.4).

The physics behind the scattering of the electrons at atoms of a solid is given by the **Bethe–Bloch equation** describing the energy dissipation per length of a fast-moving charged particle passing through condensed matter

Bethe–Bloch equation

$$-\frac{\mathrm{d}E}{\mathrm{d}x} = \frac{4\pi n z^2}{m_\mathrm{e} c_0^2 \beta^2} \cdot \left(\frac{e^2}{4\pi\varepsilon_0}\right)^2 \cdot \left[\ln\left(\frac{2m_\mathrm{e} c_0^2 \beta^2}{I \cdot (1-\beta^2)}\right) - \beta^2\right]. \tag{2.22}$$

Thereby represents I an averaged excitation potential of the scattering material, z the charge number of the particle, and n the electron density in the material.

This apparatus is today used routinely in medical and technical applications in detecting objects within a body. For instance the physician uses X-rays to get insight into the human body, not only looking at bones. Today, with the high sensitivity and the high selectivity of the X-ray detectors, and tomography techniques, too, makes it possible to detect soft tissue, allowing the determination of density differences in

tissues. In technical applications, X-rays are applied to detect defects in solid materials, like micro-cracks in alloys, and also in product quality control, e.g. detecting foreign objects in cups and bottles.

2.4.2 Acceleration Perpendicular to the Velocity

A special configuration, where a charged particle features not only a constant velocity but also a constant acceleration, is given for a circular trajectory. For this configuration the velocity vector $|\boldsymbol{v}'| = \text{const}$ is orthogonal oriented to the acceleration vector $|\boldsymbol{a}'| = \text{const}$

$$\boldsymbol{a}' \perp \boldsymbol{v}'.$$

A storage ring, also called synchrotron, allows the generation of very intense X-rays. The directional radiation characteristics is slightly different from those of a collinear acceleration (Fig. 2.5) due to the fact that the acceleration vector changes in orientation all the time as well as the velocity vector.

A seen in (2.16) the power emitted per solid angle is proportional to the squared acceleration and the $dP/d\Omega$ depends also on the relative velocity $\boldsymbol{\beta}$ (Fig. 2.5):

- For a relative velocity $\beta \to 0$, the second term of (2.16) vanishes. A slow particle emits in this configuration electromagnetic radiation in propagation direction $\hat{z}$ and perpendicular to the acceleration direction $\hat{\boldsymbol{a}}'$, with the maximum power emission at $\vartheta = \pi/2$.
- For a relative velocity $\beta \approx 1$, a relativistic particle is given featuring a significant large velocity $v' \approx c_0$ emitting electromagnetic radiation predominantly being forward oriented, with the maximum power emission at $\vartheta = \pi/2$. This radiation is called *synchrotron radiation*, and the photon energy is controlled via the particle velocity. The energy distribution is also difficult to be calculated, though the acceleration value is constant its vector character induces a complex dependence of the emission characteristics in space and time of the synchrotron radiation.

The mean energy of the electromagnetic radiation is controlled by the electron velocity and the intensity by the current density of the electrons. A synchrotron emits radiation with very high brilliance from the IR to the X-ray regime. Its application is found in fundamental research and in material characterization for technical applications.

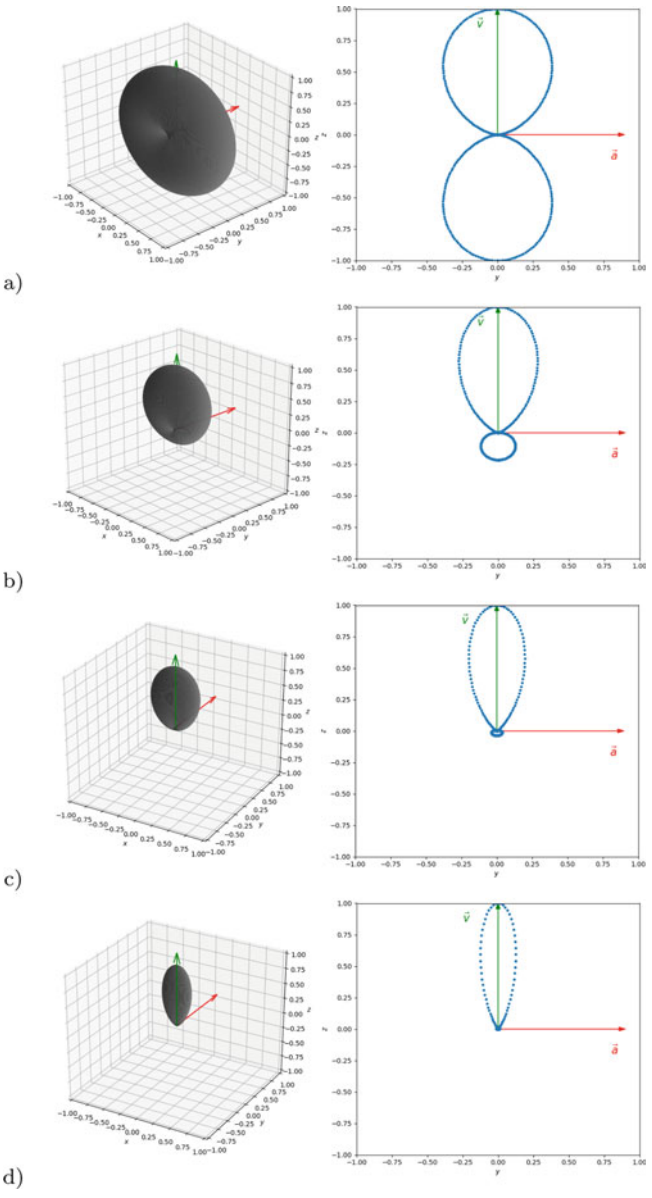

Fig. 2.5 Directional radiation characteristics of a particle accelerated with orthogonal unity vectors $\hat{\boldsymbol{a}}' \parallel \hat{\boldsymbol{v}}'$ with relative velocity parameters **a** $\beta = 0$, **b** $\beta = 0.25$, and **c** $\beta = 0.50$ and $\beta = 0.75$

2.4.3 Periodic Oscillation of a Charged Particle

The third configuration with an accelerated charged particle is given by an oscillating electron. Again, one has to set up a scalar and a vector potential representing the solution of the d'Alembert equations (2.7) and (2.8). Therefore, we need a description of the charge and current densities of a periodically oscillating charge.

It is reasonable to introduce the definition of an electric dipole described by a temporal dependence of a periodic oscillating charge. Let us now assume that a free electron is oscillating. The static electric dipole moment is then given by

Static dipole moment

$$\boldsymbol{d} = q\,\boldsymbol{b}, \tag{2.23}$$

with $\boldsymbol{b}$ representing the distance vector of the charge q from the point of origin (or the elongation of one oscillating charge). One can calculate (see [4]) that, even if the distance vector gets to zero, $b \to 0$, the charge density can be described by even a dipole getting

Charge density via dipole moment

$$\varrho = -\boldsymbol{d} \cdot \nabla\delta^3(\boldsymbol{r}), \tag{2.24}$$

using a temporal dependent dipole moment $\boldsymbol{d} = \boldsymbol{d}(c_0\,t)$. The current density is derived from the continuity equation (1.12) resulting in

$$\begin{aligned} \nabla \cdot \boldsymbol{J} &= -\frac{\partial \varrho}{\partial t} \\ &= \frac{d}{dt}\boldsymbol{d} \cdot \nabla\delta^3(\boldsymbol{r}). \end{aligned}$$

Applying now $\boldsymbol{d}\,'(\xi) = \frac{d}{d\xi}\boldsymbol{d}(\xi)$ with $\xi = c_0 t$, one gets

$$\nabla \cdot \boldsymbol{J} = c_0 \boldsymbol{d}\,'(\xi) \cdot \nabla\delta^3(\boldsymbol{r}). \tag{2.25}$$

This equation is fulfilled when one defines a time-dependent current density

Time-dependent current density

$$\boldsymbol{J} = c_0 \boldsymbol{d}\,'\delta^3(\boldsymbol{r}). \tag{2.26}$$

With the descriptions of the charge and current densities by using the dipole moment, now one can calculate the potentials. Finally, using the relation for the electric and magnetic fields, (1.27) and (1.25), one calculates the formal field equations [4], here summarized by the equations

Electric and magnetic field of an oscillating dipole

$$\boldsymbol{E}_{\mathrm{e}} = \frac{1}{4\pi\varepsilon_0}\left[-\frac{\boldsymbol{d}''}{r} + \frac{(\boldsymbol{d}''\cdot\boldsymbol{r})\,\boldsymbol{r}}{r^3} - \frac{\boldsymbol{d}'}{r^2} + \frac{3(\boldsymbol{d}'\cdot\boldsymbol{r})\,\boldsymbol{r}}{r^4} - \right. \tag{2.27}$$
$$\left. - \frac{\boldsymbol{d}}{r^3} + \frac{3(\boldsymbol{d}\cdot\boldsymbol{r})\,\boldsymbol{r}}{r^5}\right],$$
$$\boldsymbol{B}_{\mathrm{e}} = \frac{\mu_0 c_0}{4\pi}\left(\frac{\boldsymbol{d}''\times\boldsymbol{r}}{r^2} + \frac{\boldsymbol{d}'\times\boldsymbol{r}}{r^3}\right). \tag{2.28}$$

Let us now assume that the oscillating charge performs a harmonic motion, given by a periodic dipole moment

$$\boldsymbol{d}_c(c_0t) = \boldsymbol{d}_0 e^{-i\omega t} = \boldsymbol{d}_0 \exp(-i\frac{\omega}{c_0}c_0t) = \boldsymbol{d}_0 e^{-ikc_0t},$$

and using in the last equation the dispersion relation (1.71) in vacuum. $\boldsymbol{d}_c$ represents a complex dipole moment of the oscillating electron. Calculating the derivatives, one gets

$$\boldsymbol{d}_c{}'(c_0t) = -ik\boldsymbol{d}_c \quad \text{and} \quad \boldsymbol{d}_c{}''(c_0t) = -k^2\boldsymbol{d}_c. \tag{2.29}$$

Here, it is important to notify that through the integration of the scalar and vector fields, (2.7) and (2.8), the temporal dependence of the dipole moment is changed by the delta distribution $\delta(c_0t - c_0t' - |\boldsymbol{r} - \boldsymbol{r}'|)$ to a typical wave function

$$\begin{aligned}\boldsymbol{d}_c(c_0t - |\boldsymbol{r} - \boldsymbol{r}'|) &= \boldsymbol{d}_0 \exp(-i\frac{\omega}{c_0}(c_0t - |\boldsymbol{r} - \boldsymbol{r}'|))\\ &= \boldsymbol{d}_0 \exp(-i(\omega t - k|\boldsymbol{r} - \boldsymbol{r}'|)).\end{aligned}$$

The second delta distribution in the scalar fields projects $\boldsymbol{r}'$ on $\boldsymbol{r}$ getting

$$\boldsymbol{d}_c = \boldsymbol{d}_0 \exp(-i(\omega t - k\cdot r)).$$

Clearly, the physical dipole is represented only in the real part of $\boldsymbol{d}_c$

$$\boldsymbol{d} = \Re\{\boldsymbol{d_0}\exp[-i(\omega t - kr)]\} = \boldsymbol{d}_0\cos(\omega t - kr).$$

Inserting $\boldsymbol{d}_c$ into the calculated electric and magnetic fields from (2.28), one gets

$$\boldsymbol{E}_{ec} = \frac{1}{4\pi\varepsilon_0}\frac{\exp[-i(\omega t - kr)]}{r^3}\left\{[(kr)^2 + i(kr) - 1]\boldsymbol{d}_0 - \right.$$
$$\left. -[(kr)^2 + 3ikr - 3](\boldsymbol{d}_0\cdot\hat{\boldsymbol{r}})\hat{\boldsymbol{r}}\right\}$$
$$\boldsymbol{B}_{ec} = -\frac{\mu_0\,\omega}{4\pi}\frac{\exp[-i(\omega t - kr)]}{r^2}(kr + i)(\boldsymbol{d}_0\times\hat{\boldsymbol{r}}).$$

These fields of the emitted radiation can be investigated using the power series of kr distinguishing the near from the far field regimes.

Near Field kr $\ll$ 1

With the relation for a wavelength and a wave number $k = 2\pi/\lambda$, the relation $kr \ll 1$ is equivalent to $r \ll \lambda$, i.e. the investigated fields are close to the dipole itself (representing the smallest power in r)

$$\boldsymbol{E}_{ec} = \frac{1}{4\pi\varepsilon_0}\frac{\exp[-i(\omega t - kr)]}{r^3}\left\{-\boldsymbol{d}_0 + 3(\boldsymbol{d}_0 \cdot \hat{\boldsymbol{r}})\hat{\boldsymbol{r}}\right\}$$
$$\boldsymbol{B}_{ec} = -\frac{i\mu_0\,\omega}{4\pi}\frac{\exp[-i(\omega t - kr)]}{r^2}(\boldsymbol{d}_0 \times \hat{\boldsymbol{r}}).$$

It can be shown that the electric field equals an electrostatic dipole with a temporal variation. The physical fields are finally given by

$$\boldsymbol{E}_{\mathrm{e}} = \frac{1}{4\pi\varepsilon_0}\frac{3(\boldsymbol{d} \cdot \hat{\boldsymbol{r}}) - \boldsymbol{d}}{r^3}$$
$$\boldsymbol{B}_{\mathrm{e}} = \frac{\mu_0 c_0}{4\pi}\frac{\boldsymbol{d}' \times \hat{\boldsymbol{r}}}{r^2}.$$

The near fields vanish for large r due to the proportionality $1/r^2$ per field.

Far Field kr $\gg$ 1

The far field is also called the wave field or dipole field and is described by $r \gg \lambda$. Here, the investigated fields are far away from the field generating dipole. We consider only the terms $\propto kr$ with highest power and get firstly the complex description

$$\boldsymbol{E}_{ec} = \frac{1}{4\pi\varepsilon_0}\frac{\exp[-i(\omega t - kr)]}{r^3}\left\{(kr)^2\boldsymbol{d}_0 - (kr)^2(\boldsymbol{d}_0 \cdot \hat{\boldsymbol{r}})\hat{\boldsymbol{r}}\right\}$$
$$\boldsymbol{B}_{ec} = -\frac{\mu_0\,\omega}{4\pi}\frac{\exp[-i(\omega t - kr)]}{r^2}kr(\boldsymbol{d}_0 \times \hat{\boldsymbol{r}}).$$

Secondly, we can immediately take the physical description by calculating the real part, and get for the fields

$$\boldsymbol{E}_{\mathrm{e}} = \frac{1}{4\pi\varepsilon_0}\frac{(\boldsymbol{d}'' \cdot \hat{r})\hat{r} - \boldsymbol{d}''}{r} = \frac{1}{4\pi\varepsilon_0}\frac{(\boldsymbol{d}'' \times \hat{\boldsymbol{r}}) \times \hat{\boldsymbol{r}}}{r},$$
$$\boldsymbol{B}_{\mathrm{e}} = \frac{\mu_0 c_0}{4\pi}\frac{\boldsymbol{d}'' \times \hat{\boldsymbol{r}}}{r} = \frac{1}{4\pi\varepsilon_0 c_0}\frac{\boldsymbol{d}'' \times \hat{\boldsymbol{r}}}{r}.$$

It can be seen that the electric field vector $\boldsymbol{E}_{\mathrm{e}}$ is tangential to the meridian and $\boldsymbol{B}_{\mathrm{e}}$ is parallel to it. Both fields are perpendicularly oriented to each other (Fig. 2.6), and can be rewritten using (1.10) to

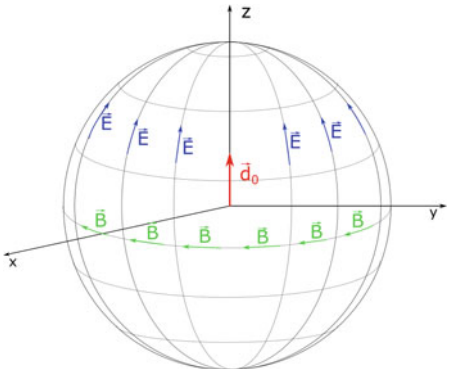

Fig. 2.6 Electric and magnetic flux lines in the far field of a dipole, dipole vector $\boldsymbol{d}_0$ oriented in z-direction

$$\boldsymbol{B}_\mathrm{e} = \frac{1}{c_0}(\hat{\boldsymbol{r}} \times \boldsymbol{E}_\mathrm{e})$$
$$\boldsymbol{E}_\mathrm{e} = c_0(\boldsymbol{B}_\mathrm{e} \times \hat{\boldsymbol{r}}).$$

These field vectors represent in the far field spherical waves and are also called dipole radiation. The Poynting vector in the far field of a dipole describes the energy flux and is given by

$$\boldsymbol{S} = \boldsymbol{E}_\mathrm{e} \times \boldsymbol{H}_\mathrm{e} = \frac{1}{\mu_0}\boldsymbol{E}_\mathrm{e} \times \boldsymbol{B}_\mathrm{e}.$$

Inserting the description of the dipole moment of the fields, one gets

$$\begin{aligned}\boldsymbol{S} &= \frac{c_0}{16\pi^2\varepsilon_0}\left(\boldsymbol{d}'' \times \hat{\boldsymbol{r}}\right)^2 \frac{\hat{\boldsymbol{r}}}{r^2} \\ &= \frac{c_0}{16\pi^2\varepsilon_0}\frac{\hat{\boldsymbol{r}}}{r^2}|\boldsymbol{d}''|^2 \sin^2\vartheta,\end{aligned}$$

introducing the plane angle ϑ between the vectors $\hat{\boldsymbol{r}}$ and $\boldsymbol{d}''$. This angle ϑ represents also the angle between $\hat{\boldsymbol{r}}$ and $-\boldsymbol{d}$ (see (2.29)).

For oscillating accelerations physically detectable is only the averaged flux, as we discussed in Sect. 1.6.3 by using (1.93). So, one calculates the temporal average of the Poynting vector

$$\begin{aligned}\langle \boldsymbol{S} \rangle &= \frac{c_0}{16\pi^2\varepsilon_0}\frac{\hat{\boldsymbol{r}}}{r^2}\left\langle |\boldsymbol{d}''|^2 \right\rangle \sin^2\vartheta \\ &= \frac{c_0}{16\pi^2\varepsilon_0}\frac{\hat{\boldsymbol{r}}}{r^2}k^4 d_0^2 \left\langle \cos^2(c_0 t) \right\rangle \sin^2\vartheta,\end{aligned}$$

Temporal averaged Poynting vector

$$\langle \boldsymbol{S} \rangle = \frac{c_0 k^4}{32\pi^2 \varepsilon_0} d_0^2 \frac{\hat{\boldsymbol{r}}}{r^2} \sin^2 \vartheta. \tag{2.30}$$

The averaged energy flux through a differential area $d\boldsymbol{a}$ (see (2.15)), i.e. the differential power, or averaged energy flux, is given by

$$d\langle P \rangle = \langle \boldsymbol{S} \rangle \cdot d\boldsymbol{a} = r^2 \langle \boldsymbol{S} \cdot \hat{r} \rangle d\Omega,$$

and the differential power per solid angle $d\Omega$ results in

Directional radiation characteristics of a dipole

$$\frac{d\langle P \rangle}{d\Omega} = \frac{c_0 k^4}{32\pi^2 \varepsilon_0} d_0^2 \sin^2 \vartheta. \tag{2.31}$$

The directional characteristics of the differential averaged energy flux per solid angle is rotational symmetric to the orientation of the dipole vector $\boldsymbol{d}_0$, and exhibits a maximum power emission at $\vartheta = \pi/2$ (Fig. 2.7). Also, no energy flux is given in direction of the dipole moment $\boldsymbol{d}$. Interestingly, this matter of fact will explain the Brewster angle in geometrical optics (see Sect. 7.8).

Integrating the differential power per solid angle over the full solid angle, one gets the total emitted averaged power of an oscillating dipole

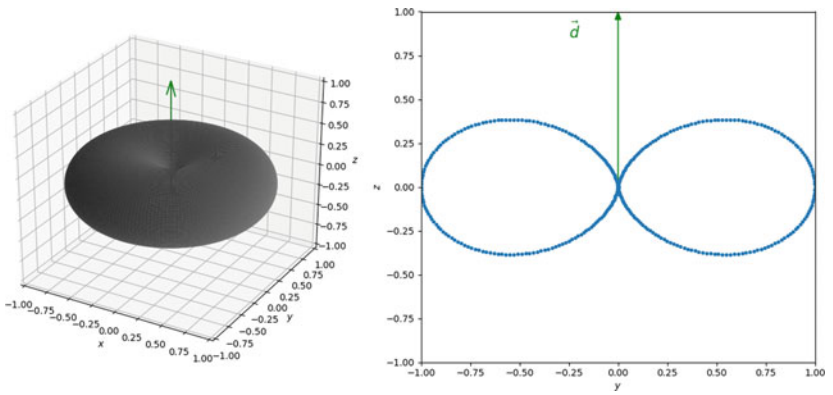

Fig. 2.7 Directional radiation characteristics of an electric dipole with dipole vector $\boldsymbol{d}_0$ oriented in z-direction

$$\langle P \rangle = \int_0^{2\pi} d\varphi \int_{-1}^{1} d\cos\vartheta \ \sin^2\vartheta \frac{c_0 k^4}{32\pi^2 \varepsilon_0} d_0^2$$
$$= \frac{c_0 k^2}{12\pi\varepsilon_0} d_0^2 = \frac{\mu_0 c_0^3 k^4}{12\pi},$$

Emitted averaged power of an oscillating dipole

$$\langle P \rangle = \frac{\mu_0}{12\pi c_0} \omega^4 d_0^2. \tag{2.32}$$

So, the power of the emitted electromagnetic radiation of an oscillating electron at the angular frequency ω scales with the fourth power in the frequency ω, and quadratic in the dipole moment d_0.

2.5 Black-Body Radiation

In this section, we will have a look at solid bodies with very specific geometries. We assume a uniform temperature of the body, and as a consequence, of each atom. Due to that, each atom features a temperature-dependent potential energy featuring an oscillation with an amplitude proportional to the temperature. We will at the moment not excite this system with any external radiation. As the atoms oscillate, they represent accelerated particles or oscillating dipoles, and will emit electromagnetic radiation.

Considering the interaction of many particles with electromagnetic radiation, one can think about an ideal body. Ideal is meant in the sense of ideal absorption and ideal emission of radiation. A black body ideally emits all electromagnetic radiation and absorbs all electromagnetic radiation. This means, in other words that the black body is in a **thermodynamic equilibrium** and features a defined temperature T. This approach was chosen at the end of the nineteenth century to target the thermal emission properties of condensed matter, so-called black bodies featuring an absolute temperature T.

The question thereby is, why is the energy distribution of the emitted radiation of a body, the so-called electromagnetic spectrum is given by a continuum, and not by discrete energy levels? The electromagnetic spectrum represents the energy distribution of the number of emitting atoms as a function of the frequency ν, and is said to be the *spectral energy density*. Two assumptions were defined to explain the discrepancy.

The first assumption we make is to assume that the atoms of a hollow body consisting of condensed matter exhibit due to its uniform temperature oscillations with an amplitude proportional to its elongation. One oscillating atom represents thereby an electric dipole given by its atomic electron distribution, and emits electromagnetic radiation, as shown in Sect. 2.4.3. The emitted electromagnetic radiation itself

is absorbed completely by other atoms[3] of the system, so that finally absorption and emission are balanced, the energy is conserved, and a constant temperature, i.e. a **thermal equilibrium** results.

The time-averaged potential energy of such an atomic oscillator is described by

Time-averaged potential energy of atomic oscillator

$$< E_{pot} >= \left\langle \frac{1}{2} m\omega^2 x^2 \right\rangle = k_B T, \tag{2.33}$$

and corresponds to the thermal energy $E_{therm} = \frac{1}{2} k_B T$ per degree of freedom of an atom, with $k_B = 1.38 \cdot 10^{-23}$ J/K representing the Boltzmann constant. Assuming also two possible polarization states of the electromagnetic radiation, we get twice this energy per excitation.

The second assumption quantifies the energy emission and absorption of radiation in a defined body: due to the constant temperature, we consider the propagation of the electromagnetic radiation in a hollow body as a steady state process. This implies that the only solution for the wave equation (1.13) is given by a standing wave, like the propagation of electromagnetic radiation within a wave guide.

As shown in solid state textbooks like [6], starting from a one-dimensional chain of oscillating atoms, the process of emission of radiation with its spectral components is described in the following. We will transfer this approach then to the three-dimensional case.

2.5.1 One-Dimensional Hollow Black Body

Let us assume a one-dimensional hollow body given in the x-direction with the length L, and vanishing dimensions in $y, z \ll x$. A propagation of an electromagnetic wave inside this hypothetical hollow body is only possible in the x-direction, and is described by the wave equation

$$\frac{\partial^2}{\partial x^2} E(x,t) = \frac{1}{c_0^2} \frac{\partial^2}{\partial t^2} E(x,t).$$

This wave equation is solved, see Sect. 1.5 and also [10], e.g. by a plane wave

$$\begin{aligned} E(x,t) &= E_0 \exp(i(\omega t + k \cdot x)) \\ &= E_0 \exp(i\omega t) \exp(ik \cdot x) \\ &= \tilde{E}(x) \exp(i\omega t) \end{aligned} \tag{2.34}$$

[3] Assuming the atoms to be from the same kind.

with the real component $E_R(x) = \Re(\tilde{E}(x)) \sim \cos(k \cdot x)$ and $k = \dfrac{\omega}{c_0}$. For a metallic hollow body in thermodynamic equilibrium, time-independent boundary conditions are given, resulting in vanishing electric fields at its ends, and are given by

$$E(0) = E(L) = 0.$$

For (2.34), this boundary condition is satisfied for $k \cdot L = j\pi$, with the mode number $j \in \mathbb{N}_0$. Substituting $k = 2\pi/\lambda$, one gets

$$\begin{aligned} L &= \frac{j\pi}{k} \\ &= \frac{j\pi\lambda}{2\pi} \\ \curvearrowright \quad \lambda_j &= \frac{2L}{j} \qquad \text{the discrete mode wavelength,} \end{aligned}$$

or using $\lambda = c_0/\nu$ one calculates the discrete mode frequency

Mode frequency in one dimension

$$\nu_j = \frac{c_0}{2L} j. \tag{2.35}$$

The distance between each mode is constant and is given by the frequency separation

$$\begin{aligned} \Delta\nu &= \nu_{j+1} - \nu_j \\ &= \frac{c_0}{2L}[(j+1) - j], \end{aligned}$$

Mode distance in one dimension

$$\Delta\nu = \frac{c_0}{2L}. \tag{2.36}$$

Each atom oscillates at a frequency ν_j and due to the dipole emission of a charged particle, its emitted radiation features the same frequency. As known from statistical mechanics, an ensemble of atoms at an equal temperature T features not only one frequency, but also a statistical distribution over a broad range of frequencies of the radiation. So we have to calculate the distribution of the modes, or mode density by counting them: for a given maximal frequency ν_{max}, we calculate the number of possible modes N by

$$N(\nu_{max}) = \frac{\nu_{max}}{\Delta\nu} = \frac{2L}{c_0}\nu_{max}. \tag{2.37}$$

So in general, the number of modes depends linearly on the frequency ν. The mode density describes the number of modes in the interval $[\nu, \nu + \Delta\nu]$, also called occupation density, and is given by

Mode density in one dimension

$$n(\nu) = \frac{dG(\nu)}{d\nu} = \frac{2L}{c_0} = \text{const.}, \tag{2.38}$$

depending not on the frequency at all. The spectral energy density of a one-dimensional hollow body is on the other hand calculated by defining an energy density per mode

$$\epsilon = \frac{E_{therm}}{L} = \frac{\frac{1}{2}k_B T}{L}.$$

Here, it is important to note that the electric field of the electromagnetic radiation is described by two polarization states, the parallel and orthogonal polarization states. This states the degeneracy $p = 2$ of each mode having the same energy. One has to count two states per mode for the spectral energy density getting

$$\begin{aligned} u(\nu) &= n(\nu)(p \cdot \epsilon) = n(\nu)\frac{2E_{therm}}{L} \\ &= \frac{2L}{c_0}\frac{k_B T}{L}, \end{aligned}$$

Spectral energy density in one-dimension

$$u(\nu) = \frac{2k_B}{c_0} T. \tag{2.39}$$

The spectral energy density increases with increasing temperature, and is called **the Rayleigh–Jeans model**. But, this spectral energy density diverges summing it up over all frequencies, describing the ultraviolet catastrophe for the overall energy emitted by a body using this one-dimensional approach

$$U = \int_0^\infty u(\nu) d\nu \to \infty.$$

The derivation for a three-dimensional hollow body should get a similar result. This was the starting point of Max Planck's interpretations, where he made two revolutionary assumptions:

1. The energy of the electromagnetic radiation is quantized, and is given by the energy of one photon

Energy of one photon

$$E_\gamma = h\nu. \tag{2.40}$$

The Planck constant itself is given by $h = 6.626 \cdot 10^{-34}$ Js.

2. The occupation density, or number of modes in the interval $[\nu, \nu + \Delta\nu]$ is not constant, but follows the Bose–Einstein statistics for boson particles, so-called bosons, with the Bose–Einstein distribution function

Bose–Einstein distribution function

$$f_{\mathrm{BE}}(\nu) = \frac{1}{e^{\frac{h\nu}{k_\mathrm{B}T}} - 1}. \tag{2.41}$$

Now, the energy per mode is given by

$$E_{therm} = E_\gamma \cdot f_{\mathrm{BE}}(\nu) = \frac{h\nu}{e^{\frac{h\nu}{k_\mathrm{B}T}} - 1}.$$

The overall energy of the electromagnetic wave with the spectral energy density for the one-dimensional hollow body using Planck's assumption does not diverge anymore. We will now directly calculate it for the three-dimensional case.

2.5.2 *Three-Dimensional Hollow Black Body*

We assume a three-dimensional hollow body featuring the size $V = L \times L \times L = L^3$. Now, electromagnetic radiation propagates in three dimensions, and the full wave equation (1.13) has to be solved. Making a separation ansatz

$$E(x, y, z) = E_x(x)E_y(y)E_z(z),$$

with $E_i \sim \sin(k_i \cdot i)$ and using the wave number k_i with $i = x, y, z$ one gets from the wave equation [7] the dispersion relation

$$\frac{\omega^2}{c_0^2} = k_x^2 + k_y^2 + k_z^2 = k^2, \tag{2.42}$$

with squared value of the wave vector $k^2 = |\boldsymbol{k}|^2$, and the wave vector $\boldsymbol{k}$. Now, as electromagnetic radiation can propagate in all spatial directions, we have to assume for each direction standing waves, and using the boundary conditions for each direction we get discrete wave numbers

$$k_i \cdot L = j_i \pi, \text{ with } i = x, y, z.$$

We get for (2.42),

$$\begin{aligned} \frac{\omega^2}{c_0^2} &= \left(\frac{j_x \pi}{L}\right)^2 + \left(\frac{j_y \pi}{L}\right)^2 + \left(\frac{j_z \pi}{L}\right)^2 \\ &= k^2. \end{aligned}$$

So, the mode number in one dimension gets in three dimensions a mode vector $\boldsymbol{\jmath}$, and we see

$$\jmath^2 = |\boldsymbol{\jmath}|^2 = j_x^2 + j_y^2 + j_z^2 = \left(\frac{kL}{\pi}\right)^2 = \left(\frac{2L}{\lambda}\right)^2 = \left(\frac{2\nu}{c_0} L\right)^2.$$

Evidently, this equation represents a sphere equation with the radius $j = \frac{2\nu}{c_0} L$.

Again, like in the one-dimensional case we calculate the number of modes. The modes are positive natural numbers $j_i \in \mathbb{N}_0$, and $j > 0$ describes an octant of a sphere. The polarization states are again two described by the degeneracy $p = 2$, and we assume the size of the hollow body to be much larger than the wavelength of the investigated radiation, with

$$L \gg \lambda \curvearrowright \nu \gg L, j \gg 1.$$

As a consequence, the mode number represents a very large number, and we can assume $j \in \mathbb{R}$ to be a continuum. The number of modes as a function of the frequency is given by

Mode number as function of frequency

$$N(\nu) = p\left(\frac{1}{8}\right)\frac{4\pi}{3} j^3 = \frac{\pi}{3}\left(\frac{2L}{c_0}\right)^3 \nu^3 = \frac{8\pi}{3}\frac{L^3}{c_0^3}\nu^3 \tag{2.43}$$

and as a function of the wave number by

Mode number as function of wave number

$$N(k) = p\frac{1}{8}\frac{4\pi}{3}\left(\frac{kL}{\pi}\right)^3 = p\frac{4\pi}{3}\left(\frac{kL}{2\pi}\right)^3 = \frac{p}{6}\frac{L^3}{\pi^2}k^3. \tag{2.44}$$

The spectral mode density is calculated by the derivative of the mode number

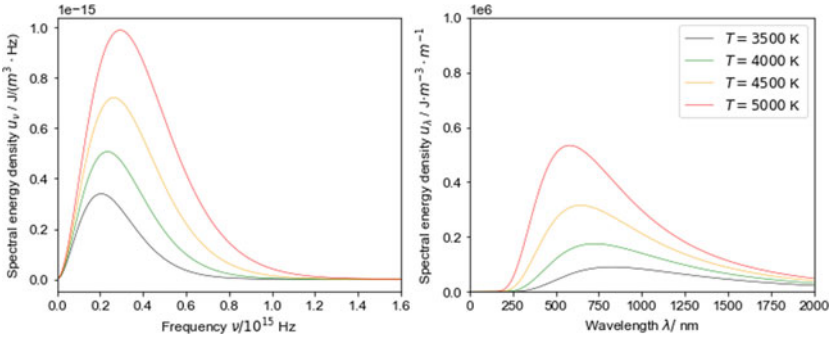
1e−15
Spectral energy density u_ν / J/(m^3 · Hz)
Frequency $\nu/10^{15}$ Hz
1e6
Spectral energy density u_λ / J·m^{-3} · m^{-1}
Wavelength λ/ nm
T = 3500 K
T = 4000 K
T = 4500 K
T = 5000 K

Fig. 2.8 Spectral energy density as a function of the frequency $u_\nu(\nu)$ (left) and as a function of the wavelength $u_\lambda(\lambda)$ (right) of a black body for different temperatures

Spectral mode density

$$n(\nu) = \frac{\partial N(\nu)}{\partial \nu} = 8\pi \frac{L^3}{c_0^3}\nu^2, \tag{2.45}$$

and represents the shell of a sphere with the radius j. The spectral energy density for a three-dimensional hollow body is given by

$$\begin{aligned} u(\nu) &= n(\nu)\frac{E_{therm}}{L^3} \\ &= 8\pi \frac{L^3}{c_0^3}\nu^2 \frac{\overline{\frac{h\nu}{e^{\frac{h\nu}{k_B T}} - 1}}}{L^3} \end{aligned}$$

representing Planck's law,

Spectral energy density as function of frequency—Planck's law

$$u_\nu(\nu) = \frac{8\pi h\nu^3}{c_0^3} \frac{1}{e^{\frac{h\nu}{k_B T}} - 1}. \tag{2.46}$$

See its distributions as a function of the frequency and the wavelength in Fig. 2.8. For increasing frequency the wavelength decreases, so $d\nu = -d\lambda$ holds and by the relation $u(\nu)d\nu = -u(\lambda)d\lambda$ one gets

$$\begin{aligned} u(\lambda(\nu)) &= -\frac{d\nu}{d\lambda}u(\nu) \quad \text{and with} \quad \nu = \frac{c_0}{\lambda} \text{ it results in} \\ &= \frac{c_0}{\lambda^2}u(\nu), \end{aligned}$$

Spectral energy density as a function of wavelength—Planck's law

$$u_\lambda(\lambda) = \frac{8\pi h c_0}{\lambda^5} \frac{1}{\exp\left(\frac{h c_0}{\lambda k_B T}\right) - 1}. \tag{2.47}$$

2.5.3 *High- and Low Photon Energy Limits*

Depending on the ratio between the photon energy and the thermal energy, two regimes can be determined for Planck's law.

Low Photon Energy and High Temperatures $h\nu \ll k_B T$

The exponential function of (2.46) can be approximated by the first two Taylor terms:

$$u(\nu) = \frac{8\pi h \nu^3}{c_0^3} \frac{1}{1 + \frac{h\nu}{k_B T} - 1}.$$

The spectral energy density scales now linear with the temperature, quadratic in frequency, and is called the *Rayleigh–Jeans law*,

Rayleigh–Jeans law

$$u(\nu) = \frac{8\pi}{c} \nu^2 k_B T. \tag{2.48}$$

Low Temperatures and High Photon Energy $h\nu \gg k_B T$

The exponential function dominates for $h\nu \gg k_B T$: $\exp(\frac{h\nu}{k_B T}) \gg 1$ making the "-1" negligible, and we get

Wien's!law

$$u(\nu) = \frac{8\pi h \nu^3}{c_0^3} \exp\left(-\frac{h\nu}{k_B T}\right). \tag{2.49}$$

The spectral energy density decays for large frequencies exponentially. This means that for small wavelengths the spectral energy density increases exponentially. This dependency is called *Wien's law*.

2.5.4 The Stefan–Boltzmann Law

The overall energy density of a body emitted at the temperature T is calculated by integration over all accessible frequencies

$$U(T) = \int_0^\infty u(\nu)d\nu = \int_0^\infty \frac{8\pi h\nu^3}{c_0^3} \frac{1}{\exp\left(\frac{h\nu}{k_B T}\right) - 1} d\nu,$$

and by substituting $x = h\nu/k_B T$ one gets

$$U(T) = \frac{8\pi k_B^4 T^4}{c_0^3 h^3} \underbrace{\int_0^\infty \frac{x^3}{\exp(x) - 1} dx}_{=\frac{\pi^4}{15}}$$

$$= \frac{8\pi^5 k_B^4}{15 c_0^3 h^3} T^4.$$

Stefan–Boltzmann law

The energy density of the radiation emitted by a black body at the temperature T is given by

$$U(T) = \frac{4}{c_0} \sigma_{SB}\, T^4 \tag{2.50}$$

with the Stefan–Boltzmann constant $\sigma_{SB} = \dfrac{2\pi^5 k_B^4}{15 c_0^2 h^3}$.

2.5.5 Wien's Displacement Law

Often, the maximum energy density is important to know when optical systems have to be designed. So, we have to take the derivative of the spectral energy density, here the one equation dependent on the wavelength, (2.47). One has to solve (numerically)

$$\frac{du(\lambda)}{d\lambda} = 0 \quad \text{and gets}$$

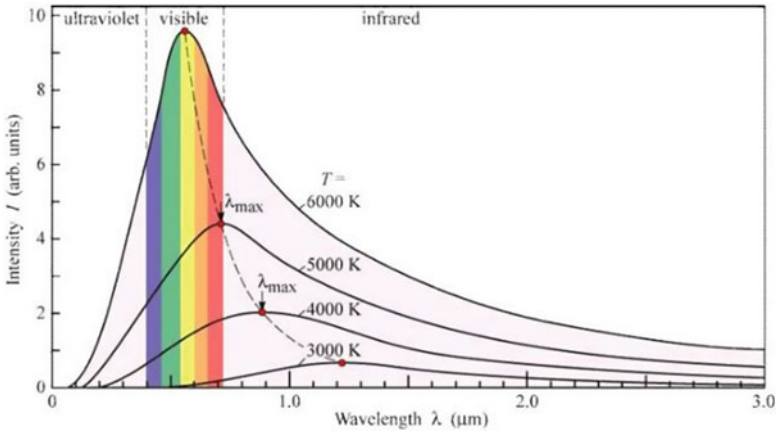

Fig. 2.9 Intensity of a black-body radiation for different temperatures [11]

Wien's Displacement Law

$$\lambda_{max} T = \frac{hc_0}{4.965 \cdot k_B} = 2.898 \cdot 10^{-3} \text{m} \cdot \text{K}. \tag{2.51}$$

The maximum wavelength scales inversely proportional to the temperature. The value 4.965 is a numerical result for the vanishing first derivative of the energy density $u(\lambda)$ (Fig. 2.9).

2.5.6 *Emitted Radiation Power*

Starting now from the spectral energy density $u(\nu)$, one gets different representations for the emitted energy; see Fig. 2.10 and the emitted power, and Fig. 2.11.

The projected area $dA_\perp$ given in the emitted energy and power denotes the "visible" area $A_\perp$ of the thermal emitter detected by an observer. The projected area element $dA_\perp$ is given by

$$dA_\perp = dA \cdot \cos\theta;$$

see Fig. 2.12.

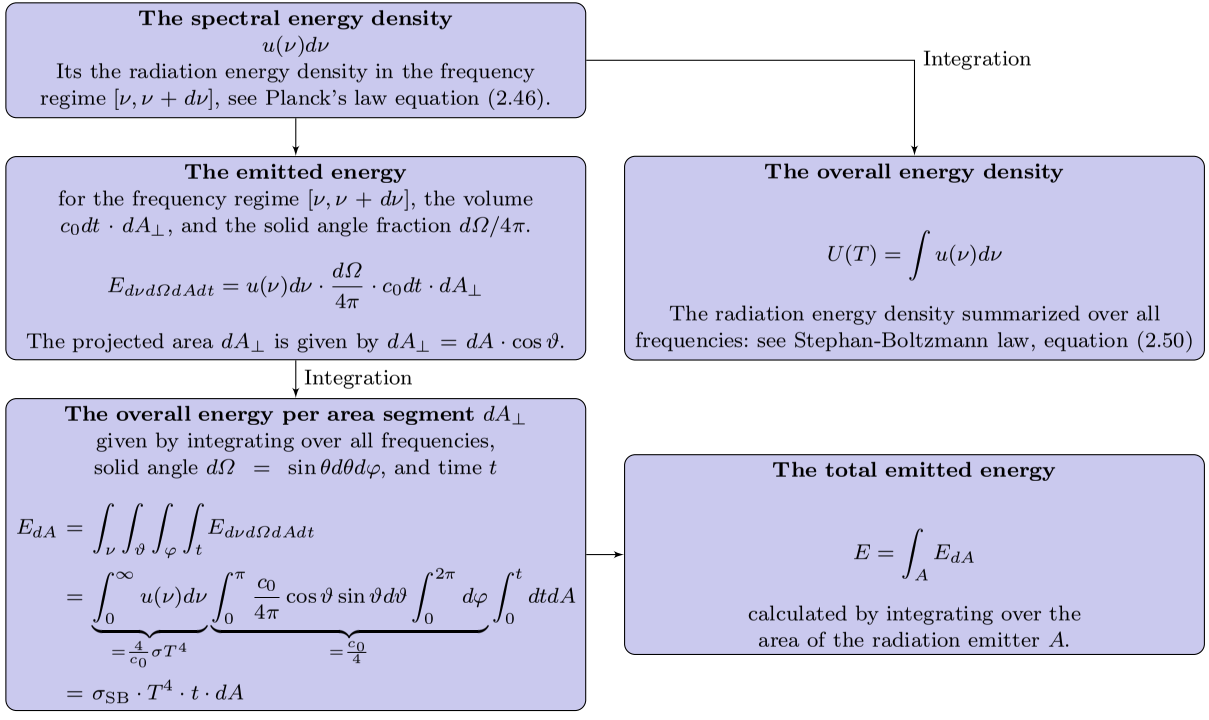
The spectral energy density
$u(\nu)d\nu$
Its the radiation energy density in the frequency regime $[\nu, \nu + d\nu]$, see Planck's law equation (2.46).
Integration
The emitted energy
for the frequency regime $[\nu, \nu + d\nu]$, the volume $c_0 dt \cdot dA_\perp$, and the solid angle fraction $d\Omega/4\pi$.
$E_{d\nu d\Omega dA dt} = u(\nu)d\nu \cdot \frac{d\Omega}{4\pi} \cdot c_0 dt \cdot dA_\perp$
The projected area $dA_\perp$ is given by $dA_\perp = dA \cdot \cos\vartheta$.
The overall energy density
$U(T) = \int u(\nu)d\nu$
The radiation energy density summarized over all frequencies: see Stephan-Boltzmann law, equation (2.50)
Integration
The overall energy per area segment $dA_\perp$
given by integrating over all frequencies, solid angle $d\Omega = \sin\theta d\theta d\varphi$, and time t
$E_{dA} = \int_\nu \int_\vartheta \int_\varphi \int_t E_{d\nu d\Omega dA dt}$
$= \underbrace{\int_0^\infty u(\nu)d\nu}_{=\frac{4}{c_0}\sigma T^4} \underbrace{\int_0^\pi \frac{c_0}{4\pi} \cos\vartheta \sin\vartheta d\vartheta \int_0^{2\pi} d\varphi}_{=\frac{c_0}{4}} \int_0^t dt dA$
$= \sigma_{SB} \cdot T^4 \cdot t \cdot dA$
The total emitted energy
$E = \int_A E_{dA}$
calculated by integrating over the area of the radiation emitter A.

Fig. 2.10 Block diagrams depicting the energy descriptions starting from the spectral energy density over the emitted energy per frequency, volume, and solid angle fraction to the overall energy per segment and finally the total emitted energy

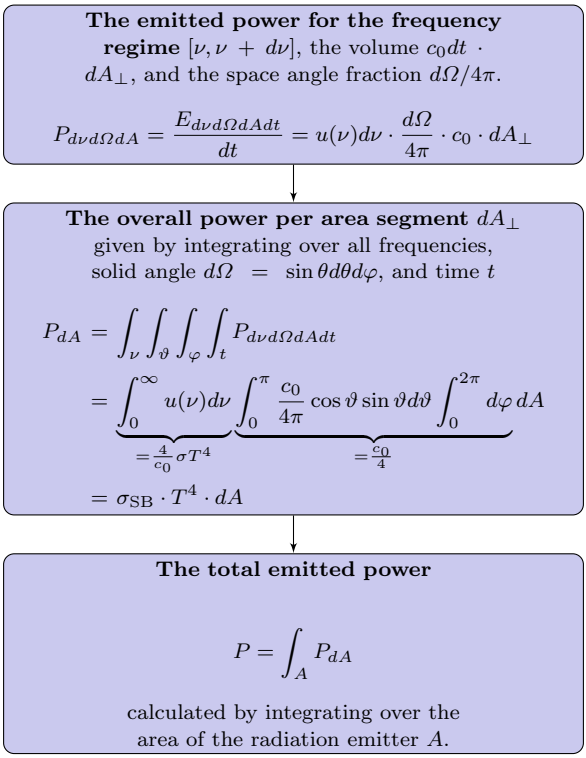
The emitted power for the frequency regime $[\nu, \nu + d\nu]$, the volume $c_0 dt \cdot dA_\perp$, and the space angle fraction $d\Omega/4\pi$.
$P_{d\nu d\Omega dA} = \frac{E_{d\nu d\Omega dA dt}}{dt} = u(\nu)d\nu \cdot \frac{d\Omega}{4\pi} \cdot c_0 \cdot dA_\perp$
The overall power per area segment $dA_\perp$ given by integrating over all frequencies, solid angle $d\Omega = \sin\theta d\theta d\varphi$, and time t
$P_{dA} = \int_\nu \int_\vartheta \int_\varphi \int_t P_{d\nu d\Omega dA dt}$
$= \underbrace{\int_0^\infty u(\nu)d\nu}_{=\frac{4}{c_0}\sigma T^4} \underbrace{\int_0^\pi \frac{c_0}{4\pi} \cos\vartheta \sin\vartheta d\vartheta \int_0^{2\pi} d\varphi}_{=\frac{c_0}{4}} dA$
$= \sigma_{SB} \cdot T^4 \cdot dA$
The total emitted power
$P = \int_A P_{dA}$
calculated by integrating over the area of the radiation emitter A.

Fig. 2.11 Block diagrams depicting the power descriptions starting from the emitted power per frequency, volume, and solid angle fraction to the overall power per segment and finally the total emitted power

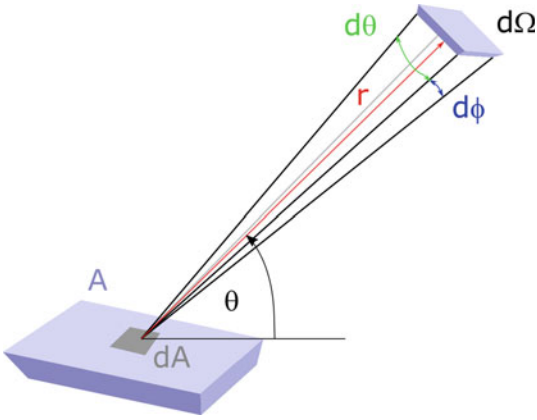

Fig. 2.12 Projected area of a thermal emitter, and solid angle of the emission

2.5.7 *Real Thermal Emitter*

We assumed for a black body that all emitted radiation is also absorbed completely by the atoms of the black body. In reality, not all absorbed radiation of a system is again re-emitted, but partly introduced into the atomic system, e.g. exiting its atomic or molecular components, or representing a system that is not in any thermodynamic equilibrium. Then heat energy dissipates.

Real emitter emitting in dependence of its temperature is described by its emissivity $\epsilon(T)$, and the emitted power is given by

Emitted thermal power

$$P_{real} = \epsilon(T) \cdot \sigma_{SB} \cdot A \cdot T^4. \tag{2.52}$$

Depending on the material and its temperature, ϵ can vary between 0.06 for cold iron and 0.91 for water or wood.

2.6 Laser-Generated X-Rays

Electrons accelerated in an electric field emit radiation; see Sect. 2.3. Laser radiation features oscillating electric fields. It is not remarkable that electrical charges in strong electric fields given, e.g. at high pulse energies and ultrashort pulse duration, emit radiation. But, increasing the intensities of the radiation above about 10^{11} W/cm^2, and allowing an interaction with electrons, ions in a laser-generated ablation plume results in the emission of X-rays with photon energies up to 10–15 keV; see Fig. 2.13.

By irradiating stainless steel with pulsed ultra-fast laser radiation setting the laser parameters enabling ablation, an X-ray spectrum is detected featuring a contin-

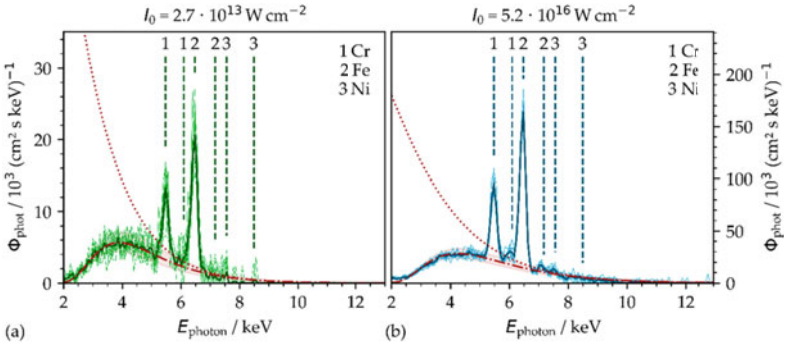

Fig. 2.13 X-ray photon flux Φ_γ for low peak intensity **a** $I_0 = 2.7 \times 10^{13}$ Wcm^{-2} and high peak intensity **b** $I_0 = 5.2 \times 10^{16}$ Wcm^{-2} (35° detection angle and 100 mm distance) [8]

uum spectrum with discrete characteristic lines of the elemental constituents of the steel; see Fig. 2.13a [8]. The spectral X-ray photon distribution follows a Maxwell–Boltzmann distribution, computed for vacuum by a dotted line representing the non-attenuated X-ray emission, and for ambient air by a dashed line, reproducing well the measured continuum spectrum. Due to absorption of the low energy part of the X-ray radiation, a hardening takes place, i.e. the low-energy fraction of the X-ray spectrum has been filtered (removed) resulting in an X-ray spectrum with high-energy photons only.

Increasing the peak intensity of the laser radiation about three orders of magnitude, from $I_0 = 2.7 \times 10^{13}$ Wcm^{-2} to $I_0 = 5.2 \times 10^{16}$ Wcm^{-2}, increases the X-ray-photon flux by a factor of 50, as well as the maximum flux to higher photon energies; see Fig. 2.13b.

The differences of the X-ray photon spectra can be attributed to the different mechanisms of laser–plasma interaction and electron plasma heating that largely depend on the irradiating conditions. So, radiation at lower intensity ($I_0 < 10^{14}$ Wcm^{-2}) will be primarily absorbed in an underdense corona region of the plasma by **inverse bremsstrahlung**. The excited electrons will be accelerated in the Coulomb field of the radiation resulting in the emission of a bremsstrahlung continuum. This free–free generation[4] of bremsstrahlung X-ray photons is inefficient and yields only a low amount of X-ray photons per laser pulse [8].

By contrast, **resonance absorption** is suggested as the dominant mechanism for radiation at high peak intensity, $I_0 > 10^{15}$ Wcm^{-2}. This collisionless process is most efficient for parallelly polarized laser radiation at a large incident angle with respect to the plasma surface. The laser energy will be transferred to the electron plasma in the region of the critical plasma density, where the electron plasma frequency equals the laser frequency. The highly excited plasma electrons interact with the bound electrons of the target atoms by collisional impact ionization, generating additional free electrons and leaving vacant energy levels at the atoms [8].

Important for safety at work is the determination of the X-ray dose. Thereby, threshold values for dose rates at the workplace are regulated by national law. Using ultra-fast pulsed laser radiation in the range from $0.24 < t_p < 10$ ps and ablating for example steel, the directional dose rate increases dramatically with the increasing intensity of the laser radiation; see Fig. 2.14. For example, an overall directional dose of $H = 1$ mSv is reached after 1000 h[5] when using ultra-fast laser radiation ablating steel with a peak intensity of about $I_0 = 20 \cdot 10^{13}$ W/cm^2.

High-repetition rate ultra-fast lasers up to the GHz and multi-pulse burst ultra-fast laser radiation are becoming common in industrial applications. There, these sources are used for ablation purposes. One observes that the interaction of the radiation with the plasma gets stronger, when tailored laser radiation is used, i.e. pulse burst with multi-pulses. Using laser radiation with repetition rates in the kHz to MHz featuring, e.g. double-pulses with a pulse separation time of about 440 ps, the photon flux of

[4] Free–free generation intends the interaction of free electrons with quasi-free electrons. As a three-body interaction is given, a little part of the kinetic energy is transferred to the participating ions.

[5] The natural overall dose each person gets by environmental influences is about 1 mS.

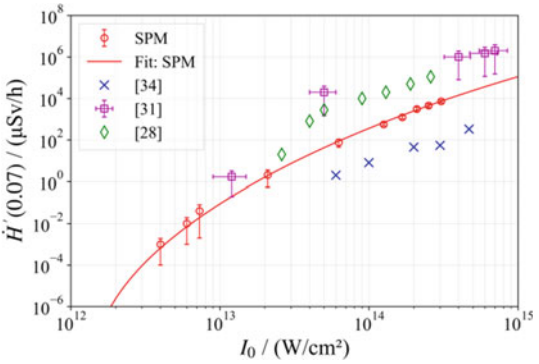

Fig. 2.14 Measured directional dose rate $\dot{H}'(0.07)$ for single-pulse ablation of stainless steel as a function of the intensity compared to the theoretical values (red line) as well as to the results of other authors [9]

X-ray is increased dramatically; see Fig. 2.15b. Further increase of the number of pulses in the burst to three or four pulses, see Fig. 2.15c, d, does not increase the photon flux. The interplay between the plasma generated by the first pulse with the following pulses results in a plasma changing its properties in space and time. As the radiation interacts not only with the plasma, but also with the substrate ablating additional material, this process is very complex.

By irradiating stainless steel using MHz bursts, a maximum X-ray dose rate of approximately $\dot{H}' = 35 \cdot 10^3 \mu\text{Sv/h}$ is measured, being five times higher than for single-pulse ablation at the same overall fluence; see Fig. 2.16. Again, at a number of pulses around two a maximum directional dose rate is detectable. These findings

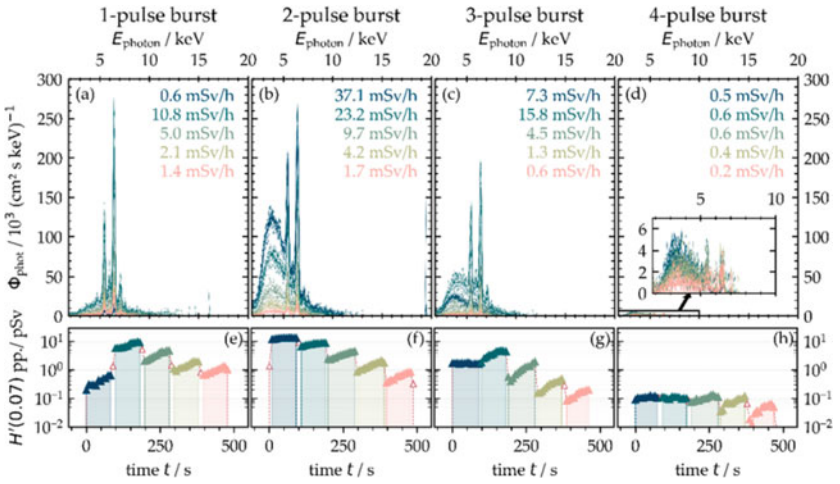
1-pulse burst
2-pulse burst
3-pulse burst
4-pulse burst
E_{photon} / keV
(a) 0.6 mSv/h 10.8 mSv/h 5.0 mSv/h 2.1 mSv/h 1.4 mSv/h
(b) 37.1 mSv/h 23.2 mSv/h 9.7 mSv/h 4.2 mSv/h 1.7 mSv/h
(c) 7.3 mSv/h 15.8 mSv/h 4.5 mSv/h 1.3 mSv/h 0.6 mSv/h
(d) 0.5 mSv/h 0.6 mSv/h 0.6 mSv/h 0.4 mSv/h 0.2 mSv/h
Φ_{phot} / 10^3 (cm² s keV)$^{-1}$
(e) (f) (g) (h)
$H'(0.07)$ pp./ pSv
time t / s

Fig. 2.15 The spectral X-ray photon flux and X-ray emission dose rate (**a**–**d**) as well as the X-ray dose per pulse (**e**–**h**) as a function of time, representing the number of irradiations (scan crossings). The intra-burst pulse number was varied between 1 (**a**) and 4 (**d**). (burst repetition frequency f_p= 400 kHz monitored at 100 mm distance, 35° detection angle) [8]

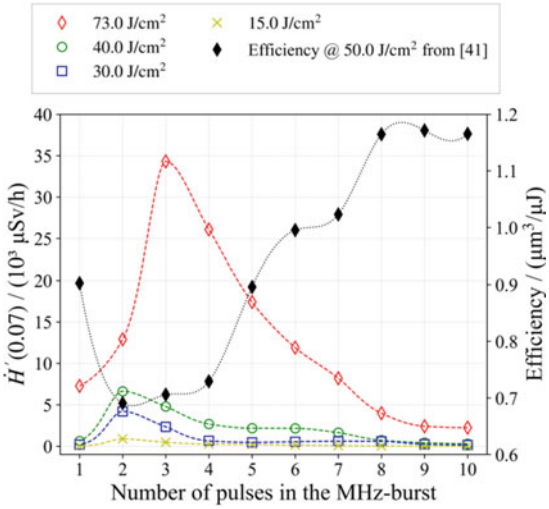

Fig. 2.16 X-ray dose rates $\dot{H}'(0.07)$ and the ablation efficiency at a total fluence of $H = 50\ \mathrm{Jcm}^{-2}$ per burst using the a multi-pulse burst as a function of the total fluence per burst and the number of pulses with a pulse duration of 0.24 ps. The determined X-ray dose rates correspond to the left ordinate and the ablation efficiencies (black dotted graph) to the right ordinate. The dashed lines are used to guide the eye [9]

make the usage of laser radiation in material processing applications more elaborate, as additional protection against X-ray radiation has to be added. Commonly, using steel as walls for the shielding of laser radiation, also the X-rays can be blocked efficiently, assuring safety.

2.7 Concluding Remarks

This section has shown that the dynamics of a free electron in an electromagnetic field has to be calculated with respect to the Maxwell equations. An electron at rest is accelerated in an electromagnetic field and gains energy from it. But in the case of a temporally limited lasting electromagnetic field (a so-called electromagnetic pulse) after the interaction with the field, the electron returns to rest, again. The energy of the electron is dissipated back into the field by emitted radiation. As one important consequence, accelerated free charges emit electromagnetic radiation.

The special case of a periodic oscillation of a charge results in the emission of radiation in the far field as spherical electromagnetic waves. This case is called also the dipole emission. Its directional radiation characteristics will be important for the description of the interaction of radiation with non-free electrons, so-called bounded electrons, especially for atoms, molecules, and condensed matter. We will be able to discuss the dipole emission of atoms and molecules, so-called elastic scattering, and will see also there the emitted power scales with the fourth power in the angular frequency.

The statistical description of atoms oscillating due to their temperature in condensed matter result in Planck's law for black-body radiation, as well as the Stefan–

Boltzmann law. Also, using ultra-fast laser radiation induces fast oscillations of electrical charges in a plasma inducing X-ray generation. As high-energy electrons are involved, complex secondary processes, like impact ionization, take place.

References

1. F.J. Duarte, *Quantum Optics for Engineers* (CRC Press, 2017)
2. U. Hohenester, *Nano and Quantum Optics: An Introduction to Basic Principles and Theory* (Springer International Publishing, 2020)
3. B.R. Kusse, E.A. Westwig, *Mathematical Physics: Applied Mathematics for Scientists and Engineers* (Wiley-VCH Weinheim, 2011)
4. S. Brandt, H.D. Dahmen, *Elektrodynamik* (Springer, Heidelberg, 2005)
5. https://de.wikipedia.org/wiki/Duane-Hunt-Gesetz
6. C. Kittel, *Introduction to Solid State Physics*, 9th edn. (Wiley, 2018)
7. T. Fließbach, *Elektrodynamik* (Springer, Berlin Heidelberg, 2012)
8. J. Schille, S. Kraft, T. Pflug, C. Scholz, M. Clair, A. Horn, U. Loeschner, Study on x-ray emission using ultrashort pulsed lasers in materials processing. Materials **14**, 4537 (2021)
9. Daniel Metzner, Markus Olbrich, Peter Lickschat, Alexander Horn, Steffen Weißmantel, X-ray generation by laser ablation using MHz to GHz pulse bursts. J. Laser Appl. **33**, 032014 (2021)
10. https://qudev.phys.ethz.ch/content/science/BuchPhysikIV/PhysikIVch5.html
11. https://chriscolose.wordpress.com/2010/02/18/greenhouse-effect-revisited/

Part II
Interaction of Particles with Electromagnetic Radiation

This part of the book is dedicated to the interaction of single particles, like electrons, atoms, molecules, or atomic clusters. We will introduce in Chap. 3 a semi-classical model describing the movement of the electron, being free, quasi-free, or bounded. With this, we will have a dipole description of a charge, allowing to apply the dependencies derived in the previous part and being able to calculate the emitted differential power of the radiation.

It's a cloud to describe the interaction of radiation with atoms as an elastic scattering process thereby introducing a cross-section for scattering. Doing this we will now be able to describe the "efficiency" for scattering and can describe the Rayleigh, resonant, and Thomson scattering. We made all this from a classical point of view using the Maxwell equations and Newton's laws. Alternatively, elastic scattering can also be described by a quantum mechanical excitation of an atom at the ground state by absorption of one photon into an excited state, and afterward the emission of a photon with the same energy by the so-called spontaneous emission.

The next Chap. 4 will focus on inelastic scattering going hand-in-hand with the absorption of radiation. Many processes, like inverse Bremsstrahlung, Raman scattering, or photo-ionization can be named and are described. Also, the non-linear processes are described, as using laser radiation these processes get probable. Thereby we will talk about tunnel- and multi-photon ionization and handle with the Keldysh parameter. As a specialty using intense ultra-fast laser radiation, above-threshold multi-photon ionization allowing to generate higher harmonics of the radiation will be discussed. Compton scattering and pair production close this part, being of interest for high-energy radiation, like X-ray or gamma radiation.

At the end of this part of the book, we start in Chap. 5 to increase the number of particles interacting with radiation. Therefore, we introduce the attenuation coefficient of dense matter and deduce the first time Lambert–Beer's law. As a preparation for the interaction with condensed matter, we increase here the particle density reaching a level, where coherent scattering takes place, distinguishing the scattering of light at clouds from the incoherent scattering at the molecules of the surrounding ambient gas.

Chapter 3
Elastic Scattering at Charged Particles

Abstract The interaction of charged particles with electromagnetic radiations describes the reaction of charges when forces due to the electric and magnetic fields are present. In the following sections, the interaction of one electron is described first. Therefore, we will realize that free electrons oscillate by the interaction with electromagnetic radiation. For the sake of simplicity, we will start over with bounded electrons. Many free charges, like electrons, represent possibly a plasma state or metal, and its dynamics has to be described by magneto-hydrodynamics, but this will not be the scope of this book.

3.1 Free Electron

Now we recover the discussions started in Sect. 2.3 on the free electron being accelerated in an external electromagnetic field. We discussed in the last chapter the acceleration of free charges and found the consequence of the emission of electromagnetic radiation. Now, looking again at the equation of motion, see (2.2), the equation has in order to fulfill energy conservation to be expanded by an energy drain term. Typically, in classical mechanics, an energy drain is represented by a dissipative force, also called a friction or a perturbance.

This means that we have to deduce a perturbance, i.e. the emission of radiation, to fulfill an energy drain for a free electron, represented, e.g. by a velocity dependent friction force

$$\boldsymbol{F}_{\mathrm{em}} = -m_{\mathrm{e}}\Gamma_{\mathrm{em}}\boldsymbol{v},$$

with Γ_{em} being a damping coefficient. A free electron fulfills an oscillatory movement when driven by an external force here given by the electric field of the radiation. The equation of motion of an electron looks now like

$$m_{\mathrm{e}}\ddot{\boldsymbol{r}}_0 + m_{\mathrm{e}}\Gamma_{\mathrm{em}}\dot{\boldsymbol{r}}_0 = -e\boldsymbol{E}_0\exp(-i(\omega t - \boldsymbol{k}\cdot\boldsymbol{r}_0)), \tag{3.1}$$

where $\boldsymbol{E}_0$ represents the constant electric field vector and ω the angular frequency of the external electromagnetic wave.

© Springer Nature Switzerland AG 2022

A. Horn, *The Physics of Laser Radiation–Matter Interaction*,
https://doi.org/10.1007/978-3-031-15862-9_3

3.1.1 Radiation Force

Next, before we solve the differential equation (3.1), we have to quantify the damping coefficient Γ_{em}. First, an electron perturbated by the external electromagnetic field is periodically accelerated and emits electromagnetic radiation. The emission is proportional to the squared averaged acceleration, see (2.19). Second, the averaged emitted power is also equal to the averaged emitted power of a dipole, see (2.32). This fact can easily be seen by writing a time-dependent dipole moment of the oscillating electron

$$\boldsymbol{d} = \boldsymbol{d}_0 \cos(\omega t) = q_{\mathrm{e}} \boldsymbol{r}_0 \cos(\omega t) = q_{\mathrm{e}} \boldsymbol{r}(t).$$

One gets on this way a time-dependent vector of the location, the velocity and the acceleration of an electron by

$$\begin{aligned} \boldsymbol{r}(t) &= \boldsymbol{r}_0 \cdot \cos(\omega t) \\ \Rightarrow \quad \ddot{\boldsymbol{r}} &= \boldsymbol{a} = -\omega^2 \boldsymbol{r}(t). \end{aligned}$$

We see again that the power of the emitted radiation scales, as given in (2.19) and (2.32), by the squared static dipole moment $\boldsymbol{d}_0 = q_{\mathrm{e}} \boldsymbol{r}_0$ and the fourth power in the angular frequency, or by the squared acceleration

$$\langle P \rangle \propto \omega^4 \boldsymbol{d}_0{}^2 = q_{\mathrm{e}}^2 \boldsymbol{a}^2.$$

The emitted radiation power of the system is given by the scalar product of the velocity of the electron with all acting forces

$$P = \boldsymbol{F}_{\mathrm{rad}} \cdot \boldsymbol{v}. \tag{3.2}$$

An accelerated electron emits radiation, so the averaged power using a radiation force should not vanish, and using (2.19) is given by

$$\begin{aligned} \langle P \rangle &= \langle \boldsymbol{F}_{\mathrm{rad}} \cdot \boldsymbol{v} \rangle \\ &\overset{(2.19)}{=} -\frac{q_{\mathrm{e}}^2 \mu_0}{6\pi c_0} \langle \boldsymbol{a}^2 \rangle \\ &= -\frac{q_{\mathrm{e}}^2 \mu_0}{6\pi c_0} \langle \dot{\boldsymbol{v}}^2 \rangle. \end{aligned} \tag{3.3}$$

The negative sign here denotes that electromagnetic radiation is emitted with the given power representing a power drain. Looking closer at the term $\langle \boldsymbol{a}^2 \rangle = \langle \dot{\boldsymbol{v}}^2 \rangle$, one can rewrite this equation by partial integration

$$\langle \dot{\boldsymbol{v}}^{\,2} \rangle = \frac{1}{T} \int_t^{t+T} \mathrm{d}t' \, \dot{\boldsymbol{v}} \cdot \dot{\boldsymbol{v}}$$
$$= \frac{1}{T} \left[\dot{\boldsymbol{v}} \cdot \boldsymbol{v}|_t^{t+T} - \int_t^{t+T} \mathrm{d}t' \, \ddot{\boldsymbol{v}} \cdot \boldsymbol{v} \right].$$

Due to the anti-symmetry resulting from the scalar product of the velocity with the location vectors, $\dot{\boldsymbol{v}} \cdot \boldsymbol{v}$ vanishes over one period getting

$$\langle \dot{\boldsymbol{v}}^{\,2} \rangle = -\langle \ddot{\boldsymbol{v}} \cdot \boldsymbol{v} \rangle.$$

Comparing the last equation with (3.3), one gets $\langle \dot{\boldsymbol{v}}^{\,2} \rangle = -\langle \ddot{\boldsymbol{v}} \cdot \boldsymbol{v} \rangle$ and inserting it into (3.3), one gets for the time-averaged emitted power

$$\langle P \rangle = \frac{q_\mathrm{e}^2 \mu_0}{6\pi c_0} \langle \ddot{\boldsymbol{v}} \cdot \boldsymbol{v} \rangle.$$

We extract now, comparing $\langle P \rangle = \langle \boldsymbol{F}_\mathrm{rad} \cdot \boldsymbol{v} \rangle$ with the last equation, the radiation force of a driven oscillating electron

Radiation force of a driven electron

$$\boldsymbol{F}_\mathrm{rad} = \frac{q_\mathrm{e}^2 \mu_0}{6\pi c_0} \ddot{\boldsymbol{v}}. \tag{3.4}$$

This force is proportional to the change in acceleration of the electron. The new trajectory of the free electron is described by a perturbation, like the vector $\boldsymbol{r}(t)$. The first time derivative of the electron location is given by

$$\boldsymbol{v} = \frac{\mathrm{d}\boldsymbol{r}}{\mathrm{d}t}.$$

The motion of the electron is periodic, so we can make the ansatz for the velocity of the oscillating electron by $\boldsymbol{v} = \boldsymbol{v}_0 e^{i\omega \cdot t}$ calculating its second derivative getting

$$\ddot{\boldsymbol{v}} = -\omega^2 \boldsymbol{v}.$$

The radiation force can now be rewritten using the classical description of a frictional force being proportional to the velocity

$$\boldsymbol{F}_\mathrm{rad} = -m_\mathrm{e} \Gamma_\mathrm{em} \boldsymbol{v},$$
$$= -\frac{q_\mathrm{e}^2 \mu_0}{6\pi c_0} \omega^2 \boldsymbol{v}.$$

One reads from that last equation the damping coefficient for a free electron given by

Damping coefficient for a free electron

$$\Gamma_{\mathrm{em}}(\omega) = \frac{q_{\mathrm{e}}^2 \mu_0 \omega^2}{6\pi c_0 m_{\mathrm{e}}}. \tag{3.5}$$

A value for the damping coefficient can now be calculated inserting all natural constants for electromagnetic radiation with an angular frequencies $\omega \approx 10^{14}$ Hz getting $\Gamma_{\mathrm{em}} \approx 10^5$ 1/s. The damping constant represents a frequency much smaller than the angular frequency of the radiation

$$\Gamma_{\mathrm{em}}(\omega) \ll \omega,$$

confirming the perturbation character of the dissipative radiation force $\boldsymbol{F}_{\mathrm{rad}}$, and of the emission of electromagnetic radiation by the interaction of an external field with a free electron.

3.1.2 External Field

The external force can be represented by a deliberate electromagnetic field acting on the charged particle, here given by the electron with $q = -e$

$$\boldsymbol{F}_{\mathrm{em}} = -e\boldsymbol{E}_0 \exp(-i(\omega t - \boldsymbol{k} \cdot \boldsymbol{r}_0)).$$

The amplitude of the electron trajectory $\boldsymbol{r}_0$ is assumed to be a_0, and is expected here to be much smaller than the wavelength of the external electric field strength $r_0 = a_0 \ll \lambda$, see first calculations in Sect. 2.3 by (2.3). This approximation is valid for all electromagnetic radiation, from radio waves to UV waves. Using the wave number $k = 2\pi/\lambda$, one gets for the electric field, applying an approximation for the exponential function, a plane wave

$$\begin{aligned}
\boldsymbol{E} &= \boldsymbol{E}_0 e^{-i\omega\cdot t} e^{i\frac{2\pi a_{\mathrm{B}}}{\lambda}\hat{k}\cdot\hat{a}_0} \\
&= \boldsymbol{E}_0 e^{-i\omega\cdot t}\left[1 + \mathcal{O}\left(\frac{a_0}{\lambda}\right)\right] \\
&\approx \boldsymbol{E}_0 e^{-i\omega\cdot t}.
\end{aligned}$$

As shown in Fig. 3.1, due to the small amplitudes a_0 compared to the applied wavelength λ of the radiation the external field can be represented now as a plane wave

$$\boldsymbol{E} = \boldsymbol{E}_0 e^{-i\omega t}.$$

We get finally the equation of motion for a free electron interacting with an external field by

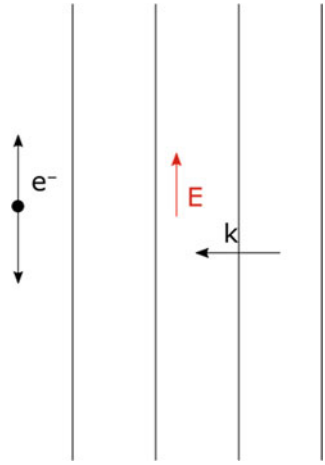

Fig. 3.1 Free electron interacting with an external electric field

Equation of motion of a free electron

$$m_e \ddot{\boldsymbol{r}}_0 + m_e \Gamma_{em} \dot{\boldsymbol{r}}_0 = -e\boldsymbol{E}_0 e^{-i\omega t}. \tag{3.6}$$

3.1.3 Dipole Moment and Differential Power per Solid Angle

The equation of motion determined in the last section represents a damped motion of a particle with a harmonic driving force with an angular frequency ω. As known from classical mechanics, this equation represents a linear inhomogeneous differential equation of second order with constant coefficients. Usually, a general solution for the homogeneous differential equation has to be found first, and additionally, a special solution for the inhomogeneous one is needed too. Here, the homogeneous solution due to the damping term vanishes for large times, so that only the special solution is of interest for a stationary process.

We take the exponential ansatz $\boldsymbol{r}_0 = \boldsymbol{a}e^{-i\omega t}$ with a constant amplitude vector $\boldsymbol{a} = \text{const}$, and calculating its derivatives, one gets the characteristic equation for the differential equation (3.6)

$$\left(-\omega^2 - i\omega\Gamma_{em}\right)\boldsymbol{a} = -\frac{e}{m_e}\boldsymbol{E}.$$

The amplitude vector $\boldsymbol{a}$ of an electron, driven by an external field $\boldsymbol{E}$ gets to

$$\boldsymbol{a} = -\frac{e}{m_e}\frac{1}{\left(-\omega^2 - i\omega\Gamma_{em}\right)}\boldsymbol{E} \tag{3.7}$$

and the trajectory of free electron results using the plane wave approximation described in Sect. 3.1.2 to

$$\boldsymbol{r}_0(t) = \frac{e}{m_e\omega}\frac{1}{(\omega + i\,\Gamma_{em})}\boldsymbol{E}_0 e^{-i\omega t}.$$

One sees that this trajectory represents a periodic oscillation of the electron induced by the external field with the frequency ω. The amplitude scales by the reciprocal frequency. We know that this periodic movement can be described by a time-varying dipole moment. As defined, the dipole moment of a charged particle is given by (2.23), and gets in our case to

$$\begin{aligned}\boldsymbol{d}(t) &= -e\boldsymbol{r}_0(t)\\ &= -e\boldsymbol{a}e^{-i\omega t} = \boldsymbol{d}_0 e^{-i\omega t}\\ &= \frac{e^2}{m_e\omega}\frac{1}{(\omega + i\,\Gamma_{em})}\boldsymbol{E}_0 e^{-i\omega t}.\end{aligned}$$

Introducing the electric polarizability

$$\alpha_e = \frac{e^2}{m_e\omega}\frac{1}{(\omega + i\,\Gamma_{em})}, \tag{3.8}$$

we see that the induced dipole moment is collinear to the inducing electric field, and is directly proportional to the electric field strength

$$\boldsymbol{d}(t) = \alpha_e \boldsymbol{E}. \tag{3.9}$$

So, the free electron interacting with the external field exhibits a time-dependent dipole moment, which in consequence emits electromagnetic radiation as spherical waves in the far field, see (2.30) and (2.31). The averaged power per solid angle of the emitted radiation can be expressed by

$$\begin{aligned}\frac{\mathrm{d}\langle P\rangle}{\mathrm{d}\Omega} &\overset{(2.31)}{=} \frac{c_0 k^4}{32\pi^2\varepsilon_0}|\boldsymbol{d}_0|^2\,\sin^2\vartheta\\ &= \frac{c_0 k^4}{32\pi^2\varepsilon_0}|\alpha_e|^2\,|\boldsymbol{E}_0|^2\sin^2\vartheta\\ &= \frac{c_0 k^4}{32\pi^2\varepsilon_0}\left|\frac{e^2}{m_e\omega}\frac{1}{(\omega + i\,\Gamma_{em})}\right|^2|\boldsymbol{E}_0|^2\sin^2\vartheta.\end{aligned}$$

Averaged emitted power per solid angle

$$\frac{\mathrm{d}\langle P\rangle}{\mathrm{d}\Omega} = \frac{c_0\,\omega^4}{32\pi^2\varepsilon_0}\left(\frac{e^2}{m_\mathrm{e}c_0^2\omega}\right)^2 \frac{1}{\omega^2+\Gamma_\mathrm{em}^2}\,|\boldsymbol{E}_0|^2\sin^2\vartheta \tag{3.10}$$

In summary, we can state that:

- The incoming electromagnetic wave induces a time-dependent, periodic oscillating dipole moment of the free electron.
- The periodic oscillating electronic dipole emits electromagnetic radiation as spherical waves.
- The emitted electromagnetic radiation features the same frequency (or wavelength) as the inducing one and has the same photon energy. This process is called *elastic scattering of electromagnetic radiation*, or elastic photon scattering.
- The emission characteristics of the oscillating free electron is equivalent to the one of a time-dependent dipole: No emission in the direction of the electric field strengths, and a radial symmetric maximal emission orthogonal to the electric field strength vector at $\vartheta = \pi/2$.
- The elastic scattering of unpolarized electromagnetic radiation at such electrons results in dependence of the polarization grade/state on the observation point: orthogonal observation to a scatterer results in fully linear polarized scattered radiation. For all other observation angles, a mixed polarization state results.

3.2 Bounded Electron

Electrons are often bounded to protons and neutrons forming an electrically neutral atom. The electrical neutrality depends on the distance of the electrons from the considered atom, meaning that at distances close to the region occupied by the electrons, electrical fields are still given. This states that an external electromagnetic field can, even at a small field strength, interact with the outer electrons of an atom or a molecule, the so-called *weakly bounded electrons*, or also called *valence electrons*. Electrons closer to the nucleus are shielded by the outer electrons, so they are not interacting significantly with external radiation at small field strengths.

3.2.1 Equation of Motion of a Weakly-Bounded Electron

Knowing the position of the electron as a function of time, one can get the acceleration, and in consequence as we have seen in the section before, the emitted power of the radiation. In order to describe the trajectory of an electron in an atom (classical approach), an equation of motion has to be defined therefore.

Before we start investigating an electron bounded to an atom, let us first have a look on a moving electron with constant velocity $|\boldsymbol{v}|$ in a homogeneous and constant magnetic field $\boldsymbol{B}$. The velocity of the electron is directed orthogonally to the magnetic field, i.e. $\boldsymbol{v} \perp \boldsymbol{B}$, so that from the Lorentz force

$$\boldsymbol{F}_{\mathrm{L}} = q_{\mathrm{e}} \boldsymbol{v} \times \boldsymbol{B}$$

one gets a vanishing power

$$P = \boldsymbol{F}_{\mathrm{L}} \cdot \boldsymbol{v} = 0,$$

expressing that the electron is moving on a circular trajectory, but not loosing any "mechanical" energy per time, and sustaining at an unchanged rotational radius.

As we learned in Sect. 2.4.2, a free electron on a circular trajectory represents an accelerated charged particle, and in consequence, it emits electromagnetic radiation. This, in turn, represents a continuous energy loss of the rotating electron, contradicting the aforementioned consideration of no-power loss of a particle moving in a magnetic field. This means that there has to be added an additional force describing the dissipative process during the curling of the electron. Experimentally, one observes that a charged particle on a circular trajectory looses energy, resulting in the case of an electron moving in a magnetic field in a spiral trajectory with decreasing radius.

On contrary, from quantum mechanics, we know that a bounded electron, even moving on a circular trajectory, does not emit any electromagnetic energy at all. The Bohr's model describes a circular trajectory of an electron in the potential of a positively charged nucleus, being energy-fixed on discrete, so-called quantized energy levels, representing the main quantum number n. Due to the Heisenbergs uncertainty principle in Bohr's model, only a discrete transition with a quantized angular momentum (or energy), given by

$$L = m_{\mathrm{e}} v r = n\hbar = L_n \tag{3.11}$$

is allowed with a discrete quantum number $n \in \mathbb{N}$ (Bohr's postulate, see Infobox on next page). On the other hand, one calculates, assuming an equilibrium between the Coulomb and the centrifugal forces, both radial oriented,

$$\begin{aligned} F_{\mathrm{C}} &= F_{\mathrm{Z}} \\ \frac{1}{4\pi\varepsilon_0}\frac{e^2}{r^2} &= \frac{m_{\mathrm{e}} v^2}{r} \end{aligned}$$

the classical radius of a hydrogen atom

Classical radius of hydrogen atom

$$r_\mathrm{e} = \frac{1}{4\pi\varepsilon_0}\frac{e^2}{m_\mathrm{e}v^2}. \tag{3.12}$$

Inserting the quantized velocity taken from (3.11), one gets the radius of a hydrogen-like atom

$$r_\mathrm{e}^n = \frac{n^2\hbar^2 4\pi\varepsilon_0}{e^2 m_\mathrm{e}},$$

with the main quantum number n representing the trajectories of the electrons, or the so-called shells: the K-shell is given by the quantum number $n = 1$, the L-shell by $n = 2$, the M-shell by $n = 3$, and so on. For $n = 1$, one gets the Bohr radius, the Bohr velocity, and acceleration of an electron within a hydrogen atom, and the angular frequency there:

Bohr radius–velocity–acceleration

$$r_\mathrm{B} = \frac{\hbar^2 4\pi\varepsilon_0}{e^2 m_\mathrm{e}} \tag{3.13}$$

$$v_\mathrm{B} = \frac{e^2}{4\pi\varepsilon_0\hbar} \tag{3.14}$$

$$a_\mathrm{B} = \frac{4\pi\varepsilon_0\hbar^2}{e^2 m_\mathrm{e}} \tag{3.15}$$

$$\text{and} \quad \omega_0 = \frac{v_\mathrm{B}}{a_\mathrm{B}}. \tag{3.16}$$

One calculates easily that the Bohr radius results to $a_\mathrm{B} = 0.53 \cdot 10^{-10}$ m, the Bohr velocity $v_\mathrm{B} = \alpha \cdot c_0 \approx 2 \cdot 10^6$ m/s with the hyperfine structure constant $\alpha \approx 1/137$, and the angular frequency $\omega_0 = 4.1 \cdot 10^{16}$ Hz.

Info Box: The Bohr's postulate

We have to clarify the contradiction that, on the one hand, a bounded electron moving on a circular trajectory within an atom does not emit electromagnetic radiation, and on the other hand, an accelerated electron emits radiation.
Due to the Coulomb force acting between the electron and the proton(s) of the atomic core, a quantum mechanical description results, as the electron described as a wave packet, features now discrete energy. A transition to another energy level is only possible by absorption of specific energy portions. Typical energy portions for atoms range in the 10 to 100 eV-regime. This means that for visible radiation, no excitation of an atom by absorption of radiation is possible.
A bounded electron being accelerated in an external electromagnetic field will follow this field by the acting force of the field. The motion around the atom is little perturbated by this external field, meaning also that the energy absorbed by the electron is much smaller than the excitation energy from a lower shell into a higher shell.
A time-limited perturbance on the electron, e.g. induced by an external electromagnetic field, increases the kinetic energy of the electron temporally, but being accelerated, the electron emits very quickly the energy by emission of electromagnetic radiation resulting in average no absorbed energy. Thereby the Heisenberg uncertainty principle holds, as the temporal energy increase ΔE is emitted quickly in the time Δt maintaining $\Delta E \cdot \Delta t \leq h$.
The Bohr's postulate is fulfilled while the averaged energy of the electron is unchanged.

This means that we have for a perturbance, i.e. the emission of radiation, to define an energy drain for the bounded electron, represented, e.g. by a velocity dependent friction force

$$\boldsymbol{F}_{\mathrm{em}} = -m_{\mathrm{e}} \Gamma_{\mathrm{em}} \boldsymbol{v}, \tag{3.17}$$

with Γ_{em} being the damping coefficient for emission. The electron fulfills a circular movement, given by a harmonic force being proportional to $\omega_0^2 \boldsymbol{r}_0$ with an external force given by the electric field of the radiation. The equation of motion of the electron looks now like

$$m_{\mathrm{e}} \ddot{\boldsymbol{r}}_0 + m_{\mathrm{e}} \Gamma_{\mathrm{em}} \dot{\boldsymbol{r}}_0 + m_{\mathrm{e}} \omega_0^2 \boldsymbol{r}_0 = -e \boldsymbol{E}_0 \exp(-i(\omega t - \boldsymbol{k} \cdot \boldsymbol{r}_0)), \tag{3.18}$$

where ω_0 represents the harmonic angular frequency of the electron in the atom, E_0 the constant electric field vector, and ω the angular frequency of the external electromagnetic wave. The circular motion of the electron is represented by the radius $\boldsymbol{r}_0$.

3.2.2 Radiation Force

Again, like for the free electron, we have to quantify the damping coefficient Γ_{em}, comparable to Sect. 3.1.1. Also, here the power of the emitted radiation scales, as given in (2.19) and (2.32) with the static dipole moment $\boldsymbol{d}_0 = q_\mathrm{e}\boldsymbol{r}_0$ with the fourth power in the angular frequency, or with the squared acceleration

$$\langle P\rangle \propto \omega^4 \boldsymbol{d}_0{}^2 = q_\mathrm{e}^2 \boldsymbol{a}^2.$$

The power of the system consisting of an atom with a bounded electron is given by the scalar product of the velocity of the electron with all acting forces

$$P = \boldsymbol{v}\cdot(\boldsymbol{F}_C + \boldsymbol{F}_z + \boldsymbol{F}_\mathrm{rad}).$$

The Coulomb and centrifugal forces are radially oriented and perpendicular to the velocity vector of the electron, not contributing to the power of this system. On the contrary, an accelerated electron emits radiation, so the averaged power with a radiation force is non-zero, and using (2.19), is given again by (3.3),

$$\langle P\rangle = -\frac{q_\mathrm{e}^2\mu_0}{6\pi c_0}\langle \dot{\boldsymbol{v}}^2\rangle.$$

Similar to the free electron, we extract now using $\langle P\rangle = \langle \boldsymbol{F}_\mathrm{rad}\cdot\boldsymbol{v}\rangle$ the radiation force

Radiation force

$$\boldsymbol{F}_\mathrm{rad} = \frac{q_\mathrm{e}^2\mu_0}{6\pi c_0}\ddot{\boldsymbol{v}}, \tag{3.19}$$

being again proportional to the change in acceleration of the electron. The trajectory of the electron around the atom is described by an undisturbed circular motion given by $|\boldsymbol{r}_0| = a_\mathrm{B}$ equal to the Bohr radius, and a perturbation $\boldsymbol{r}'$ resulting in an overall trajectory $\boldsymbol{r} = \boldsymbol{r}_0 + \boldsymbol{r}'$, with $|\boldsymbol{r}'| \ll |\boldsymbol{r}_0|$. The first time derivative can be approximated by the velocity of the electron around the atom, i.e. Bohr velocity, see (3.14)

$$\boldsymbol{v} = \frac{\mathrm{d}\boldsymbol{r}}{\mathrm{d}t} = \frac{\mathrm{d}\boldsymbol{r}_0}{\mathrm{d}t} + \mathcal{O}(\frac{\boldsymbol{r}'}{r_0}) \approx \boldsymbol{v}_0.$$

The motion of the electron is periodic, so we can make the ansatz for the velocity by $\boldsymbol{v} = \boldsymbol{v}_0 e^{i\omega_0\cdot t}$ calculating the second derivative getting $\ddot{\boldsymbol{v}} = -\omega_0^2\boldsymbol{v}$. The radiation force can now be rewritten using the classical description of a frictional force being proportional to the velocity

$$\begin{aligned}\boldsymbol{F}_{\text{rad}} &= -m_{\text{e}}\Gamma_{\text{em}}\boldsymbol{v},\\ &= -\frac{q_{\text{e}}^2\mu_0}{6\pi c_0}\omega_0^2\boldsymbol{v}.\end{aligned}$$

One reads from that last equation the damping coefficient to

Damping coefficient of a weakly-bounded electron

$$\Gamma_{\text{em}} = \frac{q_{\text{e}}^2\mu_0\omega_0^2}{6\pi c_0 m_{\text{e}}}. \tag{3.20}$$

It should be noted that the difference in this damping constant is composed of constants, contrary to the damping constant of a free electron being dependent on the angular frequency of the external force, see (3.5). A value for the damping coefficient can now be calculated by inserting all natural constants getting $\Gamma_{\text{em}} \approx 10^{11}$ 1/s. It represents a frequency much smaller than the atomic angular frequency

$$\Gamma_{\text{em}} \ll \omega_0,$$

confirming the perturbation character of the dissipative radiation force $\boldsymbol{F}_{\text{rad}}$, and of the emission of electromagnetic radiation by the interaction of an external field with the hydrogen atom.

3.2.3 External Field

The external force can be represented by a deliberate electromagnetic field, here given by

$$\boldsymbol{F}_{\text{em}} = -e\boldsymbol{E}_0 e^{-i(\omega t - \boldsymbol{k}\cdot\boldsymbol{r}_0)}.$$

The radius of the electron trajectory $\boldsymbol{r}_0$ is assumed to be the Bohr radius a_{B}, and is expected here to be much smaller than the wavelength of the external electric field strength $r_0 = a_{\text{B}} \ll \lambda$. This approximation is valid for all electromagnetic radiation, from the radio waves to the X-rays.

Using $k = 2\pi/\lambda$, one gets for the electric field using an approximation for the exponential function

$$\begin{aligned}\boldsymbol{E} &= \boldsymbol{E}_0 e^{-i\omega\cdot t} e^{i\frac{2\pi a_{\text{B}}}{\lambda}\hat{k}\cdot\hat{a}_{\text{B}}}\\ &= \boldsymbol{E}_0 e^{-i\omega\cdot t}\left[1 + \mathcal{O}\left(\frac{a_{\text{B}}}{\lambda}\right)\right]\\ &\approx \boldsymbol{E}_0 e^{-i\omega\cdot t}\end{aligned}$$

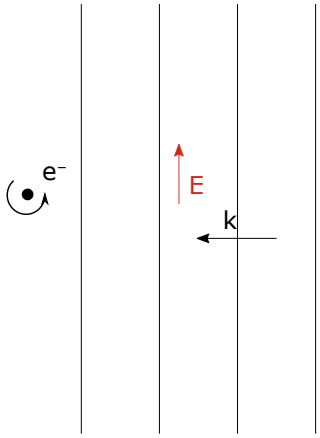

Fig. 3.2 Bounded electron circulation a positive nucleus and interacting with an external electric field

As shown in Fig. 3.2, the external field represents a plane wave, due to the small atomic radius r_0 compared to the applied wavelength λ

$$\boldsymbol{E} = \boldsymbol{E}_0 e^{-i\omega t}. \tag{3.21}$$

We get finally the equation of motion for a bounded electron of a hydrogen atom interacting with an external field

Equation of motion of one weakly bounded electron

$$m_\mathrm{e}\ddot{\boldsymbol{r}}_0 + m_\mathrm{e}\Gamma_\mathrm{em}\dot{\boldsymbol{r}}_0 + m_\mathrm{e}\omega_0^2\boldsymbol{r}_0 = -e\boldsymbol{E}_0 e^{-i\,\omega t}. \tag{3.22}$$

3.2.4 Dipole Moment and Differential Power per Solid Angle

The equation of motion determined in the last section represents a damped harmonic oscillator at ω_0 with a harmonic driving force at the angular frequency ω. As known from classical mechanics, this equation represents a linear inhomogeneous differential equation of second order with constant coefficients. Usually, a general solution for the homogeneous differential equation has to be found first, and additionally, a special solution for the inhomogeneous one is added first. Here, the homogeneous solution of a damped oscillator vanishes for large times so that only the special solution remains.

We take the ansatz for the location of the electron $\boldsymbol{r}_0 = \boldsymbol{a}e^{-i\omega t}$ with $\boldsymbol{a} = \text{const}$, and calculating the derivatives, one gets the characteristic equation for this differential equation

$$\left(-\omega^2 - i\omega\Gamma_{\text{em}} + \omega_0^2\right)\boldsymbol{a} = -\frac{e}{m_{\text{e}}}\boldsymbol{E}_0.$$

So, the amplitude vector $\boldsymbol{a}$ of the electron in the hydrogen atom, driven by an external field $\boldsymbol{E}_0$ gets to

$$\boldsymbol{a} = -\frac{e}{m_{\text{e}}}\frac{1}{\left(\omega_0^2 - \omega^2 - i\omega\Gamma_{\text{em}}\right)}\boldsymbol{E}_0, \tag{3.23}$$

and the location of the bounded electron results to

$$\boldsymbol{r}_0(t) = -\frac{e}{m_{\text{e}}}\frac{1}{\left(\omega_0^2 - \omega^2 - i\omega\Gamma_{\text{em}}\right)}\boldsymbol{E}_0 e^{-i\omega t}.$$

One sees that this trajectory represents a periodic oscillation of the electron with the frequency ω, induced by the external field. And we know that this periodic movement can be described by a time-varying dipole moment. As defined, the dipole moment of a charged particle is given by (2.23), and gets to

$$\begin{aligned}\boldsymbol{d}(t) &= -e\boldsymbol{r}_0(t)\\ &= -e\boldsymbol{a}e^{-i\omega t} = \boldsymbol{d}_0 e^{-i\omega t}\\ &= \frac{e^2}{m_{\text{e}}}\frac{1}{\left(\omega_0^2 - \omega^2 - i\omega\Gamma_{\text{em}}\right)}\boldsymbol{E}_0 e^{-i\omega t}\\ &= \frac{e^2}{m_{\text{e}}}\frac{1}{\left(\omega_0^2 - \omega^2 - i\omega\Gamma_{\text{em}}\right)}\boldsymbol{E}(t).\end{aligned}$$

With the

Electric polarizability

$$\alpha_{\text{e}} = \frac{e^2}{m_{\text{e}}}\frac{1}{\left(\omega_0^2 - \omega^2 - i\omega\Gamma_{\text{em}}\right)}, \tag{3.24}$$

we see that the induced dipole moment is collinear to the inducing electric field, and directly proportional to the electric field strength

$$\boldsymbol{d}(t) = \alpha_{\text{e}}\boldsymbol{E}(t). \tag{3.25}$$

So, the bounded electron interacting with an external field exhibits a time-dependent periodic dipole moment, which in consequence emits electromagnetic radiation, see (2.31). The averaged power per solid angle of the emitted radiation can be expressed by

$$\begin{aligned}\frac{d\langle P\rangle}{d\Omega} &\overset{(2.31)}{=} \frac{c_0 k^4}{32\pi^2\varepsilon_0}|\boldsymbol{d}_0|^2 \sin^2\vartheta \\ &= \frac{c_0 k^4}{32\pi^2\varepsilon_0}|\alpha_\mathrm{e}|^2\,|\boldsymbol{E}_0|^2 \sin^2\vartheta \\ &= \frac{c_0 k^4}{32\pi^2\varepsilon_0}\left|\frac{e^2}{m_\mathrm{e}}\frac{1}{\left(\omega_0^2-\omega^2-i\omega\Gamma_\mathrm{em}\right)}\right|^2 |\boldsymbol{E}_0|^2 \sin^2\vartheta.\end{aligned}$$

Averaged emitted power per solid angle

$$\frac{\mathrm{d}\langle P\rangle}{\mathrm{d}\Omega} = \frac{c_0\,\omega^4}{32\pi^2\varepsilon_0}\left(\frac{e^2}{m_\mathrm{e}c_0^2}\right)^2 \frac{1}{(\omega_0^2-\omega^2)^2+\omega^2\Gamma_\mathrm{em}^2}\,|\boldsymbol{E}_0|^2 \sin^2\vartheta \qquad (3.26)$$

In summary, we can state that for a bounded electron:

- The incoming electromagnetic wave induces a dipole moment in the atom.
- The periodic oscillating atomic dipole emits electromagnetic radiation.
- The emitted electromagnetic radiation features the same frequency (or wavelength) as the inducing one. Again, the emitted electromagnetic radiation has the same photon energy featuring an elastic scattering.
- The emission characteristics of the electron is equivalent to the one of a time-dependent dipole.

3.3 Cross-Section

Knowing the emitted differential power per solid angle, we introduce now the differential cross-section defined as

$$\frac{\mathrm{d}\sigma}{\mathrm{d}\Omega} = \frac{\left(\frac{\text{Scattered photons}}{\text{time}\cdot\text{solid angle}}\right)}{\left(\frac{\text{Incident number of photons}}{\text{time}\cdot\text{solid angle}}\right)} = \frac{\left(\frac{\text{Emitted power}}{\text{solid angle}}\right)}{\left(\frac{\text{Incident power}}{\text{area}}\right)}.$$

We see that on the right side, one can place for the numerator and denominator the differential power per solid angle and the averaged value of the Poynting vector getting

$$\frac{\mathrm{d}\sigma}{\mathrm{d}\Omega} = \frac{\frac{\mathrm{d}\langle P\rangle}{\mathrm{d}\Omega}}{\langle|\boldsymbol{S}|\rangle}.$$

With the (1.94) and (3.26), one gets for the differential cross-section

$$\frac{\mathrm{d}\sigma}{\mathrm{d}\Omega} = \frac{\frac{c_0\,\omega^4}{32\pi^2\varepsilon_0}\left(\frac{e^2}{m_e c_0^2}\right)^2 \frac{1}{(\omega_0^2-\omega^2)^2+\omega^2\Gamma_{em}^2}\,|\boldsymbol{E}_0|^2\sin^2\vartheta}{\frac{1}{2}c_0\cdot\varepsilon_0\,|\boldsymbol{E}_0|^2} \tag{3.27}$$

$$= \left(\frac{e^2}{4\pi\varepsilon_0 m_e c_0^2}\right)^2 \frac{\omega^4\sin^2\vartheta}{(\omega_0^2-\omega^2)^2+\omega^2\Gamma_{em}^2}. \tag{3.28}$$

Introducing the classical electron radius r_c being derived from the assumption that the energy of an electron at rest is equivalent to the potential energy of the electron, given by

$$E_{rest} = E_{pot}, \text{ and}$$
$$m_e c_0^2 = \frac{1}{4\pi\varepsilon_0 r_c},$$

one gets

Classical electron radius

$$r_c = \frac{1}{4\pi\varepsilon_0}\frac{e^2}{m_e c_0^2}, \tag{3.29}$$

rewriting the differential cross-section to

Differential cross-section

$$\frac{\mathrm{d}\sigma}{\mathrm{d}\Omega} = r_c^2 \frac{\omega^4}{(\omega_0^2-\omega^2)^2+\omega^2\Gamma_{em}^2}\sin^2\vartheta \tag{3.30}$$

$$= r_c^2 \frac{\omega^4}{(\omega_0^2-\omega^2)^2+\omega^2\Gamma_{em}^2}\frac{1-\cos 2\vartheta}{2}. \tag{3.31}$$

One remark about the scattering angle: The scattering angle ϑ is attributed to the orientation of the electric field vector $\boldsymbol{E}$, see Fig. 3.3. Sometimes the deviation angle Θ from the straight propagation direction $\boldsymbol{k}$, a as used in particle physics for scattering experiments is used

$$\Theta = \frac{\pi}{2} - \vartheta,$$

resulting now in a little different writing of the differential cross-section

$$\frac{\mathrm{d}\sigma}{\mathrm{d}\Omega} = r_c^2 \frac{\omega^4}{(\omega_0^2-\omega^2)^2+\omega^2\Gamma_{em}^2}\frac{1+\cos^2\Theta}{2}.$$

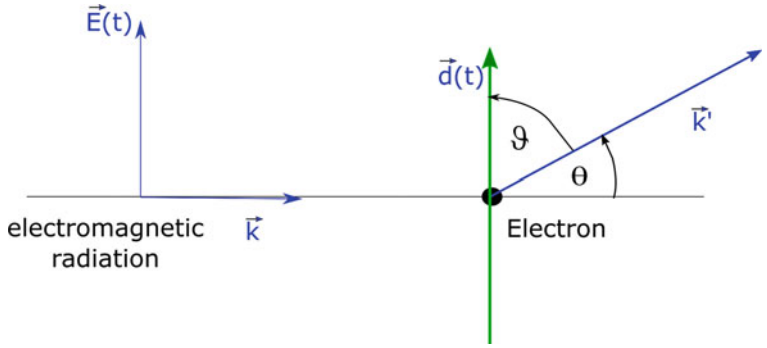

Fig. 3.3 Definitions for the scattering angle θ versus deviation angle Θ

The total cross-section of the scattered electromagnetic radiation at an atom is calculated by integrating the differential cross-section over the solid angle $\mathrm{d}\Omega$

$$\begin{aligned}\sigma &= \int \frac{\mathrm{d}\sigma}{\mathrm{d}\Omega}\mathrm{d}\Omega \\ &= \frac{8\pi}{3} r_\mathrm{c}^2 \frac{\omega^4}{(\omega_0^2-\omega^2)^2+\omega^2\Gamma_\mathrm{em}^2}\end{aligned} \tag{3.32}$$

getting

Total cross-section for elastic scattering

$$\sigma(\omega_0,\omega) = \sigma_\mathrm{Th}\frac{\omega^4}{(\omega_0^2-\omega^2)^2+\omega^2\Gamma_\mathrm{em}^2}, \tag{3.33}$$

introducing also the so-called the Thomson cross-section

Total cross-section for Thomson scattering

$$\sigma_\mathrm{Th} = \frac{8\pi}{3} r_\mathrm{c}^2 \tag{3.34}$$

The Thomson cross-section is also defined as the limes of the total cross-section for large ω, with

$$\lim_{\omega\to\infty}\frac{\omega^4}{(\omega_0^2-\omega^2)^2+\omega^2\Gamma_\mathrm{em}^2} = 1, \text{ getting } \lim_{\omega\to\infty}\sigma = \sigma_\mathrm{Th}. \tag{3.35}$$

One can see from (3.32) that the unity of the total cross-section represents an area

$$[\sigma] = m^2.$$

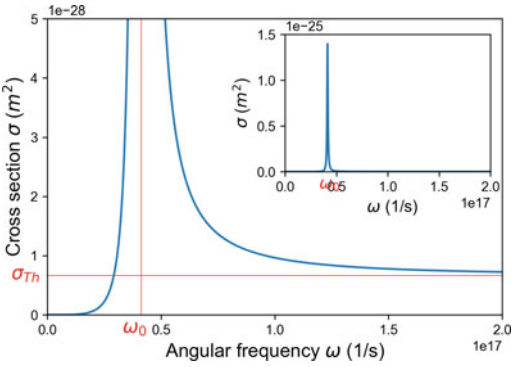

Fig. 3.4 Total cross-section σ as function of the angular frequency ω for a bounded electron

Usually, as the numbers are very small, the unit for the total cross-section is given in *barn*:

$$1\,\mathrm{b} = 10^{-24}\,\mathrm{cm}^2 = 10^{-28}\,\mathrm{m}^2. \tag{3.36}$$

The total cross-section can be subdivided into three regimes, first the Rayleigh scattering for an angular frequency well below the atomic frequency $\omega \ll \omega_0$, second the resonant scattering at the atomic frequency $\omega = \omega_0$, and third the Thomson scattering at a frequency well above ω_0 (see Fig. 3.4):

- **Rayleigh scattering for low-energy photons** ($\boldsymbol{\omega \ll \omega_0}$):
  For atomic frequencies ω_0 well above the frequency of the electromagnetic radiation, an approximation is found

Total cross-section for Rayleigh scattering

$$\sigma_\mathrm{R} = \sigma_\mathrm{Th}\frac{\omega^4}{\omega_0^4}. \tag{3.37}$$

The Rayleigh scattering is the one prominent example explaining the blue color of our sky, see Fig. 3.5. By looking at the fraction of the cross-sections at frequencies for the red and blue spectral components of the visible radiation

$$\frac{\sigma_\mathrm{blue}}{\sigma_\mathrm{red}} = \frac{\omega_\mathrm{blue}^4}{\omega_\mathrm{red}^4} = \frac{\lambda_\mathrm{red}^4}{\lambda_\mathrm{blue}^4} = \frac{(800\,\mathrm{nm})^4}{(400\,\mathrm{nm})^4} \approx 16, \tag{3.38}$$

one sees that visible electromagnetic radiation of the shorter wavelengths, the so-called blue light, is scattered 16 times more stronger at the atoms and molecules in the atmosphere (prominent representatives are nitrogen and oxygen molecules) than red light. Vice versa, a sunset featuring a red sun disc is explained by the reduced amount of the blue component in the transmitted "white" radiation through the atmosphere.

Fig. 3.5 Blue sky by elastic scattering of sunlight at the nitrogen and oxygen molecules in the atmosphere (left) and red sun at sunset (right)

- **Resonant scattering at $\omega = \omega_0$**:
  For the limes of the angular frequency ω of the electromagnetic radiation versus the atomic frequency ω_0, one gets the relation

Total cross-section for resonant scattering

$$\sigma_{\text{res}} = \sigma_{\text{Th}} \frac{\omega_0^2}{\Gamma_{\text{em}}^2}. \tag{3.39}$$

The photon energy at $\omega = \omega_0 = 4.1 \cdot 10^{16}$ Hz is about 17 eV, representing soft X-ray radiation with a wavelength of about $\lambda_0 = 45$ nm. As one can extract from the (3.14), the frequency ω_0 scales with $(n_k)^{3/2}$ of the nuclear charge, meaning that the heavier an atom is, the larger gets the resonance frequency, and the smaller its wavelength. For iron, the resonance scattering takes place at $E_{\text{res}} = 14.4$ keV, representing a wavelength of $\lambda_{\text{res}} \approx 86$ pm. Applications like resonance fluorescence spectroscopy or the Mößbauer effect apply photons at the resonance frequency.

- **Thomson scattering for $\omega \gg \omega_0$** :
  As seen from (3.35), the limes for very large angular frequencies of the electromagnetic radiation results in the Thomson cross-section σ_{Th}, see (3.34). At large photon energies in the X-ray and gamma-ray regime elastic scattering converges versus a constant value being equal to $\sigma_{\text{Th}} = 0.665 \cdot 10^{-24}\,\text{cm}^2$.

3.4 Polarization of Scattered Radiation

Elastic scattering of electromagnetic radiation exhibits an emission characteristic proportional to $\sin^2 \vartheta$, expressing that in direction of the electric field vector, no scattered radiation will be emitted. One consequence is that unpolarized radiation,

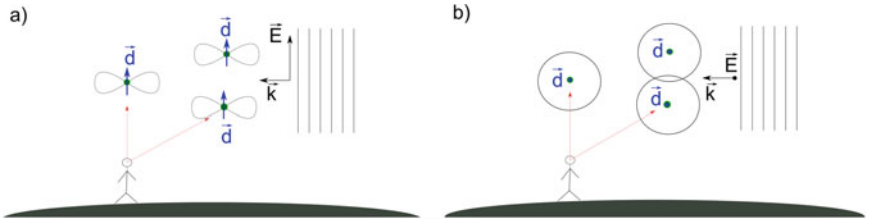

Fig. 3.6 Blue sky by elastic scattering of sun light at the nitrogen and oxygen molecules in the atmosphere (left) and red sun at sunset (right)

being scattered and detected orthogonally to the connecting line between the scattering atom and the radiation source, will be completely linear polarized orthogonally to the plane spanned by the scatterer, the source, and the detector (Fig. 3.6).

Scattering atoms or molecules, not being orthogonal oriented to the detector, emit radiation being partially polarized. The detector will measure also components of the radiation complanar to the plane spanned by the scatterer, the source and the detector. Contrary, this has a consequence that the radiation detected orthogonally to the emitter, i.e. looking up into the sky, will be fully linear polarized, see Fig. 3.6b.

3.5 Photo-Excitation of Atoms

3.5.1 Linear Scattering

Increasing the photon energy of the electromagnetic radiation quantized atomic or molecular excitation processes from one quantum state into another gets probable, resulting in an excited bounded electron with increased energy: the atom is excited and the process is called **resonant excitation by absorption**, see Fig. 3.7a. In the quantum world, a photon is thereby absorbed and, in principle, a totally inelastic scattering takes place. But, if we talk about scattering, meaning the absorption and the emission of a photon after excitation of the atom, then we have again an elastic scattering process:

$$\text{Absorption:} \qquad \text{atom} + \gamma \rightarrow (\text{atom})^*$$

$$\text{Emission:} \qquad (\text{atom})^* \rightarrow \text{atom} + \gamma.$$

Bear in mind that contrary to the non-resonant elastic scattering, where the cross-section is very low, the linear scattering results always in the absorption of the complete photon, and depicts the corpuscular property of the electromagnetic radiation.

The absorbed energy $\Delta E = h\Delta\nu$ of an atom with an atomic number Z is equivalent to

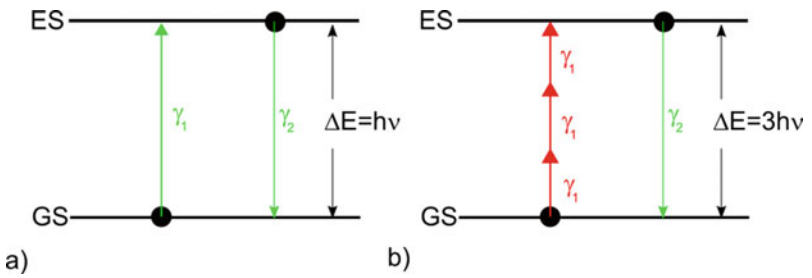

Fig. 3.7 Linear photo-excitation (**a**) and Multi-photon excitation of an atom (**b**) from ground state (GS) to an excited state (ES) by simultaneous absorption of $n = 3$ photons with the energy $E_\gamma = h\nu$ and spontaneous emission of one photon with the energy $E_{\gamma_2} = nE_{\gamma_1}$

$$\begin{aligned} \Delta E &= \left(\frac{1}{n_1^2} - \frac{1}{n_2^2}\right)\left(\frac{e^2}{4\pi\varepsilon_0}\right)\frac{m_e Z^2}{2\hbar^2} \\ &= \left(\frac{1}{n_1^2} - \frac{1}{n_2^2}\right) Z^2 E_R, \end{aligned} \tag{3.40}$$

with the Rydberg energy $E_R = \left(\frac{e^2}{4\pi\varepsilon_0}\right)\frac{m_e}{2\hbar^2} = 13.6$ eV. The Rydberg energy accords to the energy necessary for ionization of a hydrogen atom ($Z = 1$, $n_1 = 1$, and $n_2 = \infty$). The energy difference ΔE is still discrete, and the photon energies range from 1 to 3 eV in the VIS range to some ten eV in the deep UV range.

One typical application is the atomic emission spectroscopy, and an often described phenomenon is the Fraunhofer absorption lines in the solar spectrum being a typical photo-excitation process in the solar atmosphere.

Now, as every excited state of an atom is unstable, it will relax by **spontaneous emission** of radiation at the same photon energy needed for excitation (Fig. 3.7a). Looking at the absorption of the radiation and the emission, we can observe an elastic scattering of the electromagnetic radiation. As the coherent excitation of the electron states only for some nanoseconds, and the wave function of the excited electron de-phases within tens of femtoseconds, no coherence is given between this initially excited electron to the electron closely before de-excitation. The phase relation of the emitted radiation by spontaneous emission is totally un-correlated to the exciting radiation, and is called totally incoherent. This means also that the emission is isotropic resulting in a spherical wave emission when talking about electromagnetic radiation.

3.5.2 Non-linear Scattering

The process of photo-excitation is described by the absorption of one photon. In principle, it can be shown that increasing the photon density of photons with an

energy being only a fraction n of the energy difference ΔE to excite an atom, see (3.40), a simultaneous absorption of n photons is possible

$$\text{Absorption:} \qquad \text{atom} + n \cdot \gamma \rightarrow (\text{atom})^*.$$

This process is called **multi-photon absorption**, or a n-photon absorption, see Fig. 3.7b.

Again, as for scattering a photon is emitted, this process is called multi-photon scattering. Contrary to the linear scattering process, here the photon energy of the emitted radiation is n times the photon energy of the incoming radiation E_{γ_1}.

$$\text{Emission:} \qquad (\text{atom})^* \rightarrow \text{atom} + n \cdot \gamma.$$

As the overall energy of the photons is preserved, this process is still an elastic scattering process

$$\begin{aligned} n\gamma_1 &\rightarrow \gamma_2 \\ nE_{\gamma_1} &= E_{\gamma_2} \end{aligned}$$

As again a spontaneous emission takes place, no phase information by the exciting photons is given anymore, and the emission direction of the photons is of statistical nature being isotropic in space and totally incoherent.

Chapter 4
Inelastic Scattering and Absorption

Abstract Up to now only elastic scattering has been discussed, where electromagnetic radiation impinges on an electronics system, e.g. a simple hydrogen atom or molecule with at least one bounded electron. More exactly, one weakly bounded electron scatters electromagnetic radiation with the same wavelength, frequency, or in terms of energy, the same photon energy. This happens, when the photon energy is not equal to or larger than the excitation or ionization energy of the atomic system (e.g. photo-excitation or photo-ionization). This case is often written as non-resonant process . In short, for scattered photons having the same energy as the incoming one, the scattering process is energy conserved. One can imagine that comparable to classical mechanics, also inelastic scattering is possible where the kinetic energy is not preserved, and absorption takes place. Inelastic scattering can be observed at different photon energies from low-energy photons in the meV to eV regime of UV-VIS-NIR radiation and further increased well above the energies for Thomson scattering in the keV regime. Here, we discuss free carrier absorption or inverse Bremsstrahlung, Raman scattering, Photo-electro chemical excitation or Photo-excitation, Photo-ionization or Photo-effect, Non-linear photo-ionization, Compton scattering, and Pair production.

4.1 Free Carrier Absorption—Inverse Bremsstrahlung

Free electrons can absorb radiation in a non-resonant process called free carrier absorption or inverse bremsstrahlung. This process is only possible in combination with heavy charged particles as a collision partner, such as ions or atomic nuclei. The third acting particle, in this case the ion/nucleus, is needed for energy and momentum conservation; see Fig. 4.1. Both cannot be conserved if only a photon interacts with an electron, as then we have only elastic scattering; see Sect. 3.1. So, in order to take place inverse bremsstrahlung, a sufficient high density of quasi-free electrons is needed.

Free or quasi-free electrons are given, e.g. in metals, a dense plasma, and as well, in an excited dielectric. Dielectrics, e.g. excited by multi-photon absorption of ultra-fast laser radiation, feature also free electrons in the conduction band.

© Springer Nature Switzerland AG 2022

A. Horn, *The Physics of Laser Radiation–Matter Interaction*,
https://doi.org/10.1007/978-3-031-15862-9_4

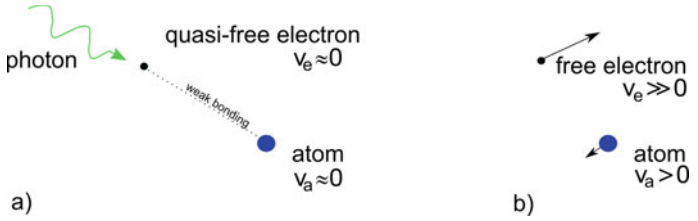

Fig. 4.1 Free carrier absorption of a photon at a quasi-free electron. Quasi-free means that the electron interacts weakly with an atom or molecule. Before photon absorption (**a**) and after photon absorption (**b**). The electron gains kinetic energy, and also the atom/molecule. But due to the large mass difference, the transferred energy to the electron is much larger

The context of absorption of electromagnetic radiation in metals is described by intraband excitation, described separately in Sect. 12.3.

In one way, inverse bremsstrahlung takes place in a laser-produced plasma. For this process, a plasma should be collisional meaning that the density of the charges is large enough to allow interaction between the constituents. When an electron collides with an ion or passes close to it, it can absorb electromagnetic radiation resulting in an increase in its kinetic energy. After multiple collisions, the energy distribution of the accelerated electrons thermalizes by scattering with not accelerated electrons, finally rising the plasma temperature. Inverse bremsstrahlung is one important way to deposit laser energy into the plasma, e.g. a laser-generated plasma by non-linear excitation of dielectrics or in inertial confinement fusion [1].

Often, inverse bremsstrahlung is described in the context of Kramers' opacity law. It describes the opacity of a medium in terms of the density and temperature, assuming that the opacity is dominated by absorption in a plasma by

- **bound-free absorption**. Absorption of radiation takes place during ionization of a bound electron, see Sect. 4.3, or
- **free-free absorption**, where absorption of radiation takes place when an electron scatter at a free ion, the so-called inverse bremsstrahlung; see [2].

As shown in Fig. 4.2, the free electrons in a plasma, or quasi-free electrons within the conduction band of metals, or in the conduction band of a dielectric gain optical energy absorbing electromagnetic radiation by inverse bremsstrahlung [3]. As a consequence, electrons reach kinetic energies large enough to ionize further atoms by impact ionization with other quasi-free electrons generating new free electrons; see also Sect. 13.4. This process can develop exponentially in the electron number if the scattering rate of the ballistic electrons is high enough, resulting in an avalanche ionization. The electron density grows such fast that during irradiation the optical property of the dielectric or plasma gets highly absorbing; see more in Chap. 12.

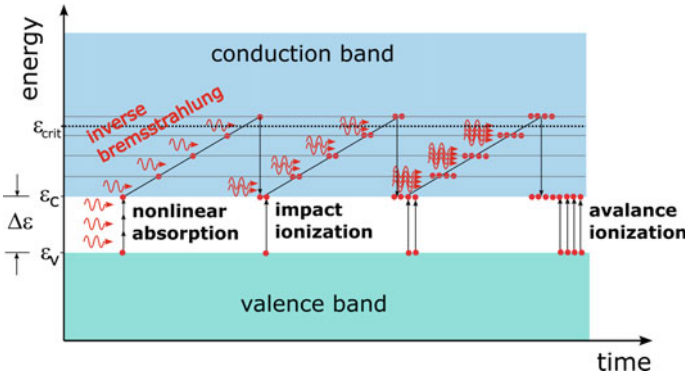

Fig. 4.2 A schematic of the laser-induced optical breakdown processes in dielectrics

4.2 Raman Scattering

Generally, this inelastic scattering is given for molecules with vibrational and rotational modes, so-called vibronic modes. An excited molecule exhibits an excited vibronic mode.

The Raman scattering can be described on the one hand by the Stokes scattering, where a molecule in the ground state absorbs energy and is excited (Fig. 4.3a). The scattered radiation features a smaller photon energy $E'_\gamma < E_\gamma$ and the molecule ends into an excited vibronic state:

$$\text{molecule} + \gamma \rightarrow (\text{molecule})^* + \gamma'.$$

Starting from an excited molecule the anti-Stokes scattering is described by emission of higher energy photons $E_\gamma < E'_\gamma$ by de-excitation of the molecule into the ground state (Fig. 4.3b):

$$(\text{molecule})^* + \gamma \rightarrow \text{molecule} + \gamma'.$$

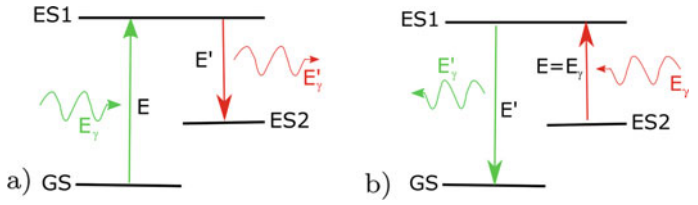

Fig. 4.3 Term schemes of the Raman scattering with **a** Stokes scattering and **b** anti-Stokes scattering

Raman scattering is applicable for single molecules, or also compounds of them. As described in Sect. 14.4, condensed matter features the collective movement of atoms, especially an oscillation behavior. The so-called phonon state represents a quantized state of collective atomar motions. Its energy ranges from the meV to eV. Thereby one differs between optical and acoustical phonons. Raman scattering is given by the scattering of photons with optical phonon states, whereas the scattering of photons with acoustical phonons is called Brillouin scattering. Both techniques enable the analysis of the crystal properties of solids.

4.3 Photo-Ionization or Photo-Effect

An important case for photo-excitation is the complete separation of one electron from an atom or molecule by resonant absorption of one photon, the so-called **ionization of an atom**

$$\text{atom} + \gamma \rightarrow (\text{atom})^+ + \text{e}^-.$$

This process is also called the photo-electric effect. First, one has to distinguish between the internal and the external photo-effect. The *internal photo-effect* is attributed to the change in electrical conductivity of semiconductors induced by the absorption of photons; see Sect. 12.2. E.g. the photo-voltaic effect is one example of the internal photo-effect, where electron–hole pairs are formed by irradiation; see also Sect. 12.2.2.

Real photo-ionization is described by the *external photo-electric effect*, explained by Albert Einstein in 1905, where an atom or a molecule is excited by electromagnetic radiation emitting an electron. Here, the view on electromagnetic radiation as particles, so-called photons, is important for the description. The electron resulting from photo-ionization represents a free electron, in contrast to a bounded one, whereby the photon is fully absorbed; see Fig. 4.4. Looking at (3.40), an ionization is given for $n_2 = \infty$. Typical experiments for the photo-effect are used, e.g. to determine the Planck constant h. Photo-ejected electrons by electromagnetic radiation with a frequency ν exhibit a kinetic energy, given by

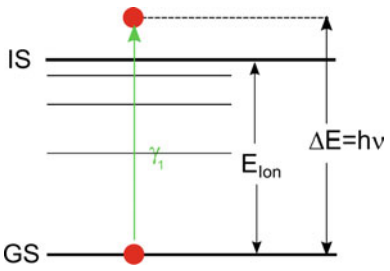

Fig. 4.4 Ionization of an atom or molecule by linear absorption of one photon by exciting an electron from the ground state (GS) above the ionization state (IS) n_∞

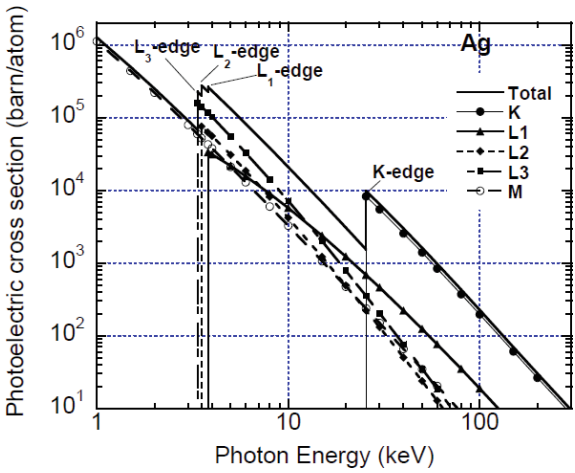

Fig. 4.5 Cross-section σ_{pe} for the photo-effect for Ag as function of the photon energy E_γ [4]

$$E_{\text{kin}} = h\nu - \varphi,$$

which is equal to the photon energy minus a material-specific work function φ. Important here is that contrary to the elastic scattering, no electromagnetic radiation, here best described in the particle view, exists anymore. The energy of the radiation is totally absorbed in quantized steps. The photo-ionization has a threshold-like character: not the intensity of the radiation, but the photon energy determines the photo-ionization process.

The **total cross-section for the photo-effect** for atoms with the atomic number Z is generally given by [4]

Total cross-section for the photo-effect

$$\sigma_{\text{pe}} \propto \begin{cases} \frac{Z^4}{E_\gamma^3} & \text{for low-energy photons } E_\gamma \\ \frac{Z^5}{E_\gamma} & \text{for high-energy photons } \epsilon \gg 1 \end{cases} \tag{4.1}$$

with the reduced photon energy $\epsilon = \dfrac{E_\gamma}{m_e c^2}$, describing a falling cross-section for increasing photon energy, and a strong increasing in the cross-section for increasing atomic number Z (Fig. 4.5). The cross-section increases step-like at specific energies, due to a strongly increased probability for photo-ionization of an electron being on a closer shell to the nucleus, resulting in so-called **absorption edges**. In Fig. 4.5, for example, at lower energies, the electrons of the element silver are photo-ionized, thereby the cross-section decreasing with increasing photon energy, but jumping to larger values when the electrons of the L-shell and then of the K-shell are ionized.

The absorption of a photon indicates that the momentum is conserved. This is only possible when the electron is bounded to a nucleus, and the nucleus takes the recoil momentum of the emitted electron (the overall momentum before scattering is zero!). The largest cross-section is attributed to K-shell electrons featuring the strongest binding to the nucleus. In the non-relativistic Born approximation, and far away from any absorption edge, one gets a total cross-section for [5]

Total cross-section for K-shell ionization

$$\sigma_{\mathrm{pe}}^{K} = \begin{cases} \left(\frac{32}{\epsilon^7}\right)^{1/2} \alpha^4 \, Z^5 \, \sigma_{\mathrm{Th}} & \text{for low-energy photons} \\ 4\pi r_{\mathrm{e}}^2 Z^5 \alpha^4 \frac{1}{\epsilon} & \text{for high-energy photons } \epsilon \gg 1 \end{cases} \tag{4.2}$$

with the reduced photon energy

$$\epsilon = \frac{E_\gamma}{m_{\mathrm{e}} c^2}, \tag{4.3}$$

the Thomson cross-section σ_{Th}, and the hyper-fine structure constant α.

4.4 Ponderomotive Energy and Force

Free electrons can absorb for larger intensities of the electromagnetic radiation, like high-intensity laser radiation, optical energy in form of **cycle-averaged quiver energy**.

Assuming linear-polarized electromagnetic radiation with the electric field strength given by

$$E = E_0 \cos \omega t,$$

an electron is accelerated by the force $F = m_{\mathrm{e}} a = q_{\mathrm{e}} E_0 \cos \omega t$, and the position of the electrons results then to

$$\begin{aligned} x &= -\frac{a}{\omega^2} \\ &= -\frac{q_{\mathrm{e}} E_0}{m_{\mathrm{e}} \omega^2} \cos \omega t. \end{aligned}$$

Now, the electron experiencing a harmonic motion features a time-averaged potential energy from $\langle E_{\mathrm{pot}} \rangle = 1/2k \langle x^2 \rangle$ with $\omega^2 = k/m_{\mathrm{e}}$, using the derived position of the electron, and averaging the $\cos^2$ function over time, one gets

$$\langle E_{\text{pot}} \rangle = \frac{1}{2} m_e \omega^2 \langle x^2 \rangle$$
$$= \frac{q_e^2 E_0^2}{4 m_e \omega^2},$$

the so-called **poderomotive energy** of a free electron.

Ponderomotive energy

$$U_P = \frac{q_e^2 E_0^2}{4 m_e \omega^2}. \tag{4.4}$$

Using the intensity of the radiation, see (1.94), one gets

$$U_P = \frac{2 q_e^2 I}{2 m_e c_0 \epsilon_0 \omega^2}. \tag{4.5}$$

Solving this equation with the adequate numbers, one gets the following relation:

$$U_P = 9.3 \cdot 10^{-14} I \lambda^2;$$

applying the intensity I in W/cm^2 and the wavelength λ in μm results in a ponderomotive energy in electronvolts eV.

Exemplary, using laser radiation with a wavelength of about 1 μm with intensities of $I = 1 \cdot 10^{13}$ W/cm^2, a ponderomotive energy of the electrons of about 1 eV results. Increasing the intensity to $I = 1 \cdot 10^{15}$ W/cm^2 results in an electron ponderomotive energy of about 100 eV.

A **ponderomotive force** is a non-linear force that a charged particle, here an electron, experiences in an inhomogeneous oscillating electromagnetic field. It causes the electron to move toward the area of the weaker electric field strength, rather than oscillating around an initial point as happens in a homogeneous field. This occurs because the electron features a greater magnitude of force during the half of the oscillation period while it is in the region with stronger field. The net force during one period in the weaker region in the second half of the oscillation does not compensate for the net force of the first half, and so over a complete cycle, the particle moves toward the region of lesser force.

The ponderomotive force F_p is expressed by

Ponderomotive force

$$\boldsymbol{F}_P = -\frac{q_e^2}{4 m_e \omega^2} \nabla \boldsymbol{E}_0^2. \tag{4.6}$$

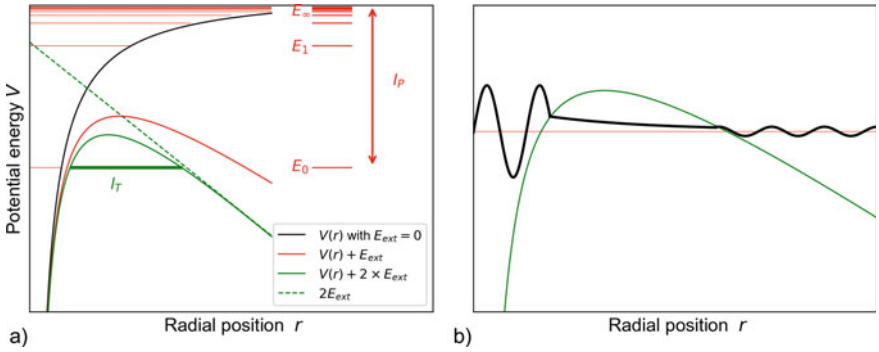

Fig. 4.6 Mechanism of single ionization of atoms using hydrogen as an example: **a** The potential described also with the energy levels until ionization level E_∞, without any external field added (black), with increasing field strength of electromagnetic radiation E_{ext} resulting in decreasing tunnel barrier width l_{T}. **b** Electron described quantum mechanically by a wave function tunneling the barrier, therein described by an exponentially decaying function, and resulting in a free electron wave function

4.5 Non-linear Photo-Ionization

Atoms and molecules can be ionized even for photon energies smaller than the energy difference between the ground state and an excited state above the ionization level of an atom, when the intensity of the photons is high enough to induce **multi-photon ionization MPI**, or the field strength of the radiation is intense enough to induce **tunnel ionization TI**. Both processes induce the same final state, starting from the same initial state, so that physically we are speaking about the same process of photo-ionization, even though its descriptions are different.

4.5.1 Tunnel Ionization

The process involved in tunnel ionization is quantum tunneling. The potential of an atom being proportional to $\propto r^{-1}$ is modified by a DC external field E_{ext} being proportional to $\propto -E_{\text{ext}}$. The external electrical field distorts the potential of an atom, see Fig. 4.6a, generating a definite barrier of width l_{T}. As known from quantum mechanics, a particle described by a periodical wave function can pass through a barrier of width l, the so-called **quantum tunneling**. This results in a transmission of this particle through the barrier; see Fig. 4.6b.

As the atomic potential is distorted from an external DC electrical field, the valence electron of an atom, being the weakest-bounded electron, features a tunnel probability for ionization, depending on the ionization energy I_{P} and the field strength E_0 generating a definite barrier of width l_{T}. The probability for photo-ionization by tunnel ionization or also ionization rate is described by [6]

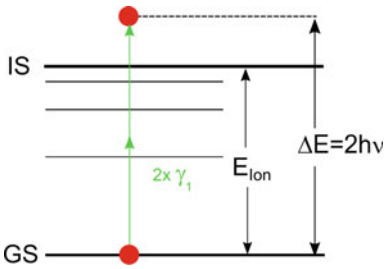

Fig. 4.7 Ionization of an atom or molecule by multi-photon absorption, i.e. the simultaneous absorption of two photons from the ground state GS above the ionization state IS

Ionization rate

$$\left(\frac{\mathrm{d}n_\mathrm{e}}{\mathrm{d}t}\right)_{TI} = \frac{\sqrt{6\pi}}{4}\frac{I_\mathrm{P}}{\hbar}\left(\frac{e\hbar E_{ext}}{m_\mathrm{e}^{1/2} I_\mathrm{P}^{3/2}}\right)^{1/2} \times \\ \times \exp\left(-\frac{4}{3}\frac{\sqrt{2m_\mathrm{e}} I_\mathrm{P}^{3/2}}{e\hbar E_\mathrm{ext}}\left(1 - \frac{m_\mathrm{e}\omega_\mathrm{em}^2 I_\mathrm{P}}{5e^2 E_\mathrm{ext}^2}\right)\right), \qquad (4.7)$$

with the ionization energy I_P.

4.5.2 Multi-photon Ionization

Is the photon density within the interaction volume of focused laser radiation large enough, i.e. at larger intensities of the laser radiation, then a multi-photon transition between the ground state and an excited state above the ionization level by **simultaneous absorption** of n photons gets probable, one speaks about a **n-photon ionization**, or more general a multi-photon ionization; see Fig. 4.7. Thereby the probability for ionization is described in general by the ionization rate

$$\frac{\mathrm{d}n_\mathrm{e}}{\mathrm{d}t} = \sigma_\mathrm{N} I^N,$$

with the generalized N-photon ionization cross-section σ_N.

For multi-photon ionization MPI, the probability for photo-ionization is described by [6]

Ionization rate for multi-photon ionization

$$\left(\frac{\mathrm{d}n_\mathrm{e}}{\mathrm{d}t}\right)_{MPI} = A\left(\frac{I_\mathrm{P}}{\hbar\omega_\mathrm{em}}\right)^{3/2}\omega_\mathrm{em}\Phi\left(\sqrt{2\left\langle\frac{\tilde{I}_\mathrm{P}}{\hbar\omega_\mathrm{em}}+1\right\rangle-\frac{2\tilde{I}_\mathrm{P}}{\hbar\omega_\mathrm{em}}}\right)\times$$
$$\times\exp\left(2\left\langle\frac{\tilde{I}_\mathrm{P}}{\hbar\omega_\mathrm{em}}+1\right\rangle-\frac{\tilde{I}_\mathrm{P}}{\hbar\omega_\mathrm{em}}\left(1+\frac{e^2E_{ext}^2}{2m_\mathrm{e}\omega_\mathrm{em}^2I_\mathrm{P}}\right)\right)$$
$$\times\left(\frac{e^2E_\mathrm{ext}^2}{8m_\mathrm{e}\omega_\mathrm{em}^2I_\mathrm{P}}\right)^{\left\langle\tilde{I}_\mathrm{P}/\hbar\omega_\mathrm{em}+1\right\rangle} \tag{4.8}$$

where A is a numerical factor in the order of unity, and $\tilde{I}_\mathrm{P}$ represents the extended ionization energy calculated by the ionization potential plus the ponderomotive energy, see Sect. 4.4,

$$\tilde{I}_\mathrm{P} = I_\mathrm{P} + U_\mathrm{P} = I_\mathrm{P} + \frac{e^2E_\mathrm{ext}^2}{4m_\mathrm{e}\omega^2} = I_\mathrm{P}\left(1+\frac{1}{2\gamma^2}\right).$$

The factor $\left\langle\tilde{I}_\mathrm{P}/\hbar\omega_\mathrm{em}+1\right\rangle$ describes the integer part of the multi-photon ionization order, meaning how many photons are needed to induce an ionization, and Φ represents the probability integral, also called Dawson integral.

4.5.3 Keldysh Parameter for Atoms

The probability whether multi-photon ionization MPI or tunnel ionization TI is dominating the excitation can be characterized by the Keldysh parameter [6]. Thereby, the Keldysh parameter γ can now be defined in a first approximation for atoms as the ratio of the Keldysh tunnel time t_T and the radiation oscillation period

$$\gamma \propto \frac{t_\mathrm{T}}{T_0},$$

with the radiation oscillation period

$$T_0 = \frac{2\pi}{\omega_\mathrm{em}}$$

for electromagnetic radiation at the frequency ω_em. This means that the Keldysh parameter decreases when the tunnel time is smaller than the oscillation period of an electron, induced by the external field, within the atomic potential.

Here, the tunnel time can be interpreted as the time $t_\mathrm{T} = l/v$ an electron with velocity

$$v = \sqrt{\frac{2I_\mathrm{P}}{m_\mathrm{e}}} \tag{4.9}$$

takes to cross a potential barrier of width

$$l_\mathrm{T} = \frac{I_\mathrm{P}}{eE_\mathrm{ext}}, \tag{4.10}$$

where I_P is the electron binding energy or the ionization energy, and E_ext is the electric field strength of the radiation; see Fig. 4.6a [7].

The tunneling frequency ω_T represents then the reciprocal tunneling time t_T and is calculated using (4.9) and (4.10) by

$$t_\mathrm{T}(t) = \frac{\sqrt{\frac{1}{2}m_\mathrm{e}I_\mathrm{P}}}{eE_\mathrm{ext}(t)} = \nu_T^{-1} = \frac{2\pi}{\omega_\mathrm{T}},$$

with the electron mass m_e, the elementary charge e, and the instantaneous electrical field strength E_ext of the radiation, describing the actual field strength, and often approximated by the peak field strength in pulsed radiation.

One calculates now the Keldysh parameter to

$$\gamma = 4\pi\frac{t_\mathrm{T}}{T_0} = \omega_\mathrm{em}\frac{\sqrt{2m_e I_\mathrm{P}}}{eE_\mathrm{ext}}.$$

Analogous, the Keldysh parameter represents the fraction between a tunneling frequency ω_t and the frequency of the electromagnetic field ω_em

$$\gamma = 4\pi\frac{\omega_\mathrm{em}}{\omega_\mathrm{T}}$$

Keldysh parameter for atoms

$$\gamma = \omega_\mathrm{em}\frac{\sqrt{2m_e I_\mathrm{P}}}{eE_\mathrm{ext}}. \tag{4.11}$$

In case the frequency of the radiation is much smaller than the tunneling frequency, then the electrical field strength of the radiation changes much slower than the time an electron needs to tunnel, favoring tunnel ionization. A classical description of the nearly-DC field distortion is then possible; see Fig. 4.6a. More details are given in Sect. 4.5.1. Here, the Keldysh parameter is much smaller than unity.

Keldysh parameter faworing tunnel ionization

$$\gamma \ll 1.$$

Looking at (4.11) tunnel ionization gets probable when the frequency of the radiation is small and the field strength, i.e. its intensity is large. So, high-intensity IR radiation will more probably ionize by tunnel ionization.

In the other case, the frequency of the electromagnetic radiation is much larger than the tunneling frequency, and an instantaneous process by multi-photon ionization takes place, and a process described by quantized photons is necessary, with the Keldysh parameter now being much smaller than unity.

Keldysh parameter favoring multi-photon ionization

$$\gamma \gg 1.$$

Multi-photon ionization gets probable for frequencies larger than the intensities, meaning that UV radiation will probably induce ionization by MPI.

An overall rate for photo-ionization of an atom is now given by [6]

$$\left(\frac{\mathrm{d}n_\mathrm{e}}{\mathrm{d}t}\right)_{PI} = \sqrt{\frac{2I_\mathrm{P}}{\hbar}}\omega_\mathrm{em}\left(\frac{\gamma}{\sqrt{1+\gamma^2}}\right)^{3/2} S\left(\gamma, \frac{\tilde{I}_\mathrm{P}}{\hbar\omega_\mathrm{em}}\right) \times \exp\left\{-\frac{2\tilde{I}_\mathrm{P}}{\hbar\omega_\mathrm{em}}\left(\sinh^{-1}\gamma - \gamma\frac{\sqrt{1+\gamma^2}}{1+2\gamma^2}\right)\right\}, \tag{4.12}$$

where the effective potential is hereby calculated to

$$I_\mathrm{P} = \frac{2I_\mathrm{P}}{\pi}\frac{\sqrt{1+\gamma^2}}{\gamma}\mathcal{E}\left(\frac{1}{\sqrt{1+\gamma^2}}\right).$$

The function S is calculated by

$$S(\gamma, x) = \sum_{j=0}^{\infty} \exp\left\{-2\left(\langle x+1\rangle - x + j\right)\left(\sinh^{-1}\gamma - \frac{\gamma}{\sqrt{1+\gamma^2}}\right) \times \Phi\left(\sqrt{\frac{2\gamma}{\sqrt{1+\gamma^2}}\left(\langle x+1\rangle - x + j\right)}\right)\right\},$$

with the probability integral or Dawson integral Φ [6], and using again with $\langle x\rangle$ the integer part of x. Even these equations and also those of the tunnel and multi-photon are very extensive, from an engineering point of view Keldysh solved them, and we

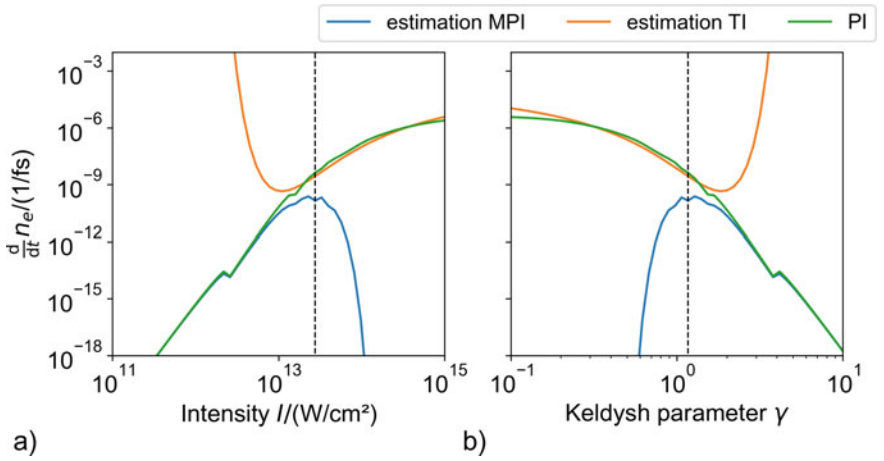

Fig. 4.8 Photo-ionization of an atom or molecule with $I_P = 9$ eV described by the Keldysh model. Photo-ionization rate plotted by approximations for tunnel and multi-photon ionization, as well as the photo-ionization rate by general model as function of the intensity of the radiation (**a**) and as function of the Keldysh parameter γ (**b**)

can plot them easily using any mathematical program the ionization probabilities for tunnel, multi-photon, and the photo-ionization; see Fig. 4.8a.

One observes that photo-ionization increases exponentially with increasing intensity of the radiation (the plot is double-log), and that for small intensities multi-photon ionization dominates, whereas at larger intensities tunnel ionization takes place. Also, the distinction of the two approximations by the Keldysh parameter is well-given in Fig. 4.8b.

4.5.4 Above-Threshold Multi-photon Ionization

Above-threshold ionization (ATI) is a special form of photo-ionization in which the atom absorbs more photons than would be necessary to reach the ionization threshold. This effect occurs with atoms in strong pulsed laser fields (especially with a pulse duration in the ps and fs range), since very high photon intensities can prevail. Thus, in an energy spectrum of photo-electrons, in addition to the first-order photo-electrons, which absorb only as many photons as are necessary for ionization, other electrons appear with energies that are just many times the energy of a photon higher than those of the first-order electrons; see Fig. 4.9a.

The reason is that the energy of the excess absorbed photons is directly converted into kinetic energy of the photo-electrons. If E_B is the binding energy of an emitted electron so its kinetic energy is calculated to

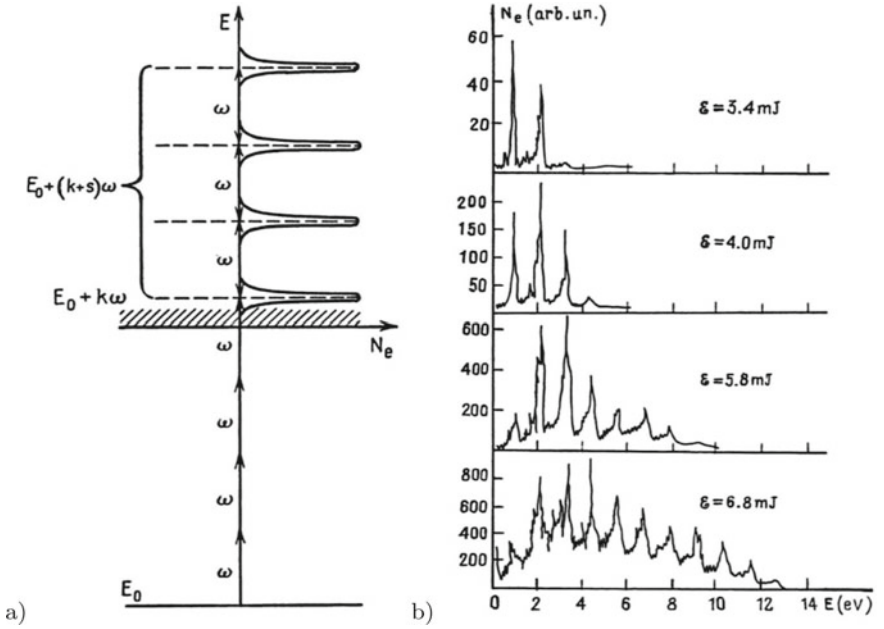

Fig. 4.9 **a** Principle of above-threshold multi-photon ionization process by absorption of N photons until ionization, and subsequent excitation of the free electron by further absorption of photons [8]. **b** Electron spectra of Xe gas for different excitation energies of the laser radiation (wavelength $\lambda = 1064$ nm, pulse duration $t_\mathrm{p} = 150$ ps) (Reprinted with the permission from [9], ©The Optical Society)

$$E_\mathrm{kin} = N \cdot E_\gamma - E_\mathrm{B}$$

where $E_\gamma = h\nu$ is the energy of a photon and N is the number of absorbed photons. N must be at least large enough so that $NE_\gamma > E_\mathrm{B}$. Such an energy spectrum for xenon atoms ionized with an fs titanium-sapphire laser radiation is shown in Fig. 4.9b.

4.6 Compton Scattering

Further increasing the photon energy makes Compton scattering probable. Thereby a weakly bounded electron interacts with the radiation and part of the photon energy is absorbed by the electron gaining kinetic energy. The nucleus together with the electron fulfill the conservation of momentum. The angle between the incoming photon and the scattered photon is given by Θ_γ. The electron initially at rest is scattered at an angle Θ_e; see Fig. 4.10.

The energy of the photon must be diminished because the electron now takes kinetic energy $E'_\mathrm{e} = E_\gamma - E'_\gamma$, and the photon energy is reduced to

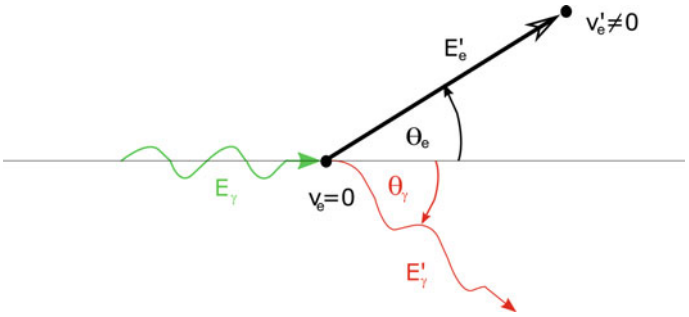

Fig. 4.10 Principle of Compton scattering [5]

Photon energy of Compton-scattered photon

$$E'_\gamma(\Theta_\gamma) = \frac{E_\gamma}{1 + \frac{E_\gamma}{m_e c_0^2}(1 - \cos\Theta_\gamma)} = \frac{E_\gamma}{1 + \epsilon(1 - \cos\Theta_\gamma)}. \tag{4.13}$$

Thereby the reduced photon energy (4.3) is used. One sees that the energy transferred to the electron as a function of Θ_γ is of continuous nature and is maximal for $\Theta_\gamma = \pi$ describing the back-scattering of the photon with the smallest photon energy

$$E'_{\gamma,\min}(\pi) = \frac{E_\gamma}{1 + 2\epsilon},$$

and for the electron the largest kinetic energy

$$E'_{e,\max} = \frac{2\epsilon}{1 + 2\epsilon} E_\gamma,$$

representing the Compton edge in photo-electron spectroscopy. The total cross-section for Compton scattering using high-energy photons is given by

Total cross-section for Compton scattering

$$\sigma_c = \frac{m_e c_0^2}{E_\gamma} \pi r_c^2 \left(\frac{1}{2} + \ln \frac{2E_\gamma}{m_e c_0^2} \right) = \frac{\pi r_c^2}{\epsilon} \left(\frac{1}{N2} + \ln 2\epsilon \right) \tag{4.14}$$

and depends on the number of electrons per atom Z, so that $\sigma_{\text{atomic}} = Z \cdot \sigma_c$.

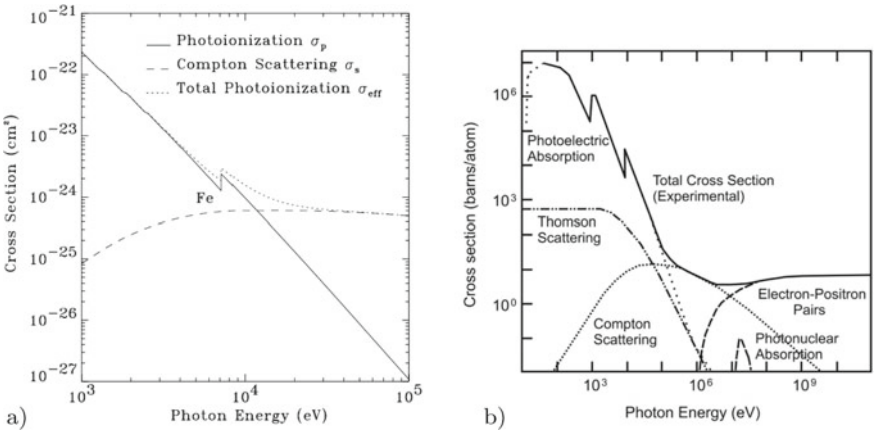

Fig. 4.11 **a** Cross-section for Compton scattering of Fe [10], **b** Overall elastic an inelastic cross-section of Cu [4]

4.7 Pair Production

High-energy electromagnetic radiation can interact with the nucleus of atoms when the photon energy is larger than two times the rest mass of the electron ($E_\gamma = 2 \times 0.511\,\text{MeV} = 1.022\,\text{MeV}$) generating one electron and one positron

$$\gamma \rightarrow e^- + e^+.$$

Due to the conservation of momentum, the nucleus gains a recoil. The total cross-section for pair production at an atom is given by [5].

Total cross-section for pair production

$$\sigma_{\text{PP}}^K = 4\alpha r_c^2 Z^2 \left(\frac{7}{9} \ln 2\epsilon - \frac{109}{54} \right). \tag{4.15}$$

The overall total cross-section for all elastic and inelastic scattering processes for copper is given in Fig. 4.11b.

References

1. N. Firouzi Farrashbandi, M. Eslami-Kalantari, Calculation of the inverse bremsstrahlung absorption in unmagnetized plasmas. Contrib. Plasma Phys. **60**, 0863–1042 (2020). https://doi.org/10.1002/ctpp.201900054
2. https://en.wikipedia.org/wiki/Kramers'_opacity_law

3. Y.R. Davletshin, A computational analysis of nanoparticle-mediated optical breakdown. Ph.D. Thesis, Ryerson University, Oronto, Ontario, Canada, 2017
4. H. Hirayama, *Lecture Note on Photon Interactions and Cross Sections*. KEK, High Energy Accelerator Research Organization, 1-1, Oho, Tsukuba, Ibaraki, 305-0801 Japan, 2000
5. C. Grupen, B. Shwartz, *Particle Detectors* (Cambridge University Press, 2008)
6. L.V. Keldysh, Ionization in the field of a strong electromagnetic wave. Sov. Phys. JETP **20**, 1307 (1965)
7. C.R. McDonald et al., J. Phys: Conf. Ser. **594**, 012019 (2015)
8. M.V. Fedorov, *Interaction of Intense Laser Light with Free Electrons* (CRC Press, 1991), ISBN 3718651262
9. G. Petite, P. Agostini, F. Yergeau, Intensity, pulse width, and polarization dependence of above-threshold-ionization electron spectra. J. Opt. Soc. Am. B **4**(5), 765–769 (1987)
10. https://www.aanda.org/articles/aa/full/2005/36/aa2889-05/aa2889-05.fig.html

Chapter 5
Scattering by Many Charges

Abstract This chapter will deal with the interaction of electromagnetic radiation with many atoms. We will start to add the scattering amplitudes, i.e. the sum of the total cross-sections of many atoms to get the attenuation coefficient. This is a good approach as long as the coherence of the radiation can be omitted. We will see in the first section that concentrating many scatterers within a volume having a mean length being smaller than the coherence length of the radiation results in a much stronger scattering of the radiation.

5.1 Attenuation Coefficient

Radiation interacting with atoms can, as we have seen in the previous chapter, be scattered, and partially or totally absorbed. The intensity of incident electromagnetic radiation I_0 attenuated by scattering and/or absorption, assuming an atom density $n = N/V$ within the volume V, containing N identical atoms, is given by

$$dI = I_0 \, \mu \, dx, \tag{5.1}$$

with $\mu = \mu_a + \mu_s$ defined as the **attenuation coefficient** composed of the absorption and the scattering coefficients. The attenuation coefficient is described by

Attenuation coefficient

$$\mu = n \, \sigma_\mathrm{T} \tag{5.2}$$

using the overall cross-section

Overall cross-section

$$\sigma_\mathrm{T} = \sum \sigma_i \tag{5.3}$$

with $i = a, s$ containing all cross-sections for elastic scattering and inelastic scattering.

© Springer Nature Switzerland AG 2022

A. Horn, *The Physics of Laser Radiation–Matter Interaction*,
https://doi.org/10.1007/978-3-031-15862-9_5

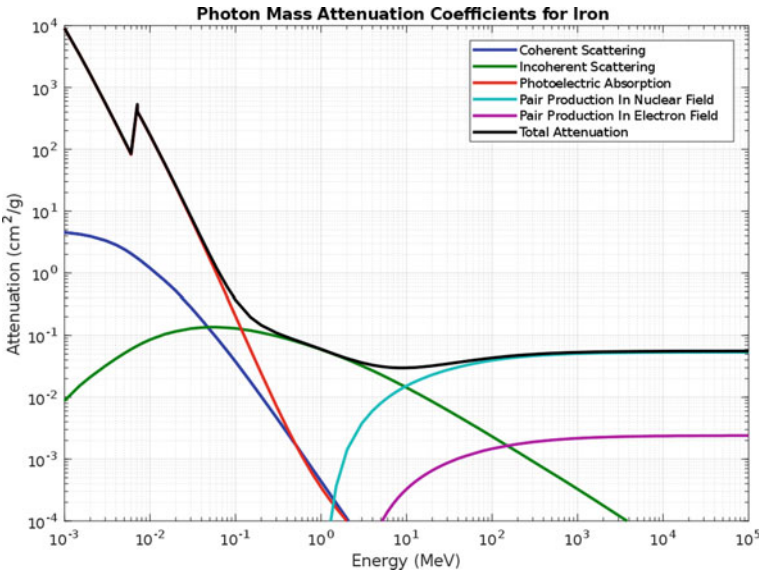

Fig. 5.1 Mass attenuation coefficient for iron [1]

The intensity of the radiation as a function of the propagation direction is then given by integration by parts of (5.1) getting

Lambert–Beer's Law

$$I(x) = I_0 e^{-\mu \cdot x} \tag{5.4}$$

describing the *Lambert–Beer's law* for individual scattering and absorption.[1] Dividing the attenuation coefficient by the density of the investigated matter ϱ, one calculates the **mass attenuation coefficient**, see also Fig. 5.1,

$$\mu^{\mathrm{m}} = \frac{\mu}{\varrho}.$$

5.2 Coherent Scattering

In principle, the scattering power scales with the number density of the scatterer, as described before using the attenuation coefficient. But, up to now we did not consider the wave properties of electromagnetic radiation, especially the possibility of **interference**. Assuming now N atoms, see Fig. 5.2 each one being located at the position $\boldsymbol{r}_j$, and each scatterer carrying a dipole moment proportional to the electric

[1] If only elastic scattering is supposed, no energy is absorbed.

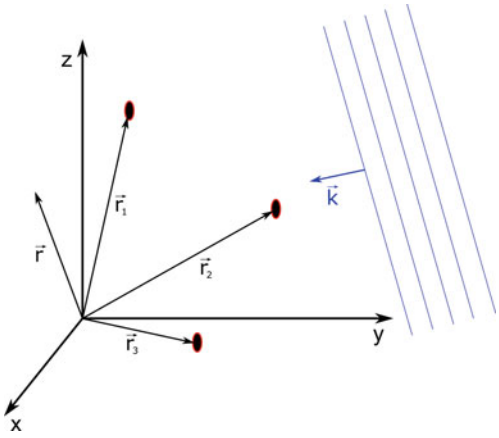

Fig. 5.2 Coherent scattering given by three scatterers

field of the electromagnetic radiation

$$\boldsymbol{d}_j \sim \boldsymbol{E}(\boldsymbol{r}_j).$$

Each dipole moment carries a phase $\propto \exp(i\boldsymbol{k}\cdot\boldsymbol{r}_j)$ representing the path length between the incoming wave and the scatterer (see Fig. 5.2). Also, we have a phase factor given by $\exp(-ik\boldsymbol{e}_r\cdot\boldsymbol{r}_j)$ representing the path length between each scatterer and the point of observation $\boldsymbol{r}$. Introducing $\boldsymbol{q}=\boldsymbol{k}-k\boldsymbol{e}_r$, the differential cross-sections of each scatterer is summed up considering all phase factor differences, and keeping in mind that $d\sigma/d\Omega \propto |\boldsymbol{d}|^2$ one gets [2].

Differential cross-sections for many scatterers

$$\left(\frac{d\sigma}{d\Omega}\right)_N = \frac{d\sigma}{d\Omega}\left|\sum_{j=1}^{N}\exp(i\boldsymbol{q}\cdot\boldsymbol{r}_j)\right|^2 = \frac{d\sigma}{d\Omega}\,|F(\boldsymbol{q})|^2\,. \tag{5.5}$$

The **form factor** $F(\boldsymbol{q})$ represents the Fourier transform of the density distribution $\sum_j \delta(\boldsymbol{r}-\boldsymbol{r}_j)$ of the scatterer positions, and is a measure of the scattering amplitude of a wave per the single atom.

Looking closer at the form factor knowing that the squared absolute value of a complex function is equal to the product of the function with its conjugate complex one, we get

$$|F(\boldsymbol{q})|^2 = \sum_{i=1}^{N}\sum_{j=1}^{N}\exp(i\boldsymbol{q}\cdot(\boldsymbol{r}_i-\boldsymbol{r}_j)) = N + 2\sum_{i=2}^{N}\sum_{j=1}^{i-1}\cos(\boldsymbol{q}\cdot(\boldsymbol{r}_i-\boldsymbol{r}_j)). \tag{5.6}$$

Hereby in the second equation, the summation for $i = j$ results in N, and the summation at $i \neq j$ of (i, j) and (j, i) terms were merged.

There is a strong dependence of the form factor on the distance between the scattering particles, which is described by the overall volume, given by the radius R and containing all scatterers $|\boldsymbol{r}_j| \leq R$, and the wavelength of the radiation λ.

- **Small systems** containing N particles for $R \ll \lambda$ result in $\boldsymbol{q} \cdot (\boldsymbol{r}_i - \boldsymbol{r}_j) \ll 1$, and in consequence only $\cos(\boldsymbol{q} \cdot (\boldsymbol{r}_i - \boldsymbol{r}_j)) \approx 1$ of the exponential function remains. The double summation in the form factor, first equation in (5.6), results in N^2. This is called **coherent scattering**.
- **Large systems** with N particles for $R \gg \lambda$ have an equal amount of terms with cos-function existing (second term in (5.6)), but with opposite signs (change $i \leftrightarrow j$), erasing each other. Only the summands with $i = j$ remain, resulting in an overall sum equal N, describing the so-called **incoherent scattering**.

The differential cross-section of many scatterers $N \gg 1$ results in two different strong scattering behavior

Differential cross-section for coherent and incoherent scattering

$$\left(\frac{d\sigma}{d\Omega}\right)_N \approx \frac{d\sigma}{d\Omega} \begin{cases} N^2 & \text{for } R \ll \lambda : \text{coherent scattering} \\ N & \text{for } R \gg \lambda : \text{incoherent scattering} \end{cases} \tag{5.7}$$

A typical example is the formation of a cloud or the formation of fog: air saturated with water vapor will form small droplets, in case the temperature decreases quickly. Before this formation, the distance of the vapor molecules is comparable to the ones of air molecules, an incoherent scattering proportional to N results. Small droplets formed at a much higher density and with a radius of about $R = 20\,\text{nm} \ll \lambda_{\text{VIS}}$

Fig. 5.3 Clouds scatter sunlight coherently, and for all wavelengths approximately similarly strong

($\lambda_{VIS} \approx 500$ nm), like in a cloud, scatters radiation coherently, resulting in a highly attenuating system, like the fog or a white cloud in the sky. Due to multiple scattering, reflection, and refraction in the droplets, the wavelength selectivity of the cross-section is averaged by stochastic color mixing resulting in white scattered cloud formations (Fig. 5.3).

As the droplet size grows and the radius becomes larger, in the range of the wavelength of the radiation, the cross-section decreases again rapidly. Rain droplets are typically not scattering strongly anymore, but transmitting most of the radiation like dielectrics do (see Chap. 7).

References

1. https://en.wikipedia.org/wiki/Mass_attenuation_coefficient
2. T. Fließbach, *Elektrodynamik* (Springer-Verlag, Berlin Heidelberg, 2012)

Part III
Interaction with Condensed Matter Without Absorption

As no absorption is given, elastic scattering prevails and features a small damping coefficient. Radiation interacts with matter, but only a small part of the radiation is scattered. Condensed matter featuring these properties are called dielectrics. Due to this, we observe many phenomena of the linear optics. In Chap. 6, we investigate generally scattering in condensed matter, also determining the effects of electric fields on dielectrics, where polarization is induced. As one consequence, we introduce the Maxwell equation in matter and deduce the Lorentz model for the induced polarization in matter. This central model allows us to determine, using the Maxwell equations, to establish a dielectric function and from there a complex refractive index of dielectrics. As condensed matter can be built by many different atoms or molecules, also different oscillatory behavior of the electrons are expected and discussed.

One important consequence of condensed matter and the coherent elastic scattering is the directionality of radiation in matter. A laser beam entering a dielectric will mostly propagate further as a beam, and only little amount of radiation is scattered isotropically in space. Similarly, as only a small part of radiation is scattered at all, depending on the frequency of the radiation with respect to the oscillatory frequency of the scatterer, the overlap of the scattered with the non-scattered radiation results in a phase velocity being smaller or larger than the speed of light in vacuum.

Linear optics is the great consequence of scattering of radiation without absorption and is discussed in Chap. 7. Here, we start again from the Maxwell equations firstly determining the conditions of the electric and magnetic fields at boundaries, i.e. the transition from one optical medium to another. We then determine the Fresnel equations depicting the energy transport through the boundary as transmitted radiation and back into the first medium as reflected radiation. We will also look closely at the Brewster angle and its physical interpretation, as well as at the critical angle for total reflection.

The last Chap. 8 discusses the optics for radiation at high intensities, where non-linear processes are given, and classifies the non-linear optics. We determine firstly the principal equation of non-linear optics, and in the following we describe, again using the semi-classical approach used for the elastic scattering process for condensed matter, non-linear quadratic repulsive forces of the electrons interacting with electromagnetic radiation. A non-linear polarization of matter results, which we use to solve the principal equation using some approximations. Second-order pro-

cesses are deviated describing the second-harmonic generation, and determining the Manley–Rowe relations also three-wave mixing is described, being the non-linear process in optical parametric amplifiers and oscillators. Applying non-linear cubic forces third-order processes like four-wave mixing, third-harmonic generation, the Kerr effect by four-wave mixing, and self-focusing is described.

Chapter 6
Scattering in Matter

Abstract Now taking the knowledge on the interaction of electromagnetic radiation with atoms, we have to determine macroscopic measures in the condensed state. But as the number of scatterers per cubic centimeter is a very large number in the range of $n \approx 10^{23}$, a simple coherent addition of all scattered fields is not possible. Historically given, and also a very elegant approach is to derive first an understanding of the macroscopic reaction of matter interacting with electromagnetic radiation by applying the Maxwell equations. For sake of simplicity, we will only look at the electric fields. Knowing the reaction of matter, we will call it the polarization density, and we will be able to compare it with our scattering model of a single dipole. This will be called the Lorentz model.

6.1 Reversible and Irreversible Interaction

Depending on the matter state and the intensity of the radiation, different processes are given. So, one has to distinguish between **reversible** and **non-reversible interactions**, meaning that in the first case the condensed matter restores its state completely without any chemical or physical modification after irradiation. Here, we talk about the *linear optics*. In the second case, the state of the matter changes resulting after irradiation in matter with different physical properties, e.g. change in the crystal structure, the concentration of the chemical compounds, or its chemistry. To achieve a phase change, energy is needed; why the *absorption* of radiation is necessary, see Fig. 6.1.

Electromagnetic radiation interacting with condensed matter will primarily interact with electrons. This is true for intensities of radiation being much smaller than the atomic electric fields, being below 10^{14} W/cm^2. Depending on the state of the condensed matter, the electrons are quasi-free or bounded.

As one has seen in the previous sections, bounded electrons feature an *elastic scattering* without absorption of radiation. This is also true for bounded electrons in condensed matter at small photon energies compared to the resonance frequency (no X-rays) of the bounded electron, and for small intensities (no Raman scattering). This condensed matter is called a **dielectric**, and the process of interaction with radiation

© Springer Nature Switzerland AG 2022

A. Horn, *The Physics of Laser Radiation–Matter Interaction*,
https://doi.org/10.1007/978-3-031-15862-9_6

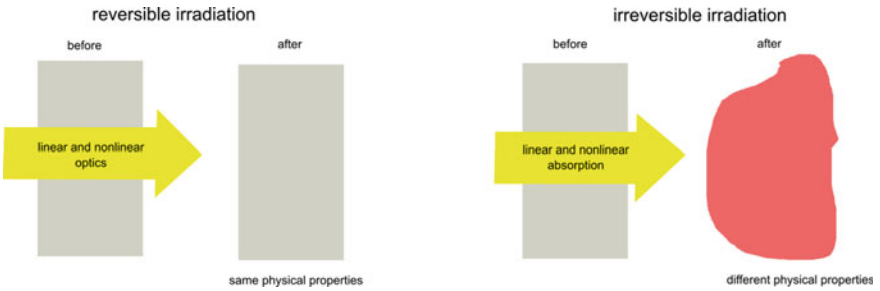

Fig. 6.1 Reversible and irreversible processes describing linear and non-linear optics (left) and linear and non-linear absorption followed by irreversible phase changes (right)

is described as linear optics with the laws of reflection and refraction. Differently, **metals** feature quasi-free and bounded electrons. There *inelastic scattering* of the electrons takes place, and the optical energy is absorbed and deposited into matter forcing the heating of the condensed matter. In both cases of matter, the dielectric or the metal, a **linear absorption process** takes place; see Fig. 6.2.

Increasing the intensity in a metal results in an increased deposition in the matter of optical energy per time. The process is still linear. Contrary, dielectrics will start to interact only non-linearly with the radiation due to its needed large electric fields, inducing non-linear repulsive force of the dielectric constituents. Depending on the

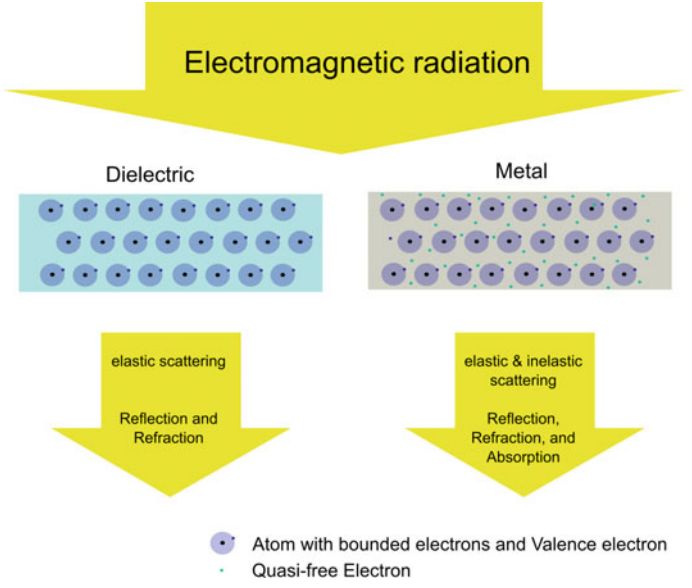

Fig. 6.2 Linear interaction of electromagnetic radiation with condensed matter: dielectrics feature only bounded electrons (left) and metals feature bounded and quasi-free electrons (right)

intensity of the radiation, one distinguishes again in reversible and non-reversible non-linear interaction. In the first case, we talk about **non-linear optics**, and in the second case, we talk about **non-linear absorption**.

6.2 Maxwell Equations in Matter

Now, the approach is straightforward: we are looking for the paths condensed matter interacts with radiation. So, we are looking for a description of the optical property of condensed matter, here especially the emission of radiation by the dipoles after irradiation. Therefore, we will determine the surface charge densities induced by electric fields in a dielectric, because like in a capacitor, charges separated in space represent a dipole.

One value being important in optics is the **refractive index**, describing the change in the velocity of the electromagnetic radiation entering matter c_{M} compared to the speed of light in vacuum c_0

Refractive index

$$n = \frac{c_0}{c_{\mathrm{M}}}. \tag{6.1}$$

We will see that this very important relation will be described via the surface charges in a capacitor. Also, later we will see that in practice, the refractive index is a complex number $\tilde{n} \in \mathcal{C}$, where the above given value n represents just the real part of $\tilde{n}$.

Microscopically, each atom represents a scatterer, or analogous each atom represents a point source emitting spherical waves.[1] We omit this approach (see for example here [1, 2] for an adequate description) and start describing the reaction, i.e. the answer of a dielectric material when a static and constant electric field acts on it. Later we will move on to oscillating fields.

Starting with a charged capacitor consisting of two electrodes spaced by b and featuring an electrode area a, we found that the electrostatic field strength scales with the surface charge, see (1.33), and the **capacity** is given by

$$C_0 = \frac{q_0}{U_0};$$

see Fig. 6.3a.

Introducing a dielectric into the capacitor the amount of charges on the electrodes does clearly not change, $q_0 = \text{const.}$[2] But now, one observes that the voltage between the two plates is reduced $U < U_0$ proportional to the capacity C_D of the capacitor

[1] This is for distances large compared to the dipole amplitude.

[2] The plates are electrically isolated from the surrounding.

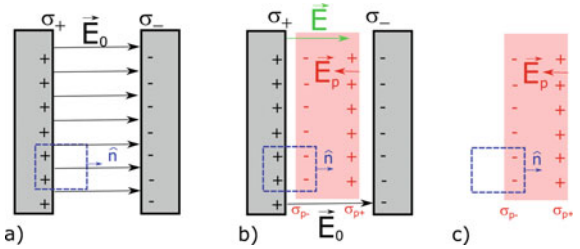

Fig. 6.3 Electric field strengths $\boldsymbol{E}_0$, $\boldsymbol{E}$, and $\boldsymbol{E}_\mathrm{p}$ in a charged capacitor without dielectric (**a**), with a dielectric (**b**), and without the capacitor plates (**c**) [2]

$$U = \frac{q_0}{C_D}.$$

The decrease in voltage introducing an dielectric is equivalent to the increase in charges at a constant voltage. So, we define an "amplification" factor, the so-called **relative permittivity** or relative dielectric constant

Relative permittivity

$$\epsilon_\mathrm{r} = \frac{C_D}{C_0} = \frac{\epsilon}{\varepsilon_0}. \tag{6.2}$$

The relative permittivity represents also the fraction between the absolute permittivity ϵ and the vacuum permittivity ε_0.

As the **voltage in a capacitor** is given by the formation of the electric field strength E_0 and the distance between the plates b,

$$U_0 = E_0 b,$$

one gets for the reduced voltage the electric field strength E in the dielectric

$$\begin{aligned} E &= \frac{U}{b} \\ &= \frac{q_0}{C_D \cdot b}, \quad \text{and using (1.33) for } q_0 \\ &= \frac{U_0 \cdot C_0}{C_D \cdot b}, \quad \text{and using } E_0 = U_0/b \end{aligned}$$

Electric field strength in the dielectric

$$E = \frac{1}{\epsilon_\mathrm{r}} E_0. \tag{6.3}$$

Introducing a dielectric, the electric field strength is reduced by the relative permittivity ϵ_r. This can be interpreted as the **influence** of the initial electric field strength on the induced dipoles in the dielectric.

Thereby, the induced dipoles in the dielectric have different properties and we distinguish two **classes of dipoles**:

- *Static dipole*: In case the condensed matter is liquid, one can imagine that molecules of the fluid exhibit a constant dipole moment, like the water molecules, with a more electronegative oxygen atom compared to the hydrogen atoms. The water molecules feature molecular dipole moments and will align by **rotation** in the electrostatic field.
- *Dynamic dipole*: Atoms and molecules represent electrical neutral entities with vanishing dipole moment. Interaction with a constant or time-dependent electric field will result in a relative **displacement** of the electron (cloud) respective to the positive nucleus resulting in a constant or timedependent dipole moment.

The resulting electric field strength $\boldsymbol{E}$ is understood as the addition of the initial field strength with an induced opposite field, the so-called **electric polarization** $\boldsymbol{E}_p$ (Fig. 6.3b)

$$\boldsymbol{E} = \frac{1}{\epsilon_r}\boldsymbol{E}_0 = \boldsymbol{E}_0 + \boldsymbol{E}_p.$$

The electric polarization is proportional to the electric field strength and can be rewritten for the electric field strength in the dielectric, too

$$\begin{aligned}\boldsymbol{E}_p &= \left(\frac{1}{\epsilon_r} - 1\right)\boldsymbol{E}_0 \\ &= -(\epsilon_r - 1)\frac{1}{\epsilon_r}\boldsymbol{E}_0 \\ &= -(\epsilon_r - 1)\boldsymbol{E}\end{aligned}$$

Electric polarization

$$\boldsymbol{E}_p = -\chi_e \boldsymbol{E}. \tag{6.4}$$

The strength of the induced polarization is described by the **electric susceptibility**

Electric susceptibility

$$\chi_e = \epsilon_r - 1. \tag{6.5}$$

In order to get the induced dipole moment in the dielectric, we see that the electric polarization given here results in surface charge densities σ_p on the dielectric surfaces (Fig. 6.3b). We determine these charges by applying the approach used in Sect. 1.6.1 and using Maxwell equation (1.8) and the Gauß law getting the flux of the electric

field strength through the surfaces of a defined volume. In Fig. 6.3, the blue dashed box represents the side view of this volume V. The electric flux in Fig. 6.3a is defined as

$$\begin{aligned}\Psi^e &= \varepsilon_0 \int_V \nabla \cdot \boldsymbol{E}_0 \, \mathrm{d}V \\ &= \varepsilon_0 \oint_{(V)} \boldsymbol{E}_0 \cdot \mathrm{d}\boldsymbol{a} = \varepsilon_0 \oint_{(V)} \boldsymbol{E}_0 \cdot \hat{\boldsymbol{n}} \, \mathrm{d}a \\ &\overset{(1.8)}{=} \int_V \varrho_0 \mathrm{d}V = q_0 = \oint_{(V)} \sigma \, \mathrm{d}a.\end{aligned}$$

Comparing the results of the last two lines, we get the description of the electric field strength for the capacitor with the **surface charge densities**

$$\boldsymbol{E}_0 \cdot \hat{\boldsymbol{n}} = \frac{\sigma}{\varepsilon_0}, \tag{6.6}$$

and for the electric field strength with an dielectric, the electric field strength in the dielectric by

$$\boldsymbol{E} \cdot \hat{\boldsymbol{n}} = \frac{\sigma + \sigma_\mathrm{p}}{\varepsilon_0} = \frac{\sigma_\mathrm{eff}}{\varepsilon_0},$$

with the **effective surface charge density** $\sigma_\mathrm{eff} = \sigma + \sigma_\mathrm{p}$. Finally, we get the relation for the electric polarization, see Fig. 6.3c), to

$$\boldsymbol{E}_\mathrm{p} \cdot \hat{\boldsymbol{n}} = \frac{\sigma_\mathrm{p}}{\varepsilon_0}.$$

The **polarization surface charge density** is proportional to the electric field strength and consequently dependent on the surface charge density of the capacitor

$$\begin{aligned}\sigma_\mathrm{p} &= \varepsilon_0 \boldsymbol{E}_\mathrm{p} \cdot \hat{\boldsymbol{n}} \\ &= -\varepsilon_0 \chi_\mathrm{e} (\boldsymbol{E} \cdot \hat{\boldsymbol{n}}) \\ &= -\varepsilon_0 \chi_\mathrm{e} \frac{1}{\epsilon_\mathrm{r}} (\boldsymbol{E}_0 \cdot \hat{\boldsymbol{n}}) = -\varepsilon_0 \chi_\mathrm{e} \frac{1}{\epsilon_\mathrm{r}} \frac{\sigma}{\varepsilon_0}\end{aligned}$$

Polarization surface charge density

$$\sigma_\mathrm{p} = -\frac{\epsilon_\mathrm{r} - 1}{\epsilon_\mathrm{r}} \sigma. \tag{6.7}$$

Now, looking on the dielectric and imaging the capacitor plates far away but still acting with its constant field, we detect two opposite signed surface charge densities $\sigma^\pm$ on the dielectric spaced by b. The surface charge is given by $-\sigma_\mathrm{p} \cdot a$, with a

representing the surface area of the dielectric.[3] The **dipole moment** of the dielectric, induced by an external electric field strength, is calculated by

$$\boldsymbol{d}_{\mathrm{de}} = d_{\mathrm{de}}\,\hat{\boldsymbol{n}} = q\,b\,\hat{\boldsymbol{n}} = -\sigma_{\mathrm{p}}\,a\,b\,\hat{\boldsymbol{n}} = -\sigma_{\mathrm{p}} V \hat{\boldsymbol{n}}$$

Assuming in the dielectric volume N atomar dipoles getting a **number density of the dipoles** $n_{\mathrm{d}} = N/V$ of many atomar dipoles $\boldsymbol{d}$, one calculates an **overall dipole moment**

$$N\,\boldsymbol{d} = n_{\mathrm{d}}\,\boldsymbol{d}\,V = \boldsymbol{P}\,V, \tag{6.8}$$

with the dipole moment density $\boldsymbol{P}$, the so-called **polarization**.

$$\begin{aligned}\boldsymbol{P} &= -\sigma_{\mathrm{p}}\hat{n} = -\varepsilon_0 \boldsymbol{E}_{\mathrm{p}} \\ &= \varepsilon_0 \chi_{\mathrm{e}} \boldsymbol{E} \\ &= \varepsilon_0(\epsilon_{\mathrm{r}} - 1)\boldsymbol{E}.\end{aligned}$$

We have got a relation between the polarization and the external field, as well as the electric susceptibility, representing the dipole properties of the dielectric.

Comparing now the first calculated dipole moment using the polarization surface charge density from the Maxwell equation and the one using atomar dipoles, we get the dipole moment density, i.e. the polarization rewritten to

Polarization

$$\boldsymbol{P} = n_{\mathrm{d}}\,\boldsymbol{d} = \varepsilon_0 \chi_{\mathrm{e}} \boldsymbol{E}. \tag{6.9}$$

So, electric fields in matter induce a polarization. The resulting field, the so-called **displacement field in matter** is given by the **material equation**

Displacement field in matter

$$\boldsymbol{D} = \epsilon_0 \boldsymbol{E} + \boldsymbol{P}. \tag{6.10}$$

Assuming a linear and isotropic material, the relative permittivity ϵ_{r} and the electric susceptibility χ_{e} are a scalar function and we can write for the displacement field

$$\boldsymbol{D} = \varepsilon_0 \epsilon_{\mathrm{r}} \boldsymbol{E},$$

with the **linear polarization**

[3] The minus sign results from the opposite direction of the electric polarization vector $\boldsymbol{E}_{\mathrm{p}}$ to the inducing field $\boldsymbol{E}_0$.

Linear polarization

$$\boldsymbol{P} = \varepsilon_0(\epsilon_\mathrm{r} - 1)\boldsymbol{E}. \tag{6.11}$$

As shown in standard textbooks of electrodynamics [2], the reaction of matter on a magnetic field will result in an analogous reaction field as the polarization (density), the so-called **magnetization**. The magnetization $\boldsymbol{M}$ connects the magnetic field strength $\boldsymbol{H}$ with the magnetic induction $\boldsymbol{B}$

Magnetic field strength

$$\boldsymbol{H} = \frac{1}{\mu_0}\boldsymbol{B} - \boldsymbol{M}. \tag{6.12}$$

Assuming a linear and isotropic material, the **relative permeability** μ_r and the **magnetic susceptibility**

Magnetic suszeptibility

$$\chi_\mathrm{m} = \left(1 - \frac{1}{\mu_\mathrm{r}}\right) \tag{6.13}$$

are a scalar function and we can write for the magnetic field strength by

$$\boldsymbol{H} = \frac{1}{\mu_0\mu_\mathrm{r}}\boldsymbol{B} \tag{6.14}$$

with the **linear magnetization**

$$\boldsymbol{M} = \frac{1}{\mu_0}\left(1 - \frac{1}{\mu_\mathrm{r}}\right)\boldsymbol{B} = \frac{1}{\mu_0}\chi_\mathrm{m}\boldsymbol{B}.$$

We can now rewrite the Maxwell equations in matter with the material equations as

Maxwell equations in matter

$$\nabla \times \boldsymbol{E} = -\frac{\partial \boldsymbol{B}}{\partial t} \tag{6.15}$$

$$\nabla \cdot \boldsymbol{D} = \varrho \tag{6.16}$$

$$\nabla \times \boldsymbol{H} = \boldsymbol{J} + \frac{\partial \boldsymbol{D}}{\partial t} \tag{6.17}$$

$$\nabla \cdot \boldsymbol{B} = 0. \tag{6.18}$$

Material equations

$$\boldsymbol{D} = \epsilon_0 \boldsymbol{E} + \boldsymbol{P} \tag{6.19}$$

$$\boldsymbol{H} = \frac{1}{\mu_0}\boldsymbol{B} - \boldsymbol{M}. \tag{6.20}$$

6.3 Lorentz Model

Up to now, we worked with a static field, but w.l.o.g.[4] dynamic fields are allowed, as long as the dipoles can follow the oscillating fields. So, one can take as well electromagnetic fields as an external field. We calculated for an oscillating dipole, see (3.25), $\boldsymbol{d}(t) = \alpha_\mathrm{e}\boldsymbol{E} = -\varepsilon_0 \boldsymbol{E}_\mathrm{p}$, expanding it by the number density of the dipoles n_d (for N dipoles per volume V) on the one hand the dipole moment density as function of the atomar dipole moment, see (6.8), and on the other hand the relation between dipole moment density and the electric susceptibility

$$\begin{aligned} \boldsymbol{P} &= n_\mathrm{d}\, \boldsymbol{d} \\ &= \frac{n_\mathrm{d}\, e^2}{m_\mathrm{e}} \frac{1}{\left(\omega_0^2 - \omega^2 - i\omega\Gamma_\mathrm{em}\right)} \boldsymbol{E} \\ &\stackrel{!}{=} \varepsilon_0 \tilde{\chi}_\mathrm{e} \boldsymbol{E}. \end{aligned} \tag{6.21}$$

Take care that here the electric susceptibility is now a complex function, $\tilde{\chi}_\mathrm{e} \in \mathbb{C}$. So, when electromagnetic radiation interacts with a dielectric, it induces oscillating dipoles, which on its part induce an electromagnetic polarization field given by the dipole equation. The strength of this field is given by the number density of the dipoles and is proportional to the electric field strength $\boldsymbol{E}$. The "reaction term" is written to

$$\varepsilon_0 \tilde{\chi}_\mathrm{e} = \varepsilon_0(\tilde{\epsilon}_\mathrm{r} - 1) = \frac{n_\mathrm{d}\, e^2}{m_\mathrm{e}} \frac{1}{\left(\omega_0^2 - \omega^2 - i\omega\Gamma_\mathrm{em}\right)}.$$

As one can see, the relative permittivity $\tilde{\epsilon}_\mathrm{r}$ is a complex number, and its description is called the **Lorentz model** describing the **dielectric function**

The Lorentz model and the dielectric function

$$\tilde{\epsilon}_\mathrm{r} = \epsilon_1 + i\epsilon_2 = 1 + \frac{n_\mathrm{d}\, e^2}{m_\mathrm{e}\varepsilon_0} \frac{1}{\left(\omega_0^2 - \omega^2 - i\omega\Gamma_\mathrm{em}\right)} \in \mathbb{C}. \tag{6.22}$$

[4] without loss of generality (German: ohne Beschränkung der Allgemeinheit o.B.d.A.)

The speed of light in vacuum is given by (1.10) and can be expanded using (6.2) for the **speed of light in matter** to

$$c_{\mathrm{M}} = \frac{1}{\sqrt{\epsilon\mu}} = \frac{1}{\sqrt{\epsilon_{\mathrm{r}}\varepsilon_0\mu_{\mathrm{r}}\mu_0}} = \frac{c_0}{\sqrt{\epsilon_{\mathrm{r}}\mu_{\mathrm{r}}}}. \tag{6.23}$$

The refractive index n, see (6.1), gets now complex

$$\tilde{n} = \sqrt{\tilde{\epsilon}_{\mathrm{r}}\mu_{\mathrm{r}}},$$

and assuming for instance that the relative permeability is unity, $\mu_{\mathrm{r}} \approx 1$ one can write the Lorentz model describing the **dispersion relation**

Dispersion relation

$$\tilde{n}^2 = \tilde{\epsilon}_{\mathrm{r}} = 1 + \left(\frac{n_{\mathrm{d}}\, e^2}{\varepsilon_0\, m_{\mathrm{e}}}\right) \frac{1}{\left(\omega_0^2 - \omega^2 - i\omega\Gamma_{\mathrm{em}}\right)}, \tag{6.24}$$

and introducing the plasma frequency

Plasma frequency

$$\omega_{\mathrm{p}} = \sqrt{\frac{n_{\mathrm{d}}\, e^2}{\varepsilon_0\, m_{\mathrm{e}}}}, \tag{6.25}$$

one gets for the dispersion relation

$$\tilde{n}^2 = 1 + \omega_{\mathrm{p}}^2 \frac{1}{\left(\omega_0^2 - \omega^2 - i\omega\Gamma_{\mathrm{em}}\right)}. \tag{6.26}$$

Complex refractive index

The refractive index $\tilde{n}$ represents a complex number: $\tilde{n} \in \mathbb{C}$ and is given for $\mu_{\mathrm{r}} = 1$ by

$$\tilde{n} = n - i\kappa = \sqrt{1 + \frac{\omega_{\mathrm{p}}^2}{\left(\omega_0^2 - \omega^2 - i\omega\Gamma_{\mathrm{em}}\right)}}. \tag{6.27}$$

Here, we define the **refractive index** as the real part of the complex refractive index $n = \Re(\tilde{n})$ and the **extinction coefficient** as the imaginary part of the complex refractive index $\kappa = \Im(\tilde{n})$.

6.4 Refractive Index

Recalling the equation of motion (3.18), one can now compute the amplitude of each oscillating electron, see (3.23)

$$\boldsymbol{a} = a\,\hat{a} = a\,\hat{E}_0,$$

by describing its value a using the Euler description of a complex number, using its amplitude $|\boldsymbol{a}|$ and phase φ

$$\begin{aligned} a &= |\boldsymbol{a}| e^{i\varphi} \\ &= \frac{e\,E_0}{m_\mathrm{e}\sqrt{\left(\omega_0^2 - \omega^2\right)^2 + \omega^2 \Gamma_\mathrm{em}^2}}\, e^{i\varphi} \end{aligned}$$

with the phase[5]

$$\varphi = \arctan\left(\frac{\Gamma_\mathrm{em}\,\omega}{m_\mathrm{e}\,(\omega_0^2 - \omega^2)}\right). \tag{6.28}$$

Obviously, the weakly bounded electron in the atom is driven by the electric field $\boldsymbol{E}_0$ oscillating with the frequency ω. Calculating the amplitude with the damping coefficient Γ_em from (3.20) results in a very sharp peak at the harmonic angular frequency of the electron in the atomic system ω_0, so-called resonance frequency (Fig. 6.4). Due to the very sharp peak, also the phase of the electron changes abruptly at ω_0 from zero to π. Increasing the damping coefficient by many orders of magnitude, the amplitude gets broader in the full width at half maximum (FWHM), and the phase changes smoothly.

As learned, an oscillating electron represents an accelerated particle, featuring its maximum acceleration at the reversal points of the electron trajectory (see Sect. 2.3.3). Looking at the electron's phase, this maximum acceleration is reached at the phase $\varphi_\mathrm{e} = \pi$. Substantially the electron starts to emit at $\varphi_\mathrm{e} = \pi/2$ resulting in a phase shift of the emitted radiation to the oscillating electron of at least $\pi/2$.

So, the phase of the emitted radiation starts with $\varphi_\mathrm{em} = \pi/2$ and results at the resonance frequency ω_0 to $\varphi_\mathrm{em} = \pi$, and above ω_0 getting close to $\varphi_\mathrm{em} = 3/2\pi$, depending on the damping coefficient Γ_em. For weak attenuation, the phase changes abruptly by π.

In condensed matter, the dipole moment of each scatterer is given by the amplitude and the phase and scales by the dipole density n_d. The response of the matter to electromagnetic radiation is given by the relative permittivity $\tilde{\epsilon}$. The squared complex refractive index, being equal to the relative permittivity $\tilde{\epsilon}$, can be written by a real and an imaginary part by multiplying the conjugate complex part of the denominator,

[5] The phase of a complex number $a = \Re(a) + i\Im(a)$ is defined by $\tan\varphi = \frac{\Im(a)}{\Re(a)}$.

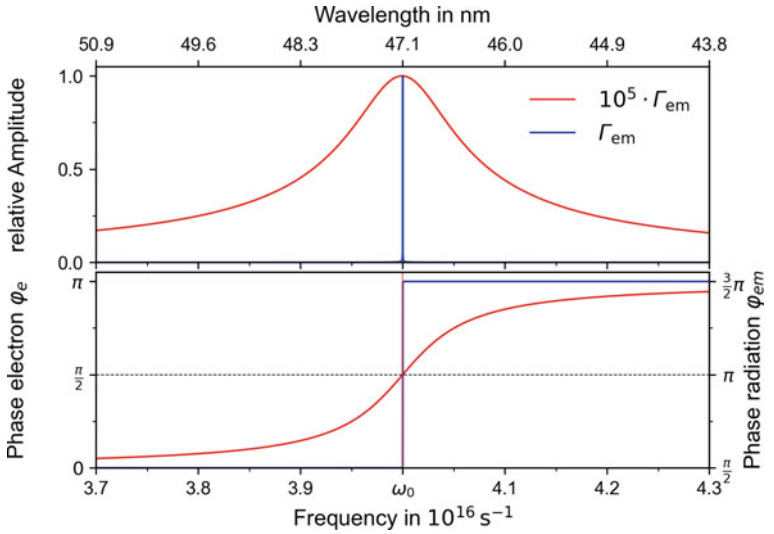

Fig. 6.4 Relative amplitude (top) and phase (bottom) of the oscillating electron with two damping coefficients Γ_{em}, and the phase of the emitted radiation (bottom, right axes)

$$\tilde{n}^2 = 1 + \frac{\omega_\mathrm{p}^2}{\left(\omega_0^2 - \omega^2 - i\omega\Gamma_{\mathrm{em}}\right)} \frac{\left(\omega_0^2 - \omega^2 + i\omega\Gamma_{\mathrm{em}}\right)}{\left(\omega_0^2 - \omega^2 + i\omega\Gamma_{\mathrm{em}}\right)} \tag{6.29}$$

$$= \underbrace{1 + \frac{\omega_\mathrm{p}^2(\omega_0^2 - \omega^2)}{\left(\omega_0^2 - \omega^2\right)^2 + \omega^2\Gamma_{\mathrm{em}}^2}}_{\Re(\tilde{n}^2)} + i \underbrace{\frac{\omega_\mathrm{p}^2\omega\ \Gamma_{\mathrm{em}}}{\left(\omega_0^2 - \omega^2\right)^2 + \omega^2\Gamma_{\mathrm{em}}^2}}_{\Im(\tilde{n}^2)}. \tag{6.30}$$

The squared complex refractive index $\tilde{n}^2$ represents a complex number, and also $\tilde{n} = n - i\kappa$

$$\begin{aligned} \tilde{n}^2 = \tilde{\epsilon} &= \epsilon_1 + i\epsilon_2 \\ (n - i\kappa)^2 &= \\ \left(n^2 - \kappa^2\right) - i(2n\kappa) &= \end{aligned}$$

and we can write the identity using the relative permittivity, now being complex $\tilde{\epsilon} = \epsilon_1 + i\epsilon_2$, too

$$\epsilon_1 = n^2 - \kappa^2 \tag{6.31}$$

$$\epsilon_2 = -2n\kappa. \tag{6.32}$$

One sees, assuming a *vanishing damping coefficient* Γ_{em}, that the relative permittivity $\tilde{\epsilon}$ gets a real number

$$\epsilon_1 = \Re(\tilde{n}^2) = \left(n^2 - \kappa^2\right) \xrightarrow{\Gamma_{\text{em}} \to 0} 1 + \frac{\omega_\text{p}^2}{\omega_0^2 - \omega^2}$$
$$\epsilon_2 = \Im(\tilde{n}^2) = -2n\kappa \qquad \xrightarrow{\Gamma_{\text{em}} \to 0} 0.$$

Assuming now a *small scatterer density* so that $\omega_\text{p} \ll \omega_0$ is valid, and also assuming a small extinction coefficient $\kappa \ll n$ because of a small damping constant Γ_{em}, we get

$$\Re(\tilde{n}^2) = \epsilon_1 \approx n^2$$

allowing us to approximate the refractive index using (6.30) by

Refractive index for weak damping

$$n = \sqrt{1 + \frac{\omega_\text{p}^2(\omega_0^2 - \omega^2)}{\left(\omega_0^2 - \omega^2\right)^2 + \omega^2\Gamma_{\text{em}}^2}}. \tag{6.33}$$

As the second summand in the square root is for $\omega \ll \omega_0$ small compared to 1,

$$\frac{\omega_\text{p}^2(\omega_0^2 - \omega^2)}{\left(\omega_0^2 - \omega^2\right)^2 + \omega^2\Gamma_{\text{em}}^2} \ll 1,$$

one can approximate the square root by

$$n = 1 + \frac{1}{2}\frac{\omega_\text{p}^2(\omega_0^2 - \omega^2)}{\left(\omega_0^2 - \omega^2\right)^2 + \omega^2\Gamma_{\text{em}}^2} \approx 1,$$

meaning that the refractive index far away from a resonance is about unity. Now taking (6.32), we can compute the extinction coefficient to

The extinction coefficient for weak damping

$$\kappa = -\frac{1}{2}\frac{\omega_\text{p}^2\omega\ \Gamma_{\text{em}}}{\left(\omega_0^2 - \omega^2\right)^2 + \omega^2\Gamma_{\text{em}}^2}. \tag{6.34}$$

Plotting the refractive index n and the extinction coefficient κ for this assumptions, one observes two regimes for the frequency of the external field separated by the resonance frequency ω_0 (Fig. 6.5):

- $\boldsymbol{\omega < \omega_0}$: The value of the refractive index is still larger than unity. In consequence, the speed of light in the medium is smaller than the speed of light in vacuum; see (6.23).
- $\boldsymbol{\omega > \omega_0}$: The value of the refractive index is still smaller than unity. In consequence, the speed of light in the medium is larger than the speed of light in vacuum.

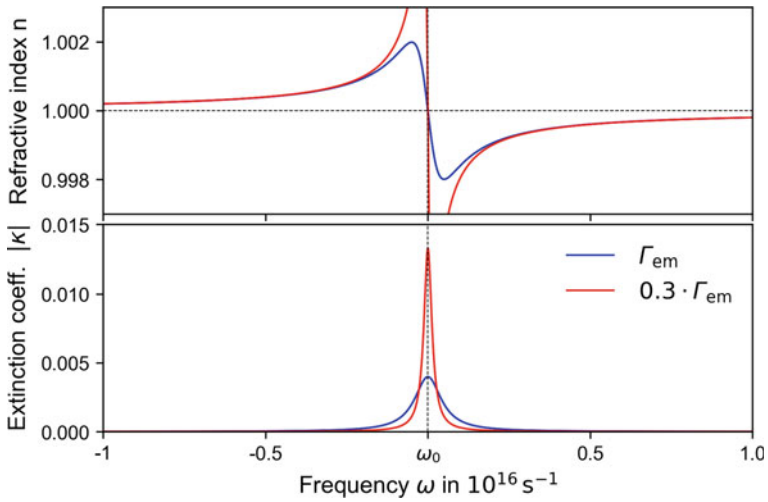

Fig. 6.5 Refractive index n (top) and value extinction coefficient $|\kappa|$ (bottom) for a scatterer concentration $n_p = 1 \cdot 10^{21}\,m^{-3}$ and two damping coefficients $\Gamma_{em} = 1 \cdot 10^{10}$ 1/s (blue), and $\Gamma_{em} = 0.3 \cdot 10^{10}$ 1/s (red). The resonance frequency ω_0 is located at absorption peak

The region of the refractive index with a positive slope $\boldsymbol{dn/d\omega > 0}$ is called **normal dispersion**. The region with negative slope $\boldsymbol{dn/d\omega < 0}$ is called **anomalous dispersion**. The full width at half maximum (FWHM) is about six orders of magnitudes smaller than the resonance frequency ω_0, so the extinction coefficient is a very sharp distributed function around ω_0.

6.5 Many Different Scatterers

Condensed matter consists often of many different types of atoms. So, e.g. fused silica represents a solid transparent dielectric composed of the atoms silicon (Si) and oxygen (O), often written as a-SiO_2 (amorphous quartz). Depending on the investigated wavelength regime, a number of resonant frequencies of these atoms can be given. Assuming that the matter consists of m different resonances, the **oscillator strength of one resonant frequency** $\boldsymbol{\omega_{0i}}$ is given by

$$f_i = \frac{N_i}{N},$$

where N_i denotes the number density of each kind of resonant atoms at ω_{0i}, and the total particle density of the resonant atoms is given by $N = \Sigma_i N_i$ with $i = 1, \ldots, m$. The oscillator strengths are normalized by

$$\sum_{i=1}^{m} f_i = 1.$$

In analogy to the calculation of $\tilde{n}^2$ with one scatterer, one resonance ω_0, and a density of dipoles n_d, (6.24), now we can generalize to m different resonant atoms getting

$$\begin{aligned}\tilde{n}^2 &= \tilde{\epsilon}_\mathrm{r} = \chi_\mathrm{e} + 1 \\ &= \epsilon_1 + i\epsilon_2 \\ &= 1 + \omega_\mathrm{p}^2 \sum_{i=1}^{m} \frac{f_i}{\omega_{0i}^2 - \omega^2 - i\omega\Gamma_{\mathrm{em},i}},\end{aligned}$$

taking into account that each resonance frequency ω_{0i} has its damping constant $\Gamma_{\mathrm{em},i}$. One calculates the real and imaginary parts of $\tilde{n}^2$ being equal to the to relative permittivity $\tilde{\epsilon}_\mathrm{r}$. The relative permittivity is often also called the dielectric function.

Relative permittivity or dielectric function for many oscillators

$$\epsilon_1 = n^2 - \kappa^2 = 1 + \omega_\mathrm{p}^2 \sum_{i=1}^{m} \frac{(\omega_{0i}^2 - \omega^2) f_i}{(\omega_{0i}^2 - \omega^2)^2 + \omega^2 \Gamma_{\mathrm{em},i}^2} \tag{6.35}$$

$$\epsilon_2 = -2n\kappa = \omega_\mathrm{p}^2 \sum_{i=1}^{m} \frac{f_i\, \omega\, \Gamma_{\mathrm{em},i}}{(\omega_{0i}^2 - \omega^2)^2 + \omega^2 \Gamma_{\mathrm{em},i}^2}. \tag{6.36}$$

Assuming one resonance frequency, an example is given in Fig. 6.6a for crown glass, thereby plotting the measured refractive index as function of $(n^2-1)^{-1}$ in the wavelength regime 388 nm $< \lambda <$ 728 nm as function of $1/\lambda^2$. For vanishing damping constant Γ_{em}, a linear dependence is expected, and as seen in Fig. 6.6a, the dependence is also compared by measurements [3].

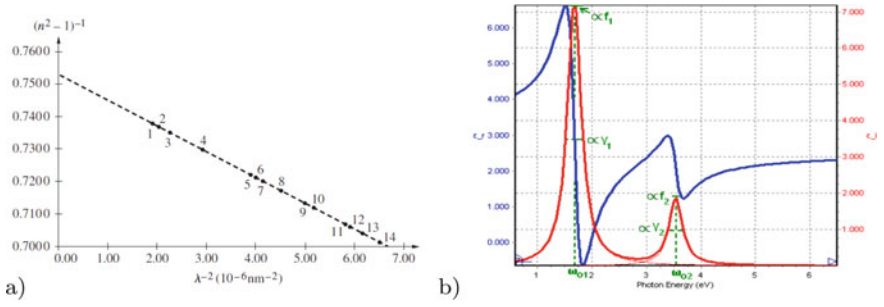

Fig. 6.6 Linear dependence of $(n^2-1)^{-1}$ as function of $1/\lambda^2$ for crown glass assuming one resonant frequency (Reproduced from [3], with the permission of American Association of PhysicsTeachers) (**a**), and double resonance in CuPc (Copper phthalocyanine) (**b**) [4]

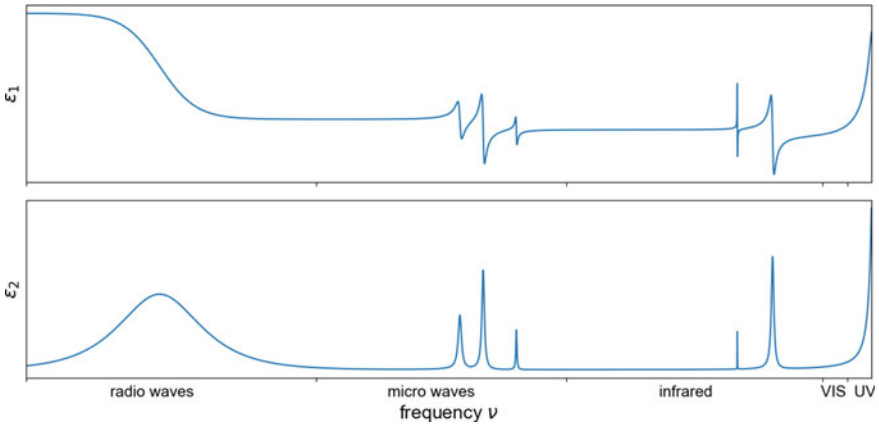

Fig. 6.7 Real and imaginary parts of the permittivity calculated for the dielectric PMMA using equations (6.35) and (6.36)

Using spectroscopic ellipsometry, see Sect. 17, the real and the imaginary parts of the complex permittivity $\tilde{\epsilon}_\mathrm{r}$ are detectable. As exemplary shown for CuPc (copper phthalocyanine, phthalocyanine blue) in Fig. 6.6b, the constituents ϵ_1 and ϵ_2 of the complex permittivity are detected, and by a program [4], the two resonance frequencies, as well as its damping constants are approximated to the measured data. Alternatively, the real and imaginary parts of the permittivity are calculated for the polymer poly(methyl methacrylate) PMMA using equations (6.35) and (6.36) assuming resonant frequencies for vibrational transitions in the infrared, rotational transitions in the micro wave regime and electronic transitions in the UV for PMMA (Fig. 6.7).

Matter exists often in a solid state, and **anisotropic optical properties** can be given. So, knowing that the electron distributions within atoms are in reality not homogeneous distributed, i.e. the crystal lattice features different distances between the atoms, also the response of each atom will be dependent on the orientation of the electron distribution relative to the electric field. E.g. the tetragonal crystal structure of the carbon atoms in diamond results from the sp^3-hybridization of the carbon electrons.

This means that the scattering efficiency not only depends on the atom type with its resonance frequency and damping constant, but also on the **crystal orientation** with respect to the electric field vector. This effect is called **birefringence** and gives rise to a **tensor description** for the complex electric permittivity

$$\underline{\underline{\tilde{\epsilon}}}_\mathrm{r} = \begin{pmatrix} \tilde{\epsilon}_{11} & \tilde{\epsilon}_{12} & \tilde{\epsilon}_{13} \\ \tilde{\epsilon}_{21} & \tilde{\epsilon}_{22} & \tilde{\epsilon}_{23} \\ \tilde{\epsilon}_{31} & \tilde{\epsilon}_{32} & \tilde{\epsilon}_{33} \end{pmatrix},$$

as well for the electric susceptibility $\underline{\underline{\tilde{\chi}}}_{\mathrm{e}}$, both representing a tensor of second rank, i.e. $\underline{\underline{\tilde{\epsilon}}}_{\mathrm{r}}, \underline{\underline{\tilde{\chi}}}_{\mathrm{e}} \in \mathbb{C}^2$. Due to the symmetric properties of these tensors, diagonalization of the tensor is possible and *up to* three in the crystal orthogonally oriented relative permittivities $\tilde{\epsilon}_{r1}$, $\tilde{\epsilon}_{r2}$, and $\tilde{\epsilon}_{r3}$ result.

6.6 Wave Equation in Matter

Starting from the Maxwell equations in matter (6.15) to (6.18) using the material (6.19) and (6.20) we can now derive the wave equations for the electromagnetic radiation propagating in matter.

Again, by applying the curl on the Maxwell equation (6.15) and assuming no charge and current densities, one gets

$$\nabla \times (\nabla \times \boldsymbol{E}) = -\nabla \times \frac{\partial \boldsymbol{B}}{\partial t}.$$

Assuming now an **isotropic and homogenous dielectric**, we can use the linear relation between the fields, e.g. $\boldsymbol{B} = \mu_0 \mu_{\mathrm{r}} \boldsymbol{H}$, and using (6.17) one gets for the right side

$$\begin{aligned} -\Delta \boldsymbol{E} &= -\mu_0 \mu_{\mathrm{r}} \frac{\partial}{\partial t} \nabla \times \boldsymbol{H} \\ &= -\mu_0 \mu_{\mathrm{r}} \frac{\partial^2 \boldsymbol{D}}{\partial t^2} \\ &= -\mu_0 \mu_{\mathrm{r}} \frac{\partial^2 (\varepsilon_0 \boldsymbol{E} + \boldsymbol{P})}{\partial t^2}. \end{aligned}$$

The last equation uses the material (6.19) and describes the dependence of the wave equation on the polarization density. Finally, we get the principal equation of the linear optics.

Principal equation of linear optics

$$\Delta \boldsymbol{E} - \mu_0 \mu_{\mathrm{r}} \varepsilon_0 \frac{\partial^2 (\boldsymbol{E})}{\partial t^2} = \mu_0 \mu_{\mathrm{r}} \frac{\partial^2 \boldsymbol{P}}{\partial t^2}. \tag{6.37}$$

In the case the polarization density is linearly proportional to the electric field strength, like (6.9) $\boldsymbol{P} = \varepsilon_0 \tilde{\chi}_{\mathrm{e}} \boldsymbol{E}$, one gets again a homogeneous wave equation

$$
\begin{aligned}
-\Delta \boldsymbol{E} &= -\mu_0\mu_\mathrm{r}\frac{\partial^2(\varepsilon_0\boldsymbol{E}+\varepsilon_0\tilde{\chi}_\mathrm{e}\boldsymbol{E})}{\partial t^2} = -\mu_0\mu_\mathrm{r}\frac{\partial^2(\varepsilon_0\overbrace{(1+\tilde{\chi}_\mathrm{e})}^{\tilde{\epsilon}_\mathrm{r}}E)}{\partial t^2} \\
&= -\mu_0\mu_\mathrm{r}\varepsilon_0\tilde{\epsilon}_\mathrm{r}\frac{\partial^2\boldsymbol{E}}{\partial t^2} \\
&= -\frac{1}{c_\mathrm{M}^2}\frac{\partial^2\boldsymbol{E}}{\partial t^2}.
\end{aligned}
$$

The only difference between the solution in vacuum and this one is found in the wave velocity being now the speed of light in matter c_M, (6.23). The described properties of the electromagnetic radiation in the matter are comparable to those in vacuum, with the only difference in the wave velocity being now the speed of light in matter c_M!

As described in Sect. 6.5, solid matter can feature an anisotropic permittivity, resulting in three wave equations for the main relative permittivities of the main axis of the birefringent crystal with different speeds of light for each crystal axis orientation. These wave equations are called *the principal equation of linear optics with birefrigence*.

Principal equation of linear optics with birefrigence

$$
\Delta\boldsymbol{E} - \mu_0\mu_\mathrm{r}\frac{\partial^2(\varepsilon_0\boldsymbol{E}+\varepsilon_0\underline{\underline{\tilde{\chi}}}_\mathrm{e}\boldsymbol{E})}{\partial t^2} = 0. \tag{6.38}
$$

6.7 Straight Propagation in Condensed Matter

As seen in Sect. 5.2, the distance between scattering atoms in relation to the wavelength of the applied radiation influences the scattering behavior dramatically. One can show that the phase relation between the scattering atoms or molecules vanishes for large distances $l \gg \lambda$ between the scatter. The scatterer emits independent of each other without any coherence, and so any interference effect. The overall scatterer power represents the algebraic sum of each atom's scattering power, depicting incoherent scattering.

Now, considering the condensed matter, the distance between the atoms, i.e. the scatterer, is usually well below the wavelength of common (laser) radiation, and additionally, the periodicity of the atom locations is now very high!

Without a stringent calculation, we show that the propagation of radiation in condensed matter is predominantly continued in the propagation direction of the incoming radiation, when the distance between the atoms is well below the wavelengths of the radiation [5]. Two atoms are interacting with a primary plane wave, first the atom A (Fig. 6.8a), then later the atom B (Fig. 6.8b). The atoms emit the

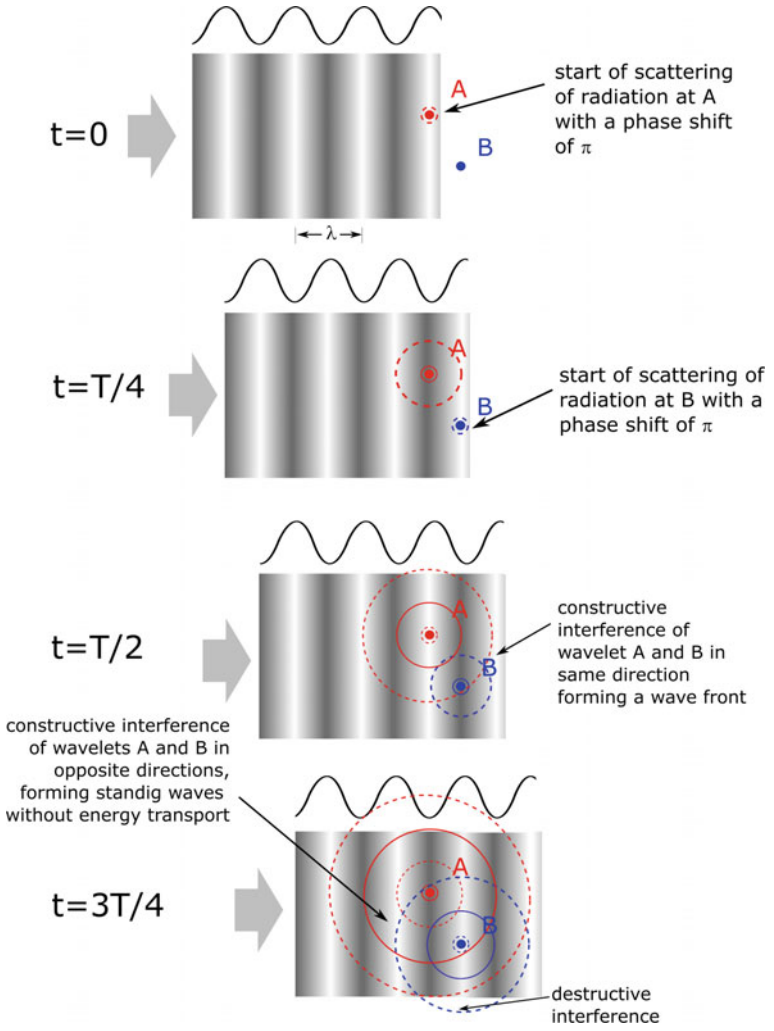

Fig. 6.8 Phase relation for forward scattering

radiation with a phase shift of π to the incoming radiation. Later we will see that this assumption is often valid. In propagation direction, the emitted radiation of the atoms A and B is in phase and called **forward scattered radiation** (Fig. 6.8c, d). This fixed phase dependence is independent of the distance between the atoms, as long as its distance is well below the wavelength of the radiation. Because of the symmetry introduced by the radiation itself, all the scattered waves add constructively in the forward direction with each other forming a scattered wave, the scattered radiation.

What about the **backwards scattered radiation**? Looking at Fig. 6.8 gives us the impression that also scattered radiation should be emitted in reversed direction.

Imagine two atoms, like atom A, the other being located like atom B, the wavelets of A will interfere with B also between both atoms, where the radiation of A moving in the propagation direction, whereas the radiation of B counterpropagating, we can write for the sum of both (assuming plane waves)

$$\boldsymbol{E}_{\text{sum}} = \boldsymbol{E}_0 \underbrace{\mathrm{e}^{i(kx-\omega t)}}_{\text{atom A}} + \underbrace{\mathrm{e}^{i(-kx-\omega t)}}_{\text{atom B}}),$$

where the radiation of A moves in the positive z-direction and of atom B in the opposite direction $-z$. One sees that now a standing wave is formed,

$$\boldsymbol{E}_{\text{sum}} = \boldsymbol{E}_0 \mathrm{e}^{-i\omega t)} \left(\mathrm{e}^{i(kx} + \mathrm{e}^{i(-kx)}\right) = \boldsymbol{E}_0 \mathrm{e}^{-i\omega t)} 2\cos(kz).$$

As well known, this is not anymore a wave transporting energy anywhere, as standing waves feature only localized energy. In fact, no radiation is scattered backwards!

Lateral scattering, i.e. the perpendicular propagation of scattered radiation, is still given as discussed before. But, further increasing the scatterer density like our atmosphere at ground results in $3 \cdot 10^6$ atoms in a cube λ^3 with the edge length $\lambda = 500$ nm. Here, the phase relations are not deliberate, and interference will be dominant. Again in forward direction constructive interference takes place, but perpendicularly destructive interference cancels all radiation. Image a chain of atoms being excited by radiation, and all these atoms scatter radiation at the same time; see Fig. 6.9. Due to the high atom density, one finds always two atoms in the chain emitting wavelets, here given by atoms A and B that are phase separated by $\Delta\varphi = k \cdot l = (2n+1)\pi$, with $l \gg \lambda$ and $\mathbb{N}_0$. Now, interference takes place, but destructively.

Liquids, being thousand times denser than a gas should scatter 1000 times stronger in all directions (depending on the polarization state of the incoming radiation!), but due to the destructive interference of colinear scatterer, lateral scattering is inhibited in the perpendicular direction. Further increasing the atom density to those of condensed matter will also increase the atomic order in the solids, making interference further selective regarding the propagation direction due to a precise phase relation between the atoms.

Because in **condensed matter** much more atoms are allocated within the wavelength λ of the radiation, $l \gg \lambda$,[6] the more dense, uniform, and ordered the medium gets, the more atoms will participate to the lateral destructive interference, and the smaller will be the amount of non-forward scattered radiation. Thus, most of the energy will go into the forward direction, and **the beam will advance essentially undiminished in intensity and unchanged in direction and geometry**. This is why in optics the definition of a **ray** is allowed, as radiation passing through dense media will not change its geometry.

[6] The ratio $l/\lambda \ll 1$ depicts a nearly-continuous distribution of atoms in condensed matter compared to the wavelength of the radiation.

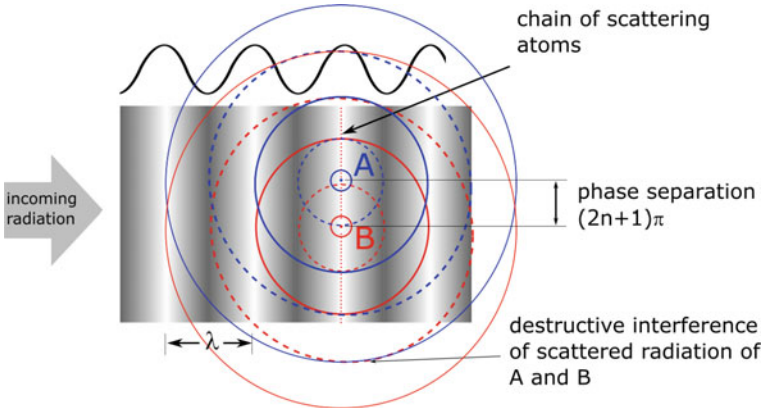

Fig. 6.9 Chain of atoms scattering incoming radiation. The radiation of two atoms scattering at a phase separation $(2n + 1)\pi$ interferes destructively

6.8 Speed of Light in Media

It sounds embarrassing that in a medium the speed of light is larger than the speed of light in vacuum. The special theory of relativity is defined as the maximum velocity of everybody being limited to the speed of light in vacuum. This conflict is simply solved, remembering that one atom scatters only a small amount of the incoming radiation. So, the relative scattered intensity of the radiation passing one meter of matter at a density $n_\mathrm{d} = 1 \cdot 10^{21}\ \mathrm{m}^{-3}$ gets to

$$I/I_0 = \exp(-\mu x) = \exp(-n_\mathrm{d}\sigma x) \approx 10^{-7}.$$

Assuming an incoming periodic oscillating electromagnetic wave with the frequency $\boldsymbol{\omega < \omega_0}$ given here by its electric field strength

$$E_\mathrm{in} = E_0 \sin(\omega\, t),$$

one can calculate the electric field strength of the scattered matter by

$$\begin{aligned} E_\mathrm{scat} &= \sigma E_0 \sin(\omega\, t - \pi/2) \\ &= -\sigma E_0 \cos(\omega\, t), \end{aligned}$$

with the total cross-section $\sigma = 0.1$ and the phase shift of $\pi/2$; see Fig. 6.10. The phase shift of $\pi/2$ is non-trivial, as the phase relation between exciting radiation and scattered radiation varies, depending on the applied frequency ω and the resonance frequency ω_0 of the scattering atom; see Sect. 6.4 and (6.28).

This means that 90% of the incoming radiation is not scattered at all, and the resulting superposed electric field reads to

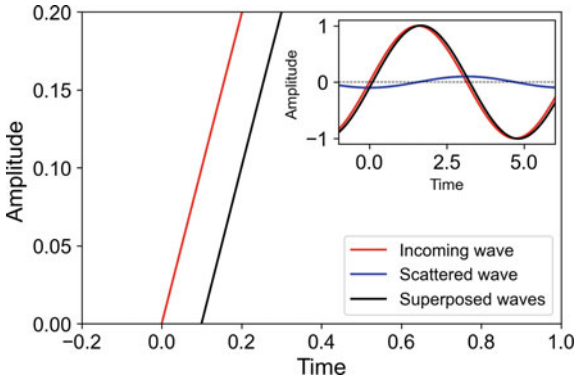

Fig. 6.10 Incoming, scattering, and superposed electromagnetic waves for a retardation at $\omega < \omega_0$ resulting in $c_M < c_0$

$$E_{sup} = E_{in} + E_{scat}.$$

The superposed electric field E_{sup} results as a **retarded wave** compared to the incoming wave; see Fig. 6.10. The retardation accumulates per scattering process resulting in a final delay passing through the matter and represents a speed of light c_M smaller than the speed of light in vacuum c_0. This case is given using electromagnetic radiation with $\omega \ll \omega_0$, like visible radiation (VIS) in dielectrics, depicting a **speed of light in matter smaller than in vacuum $c_M < c_0$**.

When irradiating matter with radiation at $\boldsymbol{\omega > \omega_0}$, an additional phase shift of $\Delta\varphi \leq \pi$ is given, see Fig. 6.4, with an electric field strength of the scattered matter given by

$$E_{scat} = \sigma E_0 \sin(\omega\, t - \pi/2 - \pi) = \sigma E_0 \cos(\omega\, t).$$

A superposed wave results, being an **anticipated wave** to the incoming one, see Fig. 6.11, depicting a **speed of light in matter larger than in vacuum $c_M > c_0$**. This case happens using, e.g. X-rays in dielectrics.

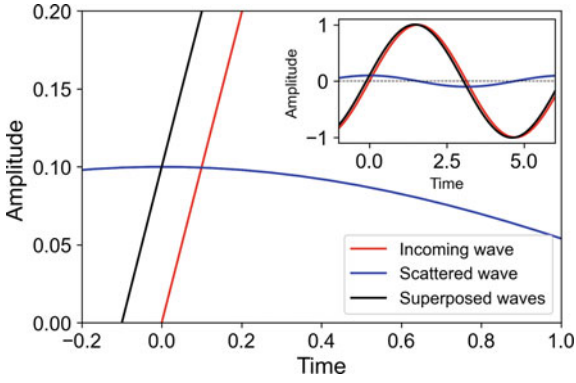

Fig. 6.11 Incoming, scattering, and superposed electromagnetic waves for an anticipation at $\omega > \omega_0$ resulting in $c_M > c_0$

In fact, the electromagnetic wave still propagates at the speed of light in vacuum c_0, but the resulting overall velocity, the so-called **phase velocity**, is calculated to be smaller or larger than the speed of light in vacuum depending on the frequency of the radiation in relation to the atomic frequency of the scatterer.

References

1. T. Fließbach, *Elektrodynamik* (Springer, Berlin, Heidelberg, 2012)
2. S. Brandt, H.D. Dahmen, *Elektrodynamik* (Springer, Heidelberg, 2005)
3. N. Gauthier, Wavelength dependence of the refractive index. Phys. Teach. **25**, 502–503 (1987). https://doi.org/10.1119/1.2342347
4. http://www.horiba.com/fileadmin/uploads/Scientific/Downloads/OpticalSchool_CN/TN/ellipsometer/Lorentz_Dispersion_Model.pdf
5. E. Hecht, *Optics* 5th ed., Global edition (Boston, Columbus, Indianapolis, Pearson Global Edition, 2017)

Chapter 7
Linear Optics

Abstract Understanding now the meaning of the complex refractive index for the transmission of electromagnetic radiation through a dielectric material, it is practical and also necessary to discuss the transition of the radiation from one medium with the refractive index $\tilde{n}_1$ into another medium with the refractive index $\tilde{n}_2$. The physical separation is called the *interface* between two media. Contrary to radiation propagating only through one dense medium where we saw that no radiation is scattered backwards, now we have to allow the back-scattering, the so-called reflection at boundaries. We will start here with non-absorbing dielectrics, meaning that the refractive index is purely real $\tilde{n} = n$.

7.1 Steadiness of Fields

In order to describe the process of energy transmission through a boundary from one medium to another, and possibly determine the absorbed energy, too, firstly the dependence of the electric field strengths for the incoming, the reflected, and the transmitted radiation have to be calculated.

The transition of the electric and magnetic field strengths from one medium to another through a boundary is described in the electrostatic and magnetostatics using the Maxwell equations and calculating the flux of the change in the magnetic field strength in time through the surface A, see Fig. 7.1, by calculating the surface integral of the Maxwell equation (6.15)

$$\int_A \nabla \times \boldsymbol{E} \cdot \mathrm{d}\boldsymbol{a} = \oint_{(A)} \boldsymbol{E} \cdot \mathrm{d}\boldsymbol{l} = -\int_A \frac{\partial \boldsymbol{B}}{\partial t} \cdot \mathrm{d}\boldsymbol{a}.$$

Being interested in the transition of the fields at the boundary, the flux is calculated for vanishing width of the area A:

$$-\lim_{l_2, l_4 \to 0} \int_A \frac{\partial \boldsymbol{B}}{\partial t} \cdot \mathrm{d}\boldsymbol{a} = 0$$

$$\lim_{l_2, l_4 \to 0} \oint_{(A)} \boldsymbol{E} \cdot \mathrm{d}\boldsymbol{l} = \boldsymbol{E}_1 \cdot \boldsymbol{l}_1 + \boldsymbol{E}_2 \cdot \boldsymbol{l}_3.$$

© Springer Nature Switzerland AG 2022

A. Horn, *The Physics of Laser Radiation–Matter Interaction*,
https://doi.org/10.1007/978-3-031-15862-9_7

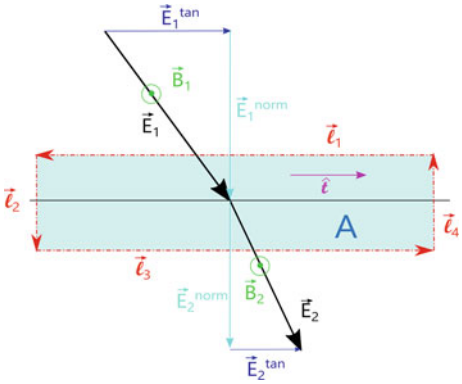

Fig. 7.1 Interface conditions for electromagnetic fields

With $\boldsymbol{l}_1 = -l\hat{\boldsymbol{t}}$ and $\boldsymbol{l}_3 = l\hat{\boldsymbol{t}}$, using a tangential unity vector $\hat{t}$, see Fig. 7.1, one gets

$$(\boldsymbol{E_1} \cdot \hat{\boldsymbol{t}})\, l = (\boldsymbol{E_2} \cdot \hat{\boldsymbol{t}})\, l.$$

Equivalent to this means that the tangential components of the electric field strengths are continuous across the interface

Continuity condition for tangential components of the electric field

$$\boldsymbol{E}_1^{\tan} = \boldsymbol{E}_2^{\tan}. \tag{7.1}$$

Similarly, one can argue, using from a magnetostatic point of view (6.17), that the tangential magnetic field strengths $\boldsymbol{H}$ are continuous across the interface

Continuity condition for tangential components of the magnetic field

$$\boldsymbol{H}_1^{\tan} = \boldsymbol{H}_2^{\tan}. \tag{7.2}$$

Both (7.1) and (7.2) represent the **continuity equations for the electric and magnetic fields**.

7.2 S-Polarized Radiation

With this continuity equations, we are now able to apply a plane electromagnetic wave crossing from one medium with the refractive index $\tilde{n}_1$ through a boundary to another medium with the refractive index $\tilde{n}_2$ (Fig. 7.2). At the moment, we assume that both media are dielectrics with vanishing imaginary parts, so $n_1, n_2 \in \mathbb{R}$. In the subsequent section, we will return to the complex writing.

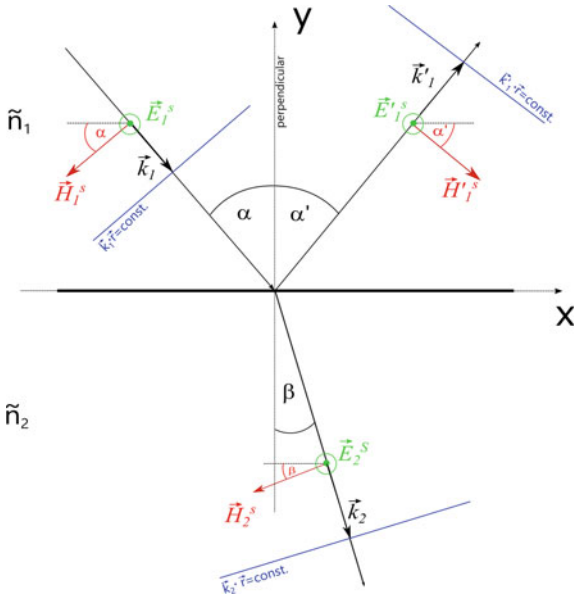

Fig. 7.2 Electric and magnetic field vectors for incoming, reflected, and transmitted s-polarized radiation

The interface normal vector, the so-called perpendicular, defines together with the incoming propagation vector $\boldsymbol{k}_1$ the **plane of incidence**. The incident electric and magnetic fields are perpendicularly oriented to $\boldsymbol{k}_1$. The electric field strength can be described by two orthogonal vectors, the **parallel electric field vector** $\boldsymbol{E}_1^{\mathrm{p}}$ and the **orthogonal electric field vector** $\boldsymbol{E}_1^{\mathrm{s}}$, representing its orientations with respect to the plane of incidence

$$\boldsymbol{E}_1 = \boldsymbol{E}_1^{\mathrm{p}} + \boldsymbol{E}_1^{\mathrm{s}}.$$

So, for the further discussion of the propagation of electromagnetic radiation from one medium to another, it is adequate to describe its propagation with two orthogonal oriented electric fields, so-called **s-polarized radiation** (see Fig. 7.2) and parallelly oriented fields, so-called **p-polarized radiation**; see Sect. 7.3.

The incoming plane electromagnetic wave can be expressed by the electric field strength

$$\begin{aligned}\boldsymbol{E}_1^{\mathrm{s}} &= \boldsymbol{E}_{10}^{\mathrm{s}} \exp\left(i(\omega\, t - \boldsymbol{k}_1 \cdot \boldsymbol{r})\right) \\ &= E_{10}^{\mathrm{s}} \exp\left(i(\omega\, t - \boldsymbol{k}_1 \cdot \boldsymbol{r})\right) \hat{z},\end{aligned}$$

with the constant amplitude E_{10}^{s}, and the wave number vector

$$\boldsymbol{k}_1 = (k_{1x}, k_{1y}, k_{1z}) = k_1(\hat{k}_{1x}, \hat{k}_{1y}, \hat{k}_{1z}) = k_1 \hat{k}_1.$$

Evidently, the propagation direction is tangential to the interface: $\hat{z} = \hat{t}$. Accordingly for the reflected and transmitted radiation, one gets

$$\begin{aligned} \boldsymbol{E}_1^{\mathrm{s}'} &= E_{10}^{\mathrm{s}'} \exp\left(i(\omega' t - \boldsymbol{k}_1' \cdot \boldsymbol{r})\right) \hat{z} \\ \boldsymbol{E}_2^{s} &= E_{20}^{s} \exp\left(i(\omega'' t - \boldsymbol{k}_2 \cdot \boldsymbol{r})\right) \hat{z}. \end{aligned}$$

The incoming electromagnetic radiation induces in the atoms of the medium with the refractive index n_2 electric dipoles being oriented in the same direction as the electric field vector, and the resulting reflected and transmitted electric field vectors will be oriented as well in the same direction. At the moment, the angular frequencies ω' and ω'', as well as the wave vectors $\boldsymbol{k}_1'$ and $\boldsymbol{k}_2$ are chosen arbitrarily.

Due to the steady continuation of the tangential electric field vectors passing through a boundary, see (7.1) and (7.2), the tangential components of $\boldsymbol{E}$ and $\boldsymbol{H}$ are continuous,

Boundary conditions for electromagnetic fields

$$\boldsymbol{E}_1^{\tan} + \boldsymbol{E}_1^{\tan'} = \boldsymbol{E}_2^{\tan} \tag{7.3}$$
$$\boldsymbol{H}_1^{\tan} + \boldsymbol{H}_1^{\tan'} = \boldsymbol{H}_2^{\tan}. \tag{7.4}$$

Holding in mind that in the case of s-polarized radiation the tangential fields are given by

$$\begin{aligned} &\boldsymbol{E}_1^{\tan} = E_1^{\mathrm{s}} \hat{z}, && \boldsymbol{E}_1^{\tan'} = E_1^{\mathrm{s}'} \hat{z}, && \boldsymbol{E}_2^{\tan} = E_2^{\mathrm{s}} \hat{z}, \\ &\boldsymbol{H}_1^{\tan} = -H_1^{\mathrm{s}} \cos(\alpha) \hat{x}, && \boldsymbol{H}_1^{\tan'} = H_1^{\mathrm{s}'} \cos(\alpha') \hat{x}, && \boldsymbol{H}_2^{\tan} = -H_2^{\mathrm{s}} \cos(\beta) \hat{x}\,, \end{aligned}$$

we can write them at the boundary with $y = 0$, and knowing that all wave number vectors are coplanar in the $x - y$ plane, i.e. $\boldsymbol{k}_{iz} = 0$ for $i = 1, 2, 3$, getting for the electric fields

$$\begin{aligned} \boldsymbol{E}_1^{\mathrm{s}}\big|_{y=0} + \boldsymbol{E}_1^{\mathrm{s}'}\big|_{y=0} &= \boldsymbol{E}_2^{\mathrm{s}}\big|_{y=0} \\ \left(E_{10}^{\mathrm{s}} e^{i(\omega t - \boldsymbol{k}_1 \cdot \boldsymbol{r})} \hat{z} + E_{10}^{\mathrm{s}'} e^{i(\omega' t - \boldsymbol{k}_1' \cdot \boldsymbol{r})}\right) \hat{z}\Big|_{y=0} &= E_{20}^{s} e^{i(\omega'' t - \boldsymbol{k}_2 \cdot \boldsymbol{r})} \hat{z}\Big|_{y=0} \\ E_{10}^{\mathrm{s}} e^{i(\omega t - k_1 x \sin\alpha)} + E_{10}^{\mathrm{s}'} e^{i(\omega' t - k_1' x \sin\alpha')} &= E_{20}^{s} e^{i(\omega'' t - k_2 x \sin\beta)} \end{aligned} \tag{7.5}$$

and for the magnetic fields

$$\boldsymbol{H}_1^{\mathrm{s}}\big|_{y=0} + \boldsymbol{H}_1^{\mathrm{s}'}\big|_{y=0} = \boldsymbol{H}_2^{\mathrm{s}}\big|_{y=0} \tag{7.6}$$

$$\left(-\cos\alpha H_{10}^{\mathrm{s}} e^{i(\omega\, t - \boldsymbol{k}_1\cdot\boldsymbol{r})}\hat{z} + \cos\alpha' H_{10}^{\mathrm{s}'} e^{i(\omega'\, t - \boldsymbol{k}_1'\cdot\boldsymbol{r})}\right)\hat{x}\Big|_{y=0} =$$

$$= -\cos\beta H_{20}^{s} e^{i(\omega''\, t - \boldsymbol{k}_2\cdot\boldsymbol{r})}\hat{x}\Big|_{y=0}$$

$$-\cos\alpha H_{10}^{\mathrm{s}} e^{i(\omega\, t - k_1 x\sin\alpha)} + \cos\alpha' H_{10}^{\mathrm{s}'} e^{i(\omega'\, t - k_1' x\sin\alpha')} =$$

$$= -\cos\beta H_{20}^{s} e^{i(\omega''\, t - k_2 x\sin\beta)}.$$

Assuming an infinite extended plane wave, the three exponential functions have independently to be valid for all times t resulting in equal angular frequencies

$$\omega = \omega' = \omega'' \tag{7.7}$$

and the spatial coordinate x, meaning

$$k_1 x\sin\alpha = k_1' x\sin\alpha' = k_2 x\sin\beta. \tag{7.8}$$

The relation (7.7) expresses that all frequencies are equal, describing **energy conservation**, or equivalently an elastic scattering process.

On the other hand, because the speed of light in medium 1 is equal to $c_1 = \omega/k_1 = \omega/k_1'$, it results in $k_1 = k_1'$, and consequently the sinus are equally depicting the **law of reflection**

Law of reflection

$$\alpha = \alpha'. \tag{7.9}$$

From (7.8), now one gets

$$k_1 x\sin\alpha = k_2 x\sin\beta,$$

and remembering the dispersion relation $k_i = \frac{\omega}{c_i}$, and the refractive index $n_i = c_0/c_i$, one gets

$$k_i = \frac{n_i\omega}{c_0},$$

with the media $i = 1, 2$ and one resumes **Snell's law for refraction**

Snell's law for refraction

$$n_1\sin\alpha = n_2\sin\beta. \tag{7.10}$$

From the continuity relations for the electric and magnetic field vectors, see (7.5) and (7.6), the exponential functions are now canceled, resulting in

$$E_{10}^{s} + E_{10}^{s'} = E_{20}^{s} \tag{7.11}$$

$$\cos\alpha \left(-H_{10}^{s} + H_{10}^{s'}\right) = -\cos\beta H_{20}^{s}. \tag{7.12}$$

Using plane electromagnetic radiation, we know the dependence of the magnetic field to the electric field strengths, see (1.75), getting $B_i = 1/c_0 E_i$. Additionally, remembering the linear dependence between the magnetic induction field an the magnetic field strength, see (6.14), we get for the magnetic field strengths

$$H_{i0} = \frac{1}{\mu_0 \mu_{ri}} B_{i0} = \frac{1}{c_{Mi} \mu_0 \mu_{ri}} E_{i0} = \sqrt{\frac{\varepsilon_0 \epsilon_{ri}}{\mu_0 \mu_{ri}}} E_{i0}. \tag{7.13}$$

One substitutes now in (7.12) the magnetic field strengths by the electric field strengths and gets

$$\cos\alpha \sqrt{\frac{\varepsilon_0 \epsilon_{r1}}{\mu_0 \mu_{r1}}} \left(-E_{10}^{s} + E_{10}^{s'}\right) = -\cos\beta \sqrt{\frac{\varepsilon_0 \epsilon_{r2}}{\mu_0 \mu_{r2}}} E_{20}^{s}$$

or

$$E_{10}^{s} - E_{10}^{s'} = \frac{\cos\beta}{\cos\alpha} \sqrt{\frac{\mu_{r1} \epsilon_{r2}}{\epsilon_{r1} \mu_{r2}}} E_{20}^{s}. \tag{7.14}$$

The square root can also be expressed using Snell's law, see (7.10), getting

$$\sqrt{\frac{\mu_{r1} \epsilon_{r2}}{\epsilon_{r1} \mu_{r2}}} = \sqrt{\frac{\mu_{r1} \epsilon_{r2}}{\epsilon_{r1} \mu_{r2}} \frac{\mu_{r1} \mu_{r2}}{\mu_{r1} \mu_{r2}}} = \frac{n_2}{n_1} \frac{\mu_{r1}}{\mu_{r2}} = \frac{\sin\alpha}{\sin\beta} \frac{\mu_{r1}}{\mu_{r2}}. \tag{7.15}$$

One can now get the amplitude of the incoming electric field by adding (7.11) with (7.14) and gets

$$2E_{10}^{s} = \left(1 + \frac{\sin\alpha}{\sin\beta} \frac{\cos\beta}{\cos\alpha} \frac{\mu_{r1}}{\mu_{r2}}\right) E_{20}^{s}, \tag{7.16}$$

or getting the amplitude of the reflected electric field by subtracting (7.11) from (7.14)

$$2E_{10}^{s'} = \left(1 - \frac{\sin\alpha}{\sin\beta} \frac{\cos\beta}{\cos\alpha} \frac{\mu_{r1}}{\mu_{r2}}\right) E_{20}^{s}.$$

The **first Fresnel equation**, the so-called **reflection coefficient for s-polarized radiation** or relative reflection coefficient, is given by the fraction of the reflected to incoming electric field strengths, here for s-polarized radiation

$$r^{\mathrm{s}} = \frac{E_{10}^{\mathrm{s}'}}{E_{10}^{\mathrm{s}}} = \frac{\left(1 - \frac{\sin\alpha}{\sin\beta}\frac{\cos\beta}{\cos\alpha}\frac{\mu_{r1}}{\mu_{r2}}\right)}{\left(1 + \frac{\sin\alpha}{\sin\beta}\frac{\cos\beta}{\cos\alpha}\frac{\mu_{r1}}{\mu_{r2}}\right)}$$
$$= \frac{\cos\alpha\sin\beta - \frac{\mu_{r1}}{\mu_{r2}}\sin\alpha\cos\beta}{\cos\alpha\sin\beta + \frac{\mu_{r1}}{\mu_{r2}}\sin\alpha\cos\beta}.$$

Reflection coefficient for s-polarized radiation

$$r^{\mathrm{s}} = \frac{\mu_{r2}\cos\alpha\sin\beta - \mu_{r1}\sin\alpha\cos\beta}{\mu_{r2}\cos\alpha\sin\beta + \mu_{r1}\sin\alpha\cos\beta}. \tag{7.17}$$

The relative reflectivity can be plotted in dependence of the reflectance angle α and also in dependence on the refractive index of the two dielectrics. One has to distinguish two cases, first, the radiation passing from an optical thin medium to an optical thick one, $n_1 < n_2$ (Fig. 7.3), and second, the radiation passing from an optical thick to an optical thin one, $n_1 > n_2$ (Fig. 7.8). In this section, we talk about the first one and will discuss the effects of $n_1 > n_2$ in Sect. 7.9.

The reflection coefficient for s-polarized radiation is still negative, see Fig. 7.3, meaning that the reflected radiation features every time a **phase shift** of $\Delta\varphi = -\pi$, as the reflected electric field strength is given by $E_{10}^{\mathrm{s}'} \propto \exp(-i\pi) = -1$.

The **second Fresnel equation**, **transmission coefficient for s-polarized radiation**, or relative transmission coefficient is calculated by using (7.16)

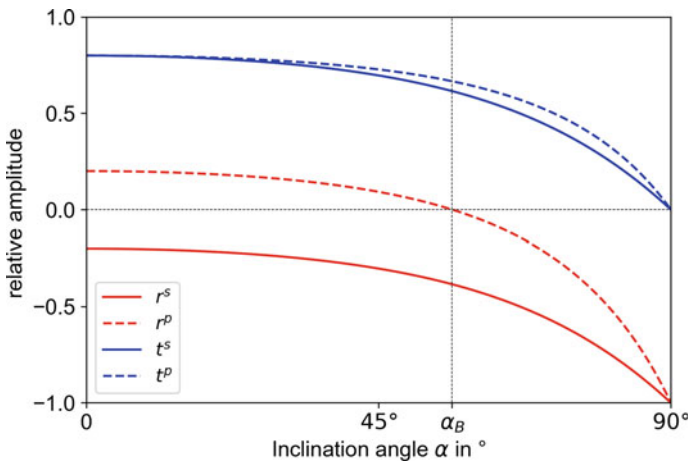

Fig. 7.3 Relative reflectivity and transmittivity for s- or p-polarized radiation passing through an interface from medium 1 with n_1 to medium 2 with n_2 and $n_1 < n_2$ (for nonmagnetic materials $\mu_{r1} = \mu_{r2} = 1$)

$$t^{\mathrm{s}} = \frac{E_{20}^{\mathrm{s}}}{E_{10}^{\mathrm{s}}} = \frac{2}{1 + \frac{\sin\alpha}{\sin\beta}\frac{\cos\beta}{\cos\alpha}\frac{\mu_{r1}}{\mu_{r2}}}$$
$$= \frac{2\sin\beta\cos\alpha}{\sin\beta\cos\alpha + \frac{\mu_{r1}}{\mu_{r2}}\sin\alpha\cos\beta}$$

Transmission coefficient for s-polarized radiation

$$t^{\mathrm{s}} = \frac{2\mu_{r2}\sin\beta\cos\alpha}{\mu_{r2}\sin\beta\cos\alpha + \mu_{r1}\sin\alpha\cos\beta}. \tag{7.18}$$

Here, the transmission coefficient for s-polarized radiation features for all inclination angles no phase shift at all; see Fig. 7.3.

7.3 P-Polarized Radiation

The approach for the p-polarized radiation is analogous: using the continuity equations, we apply a plane electromagnetic wave crossing from one medium with the refractive index $\tilde{n}_1$ through a boundary to another medium with the refractive index $\tilde{n}_2$; see Fig. 7.4.

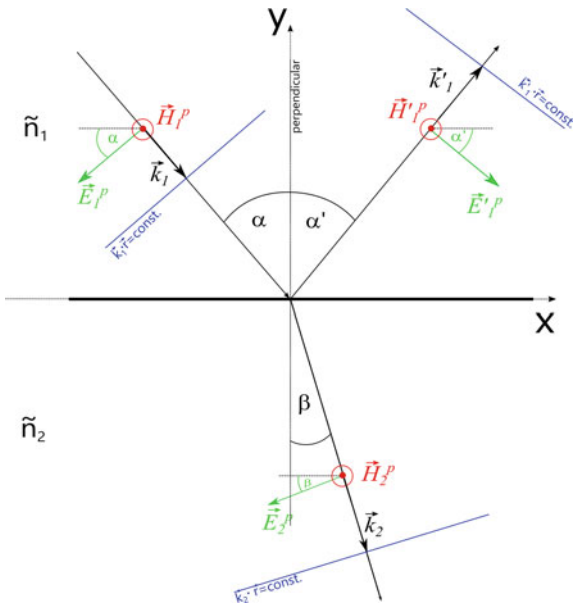

Fig. 7.4 Electric and magnetic field vectors for incoming, reflected, and transmitted p-polarized radiation

Again, we assume that both media are dielectrics with vanishing imaginary parts, so $n_1, n_2 \in \mathbb{R}$. Now the polarization of the electric field vectors is parallel to the plane of incidence. The steady continuity of the tangential components are still valid, (7.3) and (7.4), and can be written as With the same argumentations as for the s-polarized

$$\boldsymbol{E}_1^{\tan} = -\cos\alpha E_1^{\mathrm{p}}\hat{x} \quad \boldsymbol{E}_1^{\tan'} = \cos(\alpha')E_1^{\mathrm{p}'}\hat{x} \quad \boldsymbol{E}_2^{\tan} = -\cos(\beta)E_2^{\mathrm{p}}\hat{x}$$

$$\boldsymbol{H}_1^{\tan} = H_1^{\mathrm{p}}\hat{z} \qquad \boldsymbol{H}_1^{\tan'} = H_1^{\mathrm{p}'}\hat{z} \qquad \boldsymbol{H}_2^{\tan} = H_2^{\mathrm{p}}\hat{z}$$

radiation, we get again the law for reflection and Snell's law, and the boundary equations

$$\cos\alpha\left(-E_{10}^{\mathrm{p}} + E_{10}^{\mathrm{p}'}\right) = -\cos\beta E_{20}^{p} \tag{7.19}$$

$$H_{10}^{\mathrm{p}} + H_{10}^{\mathrm{p}'} = H_{20}^{p}. \tag{7.20}$$

The magnetic field is substituted by the relation with the electric field getting

$$E_{10}^{\mathrm{p}} - E_{10}^{\mathrm{p}'} = \frac{\cos\beta}{\cos\alpha}E_{20}^{p}$$

$$E_{10}^{\mathrm{p}} + E_{10}^{\mathrm{p}'} = \frac{\sin\alpha}{\sin\beta}\frac{\mu_{r1}}{\mu_{r2}}E_{20}^{p}.$$

The reflectivity coefficient is now calculated using these equations, see Fig. 7.4, given by

$$r^{\mathrm{p}} = \frac{E_{10}^{\mathrm{p}'}}{E_{10}^{p}}.$$

One gets adding the two relations

$$2E_{10}^{\mathrm{p}} = \left(\frac{\cos\beta}{\cos\alpha} + \frac{\mu_{r1}}{\mu_{r2}}\frac{\sin\alpha}{\sin\beta}\right)E_{20}^{p}$$

and by subtracting the second from the first relation

$$2E_{10}^{\mathrm{p}'} = \left(\frac{\mu_{r1}}{\mu_{r2}}\frac{\sin\alpha}{\sin\beta} - \frac{\cos\beta}{\cos\alpha}\right)E_{20}^{p}.$$

Finally, the **third Fresnel equation**, or **reflection coefficient for p-polarized radiation**, is derived as

$$r^{\mathrm{p}} = \frac{\frac{\mu_{r1}}{\mu_{r2}}\frac{\sin\alpha}{\sin\beta} - \frac{\cos\beta}{\cos\alpha}}{\frac{\cos\beta}{\cos\alpha} + \frac{\mu_{r1}}{\mu_{r2}}\frac{\sin\alpha}{\sin\beta}} = \frac{\frac{\mu_{r1}}{\mu_{r2}}\sin\alpha\cos\alpha - \sin\beta\cos\beta}{\sin\beta\cos\beta + \frac{\mu_{r1}}{\mu_{r2}}\sin\alpha\cos\alpha},$$

Reflection coefficient for p-polarized radiation

$$r^{\mathrm{p}} = \frac{\mu_{r1}\sin\alpha\cos\alpha - \mu_{r2}\sin\beta\cos\beta}{\mu_{r2}\sin\beta\cos\beta + \mu_{r1}\sin\alpha\cos\alpha}. \tag{7.21}$$

Here, the reflection coefficient for p-polarized radiation features for inclination angles smaller than the **Brewster angle** α_{B}, see also Sect. 7.8, no phase shift, but above α_{B} a phase shift of $\Delta\varphi = -\pi$; see Fig. 7.3.

The **fourth Fresnel equation**, or **transmission coefficient for p-polarized radiation**, or relative transmission coefficient is calculated by using (7.16)

$$t^{\mathrm{p}} = \frac{E_{20}^{\mathrm{p}}}{E_{10}^{\mathrm{p}}} = \frac{2}{\frac{\cos\beta}{\cos\alpha} + \frac{\mu_{r1}}{\mu_{r2}}\frac{\sin\alpha}{\sin\beta}} = \frac{2\sin\beta\cos\alpha}{\sin\beta\cos\beta + \frac{\mu_{r1}}{\mu_{r2}}\sin\alpha\cos\alpha},$$

Transmission coefficient for p-polarized radiation

$$t^{\mathrm{p}} = \frac{2\mu_{r2}\sin\beta\cos\alpha}{\mu_{r2}\sin\beta\cos\beta + \mu_{r1}\sin\alpha\cos\alpha}. \tag{7.22}$$

Similar to the s-polarized radiation, the transmission coefficient for p-polarized radiation features for all inclination angles with no phase shift at all; see Fig. 7.3.

7.4 Boundary Conditions with Complex Refractive Index

Let us now assume that the **refractive index is complex** $\tilde{n} \in \mathbb{C}$ with $\tilde{n} = n - i\kappa$. Snell's equation is generalized to

$$\tilde{n}_1 \sin\alpha = \tilde{n}_2 \sin\beta.$$

Using this relation, we can also generalize the Fresnel equations from the last section substituting the trigonometric relations with the complex refractive index.

The Fresnel equations for complex refractive index

For s-polarized electromagnetic radiation:

$$r^{\mathrm{s}} = \frac{E_{10}^{\mathrm{s}'}}{E_{10}^{\mathrm{s}}} = \frac{\tilde{n}_1 \cos\alpha - \tilde{n}_2 \frac{\mu_{r1}}{\mu_{r2}} \cos\beta}{\tilde{n}_1 \cos\alpha + \tilde{n}_2 \frac{\mu_{r1}}{\mu_{r2}} \cos\beta} \tag{7.23}$$

$$t^{\mathrm{s}} = \frac{E_{20}^{\mathrm{s}}}{E_{10}^{\mathrm{s}}} = \frac{2\tilde{n}_1 \cos\alpha}{\tilde{n}_1 \cos\alpha + \tilde{n}_2 \frac{\mu_{r1}}{\mu_{r2}} \cos\beta}. \tag{7.24}$$

For p-polarized electromagnetic radiation:

$$r^{\mathrm{p}} = \frac{E_{10}^{\mathrm{p}'}}{E_{10}^{p}} = \frac{\tilde{n}_2 \frac{\mu_{r1}}{\mu_{r2}} \cos\alpha - \tilde{n}_1 \cos\beta}{\tilde{n}_2 \frac{\mu_{r1}}{\mu_{r2}} \cos\alpha + \tilde{n}_1 \cos\beta} \tag{7.25}$$

$$t^{\mathrm{p}} = \frac{E_{20}^{\mathrm{p}}}{E_{10}^{\mathrm{p}}} = \frac{2\tilde{n}_1 \cos\alpha}{\tilde{n}_2 \frac{\mu_{r1}}{\mu_{r2}} \cos\alpha + \tilde{n}_1 \cos\beta}. \tag{7.26}$$

7.5 Fresnel Equations for Transparent Dielectrics

Many dielectrics feature a **vanishing extinction coefficient** κ and are **nonmagnetic** with $\mu_{r1} = \mu_{r2} = 1$ getting a simplified description of the Fresnel equation r^{s}, t^{s}, r^{p}, and t^{p}; see (7.17), (7.18), (7.21), and (7.22). Using also the addition theorems for trigonometric functions, one gets

$$\begin{aligned}
r^{\mathrm{s}} &= \frac{\cos\alpha \sin\beta - \sin\alpha \cos\beta}{\cos\alpha \sin\beta + \sin\alpha \cos\beta} = \frac{\sin(\beta - \alpha)}{\sin(\alpha + \beta)} \\
t^{\mathrm{s}} &= \frac{2 \sin\beta \cos\alpha}{\sin\beta \cos\alpha + \sin\alpha \cos\beta} = \frac{2 \sin\beta \cos\alpha}{\sin(\alpha + \beta)} = 1 + r^{\mathrm{s}} \\
r^{\mathrm{p}} &= \frac{\sin\alpha \cos\alpha - \sin\beta \cos\beta}{\sin\beta \cos\beta + \sin\alpha \cos\alpha} = -\frac{\tan(\beta - \alpha)}{\tan(\alpha + \beta)} \\
t^{\mathrm{p}} &= \frac{2 \sin\beta \cos\alpha}{\sin\beta \cos\beta + \sin\alpha \cos\alpha} = \frac{n_1}{n_2}(1 - r^{\mathrm{p}}),
\end{aligned}$$

and using for t^{p} again the (7.15), here $\frac{n_2}{n_1} = \frac{\sin\alpha}{\sin\beta}$.

7.6 Reflectance and Transmittance

Knowing the electric field strength relations for the reflection and the transmission, i.e. the Fresnel equations, one can now determine the relative reflected and transmitted power. The metrology used to determine this value is called **photometry**. Now, as we know the Poynting vector for a plane wave traveling through a medium with the permittivity ϵ_r and the permeability μ_r, see also (1.91), can be written using (1.54) and calculating the intensity

$$\begin{aligned} I &= \langle |\boldsymbol{S}| \rangle = \langle |\boldsymbol{E} \times \boldsymbol{H}| \rangle \\ &= \frac{1}{2} |\boldsymbol{E} \times \frac{1}{\mu_0 \mu_r} \frac{1}{c_M} \boldsymbol{E}| \\ &= \frac{1}{2} \sqrt{\frac{\varepsilon_0 \epsilon_r}{\mu_0 \mu_r}} |\boldsymbol{E}|^2 \\ &= \frac{1}{2} \varepsilon_0 c_0 \sqrt{\frac{\epsilon_r}{\mu_r}} |\boldsymbol{E}|^2. \end{aligned}$$

Hold in mind that now the relations between the field, see (1.65), are now applied in matter, with the speed of light in matter c_M (e.g. $\boldsymbol{B} = 1/c_M \boldsymbol{E}$ and $\boldsymbol{H} = 1/(\mu_0 \mu_r) \boldsymbol{B}$).

For nonmagnetic material, we can set $\mu_r = 1$ and using the refractive index $n = \sqrt{\epsilon_r}$ we get the intensity in matter

Intensity in matter

$$I = \frac{1}{2} \varepsilon_0 \, c_0 \, n \, \boldsymbol{E}_0^2. \tag{7.27}$$

On the other hand, remembering that the irradiated area depends on the inclination angle α to the surface normal (Fig. 7.5), one defines the **reflectance R** as the relative reflected power, i.e. the fraction of the reflected power to the incoming power for s- or p-polarized radiation

$$R^{(s/p)} = \frac{P_1^{'}}{P_1} = \frac{I_1^{'} \cos \alpha}{I_1 \cos \alpha} = \frac{c_0 n_1 \cdot \boldsymbol{E}_{10}^{'2} \cos \alpha}{c_0 n_1 \cdot \boldsymbol{E}_{10}^2 \cos \alpha} = \left| r^{(s/p)} \right|^2.$$

The reflectance starts for both polarization states (s or p) at vanishing inclination angle at a value larger than zero, increasing steadily for s-polarized radiation until unity at 90°, whereas the reflectance for p-polarized radiation decreases to zero firstly until the Brewster angle and then increasing steadily until unity for an inclination angle of 90°; see Fig. 7.6.

As well, the **transmittance T** is defined as the relative transmitted power, i.e. the fraction of the transmitted power to the incoming power for s- or p-polarized radiation

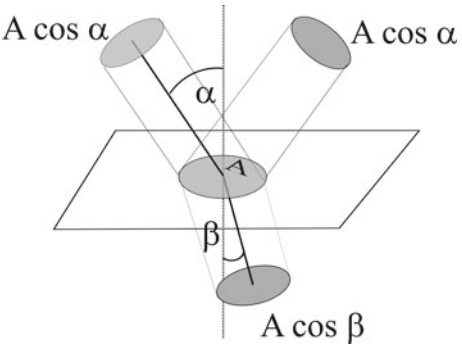

Fig. 7.5 Incoming, reflected, and transmitted power through a dielectric interface

$$T^{(s/p)} = \frac{P_2}{P_1} = \frac{I_2 \cos\beta}{I_1 \cos\alpha} = \frac{c_0 n_2 \cdot \boldsymbol{E}_{20}^2 \cos\beta}{c_0 n_1 \cdot \boldsymbol{E}_{10}^2 \cos\alpha} = \frac{n_2 \cos\beta}{n_1 \cos\alpha} \left| t^{(s/p)} \right|^2 .$$

Inversely to the reflectance, the transmittance starts again from one value for both polarization states, decreases steadily for s-polarized radiation until zero for an inclination angle of 90°, and increases first until unity for p-polarized radiation at the Brewster angle, then decreasing steadily to zero until 90° inclination angle; see Fig. 7.6.

But, as one can see, every time and for each polarization state the relation

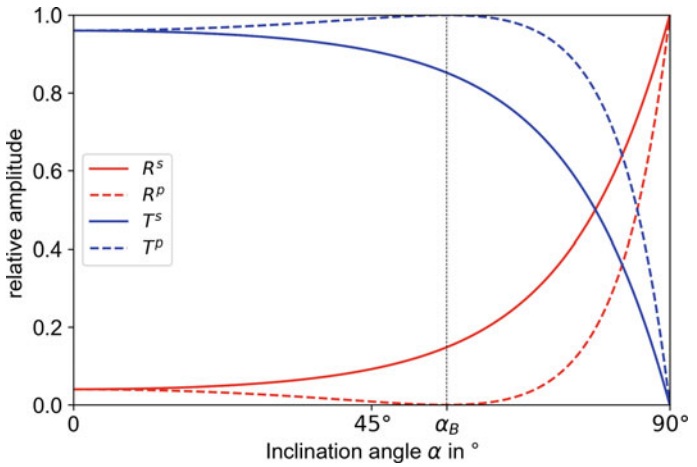

Fig. 7.6 Reflectance as well as transmittance for s- or p-polarized radiation passing through an interface from medium 1 with n_1 to medium 2 with n_2 and $n_1 < n_2$ (for nonmagnetic materials $\mu_{r1} = \mu_{r2} = 1$)

Energy conservation at boundaries

$$R + T = 1 \tag{7.28}$$

holds, confirming the **energy conservation**. Thereby, we used the reflectance R and transmittance T described by the Fresnel equations, the refractive indices n_1 and n_2, and the inclination angels α and β.

Reflectance and transmittance for transparent media

$$R^{(s/p)} = \left|r^{(s/p)}\right|^2 \tag{7.29}$$

$$T^{(s/p)} = \frac{n_2 \cos\beta}{n_1 \cos\alpha} \left|t^{(s/p)}\right|^2. \tag{7.30}$$

7.7 Nearly Perpendicular Irradiation

To get rid of the values of the reflection and transmission coefficients as well as reflectance and transmittance at perpendicular inclination angle, see Figs. 7.3 and 7.6, we look at a dielectric irradiated nearly perpendicular to its boundary described by the angles $\alpha, \beta \ll 1$, resulting in

$$n_1 \sin\alpha = n_2 \sin\beta \quad \rightarrow \quad n_1\,\alpha = n_2\,\beta \quad \rightarrow \quad \alpha = \frac{n_2}{n_1}\beta = n\,\beta$$

$$\curvearrowright \quad r^{\mathrm{s}} \approx \frac{\beta - \alpha}{\alpha + \beta} = \frac{\beta - n\,\beta}{n\,\beta + \beta} = \frac{1-n}{1+n} = -\frac{n-1}{n+1}$$

Reflection coefficient at perpendicular inclination

$$r^{\mathrm{p}} \approx -\frac{\beta - \alpha}{\alpha + \beta} = -\frac{1-n}{1+n} = \frac{n-1}{n+1} = -r^{\mathrm{s}} = r. \tag{7.31}$$

The reflection coefficient at perpendicular inclinations is for s- and p-polarized radiation equal.

For example, calculating the reflection coefficient for normal incident radiation from air ($n_1 \approx 1$) onto glass ($n_2 = 1.5$), one calculates a reflection coefficient of $r = 0.2$, and gets a reflectance $R = r^2$ of about 4% of the radiation (see Fig. 7.3).

7.8 Brewster Angle

Observing the relative reflectivity coefficients, one deduces that for the p-polarized radiation r^{p} vanishes at a definite inclination angle, the so-called **Brewster angle**, when the sum of the incident inclination angle α and the transmitted angle β gets 90°, which one can write as

$$r^{\mathrm{p}} = 0 \quad \leftrightarrow \quad \alpha_{\mathrm{B}} + \beta = \frac{\pi}{2} \quad \leftrightarrow \quad n_1 \sin\alpha_{\mathrm{B}} = n_2 \sin\left(\frac{\pi}{2} - \alpha_{\mathrm{B}}\right)$$

defining the Brewster angle α_{B}:

Brewster angle

$$\alpha_{\mathrm{B}} = \arctan\left(\frac{n_2}{n_1}\right). \tag{7.32}$$

The Brewster angle is valid for both cases of refractive index difference at the boundary, $n_1 < n_2$ and $n_1 > n_2$ (Figs. 7.3 and 7.8). The physical interpretation is illustrative of the dipole approach chosen to describe the emission of radiation after excitation. The electric field vector for the incoming p-polarized radiation striking the interface at the Brewster angle α_{B} is oriented exactly into the direction of the transmitted radiation direction. This implies that the dipoles given by the atoms at the interface n_2 are all oriented in the alleged direction of the reflected radiation. But, as we learned in Sects. 2.4.3 and 3.2.4, **a dipole never emits radiation into the dipole direction**.

7.9 Critical Angle for Total Reflection

For radiation passing an interface from **an optical thicker medium to an optical thinner one**, $n_1 > n_2$, one observes that all angles follow the relation $\beta > \alpha$; see Fig. 7.7. This also means that an inclination angle α exists, where the refracted beam gets parallel to the surface, $\beta = 90°$. This results, computing it into Snell's law, in $n_1 \sin\alpha_T = n_2 \sin(90°)$ getting the so-called **critical angle for total reflection**

The critical angle for total reflection

$$\alpha_T = \arcsin\left(\frac{n_2}{n_1}\right). \tag{7.33}$$

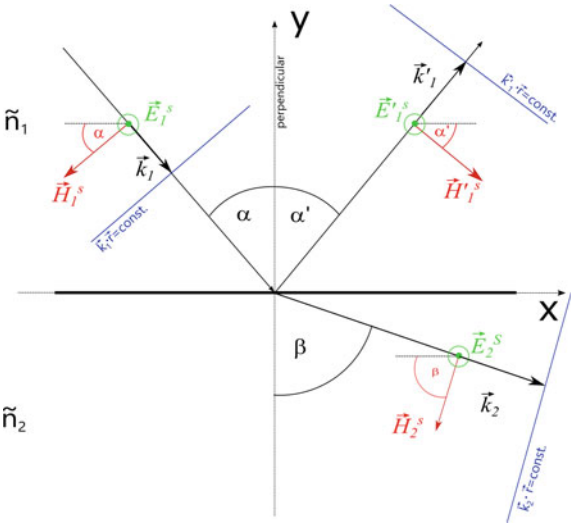

Fig. 7.7 Electric and magnetic field vectors for incoming, reflected, and transmitted s-polarized radiation

Obviously, radiation striking a boundary with an inclination angle $\alpha > \alpha_T$ will be completely **internally reflected**, given by the reflection and transmission coefficients (Fig. 7.8), and by the reflectance and transmittance (Fig. 7.9).

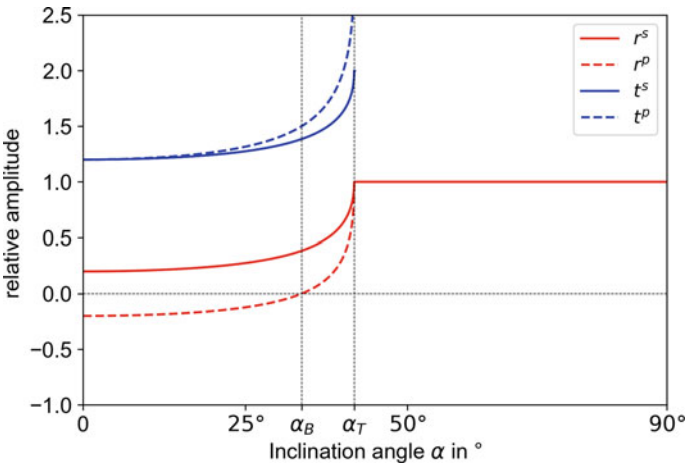

Fig. 7.8 Relative reflectivity and transmittivity for s- or p-polarized radiation passing through an interface from medium 1 with n_1 to medium 2 with n_2 and $n_1 > n_2$ (for nonmagnetic materials $\mu_{r1} = \mu_{r2} = 1$)

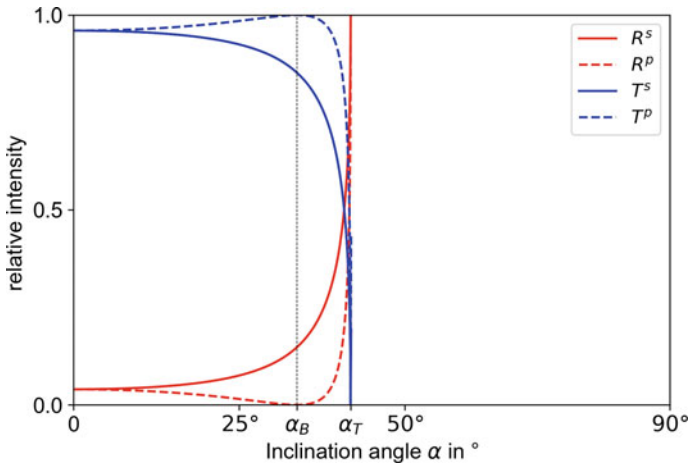

Fig. 7.9 Reflectance as well as transmittance for s- or p-polarized radiation passing through an interface from medium 1 with n_1 to medium 2 with n_2 and $n_1 > n_2$ (for nonmagnetic materials $\mu_{r1} = \mu_{r2} = 1$)

Snell's law has to be expanded, because for $\alpha > \alpha_T$ it follows that $|\sin\beta| > 1$, which is not possible for real numbers β. This implies that for an inclination $\alpha > \alpha_T$ the transmission angle has to be described by a complex number: $\beta \in \mathbb{C}$ with

$$\beta = \frac{\pi}{2} + i\beta_i .$$

One gets for the Fresnel equations, using the relations for trigonometric functions,

$$\sin\beta = \sin(\pi/2 + i\beta_i) = \cos(i\beta_i) = \cosh\beta_i \tag{7.34}$$

$$\cos\beta = \cos(\pi/2 + i\beta_i) = -\sin(i\beta_i) = -i\sinh\beta_i , \tag{7.35}$$

the **reflection coefficients for s-polarized radiation for an inclination angle $\alpha > \alpha_T$**, introducing the complex function $z = \alpha - i\beta_i$, and its conjugate complex $\bar{z} = \alpha + i\beta_i$, getting

$$r^{\mathrm{s}} = \frac{\sin(\beta-\alpha)}{\sin(\alpha+\beta)} = \frac{\sin(\pi/2-\alpha+i\beta_i)}{\sin(\pi/2+\alpha+i\beta_i)} = \frac{\cos(\alpha-i\beta_i)}{\cos(\alpha+i\beta_i)} \tag{7.36}$$

$$= \frac{e^{iz}+e^{-iz}}{e^{i\bar{z}}+e^{-i\bar{z}}} = \frac{|W_{\mathrm{s}}|e^{i\varphi_{\mathrm{s}}}}{|W_{\mathrm{s}}|e^{-i\varphi_{\mathrm{s}}}} = e^{2i\varphi_{\mathrm{s}}} . \tag{7.37}$$

Thereby, we used in the last row $W_{\mathrm{s}} = e^{iz} + e^{-iz}$. Apparently, the relative reflection coefficient is now a complex number, $r^{\mathrm{s}} \in \mathbb{C}$ with $|r^{\mathrm{s}}| = 1$. The phase φ_1 is calculated by separating the complex number W_{s} in real and imaginary parts, and by the argument and the phase

$$
\begin{aligned}
W_\mathrm{s} &= e^{iz} + e^{-iz} \\
&= e^{\beta_i}(\cos\alpha + i\sin\alpha) + e^{-\beta_i}(\cos\alpha - i\sin\alpha) \\
&= \underbrace{\left(e^{\beta_i} + e^{-\beta_i}\right)\cos\alpha}_{x} + i\underbrace{\left(e^{\beta_i} - e^{-\beta_i}\right)\sin\alpha}_{y} \\
&= x + iy = |W_\mathrm{s}|e^{i\varphi_\mathrm{s}}.
\end{aligned}
$$

The phase φ_s of the complex number W_s is defined by

$$
\tan\varphi_\mathrm{s} = \frac{y}{x} = \frac{e^{\beta_i} - e^{-\beta_i}}{e^{\beta_i} + e^{-\beta_i}}\tan\alpha = \tanh\beta_i \tan\alpha
$$

and can be calculated getting β_i from Snell's law

$$
n_1 \sin\alpha = n_2 \cosh\beta_i \quad \curvearrowright \quad \beta_i = \operatorname{arccosh}\left(\frac{n_1\sin\alpha}{n_2}\right),
$$

and results in

Phase for s-polarized radiation and $\alpha > \alpha_T$

$$
\tan\varphi_\mathrm{s} = \tanh\left(\operatorname{arccosh}\left(\frac{n_1\sin\alpha}{n_2}\right)\right)\tan\alpha. \tag{7.38}
$$

The **reflection coefficients for p-polarized radiation for $\alpha > \alpha_T$** results analogous to

$$
\begin{aligned}
r^\mathrm{p} &= \frac{\tan(\beta-\alpha)}{\tan(\alpha+\beta)} = \frac{\tan(\pi/2-\alpha+i\beta_i)}{\tan(\pi/2+\alpha+i\beta_i)} = -\frac{\cot(\alpha-i\beta_i)}{\cot(\alpha+i\beta_i)} \\
&= -\frac{\cos(\alpha-i\beta_i)}{\sin(\alpha-i\beta_i)}\frac{\sin(\alpha+i\beta_i)}{\cos(\alpha+i\beta_i)} \\
&= -\frac{e^{iz}+e^{-iz}}{e^{iz}-e^{-iz}}\frac{e^{i\bar{z}}-e^{-i\bar{z}}}{e^{i\bar{z}}+e^{-i\bar{z}}} \\
&= -\frac{W_\mathrm{p}}{W_\mathrm{s}}\frac{\overline{W}_\mathrm{s}}{\overline{W}_\mathrm{p}} = -e^{2i(\varphi_\mathrm{p}-\varphi_\mathrm{s})},
\end{aligned} \tag{7.39}
$$

using in the last row again $W_\mathrm{s} = e^{iz} + e^{-iz} = |W_\mathrm{s}|e^{i\varphi_\mathrm{s}}$ and $W_\mathrm{p} = e^{iz} - e^{-iz} = |W_\mathrm{p}|e^{i\varphi_\mathrm{p}}$ with $z = \alpha + i\beta_i$ and its conjugate complex values $\overline{W}_\mathrm{s}$, $\overline{W}_\mathrm{p}$, and $\bar{z}$.

Again, to get the phase φ_p one calculates it by separating the complex number W_p in real and imaginary parts:

$$
\begin{aligned}
W_\mathrm{p} &= e^{iz} - e^{-iz} \\
&= e^{\beta_i}(\cos\alpha + i\sin\alpha) - e^{-\beta_i}(\cos\alpha - i\sin\alpha)
\end{aligned} \tag{7.40}
$$

$$= \underbrace{\left(e^{\beta_i} - e^{-\beta_i}\right)\cos\alpha}_{x} + i\,\underbrace{\left(e^{\beta_i} - e^{-\beta_i}\right)\sin\alpha}_{y}$$

$$= x + iy = |W_\mathrm{p}|e^{i\varphi_\mathrm{p}}. \tag{7.41}$$

The phase of the complex number W_p is defined by

$$\tan\varphi_\mathrm{p} = \frac{y}{x} = \frac{e^{\beta_i} + e^{-\beta_i}}{e^{\beta_i} - e^{-\beta_i}}\tan\alpha = \frac{1}{\tanh\beta_i}\tan\alpha.$$

Phase for p-polarized radiation and $\alpha > \alpha_T$

$$\tan\varphi_\mathrm{p} = \frac{1}{\tanh\left(\operatorname{arccosh}\left(\frac{n_1\sin\alpha}{n_2}\right)\right)}\tan\alpha. \tag{7.42}$$

One gets the relation between the phases φ_s and φ_p for radiation containing s- and p-polarized radiation components,

$$\tan\varphi_\mathrm{s}\tan\varphi_\mathrm{p} = \tan^2\alpha. \tag{7.43}$$

The reflectivity coefficients r^s ms r^p of the radiation passing from an optical thick to an optical thin medium at an incident angle $\alpha > \alpha_T$ will represent for both polarization states complex numbers, and feature a value of unity: $|r^\mathrm{s}| = |r^\mathrm{p}| = 1$. But, the phases of the s- and p-polarized radiation components are different, meaning that linear polarized radiation striking an interface from an optical thicker medium to a thinner $n_1 > n_2$, featuring a polarization state being composed of s- and p-polarized radiation, will result in **elliptical polarized reflected radiation**.

7.10 Internal Reflection and Evanescent Waves

Again, radiation striking on an interface from **an optical thicker medium to an optical thinner one**, $\boldsymbol{n_1 > n_2}$, at an **inclination angle** $\boldsymbol{\alpha > \alpha_T}$ will be **totally internal reflected**. We are now asking about the fields in the region of the optical thinner medium close to the interface. From the atomic point of view, e.g. the optical thinner medium can be a vacuum, and no atoms are there given.

So, the atoms from the optically thicker medium being at the interface will emit spherical waves (in the far field), which will interfere with the other emitted waves. From the energetic point of view, the boundary atoms will transmit also some radiation in the optical thinner medium 2, but being destructively erased: The electric field strength in the medium 2 for $\alpha < \alpha_T$ is given by

$$\boldsymbol{E}_2^{\mathrm{s}} = E_{20}^{s} e^{i(\omega\, t - k_2(x \sin\beta - y\cos\beta))}\hat{\boldsymbol{z}}$$

using $k_2 = \frac{n_2}{n_1} k_1$. Exceeding now for β the critical angle, β gets complex: $\beta \to \pi/2 + i\beta_i$ and the electric field strength becomes, using (7.34) and (7.35),

$$\begin{aligned}\boldsymbol{E}_2^{\mathrm{s}} &= E_{20}^{s} e^{i(\omega\, t - k_2(x\cosh\beta_i + iy\sinh\beta_i))}\hat{\boldsymbol{z}} \\ &= E_{20}^{s} e^{i(\omega\, t - k_2 x\cosh\beta_i)} e^{-yk_2\sinh\beta_i}\hat{\boldsymbol{z}}. \end{aligned} \tag{7.44}$$

The magnitude of the magnetic field strength in medium 2 driven by (7.13) is given by

$$H_2 = \sqrt{\frac{\varepsilon_0\epsilon_{r2}}{\mu_0\mu_{r2}}} E_2.$$

But, as the magnetic field strength is parallelly oriented to the incident plane and given by $\boldsymbol{H}_2^{\mathrm{s}} = (H_x, H_y)$, the vector components are now written to

$$\begin{aligned} H_x &= = -H_2\cos\beta = i\,H_2\sinh\beta_i \\ &= i\sqrt{\frac{\varepsilon_0\epsilon_{r2}}{\mu_0\mu_{r2}}}\sinh\beta_i\, E_{20}^{s} e^{i(\omega\, t - k_2 x\cosh\beta_i)} e^{-yk_2\sinh\beta_i} \\ H_y &= -H_2\sin\beta = -H_2\cosh\beta_i \\ &= -\sqrt{\frac{\varepsilon_0\epsilon_{r2}}{\mu_0\mu_{r2}}}\cosh\beta_i\, E_{20}^{s} e^{i(\omega\, t - k_2 x\cosh\beta_i + iy\sinh\beta_i)} \\ &= -\sqrt{\frac{\varepsilon_0\epsilon_{r2}}{\mu_0\mu_{r2}}}\cosh\beta_i\, E_{20}^{s} e^{i(\omega\, t - k_2 x\cosh\beta_i)} e^{-yk_2\sinh\beta_i}. \end{aligned}$$

The resulting electromagnetic field features an electric field strength oriented in the z-direction and a magnetic field strength in the x-y plane, but the fields are not orthogonally oriented anymore: $\boldsymbol{k}_2$ is not orthogonal to $\boldsymbol{H}_2^{\mathrm{s}}$. **The electromagnetic radiation is no longer transversal**.

The penetrating fields are attenuated in the y-direction as $y < 0$, see Fig. 7.7, whereas in the x-direction a wave solution is given. So, there exist electromagnetic fields in the optic thinner medium 2! For a given radiation with wavelength λ_1, one can define an **optical penetration depth**, where the amplitude of the electric field of (7.44) is reduced to $1/e$ of the original field strength, given by

Optical penetration depth

$$l_{\mathrm{opt}} = \frac{1}{k_2} = \frac{\lambda_2}{2\pi}, \tag{7.45}$$

with $\lambda_2 = (n_2/n_1)\lambda_1$. As an example, using the transition of radiation with the wavelength $\lambda = 600$ nm from glass ($n_1 = 1.5$) to air ($n_2 \approx 1.0$), one calculates an optical penetration depth $l_{\mathrm{opt}} \approx 60$ nm.

The energy flux, i.e. the Poynting vector is calculated by

$$\begin{aligned}
\boldsymbol{S}_2^{\mathrm{s}} &= \boldsymbol{E}_2^{\mathrm{s}} \times \boldsymbol{H}_2^{\mathrm{s}} \\
\begin{pmatrix} S_x \\ S_y \\ S_z \end{pmatrix} &= \begin{pmatrix} 0 \\ 0 \\ E_z \end{pmatrix} \times \begin{pmatrix} H_x \\ H_y \\ 0 \end{pmatrix} = \begin{pmatrix} -E_z H_y \\ E_z H_x \\ 0 \end{pmatrix} \\
&= (E_{20}^s)^2 \sqrt{\frac{\varepsilon_0 \epsilon_{r2}}{\mu_0 \mu_{r2}}} \begin{pmatrix} \cosh \beta_i e^{2i(\omega\, t - k_2 x \cosh \beta_i)} e^{-2k_2 y \sinh \beta_i} \\ i \sinh \beta_i e^{2i(\omega\, t - k_2 x \cosh \beta_i)} e^{-2k_2 y \sinh \beta} \\ 0. \end{pmatrix}
\end{aligned}$$

Detectable are only real values of the Poynting vector $\boldsymbol{S}$, so holding in mind that $i = \exp(i\pi/2)$ one gets for the x-component of the Poynting vector S_x

$$\Re(S_x) = (E_{20}^s)^2 \sqrt{\frac{\varepsilon_0 \epsilon_{r2}}{\mu_0 \mu_{r2}}} \cosh \beta_i e^{-2k_2 y \sinh \beta_i} \cos^2(\omega\, t - k_2 x \cosh \beta_i)$$

and for the y-component S_y one gets

$$\begin{aligned}
\Re(S_y) &= -(E_{20}^s)^2 \sqrt{\frac{\varepsilon_0 \epsilon_{r2}}{\mu_0 \mu_{r2}}} \sinh \beta_i e^{-2k_2 y \sinh \beta_i} \cdot \\
&\quad \cdot \cos(\omega\, t - k_2 (x \cosh \beta_i)) \cos(\omega\, t - k_2 (x \cosh \beta_i) + \pi/2) \\
&= (E_{20}^s)^2 \sqrt{\frac{\varepsilon_0 \epsilon_{r2}}{\mu_0 \mu_{r2}}} \sinh \beta_i e^{-2k_2 y \sinh \beta_i} \cos(\omega\, t - k_2 (x \cosh \beta_i)) \cdot \\
&\quad \cdot \sin(\omega\, t - k_2 (x \cosh \beta_i))
\end{aligned}$$

with the real part of S_y given by

$$\Re(S_y) = (E_{20}^s)^2 \sqrt{\frac{\varepsilon_0 \epsilon_{r2}}{\mu_0 \mu_{r2}}} \sinh \beta_i\, e^{-2k_2 y \sinh \beta} \cos(2\omega\, t - 2k_2 x \cosh \beta_i).$$

The temporal average gets for the components of the Poynting vector to

$$\begin{aligned}
< \Re(S_x) > &= \frac{1}{2} (E_{20}^s)^2 \sqrt{\frac{\varepsilon_0 \epsilon_{r2}}{\mu_0 \mu_{r2}}} \cosh \beta_i e^{-2k_2 y \sinh \beta_i} \\
< \Re(S_y) > &= 0,
\end{aligned}$$

as shown in (1.93), describing an energy flux in the x-direction. The temporal average vanishes for S_y, see Fig. 7.10, proving that **for a total internal reflection no energy is transmitted at all**.

The tangential component of the Poynting vector $\boldsymbol{S}_x$ scales in y direction (into the medium 2) with an exponentially decaying amplitude describing the **evanescent wave**. Here, the analogy to the quantum mechanical **tunnel effect** is given, e.g. see Sect. 4.5.1 for the process description. The evanescent wave, even not transporting any energy into the second media, interacts with its constituents, meaning that subsequent processes are possible, like the excitation of matter in the medium 2.

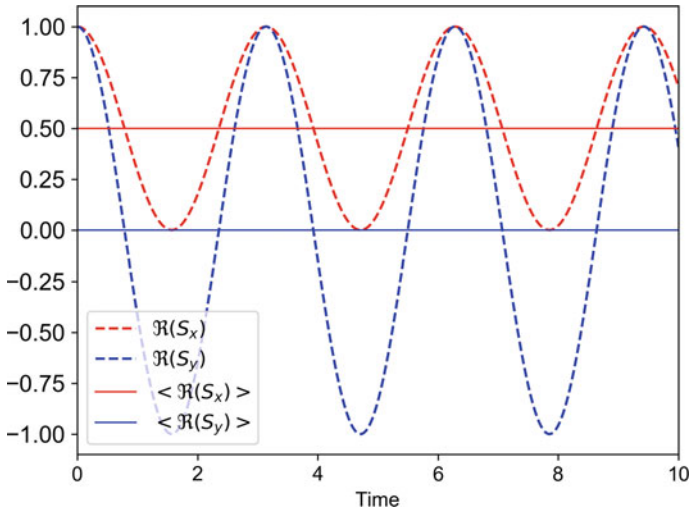

Fig. 7.10 Components of the Poynting vector $\Re(S_x)$ and $\Re(S_x)$ (dashed lines), and its temporal averages (straight lines)

One example is the formation of periodical structures in matter, the so-called ripple, where its formation is also described by the interaction of evanescent waves with matter, inducing polarized matter states, so-called **polarons**, which itself interacts with radiation; see also Sect. 1.7.2.

Chapter 8
Non-linear Optics

Abstract In this chapter, the non-linear interaction of electromagnetic radiation with negligible absorption, typical for dielectrics, will be discussed. First, the Maxwell equations will be adopted to develop the wave equation, then, introducing matter its reaction by the polarization density will be considered. Second, the non-linear reaction will be separated, and for two kinds of crystal symmetries in dielectrics the resulting optical properties will be calculated. (For this chapter, the textbook will follow closely the lecture notes of Prof. Sauerbrey, held in 2007 at the Technical University of Dresden. Many thanks to Prof. Sauerbrey!)

8.1 Principal Equations of Non-linear Optics

Starting from the Maxwell equations in matter (6.15) to (6.18) using the material (6.19) and (6.20), we can derive the wave equations for the electromagnetic radiation propagating in matter.

Again, by applying the curl on the Maxwell equation (6.15), assuming no charge and current densities, one gets

$$\nabla \times (\nabla \times \boldsymbol{E}) = -\nabla \times \frac{\partial \boldsymbol{B}}{\partial t}.$$

Assuming now an isotropic and homogeneous dielectric, we can use the linear relation between the fields, e.g. $\boldsymbol{B} = \mu_0 \mu_r \boldsymbol{H}$, we get the (6.17)

$$\begin{aligned} -\Delta \boldsymbol{E} &= -\mu_0 \mu_r \frac{\partial}{\partial t} \nabla \times \boldsymbol{H} \\ &= -\mu_0 \mu_r \frac{\partial^2 \boldsymbol{D}}{\partial t^2} \\ &= -\mu_0 \mu_r \frac{\partial^2 (\varepsilon_0 \boldsymbol{E} - \boldsymbol{P})}{\partial t^2}. \end{aligned}$$

In general, the relative permittivity $\tilde{\epsilon}_r$ and the relative permeability μ_r represent tensors of second rank $\underline{\underline{\tilde{\epsilon}}}_r$ and $\underline{\underline{\mu}}_r$ describing electric and magnetic anisotropies of

© Springer Nature Switzerland AG 2022

A. Horn, *The Physics of Laser Radiation–Matter Interaction*,
https://doi.org/10.1007/978-3-031-15862-9_8

matter. The last equation applies the material (6.19) and explains the dependence of the wave equation on the polarization density:

- In the case the **polarization density is linearly proportional** to the electric field strength, like (6.9) with $\boldsymbol{P} = \varepsilon_0 \chi_\mathrm{e} \boldsymbol{E}$, one gets again a homogeneous wave equation

$$\begin{aligned} -\Delta \boldsymbol{E} &= -\mu_0 \mu_r \frac{\partial^2(\varepsilon_0 \boldsymbol{E} - \varepsilon_0 \chi_\mathrm{e} \boldsymbol{E})}{\partial t^2} = -\mu_0 \mu_r \frac{\partial^2(\varepsilon_0 \overbrace{(1-\chi_\mathrm{e})}^{\epsilon_r} E)}{\partial t^2} \\ &= -\mu_0 \mu_r \varepsilon_0 \epsilon_r \frac{\partial^2 \boldsymbol{E}}{\partial t^2} \\ &= -\frac{1}{c_M^2} \frac{\partial^2 \boldsymbol{E}}{\partial t^2}. \end{aligned}$$

  The only difference between the solution in vacuum and this one is found in the wave velocity being now the **speed of light in matter c_M**, (6.23).
  As described in Sect. 6.5, solid matter can feature an anisotrope permittivity, resulting in three-wave equation for the main relative permittivity coefficients of the tensor $\underline{\underline{\epsilon}}_r$ given for the main axis of the birefringent crystal. For each crystal axis orientation, a different speed of light results. These wave equations are called **the principal equation of linear optics**.

Principal equation of linear optics

$$\Delta \boldsymbol{E} - \mu_0 \mu_r \frac{\partial^2(\varepsilon_0 \boldsymbol{E} - \boldsymbol{P})}{\partial t^2} = 0. \tag{8.1}$$

- In the case the **polarization density is non-linearly proportional** to the electric field, one can describe the polarization density as a power series approach, written as a superposition of a linear and a non-linear polarization density

$$\begin{aligned} \boldsymbol{P} &= \varepsilon_0 \sum_j \underline{\underline{\chi}}_\mathrm{e}^{(j)} \boldsymbol{E}^j \\ &= \boldsymbol{P}^\mathrm{L} + \boldsymbol{P}^\mathrm{NL} = \varepsilon_0 \underline{\underline{\chi}}_\mathrm{e}^{(1)} \boldsymbol{E} + \boldsymbol{P}^\mathrm{NL}, \end{aligned}$$

  with the linear susceptibility $\underline{\underline{\chi}}_\mathrm{e}^{(1)}$ of second rank, and the $(j+1)$th-ranked non-linear susceptibility tensors $\underline{\underline{\chi}}_\mathrm{e}^{(j)}$ for $j > 1$. Assuming again isotropic media, the linear susceptibility represents a scalar χ_e. Inserting this definition of the polarization into (6.38) results in an inhomogeneous and non-linear wave equation

$$-\Delta \boldsymbol{E} = -\mu_0 \mu_r \frac{\partial^2 (\varepsilon_0 \boldsymbol{E} - \varepsilon_0 \chi_e \boldsymbol{E} - \boldsymbol{P}^{\mathrm{NL}})}{\partial t^2},$$

and using

$$1/c_M^2 = n^2/c_0^2 = \mu_0 \mu_r \varepsilon_0 \epsilon_r, \tag{8.2}$$

one gets the **principal equation of the non-linear optics**

Principal equation of non-linear optics

$$\Delta \boldsymbol{E} - \frac{1}{c_M^2} \frac{\partial^2 \boldsymbol{E}}{\partial t^2} = -\mu_0 \mu_r \frac{\partial^2 \boldsymbol{P}^{\mathrm{NL}}}{\partial t^2}. \tag{8.3}$$

In the following section, the effects of non-linear media will be discussed in detail. The **non-linear polarization density** $\boldsymbol{P}^{\mathrm{NL}}$ can be developed as a Taylor series to the power of the electric field strength vector $\boldsymbol{E}$,

Non-linear polarization density

$$\boldsymbol{P}^{\mathrm{NL}} = \varepsilon_0 \sum_{j=2}^{\infty} \underline{\underline{\chi}}_{\mathrm{e}}^{(j)} \boldsymbol{E}^j, \tag{8.4}$$

where $\underline{\underline{\chi}}_{\mathrm{e}}^{(j)}$ represents the non-linear electrical susceptibility, being a tensor of rank $j+1$, with $j > 1$. For example, the x-component of the first non-linear polarization density vector $\boldsymbol{P}^{NL(2)}$ is written to

$$P_i^{NL(2)} = \varepsilon_0 \sum_{j,k} \chi_{\mathrm{e},ijk}^{(2)} E_j E_k = \varepsilon_0 \chi_{\mathrm{e},ijk}^{(2)} E_j E_k.$$

As shown in the last equation, by using the Einstein sum convention the sums over j and k can be omitted holding in mind that a summation is given for equal indices of different variables. It should be noted that a third-rank tensor, like $\chi_{\mathrm{e}}^{(2)}$, has 27 coefficients. Due to symmetry considerations, these can be reduced to 8 non-vanishing coefficients; see [1].

8.2 Non-linear Repulsive Forces

We have seen in Sect. 3.2 that the interaction of electromagnetic radiation with bounded electrons can be described by a classical equation of motion; see (3.22). There, the overall interaction is described by the Coulomb force $\boldsymbol{F}_c = -e\boldsymbol{E}$ resulting from the interaction of an electron with the electric field strength and a repulsive

potential from the binding potential of the electron with the nucleus, and is given by the harmonic oscillator potential, resulting in the linear repulsive force $\boldsymbol{F}_{\text{rep}} = -D\boldsymbol{x}$.

Increasing the intensity of the electromagnetic radiation results in larger electric field strength. The acting repulsive force must not be anymore linear, and can be described as the Taylor series, here shown in one dimension for the x-coordinate [2]

Non-linear repulsive force

$$F_{\text{rep}} = \underbrace{-D^{(1)}x}_{\text{linear optics}} \underbrace{-D^{(2)}x^2 - D^{(3)}x^3 - D^{(4)}x^4 - \ldots}_{\text{non-linear optics}}, \tag{8.5}$$

where $D^{(i)}$ denote the spring constants. With the physical reasonable assumption that the strength of the spring constants decrease strongly with increasing non-linearity, i.e. power of x,

$$D^{(n)} \gg D^{(n+1)} \tag{8.6}$$

the power series of the repulsive force F_{rep} gets convergent. The term with $n = 1$ describes the linear harmonic oscillator by the equation of motion (3.22), and the resulting laws of the **linear optics**; see Sect. 7. For $n > 1$, the non-linear forces and resulting **non-linear optics** will be described in the following.

Depending on the optical material, the power-scale considered in the repulsive force can be differentiated between **centrosymmetric** and **non-centrosymmetric forces**, and rising in centrosymmetric and non-centrosymmetric media, defined by

$$\begin{aligned} \text{Centrosymmetric forces:} \quad & F(x) = -F(-x) \\ \text{Non-centrosymmetric forces:} \quad & F(x) \neq -F(-x). \end{aligned}$$

8.3 Second-Order Processes

Second-order processes are very common in laser physics due to the high electric field strengths generated within crystals used for laser resonators or frequency converters. In the following, we will firstly solve the equation of motion using perturbation theory getting a quantitative expression for the linear and non-linear polarization densities. Secondly, solving the non-linear principal equations we get the intensity development of the **second harmonic generation (SHG)**. This second-order process is a three-wave mixing process and will then be described in more detail for the second harmonic generation (SHG), and also for **optical parametric amplification (OPA)**. So, the second harmonic is generated by passing through a non-linear crystal, and also parametric amplifications follow a second-order process. As the linear repulsive force acts, too, with the second-order repulsive force a non-centrosymmetric repulsive force results. Commonly, non-centrosymmetric media feature such non-centrosymmetric forces.

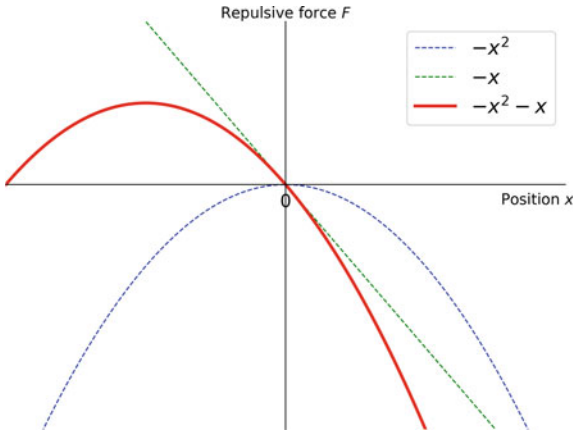

Fig. 8.1 Non-centrosymmetric force

8.3.1 Equation of Motion with Non-centrosymmetric Media

As a non-centrosymmetric repulsive force, one can write in one spatial dimension

$$F_{\text{rep}} = -D^{(1)}x - D^{(2)}x^2,$$

combining the linear force with the first non-linear one of the second order. As shown in Fig. 8.1, no centrosymmetry is given. We get now the equation of motion for one weakly bounded electron

$$\ddot{x}_0 + \Gamma_{\text{em}}\dot{x}_0 + \omega_0^2 x_0 + ax^2 = -\frac{e}{m_{\text{e}}}E_\omega \cos(\omega t), \tag{8.7}$$

using $\omega_0^2 = \frac{D^{(1)}}{m_{\text{e}}}$ and $a = \frac{D^{(2)}}{m_{\text{e}}}$. Here, we introduce also the notation for the electric field strength $\boldsymbol{E}_\omega$ highlighting as index the frequency of the radiation.

The solution of this differential equation results in the amplitude function of the electron, and from there we can calculate the dipole moment and the dipole moment density, see (6.21),

$$\boldsymbol{P}(t) = n_{\text{e}}e\boldsymbol{x}(t) = \boldsymbol{P}^{\text{L}} + \boldsymbol{P}^{\text{NL}}.$$

But, solving the non-linear differential equation is non-trivial. Doing some simplifications an analytical description can be derived. Alternatively, a numerical solution is possible every time.

The assumption from (8.6) implies that the linear force is much stronger than the non-linear one, $F^{(1)} \gg F^{(2)}$, and one gets the relation

$$x \ll \frac{D^{(1)}}{D^{(2)}} = \frac{\omega_0^2}{a},$$

making an approximation by the **perturbation theory** possible. Also, we will neglect any frictional force, i.e. $\Gamma_{\text{em}} = 0$. The ansatz used is now

$$x(t) = x^{(1)}(t) + x^{(2)}(t), \tag{8.8}$$

thereby the perturbation approximation

$$\max_t \left(x^{(1)}\right) \gg \max_t \left(x^{(2)}\right) \tag{8.9}$$

is valid, meaning that the induced linear amplitudes are much larger than the non-linear one. Using the ansatz from (8.8), one gets for the equation of motion (8.7)

$$\underbrace{\ddot{x}^{(1)}}_{I} + \underbrace{\ddot{x}^{(2)}}_{II} + \underbrace{\omega_0^2 x^{(1)}}_{III} + \underbrace{\omega_0^2 x^{(2)} + a\left(x^{(1)}\right)^2}_{IV} + \tag{8.10}$$

$$+ \underbrace{2a x^{(1)} x^{(2)} + a\left(x^{(2)}\right)^2}_{V} = -\frac{e}{m_{\text{e}}} E_\omega \cos(\omega t). \tag{8.11}$$

Due to the perturbation assumption, (8.9), the term (V) can be neglected.

In **first-order approximation**, the terms (IV) are much smaller than the one in (III), and the term (II) is much smaller than (I) resulting in an equation of motion in the first order of approximation

$$\ddot{x}^{(1)} + \omega_0^2 x^{(1)} = -\frac{e}{m_{\text{e}}} E_\omega \cos(\omega t). \tag{8.12}$$

This differential equation represents again the solution for a harmonic oscillation, and the characteristic equation of this inhomogeneous differential equation gets to

$$x^{(1)} = \frac{e/m_{\text{e}}}{\omega_0^2 - \omega^2} E_\omega \cos(\omega t). \tag{8.13}$$

In **second-order approximation**, the terms (II) and (IV) are considered getting the equation of motion

$$\ddot{x}^{(2)} + \omega_0^2 x^{(2)} = -a\left(x^{(1)}\right)^2,$$

and using the solution from the first-order approximation, (8.13) for $x^{(1)}$, one gets

$$\ddot{x}^{(2)} + \omega_0^2 x^{(2)} = -a\left(\frac{e/m_{\text{e}}}{\omega_0^2 - \omega^2} E_\omega\right)^2 \cos^2(\omega t).$$

Using the trigonometric identities[1] one rewrites last equation of motion to

$$\ddot{x}^{(2)} + \omega_0^2 x^{(2)} = -\frac{a}{2}\left(\frac{e/m_\mathrm{e}}{\omega_0^2 - \omega^2} E_\omega\right)^2 (1 + \cos(2\omega t)) .$$

Now, the inhomogeneity on the right side contains two terms, one being constant in time, the other oscillating with twice the fundamental frequency ω of the electromagnetic radiation.

To solve the last differential equation, we apply the ansatz separating the variables

$$x^{(2)} = x_1^{(2)} + x_2^{(2)}$$

getting two differential equations. The first equation marks the constant inhomogeneity

$$\ddot{x}_1^{(2)} + \omega_0^2 x_1^{(2)} = -\frac{a}{2}\left(\frac{e/m_\mathrm{e}}{\omega_0^2 - \omega^2} E_\omega\right)^2 \tag{8.14}$$

delivering the trivial and constant solution

$$x_1^{(2)} = -\frac{a}{2\omega_0^2}\left(\frac{e/m_\mathrm{e}}{\omega_0^2 - \omega^2} E_\omega\right)^2 = \text{const.}$$

The second equation marks the time-varying inhomogeneity

$$\ddot{x}_2^{(2)} + \omega_0^2 x_2^{(2)} = -\frac{a}{2}\left(\frac{e/m_\mathrm{e}}{\omega_0^2 - \omega^2} E_\omega\right)^2 \cos(2\omega t),$$

with the solution

$$x_2^{(2)} = -\frac{a}{2(\omega_0^2 - 4\omega^2)}\left(\frac{e/m_\mathrm{e}}{\omega_0^2 - \omega^2} E_\omega\right)^2 \cos(2\omega t).$$

Finally, one can now collect all partial solutions of the first- and second-order approximations $x^{(1)}$ and $x^{(2)}$, where $x^{(2)}$ is composed of $x_1^{(1)} + x_2^{(2)}$, forming the **overall amplitude function of the weakly bounded electron**

[1] $\cos(\alpha + \beta) = \cos\alpha\cos\beta - \sin\alpha\sin\beta$:
$\curvearrowright \quad \cos(2\alpha) = \cos^2\alpha - \sin^2\alpha = \cos^2\alpha - (1 - \cos^2\alpha) = 2\cos^2\alpha - 1$

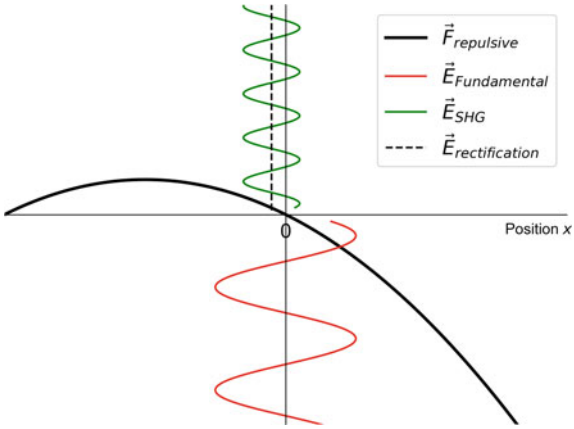

Fig. 8.2 The three induced electric fields after interaction of radiation with a non-centrosymmetric force of a non-linear non-centrosymmetric material

$$
\begin{aligned}
x(t) &= x^{(1)} + x^{(2)} = x^{(1)} + x_1^{(2)} + x_2^{(2)} \\
&= \underbrace{\frac{e/m_\mathrm{e}}{\omega_0^2 - \omega^2} E_\omega \cos(\omega t)}_{(1)} \quad \underbrace{-\frac{a}{2\omega_0^2}\left(\frac{e/m_\mathrm{e}}{\omega_0^2 - \omega^2}\right)^2 E_\omega^2}_{(2)} - \\
&\quad \underbrace{-\frac{a}{2(\omega_0^2 - 4\omega^2)}\left(\frac{e/m_\mathrm{e}}{\omega_0^2 - \omega^2}\right)^2 E_\omega^2 \cos(2\omega t)}_{(3)} .
\end{aligned}
$$

The overall solution includes three terms, as shown also in Fig. 8.2:

1. The first term (1) represents the **harmonic oscillation** observed also for small electric field strengths, the frequency being equal to the frequency of the exciting external electric field strength, representing linear optics; see Sect. 3.2.4. As many oscillators are given with a density n_osc, a **linear polarization density** $\boldsymbol{P}^\mathrm{L}$ is induced, analogous to (6.21).
2. The second term (2) depicts a **constant value**, or an oscillation with a frequency $\omega = 0$. This term describes the **optical rectification** used, e.g. for the generation of THz-radiation.
3. The last term (3) represents an oscillation of the electron at twice the frequency of the exciting field, and is proportional to the squared electric field strength. A **non-linear polarization density** $\boldsymbol{P}^\mathrm{NL}$ is induced, resulting in the emission of radiation at twice the frequency, the so-called **second harmonic generation (SHG)**.

8.3.2 Non-linear Polarization Density

As described in Sect. 3.2.4, the amplitude of the oscillating electron corresponds to a time-dependent electric dipole, which in turn results in applying the Lorentz model and, see (6.21), in an induced electric polarization density; see (6.21). In consequence, a relative electric permittivity ϵ_r results; see (6.22). So, we get for the three amplitude functions $x^{(1)} + x_1^{(2)} + x_2^{(2)}$ three polarization densities in matter, as derived in (6.21), and are written as

$$\begin{aligned} P(t) &= n_d d = -e n_d x(t) \\ &= -e n_d (x^{(1)} + x_1^{(2)} + x_2^{(2)}) \\ &= P_\omega^{\mathrm{L}}(t) + P_0^{\mathrm{NL}}(t) + P_{2\omega}^{\mathrm{NL}}(t), \end{aligned}$$

with the three polarization densities

$$P_\omega^{\mathrm{L}}(t) = \frac{e^2/m_\mathrm{e}}{\omega_0^2 - \omega^2} E_\omega \cos(\omega t) = P_\omega^{\mathrm{L}} \cos(\omega t) \tag{8.15}$$

$$P_0^{\mathrm{NL}}(t) = -\frac{a \cdot n_d \cdot e}{2\omega_0^2} \left(\frac{e/m_\mathrm{e}}{\omega_0^2 - \omega^2} \right)^2 E_\omega^2 = P_0^{\mathrm{NL}} = \text{const.} \tag{8.16}$$

$$P_{2\omega}^{\mathrm{NL}}(t) = -\frac{a \cdot n_d \cdot e}{2(\omega_0^2 - 4\omega^2)} \left(\frac{e/m_\mathrm{e}}{\omega_0^2 - \omega^2} \right)^2 E_\omega^2 \cos(2\omega t) \tag{8.17}$$

$$= P_{2\omega}^{\mathrm{NL}} \cos(2\omega t). \tag{8.18}$$

Now, the variables P_ω^{L}, P_0^{NL}, and $P_{2\omega}^{\mathrm{NL}}$ represent time-independent amplitude functions of the polarization densities.

We understand now the generation of new radiation components by the two induced non-linear additional polarization densities, resulting in the dipole emission of two non-linear electric fields traveling through matter; see Fig. 8.2.

8.3.3 Differential Equation for the Second Harmonic Field

We will not focus on the time-dependent non-linear polarization density $P_{2\omega}^{\mathrm{NL}}(t)$ first. In order to get the electric fields after non-linear interaction of high intense radiation with non-centrosymmetric matter—we expect three of them—one has to solve the principal equation of non-linear optics (8.3). For the non-linear acting forces and the resulting amplitude $x_2^{(2)}$, we have to make the ansatz using a real electric field $E \in \mathbb{R}$ by the linear combination of a complex plane wave and its complex conjugate, in the following abbreviated by c.c.

$$E(z,t) = \frac{1}{2}\left(E_{2\omega}(z)e^{-i(2\omega t - k_{2\omega}z)} + \underbrace{E^*_{2\omega}(z)e^{+i(2\omega t - k_{2\omega}z)}}_{\text{c.c.}} \right),$$

as the principal equation of non-linear optics does not follow anymore the superposition principle. There, the amplitude $E_{2\omega}$, its conjugate complex value $E^*_{2\omega}$, and the wave number

$$k_{2\omega} = n_{2\omega}\frac{2\omega}{c_0} \tag{8.19}$$

are given for the **frequency-doubled plane wave** using the refractive index at the doubled frequency $n_{2\omega}$, as this radiation propagates at the speed of light $c_{2\omega} = c_0/n_{2\omega}$.

As shown in standard laser textbooks, like [3], we approximate the spatial development of the envelope of the electric field $E_{2\omega}(z)$, because the amplitude envelope is changing much slower than the electric field strength,

Slow varying envelope approximation

$$k_{2\omega}E_{2\omega} \gg \frac{\partial E_{2\omega}}{\partial z}, \tag{8.20}$$

applying the so-called **slow varying envelope approximation** (SVEA), meaning in one dimension for the second derivative of the electric field $E_{2\omega}(z)$

$$k_{2\omega}\frac{\partial E_{2\omega}}{\partial z} \gg \frac{\partial^2 E_{2\omega}}{\partial z^2}. \tag{8.21}$$

Solving now the principal equation of non-linear optics, see (8.3), firstly the second derivative in space has to be calculated using the SVEA, and getting in one dimension

$$\Delta E = \frac{\partial^2 E}{\partial z^2} \approx \frac{1}{2}\left(2ik_{2\omega}\frac{\partial E_{2\omega}}{\partial z} - k^2_{2\omega}E_{2\omega} \right) e^{-i(2\omega t - k_{2\omega}z)} + c.c., \tag{8.22}$$

replacing thereby the conjugate complex part by the abbreviation $c.c.$. Secondly, using $\frac{1}{c_M^2} = \frac{n^2_{2\omega}}{c_0^2}$ the time derivative gets now to

$$\frac{n^2_{2\omega}}{c_0^2}\frac{\partial^2 E}{\partial t^2} = -\frac{1}{2}\frac{4\omega^2 n^2_{2\omega}}{c_0^2}\left(E_{2\omega}(z)e^{-i(2\omega t - k_{2\omega}z)} + c.c. \right). \tag{8.23}$$

Inserting both results in the principal equation of non-linear optics, and using the relation (8.19), the second term in the bracket of (8.22) is canceled by the temporal derivative from (8.23), resulting in

$$\frac{\partial^2 E}{\partial z^2} - \frac{n_{2\omega}^2}{c_0^2}\frac{\partial^2 E}{\partial t^2} = ik_{2\omega}\frac{\partial E_{2\omega}}{\partial z}e^{-i(2\omega t - k_{2\omega}z)} + c.c. \tag{8.24}$$

This equation corresponds to the left side of the principal (8.3). For the right side of the principal equation, we use now the non-linear polarization density P^{NL}, writing it similar to the electric field strength as a real function with $\mu_r = 1$, making the ansatz

$$P^{\mathrm{NL}} = \frac{1}{2}\left(P_{2\omega}^{\mathrm{NL}} e^{-2i(\omega t - k_\omega z)} + c.c.\right).$$

Here, it is important that the wave number k_ω of the polarization density is given by the incoming radiation, as the polarization density represents the overall amount of induced dipole moments in matter generated by the interaction of the electric field strength $\boldsymbol{E}$ with the weakly bounded electrons of the matter.

Now, taking the temporal derivatives of the polarization density, as written in the principal (8.3), we get

$$\begin{aligned} -\mu_0\frac{\partial^2 P^{\mathrm{NL}}}{\partial t^2} &= -\mu_0\frac{\partial^2}{\partial t^2}\frac{1}{2}\left(P_{2\omega}^{\mathrm{NL}} e^{-2i(\omega t - k_\omega z)} + c.c.\right) \\ &= -2\omega^2\mu_0\left(P_{2\omega}^{\mathrm{NL}} e^{-i2(\omega t - k_\omega z)} + c.c.\right). \end{aligned}$$

We compare now the last result with the right side of (8.24), and get

$$-2\omega^2\mu_0 P_{2\omega}^{\mathrm{NL}} e^{-2i(\omega t - k_\omega z)} + c.c. = ik_{2\omega}\frac{\partial E_{2\omega}}{\partial z}e^{-i(2\omega t - k_{2\omega}z)} + c.c.$$

The temporal dependence is equal on both sides of the equation and can be eliminated, holding in mind that we can drop the complex conjugate terms from each side and still maintain equality, getting a simple time-independent differential equation

$$\frac{\partial E_{2\omega}}{\partial z} = 2\frac{i\mu_0\omega^2}{k_{2\omega}}P_{2\omega}^{\mathrm{NL}} e^{i(2k_\omega - k_{2\omega})z}.$$

Replacing the non-linear polarization density $P_{2\omega}^{\mathrm{NL}}$ using (8.17)

$$P_{2\omega}^{\mathrm{NL}} = -\frac{a \cdot n_d \cdot e}{2(\omega_0^2 - 4\omega^2)}\left(\frac{e/m_{\mathrm{e}}}{\omega_0^2 - \omega^2}\right)^2 |E_\omega|^2 = -\bar{d}\,|E_\omega|^2$$

thereby defining a material constant, here the **non-linear polarizability** $\bar{d}$

$$\bar{d} = \frac{a \cdot n_d \cdot e}{2(\omega_0^2 - 4\omega^2)}\left(\frac{e/m_{\mathrm{e}}}{\omega_0^2 - \omega^2}\right)^2$$

and the **phase mismatch** Δk

$$\Delta k = 2k_\omega - k_{2\omega},$$

we can now rewrite the differential equation, getting

Differential equation for the second harmonic field strength

$$\frac{\partial E_{2\omega}}{\partial z} = \frac{i\omega}{n_{2\omega}}\sqrt{\frac{\mu_0}{\varepsilon_0}} \cdot \bar{d} \cdot e^{i\Delta kz} |E_\omega|^2 . \tag{8.25}$$

The change in the field strength of the second harmonic $E_{2\omega}$ depends on the material constants $n_{2\omega}$, $\bar{d}$, and Δk of the electric field strength of the fundamental E_ω.

8.3.4 Second Harmonic Generation

The increase in the second harmonic field strength depends now on the material constants $n_{2\omega}$, $\bar{d}$, and Δk, as well from the squared incoming fundamental electric field strength. Important to notice here is that also a spatial dependency is given. It can be seen, if we assume a non-changing electric field strength that due to absorption or scattering

$$E_\omega(z) \approx E_\omega(0) = E_\omega = \text{const.}, \tag{8.26}$$

one gets as solution for the second harmonic field strength assuming also a constant phase mismatch Δk

$$\begin{aligned} E_{2\omega}(z) &= \frac{i\omega}{n_{2\omega}}\sqrt{\frac{\mu_0}{\varepsilon_0}} \cdot \bar{d} \cdot |E_\omega|^2 \int_0^z e^{i\Delta kz'} dz' \\ &= \frac{i\omega}{n_{2\omega}}\sqrt{\frac{\mu_0}{\varepsilon_0}} \cdot \bar{d} \cdot |E_\omega|^2 \frac{e^{i\Delta kz} - 1}{i\Delta k} \\ &= \frac{i\omega}{n_{2\omega}}\sqrt{\frac{\mu_0}{\varepsilon_0}} \cdot \bar{d} \cdot |E_\omega|^2 e^{\frac{i\Delta kz}{2}} \frac{e^{\frac{i\Delta kz}{2}} - e^{\frac{i\Delta kz}{2}}}{i\Delta kz} \end{aligned}$$

Second harmonic field strength

$$E_{2\omega}(z) = \frac{i\omega}{n_{2\omega}}\sqrt{\frac{\mu_0}{\varepsilon_0}} \cdot \bar{d} \cdot |E_\omega|^2 \, e^{-i\frac{\Delta kz}{2}} \frac{\sin(\frac{\Delta kz}{2})}{\frac{\Delta k}{2}}. \tag{8.27}$$

Remembering the definition of the intensity, (7.27), we rewrite the linear and non-linear intensities, getting

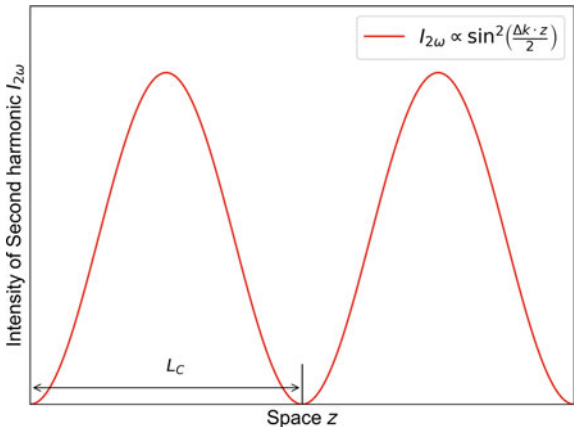

Fig. 8.3 Spatial dependence of the second harmonic intensity

$$I_\omega = \frac{n_\omega}{2}\sqrt{\frac{\mu_0}{\varepsilon_0}}\,|E_\omega|^2\,, \text{ and} \tag{8.28}$$

$$I_{2\omega} = \frac{n_{2\omega}}{2}\sqrt{\frac{\mu_0}{\varepsilon_0}}\,|E_{2\omega}|^2\,. \tag{8.29}$$

We now get the solution of (8.27) with its respective intensity

Second harmonic intensity

$$I_{2\omega}(z) = 2\left(\frac{\mu_0}{\varepsilon_0}\right)^{3/2}\frac{\omega^2\bar{d}^2}{n_\omega^2 n_{2\omega}}I_\omega^2(0)\frac{\sin^2\left(\frac{\Delta k z}{2}\right)}{\left(\frac{\Delta k}{2}\right)^2}. \tag{8.30}$$

The intensity of the second harmonic radiation changes periodically with the spatial coordinate z due to the phase mismatch Δk, which describes the difference in phase velocity of the fundamental c_ω and the second harmonic radiation $c_{2\omega}$. Only at the coherence length L_c, the phase difference of both radiations interfere constructively resulting in a maximum conversion intensity $I_{2\omega}$.

To be more precise, if at one spatial position z the fundamental radiation E_ω generates second harmonic radiation $E_{2\omega}$, at another place z the same fundamental will generate again a SH radiation $E_{2\omega}$. The primarily generated SH radiation will interfere with the second one, in case $z + L_c$ constructively, in case of $z + L_c/2$ destructively. We get a spatially modulated intensity distribution along the propagation direction of the radiation; see Fig. 8.3.

Using the relation (8.19) for the wave number of the second harmonic and for the fundamental

$$k_\omega = \frac{n_\omega \omega}{c_0} = n_\omega \frac{2\pi}{\lambda}\,,$$

we get

$$k_{2\omega} = \frac{n_{2\omega} 2\omega}{c_0} = n_{2\omega} \frac{4\pi}{\lambda},$$

and the phase mismatch is recalculated[2] as

Phase mismatch

$$\Delta k = \frac{4\pi}{\lambda} \Delta n, \tag{8.31}$$

using $\Delta n = n_\omega - n_{2\omega}$.

A coherent superposition is calculated by determining the maximum of (8.30) for

$$\frac{\Delta k L_c}{2} = \pi, \tag{8.32}$$

resulting in the coherence length

Coherence length

$$L_c = \frac{\lambda}{2\Delta n}. \tag{8.33}$$

For example, irradiating a non-linear crystal like quartz with Nd:YAG laser radiation at $\lambda = 1064$ nm generates the second harmonic radiation at $\lambda = 532$ nm. Quartz features refractive indices $n_\omega = n(1064) = 1.534$ and for the second harmonic $n_{2\omega} = n(532) = 1.547$ getting a coherence length of about $L_c \approx 40\,\mu\text{m}$.

The phase matching topic is crucial in laser technology, as the frequency conversion efficiency should not be proportional to the crystal length. But, we will not go further into this topic, as has been discussed in much more detail in other optics textbooks, like [3].

8.3.5 Three-Wave Mixing

The process of SHG can also be interpreted as the interaction of two waves at the frequencies ω_1 and ω_2, with $\omega_1 = \omega_2$; see Fig. 8.4. In the particle description, we have the interaction of two equal photons resulting in a third new one at the frequency ω_3, which is why this process is also called **three-wave mixing**.

In this case, we assume that the exciting electromagnetic field acting on the bounded electrons of the dielectric material is described by a planar linear polarized electric field

[2] As given by this equation, one can eliminate the phase matching by setting $\Delta k = 0$. This can be achieved by angle phase matching using birefringent crystals featuring different refractive indices for different angles of irradiation.

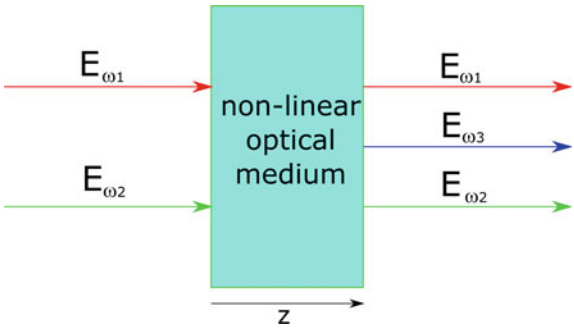

Fig. 8.4 Principle of three-wave mixing

$$\begin{aligned}\boldsymbol{E}(z,t) &= \boldsymbol{E}_1(z,t) + \boldsymbol{E}_2(z,t) \\ &= \frac{1}{2}\left(\boldsymbol{E}_1(z)\cdot e^{-i(\omega_1 t - k_1 z)} + c.c.\right) + \\ &+ \frac{1}{2}\left(\boldsymbol{E}_2(z)\cdot e^{-i(\omega_2 t - k_2 z)} + c.c.\right)\end{aligned}$$

with $\boldsymbol{E}_1$ and $\boldsymbol{E}_2$ representing the amplitude vectors of the incoming radiation, and the wave numbers defined by

$$k_j = \frac{n(\omega_j)\cdot\omega_j}{c_0} \quad \text{with } j = 1, 2.$$

Again, the equation of motion (8.12) has to be solved; see Sect. 8.3.1. One can do the approach by perturbation calculations, as shown before, getting finally a solution for the trajectory of the electron being proportional to

$$x \propto e^{-i(\omega_1+\omega_2)t} + e^{-i(\omega_1-\omega_2)t} + c.c.$$

This means that the resulting radiation features a frequency which is the sum of the incoming frequencies, the so-called sum-frequency mixing

Sum-frequency mixing

$$\omega_3 = \omega_1 + \omega_2, \tag{8.34}$$

and the difference of the incoming frequencies, the so-called difference-frequency mixing

Difference-frequency mixing

$$\omega_3 = \omega_1 - \omega_2. \tag{8.35}$$

With phase matching, one can control the outcome of the radiation featuring the sum or the difference of the incoming frequencies.

To be able to calculate the electric field of the sum-frequency radiation,[3] e.g. the SHG, we take as the electric field

$$\boldsymbol{E}_3(z,t) = \frac{1}{2}\left(\boldsymbol{E}_3(z)\cdot e^{-i(\omega_3 t - k_3 z)} + c.c.\right)$$

and get for the principal equation of non-linear optic (8.3) for each incoming field a separated non-linear polarization density vector $\boldsymbol{P}^{\mathrm{NL}} = \boldsymbol{P}_1^{\mathrm{NL}} + \boldsymbol{P}_2^{\mathrm{NL}}$ with $\boldsymbol{P}_1^{\mathrm{NL}} \propto \boldsymbol{E}_1$ and $\boldsymbol{P}_2^{\mathrm{NL}} \propto \boldsymbol{E}_2$. Written for a plane wave propagating in z-direction, we get

$$\frac{\partial^2 \boldsymbol{E}_3}{\partial z^2} - \frac{n_{\omega_3}^2}{c_0^2}\frac{\partial^2 \boldsymbol{E}_3}{\partial t^2} = \mu_0 \frac{\partial^2}{\partial t^2}\left(\boldsymbol{P}_1^{\mathrm{NL}} + \boldsymbol{P}_2^{\mathrm{NL}}\right).$$

Solving now in SVEA this equation, see Sect. 8.3.3, one gets three coupled differential equations, so-called Manley–Rowe equations

Manley–Rowe equations

$$\frac{\partial \boldsymbol{E}_1}{\partial z} = \frac{i\omega_1}{n_{\omega_1}}\sqrt{\frac{\mu_0}{\varepsilon_0}}\bar{d}e^{-i\Delta k z}\boldsymbol{E}_2^*\boldsymbol{E}_3 \tag{8.36}$$

$$\frac{\partial \boldsymbol{E}_2}{\partial z} = \frac{i\omega_2}{n_{\omega_2}}\sqrt{\frac{\mu_0}{\varepsilon_0}}\bar{d}e^{-i\Delta k z}\boldsymbol{E}_1^*\boldsymbol{E}_3 \tag{8.37}$$

$$\frac{\partial \boldsymbol{E}_3}{\partial z} = \frac{i\omega_3}{n_{\omega_3}}\sqrt{\frac{\mu_0}{\varepsilon_0}}\bar{d}e^{-i\Delta k z}\boldsymbol{E}_1\boldsymbol{E}_2 \tag{8.38}$$

with the phase mismatch

$$\Delta k = k_1 + k_2 - k_3. \tag{8.39}$$

As we will mostly deal with the intensity of the radiation, we need the value of the squared electric field $|\boldsymbol{E}|^2$. The derivative of the value of the squared intensity looks like[4]

$$\frac{\partial \left|\boldsymbol{E}_j\right|^2}{\partial z} = \frac{\partial \boldsymbol{E}_j}{\partial z}\boldsymbol{E}_j^* + \frac{\partial \boldsymbol{E}_j^*}{\partial z}\boldsymbol{E}_j. \tag{8.40}$$

[3] The described approach is as well applicable for the difference-frequency mixing by adapting the corresponding signs in the equations.

[4] The value of a complex number a is given by $|a|^2 = aa^*$, with a^* representing the conjugate complex value of a.

Multiplying each of the three differential equations with the missing electric field on the right side by $\boldsymbol{E}_j^*$, $j = 1, 2, 3$, and summing up with its conjugate complex value we get

$$\begin{aligned}
\frac{\partial \boldsymbol{E}_1}{\partial z}\boldsymbol{E}_1^* + \frac{\partial \boldsymbol{E}_1^*}{\partial z}\boldsymbol{E}_1 &= \frac{\omega_1}{n_{\omega_1}}\sqrt{\frac{\mu_0}{\varepsilon_0}}\bar{d}\left(ie^{-i\Delta kz}\boldsymbol{E}_2^*\boldsymbol{E}_3\boldsymbol{E}_1^* - ie^{i\Delta kz}\boldsymbol{E}_2\boldsymbol{E}_3^*\boldsymbol{E}_1\right)\\
\frac{\partial \boldsymbol{E}_2}{\partial z}\boldsymbol{E}_2^* + \frac{\partial \boldsymbol{E}_2^*}{\partial z}\boldsymbol{E}_2 &= \frac{\omega_2}{n_{\omega_2}}\sqrt{\frac{\mu_0}{\varepsilon_0}}\bar{d}\left(ie^{-i\Delta kz}\boldsymbol{E}_1^*\boldsymbol{E}_3\boldsymbol{E}_2^* - ie^{i\Delta kz}\boldsymbol{E}_1\boldsymbol{E}_3^*\boldsymbol{E}_2\right)\\
\frac{\partial \boldsymbol{E}_3}{\partial z}\boldsymbol{E}_3^* + \frac{\partial \boldsymbol{E}_3^*}{\partial z}\boldsymbol{E}_3 &= \frac{\omega_3}{n_{\omega_3}}\sqrt{\frac{\mu_0}{\varepsilon_0}}\bar{d}\left(ie^{-i\Delta kz}\boldsymbol{E}_1\boldsymbol{E}_2\boldsymbol{E}_3^* - ie^{i\Delta kz}\boldsymbol{E}_1^*\boldsymbol{E}_2^*\boldsymbol{E}_3\right).
\end{aligned}$$

On the left sides, we can determine the analogy to (8.40) of each electric field. It can be shown, e.g. in [1] that the three right-hand-side brackets are all equivalent, so that we can combine these equations and rewrite them to the three Manley–Rowe relations

Manley–Rowe relations

$$\begin{aligned}
\frac{1}{\omega_1}\frac{\partial}{\partial z}\left(n_{\omega_1}\sqrt{\frac{\varepsilon_0}{\mu_0}}\,|\boldsymbol{E}_1|^2\right) &= \frac{1}{\omega_2}\frac{\partial}{\partial z}\left(n_{\omega_2}\sqrt{\frac{\varepsilon_0}{\mu_0}}\,|\boldsymbol{E}_2|^2\right)\\
&= \frac{1}{\omega_3}\frac{\partial}{\partial z}\left(n_{\omega_3}\sqrt{\frac{\varepsilon_0}{\mu_0}}\,|\boldsymbol{E}_3|^2\right). \qquad (8.41)
\end{aligned}$$

These relations are written in this form, because as we can see, looking at the definition of the intensity, see (7.27), within the brackets, we have the product of the energy density with the velocity of light in the medium, representing an energy flux, i.e. an intensity

$$\frac{1}{2}n_{\omega_i}\sqrt{\frac{\varepsilon_0}{\mu_0}}\,|\boldsymbol{E}_i|^2 = \frac{1}{2}\varepsilon_0\epsilon_{ri}\frac{1}{\sqrt{\mu_0\epsilon_0\epsilon_{ri}}}\,|\boldsymbol{E}_i|^2 = \frac{1}{2}\varepsilon_0\epsilon_{ri}c_i\,|\boldsymbol{E}_i|^2 = I_i,$$

where we used $n_{\omega_i} = \sqrt{\epsilon_{ri}}$. We get finally the Manley–Rowe relation rewritten as

$$\frac{1}{\omega_1}\frac{\partial}{\partial z}(2I_1) = \frac{1}{\omega_2}\frac{\partial}{\partial z}(2I_2) = \frac{1}{\omega_3}\frac{\partial}{\partial z}(2I_3).$$

On the other hand, working with the photon description, using the photon density $n_i = N_i/V$ of the radiation with the intensity written as

$$I_i = n_i\hbar\omega_i c_0,$$

we can rewrite the Manley–Rowe relation as

$$\hbar c_0 \frac{\partial n_1}{\partial z} = \hbar c_0 \frac{\partial n_2}{\partial z} = -\hbar c_0 \frac{\partial n_3}{\partial z}$$

or working with the photon numbers N_i

$$\frac{\partial N_1}{\partial z} = \frac{\partial N_2}{\partial z} = -\frac{\partial N_3}{\partial z}.$$

Now the interpretation of the equations is easy, as we have three rate equations describing the formation of photons with the frequency ω_3 along the trajectory z by using the photons with the frequencies ω_1 and ω_2. So, we can also interpret the second harmonic generation as the **energy conservation**

$$\hbar\omega_3 = \hbar\omega_1 + \hbar\omega_2$$

and the phase matching relation, (8.39), represents the **conservation of the momentum**

$$\hbar \boldsymbol{k}_3 = \hbar \boldsymbol{k}_1 + \hbar \boldsymbol{k}_2.$$

8.3.6 *Parametric Amplification*

In parametric amplification, the difference-frequency mixing (8.35) is applied by appropriate choice of the phase matching and still, the forces are non-centrosymmetric. Again, the Manley–Rowe relations (8.41) are valid. As shown in Fig. 8.5, the incoming radiation consists of a **pump** at the frequency ω_1 and a **signal** at the frequency ω_2 and exiting are again both additionally with the difference-frequency radiation, called **idler** at ω_3. One speaks about a parametric process when both the signal and idler are amplified by the pump.

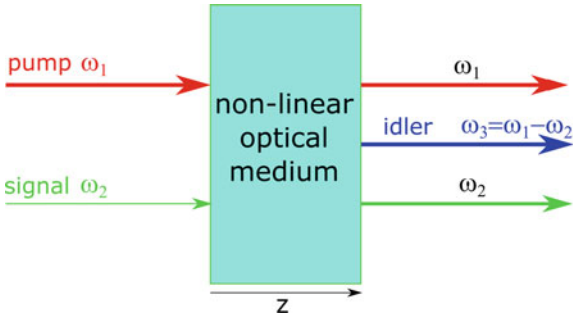

Fig. 8.5 Principle of parametric amplification

Here additionally, we take the non-depleted pump approximation (NDP) assuming that the intensity of the pump is much larger than those from the signal and idler

$$I_1 \gg I_2, I_3.$$

Additionally, we assume that within the length of the non-linear crystal, the intensity of the pump remains constant $I_1 = \text{const.}$

Starting again from the Manley–Rowe equations (8.36)–(8.38), assuming phase matching, i.e. $\Delta k = 0$, and accounting the constant pump I_3, we get (8.36) and (8.37) rewritten as

$$\frac{\partial \boldsymbol{E}_2}{\partial z} = i \left[\frac{\omega_2}{n_{\omega_2}} \sqrt{\frac{\mu_0}{\varepsilon_0}} \bar{d} \boldsymbol{E}_1(0) \right] \boldsymbol{E}_3^* \tag{8.42}$$

$$\frac{\partial \boldsymbol{E}_3}{\partial z} = i \left[\frac{\omega_3}{n_{\omega_3}} \sqrt{\frac{\mu_0}{\varepsilon_0}} \bar{d} \boldsymbol{E}_1(0) \right] \boldsymbol{E}_2^* \tag{8.43}$$

representing coupled differential equations. The values within the brackets depend not on z, so we take from this equation the second derivative,

$$\frac{\partial^2 \boldsymbol{E}_2}{\partial z^2} = i \left[\frac{\omega_2}{n_{\omega_2}} \sqrt{\frac{\mu_0}{\varepsilon_0}} \bar{d} \boldsymbol{E}_1(0) \right] \frac{\partial \boldsymbol{E}_3^*}{\partial z} \tag{8.44}$$

$$\frac{\partial^2 \boldsymbol{E}_3}{\partial z^2} = i \left[\frac{\omega_3}{n_{\omega_3}} \sqrt{\frac{\mu_0}{\varepsilon_0}} \bar{d} \boldsymbol{E}_1(0) \right] \frac{\partial \boldsymbol{E}_2^*}{\partial z} \tag{8.45}$$

and substitute the first derivatives on the right side by the conjugate complex (8.42) and (8.43) getting now to trivial differential equation for $\boldsymbol{E}_1$ and $\boldsymbol{E}_2$

$$\frac{\partial^2 \boldsymbol{E}_2}{\partial z^2} = K^2 \boldsymbol{E}_2$$

$$\frac{\partial^2 \boldsymbol{E}_3}{\partial z^2} = K^2 \boldsymbol{E}_3$$

with the constant factor

$$K = \left(\frac{\omega_2 \omega_3}{n_{\omega_2} n_{\omega_2}} \frac{\mu_0}{\varepsilon_0} \bar{d}^{\,2} |\boldsymbol{E}_1(0)|^2 \right)^{1/2}.$$

The solution with the boundary conditions

$$\boldsymbol{E}_1(z) \approx \text{const.} > 0$$

$$\boldsymbol{E}_2(0) \neq 0$$

$$\boldsymbol{E}_3(0) = 0$$

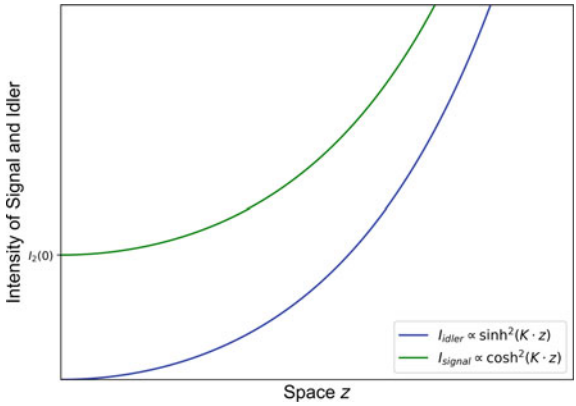

Fig. 8.6 Dependencies of the intensities of signal and idler during parametric amplification with a non-depleted pump as a function of crystal length

gets for the electric fields for signal and idler to

$$\boldsymbol{E}_2(z) = \boldsymbol{E}_2(0)\cosh(K \cdot z)$$
$$\boldsymbol{E}_3(z) = i\sqrt{\frac{\omega_3}{\omega_2}}\boldsymbol{E}_2^*(0)\sinh(K \cdot z).$$

The corresponding intensities for signal and idler get to

$$\textbf{Signal:} \quad I_2(z) = I_2(0)\cosh^2(K \cdot z) \tag{8.46}$$
$$\textbf{Idler:} \quad I_3(z) = \frac{\omega_3}{\omega_2} I_2(0)\sinh^2(K \cdot z) \tag{8.47}$$

and are shown in Fig. 8.6.

The most popular applications of parametric amplification are

1. **Optical Parametric Generation—OPG**: As one non-linear parametric process from the pump radiation signal and idler are generated following $\omega_1 = \omega_2 + \omega_3$. This process is necessary for the following process of optical parametric oscillation.
2. **Optical Parametric Oscillation—OPO**: As shown in equations (8.46) and (8.47), the amplification of signal and idler scales with crystal length. The parametric process is also enhanced by coupling the signal and/or the idler radiation within a resonator allowing to use the non-linear process as a repetitive laser pumping process; see Fig. 8.7. Very common is the degenerate OPO, where $\omega_1 = \omega_2 = \omega_3/2$.
3. **Optical Parametric Amplification—OPA**: As shown in the previous calculations, the signal is amplified by the parametric process. Using a Ti:Sapphire ultrafast laser emitting at 800 nm wavelength pump radiation, a signal is extracted from a white-light continuum generated by self-phase modulation; see Sect. 8.4.7

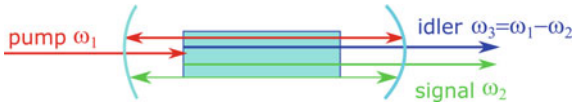

Fig. 8.7 Principle setup of an Optical Parametric Oscillator

using a little part of the pump radiation. This signal radiation is then amplified together with the idler [4].

4. **Optical Parametric Chirped Pulse Amplification—OP-CPA**: This process combines the Chirped Pulse Amplification (CPA) method with the parametric amplification. It is used to amplify ultrashort pulses very efficiently. The principle is shown in simplified form in Fig. 8.8.

8.4 Third-Order Processes

Increasing further the intensity of the laser radiation in matter induces third-order processes, described by the non-linear third-order susceptibility $\chi_e^{(3)}$. Now, also the electric field strengths scale with the third order, see (8.4), which can be interpreted as the third-harmonic generation (THG) of three equal photons, or the four-wave mixing of possibly three different photons to a fourth one. Contrary to the second-order processes, third-order processes take place in centrosymmetric, as well as in non-centrosymmetric media.

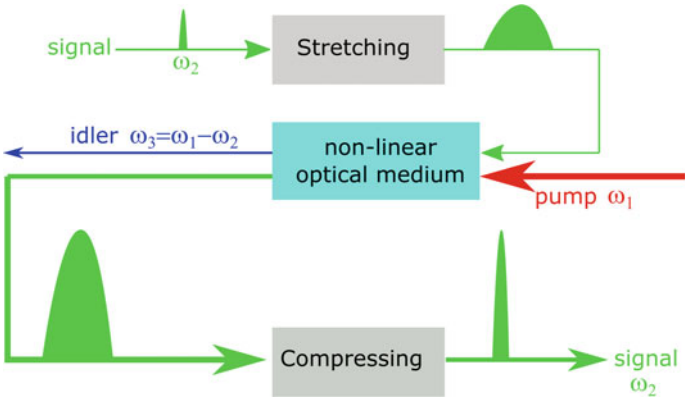

Fig. 8.8 Principle setup of an Optical Parametric Chirped Pulse Amplification (OP-CPA)

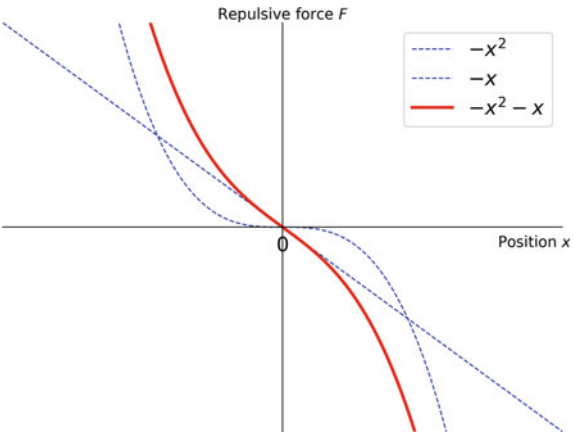

Fig. 8.9 Schematics of centrosymmetric forces

8.4.1 Equation of Motion with Centrosymmetric Media

As a centrosymmetric repulsive force, one can write

$$F_{\text{rep}} = -D^{(1)}x - D^{(3)}x^3,$$

shown in Fig. 8.9, and we get the equation of motion for one weakly bounded electron

$$\ddot{x}_0 + \Gamma_{em}\dot{x}_0 + \omega_0^2 x_0 + bx^3 = -\frac{e}{m_e}E_0\cos(\omega t), \tag{8.48}$$

using the variables $\omega_0^2 = \frac{D^{(1)}}{m_e}$ and $b = \frac{D^{(3)}}{m_e}$. Analogous to non-centrosymmetric forces, we cannot solve this differential equation analytically, but get an approximated solution by the perturbation theory. We skip here the elongated calculations and write immediately the solution for the non-linear term

$$x^{(3)}(\omega_q) = -\sum \frac{be^3 E(\omega_m)E(\omega_n)E(\omega_p)}{m_e^3 \mathcal{D}(\omega_q)\mathcal{D}(\omega_m)\mathcal{D}(\omega_p)},$$

with

$$\begin{aligned} \omega_q &= \omega_m + \omega_n + \omega_p \quad \text{with } m, n, p, q = 1, 2, 3, 4 \\ \mathcal{D}(\omega_i) &= \omega_0^2 - \omega_i^2 - i\Gamma_{em}\omega_i \quad \text{with } i = m, n, p. \end{aligned}$$

Due to symmetry, the non-linear term $x^{(2)}$ vanishes, so that the overall solution results as

$$x(t) = x^{(1)} + x^{(3)}.$$

8.4.2 Four-Wave Mixing

It can be shown that cat higher radiation intensities acting on the bounded electrons in the centrosymmetric and also non-centrosymmetric media feature a polarization density of third order in the repulsive force given by

$$\boldsymbol{P}^{\mathrm{NL}}(\omega_i) = e n_{\mathrm{e}} \boldsymbol{x}^{(3)}.$$

So, as the polarization density scales with the third power in the electric fields, its propagation in the z direction can be described by

$$\boldsymbol{P}^{\mathrm{NL}}(\omega_i) = \varepsilon_0 \chi_{\mathrm{e}}^{(3)} \left|\boldsymbol{E}(\omega, z, t)\right|^2 \boldsymbol{E}(\omega, z, t),$$

where the non-linear susceptibility $\chi_{\mathrm{e}}^{(3)}$ represents a tensor of fourth rank. One can also write this in the Einstein notation

$$P_i^{\mathrm{NL}}(\omega_A) = \varepsilon_0 \chi_{ijkl}(\omega_A, \omega_B, \omega_C, \omega_D) \epsilon_j(\omega_B) \epsilon_k(\omega_C) \epsilon_l(\omega_D),$$

making evident the four-wave mixing, where i, j, k, l represent the spatial coordinates x, y, z and A, B, C, D represent the permutation of the four involved electric fields.

Now, assuming linear polarized radiation for all three electric fields oriented in the x-direction with equal amplitude $\boldsymbol{E}_1 = \boldsymbol{E}_2 = \boldsymbol{E}_3$, we can now write the non-linear polarization density as

$$P_x^{\mathrm{NL}}(\alpha\omega, z, t) = \varepsilon_0 \chi_{xxxx}^{(3)} E^3(\omega, z, t),$$

with the coefficient $\alpha = -1, 3$. Especially, the coefficient α can be derived by calculating the resulting non-linear electric field strength, e.g. using the incoming electric field strength

$$E(\omega, z, t) = \frac{1}{2}\left(E_0(\omega, z) e^{-i(\omega t - k_\omega z)} + c.c.\right),$$

and getting its third power

$$\begin{aligned} E^3(\omega, z, t) = \frac{1}{8}\Big(&E_0^3(\omega, z) e^{-3i(\omega t - k_\omega z)} + c.c. + \\ &+ 3E_0^2 E_0^*(\omega, z) e^{-i(\omega t - k_\omega z)} + c.c.\Big). \end{aligned} \tag{8.49}$$

Therefore, we have to set up two non-linear polarization densities at the two resulting frequencies getting

$$P_x^{\mathrm{NL}} = \frac{1}{2}\left(P^{\mathrm{NL}}(3\omega, z)e^{-3i\omega t}e^{i(k_1+k_2+k_3)z} + c.c. + \right.$$
$$\left. + \; P^{\mathrm{NL}}(\omega, z)e^{-i\omega t}e^{i(k_1-k_2+k_3)z} + c.c\right).$$

One reads from the last equations that we have two different results to get the third power of the electric field strength and the non-linear polarization densities. The first represents the **third-harmonic generation (THG)** with

$$\omega_4 = 3\omega$$

where the conservation of momentum is given by

$$\boldsymbol{k}_4 = \boldsymbol{k}_1 + \boldsymbol{k}_2 + \boldsymbol{k}_3.$$

The non-linear polarization density for the third-harmonic generation reads now

$$P_x^{\mathrm{NL}}(3\omega, z, t) = \frac{1}{4}\varepsilon_0\chi^{(3)}(3\omega, \omega, \omega, \omega)E^3(\omega, z). \tag{8.50}$$

The second part of (8.49) represents the **degenerated four-wave mixing** with

$$\omega_4 = \omega - \omega + \omega,$$

with the conservation of the momentum given by

$$\boldsymbol{k}_4 = \boldsymbol{k} - \boldsymbol{k} + \boldsymbol{k}.$$

The non-linear polarization density for the degenerated four-wave mixing reads now

$$P_x^{\mathrm{NL}}(\omega, z, t) = \frac{3}{4}\varepsilon_0\chi^{(3)}(-\omega, \omega, -\omega, \omega)E^2(\omega, z)E^*(\omega, z). \tag{8.51}$$

8.4.3 Third-Harmonic Generation

Now, the principal equation of non-linear optics (8.3) is solved using the non-linear polarization density for the third-harmonic generation (8.50), applying the SVEA approximation, see page 197, and assuming non-depleting pumping (NDP), see page 207, getting analogous to the SHG the simplified differential equation in one spatial dimension

$$\frac{\partial E(3\omega)}{\partial z} = \frac{3i\omega}{8c_0 n_{3\omega}}\chi^{(3)}(3\omega)E^3(\omega)e^{i\Delta kz},$$

with the phase mismatch given by

$$\Delta k = 3k_\omega - k_{3\omega} = \frac{3\omega}{c_0}\left(n_\omega - n_{3\omega}\right).$$

We get as a solution for the intensity of the third harmonics

Intensity of the third harmonics

$$I_{3\omega}(z) = \frac{9\omega^2}{16\varepsilon_0^2 c_0^4 n_\omega^3 n_{3\omega}} \left|\chi^{(3)}(3\omega)\right|^2 I_\omega^3(0) z^2 \frac{\sin^2\left(\frac{\Delta k\cdot z}{2}\right)}{\left(\frac{\Delta k\cdot z}{2}\right)^2}, \tag{8.52}$$

describing the dependence of the intensity of the THG radiation from the third power of the incoming radiation intensity.

A phase matching is achieved, like for the SHG, for

$$\Delta\boldsymbol{k} = 3\boldsymbol{k}_\omega - \boldsymbol{k}_{3\omega} = \boldsymbol{k}_1 + \boldsymbol{k}_2 + \boldsymbol{k}_3 - \boldsymbol{k}_{3\omega} \equiv 0.$$

This equation is generally applicable for collinear as well as non-collinear incoming radiation.

8.4.4 Kerr Effect

As we have seen, two different polarization densities can result in a third-order process, and using the one for four-wave mixing, see (8.51), the principal equation of non-linear optics (8.3) results now as

$$\Delta E(\omega) + \frac{n_0^2}{c_0^2}\omega^2 E(\omega) = -\frac{3}{4}\frac{\chi^{(3)}}{c_0^2}\omega^2 \left|E(\omega)\right|^2 E(\omega).$$

Rewriting this equation, one gets again a principal equation like for linear optics,

$$\Delta E(\omega) + \frac{\omega^2}{c_0^2}\underbrace{\left(n_0^2 + \frac{3}{4}\chi^{(3)}\left|E(\omega)\right|^2\right)}_{n^2(E)} E(\omega) = 0,$$

$$\Delta E(\omega) + \frac{\omega^2}{c_0^2} n^2(E) E(\omega) = 0,$$

but one realizes that now the refractive index $n = n(E) \propto E^2$ is a function of the electric field strength,

$$n^2 = n_0^2 + \frac{3}{4}\chi^{(3)}\,|E(\omega)|^2$$
$$= \underbrace{1+\chi^{\mathrm{L}}}_{=n_0^2} + \chi^{\mathrm{NL}},$$

with the non-linear susceptibility

$$\chi^{\mathrm{NL}} = \frac{3}{4}\chi^{(3)}\,|E(\omega)|^2\,. \tag{8.53}$$

As the non-linear susceptibility $\chi^{(3)} \ll n_0^2$ is much smaller than the linear one, $\chi^{\mathrm{L}} = n_0^2 - 1 \gg \chi^{(3)}$, we can approximate the refractive index by

$$n(E) = n_0\sqrt{1+\frac{\chi^{\mathrm{NL}}}{n_0^2}} \approx n_0\left(1+\frac{1}{2}\frac{\chi^{\mathrm{NL}}}{n_0^2}\right) = n_0 + \frac{1}{2}\frac{\chi^{\mathrm{NL}}}{n_0}.$$

Using the definition of the intensity of electromagnetic radiation, (7.27) to substitute the electric field strength in (8.53), we see that now the non-linear susceptibility χ^{NL} gets to

$$\chi^{\mathrm{NL}} = \frac{3}{2}\frac{\chi^{(3)}n_0}{\varepsilon_0 c_0}I.$$

Now one can rewrite the refractive index being dependent on the intensity

$$n(I) = n_0 + \frac{3}{4}\frac{\chi^{(3)}}{\varepsilon_0 c_0}I.$$

Kerr effect

The dependence of the refractive index of a dielectric medium on the intensity of the radiation is called **Kerr effect**.

$$n(I) = n_0 + n_2 I \tag{8.54}$$

with the **Kerr coefficient**

$$n_2 = \frac{3}{4}\frac{\chi^{(3)}}{\varepsilon_0 c_0}. \tag{8.55}$$

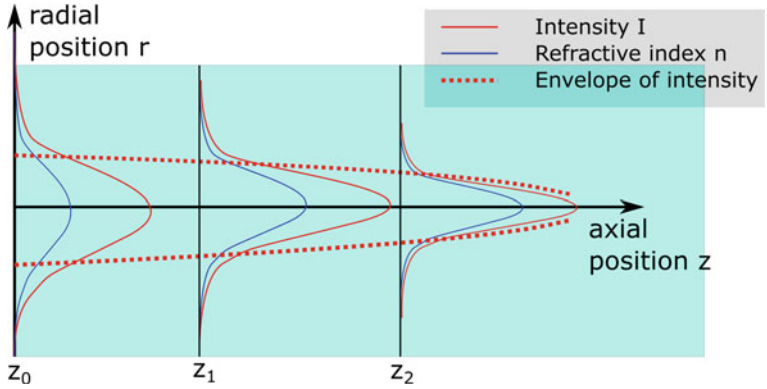

Fig. 8.10 Intensity distribution of the incoming radiation and resulting distribution of the refractive index and beam waist change within a medium due to self-focusing

8.4.5 Self-focusing

The Kerr effect is often applied in laser physics allowing to control the refractive index by tuning the intensity of the radiation. One prominent example is the **Kerr-Lens mode-locking** (KLM) of ultra-fast laser oscillators. As often laser radiation within resonators features a spatial Gaussian intensity profile, at adequate intensities a local change in the refractive index generated by femtosecond laser pulses is induced, the so-called **self-focusing**. Within a crystal, the change of intensity of the radiation induces a proportional change of the refractive index inducing a temporally limited, so-called transient **gradient-index lens** (GRIN); see Fig. 8.10. So, the laser pulse tunes the optical properties of a resonator inducing itself an optical element and changing the properties of the resonator when ultra-fast pulses are present. Doing so and setting up a laser resonator being optically stable with a transient Kerr lens will favor an ultra-fast pulsed mode instead of a cw-mode.

To describe quantitatively the propagation of the radiation by self-focusing, we have to solve the principal equation of linear optics (8.1) getting in our case

$$\Delta E - \frac{n^2(I)}{c_0^2}\frac{\partial^2 E}{\partial t^2} = 0, \tag{8.56}$$

with the intensity-dependent refractive index due to the Kerr effect

$$n^2(I) = (n_0 + n_2 I)^2 \approx n_0^2 + 2n_0 n_2 I$$

with $n_2 \ll n_0$. As the propagation of the radiation within a homogeneous and isotropic material is straight, a cylindrical symmetry can be assumed emphasizing to apply the Laplace operator in cylindrical coordinates

$$\Delta = \underbrace{\Delta_\perp}_{\text{tangential part}} + \underbrace{2ik_\omega \frac{\partial}{\partial z} + \frac{\partial^2}{\partial z^2}}_{\text{longitudinal part}}.$$

Assuming a temporal constant irradiation $\partial I/\partial t = 0$ and using a plane wave

$$E(z,t) = \frac{1}{2}\left(E_0 e^{i(k_\omega z - \omega t)} + c.c.\right)$$

the differential equations (8.56) gets, holding in mind that $k_\omega = n_0\omega/c_0$, to

$$\underbrace{\Delta_\perp E_0 + 2ik_\omega \frac{\partial E_0}{\partial z} - k_\omega^2 E_0 + \frac{\partial^2 E_0}{\partial z^2}}_{\text{tangential part}} + \underbrace{k_\omega^2 E_0 + 2k_\omega^2 \frac{n_2}{n_0} I E_0}_{\text{longitudinal part}} = 0.$$

Thus, applying the SVEA, see Sect. 8.3.3 and (8.21), now the differential equation gets to

$$\Delta_\perp E_0 + 2ik_\omega \frac{\partial E_0}{\partial z} + 2k_\omega^2 \frac{n_2}{n_0} I E_0 = 0.$$

The first term of this equation describes the diffraction due to the spatial limitation of the laser radiation, being proportional to the inverse area of the radiation $A \propto r_0^2$, r_0 representing a characteristic beam radius,

$$\Delta_\perp E_0 \approx \frac{1}{r_0^2} E_0.$$

The second term is much smaller than the first one and can here be omitted. The third term describes the **self-focusing**.

So, the first term acts against the third one getting an equilibrium for both at

$$\frac{1}{r_0^2} \approx 2k_\omega^2 \frac{n_2}{n_0} I.$$

Using the definition of the **average power**

$$P = \pi r_0^2 I,$$

we can define a critical power for self-focusing for this equilibrium, given by

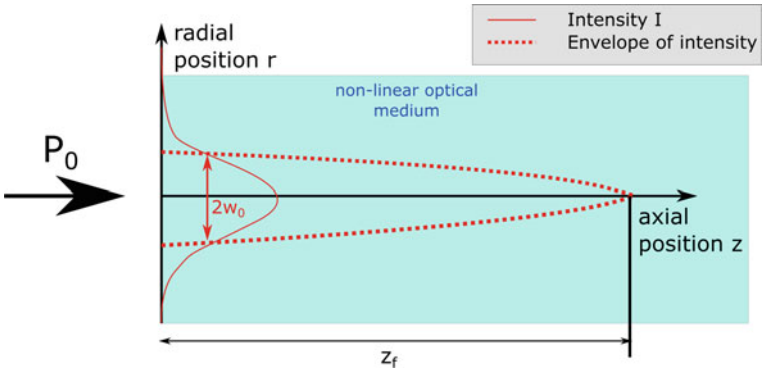

Fig. 8.11 Schematics of catastrophic self-focusing with initial beam radius at the boundary of the radiation entering the dielectrics and the position of the infinitesimal focal point

Critical power for self-focusing

$$P_{\text{crit}} = \frac{\pi n_0}{2k_\omega^2 n_0}, \text{ and using } k_\omega = \frac{2\pi}{\lambda}$$
$$= \frac{n_0 \lambda^2}{8\pi n_2}. \tag{8.57}$$

8.4.6 Catastrophic Self-focusing

The laser radiation sustains at a constant radius if the power of the radiation equals the critical power for self-focusing P_{crit}. As the power gets larger the radiation is focused, and from a geometric-optical point of view, the radiation is focused to an infinitesimal point; see Fig. 8.11. As derived in [5], the distance to this hypothetical focus point z_f is given, using as focus radius the common writing in laser technology w_0, by

$$z_{\text{csf}} = \frac{n_0 \pi w_0^2}{\lambda} \left(\frac{P_0}{P_{\text{crit}}} - 1 \right)^{-1/2}.$$

8.4.7 Self-phase Modulation

Due to the Kerr effect, the refractive index is changed, and as described in the sections before, a spatially distributed intensity results in a **spatially modulated refractive index**. Typically, ultra-fast laser radiation is not only spatially but also temporally modulated, i.e. $I = I(r, t)$, so it is straightforward to assume also a temporal modulation of the refractive index $n(I(t))$.

Starting again from a plane electromagnetic wave

$$E_{\text{in}}(z_0, t) = E_0(t)e^{i(\omega t - knz_0)}$$

entering a non-linear medium at $z = z_0$, we assume that for $z < z_0$ the refractive index is unity $n = 1$. For $z > z_0$, it follows the Kerr effect by equation (8.54) getting now an electric field strength in the non-linear medium at a deliberate position z by

$$E(z, t) = E_0(t)e^{i(\omega t - kn_0 z - kn_2 Iz)} = E_0(t)e^{i\Phi},$$

with the **time-dependent phase**

$$\Phi(t) = \omega t - kn_0 z - kn_2 I(t)z,$$

being modulated by the intensity, too.

The **effective angular frequency** ω_{eff} results now as

$$\begin{aligned}\omega_{\text{eff}} &= \frac{\mathrm{d}\Phi}{\mathrm{d}t} \\ &= \omega - kz\frac{\mathrm{d}n(t)}{\mathrm{d}t} \\ &= \omega - kzn_2\frac{\mathrm{d}I(t)}{\mathrm{d}t} \\ &= \omega_{\text{eff}}(t).\end{aligned}$$

This result depicts the temporal change in the frequency as well as the red- and blue-shifted additional spectral intensity components; see Fig. 8.12. As a consequence, the spectrum of the incoming laser radiation is broadened generating a **white-light continuum or super-continuum**. The spectrum of ultra-fast laser radiation with a pulse duration $t_{\text{p}} = 100$ fs, wavelength $\lambda = 780$ nm, and spectral width of about 20 nm, is broadened by focusing it into water generating a white-light continuum with a spectral bandwidth over 300 nm; see Fig. 8.13.

As the spectral intensity distribution is strongly connected to the temporal one by a Fourier transformation, also the temporal distribution changes due to self-phase modulation. In conclusion, we have to state that due to spatial as well as temporal

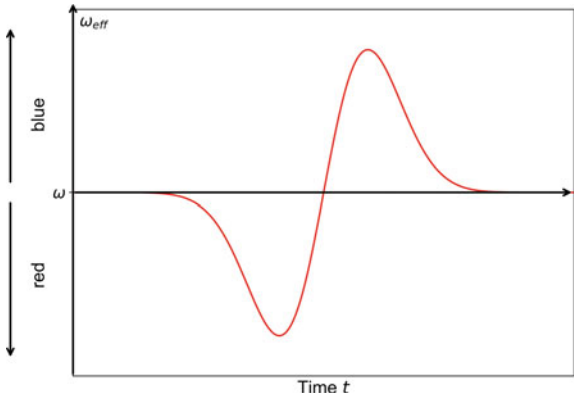

Fig. 8.12 A temporally bell-like shaped intensity distribution of ultra-fast laser radiation, like a Gaussian distribution, results in a red- and blue-shifted frequency

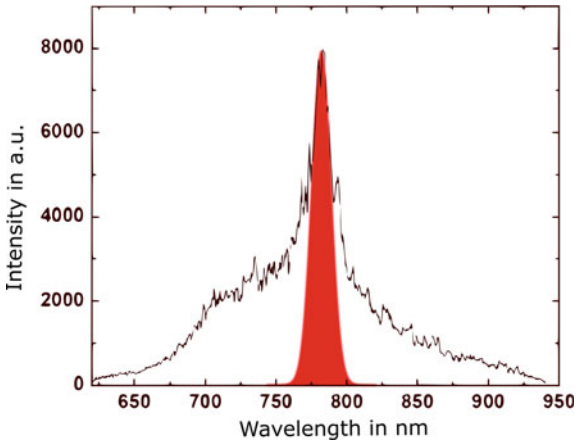

Fig. 8.13 White-light continuum generated by self-phase modulation in water using focused ultra-fast laser radiation in red (pulse duration $t_p = 100$ fs, wavelength $\lambda = 780$ Nm, and spectral width $\Delta\lambda$ of about 20 nm, modified from [6])

modulation, a refractive index change is induced, the first resulting in self-focusing and the second one in self-phase modulation. As usually, ultra-fast laser radiation exhibits both properties, and both effects appear.

References

1. R. Boyd, *Nonlinear Optics*, 4th edn. (Academic Press, Elsevier 2020)
2. R. Sauerbrey, *Nichtlineare Optik*. Lecture Notes at the TU Dresden (2007)
3. A.E. Siegman, *Lasers*, University Science Books, U.S. (17. Oktober 1990)
4. A.G. Ciriolo, M. Negro, M. Devetta, E. Cinquanta, D. Faccialá, A. Pusala, S. De Silvestri, S. Stagira, C. Vozzi, Optical parametric amplification techniques for the generation of high-energy few-optical-cycles IR pulses for strong field applications. Appl. Sci. **7**, 265 (2017). https://doi.org/10.3390/app7030265
5. Y.R. Shen, *Principles of Nonlinear Optics* (Wiley, 2002). ISBN: 978-0-471-43080-3

6. B. Anand, N. Roy, S. Siva Sankara Sai, R. Philip, Spectral dispersion of ultrafast optical limiting in Coumarin-120 by white-light continuum Z-scan. Appl. Phys. Lett. **102**, 203302 (2013)
7. E. Hecht, *Optics*, 5th edn., Global edition (Pearson, Boston, Columbus, Indianapolis, 2017)

Part IV
Interaction with Absorption

In this major part, we discuss the interaction of electromagnetic radiation with condensed matter. As Lambert–Beer's law has been firstly introduced in the last chapter, now we generalize this aspect in Sect. 10.1. From optics lectures [9], we know that the optical property of matter and also of condensed matter is mainly described by its refractive index.

As a first model describing absorption in condensed matter, the electron gas as typical model is used and described in Chap. 9. Going further, metals and semiconductors are distinguished. As matter is heated, also the temperature dependencies are investigated. Finally, in this chapter, the optical properties of an electron gas are compared to those of metals.

Getting closer to reality, the electron gas model has to be expanded by a band theory in Chap. 11. A dispersion relation for the electrons in the bands of crystals qualitatively is derived. Amorphous condensed matter does not feature dispersion relation, but still has a band structure, featuring additionally localized states.

The next Chap. 12 introduces the linear absorption of electromagnetic radiation in solid matter. Thereby, intra- and inter-band excitation in dielectrics is discussed, also using the reduced band structure. Inverse bremsstrahlung represents the predominant linear process for absorption in metals. Finally, in this chapter, we describe the optical properties of metals using the Drude–Lorentz model and plotting the complex refractive index, and also of excited matter transient optical properties are shown.

Non-linear absorption in dielectrics is discussed in Chap. 13. The electron rate equation is set up including the photo-excitation by tunnel or multiphoton excitation. After the primary excitation process, the following process of impact ionization increases the number of free electrons exponentially, allowing an avalanche ionization. As free charges are given, the radiation is deflected by it. In combination with the non-linear process, the Kerr effect, the radiation can propagate without changing strongly its diameter by channeling. We discuss thereby also the related process, the so-called filamentation formed in condensed matter.

As a consequence of the absorption of radiation by the electrons in the solid, now the collective system consisting of the quasi-free electrons within the interaction-volume is treated thermo-dynamically by setting up two heat equations; see Chap. 14. One for the electron system and the other for the phonon system. The thermo-physical parameters, i.e. the heat capacities and conductivities of both sys-

tems, and as well as the coupling parameter between both systems are derived. In consequence, the heat equations are solved numerically and examples are given for different metals.

The last Chap. 15 treats the laser-induced phase transitions. There we will talk about phase diagrams and talk about slow heating given by a quasibalance of the systems versus fast heating induced by laser radiation. Solutions of the Euler equations are given for metals in one and two spatial dimensions.

Chapter 9
Electron Gas in Condensed Matter

Abstract Electrons are given in condensed matter in different states. Depending on the matter, i.e. insulator, semiconductor, or metal, the electrons are bounded to atoms or molecules or are free. The electronic properties of many free electrons given as an electron gas are described quantum mechanically.

9.1 Periodic Potentials

Electrons are given in crystals as bounded to atoms, being free or quasi-free, and moving within the condensed matter crystal matrix. As a good representative in case of free electrons given in metals, one can speak of a spatial localized **free electron gas**. In case of bounded electrons, one has to determine the energetic states of them, and assuming a periodic crystal structure of the atoms within solid state matter, energy bands have to be introduced.

As shown in Fig. 9.1, the periodic potential of atoms in solid matter can, in first approximation, be described by a three-dimensional potential valley with the dimension of the solid. With this assumption, we describe a free electron gas in a solid. For solids where the position of the atoms is periodic, one speaks of **crystals**.

Shortly, here we want to explain the main absorption process in metals given by solids with quasi-free electrons delivered from atoms representing a crystalline state of the matter. The quasi-free electrons are called "quasi-free", because being present in the solid at large densities in the range of $n_e = 10^{21}\,\mathrm{cm}^{-1}$ they absorb the optical energy as free electrons do, but doing scattering with adjacent electrons. The energy is then deposited in the "pool" of electrons increasing its kinetic energy. As a whole, the electrons represent a thermodynamic system, and by absorption of energy its temperature increases, see Sect. 14.4 for more details.

© Springer Nature Switzerland AG 2022

A. Horn, *The Physics of Laser Radiation–Matter Interaction*,
https://doi.org/10.1007/978-3-031-15862-9_9

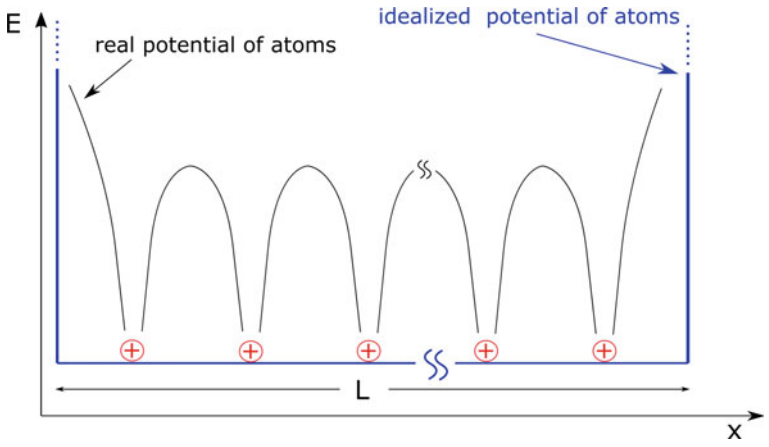

Fig. 9.1 Electrons located within a crystal represented by a periodic potential of the positive charged atoms (black) and approximation by one-dimensional potential well (blue)

9.2 Electronic Properties at Zero Temperature

Electrons are typical representatives for fermions. This implies that each entity of the fermion family is indistinguishable. This finally results in the Pauli-Principle (see Sect. 9.3), accounting that **each entity represents one specific and unique state**.

9.2.1 Quantized Wave Number and Energy

In order to describe a system consisting of many electrons in a solid as fermions, we have to describe them quantum mechanically. Starting with the simplest system, we look at one electron within an infinite-high one-dimensional potential well, see Fig. 9.2. The wave function of an electron having the mass m_e and the energy ϵ is given by solving the **stationary Schrödinger equation**

$$H\psi(x) = \epsilon\psi(x), \tag{9.1}$$

with the Hamiltonian $H = -\frac{\hbar^2}{2m}\frac{\partial^2}{\partial x^2}$. As known, we get this Hamiltonian by transferring the classical kinetic energy of the electron $H_{\text{class}} = p^2/2m$ to the given Hamiltonian introducing the impulse operator

$$p_x = -i\hbar\frac{\partial}{\partial x} = \hbar k_x.$$

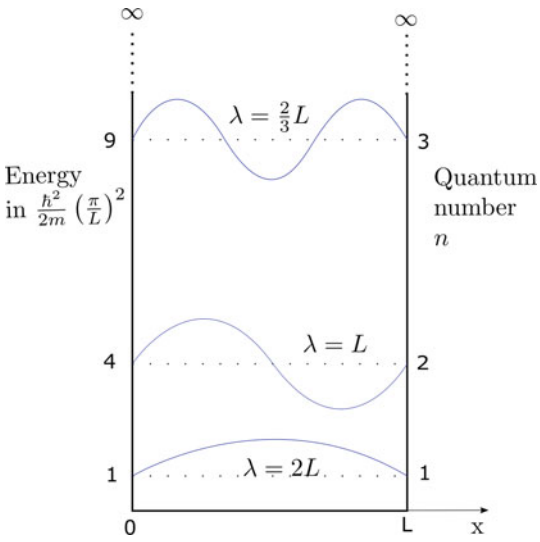

Fig. 9.2 Electron located within a one-dimensional potential well

The equation for the Hamiltonian is solved for the boundary conditions at the borders of the potential well, where the wave functions $\psi(0) = \psi(L) = 0$ are vanishing, using the harmonic function

$$\psi_n(x) = A\ \sin(k\,x) + B\ \cos(k\,x) = A\ \sin\left(\frac{2\pi}{\lambda_n}x\right) + B\ \cos\left(\frac{2\pi}{\lambda_n}x\right),$$

and fulfilling the boundary conditions. With the first boundary condition for $x = 0$ with $\psi(0) = 0$, we see that the factor B has to vanish $B = 0$, getting the wave function for the electron with the relation

$$\psi_n(x) = A\ \sin\left(\frac{2\pi}{\lambda_n}x\right).$$

Setting at the second boundary $x = L$ the boundary condition for the wave function $\psi_n(L) = 0$ results in the condition

$$\pi n = \frac{2\pi}{\lambda_n}L,$$

defining the **quantum number** $n \in \mathbb{N}_0$ and resulting in **discrete wavelengths**

$$\lambda_n = \frac{2L}{n},$$

as well **discrete wave number and discrete momentum**

$$k_{x,n} = \frac{\pi}{L} n \quad \text{and} \quad p_{x,n} = \frac{\hbar\pi}{L} n = \frac{hn}{2L}. \tag{9.2}$$

Finally, an electron in a potential well is described by the wave function

$$\psi_n(x) = A \sin\left(\frac{n\pi}{L} x\right).$$

Using the wave equation including the boundary conditions, we calculate now the derivatives to compare them with the stationary Schrödinger of (9.1)

$$\frac{\mathrm{d}\psi_n(x)}{\mathrm{d}x} = A \left(\frac{n\pi}{L}\right) \cos\left(\frac{n\pi}{L} x\right) \tag{9.3}$$

$$\frac{\mathrm{d}^2\psi_n(x)}{\mathrm{d}x^2} = -A \left(\frac{n\pi}{L}\right)^2 \sin\left(\frac{n\pi}{L} x\right) \tag{9.4}$$

getting the **quantized energy states** of the electron, representing a parabolic dependence scaling with $\epsilon_n \propto n^2$, see Fig. 9.3

Energy of a free electron in a one-dimensional potential well

$$\epsilon_n = \frac{\hbar^2}{2m_\mathrm{e}} \left(\frac{n\pi}{L}\right)^2 = \frac{\hbar^2 k_{x,n}^2}{2m_\mathrm{e}} \equiv \frac{p_{x,n}^2}{2m_\mathrm{e}}. \tag{9.5}$$

This dependence of the energy of the electron on the wave number is also called electron dispersion relation

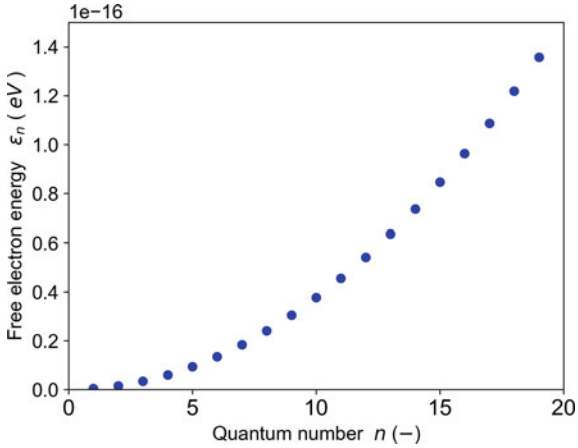

Fig. 9.3 Quantized energy of a free electron located within a one-dimensional potential well as function of the quantum number n within a crystal of length $L = 1$ m

Dispersion relation of a free electron

$$\epsilon(k) = \frac{\hbar^2}{2m_\mathrm{e}} k^2. \tag{9.6}$$

Up to now, individuality is only described by the energy of the electrons. Here, we include additionally one intrinsic property of electrons, its spin m_x being up or down. This can also be attributed to two polarization states of the electron.

Assuming now, for example, six electrons being placed within an infinite-high one-dimensional potential well, these electrons will be distributed by the number of electrons $\#_\mathrm{e}$ due to its energy and its spin within the potential well. The electron system features now two quantum numbers n and m. As the system is assumed to have no temperature, being at the absolute zero $T = 0$ K, no additional thermal energy is given to the electrons. The maximum energy of the electron system given here is called the Fermi energy

Fermi energy of a free electron gas

$$\epsilon_\mathrm{F} = \frac{\hbar^2}{2m_\mathrm{e}} \left(\frac{n_\mathrm{F}\pi}{L} \right)^2, \tag{9.7}$$

with the last electron occupying the largest quantum number, the so-called the Fermi number n_F. For $n_\mathrm{F} = 3$, we get six occupied states, see table below.

n	$\mathbf{m_x}$	$\#_\mathrm{e}$	**n**	$\mathbf{m_x}$	$\#_\mathrm{e}$
1	↑	1	3	↑	1
1	↓	1	3	↓	1
2	↑	1	4	↑	0
2	↓	1	4	↓	0

We see that each energy level is occupied by two electron states. Electrons, being fermions, feature a degenerated energy level with a degeneration $s = 2$. The largest quantum state is described by the **Fermi quantum number** n_F and one sees that the relation

$$2n_\mathrm{F} = N \quad \text{or} \quad n_\mathrm{F} = \frac{N}{2}$$

holds, with N being the overall number of electrons. The highest possible energy level, the **Fermi energy** given by (9.7) gets now to

$$\epsilon_\mathrm{F} = \frac{\hbar^2}{2m_\mathrm{e}} \left(\frac{N\pi}{2L} \right)^2.$$

Extending now the mobility of an electron into a **three-dimensional solid**, and allowing the electron to move therein freely, we have to apply our calculations on a **stationary three-dimensional Schrödinger equation**

$$H\psi_k = \epsilon_k \psi_k = -\frac{\hbar^2}{2m_e}\left(\frac{\partial^2}{\partial x^2} + \frac{\partial^2}{\partial y^2} + \frac{\partial^2}{\partial z^2}\right)\psi_k = -\frac{\hbar^2}{2m_e}\Delta\psi_k.$$

For an electron within a volume given by $V = L \times L \times L$, we get a solution of the Schrödinger equation applying the function

$$\begin{aligned}\psi_k(\boldsymbol{r}) = \psi_k(x, y, z) = A\sin(k_x \cdot x)\sin(k_y \cdot y)\sin(k_z \cdot z) + \\ + B\cos(k_x \cdot x)\cos(k_y \cdot y)\cos(k_z \cdot z).\end{aligned}$$

As in the one-dimensional case, we apply the first boundary condition with the wave function ψ_k vanishing at the borders. Finally, we get the wave function of the electron

$$\psi_k(\boldsymbol{r}) = A\sin\left(\frac{2\pi}{\lambda_x} \cdot x\right)\sin\left(\frac{2\pi}{\lambda_y} \cdot y\right)\sin\left(\frac{2\pi}{\lambda_z} \cdot z\right).$$

One makes a generalization by transferring this solution into the complex space, describing the wave function by a plane wave function

$$\psi_k(\boldsymbol{r}) = Ae^{i\boldsymbol{k}\cdot\boldsymbol{r}},$$

with the wave number vector $\boldsymbol{k} = (k_x, k_y, k_z)$ and the position vector $\boldsymbol{r} = (x, y, z)$. The second boundary condition results in $\psi_k(x + L, y, z) = \psi_k(x, y, z)$ getting the boundary wave functions

$$\begin{aligned}\psi_k(x + L, y, z) &= Ae^{ik_x(x+L)}e^{i(k_y y + k_z z)} \\ &= Ae^{ik_x x}e^{i(k_y y + k_z z)}e^{ik_x L} \\ &= \psi_k(x, y, z)e^{ik_x L},\end{aligned}$$

being solved, e.g. for $e^{ik_x L} = 1$ by $k_x L = 2\pi n_x$ and $n_x \in \mathbb{N}_0$. Resolving the relation for all coordinates, one gets the **discrete, quantized wave numbers components**

$$k_i = \frac{2\pi}{L}n_i, \tag{9.8}$$

for $i = x, y, z$, or written as a vector, the wave number is written as

Quantized wave number for an electron in a solid

$$\boldsymbol{k} = \frac{2\pi}{L}\begin{pmatrix} n_x \\ n_y \\ n_z \end{pmatrix} = \frac{2\pi}{L}\boldsymbol{n}, \tag{9.9}$$

using the **quantum number vector** $\boldsymbol{n} = (n_x, n_y, n_z)$.

The stationary Schrödinger equation is again compared to the multiple derivatives given by the Laplace operator, and one gets

$$
\begin{aligned}
H\psi_k = \epsilon_k \psi_k &= -\frac{\hbar^2}{2m_\mathrm{e}} \Delta \psi_k \\
&= \frac{\hbar^2}{2m_\mathrm{e}} (k_x^2 + k_y^2 + k_z^2) \psi_k \\
&= \frac{\hbar^2 k^2}{2m_\mathrm{e}} \psi_k ,
\end{aligned}
$$

with the value of the wave number $k = \sqrt{k_x^2 + k_y^2 + k_z^2} = \frac{2\pi}{\lambda}$. We see that the quantized energy of the electrons within a three-dimensional volume is again written by

$$
\epsilon_k = \frac{\hbar^2 k^2}{2m_\mathrm{e}} ,
$$

an in the one-dimensional case, see (9.6). The momentum of the electrons is given by

$$
\boldsymbol{p} = -i\hbar\nabla ,
$$

and one sees using (9.2.1)

$$
\boldsymbol{p}\psi_k = -i\hbar\nabla\psi_k = \hbar\boldsymbol{k}\psi_k
$$

resulting finally in

Quantized momentum and velocity of an electron

Quantized momentum:

$$
\boldsymbol{p} = \hbar\boldsymbol{k} \tag{9.10}
$$

Quantized velocity:

$$
\boldsymbol{v} = \frac{\hbar}{m_\mathrm{e}} \boldsymbol{k} . \tag{9.11}
$$

9.2.2 Density of States

Comparable to a two-dimensional case, where each wave number vector, or momentum, accounts one point with the area $\Delta k_x \cdot \Delta k_y = (2\pi/L)^2$ within a circular area of the **phase space**, see Fig. 9.4, in the three-dimensional case, one accounts that each wave number vector $\boldsymbol{k}$ points on one volume element

$$
\Delta V_{\boldsymbol{k}} = \left(\frac{2\pi}{L} \right)^3
$$

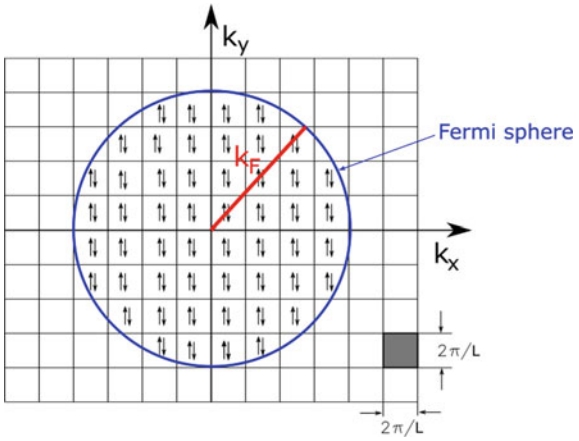

Fig. 9.4 Distribution of the states of an electron located in a 2D-potential well in the Fermi circle of radius k_F of a phase space plot

in the three-dimensional k-space, the so-called **Fermi sphere**.

As the quantum number vector $\boldsymbol{n}$ represents discrete numbers, also all physical relevant parameters get discrete. One can define for an interval $\Delta\boldsymbol{k}$ at $\boldsymbol{k}$ the number of states $\Delta\boldsymbol{n}$ given there, calculating

$$\Delta\boldsymbol{k} = \begin{pmatrix} \Delta k_x \\ \Delta k_y \\ \Delta k_z \end{pmatrix} = \frac{2\pi}{L} \begin{pmatrix} \Delta n_x \\ \Delta n_y \\ \Delta n_z \end{pmatrix} = \frac{2\pi}{L} \Delta\boldsymbol{n}.$$

The **number of states within the volume** $dV_{\boldsymbol{k}}$ for the electrons results in the product of the number of states per coordinate, Δk_x, Δk_y, and Δk_z, getting

$$\begin{aligned} \mathrm{d}N_k = \Delta n_x \Delta n_y \Delta n_z &= s \cdot \frac{L^3}{(2\pi)^3} \Delta k_x \Delta k_y \Delta k_z \\ &= 2 \frac{V}{(2\pi)^3} \Delta k_x \Delta k_y \Delta k_z \end{aligned}$$

$$\curvearrowright \quad \mathrm{d}N_k = 2 \frac{V}{(2\pi)^3} dV_{\boldsymbol{k}},$$

holding in mind that each state can be occupied by two electron spin states, so the degeneracy gets to $s = 2$.

The density of states of the electrons related to the wave number, i.e. the number of states per volume in the k-space, is written as

Density and number of states related to the wave number

$$D_{\boldsymbol{k}} = \frac{\mathrm{d}N_{\boldsymbol{k}}}{\mathrm{d}V_{\boldsymbol{k}}} = \frac{2V}{(2\pi)^3} \tag{9.12}$$

Number of states within an interval $\mathrm{d}V_{\boldsymbol{k}}$

$$\mathrm{d}N_{\boldsymbol{k}} = D_{\boldsymbol{k}}\mathrm{d}V_{\boldsymbol{k}}. \tag{9.13}$$

As the energy of the electron scales by the squared value of the wave number k^2, see (9.2.1), no angular dependence is given, and the transformation of the Cartesian volume element $dV_{\boldsymbol{k}}$ into spherical coordinates is adequate using $\mathrm{d}V_k = \mathrm{d}k_x\mathrm{d}k_y\mathrm{d}k_z = k^2\mathrm{d}k\sin\theta d\theta d\phi$

$$\mathrm{d}N_k = D_{\boldsymbol{k}}k^2\mathrm{d}k\sin\theta\mathrm{d}\theta\mathrm{d}\phi.$$

As of now, only the value of the wave number is used, no dependencies on the angels are given allowing to integrate over all angles θ and π

$$\int_{\theta=0}^{\pi}\int_{\phi=0}^{2\pi}\sin\theta\mathrm{d}\theta\mathrm{d}\phi = 4\pi.$$

Now, one writes the density of states related to the value of the wave number, i.e. the number of states per volume in the k-space by

Density and number of states related to the value of wave number

$$D_k = \frac{\mathrm{d}N_k}{\mathrm{d}k} = \frac{8\pi V}{(2\pi)^3}k^2 \tag{9.14}$$

Number of states within an interval $\mathrm{d}k$

$$\mathrm{d}N_k = D_k\mathrm{d}k. \tag{9.15}$$

We have seen that the physical relevant value for the energy of a system depends on the squared wave number, e.g. the squared radius of the Fermi sphere. The volume of the Fermi sphere is given by

$$V_k = \frac{4\pi}{3}k_{\mathrm{F}}^3.$$

with the radius

$$k_{\mathrm{F}} = |\boldsymbol{k}_{\mathrm{F}}| = \sqrt{k_{x,F}^2 + k_{y,F}^2 + k_{z,F}^2}.$$

given by all wave numbers of all states within the volume up to the highest occupied state n_{F}. The highest occupied state features the Fermi energy ϵ_{F} and the Fermi wave number $\boldsymbol{k}_{\mathrm{F}}$.

One can now calculate the overall number of states within this sphere for deliberate wave number $\boldsymbol{k}$. It is appropriate there to use again spherical coordinates writing the volume element $\mathrm{d}V_{\boldsymbol{k}} = \mathrm{d}k_x \mathrm{d}k_y \mathrm{d}k_z = k^2 \mathrm{d}k \sin\theta \mathrm{d}\theta \mathrm{d}\phi$, getting the **overall number of states** by integration using the number of states within a volume element, (9.13)

$$\begin{aligned} N &= \int \mathrm{d}N = \int_{V_{\boldsymbol{k}}} D_{\boldsymbol{k}} \mathrm{d}V_{\boldsymbol{k}} = \int_{\theta=0}^{\pi} \int_{\phi=0}^{2\pi} \int_{k=0}^{k_\mathrm{F}} D_{\boldsymbol{k}} k^2 \mathrm{d}k \sin\theta \mathrm{d}\theta \mathrm{d}\phi \\ &= \underbrace{\int_{\theta=0}^{\pi} \sin\theta \mathrm{d}\theta \int_{\phi=0}^{2\pi} \mathrm{d}\phi}_{4\pi} \int_{k=0}^{k_\mathrm{F}} D_{\boldsymbol{k}} k^2 \mathrm{d}k = \int_0^{k_\mathrm{F}} 2 \frac{4\pi V}{(2\pi)^3} k^2 \mathrm{d}k = 2 \frac{4\pi V}{3(2\pi)^3} k_\mathrm{F}^3 \\ &= \frac{V}{3\pi^2} k_\mathrm{F}^3. \end{aligned} \tag{9.16}$$

As the value of the wave number k depends not on the angles θ and ϕ, the integration over the angles results again in 4π.[1]

So, we get the Fermi wave number from (9.16)

Fermi wave number

$$k_\mathrm{F} = \left(\frac{3\pi^2 N}{V} \right)^{\frac{1}{3}}. \tag{9.17}$$

The Fermi velocity is given by the value of the Fermi momentum

$$p_\mathrm{F} = \hbar k_\mathrm{F} = m_\mathrm{e} v_\mathrm{F}$$

and results in

Fermi velocity

$$v_\mathrm{F} = \frac{\hbar k_\mathrm{F}}{m_\mathrm{e}} = \frac{\hbar}{m_\mathrm{e}} \left(\frac{3\pi^2 N}{V} \right)^{\frac{1}{3}}. \tag{9.18}$$

The occupied states of the electrons are described in the k-space by discrete points within the Fermi sphere. The electrons with the maximum energy feature the Fermi energy ϵ_F and are located on the shell of this sphere. The Fermi energy as a function of the overall number of states is written as

[1] Alternatively, one gets the number of states in the Fermi sphere by dividing the overall volume of the wave numbers by the volume of each state multiplied by its spin s, here $s = 2$ and holding in mind that $V = L^3$

$$N = s \frac{V_k}{\Delta V_k} = 2 \frac{\frac{4\pi}{3} k_\mathrm{F}^3}{\left(\frac{2\pi}{L}\right)^3} = \frac{V}{3\pi^2} k_\mathrm{F}^3.$$

$$\epsilon_\mathrm{F} = \frac{\hbar^2}{2m_\mathrm{e}} k_\mathrm{F}^2 = \frac{\hbar^2}{2m_\mathrm{e}} \left(\frac{3\pi^2 N}{V}\right)^{\frac{2}{3}}.$$

Using the **electron density**

$$n = \frac{N}{V}$$

we get for the Fermi energy as function of the electron density

Fermi energy of an electron gas

$$\epsilon_\mathrm{F} = \frac{\hbar^2}{2m_\mathrm{e}} \left(3\pi^2 n\right)^{2/3}. \tag{9.19}$$

In general, now one can write the energy of the electrons within the Fermi sphere with a variable electron number N or density n by

$$\epsilon(N) = \frac{\hbar^2}{2m_\mathrm{e}} \left(\frac{3\pi^2 N(\epsilon)}{V}\right)^{2/3} = \frac{\hbar^2}{2m_\mathrm{e}} \left(3\pi^2 n(\epsilon)\right)^{2/3} \tag{9.20}$$

The **overall energy of the electron gas as function of the Fermi wave number** is calculated by integration up to the Fermi energy

$$\begin{aligned} E &= \int_0^{\epsilon_\mathrm{F}} \epsilon(N)\mathrm{d}N = \int_{V_k} \epsilon(N) D_{\boldsymbol{k}} \mathrm{d}V_{\boldsymbol{k}} \\ &= \int_{\theta=0}^{\pi} \int_{\phi=0}^{2\pi} \int_{k=0}^{k_\mathrm{F}} \frac{\hbar^2 k^2}{2m_\mathrm{e}} \frac{2V}{(2\pi)^3} k^2 \mathrm{d}k \sin\theta \mathrm{d}\theta \mathrm{d}\phi \\ &= \frac{\hbar^2 V}{10 m_\mathrm{e} \pi^2} k_\mathrm{F}^5. \end{aligned}$$

Using (9.17), we get for the **overall energy as function of the electron density**

Overall energy of an electron gas

$$E = \frac{3(3\pi^2)^{2/3}\hbar^2 V}{10 m_\mathrm{e}} n^{5/3}. \tag{9.21}$$

9.2.3 Fermi–Dirac Distribution at $T = 0$ K

Within an localized electron gas at the absolute zero temperature all states of the electrons are occupied until the highest energy, the Fermi energy. All states have the same probability to be occupied, being equal to one. We introduce here the probability

function for a fermion to occupy a state, the so-called **Fermi–Dirac distribution** f_{FD}. Apparently, at the absolute zero temperature, this distribution represents a step function with a value equal to one for all energies below as well equal to the Fermi energy, and being zero for larger energies

Fermi–Dirac distribution f_{FD}

$$f_{\mathrm{FD}}(\epsilon) = \Theta(\epsilon_{\mathrm{F}} - \epsilon) = \begin{cases} 1, & \text{for } \epsilon \leq \epsilon_{\mathrm{F}} \\ 0. & \text{for } \epsilon > \epsilon_{\mathrm{F}} \end{cases}, \tag{9.22}$$

hereby the function Θ represents the Heavyside step function, see Fig. 9.5.

Knowing the number of electrons per energy interval allows to define the density of states as function of the energy.

Density of states related to the energy

The density of states $D(\epsilon)$ with respect to the energy, given by the derivative of the number of states

$$D_\epsilon(\epsilon) = \frac{\mathrm{d}N}{\mathrm{d}\epsilon}, \tag{9.23}$$

describes the number of occupied states by the electrons per energy interval $\mathrm{d}\epsilon$.

We rewrite the **number of states** from (9.20) getting

$$N_\epsilon(\epsilon) = \frac{V}{3\pi^2}\left(\frac{2m_{\mathrm{e}}\epsilon}{\hbar^2}\right)^{\frac{3}{2}}, \tag{9.24}$$

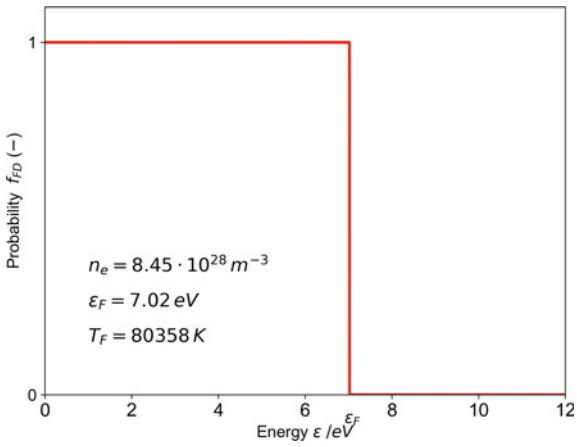

Fig. 9.5 Fermi–Dirac distribution at the absolute zero temperature for a metal, here copper with a free electron density of $n_{\mathrm{e}} = 8.45 \cdot 10^{28}\,\mathrm{m}^{-3}$

and taking the derivative, we can write the density of states[2]:

Density of states related to the energy of a free electron gas

$$D_\epsilon(\epsilon) = \frac{\sqrt{2}Vm_e^{3/2}}{\pi^2\hbar^3}\sqrt{\epsilon}. \tag{9.25}$$

Also, one can rewrite the number of states, (9.24) by taking the logarithm

$$\begin{aligned} \ln N(\epsilon) &= \frac{3}{2}\ln\epsilon + \text{const.} \\ \frac{\mathrm{d}(\ln N(\epsilon))}{\mathrm{d}\epsilon} &= \frac{\mathrm{d}(\ln N(\epsilon))}{\mathrm{d}N}\frac{\mathrm{d}N}{\mathrm{d}\epsilon} \\ \frac{3}{2}\frac{1}{\epsilon} &= \frac{1}{N(\epsilon)}\frac{\mathrm{d}N}{\mathrm{d}\epsilon} \\ \curvearrowright \quad \frac{\mathrm{d}N}{N(\epsilon)} &= \frac{3}{2}\frac{\mathrm{d}\epsilon}{\epsilon} \end{aligned}$$

getting an alternative writing for the **density of states as function also of the electron number**

$$D_\epsilon(\epsilon) = \frac{\mathrm{d}N}{\mathrm{d}\epsilon} = \frac{3N(\epsilon)}{2\epsilon}. \tag{9.26}$$

The density of states of a free electron gas related to the energy and the volume is given by

Density of states of a free electron gas related to energy and volume

$$d_\epsilon = \frac{D_\epsilon}{V} = \frac{\sqrt{2}m_e^{3/2}}{\pi^2\hbar^3}\sqrt{\epsilon}. \tag{9.27}$$

and scales with the square root of the energy, as shown in Fig. 9.6a.

One can now calculate the **number of electrons within an energy interval** at the absolute zero point $T = 0$ K by multiplying the density of states with the probability of each state given by the Fermi–Dirac distribution, (9.22), getting

$$N_\epsilon(\epsilon)d\epsilon = D_\epsilon(\epsilon)\, f_{\mathrm{FD}}(\epsilon)d\epsilon. \tag{9.28}$$

[2] Alternatively, one can start from our definition of the density of states related to the value of the wave number, (9.14), using the derivative from $\epsilon = (\hbar k)^2/(2m_e)$ to $d\epsilon = \hbar^2 k/m_e dk$ and substitute

$$D_\epsilon(\epsilon)\mathrm{d}\epsilon = D_k(k)\mathrm{d}k = \frac{8\pi V}{(2\pi)^3}k^2\mathrm{d}k = \frac{8\pi V}{(2\pi)^3}\frac{m_e\sqrt{2m_e\epsilon}}{\hbar^3}\mathrm{d}\epsilon.$$

.

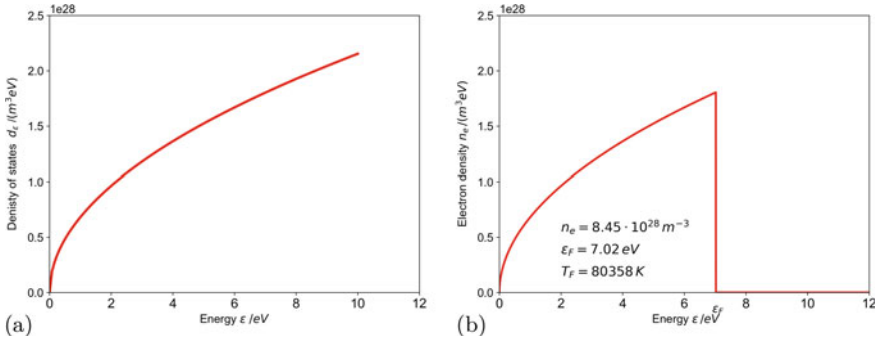

Fig. 9.6 Density of states related to the energy and the volume for a free electron gas (**a**), and electron density in an electron gas at the absolute zero temperature for copper (**b**)

The **number of states per energy interval** $[\epsilon, \epsilon + d\epsilon]$ in an electron gas, shown in Fig. 9.6 b, is written as

Number of states per energy of an electron gas at zero temperature

$$N_\epsilon(\epsilon) = D_\epsilon(\epsilon) f_{\mathrm{FD}}(\epsilon) = \frac{\sqrt{2} V m_\mathrm{e}^{3/2}}{\pi^2 \hbar^3} \sqrt{\epsilon} \Theta(\epsilon_\mathrm{F} - \epsilon). \tag{9.29}$$

Straightforward, we introduce the electron density per energy using (9.27)

Electron density per energy of an electron gas at zero temperature

$$n_\epsilon(\epsilon) = \frac{N_\epsilon(\epsilon)}{V} = d_\epsilon(\epsilon) f_{\mathrm{FD}}(\epsilon) = \frac{\sqrt{2} m_\mathrm{e}^{3/2}}{\pi^2 \hbar^3} \sqrt{\epsilon} \Theta(\epsilon_\mathrm{F} - \epsilon) \tag{9.30}$$

The **overall electron density** in the electron gas is calculated by summing up the number of electrons per energy interval and per volume for all occupied energy states, here up to the Fermi energy

$$\begin{aligned} n_\mathrm{e} &= \int_0^\infty n_\epsilon(\epsilon) \mathrm{d}\epsilon = \int_0^\infty d_\epsilon(\epsilon) f_{\mathrm{FD}}(\epsilon, T) \mathrm{d}\epsilon \\ &= \int_0^\infty \frac{\sqrt{2} m_\mathrm{e}^{3/2}}{\pi^2 \hbar^3} \sqrt{\epsilon} \Theta(\epsilon_\mathrm{F} - \epsilon) \mathrm{d}\epsilon \\ &= \frac{\sqrt{2} m_\mathrm{e}^{3/2}}{\pi^2 \hbar^3} \int_0^{\epsilon_\mathrm{F}} \sqrt{\epsilon} \mathrm{d}\epsilon, \quad \text{getting} \end{aligned}$$

Electron density for an electron gas at zero temperature

$$n_e = \frac{(2m_e\epsilon_F)^{3/2}}{3\pi^2\hbar^3}. \tag{9.31}$$

This calculus reproduces the results from (9.19).

9.3 Electronic Properties at Higher Temperatures

Increasing the temperature of a **fermion** system, like an electron gas, increases the kinetic energy of the electrons. Particles with energies close to the Fermi energy leave the Fermi sphere occupying states at higher energies.

9.3.1 Fermi–Dirac Distribution at Higher Temperatures

As a consequence, the distribution of the electrons is not a step function anymore, and is now given by a **Fermi–Dirac distribution**. The energy distribution of the states for fermions follows the Fermi–Dirac statistics [1], where the starting points are

1. Swapping two particles results in an anti-symmetric wave function ψ: None of the states of individual particles can be occupied by more than one particle (**Pauli principle**).
2. If we swaps two particles with each other, we do not get a new state, but the same state as before (**principle of indistinguishably of identical particles**).

The Fermi–Dirac distribution indicates the probability $f_{FD}(\epsilon, T)$ in an ideal Fermi gas at a given absolute temperature T that a state of energy ϵ is occupied by one of the particles, here the electrons. In statistical physics, the Fermi–Dirac distribution is derived from the Fermi–Dirac statistics for similar fermions for the important case of freedom of interaction. In case of constant density of states for the electron, $D(\epsilon) = 1$ the Fermi–Dirac distribution can be written as

Fermi–Dirac distribution

$$f_{FD}(\epsilon, T) = \frac{1}{\exp\left(\frac{\epsilon-\mu(T)}{k_B T}\right) + 1}, \tag{9.32}$$

with the **chemical potential $\mu = \mu(T)$**. For vanishing temperatures $T = 0$ K, the Fermi–Dirac distribution is equal to a Heavyside step function (9.22), and the chemical potential is equal to the Fermi energy $\mu = \epsilon_F$, see Fig. 9.5. There, all states

closely up to the chemical potential have the probability of unity, and above the probability zero.

To determine the **overall electron density**, we take the (9.30) and using the Fermi–Dirac distribution (9.32), we calculate

$$n_\mathrm{e} = \int_0^\infty n_\epsilon(\epsilon)\mathrm{d}\epsilon = \int_0^\infty d_\epsilon(\epsilon) f_\mathrm{FD}(\epsilon, T)\mathrm{d}\epsilon$$
$$= \frac{\sqrt{2}m_\mathrm{e}^{3/2}}{\pi^2\hbar^3}\int_0^\infty \frac{\sqrt{\epsilon}\mathrm{d}\epsilon}{\exp\left(\frac{\epsilon-\mu(T)}{k_\mathrm{B}T}\right)+1}$$

As shown in [2] one gets by substitution, using

$$x = \frac{\epsilon}{k_\mathrm{B}T}, \quad \mathrm{d}x = \frac{\mathrm{d}\epsilon}{k_\mathrm{B}T}, \quad \text{and}$$
$$\alpha = \frac{\mu}{k_\mathrm{B}T}. \tag{9.33}$$

the overall electron density

Overall electron density

$$n_\mathrm{e} = \frac{N_\mathrm{e}}{V} = \frac{\sqrt{2}m_\mathrm{e}^{3/2}}{\pi^2\hbar^3}\int_0^\infty \frac{x^{1/2}\mathrm{d}x}{e^{x-\alpha}+1} \tag{9.34}$$
$$= \frac{2}{\sqrt{\pi}} D_0 F_{1/2}(\alpha). \tag{9.35}$$

Here, we introduced also the **effective density of states**

$$D_0 = \frac{1}{4}\left(\frac{2m_\mathrm{e}k_\mathrm{B}T}{\pi\hbar^2}\right)^{3/2}, \tag{9.36}$$

and also the **Fermi function at index 1/2**

$$F_{1/2}(\alpha) = \int_0^\infty \frac{x^{1/2}\mathrm{d}x}{e^{x-\alpha}+1}. \tag{9.37}$$

Depending on the electron density given in matter, the Fermi function, being proportional to fraction of the electron density to the effective density

$$F_{1/2}(\alpha) \propto \frac{n_\mathrm{e}}{D_0}, \tag{9.38}$$

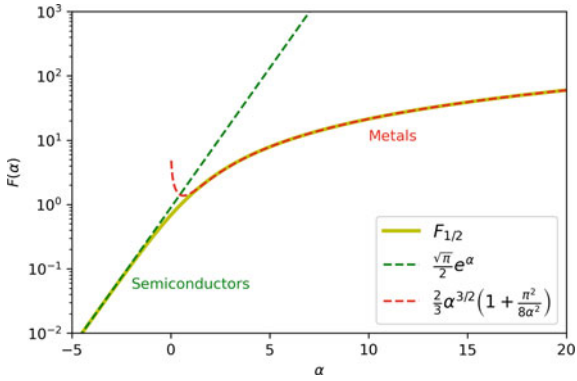

Fig. 9.7 Fermi function and approximations for negative and positive α

can be approximated analytically for high and low electron densities, see [2], representing metals or semiconductors see Fig. 9.7. Excited dielectrics feature properties comparable to semiconductors, see also Sect. 12.5.1.

9.3.2 High Electron Density: Metals

We are now able to compare the typical electron densities n_e in condensed matter with the effective density of states D_0.

As described in [2], at room temperatures the effective density of states is calculated by (9.36) to $D_0(T = 300\,\mathrm{K}) = 2.51 \cdot 10^{25}\,\mathrm{m}^{-3}$, being much smaller than the typical electron density $n_e = 8.45 \cdot 10^{28}\,\mathrm{m}^{-3}$ in metals, like copper. At this high electron densities it can be shown [2] that the Fermi function, (9.38), gets large with $F_{1/2}(\alpha) \gg 1$ for $\alpha \gg 1$, and is in that case approximated, as shown in Fig. 9.7, by the function

$$F_{1/2}(\alpha) \approx \frac{2}{3}\alpha^{3/2}\left(1 + \frac{\pi^2}{8\alpha^2}\right),$$

allowing one to calculate the chemical potential, using (9.33). Therefore, the relation between Fermi energy and the electron density, given by (9.19) is combined with the definition of the electron density via the effective density of states D_0 and the Fermi function, (9.35), getting a relation between the Fermi energy and the chemical potential, as $\alpha = \mu/(k_B T)$,

$$\epsilon_F^{3/2} = \mu^{3/2}\left(1 + \frac{\pi^2}{8}\left(\frac{k_B T}{\mu}\right)^2\right). \tag{9.39}$$

As $\alpha \propto \mu$ is large, it results that the fraction in the last equation given by $1/\alpha \ll 1$ gets very small, and the bracket in the last equation gets unity [2]. So we can approximate

$\epsilon_F \approx \mu$. Therefore we substitute as a correction term in the bracket μ by the Fermi energy ϵ_F, getting finally for a high electron density n_e the approximation of the chemical potential to

Chemical potential at high electron density

$$\mu(T) = \frac{\epsilon_F}{\left(1 + \frac{\pi^2}{8}\left(\frac{k_B T}{\epsilon_F}\right)^2\right)^{2/3}}. \tag{9.40}$$

The relation between the kinetic energy of the electrons to its property, behaving like a classical gas following the Maxwell Boltzmann statistics, or like a quantum mechanical system following the Pauli principle, can quantitatively be determined by the **degeneracy temperature** T_D. For temperatures above the degeneracy temperature T_D a Fermi gas, i.e. particle gas consisting of fermions, acts like a classical gas following the Maxwell–Boltzmann statistics. Below the degeneracy temperature T_D, a Fermi gas is described by the Fermi–Dirac statistics, see (9.32).

To determine degeneracy temperature T_D, first, one states that the **average energy per particle** is given by

$$\langle E \rangle = \frac{E}{N_e} = \frac{E}{n_e V} = \frac{3}{10 m_e}(3\pi^2 n_e)^{2/3}\hbar^2,$$

using the overall energy from (9.21). Second, this energy per particle is also equal to the kinetic energy at the degeneracy temperature T_D given by

$$\langle E \rangle = \frac{3}{2} k_B T_D. \tag{9.41}$$

Comparing this with the Fermi energy from (9.19), we get for the degeneracy temperature

Degeneracy temperature

$$T_D = \frac{1}{5 m_e k_B}(3\pi^2 n_e)^{2/3}\hbar^2 = \frac{2}{5}\frac{\epsilon_F}{k_B}. \tag{9.42}$$

Knowing the electron density of a metal n_e, the Fermi energy is calculated via (9.19), and finally a degeneracy temperature $T_D \approx 32\,\text{kK}$ results, being much higher than the ambient temperature of the electrons at 300 K. This electrons are called "**cold electrons**" and follow the Fermi–Dirac statistics.

Now, looking on the chemical potential, see (9.40), and on the fraction of the thermal energy with the Fermi energy, one realizes that this term vanishes $k_B T/\epsilon_F \ll 1$, as the energy per electron at room temperature is about $E = k_B T \approx 20\,\text{meV}$, whereas the Fermi energy is $\epsilon_F \approx 7\,\text{eV}$. One concludes that at large electron densities,

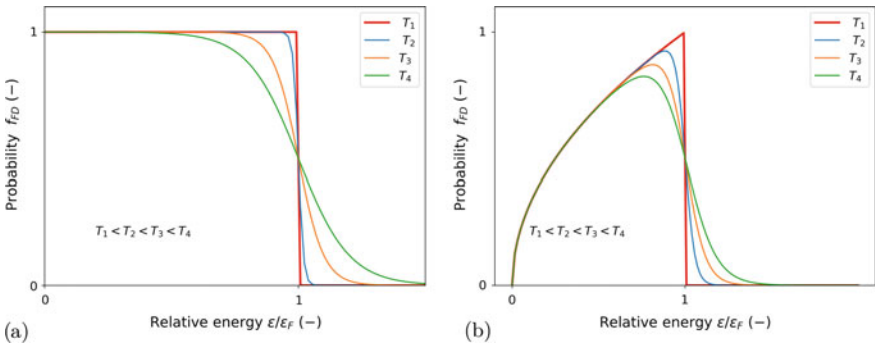

Fig. 9.8 Fermi–Dirac distribution for metals (**a**), and schematic electron density as function of the energy (**b**) at different temperature, with $T_1 < T_2 < T_3 < T_4$

the chemical potential of electrons at room temperature can be approximated to be nearly equal to the Fermi energy, and being independent of the temperature

Chemical potential for metals at room temperature

$$\mu \approx \epsilon_\mathrm{F} \tag{9.43}$$

$$\overset{(9.42)}{=} \frac{\hbar^2}{2m_\mathrm{e}}(3\pi^2 n_\mathrm{e})^{2/3}. \tag{9.44}$$

The Fermi–Dirac distribution represents approximately again a step function with most of all states being occupied for energies below $\mu(T) \approx \epsilon_\mathrm{F}$ and is written for all temperatures to

Fermi–Dirac distribution for metals

$$f_\mathrm{FD}(\epsilon, T) = \frac{1}{\exp\left(\frac{\epsilon-\epsilon_\mathrm{F}}{k_\mathrm{B}T}\right)+1}. \tag{9.45}$$

Only in the range $-k_\mathrm{B}T < \epsilon : F < k_\mathrm{B}T$, the so called **Fermi edge**, the step function is "soften up" featuring a steadily decrease in the probability for the occupation of states below μ, but featuring also states above ϵ_F with small but non-zero probability, see Fig. 9.8a. The electron density in metals now is calculated using the density of states for the free electrons, (9.25) and the Fermi–Dirac distribution for metals

$$n_\epsilon(\epsilon) = \frac{D_\epsilon \cdot f_\mathrm{FD}}{V} = d_\epsilon \cdot f_\mathrm{FD},$$

getting

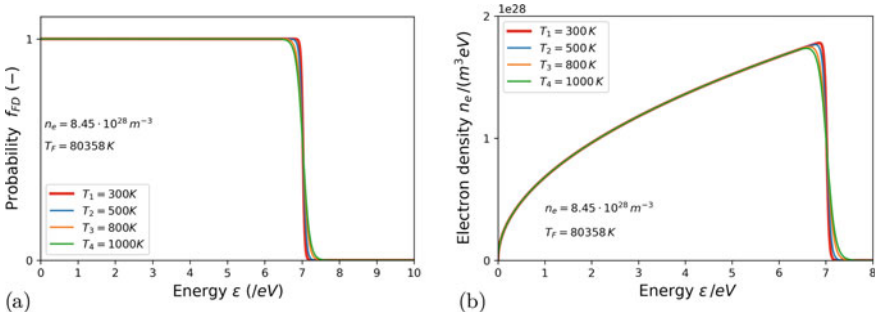

Fig. 9.9 Probability for the electrons in copper (**a**), and electron density at different temperatures (**b**)

Electron density of metals

$$n_\epsilon(\epsilon) = \frac{\sqrt{2} m_e^{3/2}}{\pi^2 \hbar^3} \frac{\sqrt{\epsilon}}{\exp\left(\frac{\epsilon - \epsilon_F}{k_B T}\right) + 1}, \tag{9.46}$$

and is depicted for different temperatures in Fig. 9.8b. With increasing temperature the states closely below the Fermi energy are depopulated and thermally excited to states above this energy forming the **Fermi tail**.

Working with real metals like copper featuring an electron density comparable to the atom density of $n_e = 8.45 \cdot 10^{28}\,\mathrm{m}^{-3}$, we can calculate the Fermi energy using (9.44) and getting a Fermi temperature above $T_F \approx 80\,\mathrm{kK}$. This results for the Fermi–Dirac distribution at typical temperatures of heated metals below its melting temperature, e.g. $T = 1.000\,\mathrm{K} \ll T_F$, in a little deviation from the step-like function of the Fermi–Dirac distribution at 0 K, as well a nearly unchanged electron density, see Fig. 9.9.

Electrons in a metal occupy almost all same states with the same probability, even at temperatures close to its melting temperature.

9.3.3 Low Electron Density: Semiconductors

Semiconductors represent materials featuring also free electrons, but at much lower electron densities, around $n_e \approx 10^{20}\,\mathrm{m}^{-3}$. Comparing this electron density with the effective density of states D_0, (9.36), one realizes that now the electron density is much smaller, $n_e \ll D_0$.

At this low electron densities, it can be shown [2] that the Fermi function (9.37) is much smaller unity, $F_{1/2} \ll 1$ with $\alpha \ll -1$, and it can be approximated as shown in Fig. 9.7 by the function

$$F_{1/2}(\alpha) = \frac{\sqrt{\pi}}{2} e^{\alpha}. \tag{9.47}$$

The **electron density for semiconductors** is then straightforward calculated by using (9.35) and getting

$$n_e = D_0 e^{\mu/(k_B T)}. \tag{9.48}$$

The chemical potential for low electron densities is determined by last equation giving

Chemical potential for low electron density

$$\mu(T) = k_B T \ln\left(\frac{n_e}{D_0}\right) = k_B T \ln\left(4 n_e \left(\frac{\pi \hbar^2}{2 m_e k_B T}\right)^{2/3}\right). \tag{9.49}$$

As $n_e \ll D_0$, the logarithm is negative and the chemical potential not only differs from the Fermi energy, but also gets negative

$$\mu(T) \ll -k_B T. \tag{9.50}$$

Now, from last equation, we can realize that the Fermi–Dirac distribution, (9.32) features a different proportionality. Rewriting it,

$$f_{FD} = \frac{1}{\exp\left(\frac{E}{k_B T}\right) \exp\left(\frac{-\mu(T)}{k_B T}\right) + 1} \tag{9.51}$$

one can see that the first exponential function is larger unity, >1, and the second one is much larger unity, $\gg 1$, so that we can simplify the distribution to

Fermi–Dirac distribution for semiconductors

$$f_{FD}^{sc} = \exp\left(\frac{-E}{k_B T}\right) \exp\left(\frac{\mu(T)}{k_B T}\right). \tag{9.52}$$

The Fermi–Dirac distribution represents a decaying exponential function, getting smaller with increasing temperatures, and featuring a very small probability even for small energies, see Fig. 9.10a.

The **electron density in a semiconductor** now is calculated using the density of states for free electrons, (9.25) and the Fermi–Dirac distribution for a semiconductor (9.52) getting

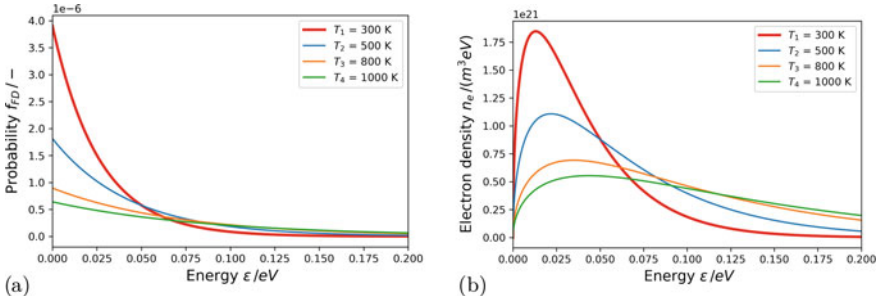

Fig. 9.10 Fermi–Dirac distribution for semiconductors (**a**) and electron densities at different temperatures of the semiconductor (equation)

Electron density getting semiconductors

$$n_\epsilon(\epsilon) = \frac{D_0 \cdot f_{\mathrm{FD}}^{\mathrm{sc}}}{V} = \frac{4n_\mathrm{e}}{\sqrt{\pi}(2k_\mathrm{B}T)^{3/2}}\sqrt{2\epsilon}\exp\left(-\frac{\epsilon}{k_\mathrm{B}T}\right). \tag{9.53}$$

As depicted for different temperatures in Fig. 9.10b, with increasing temperature the maximum of the electron density distribution decreases with increasing temperature, but featuring much more states at higher energies. In fact, the maximum of the distribution moves for larger temperatures to higher energies.

It is now also obvious that the statistics is changing from Fermi–Dirac to a **Maxwell–Boltzmann statistics**, as now the Fermi energy of a semiconductor is in the range of $\epsilon_F \approx 32\,\mu\mathrm{eV}$, getting a degeneracy temperature $T_\mathrm{D} \approx 0.15$ K, being much smaller than typical temperatures of the electrons in the range [300, 10.000] K.

As the electron density for semiconductors is very small, the probability of two electrons to be into equal states gets very unlikely, fulfilling automatically the Pauli principle.

In a semiconductor, the free electrons can be described as an ideal gas.

References

1. F. Reif, *Fundamentals of Statistical and Thermal Physics*. Series in Fundamentals of Physics (McGraw-Hill, Auckland, 1965)
2. S. Brandt, H.D. Dahmen, *Elektrodynamik* (Springer, Heidelberg, 2005)

Chapter 10
Optical Properties of an Electron Gas

Abstract Talking about absorption means in general to understand how electromagnetic radiation is transformed by interaction into other energy states, like electronic excitation energy, kinetic energy of electrons, or kinetic energy of atoms described by phonons. So, the electrons play again a major role in absorption. Depending on the matter or phase state, like metal, semiconductor, or dielectric, the optical energy is absorbed in different ways. In this chapter, the optical properties of a free electron gas and a quasi-free electron gas are described.

10.1 General Aspects—Lambert–Beer's Law

One realizes that electromagnetic radiation propagating through matter features a **complex refractive index** $\tilde{\boldsymbol{n}} = \boldsymbol{n} - \boldsymbol{i}\boldsymbol{\kappa}$, see also (6.27), and a complex wave number $\tilde{k}_{\mathrm{M}}$,

$$\tilde{k}_{\mathrm{M}}(\omega) = \frac{\omega}{c_{\mathrm{M}}} = \frac{\omega}{c_0}\tilde{n} = k_0\,\tilde{n}. \tag{10.1}$$

Thereby, the complex refractive index has to be derived from the relative permittivity, also called dielectric function $\tilde{\epsilon} = \epsilon_1 + i\epsilon_2$; see (6.35) and (6.36). At the end, it will result in the case of a one-dimensional problem,[1] an amplitude-damped electric field strength as a function of the depth x:

$$\begin{aligned}\boldsymbol{E} &= \boldsymbol{E}_0 e^{i(\omega t - \tilde{k}_{\mathrm{M}}\cdot x)} = \boldsymbol{E}_0 e^{i(\omega t - \frac{\tilde{n}\omega}{c_0}x)} = \boldsymbol{E}_0 e^{i(\omega t - \frac{(n-i\kappa)\omega}{c_0}x)} \\ &= \boldsymbol{E}_0 e^{i(\omega t - \frac{n\omega}{c_0}x)} e^{-\frac{\kappa\omega}{c_0}x}.\end{aligned}$$

The intensity of the radiation scales with the squared averaged electric field strength $I \propto |\boldsymbol{E}|^2$, and using (1.94) or (7.27) we get for the transmitted intensity

$$\begin{aligned}I(x) &= I_0 e^{-2\frac{\kappa\omega}{c_0}x} \\ &= I_0 e^{-\alpha x}\end{aligned}$$

[1] Plane wave entering with orthogonal incidence on matter.

© Springer Nature Switzerland AG 2022

A. Horn, *The Physics of Laser Radiation–Matter Interaction*,
https://doi.org/10.1007/978-3-031-15862-9_10

and one gets the Lambert–Beer's law and the absorption coefficient α

Absorption coefficient

$$\alpha(\kappa) = \frac{2\kappa\omega}{c_0} = \frac{4\pi\kappa}{\lambda_0} = 2\kappa \cdot k_0. \tag{10.2}$$

The Lambert–Beer law has also been derived from single-particle scattering processes, see (5.4), but here we introduced optical properties of matter, resulting in

Lambert–Beer's law

$$I(x) = I_0 e^{-\alpha x}. \tag{10.3}$$

Applying this formula allows one to determine the thicknesses of samples, if the absorption coefficient α of matter is known, and doing **photometry** the absorption coefficient is determined, measuring the intensity of the transmitted radiation for different sample thicknesses x.

It is important to note that the absorption coefficient α is not a constant value, but depends on the extinction coefficient κ, $\alpha = \alpha(\kappa)$. The extinction coefficient is an optical parameter being very sensitive to the properties of the involved matter, like its temperature. So, in the case of absorption of radiation by matter, its temperature increases resulting in changes of the complex refractive index $\tilde{n}$ and consequently in the absorption coefficient α.

Usually, dielectrics feature very small absorption coefficients $\alpha \ll 1$ due to the fact that absorption is only realized by the coupling strength of the valence electron with its atoms, and finally given in a very small attenuation coefficient; see (3.20). The attenuation coefficient itself depends on the resonance frequency ω_0 of the atoms, which is mainly driven by the quantum number n (see Bohr acceleration and Bohr velocity in (3.14)).

The fact that the optical energy is absorbed in matter results much more often from the absorption at quasi-free electrons, defects of the crystal, or color-centers given in the dielectrics sporadically. They allow an efficient absorption of optical energy. In general, the absorption at free charges is again described by free carrier absorption, the so-called inverse bremsstrahlung; see Sect. 4.1.

10.2 Electron Gas

Many electrons not being bounded to atoms represent in condensed matter an **electron gas**. For a low density of the electrons in this electron gas, we can assume only elastic interaction between the electrons, like **elastic scattering**. In this case, one speaks about a **free electron gas**. Allowing the electrons to interact with each other transferring energy by **inelastic scattering** is described by a **quasi-free electron gas**.

Finally, in a real matter like metals, excited dielectrics or semiconductor electrons can be given in non-bounded states. But there, the interaction between the electrons with bounded electrons is also described by quasi-free electrons in crystals.

10.2.1 Free Electron Gas

The interaction of electromagnetic radiation with metals is described by the interaction of the radiation with its electrons. As a first approach, one can assume that the atoms are arranged periodically in the solid featuring a crystal structure. At least, **one electron per atom is assumed to be free** and being allocated between these atoms. These electrons are treated here as a free electron gas, so-called **Fermi gas**.

Evidently, this approach is the first approximation, not taking into account the interaction of this electron with the lattice atoms, where more correctly we would talk about a quasi-free electron model. Also, one has to consider the quantum mechanical nature of the electron being fermions. This will be discussed afterwards in Chap. 11.

Different from an ideal dielectric material, see Sect. 6.3 where all electrons are bounded to an atom (weak binding), see (6.22), now we assume that from the N electrons given in a metallic solid, $N-1$, are weakly bounded with the damping coefficient Γ_{em}, and one is free. This free electron is not within any harmonic potential and has no resonant frequency, i.e. $\omega_0^{\mathrm{e}} = 0$, resulting in a relative permittivity, so-called **dielectric function for one free electron**

$$\begin{aligned}\tilde{\epsilon}_{\mathrm{r}} &= \tilde{\chi}_{\mathrm{e}} + 1 = \tilde{n}^2 \\ &= \underbrace{1 + \frac{\omega_{\mathrm{p},N-1}^2}{\omega_0^2 - \omega^2 - i\Gamma_{\mathrm{em}}\omega}}_{\epsilon_r(\omega)^{N-1}} - \frac{\omega_{\mathrm{p},1}^2}{\omega^2 + i\Gamma_{\mathrm{e}}\omega} \\ &= \epsilon_{\mathrm{r}}^{N-1}(\omega) - \frac{\omega_{\mathrm{p},1}^2}{\omega^2 + i\Gamma_{\mathrm{e}}\omega},\end{aligned}$$

with $\omega_{\mathrm{p},N-1}$ representing the plasma frequency; see (6.25) for an oscillator density $n_{\mathrm{e}}^{\mathrm{b}} = (N-1)/V$ for the $N-1$ weakly bounded electrons. The plasma frequency $\omega_{\mathrm{p},1}$ is given for $n_{\mathrm{e}}^{\mathrm{f}} = 1/V$, and Γ_{e} represents the damping coefficient.

Assuming now all N electrons in a solid are free, one gets the **Drude model** for a free electron gas

Drude model for a free electron gas

$$\tilde{\epsilon}_{\mathrm{r}} = \tilde{n}^2 = \epsilon_{\mathrm{r},\infty} - \frac{\omega_{\mathrm{p}}^2}{\omega^2 + i\Gamma_{\mathrm{e}}\omega}, \tag{10.4}$$

with $\omega_{\mathrm{p}} = \sqrt{n_{\mathrm{e}} e^2/(m_{\mathrm{e}}\varepsilon_0)}$ being the plasma frequency for all N electrons, and $\epsilon_{\mathrm{r},\infty}$ representing the permittivity for infinity frequency, often being set to unity $\epsilon_{\mathrm{r},\infty} = 1$.

The damping coefficient Γ_e describes the emission rate as well as the collision rate for elastic scattering of the electrons with other free electrons; see also (3.9). The collision rate dominates in the case of many electrons on the emission rate.

Now, speaking about a **free electron gas** we argue that the electrons do not interact with other electrons, expressing it by a **vanishing damping constant $\boldsymbol{\Gamma_e = 0}$**. Remembering the separation of the relative permittivity, or the complex refractive index, into the real part (e.g. as the refractive index n) and the imaginary part (e.g. the extinction coefficient κ), see (6.29), the real and imaginary components of the Drude model (10.4) get for the free electron gas with a vanishing damping constant to

$$\Re(\tilde{n}^2) = \epsilon_1 = n^2 - \kappa^2 = \lim_{\Gamma_e \to 0} 1 - \frac{\omega_p^2}{\omega^2 + \Gamma_e^2} = 1 - \frac{\omega_p^2}{\omega^2} \tag{10.5}$$

$$\Im(\tilde{n}^2) = \epsilon_2 = 2n\kappa = \lim_{\Gamma_e \to 0} \frac{-\Gamma_e \omega_p^2}{\omega(\omega^2 + \Gamma_e^2)} = 0. \tag{10.6}$$

The imaginary part of the relative permittivity vanishes for negligible damping, see Fig. 10.1, and assuming a non-zero refractive index $n \neq 0$, one gets from (10.6) a vanishing extinction coefficient $\kappa = 0$. In consequence from (10.5), the refractive index n of a free electron gas gets to

Refractive index of a free electron gas

$$n(\omega) = \sqrt{1 - \frac{\omega_p^2}{\omega^2}}. \tag{10.7}$$

The refractive index represents a real function, $n(\omega) \in \mathbb{R}$ for $\boldsymbol{\omega > \omega_p}$, see Fig. 10.1, being defined in the range $0 \leq n < 1$.

In the frequency regime $\omega > \omega_p$, electromagnetic radiation can propagate through the free electron gas without any damping.

Apparently, the refractive index gets for frequencies ω below ω_p imaginary. One can rewrite for $\boldsymbol{\omega < \omega_p}$ the refractive index (10.7) by extracting the imaginary part

$$\begin{aligned} \kappa_i(\omega) &= \sqrt{(-1)\left(\frac{\omega_p^2}{\omega^2} - 1\right)} \\ &= i\sqrt{\left(\frac{\omega_p^2}{\omega^2} - 1\right)} \in \mathbb{C}. \end{aligned}$$

For frequencies of the radiation ω below the plasma frequency ω_p, a free electron gas features an imaginary refractive index n, representing now an extinction coefficient

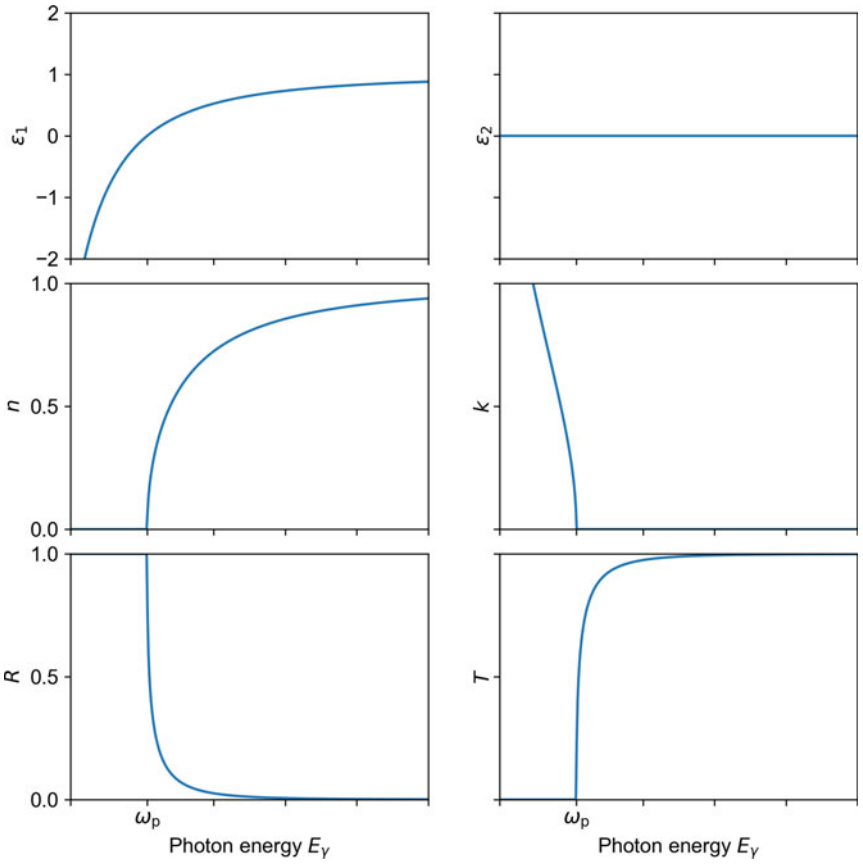

Fig. 10.1 Components of the complex relative permittivity ϵ_1, ϵ_2, and components of the complex refractive index n and κ, as well as the reflectance and transmittance for normal incident radiation on a free electron gas

$$\Im(\kappa_i) = \sqrt{\frac{\omega_\mathrm{p}^2}{\omega^2} - 1}.$$

Even the refractive index in the regime $\omega < \omega_\mathrm{p}$ is completely imaginary, no absorption results: normal incident radiation ($\alpha = 0°$) features a reflectance getting unity, see (7.31),

$$R = |r|^2 = \left|\frac{i\kappa_i - 1}{i\kappa_i + 1}\right|^2 = \frac{|i\kappa_i - 1|^2}{|i\kappa_i + 1|^2} = \frac{\kappa_i^2 + 1}{\kappa_i^2 + 1} = 1.$$

In consequence, the transmittance vanishes there, $T = 0$ (Fig. 10.1).

Electromagnetic radiation with frequencies ω below ω_p is reflected completely at a free electron gas without any attenuation by damping.

In practice, even a free electron gas is given (without any ions), the density of them must not be constant in space. For example, an electron gas generated by photoionization or by thermal emission of electrons using intense laser radiation, so-called **electron plasma**, features an electron density at a fixed time being more dense at the interaction zone, getting less dense far away from there. This means that the plasma frequency $\omega_p = \omega_p(r)$ is also changing as a function of the position, being largest at the interaction zone. So, radiation striking this electron plasma will "see" a free electron gas with a density gradient $n_e(r)$. At lower electron densities of the plasma, the radiation is transmitted, where $\omega > \omega_p$ holds. The radiation will be transmitted in this electron plasma until $\omega \leq \omega_p$, where due to an increasing electron density the plasma frequency exceeds the angular frequency of the radiation, and reflection gets then more probable. Finally, the radiation is completely reflected in the electron plasma, and one speaks about a **plasma mirror**.

Electromagnetic radiation striking a free electron gas will be optically transparent for frequencies above ω_p. As defined in (6.23), the speed of light in matter results in a free electron gas to

Speed of light in electron gas

$$c_M = \frac{c_0}{n} = \frac{c_0}{\sqrt{1 - \frac{\omega_p^2}{\omega^2}}} = \frac{\omega}{k_M} = v_p. \tag{10.8}$$

The speed of light in matter c_M is equal to the velocity of the phase front, so one calls it also **phase velocity** $\boldsymbol{v_p}$; see Sect. 1.6.4. Obviously, the speed of light in a free electron gas is anytime **larger than the vacuum speed of light** $\boldsymbol{v_p > c_0}$; see Fig. 10.2.

The **dispersion relation** for radiation propagating through a medium describes in general the relation between the wave number and the frequency. For radiation passing a free electron plasma, we get the dispersion relation

$$k_M(\omega) = \frac{\omega}{c_M} = \frac{\omega}{c_0} n(\omega, n_e) = k_0\, n(\omega, n_e) = \frac{\omega}{c_0}\sqrt{1 - \frac{\omega_p^2}{\omega^2}}. \tag{10.9}$$

The group velocity v_g represents the velocity with which the overall envelope of a pulsed radiation, see (1.97) in Sect. 1.6.4, propagates through space, and is also here defined by

$$v_g = \frac{d\omega}{dk_M}.$$

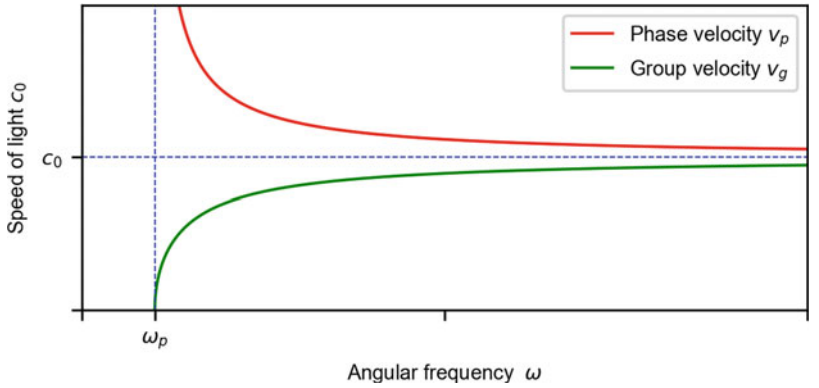

Fig. 10.2 Phase and group velocities of electromagnetic radiation in a free electron gas

One calculates the **group velocity for an electron plasma** using the given dispersion relation (10.9), reorganizing it to $\omega = \sqrt{c_0^2 k_\mathrm{M}^2 + \omega_\mathrm{p}^2}$ and taking the derivative for the wave number k_M, getting

Group velocity of a free electron plasma

$$v_\mathrm{g} = \frac{k_\mathrm{M} c_0^2}{\sqrt{c_0^2 k_\mathrm{M}^2 + \omega_\mathrm{p}^2}} = \frac{k_\mathrm{M} c_0^2}{\omega} = n(\omega, n_\mathrm{e})\, c_0. \tag{10.10}$$

Now, the **group velocity is every time smaller as the vacuum speed of light** $\boldsymbol{v_\mathrm{g} < c_0}$; see Fig. 10.2. As known, the group velocity dictates the upper velocity limit for information transfer. Any information, the simplest form given by one bit, and expressed in optics as a temporal limited emission of radiation, a so-called **pulse**, can be transferred maximally by the vacuum speed of light c_0, given by the group velocity v_g.

10.2.2 Quasi-free Electron Gas

The free electrons given in metals are not, as described in the sections before, completely free. As the next assumption, the free electrons interact with other free ones by electron–electron collisions. A collision frequency ν_ee is assumed, given also by its inverse function, the so-called **electron–electron collision time**

Electron-electron collision frequency

$$\nu_{ee} = \frac{1}{\tau_{ee}}. \tag{10.11}$$

The electron–electron collisions determine together with the electron–phonon collisions usually the thermal property of a metal, especially its **thermal conductivity**; see (12.2) and also Sect. 14.5.2. The electron–phonon collisions can be neglected as long as the electron temperature T_e is large compared to the lattice temperature, $T_e \gg T_p$.

The damping coefficient Γ_e is now not vanishing at all. As described in Sect. 10.2.1 for non-vanishing damping coefficient Γ_e, the relative permittivity $\tilde{\epsilon}_r$ gets a complex number with both, a real and an imaginary part; see (10.4). In fact, the complex refractive index of metals is written as $\tilde{n} = n - i\kappa$, equally to dielectrics.

As a consequence, Snell's law has now to be rewritten as

Snell's law

$$n_1 \sin\alpha = \tilde{n} \sin\beta, \tag{10.12}$$

implicating that the **refraction angle β is complex**, too. Remembering the propagation behavior of radiation through dielectrics from an optically dense to an optically thin medium with both purely real refractive indices, see Sect. 7.9, a complex refracted angle β resulted for inclination angles larger than a critical angle $\alpha > \alpha_T$. As a consequence, **evanescent waves** close to the boundary of these two dielectric media resulted; see Sect. 7.10.

For normal-incident radiation, where $\alpha, \beta \ll 1$ the Snell law is simplified given by $n_1\alpha = \tilde{n}\beta$, and the reflection coefficient, for example, s-polarized radiation gets to

$$r_s = \frac{\beta - \alpha}{\alpha + \beta} = \frac{\beta - \frac{\tilde{n}}{n_1}\beta}{\frac{\tilde{n}}{n_1}\beta + \beta} = \frac{1 - \tilde{n}}{1 + \tilde{n}} = r_p,$$

being equal to the reflection coefficient for p-polarized radiation. The reflectance at normal incidence is now calculated using $\tilde{n} = n - i\kappa$

$$R = |r_s|^2 = |r_p|^2 = \left|\frac{1 - \tilde{n}}{1 + \tilde{n}}\right|^2 = \frac{|1 - n - i\kappa|^2}{|1 + n + i\kappa|^2}$$

Reflectance for metals

$$R = \frac{(n-1)^2 + \kappa^2}{(n+1)^2 + \kappa^2 < 1}. \tag{10.13}$$

Different from the internal reflection of radiation in dielectrics, the **reflectance of metals will never be unity** for all n and $\kappa \neq 0$. Provided that the incidence is still normal, the reflectance R for metals gets close to unity, when

$$\left.\begin{aligned} n &\gg \kappa \\ \kappa &\gg n \\ n \text{ and } \kappa &\gg 1 \end{aligned}\right\} \quad \curvearrowright \quad R \approx 1.$$

Furthermore, the reflectance for metals will not vanish for $\omega > \omega_\mathrm{p}$, as given for a free electron gas, as well as the transmittance will not vanish for $\omega < \omega_\mathrm{p}$. Generally, calculating the dielectric function $\tilde{\epsilon}_r$ using (10.4), one can determine the complex

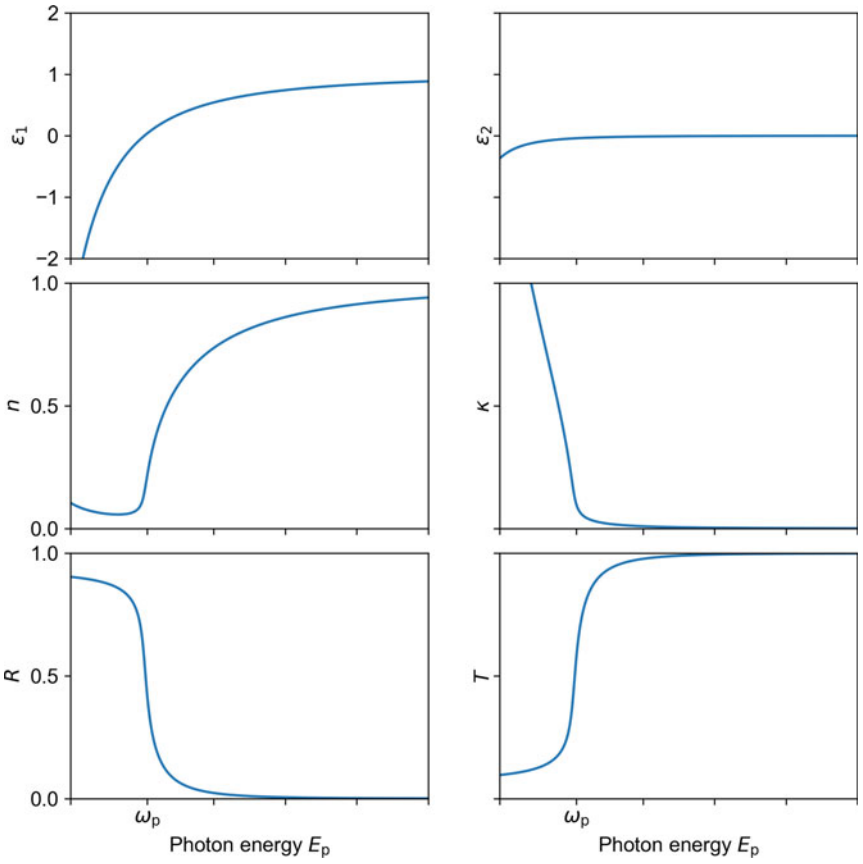

Fig. 10.3 Components of the complex relative permittivity ϵ_1, ϵ_2, and of the complex refractive index n and κ, as well as the reflectance and transmittance for normal incident radiation on a metal surface with an electron density $n_\mathrm{e} = 3 \cdot 10^{27}\,\mathrm{m}^{-3}$ getting $\omega_\mathrm{p} = 3 \cdot 10^{15}$ 1/s, and the damping coefficient $\Gamma_\mathrm{e} = 1.4 \cdot 10^{-20}$ 1/s

refractive index $\tilde{n}$ and then calculate the reflectance. This will get close to unity for decreasing ω at $\omega < \omega_p$, because n and κ are growing. The reflectance drops at $\omega > \omega_p$ due to the decreasing κ (and $n \approx 1$) and results in $T \approx 1$; see Fig. 10.3.

For example, one calculates for aluminum, assuming one free electron per atom, a plasma frequency being much larger than the angular frequency of electromagnetic radiation in the UV-VIS spectral range, resulting to be an excellent high-reflective mirror.

Contrary to dielectrics, metals exhibit for all incident angles α a complex angle of refraction β, reasoning always an **evanescent wave** at the boundary/interface. As a consequence of the interaction of laser radiation with metals, often periodic structures, so-called **ripples or laser-induced periodical surface structures LIPSS**, will result (see Sect. 1.7.2). As the refractive index of a metal is a complex number, also the reflection coefficients resulting from the Fresnel equations get complex numbers; see (7.37) and (7.39). So, for both polarization states of the radiation the reflection coefficients r_s and r_p can be written as

$$r_s = |r_s| e^{i\varphi_s} \qquad r_p = |r_p| e^{i\varphi_p},$$

introducing the phases φ_s and φ_p for orthogonal or parallel polarized radiation. The fraction of this reflection coefficients gets to

$$\frac{r_s}{r_p} = \frac{\cos(\beta - \alpha)}{\cos(\alpha + \beta)} = \frac{|r_s|}{|r_p|} e^{i(\varphi_s - \varphi_p)} \in \mathbb{C},$$

expressing a phase shift $\Delta\varphi = \varphi_s - \varphi_p$ for all incident angles α, except for $\alpha = 0°$ and $\alpha = \pi/2$. This implies that linear polarized radiation being a combination of s- and p-polarized radiation components will result in reflected **elliptical polarized radiation**, except for normal incidence, $\alpha = 0°$, and grazing incident radiation with $\alpha = \pi/2$.

Real metals feature quasi-free and bounded electrons in a crystalline atom compound. The resulting description of the complex relative permittivity now gets to a combination of the Lorentz and the Drude models resulting in the **Drude–Lorentz model**; see more in Sect. 12.6.

Chapter 11
Band Theory of Crystals

Abstract Talking about free electrons in solids one has to explain why there are freely moving electrons in many solids and why their densities n_e can differ by many orders of magnitude for different types of solids. Most solids are crystals, i.e. a regular arrangement of recurring groups of atoms or—in the simplest case—of a single type of atom, as in the case of many metals like copper or silver. In the following sections, we will talk about the periodic potentials of atoms in solids, its degenerating energy levels forming energy bands, and the differences in the energy band distribution for metals, semiconductors, and dielectrics.

11.1 Electronic Band Formation

Atoms feature **discrete energy levels**, as known from quantum mechanics, and have been described shortly in Sect. 3.5. Therefore, an excitation of a valence electron results in excited states of atoms, or if the excitation energy is much larger, then one speaks about the ionization energy for the ionization of the atoms, see Sect. 4.3.

A single atom features an atomic nucleus with an electric charge $Z \cdot e$. The number Z, which indicates the number of positive elementary charges e in the nucleus, is called the atomic number. For copper, the atomic number results in $Z = 29$. In the Coulomb field of the nucleus, the total number of Z electrons can be bound, each carrying the charge $-e$, so that an atom as a whole gets electric neutral.

Contrary to classical mechanics, the electrons within an atom can only feature very specific and discrete energy values, so-called **energy levels**, which are calculated quantum mechanically. In Fig. 11.1, on the left side, the electrostatic potential of an atomic nucleus as a function of the distance from the nucleus is schematically given, together with some corresponding energy levels. Fixing the energy zero point corresponding to the potential at infinity, all bound electron states feature negative energies. On the contrary, positive energies are referred to as free states of electrons, allowing the electron to move arbitrarily far away from the nucleus with deliberate and continuous kinetic energies. Usually, an atom is in the **ground state**, which represents the energetic state of the lowest potential energy. The **highest occupied**

© Springer Nature Switzerland AG 2022

A. Horn, *The Physics of Laser Radiation–Matter Interaction*,
https://doi.org/10.1007/978-3-031-15862-9_11

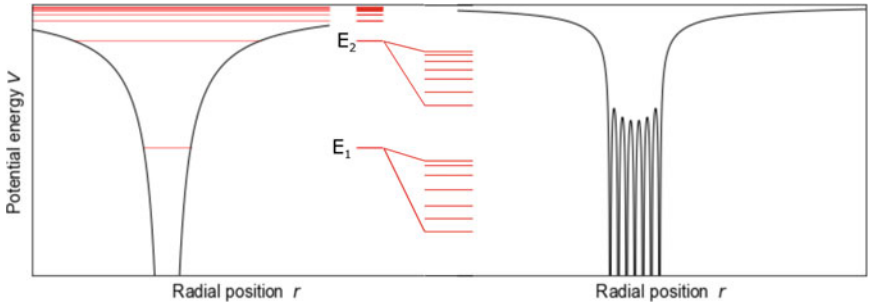

Fig. 11.1 Electrostatic potential of a simple atomic nucleus and energy levels of an electron in this potential (left). Resulting potential of several neighboring atomic nuclei (model of a crystal lattice, $N = 7$) and energy bands consisting of as many energy levels as atoms in the crystal (right)

state is characterized by the fact that all lower energy states are occupied by all electrons steadily. All possible atomic states above the highest occupied state are unoccupied.

Bringing many equal atoms together, e.g. forming a **cluster of atoms**, as shown in Figs. 11.1 right and 11.2 left, reducing the inter-atomic distance to the final distance a, induces the formation of **energy bands** for each energy level of a single atom. As the Pauli principle still holds, and all quantum numbers of the atoms at each energy level are fixed, the individual energies of the atoms at this energy level must be different for each atom of the compound.

Now, looking on **solids**, the crystal lattice of solid features, as described in solid state physics textbooks [1], a periodic potential, because of the **periodically**

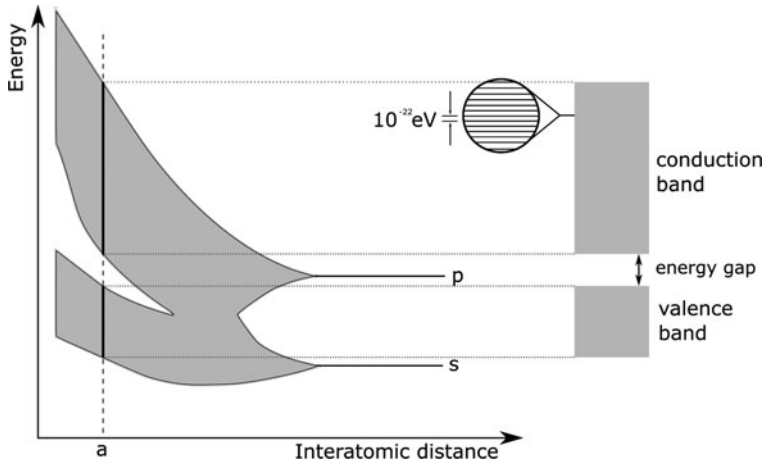

Fig. 11.2 Formation of the electron band structure with the energy levels as a function of the spacing between atoms on the left, and on the right, each atomic level splits into N levels with different energies, where N is the number of atoms. Since N is in a crystal a very large number, the adjacent levels are energetically very close together, effectively forming a continuous energy band

arranged atoms in space, shown schematically in Fig. 11.1 on the right. One observes that the potential of the individual atoms is lowered below zero everywhere inside the crystal, while it rises to zero again at the boundaries of the crystal. As the number of atoms in solids gets very large with densities in the order of 10^{28} m^{-3}, and the **energy separation scales reciprocally to the number of atoms**, typically an energy separation of 10^{-22} eV results, see Fig. 11.2 right, confirming a **quasi-continuum of energy levels** in solids, being located close to the initial discrete energy level of one atom. The discrete energy levels of the single atoms get for many atoms, by the mutual interaction between the atoms, to groups of closely neighboring energy levels, the so-called **energy bands**.

Each energy level of a single atom corresponds now to an energy band for the crystal, and due to the Pauli principle, as now the wave functions of the electrons overlap, each atomic level splits into as much energy levels as electrons are given within the band.[1] Each energy band features as many energy levels as there are atoms within the crystal, being consistent with the cluster approach of one paragraph before.

But, the number of accessible electron states in the band is twice as large as the number of atoms N in the solid, because of the degeneration into two spin-settings of the electrons, resulting in $2N$ accessible states per energy band.

As we have discussed before, one states that the difference within a band between each energy level is very small compared to the energy itself, so that a **quasi-continuum of energy levels**, like the continuous energy in a free electron gas in the band results. The bands themselves are generally separated by regions without any energy levels, the so-called **energy gaps** or band gaps, see Fig. 11.2. However, adjacent bands can also overlap, as shown later for metals and semi-metals, see Sect. 11.2.1.

The density of states within an energy band depends on the structure of the crystal, and in detail it can only be determined by quantum mechanics. Here, for our understanding, it is sufficient to note that the density of states of one specific energy band can be described by the one for a free electron gas. The density of states goes to zero at the bottom edge ϵ_b as well as at the top band edge ϵ_t with the root of the different energy to the band edge, quite corresponding to the density of states of a free electron gas in a potential well, which is proportional to the square root of the energy, see (9.25). For a free electron gas, no band structure is given. Therefore, there exists only a lower energy limit, but no upper energy limitation.

The **density of states near the bottom band edge**, $\epsilon \to \epsilon_\mathrm{b}$, is defined comparably to the free electron gas, by

$$D_\mathrm{b}(\epsilon) = \frac{\sqrt{2}Vm^{3/2}}{\pi^2\hbar^3}\sqrt{\epsilon - \epsilon_\mathrm{b}}. \tag{11.1}$$

The **density of states for the top band edge** is given for energies close to the top band edge, $\epsilon \to \epsilon_\mathrm{t}$, by an inverted square-root dependence

[1] For one fixed energy level of an atom, the quantum numbers are for all atoms equal and constant, so the energies of all atoms at that level must differ.

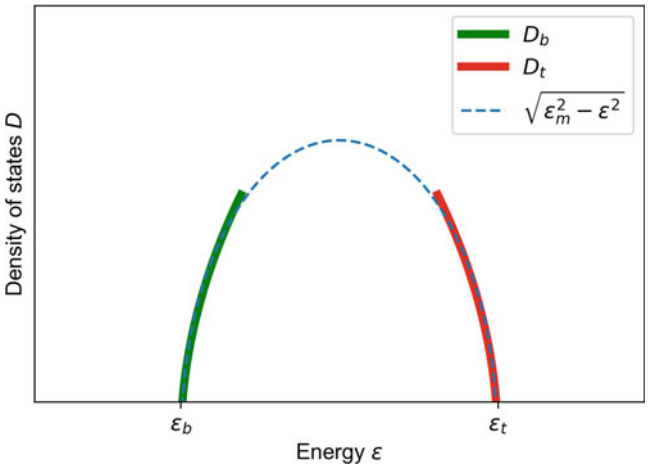

Fig. 11.3 Density of states $D(\epsilon)$ for one energy band characterized by the lower and upper energies from (11.1) and (11.2), as well by a consistent approximation $\propto \sqrt{\epsilon_{\mathrm{m}}^2 - \epsilon^2}$ with $\epsilon_{\mathrm{m}} = \epsilon_{\mathrm{b}} + (\epsilon_{\mathrm{t}} - \epsilon_{\mathrm{b}})/2$

$$D_{\mathrm{t}}(\epsilon) = \frac{\sqrt{2} V m^{3/2}}{\pi^2 \hbar^3} \sqrt{\epsilon_{\mathrm{t}} - \epsilon}. \tag{11.2}$$

An energy band structure results qualitatively by the combination of these two limiting functions, see Fig. 11.3. But in fact, its precise profile has to be determined by **ab-initio calculations** of the density of states. Some examples of ab-initio calculations are shown for different atoms in Figs. 11.4 and 11.5 [2]. In the first Fig. 11.4, the energetic lower d- and higher s/p bands for gold are given by ab-initio calcula-

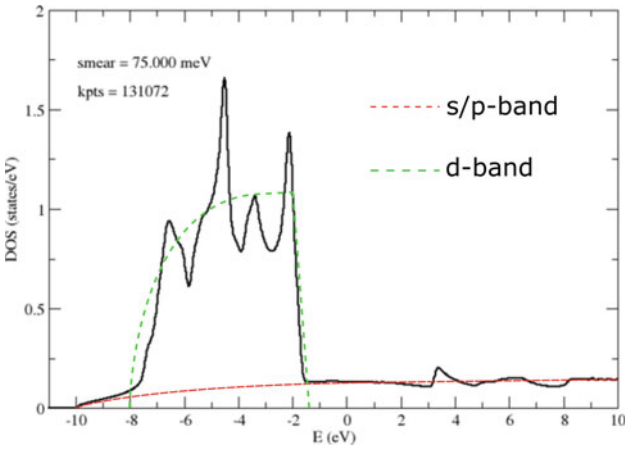

Fig. 11.4 Calculated density of states for the d- and s/p-states of gold (modified from [3])

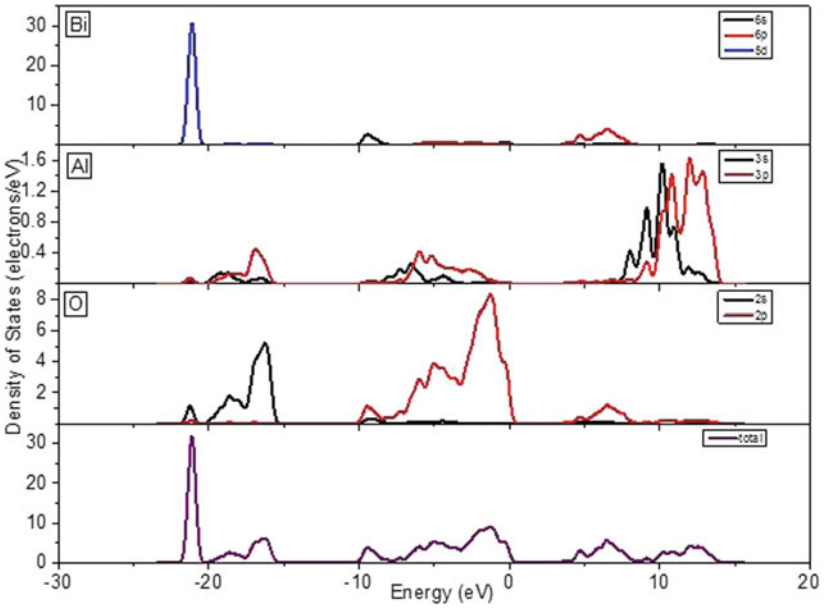

Fig. 11.5 Variation of partial density of states for bismuth, aluminum, and oxygen [2]

tion and are approximated by a square-root functional dependence. The density of state of a solid consisting of many atoms, like bismuth, aluminum, oxygen, and its resulting total density of state of the compound can be calculated too, and it is shown in Fig. 11.5 [2].

11.2 Valence and Conduction Bands

Important for the electrical as well optical properties of crystalline materials are the **population states** of the energy bands within a solid crystal. One distinguishes **fully populated, partially populated, or empty energy bands**.

In case, one energy band is completely full, and an energy gap between the adjacent bands is given, no movement of electrons in the **full band** is possible and **no electrical conductivity** results. In terms of electrostatics, an external electric field will move free electrons in a solid.[2] Clearly, if the highest energy band is completely empty, no charges therein can move. The electrons in the full band cannot gain energy, as no states are accessible anymore, and no electric conductivity results.

Electrical conductivity is only possible in solids featuring at least one partially populated energy band. In reality, solids consist of completely populated energy

[2] A movement of electrons, here, means an **excitation** of free electrons within one band to a higher energy, see Sect. 12.3.

bands, the one at highest energy called **valence band**, and at least one partially populated energy band, the so-called **conduction band**.

In the following section, we will discuss the three primary appearances of condensed crystalline matter as **metals, semiconductors or dielectrics**. We will firstly discuss its band structures and its populations at zero Kelvin temperature, and move later on to the condensed matter at higher temperatures.

11.2.1 Crystals at Absolute Zero Temperature

As described in Sect. 9.3, due to the Pauli principle, the electronic states within one energy band are consecutively populated by electrons with increasing energy, as for a free electron gas where the energy states are populated consecutively starting from the lowest energy state. At the temperature $T = 0$ K, all N electrons will populate $N/2$ states within the energy band, as each electron can feature two spin values, and each band features N energy states.

We calculate now the **energy distribution of the electrons**, i.e. the number of electrons in an energy interval $[\epsilon, \epsilon + d\epsilon]$, by multiplying the density distribution of energy states with the probability of this state, given for electrons by the Fermi–Dirac distribution, see (9.28),

$$N_\epsilon(\epsilon) = D_\epsilon(\epsilon) f_{\mathrm{FD}}(\epsilon, T). \tag{11.3}$$

As we set the temperature to $T = 0$ K, the Fermi–Dirac distribution results in a step-function, or Heaviside function,

$$\Theta(\epsilon) = f_{\mathrm{FD}}(\epsilon_{\mathrm{F}} - \epsilon).$$

Assuming a crystal with N equal atoms with the atomic number Z at a temperature $T = 0$ K, all $Z \cdot N$ electrons will populate $Z/2$ bands with energies below the Fermi energy ϵ_{F}. In case of an even atomic number, exactly $Z/2$ bands are completely populated resulting in a Fermi energy ϵ_{F}, being positioned exactly between the highest populated band and the first completely empty energy band. The full band is called **valence band (VB)**, and the region free of states between this band and the next one is called the **band gap** ΔE, see Fig. 11.6a, b. As we discussed before, this class of crystals have no free-moving electrons and are called **insulators** or dielectrics. It should also be mentioned here that a semiconductor represents at this temperature $T = 0$ K an insulator.

In case of an **uneven atomic number** Z, the highest energetic band is only half- populated by electrons, allowing now the movement of the electrons, see Fig. 11.6c, d. As one can see, the energy distribution within this partially-filled band features the same energy distribution like a free electron gas. This class of crystals are called **conductors**, and many of them are **metals**. The band structure of many metals, like alkaline metals, copper ($Z = 29$), silver ($Z = 47$), or gold ($Z = 79$)

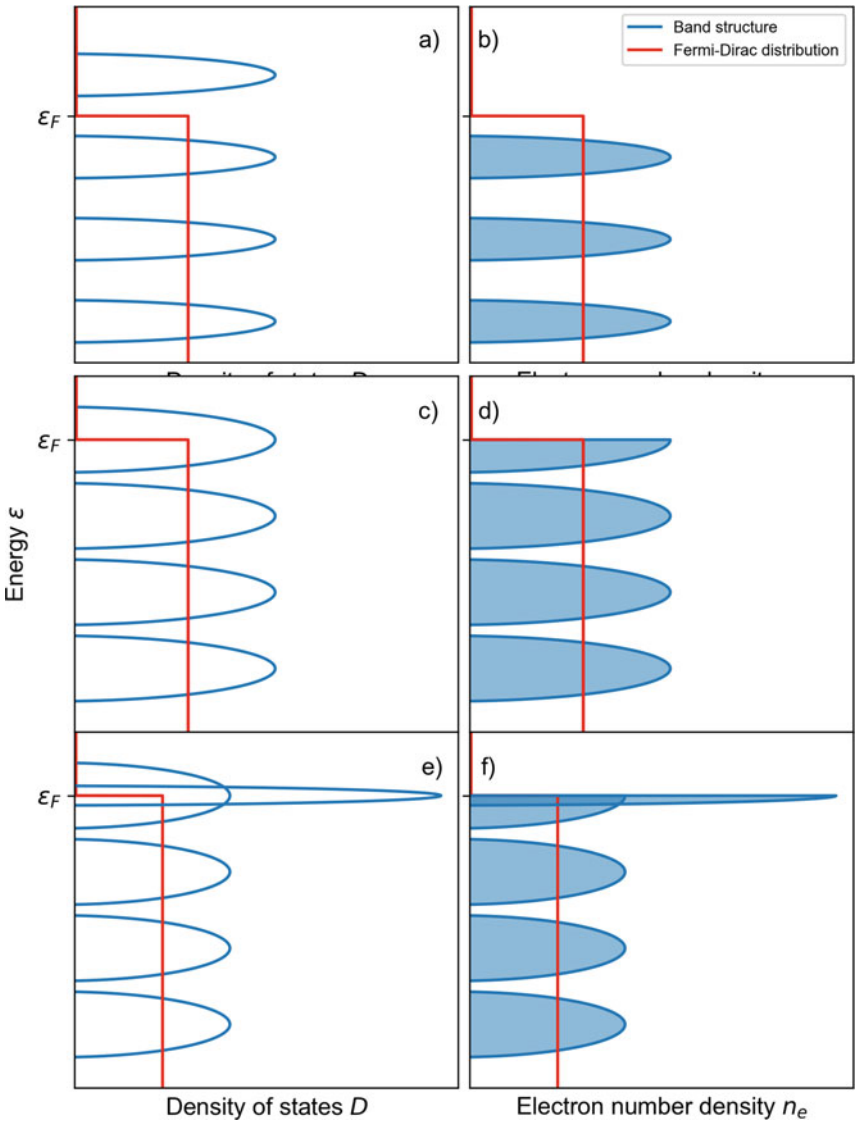

Fig. 11.6 Band structure with density of states $D(\epsilon)$, Fermi–Dirac distributions, and electron number density n_e for insulators with even number of electrons (**a**, **b**), metals with uneven number of electrons (**c**, **d**), and metals with even number of electrons and two overlapping bands (**e**, **f**)

can be described by this model. In general, the half-populated band is called the **conduction band (CB)**.

But also crystals with **even atomic number** Z can feature at $T = 0$ K **metallic** character in case two **energy bands overlap completely** in the regime around the Fermi energy ϵ_F, sharing each half of the electrons per band, see Fig. 11.6e. In the overlapping regime of the two bands energy states as well for the one as for the other band exist. In case, the atomic number of the atoms is even, one full band results. Each band will be half-populated following the Pauli principle until the Fermi energy is reached, see Fig. 11.6f. This class of conductors are represented by alkaline earth metals, like zinc ($Z = 50$), tungsten ($Z = 74$), or platinum ($Z = 78$). For totally overlapping bands, both bands will be half-populated, as shown in Fig. 11.6f, and can be described as one band with a doubled density of states representing a crystal with an uneven atomic number. Also, the partially populated band here is called the conduction band.

For **little overlapping bands** in crystals at $T = 0$ K only a small number of electrons is given in the conduction band. As one can imagine qualitatively, increasing the temperature will increase the probability of the electrons to reach higher energy levels, thereby increasing the number of electrons in the conduction band. This class of crystals is called **semi-metals**.

The conduction band features the same properties like a free electron gas, i.e. the Fermi gas. So it is expected to find the same optical behavior of quasi-free electrons interacting with phonons in a crystal, as described later in the Sect. 12.6.

11.2.2 Crystals at Higher Temperatures

Increasing the temperature of a fermionic system results in a non-step like Fermi–Dirac distribution, see Sect. 9.3.2. Consequently, the population distribution in crystal bands will change too.

Starting from an **insulator** featuring a large band gap ΔE and the Fermi energy ϵ_F at half band gap between two bands, increasing the temperature results in a broadened Fermi–Dirac distribution, see Fig. 9.8. But, as the change in probability from 1 to 0 is given in an energy range $[-k_B T, k_B T]$, as long as the band gap is larger than the thermal energy

$$\Delta E \gg k_B T,$$

nothing changes quantitatively at the final energy distribution of the electrons in the crystal. The valence band will remain completely populated and the conduction band stays empty, see Fig. 11.7a, b.

> Increasing the temperature of an insulator will not change its electrical properties, and in consequence, also not the optical properties.

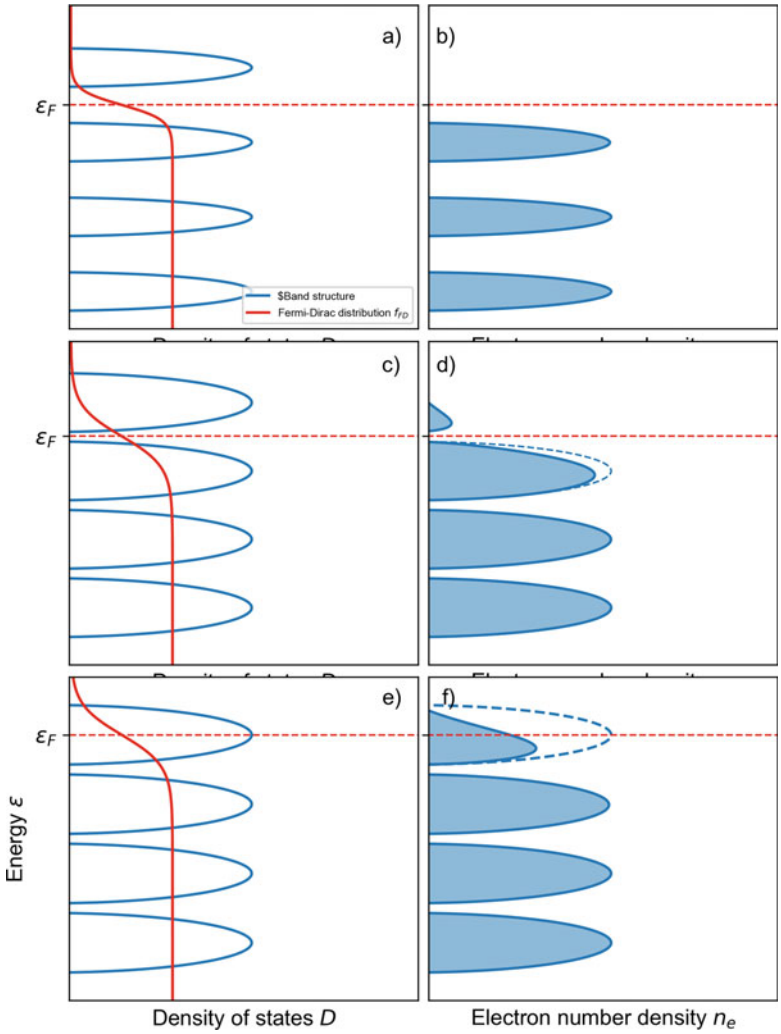

Fig. 11.7 Fermi–Dirac distributions, density of states $D(\epsilon)$ and electron number density distribution for insulators (**a**, **b**), semiconductor (**c**, **d**), and metals (**e**, **f**) at high temperatures

Moving on to other crystals, reducing the band gap into the regime

$$\Delta E \approx k_\mathrm{B} T,$$

changes the situation dramatically. When the temperature gets larger, some states in the valence band are not populated anymore, but however, some states in the conduction band will now be populated, see Fig. 11.7c, d. It is important to remember that this crystal feature any electron in the conduction band at the absolute zero

temperature: one cannot distinguish these materials, insulators or conductors, as the excitation into the conduction band and the electrical conductivity changes only with increasing temperature. This class of crystals are called **semiconductors**. Electrical conductivity is given when energy bands are not fully populated. So we have in case of semiconductors two energy bands featuring conductivity, the valence band and the conduction band. In the case of the conduction band, we have some electrons given there so that these electrons drive the electrical conductivity. Differently, in the valence band now some electrons are missing, see Fig. 11.7d, so that holes are given. As a consequence, a hole-driven electrical conductivity results.

> Increasing the temperature of a semiconductor will increase its conductivity given by electrons and holes.

Finally, **metals** featuring a band structure with the Fermi energy placed within a band will result in a more populated conduction band at higher temperatures than at $T = 0$ K, see Fig. 11.7e, f. Compared to metals at $T = 0$ K, at higher temperatures, some electronic states in the conduction band below the Fermi energy are not populated, allowing in principle, an **interband excitation** of electrons between two bands, see for further reading Sect. 12.5.3.

11.2.3 Electrons and Holes in Semiconductors

As shown in Sect. 9.3.3, one can calculate for semiconductors the density of states of the **free electrons in the conduction band** close to the band edge by shifting the energy zero point at the bottom energy edge of the conduction band and by shifting the chemical potential

$$\epsilon' = \epsilon - \epsilon_{\mathrm{cb}} \qquad \mu'(T) = \mu(T) - \epsilon_{\mathrm{cb}}, \tag{11.4}$$

getting the electron density of states to

$$D_{\mathrm{e}}(\epsilon') = \frac{\sqrt{2}Vm^{3/2}}{\pi^2\hbar^3}\sqrt{\epsilon'}.$$

Holding in mind that due to the little number of electrons, i.e. little electron density n_{e} in the conduction band of semiconductors, the Fermi-Dirac distribution is given by

$$f_{\mathrm{FD}} \approx e^{-\epsilon'/(k_{\mathrm{B}}T)} e^{\mu'(T)/(k_{\mathrm{B}}T)} = f_{\mathrm{FD}}^{\mathrm{sc}},$$

as shown in (9.52), with the chemical potential at low electron densities in the conduction band given by (9.49) with $\mu'(T) \ll k_{\mathrm{B}}T$ and the effective density of states D_0, see (9.36).

The **energy distribution of the electrons** for semiconductors, or the so-called electron number density, using (11.3) and (9.53), gets now to

$$N_{\epsilon'}(\epsilon) = 4\pi N_e m_e \frac{(2m_e(\epsilon - \epsilon_b))^{1/2}}{(2\pi m_e k_B T)^{3/2}} \exp\left(-\frac{\epsilon - \epsilon_b}{k_B T}\right),$$

and is shown in Fig. 11.7d. The **overall number of electrons in the conduction band** is calculated by integration of the electron number density

$$N_e = \int_{\epsilon_b}^{\infty} N_{\epsilon'}(\epsilon) d\epsilon = \int_0^{\infty} D_\epsilon(\epsilon') f_{FD}^{sc}(\epsilon') d\epsilon'. \tag{11.5}$$

In a strict sense, the integration should be done in the range from the bottom to the top of the conduction band. But, as the Fermi–Dirac distribution for semiconductors gets very small at the top of the conduction band, the integration limits can be expanded to infinity.

One can see that the energy distributions represents a Maxwell–Boltzmann distribution, as shown in Figs. 11.7d and 11.8b. Using the known relation (9.49), we calculate the chemical potential for electrons close to the bottom edge of the conduction band

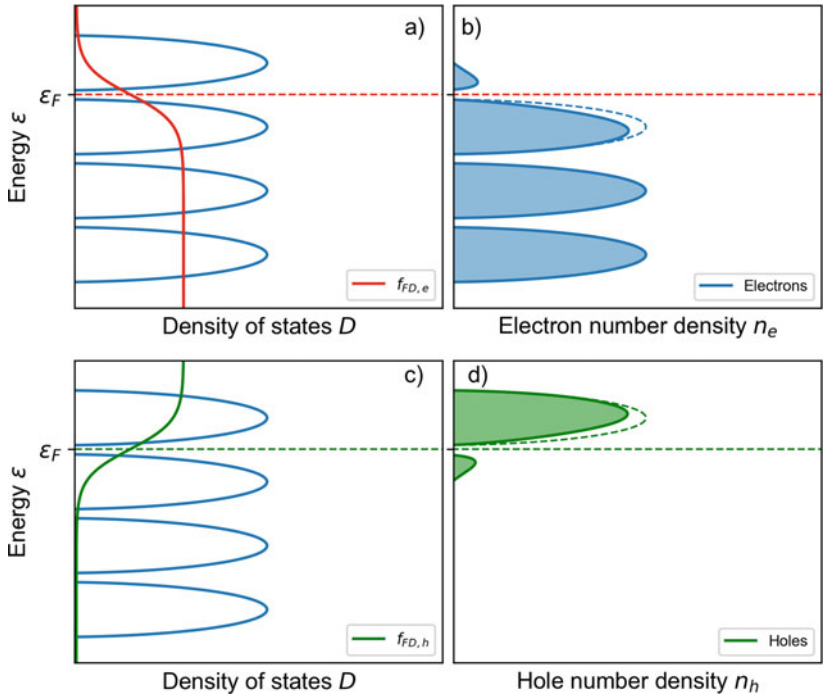

Fig. 11.8 Fermi–Dirac distributions, density of states $D(\epsilon)$ and number density distribution for electrons (**a**, **b**) and for holes (**c**, **d**) in a semiconductor

$$\mu'(T) = k_\mathrm{B} T \ln \frac{N_\mathrm{e}/V}{D_0} = k_\mathrm{B} T \ln \frac{n_\mathrm{e}}{D_0},$$

and converting it to the electron density n_e one gets

$$n_\mathrm{e} = D_0 \exp\left(\frac{\mu'}{k_\mathrm{B} T}\right), \tag{11.6}$$

with μ' representing the symmetry point of the Fermi-Dirac distribution, i.e. the chemical potential at the bottom edge of the conduction band. **Ideal semiconductors** feature as much electrons in the conduction band as holes in the valence band, so that one can write for the symmetry point in general

$$\mu = \frac{\epsilon_\mathrm{cb} + \epsilon_\mathrm{vt}}{2},$$

with the energy at the bottom of the conduction band ϵ_cb, and at the top of the valence band ϵ_vt. Transferring the zero point to the bottom of the conduction band using the (11.4), we get chemical potential at the bottom edge of the conduction band

$$\mu' = -\frac{\epsilon_{cb} - \epsilon_{vt}}{2}. \tag{11.7}$$

With (11.6) and (11.7), the **overall electron density in the conduction band** now reads as

$$\begin{aligned} n_\mathrm{e} &= D_0 \exp\left(-\frac{\epsilon_\mathrm{cb} - \epsilon_\mathrm{vt}}{2 k_\mathrm{B} T}\right) \\ &= \frac{1}{4}\left(\frac{2 m_\mathrm{e} k_\mathrm{B} T}{\pi \hbar^2}\right)^{3/2} \exp\left(-\frac{\epsilon_\mathrm{cb} - \epsilon_\mathrm{vt}}{2 k_\mathrm{B} T}\right) \end{aligned}$$

Overall electron density in semiconductors

$$n_\mathrm{e} = \frac{1}{4}\left(\frac{2 m_\mathrm{e} k_\mathrm{B} T}{\pi \hbar^2}\right)^{3/2} \exp\left(-\frac{\Delta E}{2 k_\mathrm{B} T}\right), \tag{11.8}$$

expressing the direct dependence of the electron density to the band gap, given by

Band gap

$$\Delta E = \epsilon_\mathrm{cb} - \epsilon_\mathrm{vt}. \tag{11.9}$$

Now, considering the **valence band featuring a nearly full band**, see Fig. 11.8b, the electrical conduction takes there place by the movement of the electrons, i.e. the excitation of the electrons into the little number of non-populated states within

the valence band. A moving electron will leave an unpopulated energy state, so that another electron can also move, and so on. Thus, charge transfer in an almost populated band is achieved by the movement of electrons, which corresponds to the movement into the opposite direction of non-populated states, the **defect electrons**, or the so-called **holes**.

The probability that an energy state is non-populated by an electron, or that a state is populated by a hole, is given by the complement of the Fermi–Dirac distribution for the population of an energy state by an electron

$$f_{\mathrm{FD,h}}(\epsilon) = 1 - f_{\mathrm{FD}}^{\mathrm{sc}}(\epsilon). \tag{11.10}$$

Therefore, for the non-populated states of the valence band holes are given, and a flipped Maxwell–Boltzmann distribution will be given, analogous to the electron energy distribution in the conduction band, see Fig. 11.8d.

The energy distribution for the holes of a semiconductor is calculated analogous to the electrons in the conduction band, using the complement function of the Fermi–Dirac distribution (11.10) at the symmetry point given by the chemical potential

$$\mu = \frac{\epsilon_{\mathrm{cb}} - \epsilon_{\mathrm{vt}}}{2}.$$

Using the density of states for the top energy edge, see (11.2), and replacing the top edge energy of the valence band by $\epsilon_{\mathrm{t}} = \epsilon_{\mathrm{vt}}$ one gets the **energy distribution of the holes** by

$$N_{\mathrm{h}}(\epsilon) = 4\pi N_{\mathrm{h}} m \frac{(2m(\epsilon_{\mathrm{vt}} - \epsilon))^{1/2}}{(2\pi m k_{\mathrm{B}} T)^{3/2}} \exp\left(-\frac{\epsilon_{\mathrm{vt}} - \epsilon}{k_{\mathrm{B}} T}\right),$$

representing again a Maxwell-Boltzmann distribution for the holes at the top edge of the valence band.

Equivalent to the electrons in the conduction band, we get the number density of holes in the valence band by integration, compare with (11.5). Again, within an **ideal semiconductor** the number of holes in the valence band is equal to the number of electrons in the conduction band, describing the **condition of electrical neutrality** with the density of the electrons and hole given by $n_{\mathrm{e}} = N_{\mathrm{e}}/V$ and $n_{\mathrm{h}} = N_{\mathrm{h}}/V$ reproducing (11.8),

Electron and hole density of semiconductors

$$n_{\mathrm{h}} = n_{\mathrm{e}} = \frac{1}{4}\left(\frac{2m_{\mathrm{e}} k_{\mathrm{B}} T}{\pi\hbar^2}\right)^{3/2} \exp\left(-\frac{\Delta E}{2k_{\mathrm{B}} T}\right). \tag{11.11}$$

11.2.4 Electrons in the Conduction Band of Metals

Assuming now **conductors**, i.e. metals with a half-populated upper energy band, the Fermi energy is located in the middle of this band, see Fig. 11.9. In the case of metal atoms without band overlapping and uneven atomic number the number of electrons per atom is set to one, or in the other case of two fully overlapping energy bands two electrons per atom for metal atoms are assumed. In the consequence, the number of electrons in the conduction band is given in the order of magnitude of the number of atoms in the metallic crystal, and results for copper in a large electron density of $n_e = 8.45 \cdot 10^{28}\,\mathrm{m}^{-3}$.

As shown in the Sect. 9.3.2, the Fermi-Dirac distribution

$$f_{\mathrm{FD}}(\epsilon) = \frac{1}{\exp\left(\frac{\epsilon-\mu(T)}{k_B T}\right)+1},$$

features due to the large electron densities a chemical potential nearly equal to the Fermi energy $\mu(T) \approx \epsilon_F$, and is shown in Fig. 11.9, too.

The energy distribution is again given by (11.3) and using the density of states given by the bottom edge of the conduction band, being equal to the bottom edge energy of the conduction band ϵ_{cb}

$$D_e(\epsilon) = \frac{\sqrt{2}Vm^{3/2}}{\pi^2\hbar^3}\sqrt{\epsilon-\epsilon_{cb}},$$

we can shift again the energy zero and chemical potential to

$$\epsilon' = \epsilon - \epsilon_{cb} \qquad \mu'(T) = \mu(T) - \epsilon_{cb},$$

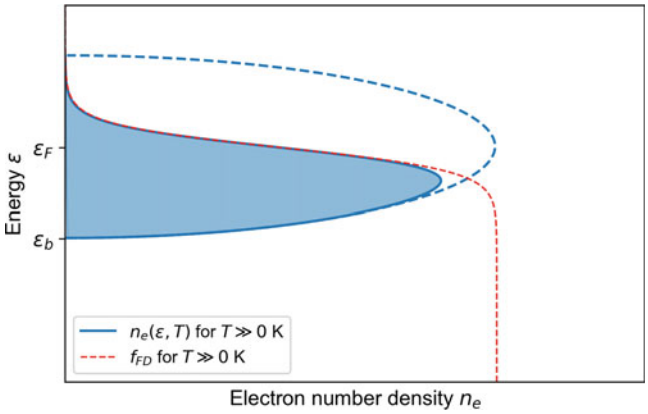

Fig. 11.9 Fermi-Dirac distribution (red dotted line), density of states $D(\epsilon)$ (blue dotted line), and energy density distribution for electrons in the conduction band of metals (blue area)

getting the energy distribution for the electrons in the conduction band to

$$N_{\epsilon'}(\epsilon') = \frac{2Vm^{3/2}}{\pi^2\hbar^3} \frac{\sqrt{\epsilon'}}{\exp\left(\frac{\epsilon'-\mu'(T)}{k_B T}\right)+1}.$$

The energy density distribution of the electrons $n_e = N_{\epsilon'}/V$, i.e. the number density of electron in the energy interval ϵ' to $\epsilon' + d\epsilon'$, is equivalent to the one of a free electron gas, when the energy zero point is positioned to the bottom edge of the conduction band, compare Fig. 11.9 with Fig. 9.8b, and (9.46).

11.3 Band Structure and Dispersion Relation in Crystals

Assuming a metallic crystal with periodically aligned atoms of same type, each atom delivering one to two free electrons, one can depict in one spatial dimension at the places of the atoms its potentials, see Fig. 11.10. The electrons in the conduction band are nearly free and can be described, in first approximation, as a free electron gas, see Sect. 9. The wave function for each electron is there approximated by a plane wave,

$$\psi(\boldsymbol{r}, \boldsymbol{k}) = \psi_0 e^{i\boldsymbol{k}\cdot\boldsymbol{r}}.$$

As shown in solid state physics [1], the wave function of a free electron (or many non-interacting free electrons) interacts with the periodic potentials of the atoms in the

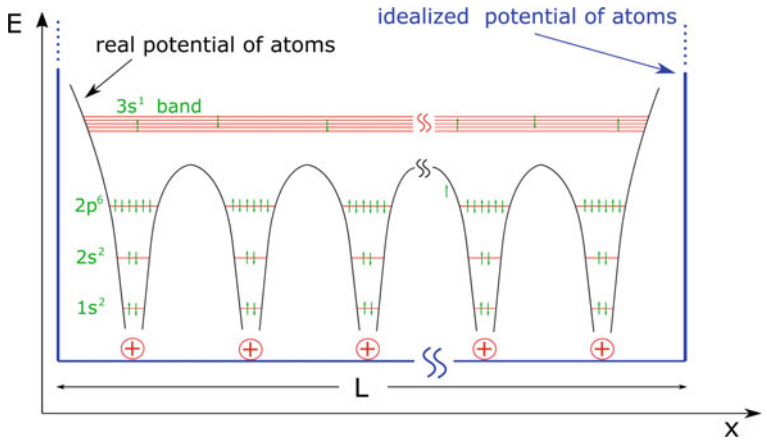

Fig. 11.10 Periodic potentials within a crystalline solid state material, here Sodium (Na) with the outer electrons representing a conduction band. There, electrons can be described, in first approximation, as free electrons

crystal, and as a consequence, the electron wave function is scattered at the potential borders. As a first approximation, each potential of the atoms can be approximated by box potentials, the so-called Kronig-Penney model.[3]

Analogous to the diffraction of X-ray at periodically aligned atoms in crystals, the electron wave function is diffracted at the atomic potentials following the **Bragg relation**. It describes the diffraction of an incoming wave featuring the wave numbers $\boldsymbol{k}$ at periodical potential of atoms in a crystal, featuring a layer separation d, and resulting in a reflected wave with the wave number $\boldsymbol{k}'$. The Bragg relation is given by the **vector for the reciprocal lattice** $\boldsymbol{G}$, and written

Bragg relation

$$\boldsymbol{G} = \boldsymbol{k} - \boldsymbol{k}', \tag{11.12}$$

and representing the **reciprocal lattice distance**

$$|\boldsymbol{G}| = G = \frac{2\pi}{d}. \tag{11.13}$$

of the separation d between successive layers of atoms. Knowing the position of the atoms in the crystal given by lattice vectors $\boldsymbol{a}_1, \boldsymbol{a}_2, \boldsymbol{a}_3$ one can biuniquely determine the reciprocal lattice vector $\boldsymbol{G}$ (see solid state text books, e.g. [1]).

A solution for the wave function of the electrons in a periodic potential is called the **Bloch function** ψ, and the corresponding electrons are referred to as **Bloch electrons**. These Bloch electrons have a fixed phase correlation with the periodicity of the reciprocal lattice G along the whole crystal.

Assuming now a one-dimensional crystal featuring periodically aligned atoms in the x-direction, and allowing only a free propagation of the electrons in the same direction, we can conclude that a wave function of an electron given by the wave number $\boldsymbol{k}$ will be diffracted in the opposite direction $\boldsymbol{k}'$ with $\boldsymbol{k} = -\boldsymbol{k}'$, due to the Bragg relation, (11.12), see Fig. 11.11. The smallest diffracted wave number $\boldsymbol{k}_{\mathrm{Br}}$ defined the **first Brillouin zone**.

As one can see in the figure, the electron wave function being deflected at the first Brillouin zone defines the two **Brillouin wave number vectors**

$$\boldsymbol{k}_{\mathrm{Br}} = \frac{1}{2}\boldsymbol{G} \quad \text{and} \quad \boldsymbol{k}'_{\mathrm{Br}} = -\frac{1}{2}\boldsymbol{G},$$

representing two counter-propagating, and in consequence also interfering waves, generating a **standing wave**. Mathematically, we can describe the interference by adding or subtracting the two waves getting two solutions of the Schrödinger equation for the standing waves

[3] https://lampx.tugraz.at/~hadley/ss1/KronigPenney/KronigPenney.php.

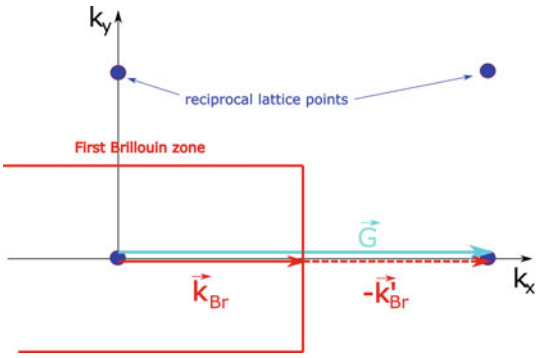

Fig. 11.11 Representation of the Bragg relation in k_x direction

$$\psi^+ \propto e^{i\boldsymbol{k}_{\mathrm{Br}}\cdot\boldsymbol{r}} + e^{i\boldsymbol{k}'_{\mathrm{Br}}\cdot\boldsymbol{r}} \qquad \psi^- \propto e^{i\boldsymbol{k}_{\mathrm{Br}}\cdot\boldsymbol{r}} - e^{i\boldsymbol{k}'_{\mathrm{Br}}\cdot\boldsymbol{r}}$$
$$\propto e^{i\frac{G}{2}\cdot x} + e^{-i\frac{G}{2}\cdot x} \qquad \propto e^{i\frac{G}{2}\cdot x} - e^{-i\frac{G}{2}\cdot x}$$

Now, the probability density functions can be calculated

$$\left|\psi^+\right|^2 \propto \cos^2\left(\frac{G}{2}x\right) \text{ and}$$
$$\left|\psi^-\right|^2 \propto \sin^2\left(\frac{G}{2}x\right),$$

and one determines the maximal probability of the electron being in the first case

$$\left|\psi^+\right|^2 : \quad x_{\max} = \frac{2\pi n}{G}, \qquad n = 0, 1, 2, \ldots$$

being located at the position of the atoms, see Fig. 11.12. This electron wave function interacts stronger with the potential of the atoms resulting in an overall energy of the electron being not only described by the kinetic energy, but also by some energy resulting from the potential of the atoms, e.g. $E = E_{\mathrm{kin}} + E_{\mathrm{pot}}$.

In the second case, the probability density function $\left|\psi^-\right|^2$ gets maximal at the first Brillouin zone, and minimal at the position of the atoms, see Fig. 11.12

$$\left|\psi^-\right|^2 : \quad x_{\max} = \frac{\pi(2n+1)}{G}, \qquad n = 0, 1, 2, \ldots$$

This electron wave functions interact much less with the potential of the atoms, and the overall energy of the electrons will be mostly of kinetic type, $E = E_{\mathrm{kin}}$.

So, the electrons featuring a Brillouin wave number $\boldsymbol{k}_{\mathrm{Br}}$ are deflected and feature a maximal probability with different energies. This means that electrons at the Brillouin zones have two energies: we observe an **energy splitting**.

Without going to much in details, we can conclude that the electrons within a conduction band feature energies being proportional to $E \propto k^2$, like a free electron

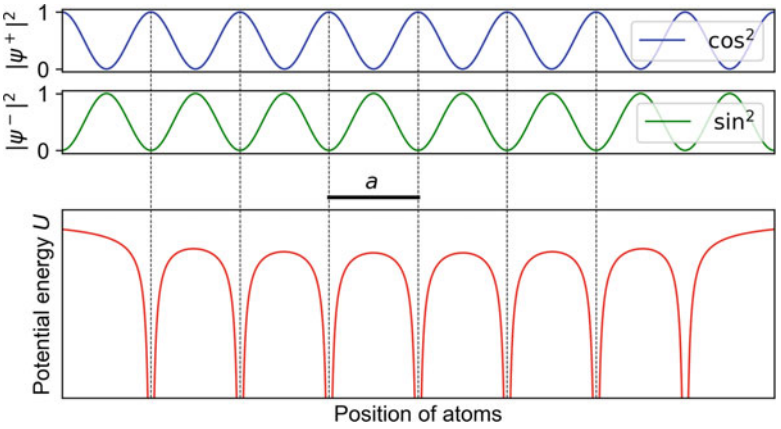

Fig. 11.12 Probability density functions $\left|\psi^{\pm}\right|^2$ of the wave functions at the Brillouin wave number $\boldsymbol{k}_{\mathrm{Br}}$ (top), and corresponding one-dimensional potential distribution for seven atoms (bottom)

gas, as long as the wave number is not close or equal to the Brillouin wave number vector $\boldsymbol{k}_{\mathrm{Br}}$. Electrons with wave numbers equal to $\boldsymbol{k}_{\mathrm{Br}}$ are deflected, resulting in two different standing waves at two different energies.

The dispersion relation of the free electron gas has to be modified at these wave numbers equal to the Brillouin wave vector, depicting there a splitting into two energies, see the **band structure plot** in Fig. 11.13.

As at $\boldsymbol{k}_{\mathrm{Br}}$ the wave functions represent standing waves, no wave propagation is given there resulting in a vanishing group velocity $v_{\mathrm{g}} = 0$, see (1.97). This results in a horizontal rising of the dispersion relation at the Brillouin zone, i.e. for $\boldsymbol{k} = \boldsymbol{k}_{\mathrm{Br}}$

$$\left.\frac{\partial \epsilon}{\partial k}\right|_{k=k_{\mathrm{Br}}} = \hbar \left.\frac{\partial \omega}{\partial k}\right|_{k=k_{\mathrm{Br}}} = \hbar v_{\mathrm{g}} \equiv 0. \tag{11.14}$$

In order to get a consistent functional description, the dispersion relations has to be adapted, to merge at the Brillouin zones with the condition of (11.14), and are shown in Fig. 11.13. Also the electron number density, the so-called electron density of states are plotted there, depicting the energetic location of the electron states. The band structure plot is consistent with the energy bands and energy gaps described in Sect. 11.1.

Thus, the energetic states of the Bloch electrons are named **extended states**, and it is sufficient to describe the energy of the electrons only for the first Brillouin zone between $k_x \leq k_{\mathrm{Br}}$. The resulting energy of all electrons together with the forbidden values of the dispersion relation ϵ represents the band structure with the energy bands and energy band gaps ΔE. Therefore, the highest occupied band is the valence band (VB) and the lowest unoccupied band is the conduction band (CB), with the band gap energy, in case both bands are separated.

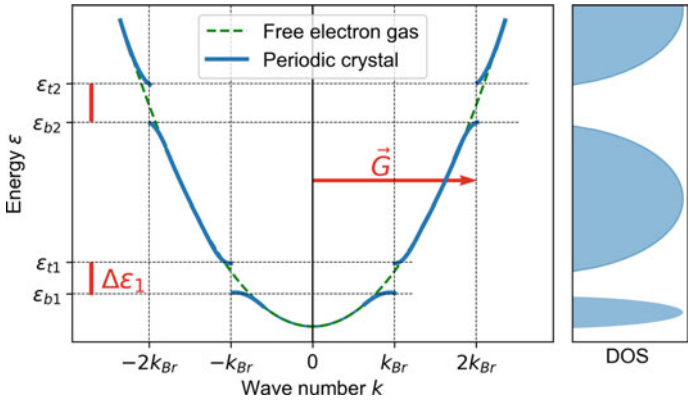

Fig. 11.13 Band structure plot with band splitting due to Bragg reflection of electronic standing waves with resulting band gaps located at the the first and second Brillouin zones (left), and density of states as function of the energy (right)

11.4 Non-crystalline Matter

The previously described band theory is based on a very fundamental property of most condensed matter, to align the atoms or molecules very periodically within the solid. This is true for nearly all metals, most semiconductors, and many dielectrics.

But, in nature also non-periodical solids exist, which like liquids feature no high symmetry by the periodical positioning of atoms in crystals. Typical solids with **no periodicity** are **glasses** or **polymers**, where one can distinguish between short-range and long-range order. In crystalline-condensed matter both orders are given, meaning that the periodicity is given for the short-range representing the region of some atoms closed to each other, and the long-ranges representing scales in the micrometer scale. Totally amorphous glasses feature short-range orders, but no long-range order at all.

Here a short sketch to **disordered matter** is given.[4] Contrary to crystals, see Fig. 11.14a, where the atoms are periodically arranged, for disordered matter, also called **amorphous materials**, the bond lengths and angles between the atoms vary strongly, resulting in a disordered atomic arrangement.

As shown in Sect. 11.1, in a crystalline dielectric or semiconductor, the density of states $D(\epsilon)$ of the electrons in the valence and conduction bands can approximately be described by a bell-shaped distribution, see Fig. 11.14b, c. Because the interaction with the periodic potential changes the energy of the electrons, also seemingly it changes the mass of the electrons, and an effective mass is assigned to the electrons

[4] The following discussion have bee extracted from [4]. I want to thank Dr. Theo Pflug for his very intense assistance during the generation of this book.

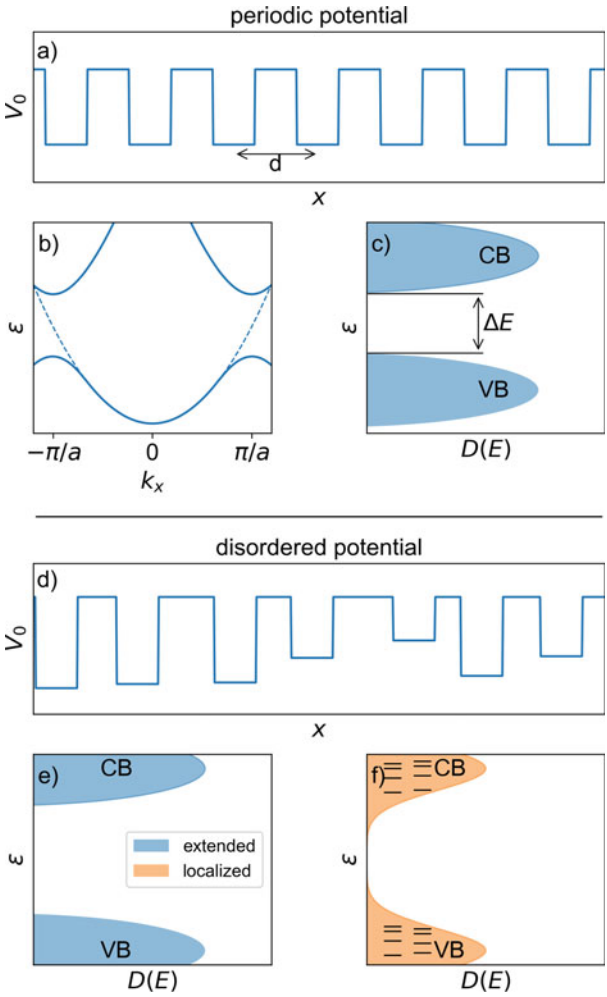

Fig. 11.14 **a** Scheme of an one-dimensional periodic potential $V_0(x)$ according to the Kronig-Penney model with the lattice constant a; **b** Dispersion relation $\epsilon(k)$ of a free electron gas (blue dashed graph), and an electron interacting with a periodic potential with the lattice constant a (blue solid graph); **c** Schematic energy band of the extended states of electrons in a periodic potential represented by the density of states $D(E)$, with the energy band gap ΔE between the valence band (VB) and the conduction band (CB); **d** Scheme of a partially disordered one-dimensional potential $V_0(x)$; **e** densities of states for a disordered potential with extended and localized states; **f** density of states of a completely disordered material [4]

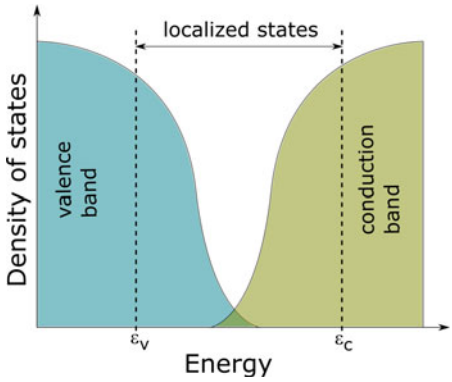

Fig. 11.15 Density N(E) of electronic states in partially disordered matter. The states between ϵ_v and ϵ_c are localized states

Effective mass of an electron

$$m^*_{e,k_x} = \hbar^2 \left(\frac{\partial^2 \epsilon}{\partial k_x^2} \right)^{-1}, \tag{11.15}$$

depending on the curvature of the corresponding dispersion relation $\epsilon(k)$.

In disordered matter each electron interacts with different potentials in its vicinity (Fig. 11.14d). Thus, no fixed phase correlation of the wave functions of the electrons along the material exists, which results in the formation of **localized energetic states**.

In consequence, the periodical potential as well as the wave functions of the electrons are no longer spatially invariant and cannot be characterized by a wave number vector $\boldsymbol{k}$, as in a crystalline material [5]. The disordered material can then only be described by a density of states D_ϵ, since the electrons cannot be assigned to a specific dispersion relation $\epsilon(k)$. Depending on the degree of disorder, which is approximately defined by the ratio of the width of the Bloch states and the spread of the width of the potentials [5], extended and localized states can overlap, resulting in a bell-shaped density of states with exponential tail states, so-called **Urbach tails** (Fig. 11.14e). A complete molecular disorder leads to vanishing continuous extended states and a discrete Gaussian density of states distribution results (Fig. 11.14f). Consequently, disordered matter features in comparison to crystals a lower polarizability and thus a smaller dielectric constant (see [4]), due to the strong Coulomb interaction of the electrons with the surrounding ions forming the localized states.

Though, in **partially disordered matter** valence and conduction bands can still be identified. These bands have delocalized electronic states, meaning that electrons in the conduction band and holes in the valence band can move, but with much lower mobility than in the corresponding bands of crystalline matter, as the localized states interact with them. The highest energy level in the valence band is now defined by the mobility edge ϵ_v, see Fig. 11.15. For energies $\epsilon_c > \epsilon > \epsilon_v$, the states are localized, which means that the charge carriers are "trapped" and cannot move freely.

For energies above ϵ_v, one speaks about the valence band tail, where the density of states $D(E)$ decreases exponentially. Thereby, the slope of the tail is given by the Urbach energy ϵ_v^0 and is a measure for the disorder in the amorphous matter; the higher the value of ϵ_v^0, the higher the disorder. The Urbach energy ϵ_v^0 can be evaluated by measuring the optical absorption coefficient $\alpha(\epsilon)$ as a function of the photon energy, and applying the so-called **Tauc plot**

$$\alpha(\epsilon) = \alpha_0 \exp\left(\frac{\epsilon - \epsilon_1}{\epsilon_v^0}\right),$$

by approximating an exponential function to the absorption coefficients with the fitting constants α_0 and ϵ_1. Due to the capture and recombination kinetics, states in the **valence band tail** do not play any role as recombination centers, but act as **traps** for the free holes. These trapped holes constitute a positive charge that can deform and reduce the internal electric field.

At higher energies the electrons are located in the conduction band tail up to ϵ_c, where the density of states $N(E)$ also follows an exponential law. As the conduction band tail is often, especially for semiconductors, much less-pronounced than the valence band tail, it does not play generally any great role. The electrons trapped within the conduction band tail do not noticeably deform the electric fields and so its potentials. The range $\epsilon_v < \epsilon < \epsilon_c$ featuring localized states is called **mobility gap** and are represented by the Urbach tails of the valence and bands.

References

1. C. Kittel, *Introduction to Solid State Physics*, 9th Ed. (Wiley, 2018)
2. G. Tse, Yu. Dapeng, The first principle study of electronic and optical properties in rhombohedral $BiAlO_3$. Mod. Phys. Lett. B **30**(03), 1650006 (2016)
3. http://dipc.ehu.es/frederiksen/inelastica/index.php/Au_FCC
4. T. Pflug, Strong field excitation of electrons into localized states of fused silica. Ph.D. Thesis, Technische Universität Chemnitz, 2022
5. C.F. Klingshirn, *Semiconductor Optics* (Springer, Berlin, Heidelberg, 2012). https://doi.org/10.1007/978-3-642-28362-8

Chapter 12
Linear Absorption

Abstract As the extinction coefficient of matter gets significantly large, the electromagnetic radiation is absorbed by the solid. In the subsequent sections, we will look at the linear absorption of radiation, being one standard process for heating matter using electromagnetic radiation. We differentiate for linear absorption between electronic and molecular excitations in solids. So, in case of an electronic excitation, electrons are excited by linear absorption from the valence into the conduction band, the so-called interband excitation, resulting in quasi-free electrons. Molecular excitation is given when specific frequencies are selected, exciting vibronic states in a band in condensed matter, so-called intraband excitation. Linear absorption is defined as the generation of an excited electron via intraband or interband excitation by absorption of one photon. When free charges are given, like in metals or in an electron plasma, then linear absorption takes place by an intraband excitation too.

12.1 Absorption in Condensed Matter

As we have seen in Chap. 11, the discrete electronic energy states of single atoms are transformed in quasi-continuous energy bands, when a large number of atoms condense into a solid. Especially, for periodically arranged atoms in solids, one speaks about a crystalline state, or about crystals.

It is important for the excitation process of solid matter by photons, the so-called absorption, to distinguish between an excitation of an electron from a valence band into a conduction band, the so-called **interband excitation**, from an excitation within one band, usually represented by a semi-populated conduction band, or a transient semi-populated valence band. In that case, one speaks about an **intraband excitation**. Here is to mention that in literature, no strong difference is given for excited or non-excited (at rest) matter, resulting in some ambiguity in the definitions. Also, in metals, all valence and conduction bands of different electronic states are treated as distinct bands, whereas in dielectrics, very often all states with full bands are treated as one valence band.

In the previous section, we have seen that depending on the population of the outermost bands of a crystal, one determines at least one fully-populated valence

© Springer Nature Switzerland AG 2022

A. Horn, *The Physics of Laser Radiation–Matter Interaction*,
https://doi.org/10.1007/978-3-031-15862-9_12

band. Depending on the matter state at the temperature $T = 0$ K, the valence band is fully populated by electrons, the conduction band is empty, and a band gap between valence and conduction band is possibly given. In case the band gap is about some few electronvolts (eV), the crystal represents a dielectric, or **insulator**. An excitation by visible electromagnetic radiation or by thermal electromagnetic radiation is not possible, resulting in a **non-electrical-conducting material**, and also in an **optical transparent material** for photon energies smaller than the band gap energy. These materials are used in linear optics for optical systems like lenses, glass plates, prisms, and so on, see Chap. 7.

In case the band gap between valence and conduction band is in the range of 1 eV or less, one speaks about a **semiconductors**. Although at $T = 0$ K the conduction band is empty, and insulator properties results, excitation of electrons with low energy photons from the valence band into the conduction band due to the small band gap gets now probable. So, an optical excitation with visible radiation is given, changing its optical properties crucially.

We summarize that condensed matter featuring a band gap between the valence and the conduction band is called dielectrics or semiconductors. Depending on the gap width, one distinguishes

- Insulators, or dielectrics with a band gap width larger 4 eV, and
- Semiconductors with a band gap width between 0.1 and 4 eV.

As the photon energy gets larger than the band gap, photo-excitation becomes probable inducing free and quasi-free electrons. The following processes after the generation of the free electrons can be much more complicated, as these charges must not recombine with the ionized atoms of the solid, but can form different transient states:

- **Free and quasi-free electrons** are moving within a specific volume, mostly defined by the excitation volume, e.g. the focal volume. These electrons can diffuse out of the volume, can interact with each other, as described more in detail later, and depending on the dielectrics, recombine within a time scale of some nano- to microseconds.
- The charges can reallocate between the atoms in the solid forming **self-trapped excitons** (STE). These STE can feature a transient lifetime, but also can be very stable over long periods of time, representing a meta-stable state.

In case the conduction band is partially populated with electrons, even at the temperature $T = 0$ K, and one speaks about **conductors**, or **metals**. Here an intraband excitation of the electrons for every photon energy is possible. The electrons in the conduction band can be described in first approximation by free or quasi-free electrons, an electron gas, or a plasma.

A crystal being heated up quickly and strongly, especially induced by **laser radiation** forming a **non-equilibrium state** between the electron and the phonon system,

features broadened Fermi distributions for the valence and conduction bands, allowing additional or alternative excitation paths. For example, as shown previously in Sect. 11.2.4, the conduction band of a metal consisting of hot electrons, i.e. fermions at high temperatures, features non-populated states closely below the Fermi energy. These states represent absorption bands, and makes now intraband excitation accessible, like **inverse bremsstrahlung**.

The absorption coefficient α is determined via the dielectric function $\epsilon(k)$, i.e. the relative permittivity $\tilde{\epsilon}_r$ given in general by the (6.35) and (6.36). But as dielectrics feature no, or a very little number of linear-absorbing particles, like free electrons or defects situated between the band gap, the approximations for the complex refractive index given by (6.33) and (6.34) holds.

Firstly, we discuss the interband excitation and then move further to the intraband excitation.

12.2 Interband Excitation

Assuming a crystal with a full valence band and an empty conduction band, i.e. an insulator or a semiconductor at low temperatures, we describe now the interband excitation, also called interband absorption.

An interband excitation gets only probable by linear absorption, i.e. excitation by one photon, when the photon energy is larger than the band gap energy

$$E_\gamma \geq \Delta E_{\text{gap}},$$

see Fig. 11.13. When we adopt this process to the band model, as described in Sect. 11.2, and holding in mind that a **photon features no mass**, so no impulse, and consequently also no wave number is given, and the excitation of an electron from the valence band into the conduction band is purely described in the band model by a **vertical shifting** of the electron energy by **absorption of one photon** (Fig. 12.1). In that way, the **energy conservation** is fulfilled.

12.2.1 Reduced Band Structure Plot

One can see in the Fig. 12.1 that the excitation ends not on the conduction band, i.e. its dispersion relation $\epsilon(k)$. As a consequence, one needs a wave number vector shifting the electron to an existing state in the conduction band described by a dispersion relation, without changing the energy, i.e. only a horizontal vector can be used and given in the figure by $\boldsymbol{p}$. Since the wave number of the initial electron in the valence state differs from the wave number of the final electron state in the conduction band

$$\boldsymbol{k} \neq \boldsymbol{k}',$$

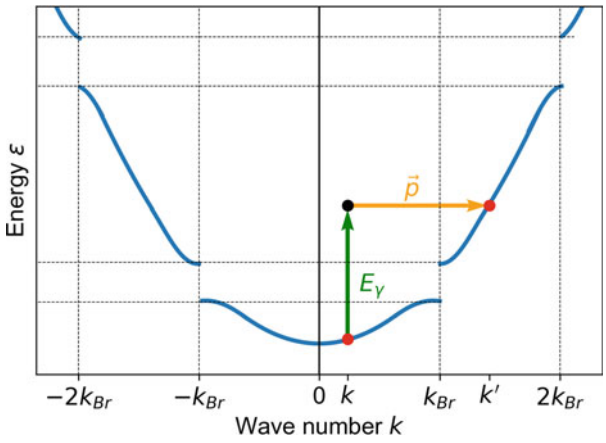

Fig. 12.1 Band structure plot with interband excitation of an electron from the valence band to the conduction band fulfilling conservation of momentum

the momentum is not conserved, $\Delta \boldsymbol{p} = \hbar(\boldsymbol{k}' - \boldsymbol{k}) \neq 0$. In order to guarantee the **conservation of momentum**, we have to shift the electron vertically getting an electron state on the conduction band. It can be shown in [1] that also here the **Bragg relation** (11.12) holds. This means that for the conservation of the momentum additionally to the momentum of the initial and final electron states, a third partner, here the crystal grid in form of the reciprocal vector $\boldsymbol{G}$

$$\boldsymbol{G} = \boldsymbol{k} - \boldsymbol{k}',$$

is needed, see Fig. 12.2a. Different from the diffraction of X-rays at crystal atoms, which represents an elastic scattering meaning $k = k'$, now the absolute value of the wave numbers before and after scattering at the Brillouin zone must differ

$$|\boldsymbol{k}| \neq \left|\boldsymbol{k}'\right|,$$

as an **inelastic electron scattering** is given.

This has very extensive consequences for the photo-excitation process. As both, energy and momentum conservation are valid, in order to fulfill both criteria for the exciting radiation with a given wavelength and, in consequence, photon energy E_γ, only electrons with a definite wave number $\boldsymbol{k}$ will be excited into the conduction band, see Fig. 12.2a.

In solid state physics, another common representation of the band structure plot is used, where the conservation of the momentum by the reciprocal vector is included. Shifting the band structure plots starting from the first Brillouin zone from the left to the right adding one reciprocal vector, and similarly subtracting one reciprocal vector from the right arm shifting it to the left side (Fig. 12.2b), one gets the **reduced!band structure plot** (Fig. 12.2c).

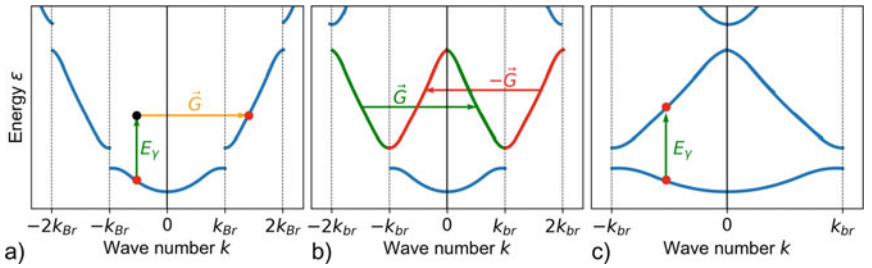

Fig. 12.2 Interband excitation of an electron from the valence band to the conduction band holding the Bragg relation (**a**), transformation of the band structure to the reduced band structure by shifting the conduction band by the Bragg vector (**b**), and interband excitation demonstrated in the reduced band structure plot (**c**)

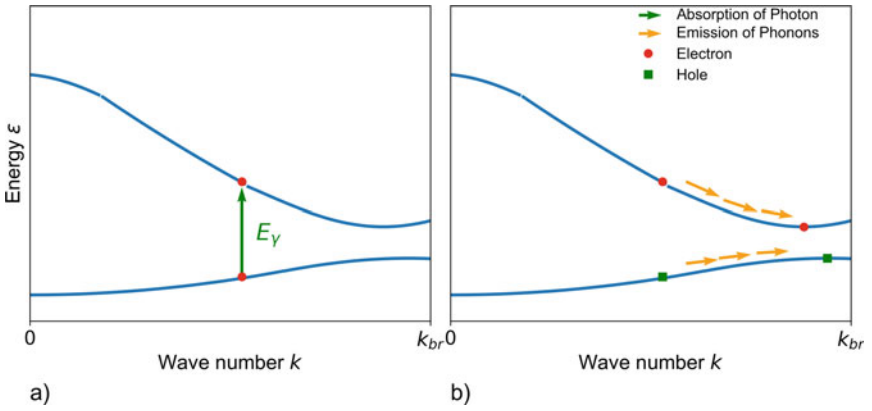

Fig. 12.3 Interband excitation by absorption of one photon with the energy E_γ of an electron from the valence to the conduction band forming a hole in the valence band (**a**). After photo-excitation, electron and hole relax by emission of phonons into the lowest energetic state of each band (**b**)

Now, energy and momentum are conserved when a photon with an energy E_γ excites an electron from the valence band into the conduction band, see also Fig. 12.3a.[1]

12.2.2 Dielectrics and Semiconductors

In dielectrics and semiconductors, featuring wide band gaps between valence and conduction bands, after excitation of the electron from the valence into the conduction band, the excited electron leaves a vacancy state, so-called **hole** in the valence band, see Fig. 12.3b. This vacancy state will, after some time, be populated by an electron

[1] As we talk about symmetric crystals, only the positive wave numbers are depicted from now on.

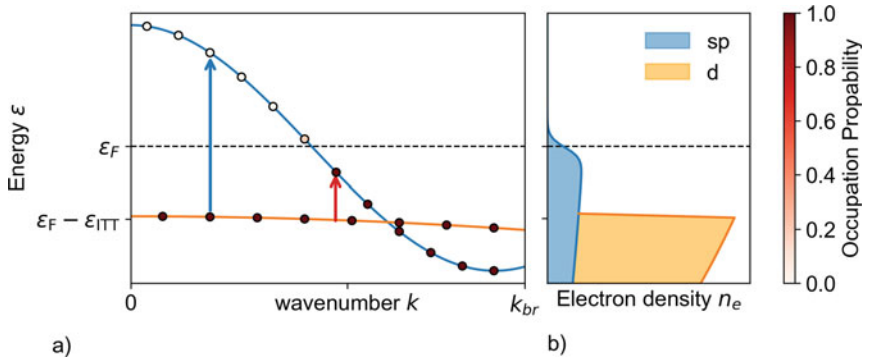

Fig. 12.4 Band structure plot of the d- and s/p-band of gold at rest (**a**) and electron density as well as its occupation probability (**b**) [2]

from a higher state on the dispersion curve of the valence band. In doing this, energy and momentum have to be still conserved, so that a third scattering partner is needed. A **phonon** has to be emitted, heating subsequently the crystal. Thereby, the phonon emission is described by a electron–phonon scattering. This process is repeated until the hole reaches the highest energy state on the dispersion curve of the valence band.

On the other hand, the electron excited into the conduction band, which is mostly unpopulated, will drive to states with lower energy, again emitting phonons until the lowest state in the conduction band is reached, and again, heating up the crystal, see Fig. 12.3b.

This process, where charges move to energetic lower states, is called **thermal relaxation** or dielectric relaxation. It is a quite fast process and lasts only about 0.1–10 ps, depending on the investigated matter and electron density. Obviously, the crystal is heated by the emitted phonons. As shown in the Fig. 12.3, the "positions" of the electron and the hole after relaxation do not coincide anymore, neither in the wave number (as shown), nor in the spatial coordinates (not shown), as electrons and holes diffuse randomly with different velocities through the solid.

12.2.3 Transition Metals

Some metals enable also interband transitions, as these metals feature fully-populated d-states at lower energies and partly-populated s/p-band at the same quantum number. Typical metals are, e.g. copper Cu, silver Ag, and gold Au. These metals feature at low temperatures (e.g. at rest) a filled d-band and a partially filled s- or s/p-bands, see Fig. 12.4 [2], compare with calculated density of states in Fig. 11.4.

An interband excitation from the d-band into the s/p-band gets probable for photons featuring energies larger than the distance between the edge of the d-band to the Fermi level (see the blue arrows in Fig. 12.4a, given by ϵ_{ITT}, the so-called **interband transition threshold** (ITT). The occupation probability in the s/p-band above ϵ_F is

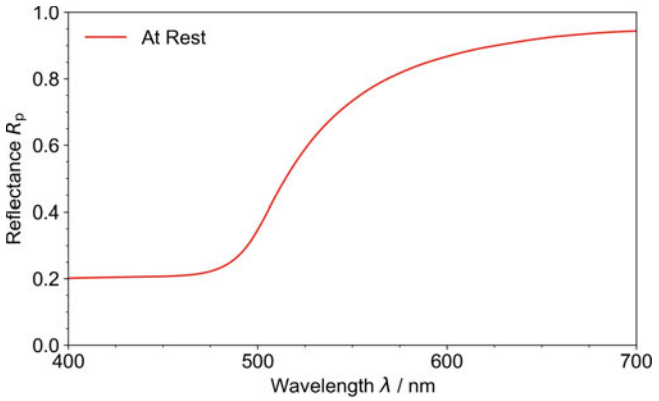

Fig. 12.5 Reflectance of p-polarized radiation for gold at little temperatures (at rest)

very low enforcing a transition, i.e. an excitation. This in fact means that the photon at the corresponding photon energies $\boldsymbol{E}_\gamma > \boldsymbol{\epsilon}_{\mathrm{ITT}}$ is absorbed resulting in a **reduced reflectance**.

On the other hand, photons with energies below the ITT, $\boldsymbol{E}_\gamma < \boldsymbol{\epsilon}_{\mathbf{ITT}}$, will feature a little probability to excite electrons from the d- into the s/p-band, as the occupation probability in the s/p-band is too large. For photons with energies below ϵ_{ITT}, an **increased reflectance** results. The density of states of the fully-populated d-band (orange) and the partially filled s/p-band up to the Fermi level ϵ_F (blue) are shown in Fig. 12.4b.

Exemplary, gold features an ITT at a wavelength of about $\lambda_{\mathrm{ITT}} = 500$ nm, which is clearly visible in its reflectance spectrum, see Fig. 12.5, with a large reflectance for $\epsilon_\gamma < \epsilon_{\mathrm{ITT}}$ and a reduced reflectance for $\epsilon_\gamma > \epsilon_{\mathrm{ITT}}$.

12.3 Intraband Excitation

Typically, the excitation of quasi-free or free electrons are described by intraband excitation. We will also see that also dielectrics and semiconductors can be excited by intraband transitions, but they must before be excited, see Sect. 12.5.1.

In principle, intraband excitation works like thermal relaxation of the electrons in the conduction band, only reversed. In case of metals featuring a quasi-free electron gas, electrons are populating the conduction band. The electrons close to the Fermi energy can absorb the photon, as they can populate free states at higher energy. As the momentum has to be conserved too, a third scattering partner, the crystal matrix, is needed. The absorption process takes place with a simultaneous absorption of a phonon. One speaks also about **inverse bremsstrahlung**, or photo-excitation.

Starting from a metal at $T = 0$ K, we depict the band structure plot and the density of states within the conduction band with the completely filled valence band and half-

filled conduction band (Fig. 12.6a). As the electrons are free, all of them close to the Fermi level in the range $\epsilon_F - E_\gamma \leq \epsilon_F$ can be excited by the electromagnetic radiation with the photon energy E_γ. So, electrons on the Fermi edge are excited most. In the density state plot, an exited electron leaves an empty state in the distribution, again close to the Fermi level, see Fig. 12.6b.

As electromagnetic radiation is delivered in pulses containing many photons, each photon excites an electron delivering a bunch of electrons above the Fermi level, see Fig. 12.6c. As shown in the density state plot, a remarkable amount of states are

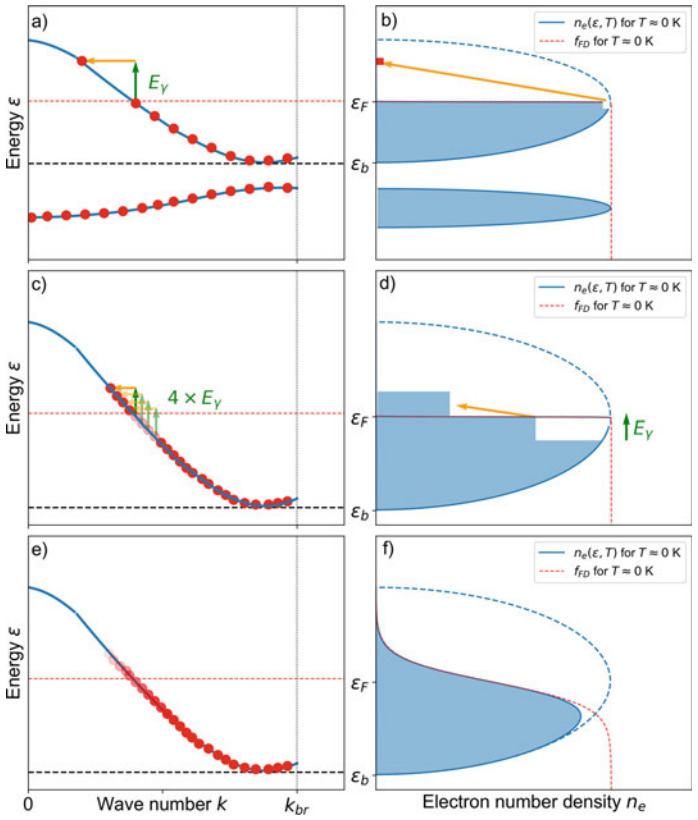

Fig. 12.6 **a** Intraband excitation of a metal by absorption of one photon with the energy E_γ of an electron from the conduction band. After photo-excitation by absorption of a phonon the electron is at a higher energy. **b** The density distribution is changed by the excited electron removing it below the Fermi level and positioning it above the Fermi level at higher energy. **c** Intraband excitation of a metal by many photons within a pulse. Many electrons close to the Fermi level are excited above ϵ_F. **d** In the density state plot, an amount of states are depopulated below the Fermi level and states above the Fermi level are populated with the excited electrons. No thermal equilibrium is given anymore and no Fermi–Dirac distribution. **e** After the inelastic scattering of excited electrons with those of the conduction band thermalization takes place. **f** The electron states are redistributed by a Fermi–Dirac distribution at higher temperature

shifted above the Fermi level, as given in Fig. 12.6d, leaving many states below the Fermi level unpopulated. It is evident that now no Fermi–Dirac distribution is given anymore, as the electrons are excited and not in any thermal equilibrium with the electrons of the conduction band. Additionally, also the electron in the conduction band are out of equilibrium as their electrons are missing.

Due to inelastic scattering processes between the excited higher energetic electrons with the remaining electrons in the conduction band, thermalization takes place within about 10–100 fs. Important is that the interaction volume as a whole features both electronic systems. Due to the non-equilibrium diffusion processes, the surrounding of the interaction volume takes place reducing the number of excited electrons in the interaction volume. As a consequence, the excited electron scatter with the conduction band electrons reaching a thermal equilibrium at higher temperature being represented by a Fermi–Dirac distribution at a higher temperature, see Fig. 12.6e, f.

12.4 Non-crystalline Matter—Disordered Matter

The last sections dealt with crystalline condensed matter, either as a metal, a semiconductor, or a dielectric. As there the periodicity of the atomic position is very high, simplified explanations for the excitation transitions were given. Now, in nature, many materials do not have a crystalline structure, but persist in a **thermodynamic meta-stable state** with non-ordered atomic positions, so-called **disordered matter** or **amorphous matter**. In Sect. 11.4, we described its properties.

Recapitulating, disorder matter can be partially- or totally-disordered. In the first case, one distinguishes between short-range and long-range order. Partially disordered matter features short-range order having electronic properties like atoms or molecules called **localized states**, but also long-range order, so-called **extended states**.

But, fully-disordered matter cannot be described via a dispersion relation, like for the free electron gas given by (9.6), or electronic states in periodic crystals represented by extended states in the band theory, see Chap. 11. Typical materials are glasses and polymers. In the second case, absolutely no short- as well long-range order exists.

As for crystalline mater, exciting amorphous, i.e. disordered dielectrics like fused silica, it is possible by an **interband excitation**. Either by applying photons with energies larger than the band gap, or ultra-fast laser radiation, a linear or nonlinear absorption is induced resulting in an excitation, see Fig. 12.7a. Disordered matter features localized states too, see Sect. 11.4. Interband excitation in disordered matter takes place from populated localized states in the valence band into empty **localized states** of the conduction band, see Fig. 12.7b.

Partially disordered dielectrics feature more channels for excitation, as there also an interband excitation from the valence band into the conduction band via **extended states** gets possible. Now, an interband excitation is given from localized states from

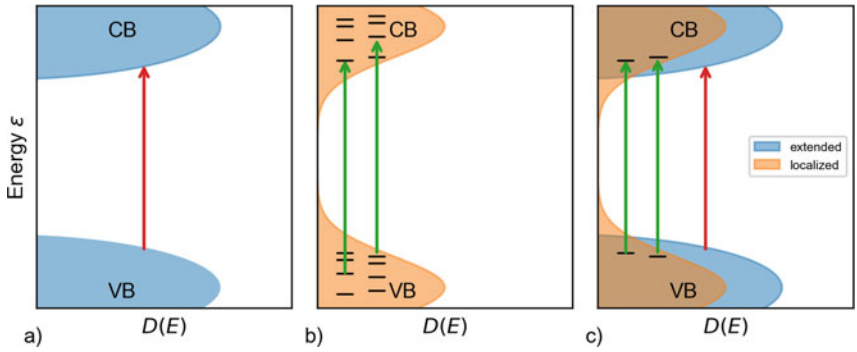

Fig. 12.7 Interband excitation in crystalline matter from extended states (**a**), in disorder matter by localized states (**b**), or in partially disordered matter by localized and extended states (**c**)

the Urbach tails of the valence and conduction band, the so-called **mobility gap** (Sect. 11.4), as well by extended state excitation from the valence into the conduction band by smaller photon energies, see Fig. 12.7c.

12.5 Excited State Transitions

An interesting process for material sciences is the definite and controlled change of the physical matter state, allowing to induce different and new excitation pathways. So, heating a metal like copper changes its optical properties, inducing an increased absorption of radiation, i.e. welding of copper by IR-laser radiation. Also, dielectrics change dramatically their optical properties when their state has been excited by nonlinear absorption, inducing spatially localized metal-like properties.

12.5.1 Dielectrics and Semiconductors

For an exited state transition, a preparing excitation step is needed, as dielectrics and semiconductors at low temperatures feature no electrons in the conduction band.

Dielectrics feature an interband excitation from the valence to the conduction band by absorption of one photon with a photon energy larger than the band gap (Fig. 12.8a), or by simultaneous absorption of many photons by multi-photon excitation, see also Sect. 13.3.3 and Fig. 12.9a.

As the irradiation of matter is every time driven by the irradiation time, and this very often is described by the pulse duration of the radiation, one can imagine that an excited electron in the conduction band is able to absorb by inverse bremsstrahlung one photon, comparably to metals, inducing an intraband excitation, see Fig. 12.8b.

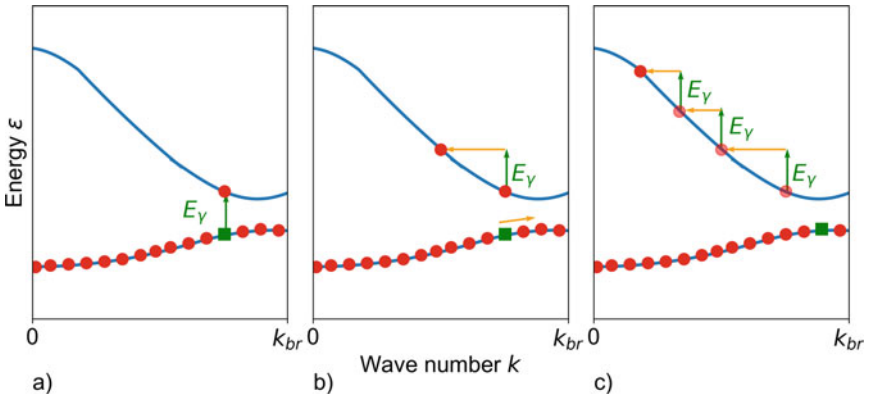

Fig. 12.8 **a** Linear excitation of an electron from the valence into the conduction band of dielectrics. **b** Intraband excitation of the excited conduction band electron to higher energy by absorption of one photon. **c** Intraband excitation by subsequent absorption of three photons

Hereby, to conserve momentum also, a phonon is generated by heating the crystal. The main difference between this excitation process to the excitation process of metals is that, for dielectrics, the electron is excited, not fulfilling the Fermi–Dirac statistics anymore.

Every excitation process needs time. This means that to excite the same electron again to a higher energy level by an intraband excitation, i.e. inverse bremsstrahlung, at least the irradiation time must be longer than the excitation time of some 10 fs. A repetitive excitation of one electron needs more time, as each excitation step takes again about 10 fs of time, so in case of four subsequent intraband excitations, the pulse duration must last at least 40 fs, see Fig. 12.8c.

Finally, extending the excitation process using many photons at the same time, first multiple-linear absorption generates many seed electrons by linear excitation of electrons from the valence band into the conduction band. As the hole concentration in the valence band is now high, the probability of intraband excitation decreases. These electrons, in turn, can now absorb subsequently many photons by intraband excitation generating an excited hot electron gas. As momentum is conserved, each excitation generates a phonon, meaning that the crystal is heated, additionally. It is important to mention that the probability for interband transition is much larger, as no phonon is needed. This means that as long the density of electrons in the valence band is large enough and the valence band is mostly empty, the interband transition will be the dominant process to the intraband transition. As the hole concentration gets in the valence band large and the electron density in the conduction band too, only a little number of electrons can further be excited by interband transitions. Then the intraband transitions will become predominant.

Although this chapter treats linear absorption processes, we introduce here firstly a nonlinear excitation process, see Chap. 13 for more detailed explanations. If the applied radiation features photon energies below the band gap of the materials, only a

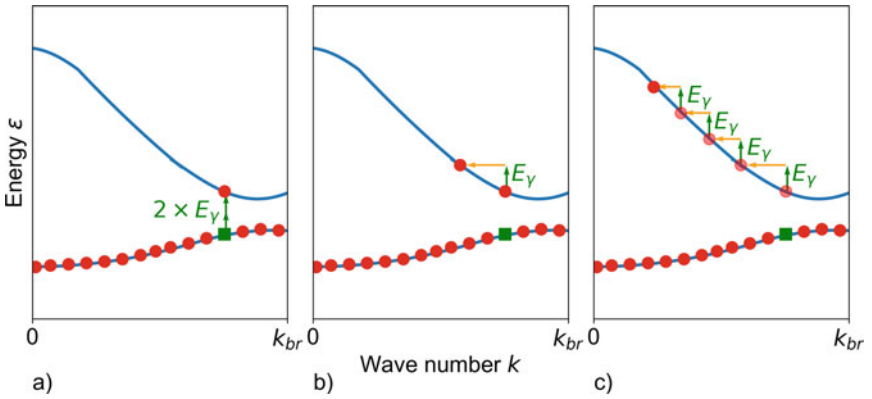

Fig. 12.9 **a** Nonlinear excitation of an electron from the valence into the conduction band of dielectrics. **b** Intraband excitation of the excited conduction band electron to higher energy by absorption of one photon. **c** Intraband excitation by subsequent absorption of four photons

nonlinear excitation enables the population of the conduction band by free electrons. This process is called **nonlinear ionization**, and is in principle demonstrated in Fig. 12.3 by applying a multiple number of photons nearly-instantaneously exciting one electron, see Fig. 12.9a.

As free electrons are now given in the conduction band, and due to adequate pulse duration, the irradiation still takes place and the electron can be excited to higher energy levels by intraband excitation, see Fig. 12.9b. Further absorption of photons will induce multiple intraband excitation generating highly-excited electrons in the conduction band, see Fig. 12.9c. Again like for the linear interband excitation, as long the electron concentration in the valence band is high, the multi-photon interband excitation will prevail over the intraband one.

Semiconductors apply in the linear absorption of electromagnetic radiation in both excitation processes. Assuming firstly a photon energy larger than the band gap, a semiconductor features at temperatures above $T > 0$ K some free electrons in the conduction band, which can easily be excited by intraband transitions, as described for metals or excited dielectrics, see Sect. 12.3. But, as the photon energy is larger than the band gap, interband excitation is more probable, generating by photo-excitation a larger number of excited electrons in the conduction band. These excited electrons can subsequently be excited by intraband processes too.

Reducing the photon energies below the band gap makes the interband excitation impossible. But on the one hand, in real semiconductors some seed electrons are every time given[2] allowing an intraband excitation. On the other hand, when the photon density is high enough, i.e. a high intensity of the radiation, a nonlinear excitation processes, like multi-photon or tunnel excitation, gets probable increasing rapidly the density of excited electrons in the conduction band. Depending on the irradiation

[2] The purity of semiconductors can be controlled very precisely, but even the purest silicon features seed electrons with a concentration of about 10^{16} 1/cm^3.

time, the seed electrons can be excited further generating a dense free electron gas, as well as a high density hole system.

12.5.2 Recombination and Meta-Stable States

Imagine that an electron in a dielectric or semiconductor is firstly excited linearly or nonlinearly from the valence band to the lowest energetic state of the conduction band (Figs. 12.8a and 12.9a). Now the electron, as not being in a thermodynamic equilibrium will thermalize, as described for metals in the previous section, from higher states of the conduction band until the lowest possible state is reached. Because the linear as well as nonlinear ionization generates also a hole in the valence band, it will thermalize populating finally the highest possible state in the valence band. This state consisting of an electron in the conduction band and a hole in the valence band represents a meta-stable state. In principle, the electron and the hole can recombine, as both attract each other electronically, thereby reducing the overall energy.

The **recombination** takes place radiatively or non-radiatively. In the first case, the radiative recombination, a photon with energy around the band gap energy is emitted. In the case of non-radiative recombination, phonons are emitted, again heating the crystal. The **recombination decay time** depends on the localization of the electrons and the hole, corresponding to the position in the band structure. In case the maximum of the valence band features the same wave number as the minimum of the conduction band, then also the electron in the conduction band and the hole in the valence band will feature equal wave number, and one speaks about a **direct electron transition**, or **direct recombination**. Differ the extrema of the bands in the k-space, so an indirect electron transitions can take place, so-called an **indirect recombination**. Electrons and holes recombine by direct recombination very fast in the nanosecond to microsecond time scale, compared to the much slower indirect recombination in the millisecond range.

As crystals are not perfect, meaning some **defects** in the crystal periodicity are depending on the quality of the material still given, electrons and holes can be trapped at such defects forming spatially-separated, meta-stable dipoles, so-called **self-trapped excitons** (STE). This self-trapped excitons decay by recombination on a much longer time scales compared to the direct and indirect recombinations, being typically in the range of seconds, days, or years, depending strongly on the material properties.

12.5.3 Excited Transition Metals

We have seen that a dielectric being excited by linear high energy photo ionization or by nonlinear processes, features a transient state in the conduction band. Also,

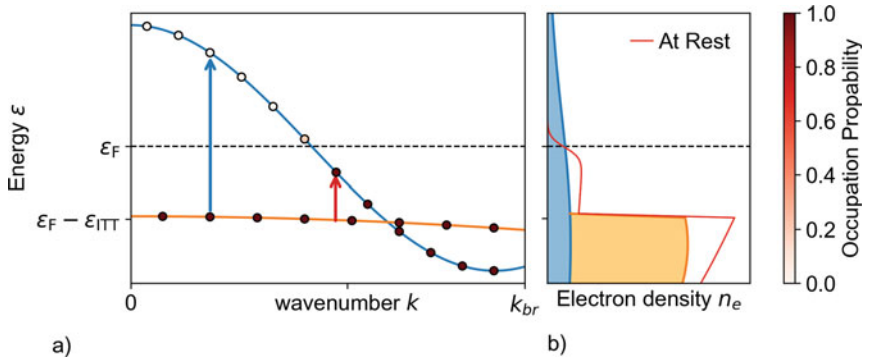

Fig. 12.10 Band structure plot of the d- and sp-band of gold at rest (**a**) and electron density as well as its occupation probability (**b**) [2]

in metals, it is possible to induce transient states allowing for example subsequent interband transitions.

Exciting gold, e.g. by irradiating it by an ultrashort laser pulse, heats the electron system by **intraband excitation**, see Sect. 12.3, and therefore, the density of the electron states is changed dramatically, see Fig. 12.10 [2]. Now, the population density at the edge of the d-band is reduced, and at the same time, the Fermi–dirac distribution is much broadened for the s/p-band decreasing the probability for transitions by photons with energies larger than ϵ_{ITT} (blue arrow). But, as more states in the s/p-band below the Fermi energy ϵ_F are now depopulated, interband transitions with photon energies below ϵ_{ITT} get more probable (red arrow). As the interband transitions for excited gold are inhibited compared to gold at rest, intraband excitation at the Fermi energy gets more probable for excited gold.

Not shown here, **interband transitions** from lower bands into the now partially populated d-band are getting also probable, opening new excitation channels. As the metal gets more excited, the electron density changes increasingly, resulting in reduced absorption of photons at energies larger ϵ_{ITT}, i.e. wavelengths smaller than

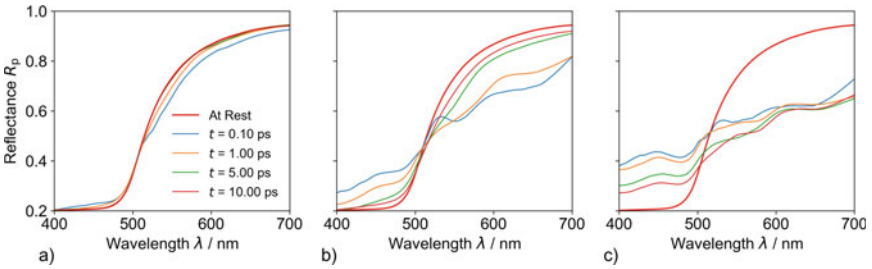

Fig. 12.11 Reflectance of the p-polarized radiation at a gold surface as function of the excitation fluence $H = 0.2\,\mathrm{J/cm^2}$ of ultra-fast pulsed radiation (**a**), $H = 2\,\mathrm{J/cm^2}$ (**b**), and $H = 8\,\mathrm{J/cm^2}$ (**c**) [2]

$\lambda_{ITT} = 500$ nm, and an increase in photon absorption for energies smaller ϵ_{ITT}, i.e. wavelengths larger λ_{ITT}, see Fig. 12.11c [2]. Also, one realizes that the relaxation time scales with the fluence, i.e. during the absorption of the optical energy at smaller fluences $H < 8\,\mathrm{J/cm^2}$ the relaxation begins within some picoseconds after excitation, see Fig. 12.11a and b. At larger fluences $H \geq 8\,\mathrm{J/cm^2}$ a large electron temperature results and the excited state lasts longer than 10 ps, see Fig. 12.11c.

12.6 Optical Properties of Metals

In this section we talk about the optical properties of metals, as firstly this matter interacts strongly with electromagnetic radiation. Depending on the intensity of the radiation, intraband excitation gets probable inducing inverse bremsstrahlung, and consequently heating of the electron system. But also transient states of dielectrics, being excited by radiation have many free electrons in the interaction volume feature metallic properties, which is why the optical properties of metals, and metallic behaving matter gets again important.

12.6.1 Non-excited Metals

Electrons moving freely in the metallic crystal are set up by the nearly restless atoms interacting with them. An atom in this case means a nucleus surrounded by bounded electrons.[3] This electrostatic interaction is not described on an atomic scale, but using solid state quantum mechanics. The high order of symmetry of the atoms in the metallic lattice allow to describe the motion of the atoms by a phonon system.

> A phonon represents a quantized vibration state of many oscillating atoms.

The collective interaction of the atoms, given by phonons, with the quasi-free electrons results in the **electron–phonon scattering** of the electrons. One can describe this interaction by the scattering frequency ν_{ep} calculating it using the mean electron–phonon collision time ep

$$\nu_{ep} = \frac{1}{\tau_{ep}}.$$

This means that the electrons are quasi-free due to the interaction with other free electrons and with the bounded electrons. The electron–phonon collision time, representing the inverse electron–phonon scattering frequency, gets important when we are looking at the thermal properties of a metal. There, the time for the energy trans-

[3] At least for a metal with one free electron per atom means that an atom with an atomic number Z features $Z - 1$ bounded electrons.

fer from the electron system to the phonon system is given by the electron–phonon relaxation time, see Sect. 14.4.

Both scattering frequencies given for this "free" electrons of the conduction band moving in a metal lattice are combined to an **overall scattering frequency**

$$\nu_e = \frac{1}{\tau_e} = \frac{1}{\tau_{ee}} + \frac{1}{\tau_{ep}}, \tag{12.1}$$

describing the average collision frequency. This frequency corresponds to the damping constant Γ_e from our atomic model, see Sect. 3.2.2 and (3.22), as the damping coefficients Γ_e represents all losses.

Average collision frequency

$$\nu_e = \nu_{ee} + \nu_{ep} = (\tau_e)^{-1} = \Gamma_e. \tag{12.2}$$

To get now the optical response of the electrons in the metal we have now to combine the description of the quasi-free electrons using the **Drude model** and the description for bounded electrons using the **Lorentz model** and get the complex relative permittivity

Drude-Lorentz model for quasi-free and bounded electrons in metals

$$\tilde{\epsilon}_r = \tilde{n}^2 = \epsilon_{r,\infty} - \frac{\omega_{pfe}^2}{\omega^2 + i\nu_e\omega} + \omega_p^2 \sum_{i=1}^{m} \frac{f_i}{\omega_{0i}^2 - \omega^2 + i\omega\Gamma_{em,i}}, \tag{12.3}$$

with $\omega_{qfe} = \omega_p\sqrt{f_0}$ representing the plasma frequency for the quasi-free electrons with the plasma frequency ω_p, ν_e its average collision frequency, and $\omega_p\sqrt{f_i}$ the plasma frequency for bounded electrons.

As now the relative permittivity for metals is complex, also the refractive index $\tilde{n}$ results as a complex number. Comparing the measured refractive index n and the extinction coefficient κ for gold with the calculated one, using two oscillators and the plasma frequency from [3], we get a good agreement, see Fig. 12.12. The calculated data is compared to measured values for the ellipsometric parameters Δ and Ψ, see also Chap. 17 and [4, 5].

12.6.2 Excited Dielectrics

As shown in Sect. 12.2.2, an excited dielectric represents matter with spatially and temporally localized metallic properties, as there now in the conduction band free electrons are given. As long as this free electrons are present, they interact with electromagnetic radiation like the free electrons in metals, see section before. But, contrary to metals at rest, excited dielectrics feature high-energetic free electrons

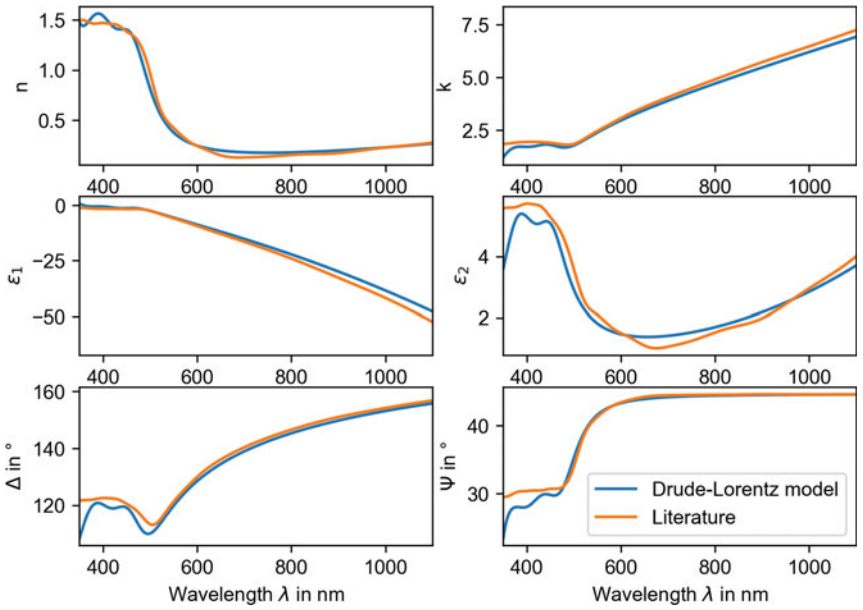

Fig. 12.12 For gold thin film Components of the complex refractive index n, κ, the complex relative permittivity ϵ_1, ϵ_2, and as well the measured and calculated ellipsometric parameters Δ and Ψ

not being in any thermodynamic equilibrium. The electrons will, depending on its kinetic energy and concentration, move toward an equilibrium by electron–electron and electron–phonon collisions, and at the same time start with relaxation processes, like recombination or formation of localized defects, like self-trapped excitons (STE).

> The higher the concentration of free electrons in the conduction band, the higher the collision frequency, and the faster the thermalization.

Strongly excited dielectrics feature free electron concentrations in the order of 10^{24} m^{-3} comparable to those of metals. At this high concentration, the relaxation into a thermal equilibrium takes place within the range of 100 fs to some picoseconds. Recombination processes take place in the range of nanoseconds to microseconds, so that a thermodynamic equilibrium is reached resulting with a **hot electron gas**.

Exciting a borosilicate glass (BK7) by ultra-fast laser radiation with one pulse (pulse duration $t_p = 70$ fs and wavelength $\lambda = 800$ nm), and detecting time-resolved the change in transmittivity as well the relative refractive index using a pump-probe Nomarski microscope (see Sect. 18), one observes after excitation an increasing absorbance within the interaction zone, oriented toward the irradiation direction[4]

[4] The green color of the background results from the ultra-fast white-light continuum pulse, being not white-balanced.

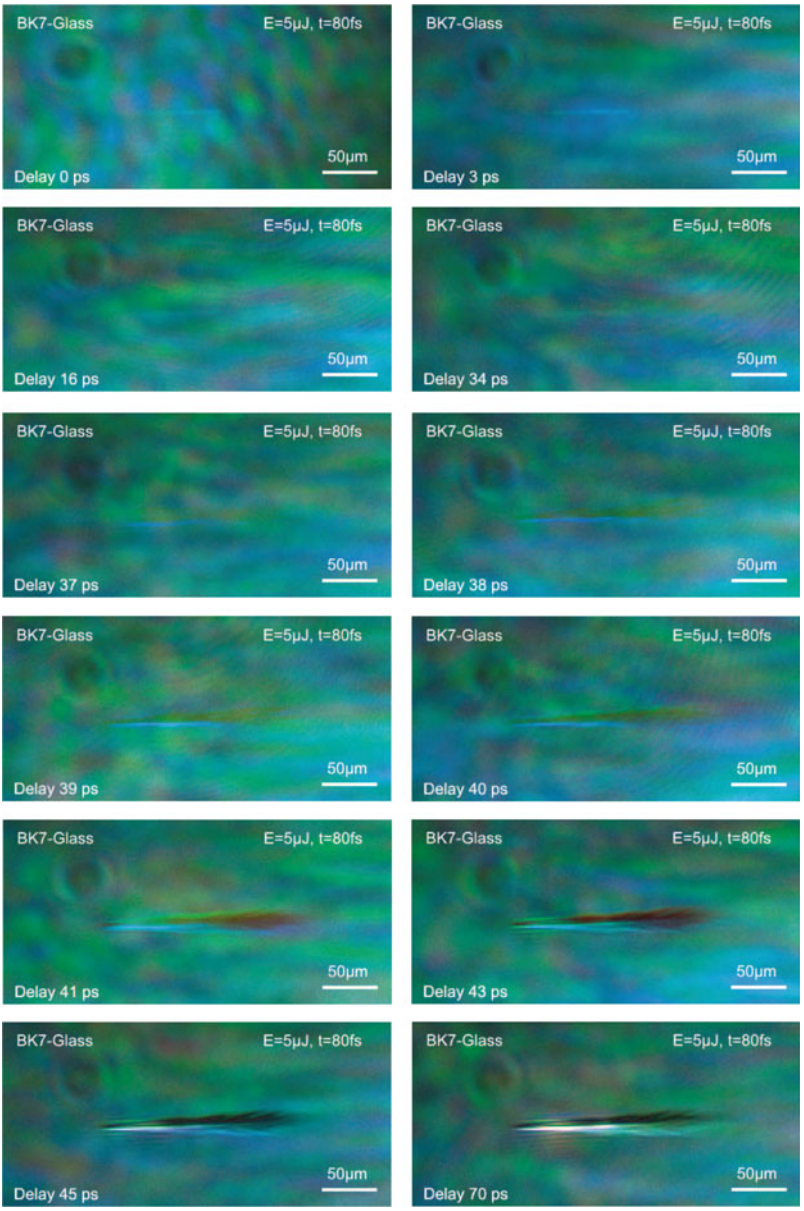

Fig. 12.13 Dynamics of the transmittance of excited BK7 glass induced by one ultra-fast laser pulse and measured by Nomarski microscopy ($t_p = 80$ fs, $\lambda = 800$ nm) [6]

Fig. 12.14 Dynamics of the refractive index of excited BK7 glass induced by one ultra-fast laser pulse and measured by Nomarski microscopy ($t_p = 80$ fs, $\lambda = 800$ nm) [6]

(Fig. 12.13) [6]. Also, one observes the filamentation on the right side of the focal region, being oriented toward the source (Fig. 12.14). Filamentation is described in more detail in Sect. 13.5.

Interestingly, depending on the intensity of the radiation a **transient as well permanent refractive index change** within the focal volume is induced. The transient induced refractive index is attributed to Four-wave mixing, see Sect. 8.4.4, where the Kerr effect, (8.54) results. Additionally, a long lasting and partly also permanent refractive index is measured, resulting from **transient localized states** of the free electrons, molecular changes in the matrix of the dielectrics, and formation of defect states. The bright blueish luminescence observed within the focal volume, e.g. Fig. 12.14 at 40 ps, is attributed to a long-lasting fluorescence of decaying transient excited states in the μs range, being detected by the CCD camera additionally to the measured ultra-fast white-light pulse.[5]

References

1. C. Kittel, *Introduction to Solid State Physics*, 9th ed. (Wiley, 2018)
2. M. Olbrich, Working title: "Time-resolved excitation of thin gold film". Ph.D. Thesis, Technische Bergakademie Freiberg, in preparation, 2022
3. A.D. Rakic, A.B. Djurisic, J.M. Elazar, M.L. Majewski, Optical properties of metallic films for vertical-cavity optoelectronic devices. Appl. Opt. **37**(22) (1998)
4. H. Fujiwara, *Spectroscopic Ellipsometry: Principles and Applications* (Wiley, Chichester, 2009)
5. P.B. Johnson, R.W. Christy, Optical constants of the noble metals. Phys. Rev. B **6**, 4370–4379 (1972)
6. A. Horn, Zeitaufgelöste Analyse der Wechselwirkung von ultrakurz gepulster Laserstrahlung mit Dielektrika. Ph.D. Thesis, RWTH Aachen, 2003, ISBN 3-8322-2068-2

[5] But, this blueish emission lasts much longer than the ultra-fast irradiation by the pump radiation, and is collected within the shutter-time of the CCD camera of approximately 1 ms.

Chapter 13
Non-linear Absorption

Abstract Non-linear absorption is mostly referred to wide-band gap materials, as dielectrics and semiconductors. There, the free-electron charge density interacting with the used radiation is very small, resulting in a vanishing extinction coefficient κ. Therefore, in linear optics we talk about transparent materials, see also the discussions on linear optics in Chap. 7.

13.1 Excitation Pathways

Electromagnetic radiation interacting with condensed matter can be absorbed. This means that the number of photons is reduced. If thereby charges, usually quasi-free electrons are generated, then we are talking about an **excitation**. Talking about dielectrics and semiconductors with nearly empty conduction bands, **linear excitation** is only possible for radiation with photon energies larger than its band gap. In case the photon energy is smaller than the band gap, only **non-linear excitation** enables to generate quasi-free electrons. The electrons in principle are not really free, as they are still within a more or less dense matter state, surrounded by atoms and/or molecules at periodic positions in case of crystals, or non-periodic positions, as in the case of amorphous matter, like glasses, liquids or gasses. In case the electrons leave the surface of the condensed matter, we speak about an effective **ionization**.

As the intensity and/or the photon energy gets large, the amount of quasi-free charges affects the optical properties of matter significantly. This will be important for excited dielectrics and semiconductors, and also metals in case of interband excitation.

Generally, depending on the photon energy and on the intensity of the laser radiation, i.e. photon number per volume and time, different excitation processes in matter take place, like **non-linear photo-excitation and impact ionization**.

As the intensity of the electromagnetic radiation gets larger, bounded electrons, here the valence electrons of a dielectric, can be excited into the conduction band by non-linear photo-excitation processes, like tunnel excitation or multi-photon excitation, see Fig. 13.1.

© Springer Nature Switzerland AG 2022

A. Horn, *The Physics of Laser Radiation–Matter Interaction*,
https://doi.org/10.1007/978-3-031-15862-9_13

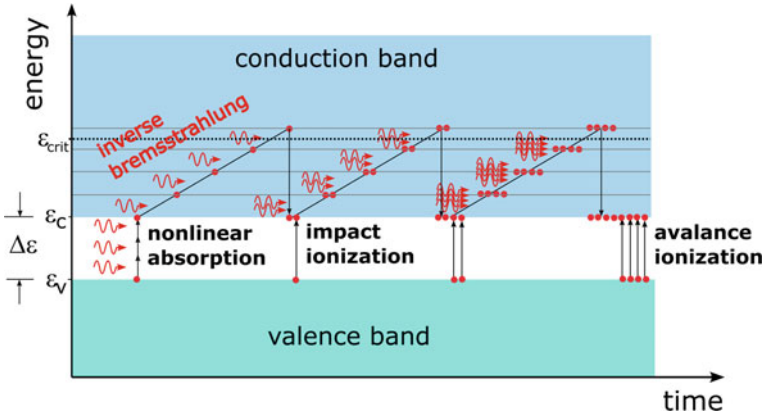

Fig. 13.1 Non-linear interband excitation of a dielectric starting from multi-photon or tunnel ionization, consecutive intraband excitations by inverse bremsstrahlung until a critical energy ϵ_{crit}, larger than the band gap energy $\Delta\epsilon$ is exceeded, followed by excitation of an additional electron into the conduction band by impact ionization. As long irradiation lasts, this processes are repeated, generating an avalanche of free electrons in the conduction band

As the dielectric, contrary to a metal, features no free electrons we can not talk about ionization here, as the electrons are still within the matrix of the condensed matter. Only processes, where the **free electrons leave the surface** of the material are really free. Then one speaks about a **photo ionization**. In case of a photon energy being larger than the band gap $E_\gamma > E_{gap}$, one talks about **linear photo-ionization**, as described in Sect. 4.3 for atoms and molecules. For condensed matter one speaks about an interband excitation, see Sect. 12.2.

> A linear absorption of radiation implicates the generation of one quasi-free electron per photon.

Using laser radiation with photon energies below the band gap $E_\gamma < E_{gap}$ makes photo-excitation only probable, when the intensity of the radiation is such large that a **non-linear absorption** of photons takes place. This is determined by the linear and non-linear absorption coefficients α, β or γ, see Sect. 13.3.3.

> Non-linear absorption takes place, when more then one photon is absorbed to generate one quasi-free electron.

Depending on the wavelength, the intensity of the radiation, and the band structure of the investigated matter, **tunnel or multi-photon absorption** gets probable, and being determined by the Keldysh parameter, see Sect. 4.5.3.

But, these excited electrons can additionally interact significantly with the electromagnetic radiation through the **inverse bremsstrahlung**, see Sect. 4.1, getting free electrons within the conduction band at high kinetic energies, see Sect. 12.5.

When quasi-free charges are generated and electromagnetic radiation is still present, then by inverse-bremsstrahlung this quasi-free electrons can absorb further optical energy by intraband excitation gaining kinetic energy, see also Sect. 12.5.

The **high-energy free electrons** can additionally scatter with the atoms of the dielectric material, exciting it further by generating additional free electrons in the conduction band, the so called **impact ionization**. In case the electric field of the radiation is still acting (or acting again by high-repetition rate pulsed radiation), this quasi-free electrons can further gain energy and generate more electrons, like a cascade. One speaks then about an **avalanche ionization**. Depending on the investigated matter, i.e. the density of the quasi-free and bounded electron, the ionization takes place when a critical energy for impact ionization is exceeded. This process is also non-linear as one electron generates one additional electron, so two electrons generate two additional electrons getting four electrons, and so on. Remembering that the free-electron density in dielectrics is at rest very small, after an avalanche process the density of free electrons in the conduction band gets as large as solid state density, with about 10^{23} e/cm^3. Now, the dielectrics features locally metallic properties, see also Sect. 12.6.2.

13.2 Electron Rate Equation

The transient dielectric function of the excited matter, represented by $\tilde{\epsilon}$ with $\tilde{\epsilon} = \epsilon_1 + i\epsilon_2 = \tilde{n}^2$, depends on the dynamics of the free-electron density, so that **self-phase modulation** takes also place, when the radiation interacts with these free electrons, see Sect. 8.4.7, modifying the radiation itself. This means that radiation interacting with matter changes its electronic properties, but doing this, also the exciting radiation is modified, e.g. by white-light generation. One can imagine that the generated radiation at higher photon energies can in principle induce different excitation path compared to the initial radiation, e.g. when the photon energy is now larger than the band gap, also linear absorption gets probable.

One can determine a rate equation for the electrons formed in the conduction band of a dielectric

Overall electron rate equation for non-linear photo excitation

$$\frac{dn_\mathrm{e}}{dt} = \frac{n_{\mathrm{VB},0} - n_\mathrm{e}}{n_{\mathrm{VB},0}} \left[\left(\frac{dn_\mathrm{e}}{dt} \right)_\mathrm{PE} + \eta n_\mathrm{e} \right] - \rho_\mathrm{rec} n_\mathrm{e}^2 - \tau_\mathrm{trap}^{-1} n_\mathrm{e}, \qquad (13.1)$$

with the impact excitation rate η, the recombination rate ρ_rec, the trapping time τ_trap, and the initial electron density in the valence band $n_{\mathrm{VB},0}$. So, the first fraction determines the relative amount of electrons in the valence band being excitable. The squared bracket includes the two excitation sources of valence electrons into the conduction band via non-linear photo-excitation (PE) and via impact ionization. The following two drains describe the reduction in the electron density in the conduction

band by recombination of the electron in the conduction band with a hole in the valence band, and the trapping of the electron in metas-table states, like self-trapped electrons. This electrons are not quasi-free anymore.

Clearly, the electrons generated within an interaction volume can diffuse out of this volume, reducing additionally the electron density. As the lateral diffusion coefficient for glasses is reported to be up to $D_{\text{diff}} \approx 10^{-3}\,\mu^2/\text{fs}$, depending on the size if the interaction volume, the diffusion has to be taken into account for time scales larger than 1 to 100 ps.

In the next sections the generation of the quasi-free electrons into the conduction band by photo-excitation processes is described in detail.

13.3 Non-linear Photo-Excitation

Non-linear photo-excitation of electrons from the valence into the conduction band in dielectrics is often referred in literature to as multi-photon ionization or tunnel ionization [1–4].

> But, the terms multi-photon excitation (MPE) and tunnel excitation (TE) are more appropriate for the non-linear excitation processes of dielectrics, because only the excitation from a ground state into an extended conduction states has to be considered.

Due to the disordered atomic structure of many amorphous dielectrics, the excited electronic states might be better described by localized tail states or excitonic states, and therefore can also not be considered as ionized nearly-free electrons, see Sect. 12.4 [5]. In fact, both processes are describing an excitation of an electron, so that after discussing the individual processes, equations for the overall non-linear photo-excitation process will be given.

13.3.1 Keldysh Parameter for Crystals

Mowing to condensed matter changes somehow the physics of the interaction with radiation, as ionization in the stronger sense described for atoms by the generation of free electrons. One has to be separated the interaction process in the **photo-excitation**, when quasi-free electrons are formed, but they are still within the solid, and **photo-ionization**, where the free electrons are outside the solid. In the following we will only talk about photo-excitation.

Now, speaking about non-linear excitation, one can use for an electron excited from the valence band into the conduction band by an interband excitation the Keldysh parameter, allowing to distinguish tunnel from multi-photon excitation. Thereby a hole in the valence band is formed.

Contrary to the non-linear photo ionization of atoms, see Sect. 4.5.3, Keldysh determined for dielectrics a different Keldysh parameter [6]:

Keldysh parameter for dielectrics

$$\gamma = \omega_{\mathrm{em}} \frac{\sqrt{m_{\mathrm{eff}} E_{\mathrm{gap}}}}{\mathrm{e} E_{\mathrm{em}}}, \tag{13.2}$$

$$= \frac{\omega_{\mathrm{em}}}{\mathrm{e}} \left(\frac{m_{\mathrm{eff}} c_0 n \varepsilon_0 E_{\mathrm{gap}}}{I_{\mathrm{em}}} \right)^{1/2}. \tag{13.3}$$

Thereby the effective electron mass m_{eff}, the band gap E_{gap}, the refractive index of matter n, and the electric field strength E_{em} or respectively the intensity of the radiation I_{em} have been introduced. Comparable to the Keldysh parameter for atoms, also for dielectrics the photo-excitation takes place by Tunnel excitation for a Keldysh parameter $\gamma \ll 1$, and becomes more probable for multi-photon excitation for a Keldysh parameter $\gamma \gg 1$.

13.3.2 Tunnel Excitation

As described in the precedent section, tunnel excitation is the more general description for a quantum mechanical process often described as tunnel ionization of atoms, see Sect. 4.5.1, and referred in quantum mechanics literature to the topics "quantum tunneling". As shown in Fig. 4.6, a potential of an atom is distorted by an external electromagnetic field, here by the instantaneous electric field of the radiation. The resulting localized potential barrier depends on the actual energy of the electron and the corresponding electrical field strength.

As we consider condensed matter, the atomic description fails and energy band models have to be used. High-intensity radiation with large electric field strengths will distort the local band structure—defined by the interaction volume—consisting of a valence and a conduction band, and resulting in a barrier similar to the atomic barrier, allowing a tunneling of the valence electrons into the conduction band, see Fig. 13.2. So, typically mid-IR ultra-fast laser radiation will more probably excite electrons of an dielectric, like poly(methyl methacrylate) (PMMA), by tunnel excitation from local tail states of the valence band into tail states of the conduction band, then by multi-photon excitation, see for more details [5].

The **electron density rate for tunnel excitation** [7] is given by

$$\left(\frac{dn_{\mathrm{e}}}{dt} \right)_{\mathrm{TE}} = \frac{2 E_{\mathrm{gap}}}{9\pi^2 \hbar} \left(\frac{m_{\mathrm{eff}} E_{\mathrm{gap}}}{\hbar^2} \right)^{3/2} \left(\frac{\hbar\omega}{E_{\mathrm{gap}} \gamma} \right)^{5/2} \times \exp\left(-\frac{\pi E_{\mathrm{gap}} \gamma}{2\hbar\omega_{\mathrm{em}}} \left[1 - \frac{\gamma^2}{8} \right] \right), \tag{13.4}$$

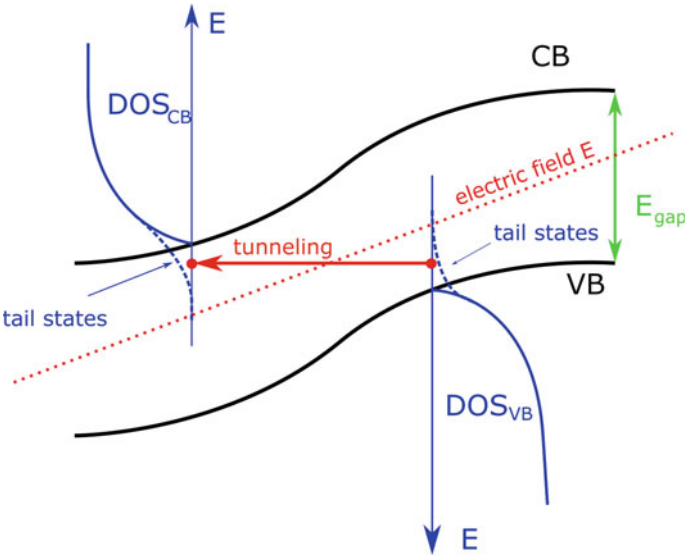

Fig. 13.2 Schematics of tunnel excitation of a dielectric. An electron in a distorted band structure can tunnel from the valence band into the conduction band via its tail states

using now the Keldysh parameter for condensed matter, (13.2). The electron density rate, also called the **probability for photo-ionization by tunnel excitation** can also be plotted as function of the electric fields by inserting the Keldysh parameter for condensed matter [6], getting

Electron density rate for tunnel excitation

$$\left(\frac{dn_e}{dt}\right)_{TE} = \frac{2}{9\pi^2}\frac{E_{gap}}{\hbar}\left(\frac{m_{eff}E_{gap}}{\hbar}\right)^{3/2}\left(\frac{e\hbar E_{em}}{m_{eff}^{1/2}E_{gap}^{3/2}}\right)^{5/2}\times$$
$$\times \exp\left(-\frac{\pi}{2}\frac{m_{eff}^{1/2}E_{gap}^{3/2}}{e\hbar E_{ext}}\left(1-\frac{1}{8}\frac{m_e\omega_{em}^2E_{gap}}{e^2E_{em}^2}\right)\right), \qquad (13.5)$$

with the band gap energy E_{gap} and the electric field strength of the electromagnetic radiation E_{em}.

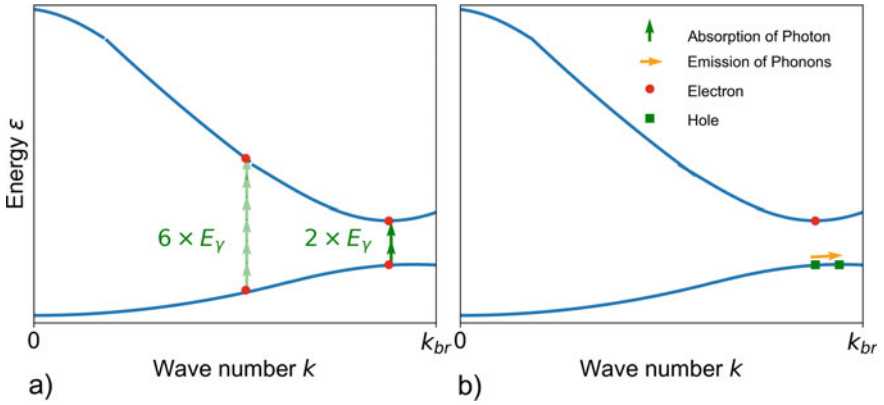

Fig. 13.3 Multi-photon excitation of a dielectric for an electron from the valence band into the empty conduction band, for 2- and 6-photon absorption (**a**). As the probability is much larger for 2-photon excitation, only 2-photon absorption takes place (**b**)

13.3.3 Multi-photon Excitation

As multi-photon excitation occurs at a high photon density, i.e. a high intensity of the radiation is given within the interaction volume, the probability for a multiple absorption of radiation through virtual states gets significant.

Multi-photon absorption in condensed matter follows the principles of single particles, but, as the inter-atomic potentials of many atoms are present, one has to describe the interband excitation of electrons from a valence into the conduction band with photon energies below the band gap, see Sect. 12.2.

As the multi-photon excitation probability scales inversely proportional to the multi-photon factor, an absorption takes places by a multiphoton excitation with the lowest possible multi-photon factor, as shown in Fig. 13.3a, where 2-Photon absorption is much more probable than a 6-photon absorption. Therefore, only a 2-photon absorption takes place exciting one electron from the valence band into the conduction band, and generating a hole in the valence band (Fig. 13.3b). In case the maximum of the valence band is not located at the same place of the minimum of the conduction band, the hole can change its position in the wave number-coordinates, as well in the spatial coordinates by electron diffusion.

As free charges are generated within condensed matter, the process is not directly a ionization process, but an rather more an excitation. We describe this within a band model, and represent the multi-photon process by a transition of an electron from the ground state often relied to the valence band into an excited state given often by the conduction band, see Fig. 13.3.

For multiphoton excitation MPE the probability for photo-excitation is described by [6]

Electron density rate for multiphoton excitation

$$\left(\frac{dn_e}{dt}\right)_{MPE} = \frac{2}{9\pi}\omega_{em}\left(\frac{m_{eff}\omega_{em}}{\hbar}\right)^{3/2} \Phi\left(\sqrt{2\left\langle\frac{\tilde{E}_{gap}}{\hbar\omega_{em}}+1\right\rangle - \frac{2\tilde{E}_{gap}}{\hbar\omega_{em}}}\right) \times$$
$$\times \exp\left(2\left\langle\frac{\tilde{E}_{gap}}{\hbar\omega_{em}}+1\right\rangle\left(1-\frac{e^2E_{em}^2}{4m_{eff}\omega_{em}^2E_{gap}}\right)\right)$$
$$\times \left(\frac{e^2E_{em}^2}{16m_{eff}\omega_{em}^2E_{gap}}\right)^{\left\langle\tilde{E}_{gap}/\hbar\omega_{em}+1\right\rangle} \tag{13.6}$$

where $\tilde{E}_{gap}$ represents the extended band gap energy calculated by the band gap energy plus the ponderomotive energy, see Sect. 4.4

$$\tilde{E}_{gap} = E_{gap} + U_P = E_{gap} + \frac{e^2E_{em}^2}{4m_e\omega_{em}^2}. \tag{13.7}$$

The factor $\left\langle\tilde{E}_{gap}/\hbar\omega_{em}+1\right\rangle$ describes the integer part of the multi-photon ionization order, meaning how many photons are needed to induce an ionization, and Φ represents the Dawson integral or probability integral.

13.3.4 Non-linear Photo-Excitation

An overall rate for **non-linear photo-excitation**, also called quasi-free electron generation rate **including the tunnel and multi-photon excitation**, is now given by [6]

Electron density rate for non-linear photo-excitation

$$\left(\frac{dn_e}{dt}\right)_{PE} = \frac{2\omega_{em}}{9\pi}\left(\frac{1+\gamma^2}{\gamma^2}\frac{m_{eff}\omega_{em}}{\hbar}\right)^{3/2} Q\left(\gamma, \frac{\tilde{E}^*_{gap}}{\hbar\omega_{em}}\right) \tag{13.8}$$
$$\times \exp\left\{-\pi\left\langle\frac{\tilde{E}^*_{gap}}{\hbar\omega_{em}}+1\right\rangle\frac{\left(\mathcal{K}\left(\frac{\gamma^2}{1+\gamma^2}\right)-\mathcal{E}\left(\frac{\gamma^2}{1+\gamma^2}\right)\right)}{\mathcal{E}\left(\frac{1}{1+\gamma^2}\right)}\right\},$$

where $\mathcal{K}$ and $\mathcal{E}$ represent elliptical integrals of first and second order, respectively. The **effective band gap energy** is hereby calculated to

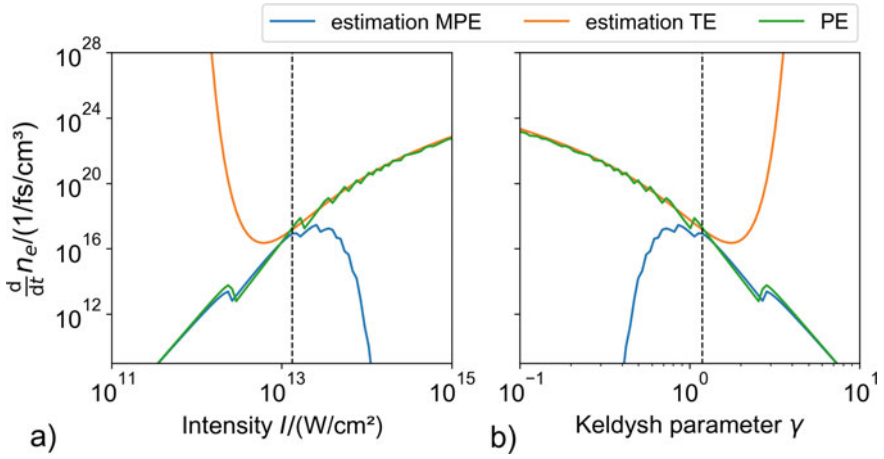

Fig. 13.4 Photo-ionization of a dielectric with $E_{\text{gap}} = 9$ eV described by the Keldysh model. The photo-excitation (PE) rate is plotted by approximations for tunnel and multi-photon excitation, as well the photo-excitation rate by the general model as function of the intensity of the radiation (**a**), and as function of the Keldysh parameter γ (**b**)

$$\tilde{E}^{*}_{\text{gap}} = \frac{2E_{\text{gap}}}{\pi}\frac{\sqrt{1+\gamma^2}}{\gamma}\mathcal{E}\left(\frac{1}{1+\gamma^2}\right).$$

The function Q is calculated by

$$Q(\gamma, x) = \sqrt{\frac{\pi}{2\mathcal{K}\left(\frac{1}{1+\gamma^2}\right)}}\sum_{j=0}^{\infty}\exp\left(-j\pi\frac{\mathcal{K}\left(\frac{\gamma^2}{1+\gamma^2}\right)-\mathcal{E}\left(\frac{\gamma^2}{1+\gamma^2}\right)}{\mathcal{E}\left(\frac{1}{1+\gamma^2}\right)}\right)$$
$$\times\, \Phi\left(\sqrt{\frac{\pi^2\,\langle x+1\rangle - 2x + j}{2\mathcal{K}\left(\frac{1}{1+\gamma^2}\right)}\mathcal{E}\left(\frac{1}{1+\gamma^2}\right)}\right),$$

with the probability integral Φ, and using again the integer part of x with $\langle x\rangle$.[1] Even this equations, and also those for the tunnel and multi-photon excitation are very extensive, from an engineering point of view, Keldysh solved them and we can plot easily using any mathematical program, the ionization probabilities for tunnel, multi-photon, and the photo-ionization. As one can see in Fig. 13.4a, the non-linear photo excitation using (13.8) is approximated by including the equations for tunnel and multi-photon excitation, (13.6) and (13.5).

[1] It should be noted that the equations for PE are altered to those from Keldysh, especially the squared values of $\lambda/(1+\gamma^2)^{1/2}$ and $(1+\gamma^2)^{-1/2}$ have been introduced for all elliptical integrals.

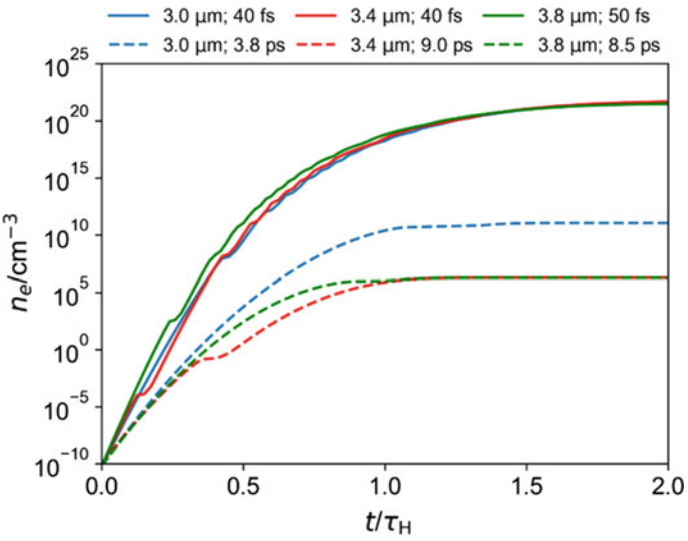

Fig. 13.5 Electron density as a function of time t normalized relative to the pulse duration of the applied radiation, depending on the wavelength λ and pulse duration τ_H [5]

Exemplary, exciting an amorphous dielectric material, here poly(methyl methacrylate) (PMMA) with ultrafast mid-IR laser radiation at wavelengths in the range of 3.0–3.8 µm, one can calculate the electron density by photo excitation using (13.8) and integrating over the irradiation time. It results as dominating process tunnel excitation, as there the Keldysh parameter gets $\gamma \ll 1$. Using femtosecond laser radiation quasi-free electrons are generated up to solid state densities of about 10^{22} 1/cm^3, contrary to picosecond laser radiation, where only 10^{10} electrons/cm^3 are generated, see Fig. 13.5 [5].

13.3.5 Two-Photon Absorption

Two-photon absorption (TPA or 2PA) is a non-linear absorption process whereby two photons are absorbed simultaneously by an atom, an ion or a molecule, and an electron is excited from a lower energy level to a higher energy level. It is refereed to a non-linear scattering, as described in Sect. 3.5.2. For example, by two-photon absorption an electron is excited from the ground to an excited state. The total energy of the excitation is equal to the sum of the two photon energies [8].

The equation describing the intensity attenuation of a laser radiation through a material undergoing single-photon absorption and two-photon absorption is given by

$$\frac{\partial I}{\partial z} = -\alpha I - \beta I^2,$$

where α is the linear absorption coefficient and β two-photon absorption constant, and is related to the second-order process, see Sect. 8.3. The absorbed power within a thickness element dz for single-photon and linear absorption is proportional to the radiation intensity, whereas the absorbed power for two-photon absorption is proportional to the intensity squared.

The two-photon absorption constant β is usually defined for a given concentration of a photo-activated material (species). The main assumption is that during interaction of the laser radiation with matter, the concentration of photo-activated species (molecules, ions, quantum dots (QDs) etc.) remains most of the time constant (e.g., it reaches equilibrium in a fraction of the irradiation time). However, for ultra-fast processes this assumption is no longer valid, and a more detailed model is usually used for numerical calculations. The central parameter of a model is a **two-photon absorption molecular cross-section** σ_{TPA}, while the density (or, population density) of the species being in ground state n is independent from the absorption constant, as follows

$$\frac{\partial I(z,t)}{\partial z} = -\sigma_{\text{TPA}} n(z,t) I^2(z,t).$$

For simplicity, here other processes are skipped from this equation—which may include single-photon, three-photon, or, generally speaking, multi-photon absorption, stimulated emission etc. Each multi-photon absorption term will have a factor of population density of the energy state from which the absorption occurs. The concentration of the photo-activated material $n_0(z,t)$ follows the corresponding rate equation

Rate equation for two-photon absorption

$$\frac{\partial n}{\partial t} = -\frac{\sigma_{\text{TPA}}}{2\hbar\omega_0} n(z,t) I^2(z,t) + k_{10}(n_0 - n), \tag{13.9}$$

where n_0 is the initial density of species and k_{10} attributes to the rate of relaxation of species from an excited to the ground state.

13.3.6 Three-Photon Absorption

Three-photon absorption (3PA) is a non-linear absorption process whereby three photons are absorbed simultaneously by an atom, ion or molecule, and an electron is excited from a lower energy level to a higher energy level. For example, three-photon absorption can excite an electron from the ground state to an excited state. The total energy of the transition is equal to the sum of the three photon energies [8].

The equation describing the **intensity attenuation** of radiation passing through a material undergoing single-photon, two-photon, and three-photon absorption is given by

$$\frac{\partial I}{\partial z} = -\alpha I - \beta I^2 - \gamma I^3,$$

where γ relates to the three-photon absorption constant and to the third-order susceptibility. The absorbed radiation in an element dz for single-photon absorption is proportional to the intensity, whereas the absorbed radiation for two-photon absorption is proportional to the intensity squared, and for three-photon absorption is proportional to the intensity cubed.

Again, the main assumption given by the two-photon absorption are used, that during interaction of the laser radiation with the matter the density of photo-activated species remains not constant most. The central parameter of the model is a **three-photon absorption molecular cross-section** σ_{3PA}, while the density of the species being in ground state n is "detached" from the absorption constant as follows

$$\frac{\partial I(z,t)}{\partial z} = -\sigma_{3PA} n(z,t) I^3(z,t).$$

One simplifies, omitting terms describing single-photon, two-photon, or, generally speaking, multi-photon absorption, linear absorption, stimulated emission etc. Each multi-photon absorption term will have a factor of population density of the energy state from which the absorption occurs. The density of the species $n(z,t)$ follows the following corresponding rate equation

Rate equation for three-photon absorption

$$\frac{\partial n}{\partial t} = -\frac{\sigma_{3PA}}{3\hbar\omega_0} n(z,t) I^3(z,t) + k_{10}(n_0 - n), \tag{13.10}$$

where n_0 is the initial concentration of species and k_{10} attributes to the rate of relaxation of species from the excited to the ground state.

13.4 Impact Ionization

Electrons already excited by linear or nonlinear photo excitation, see Fig. 13.6. They can serve as seed electrons for impact ionization, since these electrons can be further excited in a still existing electromagnetic field of the radiation (or high repetitive pulsed radiation) via inverse bremsstrahlung/free-carrier absorption by intraband excitation, see Figs. 12.9 and 13.6b. The cross-section for inelastic scattering with electrons in the valence band get significant for energies of the electrons in the conduction band being in the range of a critical energy E_{crit}, see Fig. 13.6c. This high-energy electrons collide with a ground state electrons in the valence band generating an additional excited electron within the conduction band, see Fig. 13.6c.

As long as the radiation acts on the increasing number of free electrons increasing its energy above the ionization energy, the more additional electrons are generated by

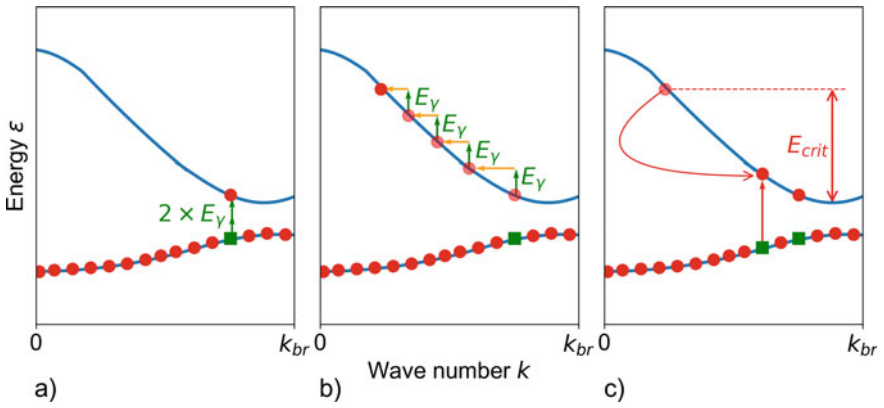

Fig. 13.6 Schematics of one collision ionization process: **a** Multiphoton or tunnel excitation of an electron from the valence into the conduction band, **b** multiple inverse bremsstrahlung exciting electron further, and **c** de excitation of conduction band electron to a lower level in the conduction band and transfer of the difference energy to a valence electron being excited into the conduction band

impact ionization, inducing an avalanche of quasi-free electrons, see also Fig. 13.1. This process of subsequent impact ionization processes is called **avalanche ionization**.

The simplest model describing avalanche ionization is given by

$$\frac{dn_\mathrm{e}}{dt} = \eta_\mathrm{av} n_\mathrm{e},$$

where the impact excitation rate η is directly proportional to the irradiation intensity

Rate equation for avalanche ionization

$$\eta = \alpha_\mathrm{av} I, \tag{13.11}$$

thereby we use an **average avalanche coefficient** α_av. This equation describes very well the impact and avalanche ionization for crystalline and amorphous materials [9], but has a leak in precision, as not considering the ponderomotive potential, or the probability for linear ionization into the conduction band, as well the collision time of the electrons, i.e. the density of the electrons.

A more elaborate model including the critical energy E_crit needed for impact ionization, is given by the **Kennedy model** [10]. There, the impact excitation rate is defined by the relative energy change due to inelastic scattering of electrons with ions or phonons, and is defined by

Kennedy model for impact ionization rate

$$\eta = \frac{1}{E_{\text{crit}}} \left(\frac{dE_{\text{gain}}}{dt} - \frac{dE_{\text{drain}}}{dt} \right), \tag{13.12}$$

where the electrons gain energy per time by inelastic scattering with higher energetic electrons. This process is proportional to the intensity of the radiation I, and scales by an oscillator term ω, driven by the scattering/collision time τ_c, and the oscillation frequency of the radiation ω

$$\frac{dE_{\text{gain}}}{dt} = \frac{2e^2 I(t)}{\epsilon_0 n c_0 m_e} \frac{\tau_c}{1 + \omega^2 \tau_c}.$$

On the other hand, electrons loose energy per time by the inelastic scattering with other electrons from the valence band, releasing an average energy E_{av} given in literature by about half of the critical energy

$$E_{\text{av}} = \frac{E_{\text{crit}}}{2}.$$

Thereby, the energy-loss process scales by the fraction of the electron mass to the ion mass M, and also by the squared frequency of the radiation, resulting in

$$\frac{dE_{\text{drain}}}{dt} = -2\omega^2 E_{\text{av}} \frac{m_e}{M} \frac{\tau_c}{1 + \omega^2 \tau_c}.$$

One central parameter in the Kennedy model is the collision time, given by the weighted average of the collision times for the electrons with other electron and electrons with phonons (or ions)

$$\tau_c = \frac{\tau_{ep} \tau_{ee}}{\tau_{ee} + \tau_{ep}}.$$

An approach to determine the collision time is, firstly, to assert that the electron-phonon collision time is for amorphous dielectrics like fused silica in the range $0.1 \leq \tau_{ep} \leq 1$ fs [9], and therefore can be omitted. Secondly, as the electrons in the conduction band of a dielectric are nearly free, they can be handled as an ideal gas and its electron-electron collision time, respectively collision frequency be calculated by the classical kinetic gas theory to

$$\frac{1}{\tau_{ee}} = \frac{4\pi\epsilon_0}{e^2} \sqrt{\frac{6}{m_e}} (k_B T_e)^{3/2},$$

with the temperature of the thermalized electron system T_e.

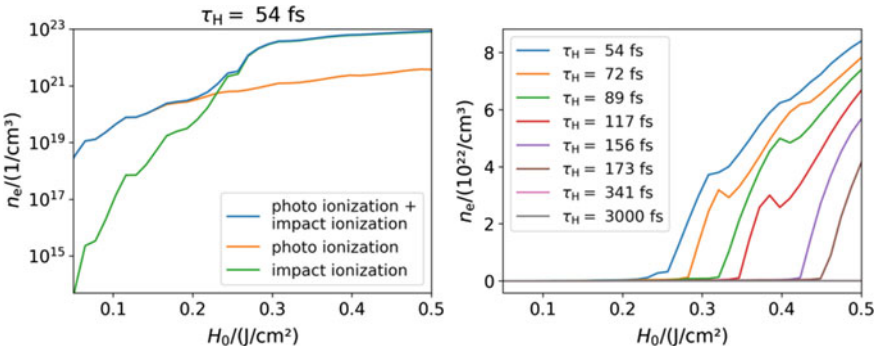

Fig. 13.7 Left: electron density n_e of P3HT as a function of the fluence of the laser radiation induced by photo-ionization (orange), impact ionization (green), and both processes (blue) after irradiation by laser radiation at the center wavelength $\lambda = 3.4\,\mu m$, and the pulse duration $\tau_H = 54$ fs. Right: comparison of the electron density n_e of P3HT induced by photo-ionization and impact ionization after laser irradiation at different pulse duration τ_H [11]

Putting the last equations together one gets for the impact ionization rate by Kennedy to

$$\eta(t) = \left(\frac{2eI(t)}{\epsilon_0 n c_0 m_e E_{crit}} - \frac{m_e \omega^2}{M} \right) \frac{\tau_c}{1 + \omega^2 \tau_c}.$$

Finally we can setup the rate equation for impact ionization omitting the last two drains terms in (13.1) describing the reduction in the number of electrons in the conduction band by recombination by a simplified equation

Simplified electron rate equation for non-linear photo excitation

$$\frac{dn_e(t)}{dt} = \left(\frac{dn_e}{dt} \right)_{PI} + \eta(t) n_e, \tag{13.13}$$

where the first therm on the right side represents the rate for photo ionization, either linearly or non-linearly, and the second term the collision ionization term.

The given rate equation for impact ionization yields a exponential growth of the electron density in time. This behavior is also called avalanche ionization. As calculated for the organic semiconductor P3HT (Poly(3-hexylthiophene-2,5-diyl)), the combination of photo ionization and impact ionization results in an exponential dependence of the electron density on the fluence H_0 of the applied radiation, see Fig. 13.7. As a consequence, the ablation threshold fluence H_{thr}, monitoring the electron density, replicates this exponential behavior, see Fig. 13.8 [11].

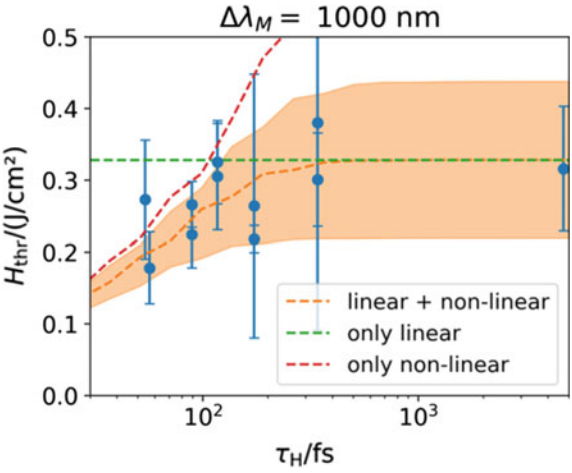

Fig. 13.8 Measured ablation threshold fluence H_{thr} of P3HT as a function of the pulse duration τ_H (blue dots) of the laser radiation in comparison with the calculated ablation threshold fluence induced by linear $H_{thr,l}$ (green dashed), nonlinear $H_{thr,nl}$ (red dashed), and the superposition of linear and nonlinear excitation $H_{thr,l+nl}$ (orange dashed and orange area) [11]

13.5 Channeling and Filamentation

The interaction of ultra-fast laser radiation with dielectrics can result in a drastic change of the propagation behavior of the radiation, and additionally in a properties change of the irradiated matter. Depending on the density of the dielectric, we distinguish channeling in dielectric fluids, and filamentation in solid dielectrics.

13.5.1 Channeling

As absorption takes place, the optical energy excites single atoms, molecules, or even many of them in condensed matter. As a consequence, ionization takes place resulting in the formation of free or quasi-free electrons. This electrons exhibit optical properties, as described in Sect. 10.2, **defocusing** the radiation.

On the other hand, high-intensity radiation induces in dielectrics the Kerr effect, see Sect. 8.4.4, resulting in case of a Gaussian shaped spatial intensity profile into **self-focusing** of the radiation. Adjusting this two processes being in balance results in an repetitive interplay of defocusing and focusing of the radiation, getting the so called **channeling**.

Depending on the focusing condition of the radiation we can observe, for high intensity ultrafast laser radiation featuring a Gaussian spatially shaped radiation, that the Kerr effect takes place inducing self-focusing during the propagation through a dielectric, like a noble gas, see Sect. 8.4.5.

As the beam waist gets smaller, the probability for non-linear absorption due to multi-photon or tunnel excitation increases, resulting in the formation of free electrons. As the intensity of the radiation scales in time, also being bell-shaped, the electron density increases proportionally, too, see Fig. 13.9.

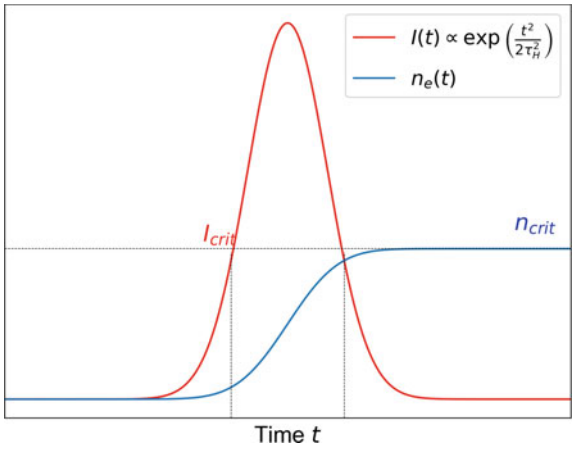

Fig. 13.9 Temporal dependence of the intensity distribution of the radiation and the resulting electron density as function of time

The electron density reaches its maximum after the irradiation. As the electron density increases, its action on the radiation gets pronounced featuring a defocusing effect due to its refractive index smaller than 1, see Sect. 10.2 and (10.7). As long as the radiation is focused into the dielectrics, the electron density is increased defocusing further the radiation until a steady-state is reached, where to a focusing follows defocusing and again focusing, and so on. This process is called channeling and shown in Fig. 13.10.

As the refractive index of the dielectrics changes due to the Kerr effect and also due to the time-dependent electron density, self-phase modulation takes place, see Sect. 8.4.7, broadening of the spectral intensity distribution of the radiation takes place along the channel. Using ultra-fast TW-laser radiation channeling is used in air investigating the chemical composition of the air. As the channels can be generated in different heights using adaptive optics, the chemical composition is investigated in heights up to some kilometers.

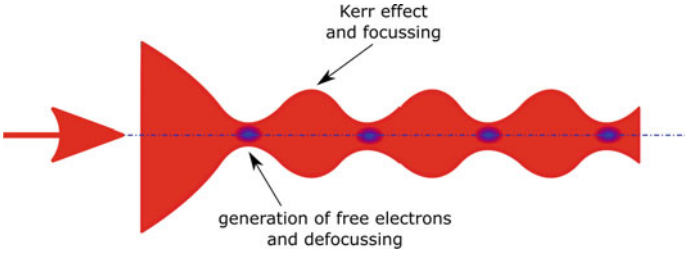

Fig. 13.10 Schematic description of the spatial dependence of the beam waist due to channeling induced by a sequence of focusing by self-focusing via the Kerr effect, and de-focusing due to free-electrons induced by photo-ionization

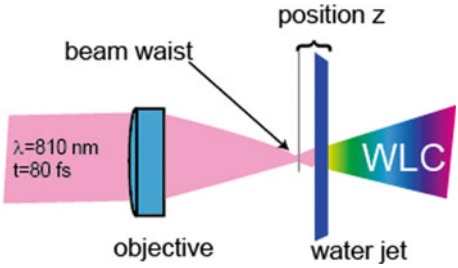

Fig. 13.11 Schematic description of the spatial dependence of the beam waist due to channeling induced by a sequence of focusing due self-focusing by the Kerr effect and de-focusing due to free-electrons induced by photo-ionization

13.5.2 Filamentation

Filamentation is complementary to the channeling. Ideally, increasing the intensity of the laser radiation, channeling should start at specific intensity i.e. at a threshold intensity. Following this, only one channel should be generated getting only stronger, when increasing the peak intensity.

In practice, due to small inhomogeneities within the spatial (and temporal) intensity distribution of the focused radiation, channeling starts at many places within the focused radiation. The larger the intensity the larger the number of spatially separated channels. This process is called **filamentation**.

Focusing ultra-fast laser radiation into a condensed dielectrics, like a water jet, shown in Fig. 13.11, as function of the average power[2] the number of filaments increases, see Fig. 13.12 [12].

Starting from an average power of $P_{av} = 0.75$ mW, a single temporal stable filament is formed within the water jet. Increasing the power increases the number of electrons and its dynamics induces a spectral broadening of the laser radiation, see filament at $P_{av} = 2.4$ mW with the whiter intensity distribution and the typical red emission-ring.

At an average power of $P_{av} = 3.5$ mW a second filament is formed, and increasing the radiation power further results in an increasing spatial separation of the two filaments inducing an interference of the two filaments, and featuring a typical modulated intensity profile of the radiation. At higher power the number of filament increases steadily, inducing additionally complex interference patterns. At very high power of $P_{av} = 200$ mW, many filaments are generated, which due to the very strong interaction with the water jet results in unstable distribution of filaments, meaning that after each pulse the position of each filaments changes resulting in a speckle-like intensity distribution. But, the overall white light continuum power remains constant.

[2] The applied laser radiation features a fixed repetition rate of $f_p = 1$ kHz and a pulse duration of $t_p = 80$ fs.

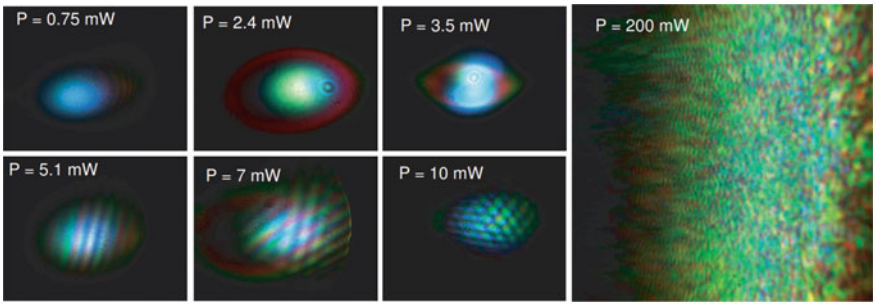

Fig. 13.12 Measured intensity distribution in the filament as function of the average laser power. With increasing power the number of filaments increases, sustaining their spatial positions and inducing partially or total interference effects. At very high power the position of the filaments vary from pulse to pulse chaotically, wheres the average intensity distribution of the white-light continuum (WLC) remains constant (wavelength $\lambda = 800$ nm, pulse duration $t_p = 80$ fs, repetition rate $f_p = 1$ kHz)

References

1. A. Kaiser, B. Rethfeld, M. Vicanek, G. Simon, Microscopic processes in dielectrics under irradiation by subpicosecond laser pulses. Phys. Rev. B: Condens. Matter Mater. Phys. **61**, 11437–11450 (2000)
2. L. Englert, B. Rethfeld, L. Haag, M. Wollenhaupt, C. SarpeTudoran, T. Baumert, Control of ionization processes in high band gap materials via tailored femtosecond pulses. Opt. Express **15**, 17855 (2007)
3. B. Rethfeld, Unified model for the free-electron avalanche in laser-irradiated dielectrics. Phys. Rev. Lett. **92**, 187401 (2004)
4. D.N. Wang, Y. Wang, C.R. Liao, *Laser Surface Engineering* (Elsevier, 2015), pp. 359–381
5. T. Pflug, M. Olbrich, A. Horn, Surface modifications of poly(methyl methacrylate) induced by controlled electronic and molecular vibrational excitation applying ultrafast Mid-IR laser radiation. J. Phys. Chem. C **123**, 20210–20220 (2019)
6. L.V. Keldysh, Ionization in the field of a strong electromagnetic wave. Sov. Phys. JETP **20**, 1307 (1965)
7. B.C. Rethfeld, Mikroskopische Prozesse bei der Wechselwirkung von Festkörpern mit Laserpulsen im Subpikosekundenbereich. Dissertation, 1999
8. http://www.simphotek.net/bckg/bckg.3pa.html
9. T. Pflug, Strong field excitation of electrons into localized states of fused silica. Ph.D. Thesis, Technische Universität Chemnitz, 2022
10. P.K. Kennedy, A first-order model for computation of laser-induced breakdown thresholds in ocular and aqueous media. I. Theory. IEEE J. Quantum Electron. **31**(12), 2241–2249 (1995). https://doi.org/10.1109/3.477753
11. T. Pflug, P. Lungwitz, M. Olbrich, A. Horn, Linear and nonlinear excitation of P3HT induced by spectral-shaped ultrafast Mid-IR laser radiation. J. Phys. Chem. C **124**(25), 13618–13626 (2020)
12. A. Horn, Zeitaufgelöste Analyse der Wechselwirkung von ultrakurz gepulster Laserstrahlung mit Dielektrika. Ph.D. Thesis RWTH Aachen, 2003, ISBN 3-8322-2068-2

Chapter 14
Heating

Abstract Laser radiation heats condensed matter by coupling optical energy into the electronic system. Depending on the properties of matter, linear, or non-linear absorption takes place. The two-temperature model is described in the following, as well the thermodynamic properties of electron and phonon systems are derived. Finally numerical solutions are presented with some examples for metals.

14.1 Process Steps of Heating

In laser technology, for example, the absorption of laser radiation is of eminent interest, because the absorbed energy primary determines the forthcoming processes. So, a solid matter absorbing optical energy can be

- **heated**, thereby also reaching some typical thresholds for re-crystallization, allowing hardening or generation of new crystal textures,
- **melted**, getting a liquid phase, allowing mixing of different substances, also initiating drilling, cutting, or ablation of matter,
- **evaporated**, enabling to drill or cut matter.

In order absorption of radiation takes place, one can state that metals absorb linearly the radiation due to the quasi-free electrons given. Looking at semiconductors the situation gets much more difficult: depending on the photon energy of the radiation, i.e. the wavelength, the radiation is little or not absorbed by the semiconductor. But, due to the small band gap the electro-optical properties are transiently changed by the irradiation resulting in a complex dynamic development of charges, i.e. the electrons and the holes. Finally, dielectrics have in the ideal case no free electrons and consequently do not absorb any radiation at low radiation intensities. There, only non-linear process will allow an absorption of radiation. Alternatively, non-perfect dielectrics or semiconductors featuring a significant concentration of defects (or dopands) have localized states and enable so interband excitation, getting a linear absorption of the radiation.

In any case, absorption takes place by linear and/or non-linear processes, the radiation is absorbed only by the quasi-free electrons being located in the conduction band of the solid. This is true for intensities of the radiation being below $I \approx 10^{18}\,\mathrm{W/cm^2}$,

© Springer Nature Switzerland AG 2022

A. Horn, *The Physics of Laser Radiation–Matter Interaction*,
https://doi.org/10.1007/978-3-031-15862-9_14

where only the interaction of the radiation with bounded and free electrons are given. Processes at larger intensities will not be discussed in this textbook.

Heating of solids represent at least a two-step process.

In the first step, the electrons absorb the optical energy thereby increasing its kinetic energies, and featuring after a thermalization process an increased average temperature T_e. In a second step this electrons, featuring a higher energy and temperature scatter with the periodically spaced atoms of the solid, called phonons, and transfer partly its energy to the phonon system increasing its average temperature T_{ph}. Doing so the solid is finally heated. The interplay of the electron and the phonon systems is described by the two-temperature model.

14.2 Two-Temperature Model

Especially, metals are a very important materials commonly used in the industrial engineering. In general, a metal represents a solid consisting of placed atoms within a lattice with periodic spacing being surrounded by quasi-free electrons located in the conduction band of the metal.

An amount of quasi-free electrons interact with the electromagnetic radiation absorbing partly the energy and getting excited (Fig. 14.1). Thereby the absorbed amount is calculated by applying the Fresnel equations for a quasi-free electron gas, see Chap. 10. The electrons absorbing the optical energy will gain energy, whereas the other quasi-free electrons will sustain at the initial energy. This excited electrons, featuring prior to the excitation a thermodynamic equilibrium with a corresponding temperature T_e, will shortly after excitation **no longer be in any equilibrium**. Within some 10th of femtoseconds the excited free electrons scatter with the other quasi-free electrons, described by the electron-electron scattering frequency, transferring energy. Doing this, the electrons recover a new thermodynamic equilibrium at a larger temperature. All the electrons gaining the energy are also called **the electron system**.

Clearly, this new state of the electrons is localized in the **interaction volume**, given by the irradiation area through the geometry of the radiation (e.g. the laser spot on the surface), and as well by the optical properties of the radiation, e.g. the extinction coefficient describing the absorption length. So, using Lambert-Beers law, see (10.3), the energy deposited in depth is calculated. A temperature difference in the electron system between the irradiated and the non-irradiated regimes will induce an energy transport by **electron diffusion** of the quasi-free electrons out of the interaction volume, and possibly also by ballistic electrons.

Ballistic electrons represent high-energy electrons not being thermalized with other electrons at all. They feature very high velocities, about ten times the thermalized one, resulting in particles featuring very high kinetic energies. At low excitation

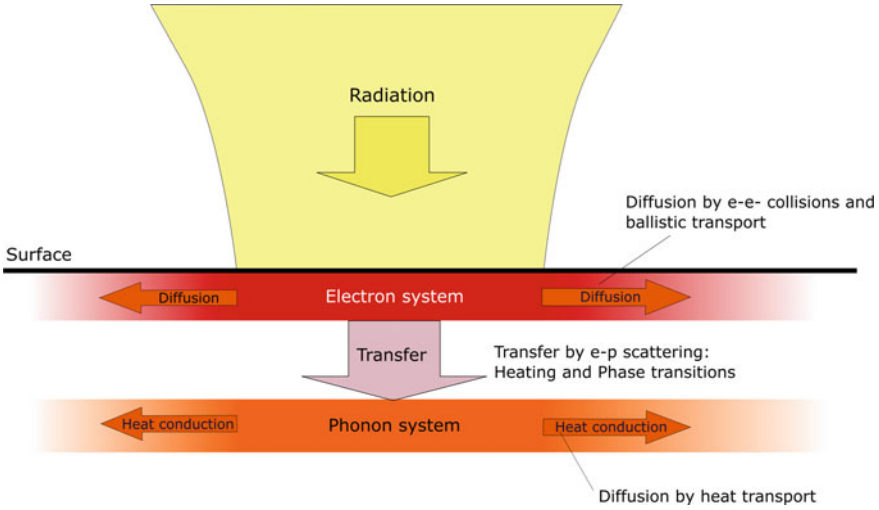

Fig. 14.1 Interaction of the radiation with condensed matter featuring quasi-free electrons, described by the two-temperature model. Here, radiation is party absorbed by the electron system. After thermalization, a heated electron system results. The heated electron system can transfer its energy to the colder electron or phonon system, heating it up, and possibly inducing phase changes

energies of the quasi-free electrons, e.g. at low electron temperatures, the cross-section for scattering of high-energy electrons, like the ballistic electrons with free electrons is small. This means that the **mean free path length of ballistic electron** can be very large, enabling electrons to escape from the interaction volume transferring energy out. But, as the energy of the quasi-free electron gets large due to higher intensity of the radiation, the cross-section for scattering gets significant inhibiting the energy diffusion by ballistic electrons further. Practically speaking, working with laser radiation inducing phase changes, like melting and ablation, results in very large electron temperatures and therefore, the probability for formation of ballistic electrons is vanishing. The cross-section for scattering of electrons with electrons is inversely proportional to its kinetic energies. This means that ballistic electrons possibly do not scatter with low-energy electrons on larger distances.

The quasi-free electrons scatter not only with each other (like particles of a gas), but also interact with the ions or atoms, not really with the nuclei, but with the bounded electrons of the condensed matter. In our model the atoms are placed in an ordered crystal structure, and the collective dynamics of the atoms is well described by phonons, or also called **the phonon system**, see Fig. 14.1. So the excited quasi-free electrons will scatter with quasi-free electrons and also will scatter with atoms, lastly described by the phonon system, thereby transferring energy.

In other words, the electron system, being heated by the electromagnetic radiation will on the other hand finally heat the phonon system. This heating of the phonon system takes place on a much longer time scale in the picosecond time regime

compared to the electron system heating. Typically, the electron system in metals is heated within some 10–100 fs. The temperature of the phonon system T_{ph} represents the temperature of the condensed phase of matter, here the solid state of a metal or a dielectric. Heating the phonon system will also induce **heat transport** out of the interaction volume, the outside of this volume being usually colder, and possibly inducing phase transitions of the matter into the liquid, the vapor, or the plasma phase state, see Chap. 15.

In order to compute all described steps, one needs to **model firstly the heating processes**

1. **The energy deposition** using the optical properties of the irradiated matter for the applied radiation, e.g. the absorption coefficient. Knowing the complex refractive index $\tilde{n}$ of the condensed matter, e.g. for metals see Sect. 12.6 and (12.3), this is easily given.
2. **The energy transfer within the electron system**, e.g. diffusion of electrons using the thermophysical properties of electrons, like the heat capacity and heat conductivity for the electron system, and the energy transfer to the phonon system. Also, one has to consider the ballistic electron diffusion at low electron temperatures.
3. **The energy diffusion in the phonon system** using the thermophysical properties of matter, like the heat capacity and heat conductivity for the phonon system.

As matter is heated, it can change its phase state and will be described by the following processes, more in detail in the next Chap. 15:

1. **The phase transitions** considering the latent heat for melting and evaporation. Also the ionization has to be added, resulting in an additional phase state, the so called *plasma state*.
2. **The melt, vapor, and plasma dynamics** have to be described by hydrodynamic and/or magneto-hydrodynamic equations.

To realize this, the heat conduction equations have to be determined for the electron and the phonon systems, first. We will instructively now derive the general heat equation.

14.3 Derivation of the Heat Equation

The heat equation describes the **energy transfer** within a body or from one body to another, without any kinetics of the atoms (no transport of matter by heat convection). Depending on the material, the energy transport is mediated by the quasi-free electrons and/or the phonons.

In our case, a solid with the volume V and the dimension $V = L \times h \times b$, representing for example a metal, is irradiated from the left side on a surface featuring an area $A_1 = h \cdot b$, see Fig. 14.2. We will firstly assume that the length L of the body is much larger than the lateral dimensions of the irradiated area $L \gg h, b$. Now, we want to apply the **one-dimensional heat conduction** in the x-direction.

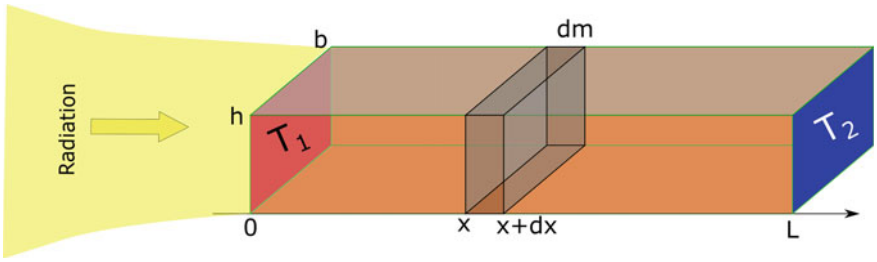

Fig. 14.2 One-dimensional heat conduction. Radiation heats from left a volume $V = h \times b \times L$ with $h, b \ll L$ interacting through the surface $A = h \cdot b$

The irradiated area on the left side features a temperature T_1, and at the position x of the solid the temperature is given by $T(x)$. The one-dimensional Fourier's law is deduced, as the heat conducted per time increment Δt, also called the **heat flow**, depends on the heat conductivity λ, the area $A = h \cdot b$, and the temperature gradient in the x-direction $\partial T/\partial x$, and is given by

$$\frac{\delta Q}{\partial t} = -\lambda \cdot A \cdot \frac{\partial T}{\partial x}. \tag{14.1}$$

For the general heat conduction in three dimensions one gets the general description:

Fourier's law

$$\frac{\delta Q}{\partial t} = -\lambda \cdot A \cdot \nabla T. \tag{14.2}$$

The necessary **heat flow** to increase the temperature within a time increment Δt of the Volume $\mathrm{d}V$ featuring the mass dm is given by its specific heat capacity c and the temperature difference ΔT, resulting in

Heat flow within the solid

$$\frac{\delta Q}{\partial t} = c \cdot dm \cdot \frac{\partial T}{\partial t}. \tag{14.3}$$

Even if the lateral dimensions h and b are small, the heat diffusing out of the volume through the lateral area $M = 2\,h \cdot L + 2\,b \cdot L$ is still given and relevant, and depends on the heat transfer coefficient α_{H}, the temperature difference at the position x between the solid temperature $T(x)$ and the ambient temperature T_{a}, representing also the initial temperature of the body prior to the irradiation, resulting in the **local heat flow**

Local heat flow

$$\frac{\delta Q}{\partial t} = -\alpha_{\mathrm{H}} \cdot M \cdot (T - T_{\mathrm{a}}). \tag{14.4}$$

The heating is primary given by the irradiation from the left area $A = b \cdot h$, and depends on the intensity decrease of the radiation $-\mathrm{d}I$ in depth, the duration of irradiation $\mathrm{d}t$, and the absorbed amount of radiation at the surface, given by the reflectance $(1 - R)$. The resulting heat increment reads to

$$\delta Q = -(1 - R)\, A\, \mathrm{d}t\, \mathrm{d}I.$$

The intensity distribution of the radiation in the body depends on the amount of energy absorbed in the depth x, so that using Lambert-Beer's law, see (5.4) and the absorption coefficient α, (10.2), one gets

$$I(x) = I_0 e^{-\alpha x}.$$

The derivative of the intensity in respect to the depth is given by

$$\frac{\mathrm{d}I}{\mathrm{d}x} = -\alpha \cdot I_0\, e^{-\alpha x} = -\alpha\, I$$

defining the decrease in intensity, e.g. the optical energy extracted from the electromagnetic field per depth

$$\mathrm{d}I = -\alpha\, I\, \mathrm{d}x.$$

The **heat flow from the surface** of the body given by the radiation is now described by

Heat flow by the radiation

$$S = \frac{\delta Q}{\partial t} = (1 - R)\alpha A\, I\, \mathrm{d}x. \tag{14.5}$$

As balance of energy holds, a heat flow into the solid results on the one side in an increase of its temperature, see (14.3), and representing the internal energy of the solid. On the other side, a heat flow per mass element $dm = \rho \mathrm{d}V = \rho A \mathrm{d}x$ is accumulated in $\mathrm{d}V$, and is given firstly by the heat per time at the surface of the volume, being introduced through the radiation using (14.5). Secondly, the heat sinks are given by the lateral areas of the volume, described by (14.4), and thirdly, the heat diffusion from the entrance area at x through the volume $\mathrm{d}V$, and out to the second area at $x + \mathrm{d}x$ is described by the Fourier's law for one spatial coordinate, see (14.1). Finally we get the overall energy flow equation

$$\frac{\delta Q}{\partial t} = c \cdot \mathrm{d}m \frac{\partial T}{\partial t} \tag{14.6}$$

$$= -\lambda_x \cdot A \left(\frac{\partial T}{\partial x}\right)_x + \lambda_{x+\mathrm{d}x} \cdot A \left(\frac{\partial T}{\partial x}\right)_{x+\mathrm{d}x} - 2\alpha_H (b+h)\mathrm{d}x(T - T_\mathrm{a}) + (1-R)A\,\alpha I\,\mathrm{d}x. \tag{14.7}$$

Now, remembering how to accomplish an approximation of a function $f(x)$ by a Taylor series,[1] we can rewrite the Fourier therms, here the second part in (14.7),

$$\begin{aligned}\lambda_{x+\mathrm{d}x} \cdot A \left(\frac{\partial T}{\partial x}\right)_{x+\mathrm{d}x} &= \lambda_x\, A \left(\frac{\partial T}{\partial x}\right)_x + \\ &+ \left[\left(\frac{\partial \lambda_x}{dx}\right)_x A \left(\frac{\partial T}{\partial x}\right)_x + \lambda_x\, A \left(\frac{\partial^2 T}{\partial x^2}\right)_x\right]\mathrm{d}x \\ &= \lambda_x\, A \left(\frac{\partial T}{\partial x}\right)_x + A \frac{\partial}{\partial x}\left(\lambda_x \frac{\partial T}{\partial x}\right)\mathrm{d}x, \end{aligned} \tag{14.8}$$

and replacing this in (14.7). One gets the one-dimensional heat equation, remembering thereby $\mathrm{d}V = \mathrm{d}x A$ and $\rho = \frac{\mathrm{d}m}{\mathrm{d}V}$

One-dimensional heat equation

$$\frac{\delta Q}{\partial t} = c \cdot \mathrm{d}m \frac{\partial T}{\partial t} = c\,\rho\,\mathrm{d}V \frac{\partial T}{\partial t} = c\,\rho\,A\,\mathrm{d}x \frac{\partial T}{\partial t} \tag{14.9}$$

$$= A \frac{\partial}{\partial x}\left(\lambda_x \frac{\partial T}{\partial x}\right)\mathrm{d}x - 2\alpha_H (b+h)\mathrm{d}x(T - T_\mathrm{a}) + (1-R)A\,\alpha I\,\mathrm{d}x. \tag{14.10}$$

Easily one sees that without sources and sinks ($\alpha_H = 0$ and $\alpha = 0$) we get

$$\frac{\delta Q}{\partial t} = c \cdot \rho \frac{\partial T}{\partial t} = \frac{\partial}{\partial x}\left(\lambda_x \frac{\partial T}{\partial x}\right),$$

and allowing now a heat conduction in all directions, we get the three-dimensional heat equation without sources and sinks for $T = T(x, y, z) = T(\boldsymbol{r})$

[1] Taylor series for a function $f(x + \mathrm{d}x) = f(x) + \left(\frac{\mathrm{d}f}{\mathrm{d}x}\right)\mathrm{d}x + \mathcal{O}(\mathrm{d}x^2)$.

Three-dimensional heat equation without sources and sinks

$$\frac{\partial T}{\partial t} = \frac{1}{c \cdot \rho} \nabla \left(\lambda(\boldsymbol{r}) \nabla T \right). \tag{14.11}$$

For a constant heat conductivity $\lambda = \text{const.}$, one gets the homogeneous heat equation

Homogenoeus heat equation

$$\frac{\partial T}{\partial t} - \frac{\lambda}{c\,\rho} \Delta T = 0. \tag{14.12}$$

14.4 Heating of Metals

As we explained in Sect. 14.2, in case of metals it is reasonable to consider two thermodynamic systems, as most metals feature quasi-free electron allowing a linear excitation of them, see Sect. 12.3. Most metals feature a crystalline atomic structure, so that one can subdivide the heating process within two systems in three equations,

1. The **electron system with the electron temperature $\boldsymbol{T}_\mathrm{e}$**, the heat capacity of the electrons c_e, and the heat conductivity of the electrons λ_e described by the heat equation for the electron system with S representing the heating source, and in our case it given by the laser radiation.

Heat equation for the electron system

$$\rho_\mathrm{e} c_\mathrm{e} \frac{\partial T_\mathrm{e}}{\partial t} - \nabla(\lambda_\mathrm{e} \nabla T_\mathrm{e}) = S - G(T_\mathrm{e})(T_\mathrm{e} - T_\mathrm{ph}). \tag{14.13}$$

2. The **phonon system with temperature of the phonons $\boldsymbol{T}_\mathrm{ph}$**, the heat capacity of the phonons c_ph, and the heat conductivity of the phonons λ_ph described by the heat equation for the phonon system

Heat equation for the phonon system

$$\rho_\mathrm{ph} c_\mathrm{ph} \frac{\partial T_\mathrm{ph}}{\partial t} - \nabla(\lambda_\mathrm{ph} \nabla T_\mathrm{ph}) = G(T_\mathrm{e})(T_\mathrm{e} - T_\mathrm{ph}). \tag{14.14}$$

3. The **heat transfer from the electron system to the phonon system** is achieved by **coupling the two thermodynamic systems**, and is realized by the electron-phonon heat flow coupling for the heat transfer from the electron to the phonon system with the electron-phonon coupling factor G.

Heat flow coupling for the electron-phonon systems

$$\frac{\delta Q}{\partial t} = G(T_\mathrm{e})(T_\mathrm{e} - T_\mathrm{ph}), \tag{14.15}$$

To solve both equations numerically, one needs apart from the optical properties of the irradiated metal, e.g. the complex refractive index, the properties of the radiation, also all thermophysical data from the investigated metal. So, the heat capacities for the electron and phonon system, as well all its heat conductivities are needed. Here, we start from the electron system, looking on its thermophysical parameters, and going forth, also to derive the parameters for the phonon system.

14.5 Thermophysical Properties of the Electron System

Assuming no heat sink due to heat conduction outside of the excitation volume, e.g. accomplishing a very short interaction time, we can write the heat equation for the electron system with an external heat source S by

$$c_\mathrm{e}\,\rho_\mathrm{e}\frac{\partial T_\mathrm{e}}{\partial t} - \nabla\,(\lambda_\mathrm{e}\nabla T_\mathrm{e}) = S - G(T_\mathrm{e})(T_\mathrm{e} - T_\mathrm{ph}). \tag{14.16}$$

So, to solve this equation we need the temperature dependence of the heat capacity for the electron system $c_\mathrm{e} = c_\mathrm{e}(T)$, the heat conductivity $\lambda_\mathrm{e} = \lambda_\mathrm{e}(T)$, and the electron-phonon coupling factor $G = G(T_\mathrm{e})$.

14.5.1 Heat Capacity of the Electron System

In principle the electron system can be described by an electron gas. Firstly, we will try a classical approach assuming this electron gas as an ideal gas. As this approach will fail, a second approach is started taking the quantum mechanical properties of the electrons into account.

Classical Approach

One gets the heat capacity for the electron system by taking the quasi-free electrons as an ideal gas, and equating the first law of thermodynamics. In general, for a solid the **specific heat capacity** is given by the relation

$$\delta Q = c\, m\, \mathrm{d}T,$$

with c the specific heat capacity. From there one calculates the specific heat capacity to

$$c = \frac{1}{m}\frac{\delta Q}{\mathrm{d}T}.$$

Also, we can define a **molar heat capacity** by

$$C = \frac{1}{n}\frac{\delta Q}{\mathrm{d}T}.$$

As known from classical thermodynamics, the absorbed heat δQ increases at constant volume the **specific internal energy** $\boldsymbol{u}$ of the system, or at constant pressure it increases the **specific enthalpy** $\boldsymbol{h}$.

In general, for condensed matter featuring a temperature $T > 0$ K the atoms fulfill an oscillatory movement, comparable to the Brownian movement of a free particle. An increase of energy results in an increase of its amplitude. Metals consist of bounded atoms and quasi-free electrons. Due to the much smaller mass of the electrons, also a much smaller heat capacity of electrons results, ending in a much higher temperature of the electron system, compared to the phonon system.

For an ideal gas one knows that the specific volumetric heat capacity c_v is given by

Specific heat capacity at constant volume

$$c_v = \left(\frac{\partial u}{\partial T}\right)_v, \tag{14.17}$$

with the specific internal energy u, and the index v determining for the heat capacity the constancy of the specific volume. One calculates the molar internal energy of a solid U_m for $N_\mathrm{A} = 6.022 \cdot 10^{23}$ atoms/mol to

$$U_\mathrm{m} = \frac{1}{2} \cdot 6\, N_\mathrm{A} T \cdot N_\mathrm{A} = 3 N_\mathrm{A} k_\mathrm{B} T = 3\, R\, T.$$

Each atom features six degrees of freedom: three oscillation directions representing the kinetic energy, with each one featuring two degrees of freedom representing the potential energy. Due to the Virial theorem[2] each oscillation consists of potential and kinetic energies, resulting in $1/2 k_\mathrm{B} T$ per oscillation mode. Thereby k_B represents the **Boltzmann constant** and $R = N_\mathrm{A} k_\mathrm{B}$ the universal gas constant.

So, the molar heat capacity for a solid results in the **Dulong-Petit law** with a constant molar heat capacity

[2] The Virial Theorem states that the average energy of an oscillating system is described by a linear force results in $2\langle E_\mathrm{kin}\rangle = 2 \cdot 1/2 k_\mathrm{B} T$.

Dulong-Petit law

$$C_{\mathrm{m}} = \frac{\partial U_{\mathrm{m}}}{\partial T} = 3R. \tag{14.18}$$

This law describes qualitatively well the heat capacity of condensed matter at higher temperatures.

Now looking on our free electron gas, we can argue similarly as for the solids, getting the molar internal energy for the electron system

$$U_{\mathrm{e}} = \frac{1}{2} \cdot 3 \cdot N_{\mathrm{A}} k_{\mathrm{B}} T = \frac{3}{2} RT,$$

as free electrons, being point-masses, feature only three degrees of freedom resulting in a molar heat capacity of $C_{\mathrm{e}} = \frac{3}{2}R$. Also here, the heat capacity is constant.

The overall molar heat capacity of a metal, consisting of atoms and, per atom one free electron (e.g. an alkaline metal), the heat capacity would be $C_{\mathrm{m}} = 3R + 3/2R = 9/2R = 4.5R$. This result is in contradiction to the experimentally given values for the molar heat capacity of many metals, ranging around $3R$ at room temperature.

Quantum Mechanical Approach

Contrary to the atoms within condensed matter, where the oscillations are described by phonons, the classical approach is not working for the free electrons, and a non-classical explanation is necessary for the electrons.

Phonons represent bosons, whereas the electrons represent fermions, which have to be described on another way. In order to calculate the internal energy of an electron system, one needs to describe, how the energies of the electrons are distributed within the condensed matter quantum mechanically.

As shown in the Sect. 9.2, where the fundamentals on the Fermi statistics have been described, and also the formal the Fermi-Dirac distribution f_{FD} has been derived. The number of states of the electron system per volume and energy step is described for free electrons using the energy density distribution $D(\epsilon)$.

The heat capacity is given again by the temperature derivative of the internal energy, see (14.17). The internal energy itself is described as the expected value for the sum over the energy of all electrons. To get the expected value of the energy of fermions, one has to look on its statistical properties, and to determine the heat capacity of the electrons, we firstly determine the molar internal energy u, see (14.17), calculating the mean energy, and applying the Fermi-Dirac distribution

$$\begin{aligned} U_{\mathrm{m,e}} &= \int_0^\infty \epsilon D(\epsilon) f_{\mathrm{FD}}(\epsilon, T) \mathrm{d}\epsilon \\ &= \int_0^\infty (\epsilon - \epsilon_{\mathrm{F}}) D(\epsilon) f_{\mathrm{FD}}(\epsilon, T) \mathrm{d}\epsilon + \int_0^\infty \epsilon_{\mathrm{F}} D(\epsilon) f_{\mathrm{FD}}(\epsilon, T) \mathrm{d}\epsilon \\ &= \int_0^\infty (\epsilon - \epsilon_{\mathrm{F}}) D(\epsilon) f_{\mathrm{FD}}(\epsilon, T) \mathrm{d}\epsilon + \epsilon_{\mathrm{F}} N. \end{aligned}$$

Finally, we take for the molar internal energy the derivative at the temperature, defining the molar heat capacity

$$\begin{aligned} C_{\mathrm{e,V}} &= \left(\frac{\mathrm{d}U_{\mathrm{m,e}}}{\mathrm{d}T}\right)_V \\ &= \frac{\mathrm{d}}{\mathrm{d}T}\int_0^\infty (\epsilon - \epsilon_\mathrm{F}) D(\epsilon) f_\mathrm{FD}(\epsilon, T)\mathrm{d}\epsilon. \end{aligned}$$

Looking on the Fermi-Dirac distribution, only close to the Fermi edge at $\epsilon = \epsilon_\mathrm{F}$ the slope differs from zero, allowing one to make the approximation $D(\epsilon) \approx D(\epsilon_\mathrm{F})$, getting now for the molar heat capacity of the electrons

$$C_{\mathrm{e,V}} = D(\epsilon_\mathrm{F}) \int_0^\infty (\epsilon - \epsilon_\mathrm{F}) \frac{\mathrm{d}f_\mathrm{FD}(\epsilon, T)}{\mathrm{d}T}\mathrm{d}\epsilon.$$

As shown in [1], for small energies $k_\mathrm{B}T \ll \epsilon_\mathrm{F}$, one gets an analytical formulation for the differentiation of the Fermi-Dirac distribution, and also the following integration is analytically solvable (see again [1], getting the molar heat capacity to

$$C_{\mathrm{e,V}} = \frac{1}{3}\pi^2 D(\epsilon_\mathrm{F}) k_\mathrm{B}^2 T.$$

Using for the density of states $D(\epsilon_\mathrm{F})$, (9.26), we can rewrite the heat capacity for a free electron gas consiting of N electron, being now proportional to the temperature, using again $\epsilon_\mathrm{F} = k_\mathrm{B}T_\mathrm{F}$ with the Fermi temperature T_F, getting

Heat capacity for a free electron gas

$$C_{\mathrm{e,V}} = \frac{\pi^2 N k_\mathrm{B}}{2T_\mathrm{F}} T. \tag{14.19}$$

The constants given in the heat capacity for a free electron gas are summarized to the **Sommerfeld parameter**

$$\gamma_\mathrm{theo} = \frac{\pi^2 N k_\mathrm{B}}{2T_\mathrm{F}}.$$

Practically, the measured Sommerfeld parameter γ_exp deviates from the theoretical one, see Table 14.1, due to an thermal effective electron mass m_th being larger than the free electron mass m_e,

$$\gamma_\mathrm{exp} = \gamma_\mathrm{theo} \frac{m_\mathrm{th}}{m_\mathrm{e}}.$$

For the transition metals Fe and Co the large deviations are attributed to the location of Fermi energy in the d-bands resulting in partially filled d-shells. The alkali metals are expected to have the best agreement with the free electron model, since these

Table 14.1 Theoretical and experimental Sommerfeld parameters Γ_{SF} in $mJmol^{-1}K^{-2}$ for different metals

	Li	Be	Na	Mg	Al	K	Ca	Cu	Zn	Ga	Rb
γ_{theo}	0.749	0.500	1.094	0.992	0.912	1.668	1.511	0.505	0.753	1.025	1.911
γ_{exp}	1.63	0.17	1.38	1.3	1.35	2.08	2.9	0.695	0.64	0.596	2.41
	Sr	Ag	Cd	In	Sn	Cs	Ba	Au	Hg	Ti	Pb
γ_{theo}	1.790	0.645	0.948	1.233	1.410	2.238	1.937	0.642	0.952	1.29	1.509
γ_{exp}	3.6	0.646	0.688	1.69	1.78	3.20	2.7	0.729	1.79	1.47	2.98

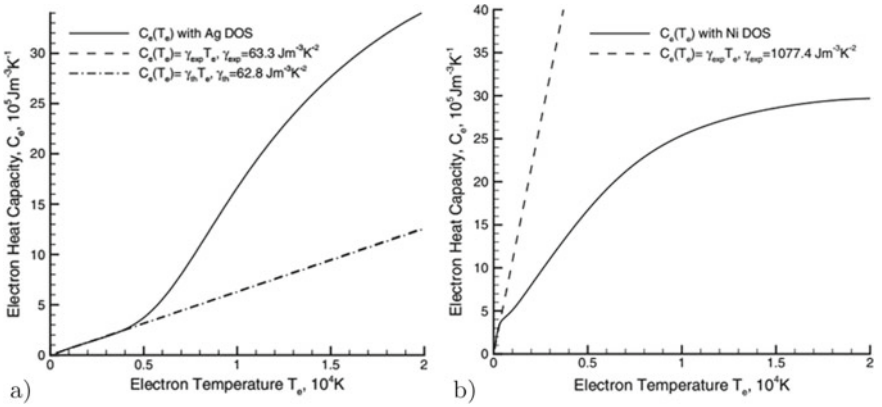
C_e(T_e) with Ag DOS
C_e(T_e)= γ_exp T_e, γ_exp=63.3 Jm^-3K^-2
C_e(T_e)= γ_fe T_e, γ_fe=62.8 Jm^-3K^-2
Electron Heat Capacity, C_e, 10^5 Jm^-3K^-1
Electron Temperature T_e, 10^4 K
a)
C_e(T_e) with Ni DOS
C_e(T_e)= γ_exp T_e, γ_exp=1077.4 Jm^-3K^-2
Electron Heat Capacity, C_e, 10^5 Jm^-3K^-1
Electron Temperature T_e, 10^4 K
b)

Fig. 14.3 Heat capacity of the electron system calculated by (14.19) and by ab-initio calculation for silver (**a**) and nickel (**b**)

metals feature only one s-electron next to a filled shell. However, even sodium, which is considered to be the closest to a free electron gas, is determined to have a γ_{exp} deviating more than 25% from the theory.

Irradiating metals with ultra-fast laser radiation or high-intensive laser radiation, very high temperatures of the electron system can be induced. Then, the linear dependence of the heat capacity of the electron on the temperature, even including the experimental Sommerfeld parameter, deviates strongly from ab-initio calculated heat capacities, as shown for the metals Ag and Ni in Fig. 14.3.

For the modeling it is appropriate to use the ab-initio calculations, being more accurate [2]. As shown in Fig. 14.4, the calculated electron heat capacity varies strongly for different metal, and is never linearly dependent on the electron temperature. Just chromium features at larger temperatures a linear behavior.

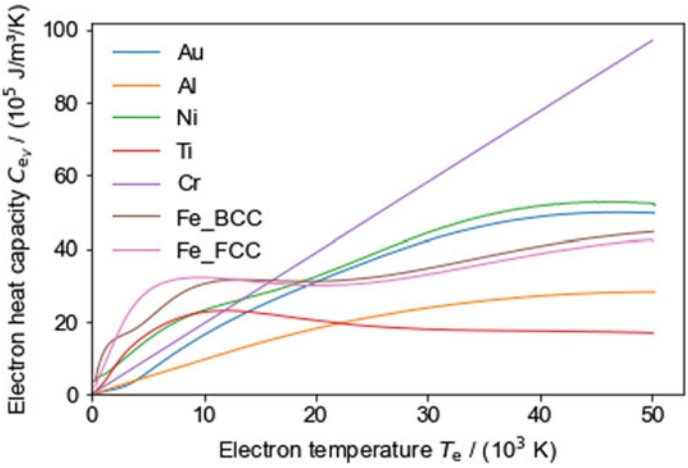

Fig. 14.4 Heat capacity of the electron system for different metals taken from literature [2]

14.5.2 Thermal Conductivity of the Electron System

The thermal conductivity of a free electron gas λ_e in one dimension is derived on one hand from Fourier's law describing the heat flow in one dimension, see (14.1), assuming a heat transport δQ in a mean scattering time of the electrons τ_e through an area A, and the characteristic length, or mean free path Δx of the electrons

$$\delta Q = -\lambda_e A \frac{\Delta T}{\Delta x} \tau.$$

On the other hand, from thermodynamics of an ideal gas we know the stored heat in the mass $\Delta m = \rho \Delta V$ using the heat capacity of the electrons, (14.3)

$$\delta Q = \Delta m c_v \Delta T = \rho c_v \Delta V \Delta T = \rho c_v A \Delta x \Delta T.$$

Comparing the transferred heat we can convert the equation writing the electron heat conductivity to

$$\lambda_e = \frac{\rho c_v \Delta x^2}{\tau}$$

The characteristic electron velocity in one dimension is described by the mean free path of the electrons Δx and the mean scattering time of the electrons τ

$$v_x = \frac{\Delta x}{\tau}.$$

Now, the heat is flowing in three dimensions, so that a characteristic squared path length by $l^2 = \Delta x^2 + \Delta y^2 + \Delta z^2$ can be determined, and with the isotropy $\Delta x = \Delta y = \Delta z$, one gets

$$\Delta x^2 = \frac{1}{3} l^2.$$

Introducing a mean electron velocity

$$v_\mathrm{e} = \frac{l}{\tau_\mathrm{e}},$$

we can determine the heat conductivity of the electrons to

$$\lambda_\mathrm{e} = \frac{1}{3} \rho c_v l v.$$

As the mean scattering time of the electrons τ_e is easier to be determined than the characteristic length, we get with $v_\mathrm{e} \cdot \tau_\mathrm{e} = l$ finally

The electron thermal conductivity

$$\lambda_\mathrm{e} = \frac{1}{3} \rho v_\mathrm{e}^2 c_v \tau_\mathrm{e}. \tag{14.20}$$

In case of a free electron gas, we take

$$c_v \cdot \rho = \frac{C_{\mathrm{e,V}}}{V}$$

from (14.19), and define its velocity by a maximum velocity with the largest kinetic energy given by the Fermi velocity of the electrons, (9.18), getting with the electron density $n_\mathrm{e} = N/V$

$$\begin{aligned} \lambda_\mathrm{e}(T_\mathrm{e}, T_\mathrm{ph}) &= \frac{1}{3} \frac{C_{\mathrm{e,V}}(T_\mathrm{e})}{V} v_\mathrm{F}^2(T_\mathrm{e}) \tau_\mathrm{e}(T_\mathrm{e}, T_\mathrm{ph}) \\ &= \frac{1}{3} \frac{\pi^2 n_\mathrm{e} k_\mathrm{B}}{2 T_\mathrm{F}} T v_\mathrm{F}^2(T_\mathrm{e}) \tau_\mathrm{e}(T_\mathrm{e}, T_\mathrm{ph}). \end{aligned}$$

The scattering time τ_e is derived from the scattering frequency of the electrons (12.1), but in practice the empiric approximation

$$\nu_\mathrm{e}(T_\mathrm{e}, T_\mathrm{ph}) = \frac{1}{\tau_\mathrm{e}(T_\mathrm{e}, T_\mathrm{ph})} = A \cdot T_\mathrm{e}^2 + B \cdot T_\mathrm{ph}, \tag{14.21}$$

is used with A and B being empirical parameters, see Table 14.2 [3].

Table 14.2 Empirical parameters for the determination of the electron scattering frequency

	Au [4]	Au [3]	Ag [4]	Cu [4]	Al [4]	Ni [5]
A in 10^7 $1/(sK^2)$	1.18	1.2	0.932	1.28	0.376	0.59
B in 10^{11} $1/(sK)$	1.25	1.23	1.02	1.23	3.9	1.4

Using for the Fermi temperature $T_\mathrm{F} = \epsilon_\mathrm{F}/k_\mathrm{B}$ and for the Fermi energy, (9.19) as well the Fermi velocity, (9.18), one gets for the thermal conductivity of the electron system now

Thermal conductivity of a free electron gas

$$\lambda_\mathrm{e}(T_\mathrm{e}, T_\mathrm{ph}) = \frac{\pi^2 n_\mathrm{e} k_\mathrm{B}^2 \tau_\mathrm{e}(T_\mathrm{e}, T_\mathrm{ph})}{3m_\mathrm{e}} T. \tag{14.22}$$

To get a more precise description of the heat capacity λ_e, the density of states of the electrons, especially for high temperatures of the electrons, has to be calculated [2].

14.5.3 Electron-Phonon Coupling Parameter

As shown in the heat equations for the electron and phonon systems (14.13) and (14.14), both equation are coupled by the coupling term, (14.16) applying the electron-phonon coupling parameter $G(T_\mathrm{e})$.

Contrary to old literature, the electron-phonon coupling parameter is not a constant, but depends non-linearly from the electron temperature T_e, as shown exemplary for the metal silver and nickel in Fig. 14.5. The electron-phonon coupling parameter describes the heat flux from the electron to the phonon system, which can be classified also by the electron-phonon coupling time

$$\tau_\mathrm{R} = \frac{C_\mathrm{e,V}}{G(T_\mathrm{e})}$$

As shown in Fig. 14.6, the electron-phonon coupling parameter as well the electron-phonon coupling time vary for many metals in a large range between some hundred femtoseconds and many tenths of picoseconds, depending strongly on the electron temperature. The plotted data results from ab-initio simulations, see [2].

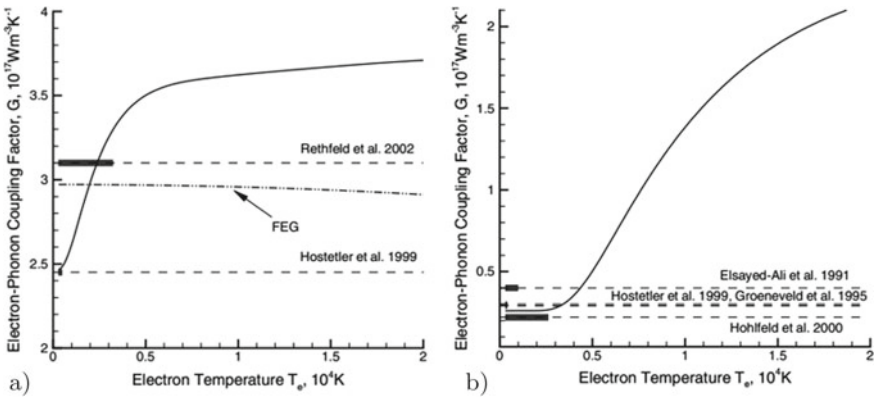

Fig. 14.5 Electron-phonon coupling parameter $G(T_\mathrm{e})$ as function of the electron temperature T_e calculated by ab-initio calculation for silver (**a**) and nickel (**b**)

14.6 Thermodynamic Properties of the Phonon System

As stated for the electron system in the previous sections, we start now for the phonon system without any heat sink, and rewrite the heat equation for the phonon system with an external heat source, coupling it to the electron system via (14.15), getting

Heat equation for the phonon system

$$c_\mathrm{p}\,\rho_\mathrm{ph}\frac{\partial T_\mathrm{ph}}{\partial t} - \nabla\left(\lambda_\mathrm{ph}\nabla T_\mathrm{ph}\right) = G(T_\mathrm{e})(T_\mathrm{e} - T_\mathrm{ph}). \tag{14.23}$$

Again, to solve this equation we need to determine the temperature dependence of the heat capacity for the phonon system c_p, and also its heat conductivity λ_ph.

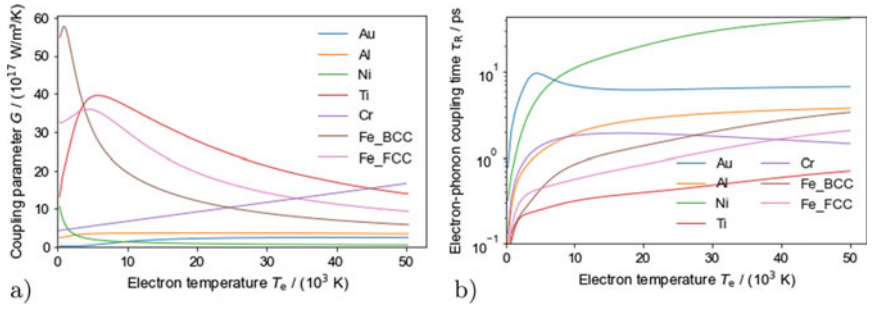

Fig. 14.6 Electron-phonon coupling parameter $G(T_\mathrm{e})$ (**a**) and electron-phonon coupling time τ_R (**b**) determined from ab-initio calculations for different metals using [2]

14.6.1 Heat Capacity of the Phonon System

The heat capacity of the phonon can be derived by determining the internal energy of the phonon system in the solid. Thinking about the movements of the atoms in a solid, one realizes that similar to the excitation of atoms due to its temperature T and followed emission of electromagnetic radiation, see Sect. 2.5, we can also describe the movement of the atoms by its **collective excitation**, the so called **phonons**, too.

As phonons feature an integral spin, they are bosons and follow the Bose-Einstein statistics. Similarly to the photons within a hollow body, phonons represent coherent oscillating atoms within a solid of volume $V = L^3$, and are described by an amplitude function of a standing wave.

Comparable to the determination of the heat capacity of the electron system, see Sect. 14.5.1, we have firstly to determine the internal energy U of the phonon system. Then, the derivative of the internal energy with the temperature will be equal to the heat capacity of the phonon system.

Again, we have to count the allowed number of states G, as for the photons in Sect. 2.5, now for the phonons as function of the wave number k, using (2.44). Here the degeneracy is $p = 3$, because phonons can oscillate transversely with two polarization states, and longitudinally with one polarization state. Assuming $p = 3$, we assume an isotropic solid having the same speed of sound c_s in all directions.

The spectral mode density as function of the angular frequency, also called density of states results

$$\frac{\mathrm{d}N}{\mathrm{d}k} = \frac{pL^3}{2\pi^2}k^2.$$

Holding in mind the **dispersion relation for sound waves, i.e. phonons**

$$k = \frac{\omega}{c_\mathrm{s}}$$

with the speed of sound in the solid c_s we get the density of states

$$\begin{aligned} D(\omega) &= \frac{\mathrm{d}N}{\mathrm{d}\omega} = \frac{\mathrm{d}N}{\mathrm{d}k}\frac{\mathrm{d}k}{\mathrm{d}\omega} \\ &= \frac{pL^3}{2\pi^2}k^2\frac{1}{c_\mathrm{s}} \\ &= \frac{pL^3}{2\pi^2}\frac{\omega^2}{c_\mathrm{s}^3}. \end{aligned}$$

The number of phonons is calculated by (2.44), and therefore we can determine a **cut-off frequency**, the so called **Debye frequency**

$$\omega_\mathrm{D} = \left(\frac{6\pi^2 c_\mathrm{s}^3\, N(\omega_\mathrm{D})}{p \cdot V}\right)^{1/3},$$

assuming a constant sound velocity c_s =const. in the solid. This is consequently called the **Debye model**.

Now we can calculate the internal energy, comparable to the one for the electron system, see (14.19). The internal energy of the phonons at the temperature T represents the sum over all energies of the phonon modes at all wave numbers $\boldsymbol{k}$ and polarization states p

$$\begin{aligned} U &= \int_0^\infty \epsilon D(\epsilon) f_{\mathrm{BE}}(\epsilon, T) \mathrm{d}\epsilon \\ &= \int_0^{\omega_\mathrm{D}} \frac{pL^3}{2\pi^2} \frac{\omega^2}{c_s^3} \frac{\hbar\omega}{e^{\frac{\hbar\omega}{k_\mathrm{B}T}} - 1} \mathrm{d}\omega \end{aligned}$$

Introducing the Debye temperature, see for the derivation [1],

Debye temperature

$$\Theta_\mathrm{D} = \frac{\hbar c_s}{k_\mathrm{B}} \left(\frac{6\pi^2 N}{c_s} \right)^{1/3}, \tag{14.24}$$

and the substitutions $x = \frac{\hbar\omega}{k_\mathrm{B}T}$ and $x_\mathrm{D} = \frac{\hbar\omega_\mathrm{D}}{k_\mathrm{B}T} = \frac{\Theta_\mathrm{D}}{T}$, one gets an integral solution for the internal energy

$$U = 9Nk_\mathrm{B}T \left(\frac{T}{\Theta_\mathrm{D}} \right)^3 \int_0^{x_\mathrm{D}} \frac{x^3}{e^x - 1} \mathrm{d}x.$$

The heat capacity of the phonon system at constant volume $C_{\mathrm{p},V}$ is determined again by differentiation the molar internal energy with respect to the temperature getting

$$C_{\mathrm{ph},V} = \left(\frac{dU}{dT} \right)_V \tag{14.25}$$

$$= 9Nk_\mathrm{B} \left(\frac{T}{\Theta_\mathrm{D}} \right)^3 \int_0^{x_\mathrm{D}} \frac{x^4 e^x}{(e^x - 1)^2} \mathrm{d}x. \tag{14.26}$$

As shown in [1] the integral solution of the internal energy converges versus a constant value for very low temperatures compared to the Debye temperature, meaning $T \ll \Theta_\mathrm{D}$ and one gets in this case the **Debye-T^3-law**

Molar heat capacity of the phonon system—Debye T^3 law

$$C_{\mathrm{ph},V} \approx \frac{12\pi^4}{5} Nk_\mathrm{B} \left(\frac{T}{\Theta_\mathrm{D}} \right)^3. \tag{14.27}$$

As the phonon temperature get much larger than the Debye temperature, with $x \ll 1$, the exponential factor within the heat capacity of (14.26) of the phonons

Table 14.3 Debye temperatures Θ_D for different materials [1]

Material	Θ_D/K	Material	Θ_D/K	Material	Θ_D/K	Material	Θ_D/K
Aluminium	428	Copper	343	Nickel	450	Silver	215
Beryllium	1440	Germanium	374	Platinum	240	Tantalum	240
Cadmium	209	Gold	170	Rubidium	56	Tin (white)	200
Caesium	38	Iron	470	Sapphire	1047	Titanium	420
Carbon	2230	Lead	105	Selenium	90	Tungsten	400
Chromium	630	Manganese	410	Silicon	645	Zinc	327

converges against $e^x - 1 \approx x$ reproducing the Dulong-Petit law, see (14.18) with $C_{ph,V} = 3Nk_B$.

Typical metals have a Debye Temperature being in the range of the room temperature at about ≈ 300 K, see Table 14.3, allowing as a good approximation there to use a **constant phonon heat capacity** following the **Dulong-Petite law**. For temperatures much higher than the Debye temperature also a constant heat capacity can be often approximated, and for laser processing of matter most solids feature temperatures being about or also well above the Debye temperatures, making again an approximation in first order with a constant heat capacity reasonable.

To get a more **precise description of the heat capacity**, the density of states of the phonons, especially when temperatures of the phonons get close to the melting temperature, or phase transitions take place, have to be calculated or measured by **phonon dispersion spectroscopy**. Phonon dispersion distributions can be calculated also by ab-initio modeling deriving the density of states for the phonon system [6].

14.6.2 Thermal Conductivity of the Phonon System

As for the electron system, again one determines the thermal conductivity of the phonons via the kinetic gas theory, see Sect. 14.5.2, and we get

Thermal conductivity of the phonon system

$$\lambda_{ph}(T_e, T_{ph}) = \frac{1}{3} v_s^2(T_{ph}) c_v \tau_e(T_e, T_{ph}), \tag{14.28}$$

using as velocity the speed of sound v_s and the scattering time τ_e from (14.21).

Getting large temperature gradients in the phonon system using pulsed laser radiation, mechanical stress is additionally induced, making a **thermo-mechanical description** of the solid necessary using the **general Euler equations** describing the continuity equation, see Chap. 15.

14.7 Numerical Approach

To calculate the electron and phonon temperatures as function of time, one needs to compute it accordingly the physical and geometrical conditions given by the experiment. Today, many different software tools exist to solve all complex mathematical tasks described in this textbook numerically, e.g. like MATHEMATICA®, MATLAB® or python™.

Generally, the heat equations have the same structure, why here a general numerical approach is shortly given. Starting from the heat equation without sources (14.11), we include now a general heat source q_V getting

$$c_\mathrm{p}(\boldsymbol{r}, T)\rho(\boldsymbol{r}, T)\frac{\partial T}{\partial t} - \nabla\left(\lambda(\boldsymbol{r}, T)\nabla T(\boldsymbol{r})\right) = q_\mathrm{V}(\boldsymbol{r}),$$

introducing also the spatial- and temperature-dependent heat capacity at constant pressure c_p and heat conductivity λ. As a first approximation, we assume isotropic and temperature-independent material parameters, meaning that heat capacity and heat conductivity are taken as constant in space and in temperature. Doing this, the heat equation simplifies to the homogeneous heat (14.12), and in our case getting

$$c_\mathrm{p}\rho\frac{\partial T}{\partial t} - \lambda\Delta T = q_\mathrm{V}(\boldsymbol{r}).$$

Using laser radiation, we apply the next simplification introducing a cylindrical symmetry of this problem, as many laser radiation features a **circular spatial intensity distribution**, like the TEM mode, or so called Gaussian fundamental mode. The heat equation gets now to

$$c_\mathrm{p}\rho\frac{\partial T}{\partial t} - \lambda\left(\frac{\partial^2 T}{\partial r^2} + \frac{\partial^2 T}{\partial z^2} + \frac{1}{r}\frac{\partial T}{\partial r}\right) = q_\mathrm{V}(\boldsymbol{r}).$$

Finally, we will here assume that a metal is irradiated featuring a thickness being d much larger than the optical absorption length, $d \gg \lambda_\mathrm{opt}$. This means that the heating source can be described as a **surface heating source** and treated as a boundary condition

$$q_\mathrm{V} = -\lambda\nabla T,$$

now with a homogeneous heat equation

$$c_\mathrm{p}\rho\frac{\partial T}{\partial t} - \lambda\left(\frac{\partial^2 T}{\partial r^2} + \frac{\partial^2 T}{\partial z^2} + \frac{1}{r}\frac{\partial T}{\partial r}\right) = 0.$$

Sometimes, in literature the thermal diffusivity α_th

Table 14.4 Thermo-physical parameters of common metals: density ρ, heat capacity c_p, head conductivity λ, thermal diffusivity α_th, and volumetric heat capacity s

Material	Ag	Al	Au	Cu	Fe	Mo	Ni	Pt
ρ/(kg/m^3)	10490	2700	19320	8920	7874	10280	8908	21450
λ/(W/(m K))	430	235	320	400	80	139	91	72
c_p/(J/(kg K))	235	897	128	385	449	254	444	130
α_th/(mm^2/s)	174.4	97.0	129.4	116.5	22.6	53.2	23.0	25.8
s/(MJ/(m^3 K))	2.47	2.42	2.47	3.43	3.54	2.61	3.96	2.79

Thermal diffusivity

$$\alpha_\mathrm{th} = \frac{\lambda}{\rho c_\mathrm{p}}, \tag{14.29}$$

and the volumetric heat capacity s are introduced

Volumetric heat capacity

$$s = \rho c_\mathrm{p}, \tag{14.30}$$

allowing to rewrite the heat equation to

$$\frac{\partial T}{\partial t} - \alpha_\mathrm{th}\left(\frac{\partial^2 T}{\partial r^2} + \frac{\partial^2 T}{\partial z^2} + \frac{1}{r}\frac{\partial T}{\partial r}\right) = 0. \tag{14.31}$$

For common metals one can now solve the heat equations using thermophysical parameters, e.g. taken from Table 14.4.

In order to solve the two coupled heat equations, a numerical solution is used. Thereby the (14.31) is solved discretizing space and time, as shown for two spatial dimensions in Fig. 14.7. One gets now the numerical recipes for the heat equation to

$$\frac{T_{i,j}^{t+1} - T_{i,j}^{t}}{\Delta t} - \alpha_\mathrm{th}\left(\frac{T_{i+1,j}^{t} - 2T_{i,j}^{t} + T_{i-1,j}^{t}}{\Delta z^2} + \right.$$
$$\left. + \frac{T_{i,j+1}^{t} - 2T_{i,j}^{t} + T_{i,j-1}^{t}}{\Delta r^2} + \frac{T_{i.j+1}^{t} + T_{i,j-1}^{t}}{r_{i,j} 2\Delta r}\right) = 0,$$

and using the approximation of the laser radiation as a surface source, we get

$$q_j = -\lambda \nabla T \approx -\lambda \frac{T_{2,j} - T_{1,j}}{\Delta z},$$

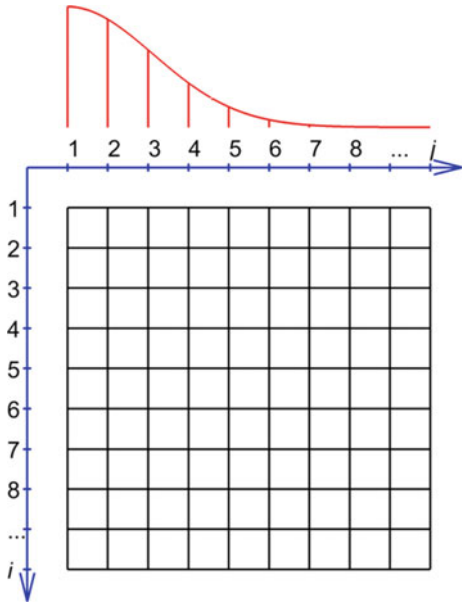

Fig. 14.7 Spatial discretization in cylindric symmetry (r, z), also of the spatial intensity distribution of the radiation

with the boundary conditions

$$T_{1,j} = T_{2,j} + \frac{q_j \cdot \Delta z}{\lambda}$$
$$= T_i + \frac{\Delta z}{\lambda}(1 - R) I_j^t.$$

14.8 Examples for Laser-Heated Metals

14.8.1 Nanosecond Laser Radiation

Irradiating metals with pulsed laser radiation with a pulse duration much larger than the electron-phonon coupling time $t_\mathrm{p} \gg \tau_\mathrm{R}$ results in coalescing of the heat equations for the electron and the phonon system to just **one heat equation**, representing a **one-temperature model** (OTM). During irradiation and heating of the electron system the transfer of the energy to the phonon system takes place nearly instantaneously compared to the irradiation time, see exemplary in Fig. 14.8 the temperature development of different metals after irradiation with one nanosecond laser pulse (pulse duration $t_\mathrm{p} = 50$ ns, beam radius $w_0 = 40$ µm, pulse energy $E_\mathrm{p} = 40$ µJ).

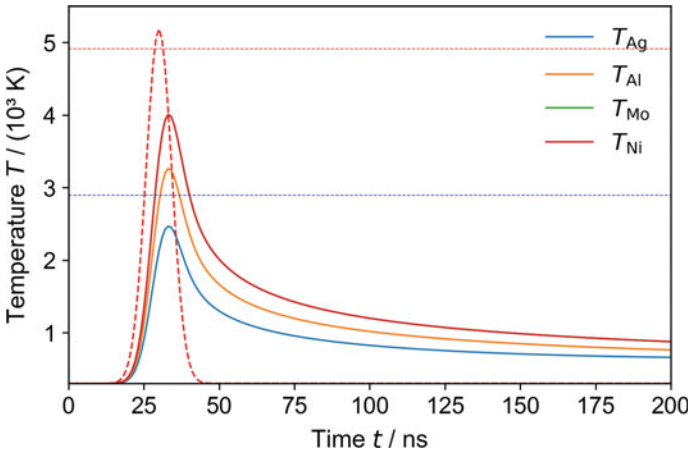

Fig. 14.8 Temperature development at the surface of different metals after irradiation with one nanosecond laser pulse (pulse duration $t_p = 10$ ns, fluence $H_0 = 0.8$ J/cm^2)

Depending on the thermal diffusivity α_{th}, see Table 14.4, the maximum of the temperatures, as well its point in time differ for different investigated metals, like Nickel, Molybdenum, Aluminum, and Silver.

14.8.2 Femtosecond Laser Radiation

Irradiating metals with pulsed laser radiation at a pulse duration much smaller than the electron-phonon coupling time $t_p \ll \tau_R$ results in two distinct processes of energy deposition for the electron and the phonon system. The electron system accumulates the optical energy nearly instantaneously, whereas the transfer of the optical energy to the phonon system is driven on the time scale of the electron-phonon coupling time τ_R, see exemplary in Fig. 14.9 the temperature development of different metals after irradiation with one femtosecond laser pulse (pulse duration $t_p = 40$ fs with a fluence $H_0 = 0.05$ J/cm^2).

Molybdenum features at the high electron temperature T_e an electron-phonon coupling time of about some picoseconds, depicting a strong interaction between the electron and phonon system, when calculated by the two-temperature model (TTM). One sees in Fig. 14.9a that after a nearly instantaneous heating of the electron system, only within about 3–4 ps the phonon system gets thermalized with the electron system. This time is in the range of the electron-phonon coupling time of molybdenum. Also one observes that the melting temperature T_M, as well the vaporization temperature T_V is exceeded, enforcing to introduce phase changes in the modeling, see Sect. 15.2. The one-temperature model describes the temperature development qualitatively well, but features to a strong heating, and a much slower cooling slope.

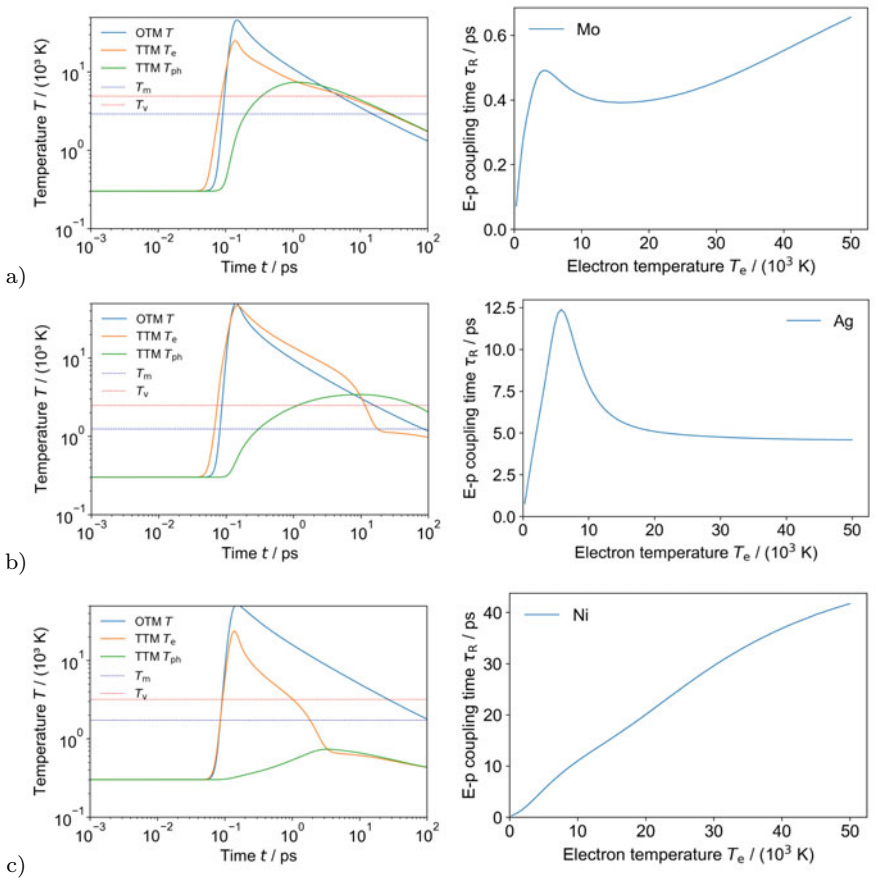

Fig. 14.9 Temperature development at the surface of different metals **a** Molybdenum, **b** Silver, and **c** Nickel after irradiation with one femtosecond laser pulse, left, and corresponding electron-phonon coupling times τ_R, right (pulse duration $t_p = 40$ fs with a fluence $H_0 = 0.05$ J/cm^2)

As the electron-phonon coupling time of other metals, like silver or nickel gets larger, also the thermalization time of the electron with the phonon system, as described by the TTM increases into the same time regime of about 10 ps, see Fig. 14.9b, c. Again, in case of silver the melting and vaporization temperatures are exceeded, whereas for nickel only heating is induced. Especially for nickel, the one-temperature model (OTM) fails completely to describe the development of the temperatures.

References

1. C. Kittel, *Introduction to Solid State Physics*, 9th ed. (Wiley, 2018)
2. Z. Lin, L.V. Zhigilei, V. Celli, Electron-phonon coupling and electron heat capacity of metals under conditions of strong electron-phonon nonequilibrium. Phys. Rev. B **77**(7), 075133 (2008)
3. X.Y. Wang, D.M. Riffe, Y. Lee, M.C. Downer, Time-resolved electron-temperature measurement in a highly excited gold target using femtosecond thermionic emission. Phys. Rev. B: Condens. Matter **50**(11), 8016–8019 (1994)
4. F. Chen, G. Du, Q. Yang, J. Si, H. Hou, Ultrafast heating characteristics in multi-layer metal film assembly under femtosecond laser pulses irradiation, in *Two Phase Flow, Phase Change and Numerical Modeling*, ed. by A. Ahsan (InTech, 2011)
5. A.M. Chen, H.F. Xu, Y.F. Jiang, L.Z. Sui, D.J. Ding, H. Liu, M.X. Jin, Modeling of femtosecond laser damage threshold on the two-layer metal films. Appl. Surf. Sci. **257**(5), 1678–1683 (2010)
6. http://pages.physics.cornell.edu/sss/debye/debye.html

Chapter 15
Phase Transitions

Abstract Laser radiation interacting with matter can be absorbed. As a consequence, the optical energy is transformed in heat, as has been described in the previous Chap. 14. As known from thermodynamics and solid state physics, the phase state of condensed matter can be changed by changing its temperature. In this chapter we investigate the thermodynamic path matter goes after excitation by laser radiation. Due to the very often very steep energy coupling, very strong thermal gradients are generated in matter inducing ultra-fast phase transitions.

15.1 Laser-Induced Phase Changes

Before talking about laser-induced heating, one has to distinguish between slow and fast heating processes. Slow processes are often described in thermodynamics within the frame of equilibrium, allowing to setup thermodynamic equation. Contrary, heating up quickly a thermodynamic system, e.g. by locally irradiation it, will result in an non-equilibrium process, much more complicated to describe as a whole.

15.1.1 Slow Heat Transfer

Matter can subsist in different phase states. Starting from the **vapor phase**, atoms or molecules will, when its temperatures decrease, start to agglomerate at a specific temperature called condensation temperature T_c, as the inter-atomar or inter-molecular binding energy gets larger than the kinetic energy of the particles itself. As a consequence, **condensation** takes place and a liquid phase is formed.

As long as vapor is present, a two-phase system prevails, and further cooling of this system will not change its temperature, but increase the amount of condensed liquid. The extracted energy is equal to the enthalpy of condensation ΔH_c, being equal in value to the enthalpy of vaporization ΔH_v given in tables.

Further energy extraction will at the end form a **one-phase state** of a **liquid**, and a continued cooling will decrease further its temperature. Reaching the solidification

© Springer Nature Switzerland AG 2022

A. Horn, *The Physics of Laser Radiation–Matter Interaction*,
https://doi.org/10.1007/978-3-031-15862-9_15

temperature T_s, atoms or molecule, or clusters will interact more strongly with each other forming either a crystalline or amorphous condensed matter phase state by **solidification**. As long as a liquid phase is given, a two-phase state together with the solid state phase persists, and energy extraction will not change its temperature, but increases the amount of solidified matter. When all liquid is solidified, further cooling will decrease now the temperature of the solid.

Laser technology operates in the opposite direction, heating solid matter e.g. by using pulsed laser radiation, where matter at room temperature is heated until the melting temperature T_m is reached and **melting** starts. Then, further heating will induce a liquid-phase generation by applying the enthalpy for melting ΔH_m. Continued heating will induce **vaporization** at the vaporization temperature T_v, where the enthalpy for vaporization ΔH_v is needed.

Using laser radiation very high temperatures can also be induced, as the intensity of laser radiation can be such high inducing that a fourth phase transition is induced by the transition into the plasma state, the so called **plasma**. Contrary to quasi-equilibrium processes described often in thermodynamics, the described phase transition in laser technology mostly proceed at any equilibrium. This means that during irradiation, a solid interaction volume is transferred to a liquid, a vapor, and a plasma phase at different positions within the interaction volume. All mentioned phase states can co-exist at the same time, and as the surrounding is only involved by the heat diffusion, a strong temperature gradient results, inducing possibly also pronounced thermo-mechanical stress.

Generally, processes involving changes of thermodynamic parameters, like pressure, temperature, and specific volume are described in thermodynamics using **phase diagrams**, see Fig. 15.1. As shown, regimes consisting of the three distinct phase states are plotted, but also regimes with mixing of phases. Often, two-dimensional representations are used, where one thermodynamic parameter is hold constant, like the $p-T$ diagram at constant specific volume, see Fig. 15.2 a, or the $T-\rho$ diagram, where the pressure is constant, and the density ρ is introduced as the reciprocate of the specific volume, see Fig. 15.2b.

Typically, in thermodynamics quasi-static changes of thermodynamic states are investigated, as there a stationary equilibrium is given. This means exemplary for a heated liquid within an adiabatic reservoir that a part of the liquid changes its phase into the gas state. The amount of vapor is limited by the **saturation vapor pressure**, and in simple systems calculated by the Clausius-Clapeyron equation. An equilibrium between the evaporating and the condensing particle then results at the **liquid-gas boundary**, see Fig. 15.2a. Again, here we describe very slow processes featuring all the time an thermal equilibrium. Further heat load will increase the amount of evaporated particles until all liquid in the reservoir is transferred to the gas state. The temperature of this system will not change as long as a liquid state is given, as the thermal energy is completely used for the evaporation of the liquid given by the enthalpy for evaporation ΔH_v. As also shown in the figure, above a **critical point** determined by the critical pressure, critical temperature, and critical density, no distinction between phases is possible anymore.

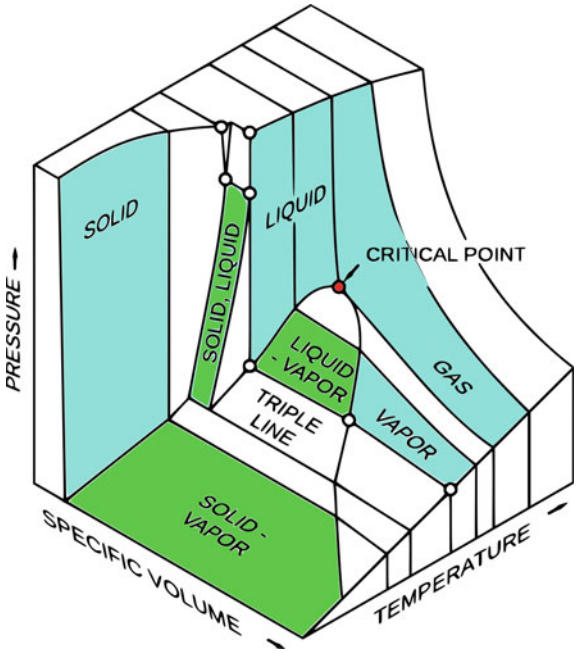

Fig. 15.1 Phase diagram plotted as function of three thermodynamic parameters, pressure, temperature, and specific volume

As a system initially featuring only one phase experiences a phase-change, two phases are in principle result for this system. But, as the transition from one phase into another one proceeds by reduction of the amount of the first phase, and an increase of the amount of the second one, also a third phase representing the mixture of the two phases can exist. One speaks about the bfcoexistence of two phases. In the $T-\rho$-diagram the phases are separated by a curve, the so called **binodal**. In case of the gas, the liquid, and the liquid-gas phase, the binodal separates this three phase states from each other, see Fig. 15.2b.

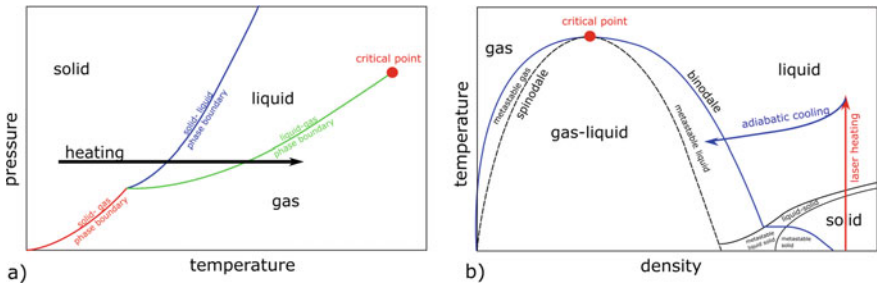

Fig. 15.2 Phase diagram plotted as function of two thermodynamic parameters **a** pressure versus temperature, and **b** temperatures versus density, i.e. reciprocal specific volume

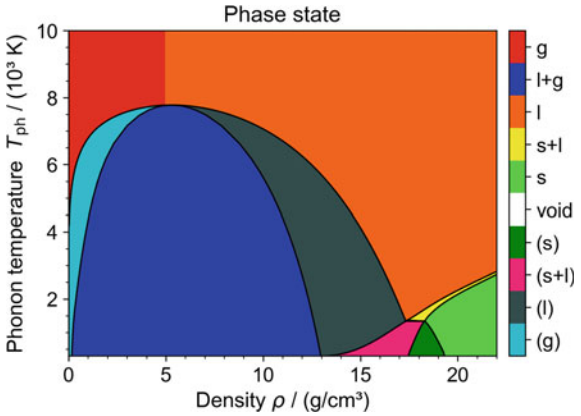

Fig. 15.3 Phase diagram of gold plotted as function of phonon temperature versus density also showing the stable states: solid s, liquid l, gas g, solid and liquid coexistence $s + l$, liquid and gas coexistence $l + g$, as well all meta-stable phase states given in brackets

In the case the heating takes place by a **quasi-static process** very slowly, the thermodynamic parameters will follow the binodal, e.g. forming a gas phase state from the liquid state by **heterogeneous boiling**, as both phase coexist with a distinct **phase interface**, and are well separated.

Phase diagrams describe also the stable and meta-stable states, as shown generally in Fig. 15.1 and for gold in Fig. 15.3.

15.1.2 Fast Heat Transfer

Heating a system fast, e.g. by laser radiation, will describe a non-equilibrium state change. Due to the very fast heat load, the matter can not immediately relax, e.g. the position of the atoms will initially, directly after heating remain at their positions resulting in an unchanged volume and density, see Fig. 15.2. Typically adiabatic processes will follow, like an **adiabatic expansion**, resulting in cooling, and an increase in volume, representing a decrease in density. Doing so, the thermodynamic parameters of a system now can cross the phase boundary, and a phase change happens rapidly. Exemplary, the heating of a system at constant pressure is shown in Fig. 15.2a, or by laser heating and adiabatic cooling in Fig. 15.2b.

The adiabatic expansion will move the system within the binodal zone, given in Fig. 15.2b. Within the binodal a region is delimited by a **spinodal**. Between the binodal and the spinodal only meta-stable phases states exist. If a heating process is fast, so that the system can not follow the binodal anymore, the thermodynamic parameters will enter this regime forming a **super-heated liquid** coming from the liquid. Featuring a phase change coming from the gas phase an **under-cooled gas** results. In both cases droplets and gas bubbles are formed, and is called **nucleation**. As this nucleation takes place everywhere in the heated phase, this process is called **homogeneous boiling**, or binodal decomposition. Getting closer to the spinodal

increases the growth of bubbles or droplets exponentially, inducing an explosive boiling, the so called **phase explosion**.

Depending on the heating conditions the system can also surpass the spinodal by adiabatic cooling, entering the **stable co-existence regime**. There, nucleation can last longer, as the system is stable, allowing the formation of larger aggregates of gas within the liquid, the so called spinodal decomposition. In the continuation the two phases will separate spontaneously by the so called **spallation**.

15.2 Heating with Phase Transitions—Modeling

Now, as phase changes take place, we have to consider for each spatial element in our previously described modeling, see Sect. 14.8, also the enthalpies for melting and vaporization. Without including any material dynamics, as the movement of molten or vaporized matter, we can again solve the heat equations for the electron and the phonon systems, see Sect. 14.7.

Exemplary, heating molybdenum featuring a melting temperature and a vaporization temperature $T_M = 2896$ K and $T_V = 4912$ K with one laser pulse, depending on the pulse duration, different heating and cooling processes are induced, and the absolute temperatures, as well slopes differ strongly when using nanosecond or femtosecond laser pulses, see Fig. 15.4.

Using nanosecond laser pulses at a pulse duration of $t_p = 10$ ns much higher pulse energies are needed to reach the vaporization temperature, here about nine times higher fluences compared to femtosecond laser radiation, see Fig. 15.4a. Solidification is only reached after about 100 ns, ten times the irradiation time.

Exciting the same metal with one femtosecond laser pulse featuring a pulse duration of $t_p = 40$ fs and a fluence of $H_0 = 0.2$ J/cm^2 induces a phase transition up to the vaporization temperature. As shown in Fig. 15.4b, the electron system is heated nearly instantaneously to very high temperatures $T_e > 10^4$ K. Only after about 1 ps the metal

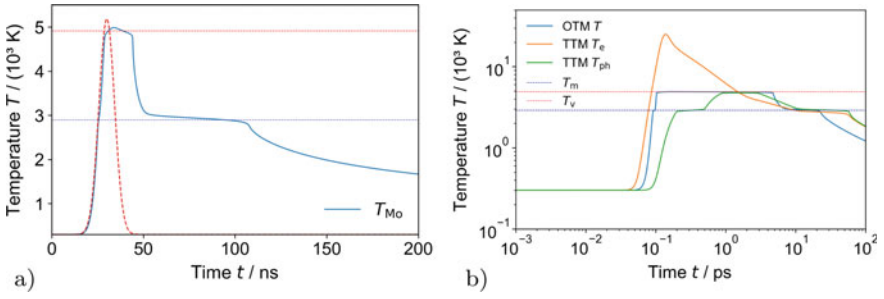

Fig. 15.4 Temperature development at the surface of molybdenum after irradiation with **a** one nanosecond laser pulse (pulse duration $t_p = 10$ ns, fluence $H_0 = 1.8$ J/cm^2), and **b** one femtosecond laser pulse (pulse duration $t_p = 40$ fs, fluence $H_0 = 0.05$ J/cm^2)

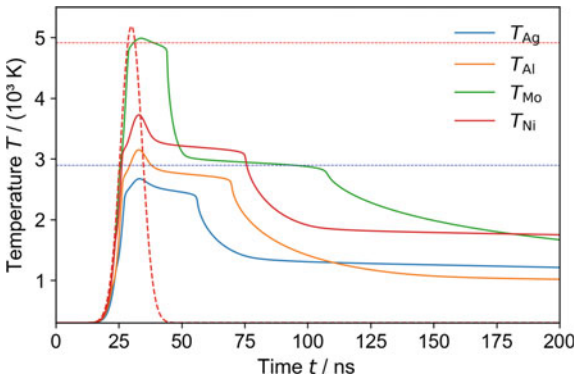

Fig. 15.5 Temperature development at the surface of the metals aluminum, silver, molybdenum, and nickel after irradiation with one nanosecond laser pulse considering phase changes (pulse duration $t_p = 10$ ns, fluence $H_0 = 1.8$ J/cm^2)

reaches the vaporization temperature T_V. After 5 ps the electron and phonon system get in thermal equilibrium. The one-temperature model (OTM) describing well the temperature development for nanosecond laser irradiation, but fails to describe the phase transitions of molybdenum when excited by femtosecond laser radiation, as there the phase transitions would take place nearly instantaneously.

Comparing different metals, here silver, aluminum, molybdenum and nickel, irradiated by a single pulses at two different pulse duration's, again one in the nanosecond regime (Fig. 15.5), the other in the femtosecond regime (Fig. 15.6), one can now visualize the phase changes of metals featuring different thermo-physical parameters, see Table 14.4.

Irradiating this metals with one nanosecond laser pulse at a pulse duration $t_p = 10$ ns and a fluence of $H_0 = 1.8$ Jcm^{-2} induces a phase changes reaching vaporization temperatures during the irradiation time, see Fig. 15.5. Depending on the thermo-physical parameters, the cooling process differs for each metal.

Irradiating the metals with femtosecond laser pulses at a pulse duration of $t_p = 40$ fs and a fluence of $H_0 = 0.2$ Jcm^{-2} induces a phase change at different times, depending on the thermo-physical parameters, and as well electron-phonon coupling parameter, see Table 14.4. One observes that the re-solidification is only reached at times in the range of 10 to some hundreds of picodeconds. Also evident is that the one-temperature model describes qualitatively the process, but fails especially for metals with strong electron-phonon coupling, see Fig. 15.5b. The thermalization of electron and phonon system is reached at about the electron-phonon coupling time, see Sect. 14.5.3.

It is obvious that this calculations are not applicable for processes where large amount of matter is molten and evaporated strongly, as there a very complex dynamics of the melt, vapor and plasma takes place and has to be considered in the modeling. This one-dimensional model description allows to describe only the initial phase transitions of single small volume elements in the nanometer scale, but fails for real laser irradiated volumes in the μm^3 scale.

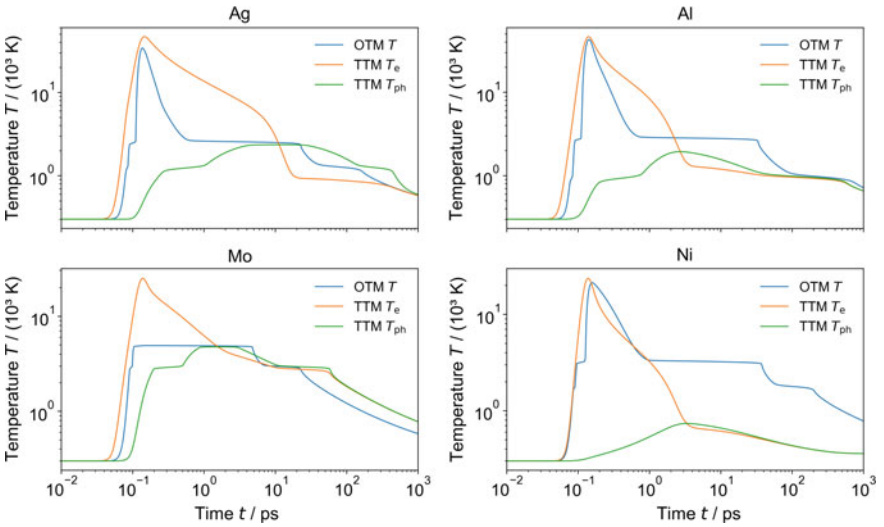

Fig. 15.6 Temperature development at the surface of the metals aluminum, silver, molybdenum, and nickel after irradiation with one femtosecond laser pulse considering phase changes (pulse duration $t_p = 40$ fs and a fluence of $H_0 = 0.2$ Jcm^{-2})

15.3 Thermo-physical Equations

Different to heating of condensed matter without phase changes, where only heat is transported spatially and temporally, inducing phase changes needs the description of matter transport.

For the interaction of ultra-fast laser radiation with matter with multiple phases, the **general Euler equations** in the convective form are needed [1]. The Euler equations represent a set of quasi-linear partial differential equations describing the flow dynamics of frictionless elastic fluids. In this textbook we will not discuss this equations into much detail.

Therefore, the continuity equation is described by

Continuity equation

$$\frac{\mathrm{d}\rho}{\mathrm{d}t} = -\rho \nabla \cdot \mathbf{u}, \tag{15.1}$$

whereby $\dfrac{\mathrm{d}}{\mathrm{d}t} = \dfrac{\partial}{\partial t} + \mathbf{u} \cdot \nabla$ represents the **total derivative**, t the time, ρ the density, $\mathbf{u} = \left(u_x, u_y, u_z\right)^{\mathrm{T}}$ the velocity in the x-, y- and z-directions.

The momentum equation is given by

Momentum equation

$$\frac{\mathrm{d}\mathbf{u}}{\mathrm{d}t} = -\frac{\nabla p}{\rho}, \tag{15.2}$$

and the extended energy equations described by the two-temperature model (TTM) are applied to consider the non-equilibrium in the energy balance between

Extended energy equations

the electron system given by

$$\frac{\mathrm{d}\epsilon_\mathrm{e}}{\mathrm{d}t} = -p_\mathrm{e}\frac{\mathrm{d}\,(1/\rho)}{\mathrm{d}t} + \frac{1}{\rho}\nabla\cdot(\lambda_\mathrm{e}\nabla T) - \frac{G}{\rho}(T_\mathrm{e} - T_\mathrm{ph}) + \frac{\dot{q}_\mathrm{V}}{\rho}, \tag{15.3}$$

and the phonon system given by

$$\frac{\mathrm{d}\epsilon_\mathrm{ph}}{\mathrm{d}t} = -p_\mathrm{ph}\frac{\mathrm{d}\,(1/\rho)}{\mathrm{d}t} + \frac{G}{\rho}(T_\mathrm{e} - T_\mathrm{ph}). \tag{15.4}$$

The indices e and ph denote the electron and phonon system, respectively, p the pressure, ϵ the specific internal energy, λ_e the thermal conductivity of the electron system, T the temperature, G the electron-phonon-coupling factor, and $\dot{q}_V$ the heat source.

Solving of the whole set of the three-dimensional equations requires a high computational effort, particularly in the case of ablation, where nucleation of cavitation bubbles, or free boundaries have to be considered among other things [1]. Thus, for the sake of simplicity, the described (15.1)–(15.4) are solved only one-dimensional along the z-direction in Lagrangian coordinates with $\mathrm{d}m = \rho\,\mathrm{d}z$, resulting in the simplified continuity equation

$$\frac{\partial(1/\rho)}{\partial t} = -\frac{\partial u_z}{\partial m}, \tag{15.5}$$

the simplified momentum equation [2]

$$\frac{\partial u_z}{\partial t} = -\frac{\partial\left(p_e + p_{ph}\right)}{\partial m}, \tag{15.6}$$

and the simplified two-temperature energy equations

$$\frac{\partial\epsilon_\mathrm{e}}{\partial t} = -p_\mathrm{e}\frac{\partial u_z}{\partial m} + \frac{\partial}{\partial m}\left(\rho\,\lambda_\mathrm{e}\frac{\partial T_\mathrm{e}}{\partial m}\right) - \frac{G}{\rho}(T_\mathrm{e} - T_\mathrm{ph}) + \frac{\dot{q}_V}{\rho}, \tag{15.7}$$

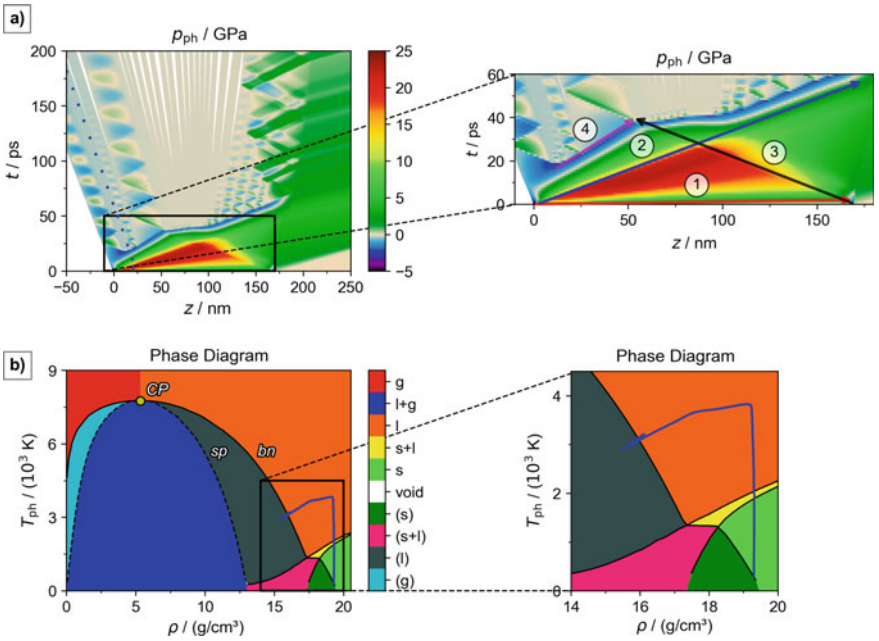

Fig. 15.7 Calculated time-space diagrams for visualizing the temporal evolution of **a** the pressure of the phonon system p_{ph} and **b** temperature-density-phase diagram of excited gold at fluences little above ablation threshold $H_0 > H_{\mathrm{thr}}$ describing spallation, according to [2]

and

$$\frac{\partial \epsilon_{\mathrm{ph}}}{\partial t} = -p_{\mathrm{ph}} \frac{\partial u_z}{\partial m} + \frac{G}{\rho} (T_{\mathrm{e}} - T_{\mathrm{ph}}), \tag{15.8}$$

wherein m represents the mass. In order to be able to solve the system of (15.5)–(15.8), the electron- and phonon pressure are derived from an equation of state. For more details see [1].

The temperature-density phase diagram of gold is calculated according to [2], see Fig. 15.7b. Different colors correspond to different phase states, wherein meta-stable phases are indicated by brackets. The dot represents the critical point (CP), bn the binodal, and sp the spinodal, respectively.

Exemplary, the irradiation of a thin gold film at moderate fluences, little above ablation threshold $H_0 > H_{\mathrm{thr}}$, is modeled by the described equations, see Fig. 15.7. The phase diagram describes the irradiation process by the very fast increase of pressure at constant volume, the so called **isochoric heating**. Thereby the interaction volume changes its phase from solid to liquid.

After the irradiation, the interaction volume and its density is reduced by an **isentropic expansion**, reaching the meta-stable liquid phase, see inset in Fig. 15.7b. Calculated are also the time-space diagrams for visualizing the temporal evolution of the pressure of the phonon system p_{ph}, see Fig. 15.7a. Even applying only an

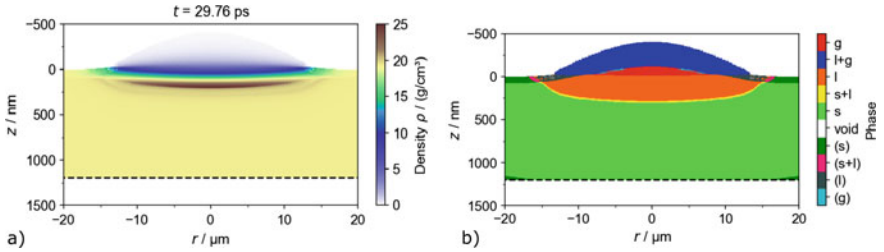

Fig. 15.8 Calculated temporal evolution of the quasi-two dimensional distribution of the density ρ (**a**), and the phase (**b**) for the time 29.76 ps after excitation of a thick gold layer ($d_z = 1000$ nm) with one laser pulse ($t_p = 40$ fs, $\lambda = 800$ nm, $H_0 = 5\,\mathrm{J/cm^2}$)

one-dimensional calculation, many information's can be extracted: The blue dots represent the evolution of a selected numerical element, and the associated values of the temperature of the phonon system and the density of this element at different time steps are depicted in the phase diagram as a blue trajectory, see Fig. 15.7b and inset. The red arrow ① in the inset of Fig. 15.7a describes the development of the shock wave propagating towards the substrate, the blue arrow ② the trajectory of the rarefaction wave propagating towards the substrate, and the black arrow ③ the trajectory of the rarefaction wave propagating towards the vacuum, which was generated by the partial reflection of the shock wave ① at the interface to the substrate. The purple arrow ④ represents the induced cavitation front of rarefaction wave ②.

A quasi-two-dimensional simulation can be derived, despite just solving the equations along the axial direction z, by considering each one-dimensional simulation for a definite fluence H of the laser radiation as a slice, giving all thermo-physical parameters as a function of the depth z. To obtain the applied fluence distribution

$$H(r) = H_0 \exp\left(-\frac{2r^2}{\omega^2}\right), \tag{15.9}$$

various one-dimensional simulations, each for a distinct fluence H, were performed, and subsequently, the slices are stacked together along the radial direction, see Fig. 15.8 for the density and the phase distribution in a gold film of 1 µm thickness 29 ps after irradiation with one ultra-fast laser pulse. This approach neglects any radial diffusion of heat and stress, but provides a natural view on the results and enables a direct comparison to the experimental ablation structures [1].

For high fluences well above ablation threshold, $H_0 \gg H_{\mathrm{thr}}$, temperatures at the surface are reached being significantly above the thermodynamical critical temperature T_{crit} at simultaneously high pressure, resulting in a super-critical fluid, see the phase diagram in Fig. 15.9.

After an isochoric strong heating where the density of matter remains unchanged, but the pressure increases dramatically over the critical pressure p_{crit}, the interaction volume relaxes by isentropic expansion reducing density and pressure reaching the binodale an spinodale close to the critical point (CP). Binodals and spinodals are

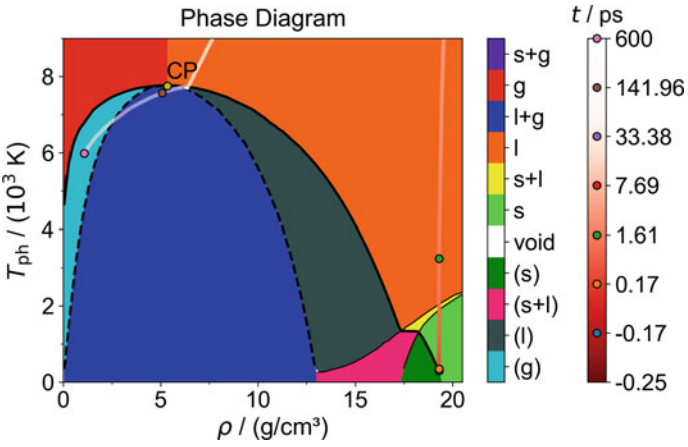

Fig. 15.9 Calculated temperature-density-phase diagram of excited gold at fluences well above ablation threshold $H_0 \gg H_{thr}$ describing phase explosion, according to [2]. The time steps of the excitation trajectory are depicted by colored circles and scaled on the right

exceeded by the relaxing system in the phase diagram, and finally the two-phase region is reached resulting in a mixture of liquid and gas. This mixture expands explosively, and this process is called a **phase explosion**, see also Fig. 15.10. The expansion of the mixture occurs in all directions, which is why the closed layer of liquid material ⑤ above the foam-like mixture ④ increases in size, see Fig. 15.10d. Furthermore, the pressure of the compression wave as well as its spatial expansion increases significantly due to the additional pressure of the recoil wave, see Fig. 15.10a.

If the densification wave is now partially reflected at the layer-substrate interface, see Fig. 15.10b, and overlaps with the thinning wave, which propagates into the direction of the substrate, an area of very low pressure is created, see Fig. 15.10c. There the melting of the material well below the melting temperature T_m starts, followed in this area by **spallation** ②. As a result, in addition to the ablation at the front side ④–⑦ of the layer, an ablation at the back side of the layer is also induced, with the ablated material being in the solid state ③.

At this high fluence, a foam-like mixture of the material is also formed at the back side of the layer ②. Furthermore, the non-ablated area ① between the ablation at the front side ④–⑦ and the ablation at the back side ② and ③ decreases, see Fig. 15.10d.

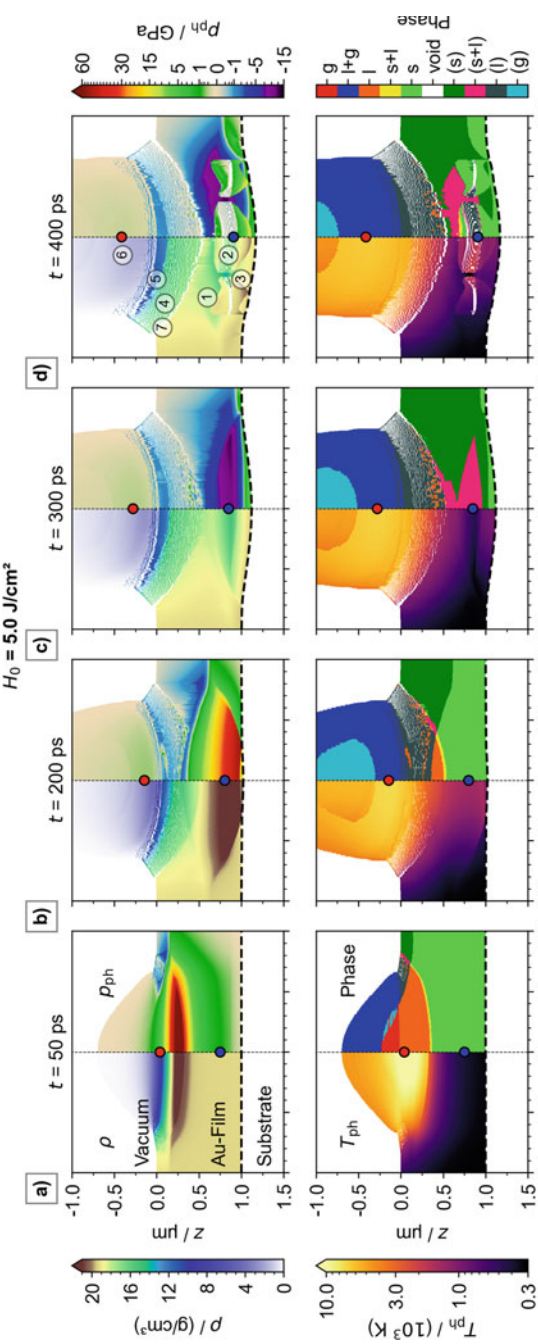

Fig. 15.10 Calculated temporal evolution of the quasi-two dimensional distribution of the density ρ, the pressure of the phonon system p_{ph}, the temperature of the phonon system T_{ph} as well as the phase for the times of **a** 50 ps, **b** 200 ps, **c** 300 ps and **d** 400 ps after excitation of a thick gold layer ($d_z + = 1000$ nm) with one laser pulse ($t_{\mathrm{p}} = 40$ fs, $\lambda = 800$ nm, $H_0 = 5$ J/cm^2). The markers ①–⑦ used are explained in the text. The rarefaction wave at the first time step of $t = 50$ ps is moving behind the shock wave propagating towards the substrate and is identical to the blue arrow in Fig. 15.7

References

1. M. Olbrich, T. Pflug, C. Wüstefeld, M. Motylenko, S. Sandfeld, D. Rafaja, A. Horn, Hydrodynamic modeling and time-resolved imaging reflectometry of the ultrafast laser-induced ablation of a thin gold film. Opt. Lasers Eng. **129**, 106067 (2020)
2. M.E. Povarnitsyn, N.E. Andreev, E.M. Apfelbaum, T.E. Itina, K.V. Khishchenko, O.F. Kostenko et al., A wide-range model for simulation of pump-probe experiments with metals. Appl. Surf. Sci. **258**(23), 9480–3 (2012)

Part V
Selected Applications in Metrology

This part describes some applications dealing with laser radiation and metrology. Laser radiation enables, due to its extraordinary properties, like directionality, monochromaticity, coherence, as well as switchability, to incorporate into **optical metrology**. In this part, we will deal with ultra-fast laser metrology, only. Due to the very short pulse durations obtainable for the laser radiation, most physical processes can be investigated with very high temporal resolution.

The simplest way to use laser radiation for metrology is to determine the change in reflectance. In Chap. 16, we describe the general principles of pump-probe methods. Then, time-resolved reflectometry is introduced, also explaining its principle setup and evaluation methods. As often the spatial distribution of the laser radiation is well determined, also a spatial-resolved investigation gets possible and is described with some examples.

To know how the surface changes after laser irradiation is a central technical question. One very powerful method to get insight into that is ellipsometry. This metrology is described in detail in Chap. 17 introducing at the end the ellipsometric equation. This metrology is, compared to reflectometry, very complex and needs much more measurement points to get the ellipsometric parameters. How to deal with this is described in the following sections, also the experimental approaches. Ellipsometry is a very surface-sensitive metrology, which is why the optics at interfaces is described here in more detail, describing at the end the reflectance at many interfaces. Ellipsometry can be expanded by imaging techniques to imaging ellipsometry, and coupling it to ultra-fast laser radiation, we get finally space- and time-resolved ellipsometry. Examples for a setup are given and some results on metals and dielectrics are given.

Observing transparent objects featuring no colors, just refractive index changes, like living cells, has moved scientists to develop microscopy techniques enabling its visualization. One technique, the Nomarski microscopy, is described in Chap. 18 and its principles are discussed. The approach to time-resolved Nomarski microscopy is then given, therefore using a non-linear process to generate ultra-fast white-light radiation. One example for dielectrics demonstrates the power of this method.

Interferometry is a phase-sensitive optical metrology, and compared to Nomarski microscopy, it is a quantitative metrology. In Chap. 19, we describe its principles and introduce space- and time-resolved interferometry. Some examples demonstrate its applicability.

Chapter 16
Reflectometry

Abstract Reflectometry is a standard technique in optics to determine physical changes at the surface of condensed matter. In metrology one distinguishes between time-resolved an integrated reflectometry. Here in this textbook we will describe the time-resolved metrology, only.

16.1 Measurement Methods

A physical process can be observed by the direct and indirect measurement method:

- In the **direct measurement method**, particles are detected, which are emitted from an interaction area. Thereby these particles can be photons, α- or β-particles, clusters etc. These particles are registered by a detector.
- In the **indirect measurement method**, the interaction area is interrogated by particles, being photons (UV-VIS-IR radiation, γ-radiation, X-radiation), elementary particles (p, n, e^-, ...), or by another defined systems. A defined system is a physical system, which features a known state, such as the polarization, the spatial and temporal intensity distribution and the phase of the radiation.

In order to achieve a temporal resolution of a detector, like a photographic plate, one has to control the photon flux into the detector, e.g. with a shutter or another optical switch. Shutter speeds of 1/10,000 s = 100 μs are achieved with electro-mechanical shutters. CCD detectors are read-out electronically, so that detection times ≈ 1 μs can be achieved.

The sensitivity of photo detectors is increased using a multi-channel plate (MCP). Thereby free electrons are generated by photons, which are accelerated by a high-voltage within the MCP, and in turn generate additional new electrons amplifying the number of electrons by a factor of about 10^6. This electrons can excite a phosphor screen inducing an optical emission being dependent of the number of electrons. This secondary light can be picked up by a photographic plate or by CCD camera. Intensified CCDs increase the light sensitivity of CCDs, and faint objects can be observed. The shutter time is controlled by the accelerating high-voltage of the MCP, and is in the range of 200 ps $\geq t <$ 1 ms.

© Springer Nature Switzerland AG 2022

A. Horn, *The Physics of Laser Radiation–Matter Interaction*,
https://doi.org/10.1007/978-3-031-15862-9_16

16.2 Pump and Probe Metrology

The Pump and Probe method is a very old procedure, which has been used for centuries. It is an indirect measurement method, as will be described in the following. As an example, an application from acoustics shall be described: When tuning a string instrument, the musician uses a tuning fork which, has been calibrated to a specific tone. This tone can be assigned to a unique frequency ν_{cal}. The sound wave of a tuning fork represent in our case the **probe pulse**. To tune one string of an instrument with an unknown frequency ν_{s}, one has to excite the string inducing vibrations, for example, by plucking it, which can be considered as the **pump pulse**. The hearing organ of the musician is very sensitive and can perceive frequency differences up 1 Hz, but is very rarely calibrated. The hearing organ is our **detector**. To tune the instrument, the musician uses the tuning fork and listens to the superposition of the sound waves of the string and the tuning fork. If the frequency difference is $\Delta\nu \approx 15\,\mathrm{Hz}$, the musician perceives an "unclean" tone. Below this frequency difference, the musician hears a mixed tone with frequency $\nu_{\mathrm{mix}} = (\nu_{\mathrm{cal}} + \nu_{\mathrm{s}})/2$, which is modulated in loudness, i.e. amplitude, with frequency $\Delta\nu = \nu_{\mathrm{cal}} - \nu_{\mathrm{s}}$. The modulation is called beat. The slower the amplitude changes, the smaller the frequency difference. Thus, the measured signal of the Pump and Probe experiment is the beat frequency of the superimposed tones. Although the ear cannot distinguish two tones that are very close in frequency, but by this Pump and Probe method the musician is able to detect the difference being able to tune the string to a defined frequency.

In laser technology, the indirect measurement method is achieved using pulsed laser radiation. The interaction region to be investigated is excited using a determined laser pulse, the so called **pump pulse**, see Fig. 16.1. The interrogation of this state is achieved also with pulsed laser radiation, which is called the **probe pulse**. In case, one laser source is used, the pump and probe pulses are optically separated by using a beam splitter. In order to change the investigation time, the probe pulse is time-shifted with respect to the pump pulse by a mechanical delay line, so that time intervals of up to a few nanoseconds can be set between pump and probe pulse, see Fig. 16.1. The probe pulse can also originate from a second radiation source. Then, a time delay is achieved by electronically tunic of the two laser sources.

The detector, which picks up the sample pulse, can be in the simplest case a photo plate, CCD, or a photo diode. The spatial resolution and the detection sensitivity are determined by the detector, whereas the temporal resolution of the measurement method is determined by the pulse duration of the probe pulse. Since an interaction volume is interrogated, the state of the pump pulse must be defined. The pump and the probe pulse must be prepared, i.e. all physically relevant quantities of the pulse, such as the spatial and temporal intensity distribution, the spectral distribution and the polarization, must be determined, see Fig. 16.2. The experiment, which is based on the indirect measurement method, must be set up in such a way that only the physical quantities of the probe pulse that can be measured by the detector. For example, a photographic plate or detector can measure intensity changes and spatial changes, see Fig. 16.2. A change in polarization is not measured with these detectors.

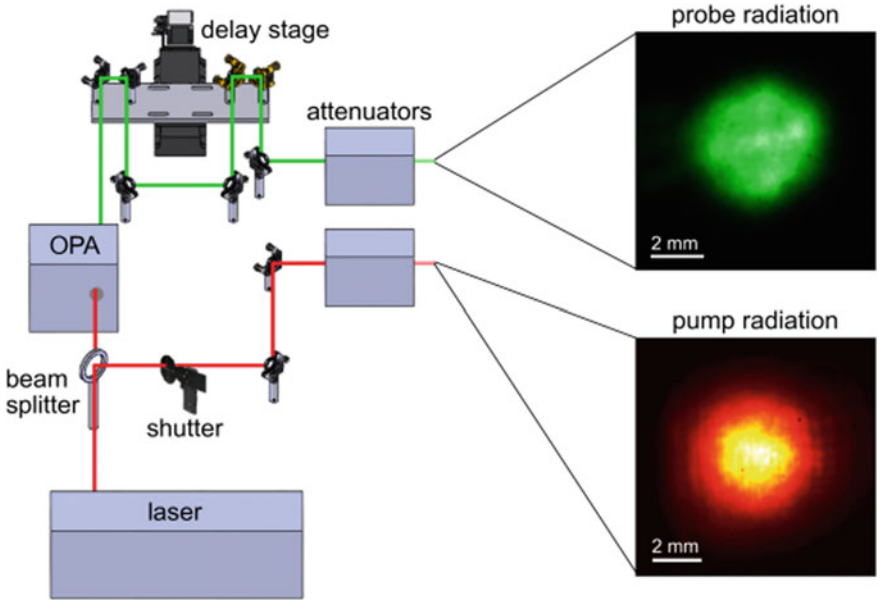

Fig. 16.1 Principle setup for the pump and probe beam lines [1]

For this purpose, the experiment must be set up, e.g. by adding a polarizer-analyzer arrangement, so that polarization changes can also be registered by the detector.

16.3 Time-Resolved Reflectometry

The determination of the change in the reflectance can give information on the dynamics of the physical properties of excited surfaces of condensed matter. For example, exciting a metallic surface by a laser pulse will induce, as describe in Chap. 15, phase changes from solid over liquid to vapor, and the plasma state, too, which can go along with changes in reflectance. Also the change in density within one phase state, changes often the reflectance.

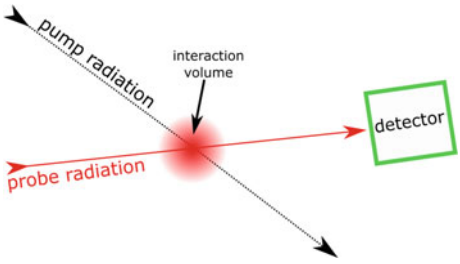

Fig. 16.2 Principle of pump-probe method. A well prepared state within the interaction volume by the pump laser radiation is interrogated by the probe radiation and measured by a detector

16.3.1 Principle and Set-Up

Usually, one separates the pump from the probe radiation at the interaction volume just by choosing different angels of incidence, see Fig. 16.3. As long as specular reflectance holds, no pump radiation will be detected. But, as surfaces of condensed matter, especially for solid matter, features at all times some defects, scattered radiation of the pump radiation can be detected. Additional blocking by narrow-band or interference filters can lower or even remove this radiation.

In principle, time-resolved reflectometry can be used during all phase change transitions of condensed matter, but due to the very strong dynamics induced by ultra-fast laser radiation, moving boundaries of solid, liquid or vapor states also change the propagation direction of the probe radiation, as the surface must not sustain at the pristine position.

> This means that modeling has to accompany the metrology giving information's about the dynamics of phases.

Combing the time-resolved reflectometry setup with optical microscopy allows to investigate laser-induced processes in the micrometer scale, as now the probe radiation is imaged on a CCD camera. Doing this, expands the functionality of the reflectometer, as now **space- and time-resolved reflectometry** is possible. A typical setup is shown in Fig. 16.4, where the inclined pump radiation is focused by a lens, and the probe radiation investigates the surface perpendicular to the surface passing through a microscopy objective, and returning the same is imaged by a tube lens onto a CCD.

In order to reduce artifacts coming from some surface topology or due to inhomogeneity of the probe radiation, and due to background radiation from external sources, four images per event are taken, as shown in Fig. 16.5a. The spatially resolved relative change of reflectance $\Delta R/R$ is then derived by

$$\frac{\Delta R}{R} = \frac{(R_i - b_i) - (R_0 - b_0)}{R_0 - b_0},$$

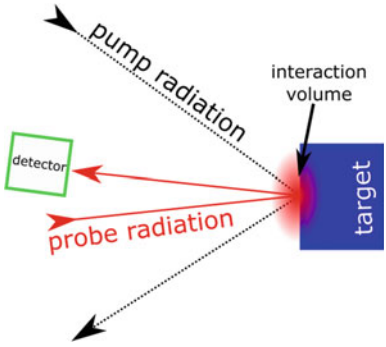

Fig. 16.3 Principle of pump-probe reflectometry [1]

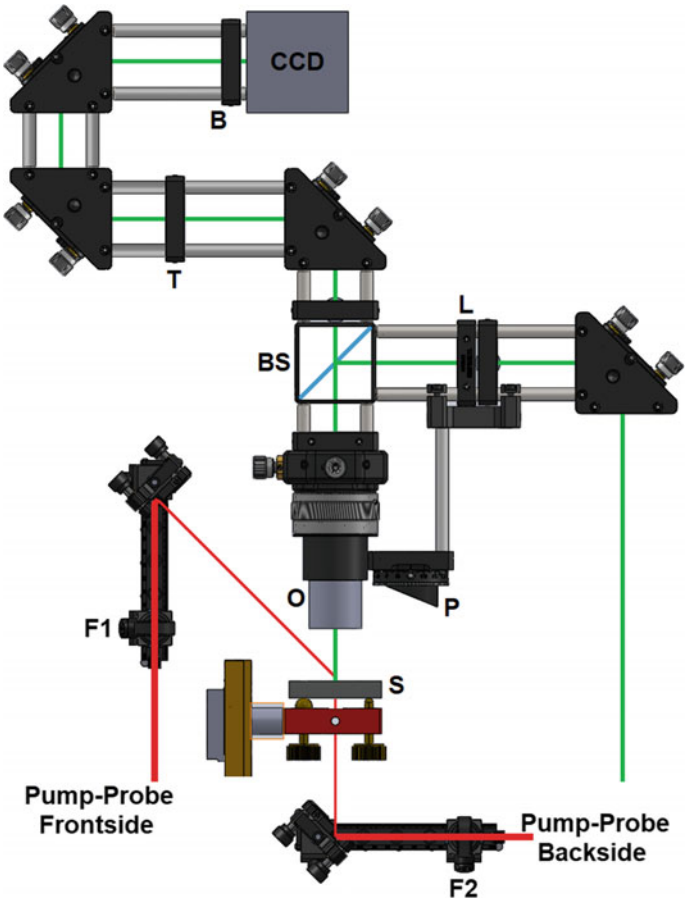

Fig. 16.4 Principle setup for the time-resolved reflectometry setup [2]

with the reflectance R_0 of the sample surface at rest, the reflectance R_i of the excited sample surface, the background noise b_0, as well as the background noise including the scattered pump radiation b_i.

16.3.2 Examples

In order to investigate the underlying physical mechanisms during laser irradiation in more detail, spatially and temporally resolved reflectometry measurements of stainless steel (EN 1.4301) are performed with the probe radiation at the wavelength

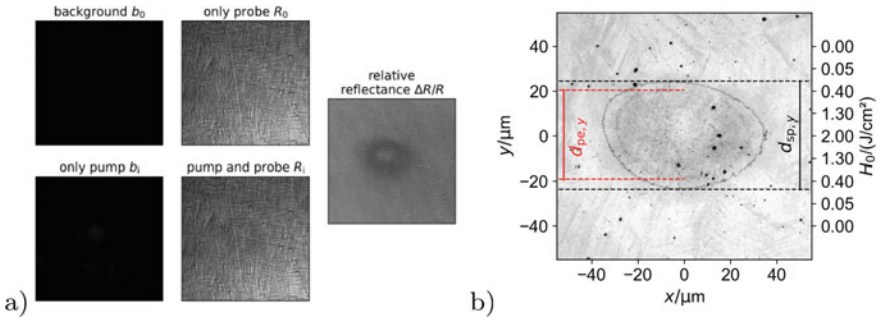

Fig. 16.5 **a** Images taken for evaluation of the space- and time resolved reflectometry: reflectance R_0 of the sample surface at rest, the reflectance R_i of the excited sample surface, the background noise b_0, as well as the background noise including the scattered pump radiation b_i. **b** Structure in stainless steel generated by single-pulsed pump radiation measured by light microscopy with the diameters of the two ablation regimes spallation $d_{\mathrm{sp},y}$ and phase explosion $d_{\mathrm{pe},y}$ [1]

$\lambda_{\mathrm{probe}} = 532$ nm and the pulse duration $t_{\mathrm{p,probe}} \approx 50$ fs, see Fig. 16.6. The ablation topology features the typical two ablation regimes for phase explosion and spallation, see Fig. 16.5b.

First, at $t < t_0 + 1$ ps, the excitation and relaxation of the electron system results in a decrease of the relative reflectance change $\Delta R/R$, whereby an annular change in terms of larger values of $\Delta R/R$ at the center compared to the values of $\Delta R/R$ at the outer area of the irradiated zone is detected, see Fig. 16.6. Second, in the range $t_0 + 1$ ps $< t < t_0 + 50$ ps, the relative reflectance change $\Delta R/R$ rapidly decreases starting from the center of the irradiated area until a minimum of $\Delta R/R = -1$ with the diameter of the phase explosion regime $d_{\mathrm{pe},y}$ is measured (Figs. 16.6 and 16.7). Afterward, at $t > t_0 + 650$ ps, the relative reflectance change $\Delta R/R$ increases

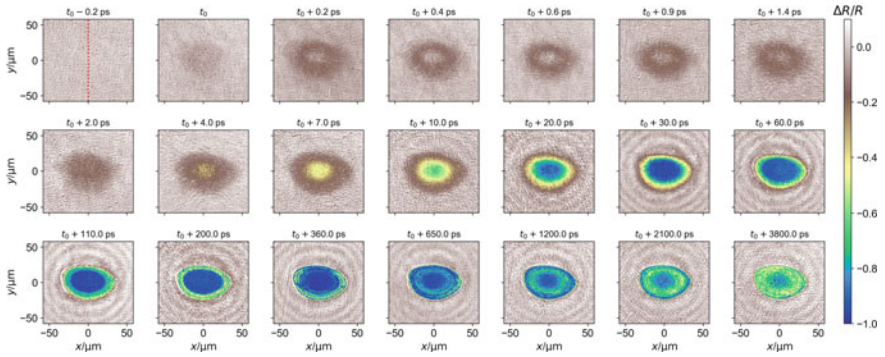

Fig. 16.6 Spatially resolved relative change of the reflectance $\Delta R/R$ of stainless steel (EN 1.4301) at the wavelength of the probe radiation $\lambda_{\mathrm{probe}} = 532$ nm and an angle of incidence $\Theta = 0°$ during and after irradiation with pump radiation at the wavelength $\lambda_{\mathrm{pump}} = 800$ nm, the fluence $H_0 = 2$ J/cm^2, the pulse duration $t_{\mathrm{p,pump}} = 40$ fs, and the angle of incidence $\Theta = 45°$. The time t_0 corresponds to the maximum of the temporal intensity distribution of the pump radiation [2]

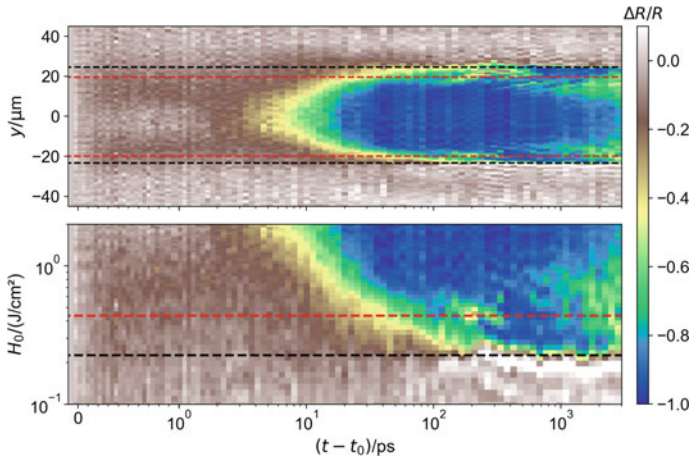

Fig. 16.7 **top**: Cross sections of the spatially resolved $\Delta R/R(y)$ at $x = 0$ (Fig. 16.6, red dashed line) plotted as a function of time relative to the time t_0 including the diameters for phase explosion (red dashed line) and spallation (black dashed line) from Fig. 16.5b; **bottom**: cross sections of the spatially resolved $\Delta R/R(y)$ at $x = 0$ plotted as a function of time, with the y-axis being assigned to the corresponding spatial fluence, according to (16.1) including the determined threshold fluences for phase explosion (red dashed) and spallation (black dashed line) from Fig. 16.5b [2]

slightly again. Third, simultaneous to the decreasing $\Delta R/R$ in the center of the irradiated area, at $t > t_0 + 50$ ps, a sharp interface between the $\Delta R/R$ at rest and the transient $\Delta R/R$ with the dimensions of spallation regime $d_{\mathrm{sp},y}$ is detectable, see Fig. 16.6. Additionally, the characteristic Newton rings become visible at $t > t_0 + 300$ ps.

In order to present the entire data in a compact manner, the cross sections of the spatially resolved relative reflectance change $\Delta R/R$ values at $x = 0$ (Fig. 16.6, red dashed line) are plotted as a function of time, see Fig. 16.7, top. Also, as the spatial intensity distribution of the radiation was measured, this relation holds, see also Sect. 1.7.1,

$$H_0(y) = \hat{H}_0 \exp\left(-\frac{8y^2}{d_y^2}\right), \tag{16.1}$$

with the beam diameter d_y assigned to the y-axis of the measured data, see Fig. 16.5 b, right axis. Knowing the spatial intensity distribution of the pump radiation allows to assign a specific fluence to each x-coordinate [2].

Irradiating a thin gold film with ultra-fast laser radiation ($\lambda = 800$ nm, $t_\mathrm{p} = 35$ fs, $H = 1.4$ J/cm^2) and determining the relative change in reflectance using probe radiation ($\lambda = 440$ nm, $t_\mathrm{p} = 60$ fs) allows the comparison with modeling of the electron phonon temperature, as well thermophysical modeling of the state of the thin film, see Sect. 15.3 and Fig. 16.8. Thereby, the comparison reveals a good agreement of the spatial construction of the relative reflectance change (a) with the behavior of

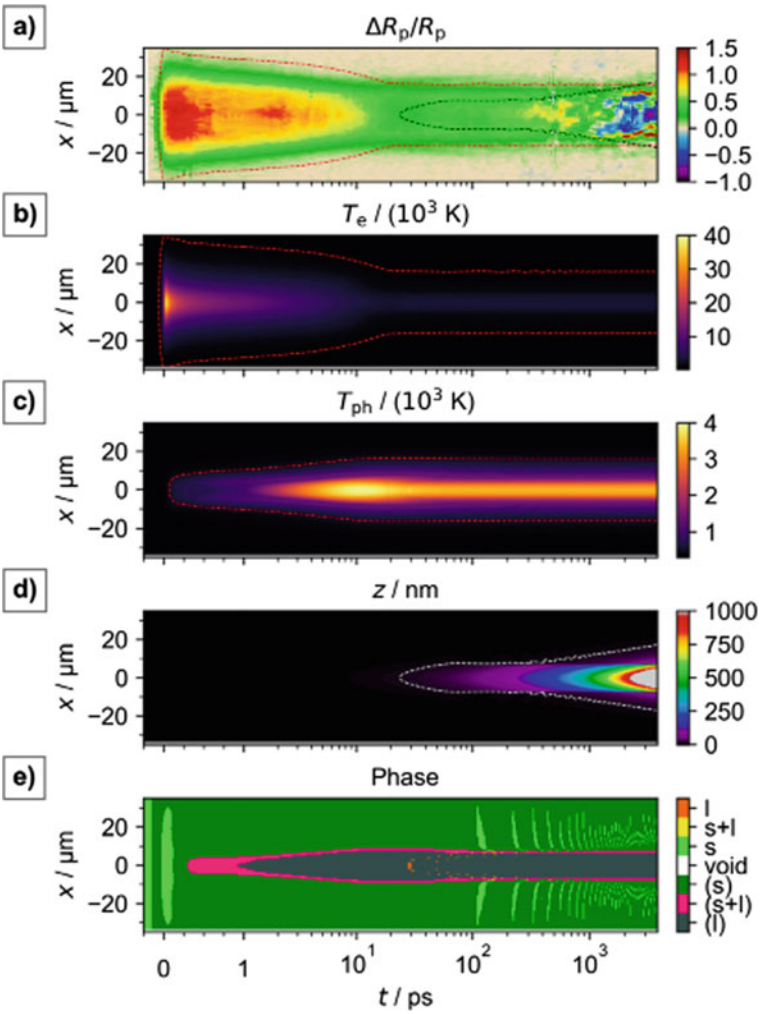

Fig. 16.8 **a** Cross-sections along the x-axis of the experimentally obtained spatially resolved relative change of reflectance $\Delta R/R$ plotted as a function of time in comparison to the simulated quasi-2D distributions on the surface of: **b** the temperature of the electron system T_e, **c** temperature of the phonon system T_p, **d** the z-coordinate of the surface and **e** phase state, respectively. The red dotted line represents the isotherm of $T_e = 600$ K, and the white as well as the black dotted lines represent a z-coordinate of the interface gold-vacuum of 10 nm [3]

the electron temperature due to cooling of the electron system by heating the phonon system, as well heat diffusion (b). Also, the increase in the relative reflectance change at delay times larger than 10 picoseconds are attributed to heating of the phonon system. At delay times larger 1 nanosecond the modeling of the surface topology (d) reveals a strong expansion due to bulging and possibly ablation, both being well detectable by reflectometry [3].

References

1. T. Pflug, Strong field excitation of electrons into localized states of fused silica. Ph.D. thesis, Technische Universität Chemnitz, 2022
2. T. Pflug, M. Olbrich, J. Winter, J. Schille, U. Löschner, H. Huber, A. Horn, Fluence-dependent transient reflectance of stainless steel investigated by ultrafast imaging pump-probe reflectometry. J. Phys. Chem. C **125**(31), 17363–17371 (2021)
3. M. Olbrich, T. Pflug, C. Wüstefeld, M. Motylenko, S. Sandfeld, D. Rafaja, A. Horn, Hydrodynamic modeling and time-resolved imaging reflectometry of the ultrafast laser-induced ablation of a thin gold film. Opt. Lasers Eng. **129**, 106067 (2020)

Chapter 17
Ellipsometry

Abstract Ellipsometry is a very sensitive technique for the detection of optical properties at surfaces, also getting information on the topology and the distribution in depth of the surface itself. This section will first introduce the principles of ellipsometry observing the dependencies of radiation being reflected at one boundary, then moving on to a thin layer with at least two boundaries, and finally talking about the dispersion relations given in ellipsometry. Finally, this section concludes with a specific application in metrology using ellipsometry, combining this fantastic method with the properties of ultra-fast laser radiation.

17.1 Fundamentals on Polarization States

Electromagnetic radiation is a transverse electromagnetic wave whose electric field strength distribution is given through[1]

$$\boldsymbol{E} = \boldsymbol{E}_0 e^{i(\omega t - \boldsymbol{k}\cdot\boldsymbol{r})}$$

with the amplitude $\boldsymbol{E}_0$, the angular frequency ω, the circular wave vector $\boldsymbol{k}$ and the position vector $\boldsymbol{r}$ of the electric field, see also Sect. 1.5. The magnetic induction $\boldsymbol{B}$ is always perpendicular oriented to the electric field strength, and can be calculated using the Maxwell equations so that the last equation is sufficient for further descriptions [4]. If the electromagnetic wave propagates in the z-direction, the electric field can be described by the linear combination of two orthogonal electric fields

$$\boldsymbol{E} = E_x\hat{\boldsymbol{x}} + E_y\hat{\boldsymbol{y}} = \boldsymbol{E}_x + \boldsymbol{E}_y.$$

The electric field strengths $\boldsymbol{E}_x$ and $\boldsymbol{E}_y$ with each phase δ_x and δ_y, and the phase difference $\Delta = \delta_x - \delta_y$ are then described by

[1] This section is derived from the master thesis of one of my past students [1], Dr. Theo Pflug, and now collaborator, see also [2, 3], and citations therein.

© Springer Nature Switzerland AG 2022

A. Horn, *The Physics of Laser Radiation–Matter Interaction*,
https://doi.org/10.1007/978-3-031-15862-9_17

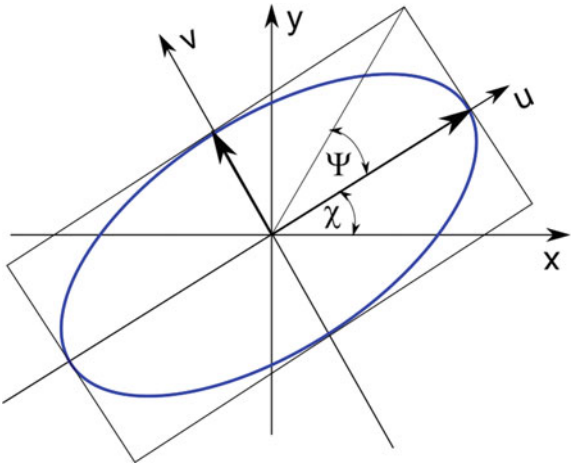

Fig. 17.1 Polarization ellipse of elliptically polarized radiation in the x-y coordinate system; Ψ is the ellipticity of polarization; χ is the angle between the x-y coordinate system and u-v coordinate system of the half-axes

$$\boldsymbol{E}_x = \boldsymbol{E}_{x,0} e^{i(\omega t - \boldsymbol{k}\cdot\boldsymbol{r})}, \text{ and}$$
$$\boldsymbol{E}_y = \boldsymbol{E}_{y,0} e^{i(\omega t - \boldsymbol{k}\cdot\boldsymbol{r} + \Delta)}.$$

The polarization state of an electromagnetic wave can be determined by a polarization ellipse, see Fig. 17.1, where $\boldsymbol{\Psi}$ represents the **ellipticity** and χ spans an angle between the large elliptical semi-axis and the coordinate system.

Using Ψ and χ, the polarization of the radiation can be determined via the **Stokes parameters** S_0, S_1, S_2, and S_3, and are calculated as follows

$$\begin{aligned}
S_0 &= E_x^2 + E_y^2 = I_{\text{sum}}, \\
S_1 &= E_x^2 - E_y^2 = I_{\text{sum}} P \cos(2\Psi)\cos(2\chi), \\
S_2 &= 2E_x E_y \cos\delta = I_{\text{sum}} P \cos(2\Psi)\sin(2\chi), \text{ and} \\
S_3 &= 2E_x E_y \sin\delta = I_{\text{sum}} P \sin(2\Psi).
\end{aligned}$$

Thereby the degree of polarization

$$P = \frac{I_{\text{pol}}}{I_{\text{sum}}}$$

is used, where I_{sum} represents the total intensity of the radiation and I_{pol} the intensity of the polarized fraction of the radiation. The normalized Stokes vector is then represented by

$$\boldsymbol{S}_N = \frac{1}{S_0}\begin{pmatrix} S_0 \\ S_1 \\ S_2 \\ S_3 \end{pmatrix} = \begin{pmatrix} S_{N,0} \\ S_{N,1} \\ S_{N,2} \\ S_{N,3} \end{pmatrix}.$$

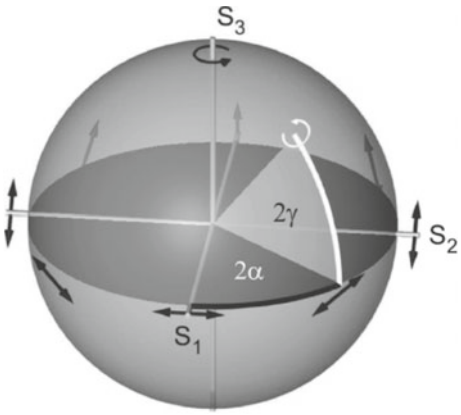

Fig. 17.2 Poincaré-sphere for the polarization state of radiation [6]

For $\delta = 0$ and $\left|S_{N,2}\right| = 1$, for example, results in linearly polarized radiation being inclined by an angle of 45° [4, 5]. For a simple description of the polarization state of an electromagnetic wave using the normalized Stokes vector, the so-called Poincaré-sphere [6] is applied, see Fig. 17.2.

The center of the sphere describes completely unpolarized, and the surface of the sphere fully polarized electromagnetic radiation. Each point within the $S_{N,1} - S_{N,2}$ plane represents partially or fully linear polarized radiation. The upper Poincaré hemisphere contains all right-turning elliptical or circular, the lower hemisphere all left-turning elliptical or circular polarization states of the radiation.

17.2 Principles of Ellipsometry

Ellipsometry determines the change of the polarization state of electromagnetic radiation with a defined wavelength by its reflection at a sample surface with the complex refractive index $\tilde{n} = n - i\kappa = n + ik$. So, the incoming linear polarized radiation is reflected at a surface and the electrical fields get, as shown in Fig. 17.3, different amplitudes and phases for the s- and p-polarization states of the radiation, resulting mostly in elliptical polarized radiation. The respective fraction between the amplitudes of the electrical field strengths in the s- and p-polarization states are described by the angle Ψ, before defined as ellipticity, with

$$\tan \Psi = \frac{\left|E'_{\mathrm{p}}\right|}{\left|E'_{\mathrm{s}}\right|}. \tag{17.1}$$

The resulting phase difference Δ results from the difference in the phases of the s- and p-polarized electric field strengths

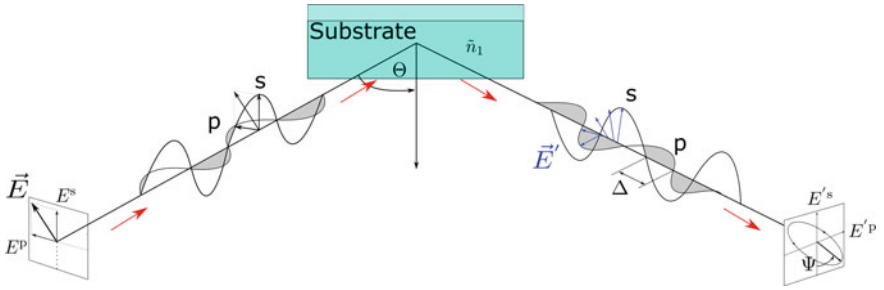

Fig. 17.3 Principle description of the electrical field strengths in an ellipsometer for the rotating analyzer method

$$\Delta = \delta_p - \delta_s.$$

As seen in Chap. 7, the Fresnel equations describe the change in the field strengths for each polarization state after reflection and transmission through a boundary by the reflection and transmission coefficients. So, we can define the change of both states by reflection introducing the fraction from the reflection coefficients

Complex ratio from the reflection coefficients

$$\rho = \frac{r^p}{r^s}. \tag{17.2}$$

As only in the ideal case the surface features only-real properties, meaning that the refractive index $\tilde{n}$ is mostly complex, also the corresponding reflection coefficients are complex, and the resulting complex ratio $\rho = r^p/r^s \in \mathbb{C}$, and we can write it in polar coordinates by

$$\begin{aligned}\rho &= \frac{|r^p|\, e^{i\delta_p}}{|r^s|\, e^{i\delta_s}} \\ &= \frac{|r^p|}{|r^s|} e^{i(\delta_p - \delta_s)} \\ &= |\rho|\, e^{i\Delta}.\end{aligned}$$

The components of the electric field strength vector of the radiation are described by the Fresnel equations, see (7.23)–(7.26) in Sect. 7.4. After reflection the electric field strengths are now given by

$$\begin{aligned}E_x &= E_{10}^{p'} = r^p E_{10}^p \\ E_y &= E_{10}^{s'} = r^s E_{10}^s.\end{aligned}$$

In the case the incoming linear polarized radiation is aligned diagonally with $\alpha = 45°$, one states that the amplitude of the incoming electric field strengths are equal, $\left|E_{10}^{\mathrm{p}}\right| = \left|E_{10}^{\mathrm{s}}\right|$, and we can rewrite the complex ratio

$$\begin{aligned}\rho &= \frac{r^{\mathrm{p}}}{r^{\mathrm{s}}} = \frac{\frac{E_{10}^{\mathrm{p}'}}{E_{10}^{\mathrm{p}}}}{\frac{E_{10}^{\mathrm{s}'}}{E_{10}^{\mathrm{s}}}} = \frac{E_{10}^{\mathrm{p}'}}{E_{10}^{\mathrm{s}'}} \\ &= \left|\frac{E_{10}^{\mathrm{p}'}}{E_{10}^{\mathrm{s}'}}\right| e^{i\Delta} \\ &= |\rho|\, e^{i\Delta}.\end{aligned}$$

Comparing now last equation with (17.1), we see that the amplitude of the complex ratio gets now

$$|\rho| = \tan \Psi,$$

and we derive the ellipsometric equation, representing the change of amplitude and phase by reflection of radiation at one boundary

Ellipsomettric equation

$$\rho = \frac{r^{\mathrm{p}}}{r^{\mathrm{s}}} = \tan \Psi e^{i\Delta}. \tag{17.3}$$

So, the fraction ρ being a complex number is now represented by its **amplitude** $\boldsymbol{\tan \Psi}$, and its **phase** $\boldsymbol{e^{i\Delta}}$.

17.3 Experimental Approach

To determine the **ellipticity** $\boldsymbol{\Psi}$ and **phase** $\boldsymbol{\Delta}$ experimentally one has to measure the refraction coefficients for the s- and p-polarization states. Usually, the incoming monochromatic radiation is linearly polarized by using a polarizer (P), see Fig. 17.4. After reflection of the radiation at an inclination angle Θ at the surface of the sample, the possibly elliptical radiation passes a second polarizes, the so called analyzer (A). There, many different ways to determine the ellipticity Ψ and phase Δ are given, like

- rotating-analyzer ellipsometry (PSAR),
- rotating-analyzer ellipsometry with compensator (PSCAR), and
- rotating-compensator ellipsometry (PSCRA).

See for a detailed description in the literature, e.g. [4]. Here the **rotating analyzer method (PSAR)** is discussed, and shown in Fig. 17.4.

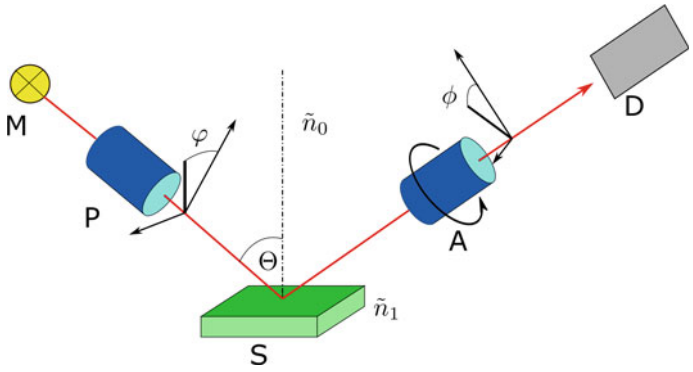

Fig. 17.4 Principle setup for an ellipsometer in the rotating analyzer method

This method offers the advantage that the polarization state of the radiation entering the polarizer (P) needs not to be firmly defined. In the chosen approach the incident radiation is linearly polarized using a polarizer, and is then predetermined. After reflection at the sample surface (S), the reflected radiation is generally elliptically polarized.

A measure for the change of the polarization state as a function of wavelength and the inclination angle of the incident radiation Θ, when reflected on a sample surface, represents the ellipsometric parameters Δ and Ψ. The values determined by the reflection at of the sample surface is indicated by the rotating analyzer (A), and measured by a detector (D) varying the analyzer angle ϕ, see Fig. 17.5 [4, 5]. The sequential rotation of the analyzer allows the intensity of the reflected radiation to be measured using the detector as a function of the analyzer angle ϕ.

The intensity curve $I(\phi)$ is approximated from the measured intensity curve, see Fig. 17.5, by varying the Fourier coefficients α_F and β_F [7], using the equation

Appoximation function

$$I(\phi) = I_0 \left(1 + \alpha_F \cos(2\phi) + \beta_F \sin(2\phi)\right). \tag{17.4}$$

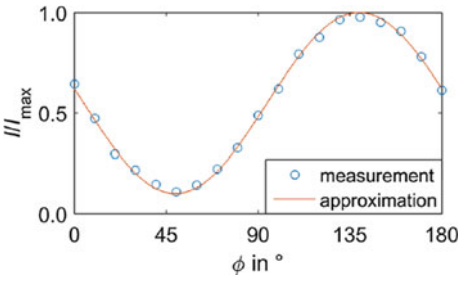

Fig. 17.5 Measured normalized intensity I of the reflected radiation on a gold surface depending on the analyzer angle ϕ, and associated approximated function $I(\phi)$ using (17.4)

The Fourier coefficients α_F and β_F describe the amplitude and phase of the approximated intensity curve.

To get a connection between the measured intensity distribution from (17.4) to the induced amplitude and phase changes by reflection by the optical properties of the investigated surface, one has to determine first the **Jones transfer matrices** for each optical element, here the polarizer **P** being rotated by the angle ϕ, the reflecting substrate surface, and the analyzer **A** rotated by the angle φ.

The Jones matrix for the reflecting surface is got by the respective Fresnel equations and the ellipsometer (17.3)

$$\begin{aligned}\mathbf{S} &= \begin{pmatrix} r^{\mathrm{p}} & 0 \\ 0 & r^{\mathrm{s}} \end{pmatrix} = r^{\mathrm{s}} \begin{pmatrix} \frac{r^{\mathrm{p}}}{r^{\mathrm{s}}} & 0 \\ 0 & 1 \end{pmatrix} \\ &= r^{\mathrm{s}} \begin{pmatrix} \tan\Psi e^{i\Delta} & 0 \\ 0 & 1 \end{pmatrix} = \frac{r^{\mathrm{s}}}{\cos\Psi} \begin{pmatrix} \sin\Psi e^{i\Delta} & 0 \\ 0 & \cos\Psi \end{pmatrix}.\end{aligned}$$

As shown in [4], one gets in the rotating-analyzer ellipsometer design, as depicted in Fig. 17.4, the overall transfer matrix by the subsequent matrix multiplications

$$\boldsymbol{E}_A = \mathbf{AR}(\phi)\mathbf{SR}(-\varphi)\mathbf{P}\boldsymbol{E}_i.$$

and inserting the matrices one gets

$$\begin{aligned}\boldsymbol{E}_A &= \begin{pmatrix} E_A \\ 0 \end{pmatrix} \\ &= \begin{pmatrix} 1 & 0 \\ 0 & 0 \end{pmatrix} \begin{pmatrix} \cos\phi & \sin\phi \\ -\sin\phi & \cos\phi \end{pmatrix} \frac{r^{\mathrm{s}}}{\cos\Psi} \begin{pmatrix} \sin\Psi e^{i\Delta} & 0 \\ 0 & \cos\Psi \end{pmatrix} \cdot \\ &\cdot \begin{pmatrix} \cos\varphi & -\sin\varphi \\ \sin\varphi & \cos\varphi \end{pmatrix} \begin{pmatrix} 1 & 0 \\ 0 & 0 \end{pmatrix} = \begin{pmatrix} E_i \\ 0 \end{pmatrix}\end{aligned} \tag{17.5}$$

Now, the usual alignment of the incoming electric field strength vector in ellipsometry is rotated by $\varphi = 45°$, and we get

$$\boldsymbol{E}_A = \begin{pmatrix} 1 & 0 \\ 0 & 0 \end{pmatrix} \begin{pmatrix} \cos\phi & \sin\phi \\ -\sin\phi & \cos\phi \end{pmatrix} \frac{r^{\mathrm{s}}}{\sqrt{2}\cos\Psi} \begin{pmatrix} \sin\Psi e^{i\Delta} \\ \cos\Psi \end{pmatrix}.$$

The electric field strength results to

$$E_A = \frac{r^{\mathrm{s}}}{\sqrt{2}\cos\Psi} \left(\cos\phi \sin\Psi e^{i\Delta} + \sin\phi\cos\Psi\right), \tag{17.6}$$

and we can now determine the intensity by $I \propto |E_A|^2$ from (1.94). We take all scalar values together in the parameter I_0, resulting in the intensity as function of the analyzer angle ϕ, given by

$$I(\phi) = I_0 \left(1 - \cos 2\phi \cos 2\Psi + \sin 2\phi \sin 2\Psi \cos \Delta\right).$$

Generalizing now for all possible polarizer angles φ, we get for the electric field strength from (17.5), omitting again the scalars,

$$E_A = \cos\varphi \cos\phi \sin\Psi e^{i\Delta} + \sin\varphi \sin\phi \cos\Psi.$$

Again, computing the intensity and applying trigonometric addition theorems one gets

$$\begin{aligned} I &= |E_A|^2 \\ &= I_0 \left[(1 - \cos 2\varphi \cos 2\Psi) + (\cos 2\varphi - \cos 2\Psi) \cos 2\phi + \right. \\ &+ \left. (\sin 2\varphi \sin 2\Psi \cos \Delta) \sin 2\phi\right] \\ &= I_0^* \left[1 + \frac{(\cos 2\varphi - \cos 2\Psi)}{(1 - \cos 2\varphi \cos 2\Psi)} \cos 2\phi + \frac{(\sin 2\varphi \sin 2\Psi \cos \Delta)}{(1 - \cos 2\varphi \cos 2\Psi)} \sin 2\phi\right]. \end{aligned}$$

The last line allows to compare with the approximation function (17.4) to determine the Fourier coefficients

$$\alpha_{\mathrm{F}} = \frac{\cos 2\varphi - \cos 2\Psi}{1 - \cos 2\varphi \cos 2\Psi} \quad \text{and} \quad \beta_{\mathrm{F}} = \frac{\sin 2\varphi \sin 2\Psi \cos \Delta}{1 - \cos 2\varphi \cos 2\Psi}.$$

Applying some trigonometric addition theorems we get another writing for the Fourier coefficients

$$\alpha_{\mathrm{F}} = \frac{\tan^2 \Psi - \tan^2 \varphi}{\tan^2 \Psi + \tan^2 \varphi} \quad \text{and} \quad \beta_{\mathrm{F}} = \frac{2 \tan \Psi \cos \Delta \tan \varphi}{\tan^2 \Psi + \tan^2 \varphi}. \tag{17.7}$$

Are polarizer before the sample surface, and analyzer after the sample surface ideally polarizing, then the ellipsometric parameters Δ and Ψ can be calculated from the Fourier coefficients α_{F} and β_{F} at a fixed polarizer angle φ [4, 8]

Ellipsometric parameters Δ and Ψ

$$\Delta = \arctan\left(\sqrt{\frac{1 + \alpha_{\mathrm{F}}}{1 - \alpha_{\mathrm{F}}}} \tan|\varphi|\right) \tag{17.8}$$

$$\Psi = \arccos\left(\frac{\beta_{\mathrm{F}}}{\sqrt{1 - \alpha_{\mathrm{F}}^2}}\right). \tag{17.9}$$

Recapitulating, using an ellipsometer and varying the analyzer angle, the so called PSA_R type, one gets a typical trigonometric dependence of the reflected intensity on the analyzer angle ϕ, Fig. 17.5, and using the approximation (17.4), we can now deter-

mine the Fourier coefficients α_F and β_F. Finally we can compute the ellipsometric parameters Δ and Ψ.

With the knowledge of the polarization state of the radiation before reflection, and the ellipsometric parameters Δ and Ψ, many material properties, such as the refractive index n and the extinction coefficient κ can be determined.

17.4 Reflection at One Interface

If the incident radiation is completely linear polarized and oriented $\varphi = 45°$ relative to the plane of incidence and $\left|E_{10}^{p}\right| = \left|E_{10}^{s}\right|$ is valid, then the ratio of $E_{10}^{p'}$ and $E_{10}^{s'}$ of the reflected radiation is directly given by the complex ratio ρ, and by the ellipsometric parameters Δ and Ψ, according to

$$\frac{E_{10}^{p'}}{E_{10}^{s'}} = \frac{r^{p}}{r^{s}} \frac{E_{10}^{p}}{E_{10}^{s}} = \frac{r^{p}}{r^{s}} = \rho = \tan\Psi e^{i\Delta}. \tag{17.10}$$

Next, the Fresnel equations for r^p and r^s, see (7.23) and (7.25), have to be rewritten, in order to have only dependencies in the incident angle Θ. Therefore, using Snell's law, (7.10), and the relative permittivities $\tilde{\epsilon}_1 = \tilde{n}_1^2$ and $\tilde{\epsilon}_2 = \tilde{n}_2^2$, we introduce the abbreviations [4]

$$\begin{aligned}
\tilde{n}_{22} &= \tilde{n}_2 \cos\beta = \tilde{n}_2 \left(1 - \sin^2\beta\right)^{1/2} = \tilde{n}_2 \left(1 - \left(\frac{\tilde{n}_1}{\tilde{n}_2}\right) \sin^2\Theta\right)^{1/2} \\
&= \left(\tilde{n}_2^2 - \tilde{n}_1^2 \sin^2\Theta\right)^{1/2} = \left(\tilde{\epsilon}_2 - \tilde{\epsilon}_1 \sin^2\Theta\right)^{1/2}, \\
\tilde{n}_{11} &= \tilde{n}_1 \cos\Theta \\
\tilde{n}_{21} &= \frac{\tilde{n}_2}{\tilde{n}_1},
\end{aligned}$$

and rewrite the reflection coefficients, assuming $\mu_{r1} = \mu_{r2} = 1$,

$$\begin{aligned}
r^{p} &= \frac{\tilde{n}_2 \cos\Theta - \frac{\tilde{n}_1}{\tilde{n}_2}\tilde{n}_{22}}{\tilde{n}_2 \cos\Theta + \frac{\tilde{n}_1}{\tilde{n}_2}\tilde{n}_{22}} \\
&= \frac{\tilde{n}_2 \frac{\tilde{n}_{11}}{\tilde{n}_1} - \frac{\tilde{n}_1}{\tilde{n}_2}\tilde{n}_{22}}{\tilde{n}_2 \frac{\tilde{n}_{11}}{\tilde{n}_1} + \frac{\tilde{n}_1}{\tilde{n}_2}\tilde{n}_{22}}.
\end{aligned}$$

Multiplying enumerator and denominator by $\tilde{n}_2/\tilde{n}_1$ one gets

$$r^{p} = \frac{\tilde{n}_2^2\tilde{n}_{11} - \tilde{n}_1^2\tilde{n}_{22}}{\tilde{n}_2^2\tilde{n}_{11} + \tilde{n}_1^2\tilde{n}_{22}} = \frac{\tilde{\epsilon}_2\tilde{n}_{11} - \tilde{\epsilon}_1\tilde{n}_{22}}{\tilde{\epsilon}_2\tilde{n}_{11} - \tilde{\epsilon}_1\tilde{n}_{22}}. \tag{17.11}$$

Analogous, the reflection coefficient for s-polarized radiation is rewritten to

$$r^s = \frac{\tilde{n}_{11} - \tilde{n}_{22}}{\tilde{n}_{11} + \tilde{n}_{22}}. \tag{17.12}$$

Now, we return to the ellipsometric equation, especially to the complex ratio ρ, inserting (17.11) and (17.12) one gets

$$\begin{aligned}\rho = \frac{r^{\mathrm{p}}}{r^{\mathrm{s}}} &= \frac{(\tilde{\epsilon}_2\tilde{n}_{11} - \tilde{\epsilon}_1\tilde{n}_{22})}{(\tilde{\epsilon}_2\tilde{n}_{11} - \tilde{\epsilon}_1\tilde{n}_{22})}\frac{(\tilde{n}_{11} + \tilde{n}_{22})}{(\tilde{n}_{11} - \tilde{n}_{22})} \\ &= \frac{\tilde{\epsilon}_2\tilde{n}_{11}^2 - \tilde{\epsilon}_1\tilde{n}_{22}^2 + (\tilde{\epsilon}_2 - \tilde{\epsilon}_1)\tilde{n}_{11}\tilde{n}_{22}}{\tilde{\epsilon}_2\tilde{n}_{11}^2 - \tilde{\epsilon}_1\tilde{n}_{22}^2 - (\tilde{\epsilon}_2 - \tilde{\epsilon}_1)\tilde{n}_{11}\tilde{n}_{22}}.\end{aligned}$$

Remembering that

$$\tilde{n}_{11}^2 = \tilde{n}_1^2 \cos\Theta = \tilde{\epsilon}_1(1 - \sin^2\Theta)$$

and

$$\tilde{n}_{22}^2 = \tilde{\epsilon}_2 - \tilde{\epsilon}_1 \sin^2\Theta,$$

we get the complex ratio to

$$\begin{aligned}\rho &= \frac{\tilde{\epsilon}_2\tilde{\epsilon}_1(1 - \sin^2\Theta) - \tilde{\epsilon}_1(\tilde{\epsilon}_2 - \tilde{\epsilon}_1\sin^2\Theta) + (\tilde{\epsilon}_2 - \tilde{\epsilon}_1)\tilde{n}_{11}\tilde{n}_{22}}{\tilde{\epsilon}_2\tilde{\epsilon}_1(1 - \sin^2\Theta) - \tilde{\epsilon}_1(\tilde{\epsilon}_2 - \tilde{\epsilon}_1\sin^2\Theta) - (\tilde{\epsilon}_2 - \tilde{\epsilon}_1)\tilde{n}_{11}\tilde{n}_{22}} \\ &= \frac{-\tilde{\epsilon}_1(\tilde{\epsilon}_2 - \tilde{\epsilon}_1)\sin^2\Theta + (\tilde{\epsilon}_2 - \tilde{\epsilon}_1)\tilde{n}_{11}\tilde{n}_{22}}{-\tilde{\epsilon}_1(\tilde{\epsilon}_2 - \tilde{\epsilon}_1)\sin^2\Theta - (\tilde{\epsilon}_2 - \tilde{\epsilon}_1)\tilde{n}_{11}\tilde{n}_{22}} \\ &= \frac{\tilde{\epsilon}_1\sin^2\Theta - \tilde{n}_{11}\tilde{n}_{22}}{\tilde{\epsilon}_1\sin^2\Theta + \tilde{n}_{11}\tilde{n}_{22}}\end{aligned} \tag{17.13}$$

Reversing the introduced abbreviations, we find

$$\rho = \frac{\tilde{\epsilon}_1\sin^2\Theta - \tilde{n}_1\cos\Theta\left(\tilde{\epsilon}_2 - \tilde{\epsilon}_1\sin^2\Theta\right)^{1/2}}{\tilde{\epsilon}_1\sin^2\Theta + \tilde{n}_1\cos\Theta\left(\tilde{\epsilon}_2 - \tilde{\epsilon}_1\sin^2\Theta\right)^{1/2}},$$

and assuming $\tilde{\epsilon}_1 = \tilde{n}_1 = 1$ we get

$$\rho = \frac{\sin^2\Theta - \cos\Theta\sqrt{\tilde{\epsilon}_2 - \sin^2\Theta}}{\sin^2\Theta + \cos\Theta\sqrt{\tilde{\epsilon}_2 - \sin^2\Theta}},$$

In order to get the unknown relative permittivity, i.e. dielectric function $\tilde{\epsilon}_2$, we have to multiply last equation by the denominator, getting

$$\rho\left(\sin^2\Theta+\cos\Theta\sqrt{\tilde{\epsilon}_2-\sin^2\Theta}\right)=\sin^2\Theta-\cos\Theta\sqrt{\tilde{\epsilon}_2-\sin^2\Theta},$$

$$\rho\cos\Theta\sqrt{\tilde{\epsilon}_2-\sin^2\Theta}+\cos\Theta\sqrt{\tilde{\epsilon}_2-\sin^2\Theta}=\sin^2\Theta-\rho\sin^2\Theta$$

$$(1+\rho)\cos\Theta\sqrt{\tilde{\epsilon}_2-\sin^2\Theta}=(1-\rho)\sin^2\Theta$$

$$\sqrt{\tilde{\epsilon}_2-\sin^2\Theta}=\frac{(1-\rho)}{(1+\rho)}\sin\Theta\tan\Theta$$

$$\tilde{\epsilon}_2-\sin^2\Theta=\left(\frac{1-\rho}{1+\rho}\right)^2\sin^2\Theta\tan^2\Theta.$$

Rearranging last equation to $\tilde{\epsilon}_2$, and using the measured ellipsometric parameters Δ and Ψ at a known angle of incidence Θ, one can calculates the complex ratio ρ, and in consequence, the dielectric function

Dielectric function of an effective medium

$$\tilde{\epsilon}_2=\sin^2\Theta\left(1+\left(\frac{1-\rho}{1+\rho}\right)^2\tan^2\Theta\right). \tag{17.14}$$

This dielectric function resembles the averaged optical properties of the complete interaction volume (of the probe radiation), and is referred to as the **effective medium**.

The complex refractive index $\tilde{n}_2$ of the sample material can now be determined, assuming again a relative permeability being unity $\mu_{r1}=\mu_{r2}=1$ for all boundaries, getting

$$\tilde{n}_2=\sqrt{\tilde{\epsilon}_2}=n_2-i\kappa_2,$$

where n_2 represents the refractive index and κ_2 the extinction coefficient [4, 5].

17.5 Reflection at Many Interfaces for Thin Layers

If a transparent thin layer of thickness d is given on a substrate, the incident radiation will be reflected and transmitted multiple times at the interfaces between the medium 0 (environment) and the medium 1 (the layer), as well the medium 1 (layer) and medium 2 (substrate). The interfaces are assumed to be parallel to each other, as shown in Fig. 17.6.

The superposition of all partially reflected radiation then results in a total reflected one. The reflection coefficients r^{p} and r^{s} at each boundary layer are now calculated, as in the case of only reflections at one boundary, according to (7.23) and (7.25). When passing through the layer with the complex refractive index $\tilde{n}_1$, the radiation gets a phase change β, given by

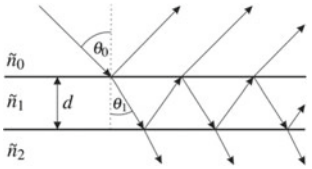

Fig. 17.6 Reflection and transmission of incident radiation in a single-layer model; the Superposition of all reflected partial beams results in the total reflected radiation

$$\beta = 2\pi\tilde{n}_1 \frac{d}{\lambda} \cos \Theta_0$$
$$\beta(d, \lambda, \Theta_0) = 2\pi 1 \frac{d}{\lambda} \sqrt{\tilde{n}_1^2 - \tilde{n}_0^2 \sin^2 \Theta_0}, \tag{17.15}$$

with the angle of refraction Θ_1, which is calculated using Snell's law of refraction, the refractive index $\tilde{n}_1$, the layer thickness d of the thin layer, and the vacuum wavelength λ of the radiation.

To describe the resulting reflected radiation, the phase β is included in the Fresnel coefficients by multiplying a phase $\exp(-i\beta)$ [4, 5, 7], and getting an infinite geometric series, the reflection coefficients r^{p} and r^{s} are computed

$$r^{\mathrm{p}} = \frac{r_{01}^{\mathrm{p}} + r_{12}^{\mathrm{p}} e^{-2i\beta}}{1 + r_{01}^{\mathrm{p}} r_{12}^{\mathrm{p}} e^{-2i\beta}} \tag{17.16}$$

$$r^{\mathrm{s}} = \frac{r_{01}^{\mathrm{s}} + r_{12}^{\mathrm{s}} e^{-2i\beta}}{1 + r_{01}^{\mathrm{s}} r_{12}^{\mathrm{s}} e^{-2i\beta}}. \tag{17.17}$$

The complex ratio ρ is then determined by

$$\rho = \frac{r_{01}^{\mathrm{p}} + r_{12}^{\mathrm{p}} e^{-2i\beta}}{1 + r_{01}^{\mathrm{p}} r_{12}^{\mathrm{p}} e^{-2i\beta}} \frac{1 + r_{01}^{\mathrm{s}} r_{12}^{\mathrm{s}} e^{-2i\beta}}{r_{01}^{\mathrm{s}} + r_{12}^{\mathrm{s}} e^{-2i\beta}}. \tag{17.18}$$

Using (17.3), Δ, and Ψ result from ρ, which in turn is calculated using (17.15) and (17.18), depending on the vacuum wavelength λ of the incident laser radiation, the angle of incidence Θ_0 of the incident radiation, the complex refractive indices of the ambient medium $\tilde{n}_0$ and the substrate $\tilde{n}_2$, and the layer thickness d and the complex refractive index $\tilde{n}_1$ of the layer.

The wavelength λ and the angle of incidence Θ of the incident laser radiation, the complex refractive indices of ambient medium $\tilde{n}_0$ and substrate $\tilde{n}_2$ are known, and the ellipsometric parameters Δ and Ψ are determined by a measurement. The layer thickness d and the complex refractive index $\tilde{n}_1$ of the layer are unknown. The calculation of the thickness and the complex refractive index of the layer with the measured ellipsometric parameters Δ and Ψ generally provide several solutions for d and $\tilde{n}_1$, since for the phase terms of the reflection coefficients in (17.16) and (17.17), we have the ambiguity

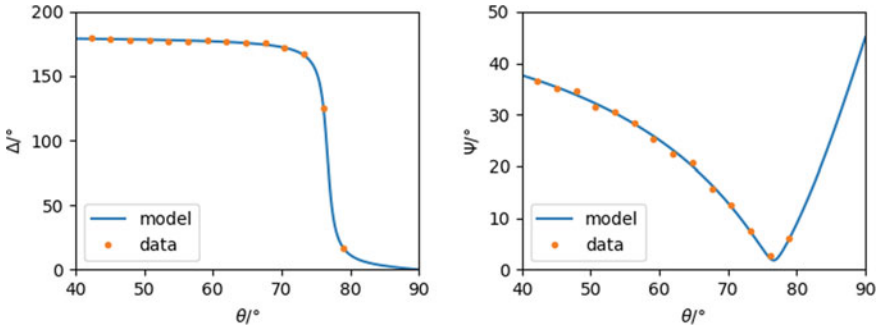

Fig. 17.7 Example of model and measurement data for Δ (left) and Ψ (right) in dependence from the angle of incidence Θ of the laser radiation

$$e^{-i2\beta} = e^{-i(2\beta+2\pi)}. \tag{17.19}$$

With a constant complex refractive index $\tilde{n}_1$, (17.15) and (17.19) get to the so-called period thickness equation d_P, with

$$d_P = d(\beta = \pi) = \frac{\lambda}{2\sqrt{\tilde{n}_1^2 - \tilde{n}_0^2 \sin^2 \Theta_0}}, \tag{17.20}$$

which is dependent on the angle of incidence Θ_0 and the wavelength λ of the laser radiation. To determine the layer thickness d and the complex refractive index $\tilde{n}_1$ explicitly, Δ and Ψ must be determined in dependence of different wavelengths λ, or angle of incidence Θ of the incident laser radiation.

To the obtained measurement data for Δ and Ψ, depending on the angle of incidence Θ or the wavelength λ of the laser radiation, a modeled dispersion curve of the ellipsometric parameters Δ and Ψ of the layer system as a function of angle of incidence Θ and wavelength λ of the laser radiation is mathematically approximated, see Fig. 17.7. The model is derived from the individual dispersion patterns of substrate, layer and ambient medium. The variable parameters of the approximation are the refractive index $\tilde{n}_1$ and the thickness d of the layer. The values of $\tilde{n}_1$ and d, fitting best the modeled dispersion of Δ and Ψ to the measurement data, are the searched values for the refractive index $\tilde{n}_1$ and the thickness d of the layer [4, 5, 7].

17.6 Layer- and Dispersion-Models

A model is defined by a predetermined system of material layers. Depending on the number of layers, the propagation of the radiation through a substrate (no layer), single-layer or multi-layer has to be modeled. Each layer is described by its dielectric

function and thus dispersion relation. The individual dispersion curves of the ellipsometric parameters Δ and Ψ can be generally used in dielectrics, semiconductors and metals. In a substrate, Δ decreases between $0° < \Theta < 90°$ always from 180° to 0°. For a dielectric, this curve features a phase jump at the Brewster angle α_B, since Δ represents the phase difference between r^{p} and r^{s}, and $\Re(r^{\mathrm{p}})$ changes sign at the Brewster angle, see Fig. 7.3.

Since r^{p} is purely real in the dielectric, the phase jump is 180°. For semiconductors and metals, this drop of Δ from 180° to 0° is continuous, since both r^{p} and r^{s} are complex numbers. Ψ reaches a minimum at the Brewster angle, since the reflectance of parallel component of the electric field strength at the Brewster angle becomes minimal.

With dielectrics the minimum reaches the value $\Psi = 0°$. With increasing extinction factor κ of the material, the minimum of Ψ gets $\Psi > 0$, see Fig. 17.8. The curves of Δ and Ψ as a function of the wavelength Λ and the angle of incidence Θ are calculated either via measured dispersion curves, or calculation models such as Sellmeier, Lorentz, Cauchy, Drude, or Fresnel equations.

The finished layer model of the sample material is composed of individual models of respective materials for a substrate, any number of layers and the ambient medium together.

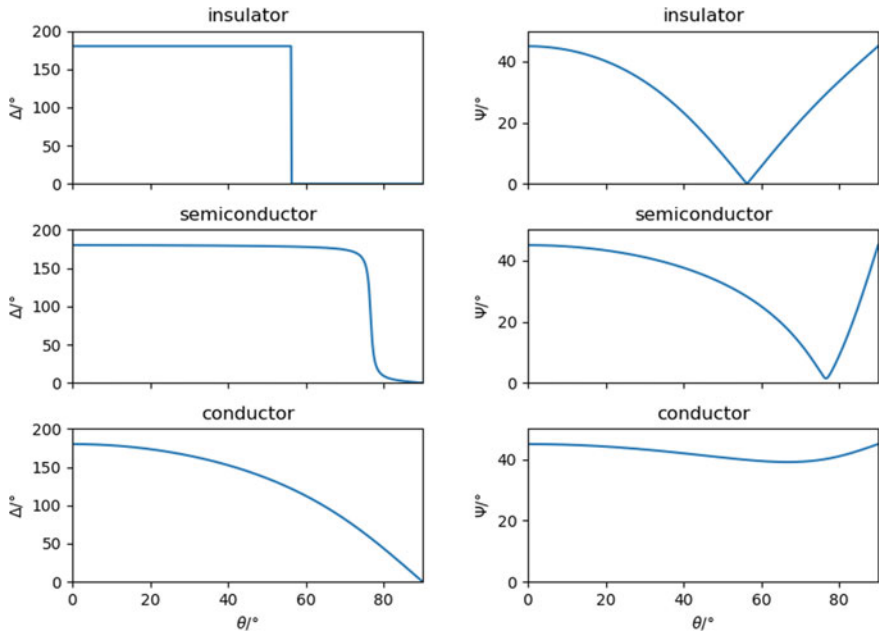

Fig. 17.8 Schematic description of the ellipsometry parameters Δ and Ψ for dielectrics, semiconductors, and metals as a function of of the angle of incidence Θ of the laser radiation at the wavelength $\lambda = 532\,\mathrm{nm}$

The resulting dispersion curves, and from there the ellipsometric parameters Δ and Ψ presented here, are calculated according to the Berreman algorithm [4], which is not discussed further in this book.

17.7 Imaging Ellipsometry

The presented ellipsometer setup usually is realized using laser radiation, and focusing the radiation to a very small spot on the surface, down to about a diameter of 50 μm. To get a spatial information, such as a topology of the optical properties of an investigated surface by ellipsometry, the relative position of the laser radiation has to be changed by moving the substrate to different locations. Doing so, a minimum spatial resolution of about the spot diameter of the focused radiation can be achieved. For each spot the data-acquisition for the rotating analyzer, or the compensator has to be accounted. To get a consistent map of the optical properties demands very long measuring times. An alternative to get with one measurement, all the spatial information of the surface is achieved by extending the ellipsometer with an imaging system.

17.7.1 Principle Set-Up

Imaging ellipsometry combines optical microscopy with ellipsometry for spatially-resolved layer-thickness and refractive index measurements of micro-structured thin-films and substrates. It is highly sensitive to single- and multi-layer ultra-thin films, ranging from mono-atomic or mono-molecular layers (sub-nm regime) up to thicknesses of several microns.

Additionally to the polarizing optics, i.e. polarizer, compensator and analysator, also imaging optics is needed to generate an image at the investigated surface of the incoming radiation, which is hereinafter imaged using microscope objectives and projectives onto a detector. As the complex refractive index depends on the wavelength, the radiation has to be monochromatic. Therefore, the radiation can be changed, e.g. using a white-light source coupled with a monochromator, or implementing different laser radiation. A commercial imaging ellipsometer featuring all this properties is given by the nanofilm EP4 from Accurion GmbH, see Fig. 17.9 [9].

Important for the set-up of an imaging ellipsometer is the optical high-quality of all optical elements. Especially the polarizing optics must feature a larger optical flatness and homogeneity. Also, in order to execute measurements at different wavelengths achromatic polarizing optics is necessary. Alternatively, this elements have to be changed at every wavelength variation.

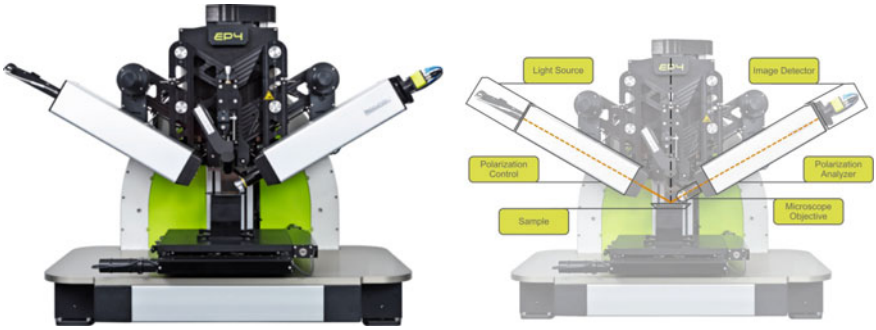

Fig. 17.9 Setup of a commercial imaging ellipsometer nanofilm EP4 from Accurion (left), and schematics of the optical elements (right) [9]

17.7.2 Spatial-Resolved Measurement

Imaging ellipsometry works in principle like the conventional elliposmetry, as shown in Sect. 17.3, where the compensator angle is varied determining the intensity of the reflected radiation. The difference is now that a complete image of the investigated surface is measured, and each pixel of the detector system, or bundles of pixels represent one measurement. Images at different compensator angels are determined, and shown in Fig. 17.10 for a transient laser-induced modification in PMMA.

For each pixel the approximation (17.4) is solved determining the Fourier coefficients α_F and β_F, see Fig. 17.11. Depending on the model used for the layer system, e.g. an effective medium, (17.14) or a distinct sequence of layers, the ellipsometric parameters, as well as the complex refractive index is determined, see Fig. 17.12.

Exemplary, the electrical properties of an organic material PEDOT:PSS have been modified without inducing any visual change of the topology using focused cw-laser radiation ($\lambda = 1064$ nm) [10]. A change in the ellipsometric parameter Δ is clearly detectable by imaging ellipsometry, see Fig. 17.13. The distances of the irradiated track have been varied demonstrating the spatial resolution of this method.

17.8 Space- and Time-Resolved Ellipsometry

Using pulsed laser radiation allows to get a temporal resolution of the investigated process, being about the pulse duration t_p of the used laser radiation. Today different ellipsometer manufacturer offer such systems with temporal resolutions into the microsecond time regime.[2] Here, an ultra-fast time-resolved, spectroscopic and imaging ellipsometer is presented.

[2] https://accurion.com/thin-film-characterization/products/nanofilm-ep4.

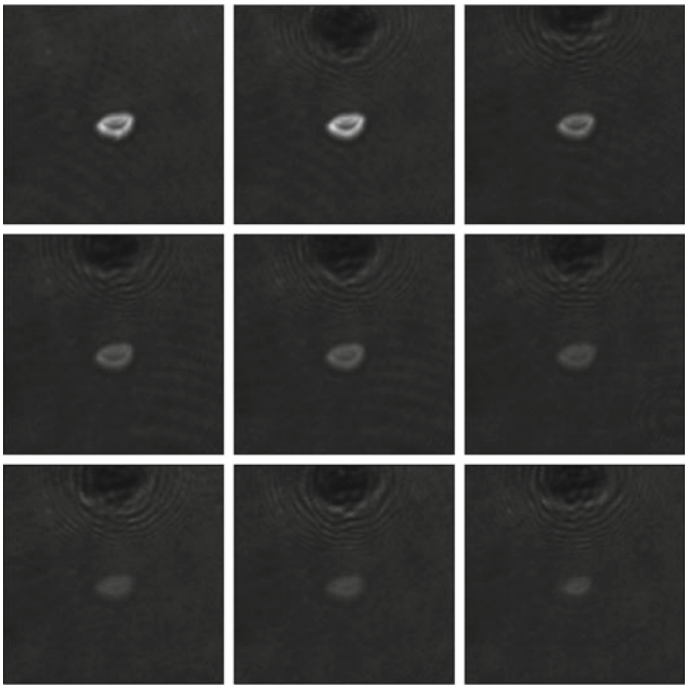

Fig. 17.10 Images taken at different compensator angels κ of a laser-induced transient modification on the surface of PMMA shown at the center of the images (Feature given at the up border represents the final structure)

17.8.1 Principle Set-Up

Combining the previously described imaging ellipsometer, see Sect. 17.7 with an ultra-fast laser source, enables a temporal resolution of about 50 fs. The set-up includes two **optical parametric amplifiers (OPA)** allowing to tune the wavelength from the UV into the mid-IR range, see Fig. 17.14. The principle function is described in Sect. 16.2, as also in this case the pump and probe techniques is adopted. Both path ways, the pump, as well the probe radiation are spectrally tunable. The radiation

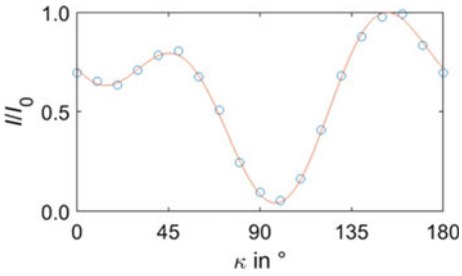

Fig. 17.11 Approximation function of one pixel of the images taken from the series in Fig. 17.10 and plotted as function of the compensator angle κ determining the Fourier coefficients α and β

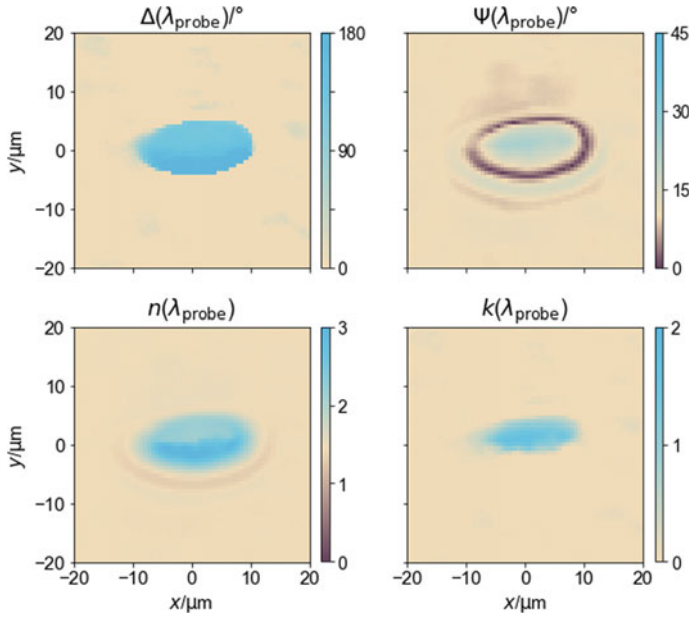

Fig. 17.12 Spatially-resolved ellipsometric parameters Δ and Ψ, as well complex refractive index $n - ik$ with the refractive index n and the extinction coefficient $k = -\kappa$ determined for each pixel of a transient laser-induced modification

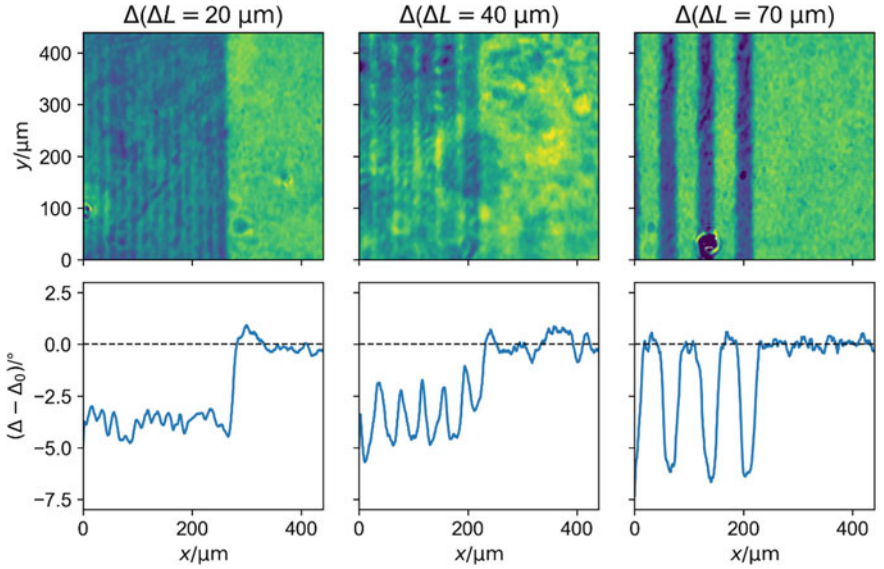

Fig. 17.13 Measured change in the ellipsometric parameter Δ of laser-modified PEDOT:PSS with the topology (top), and a cross-section (bottom) for different track distances [10]

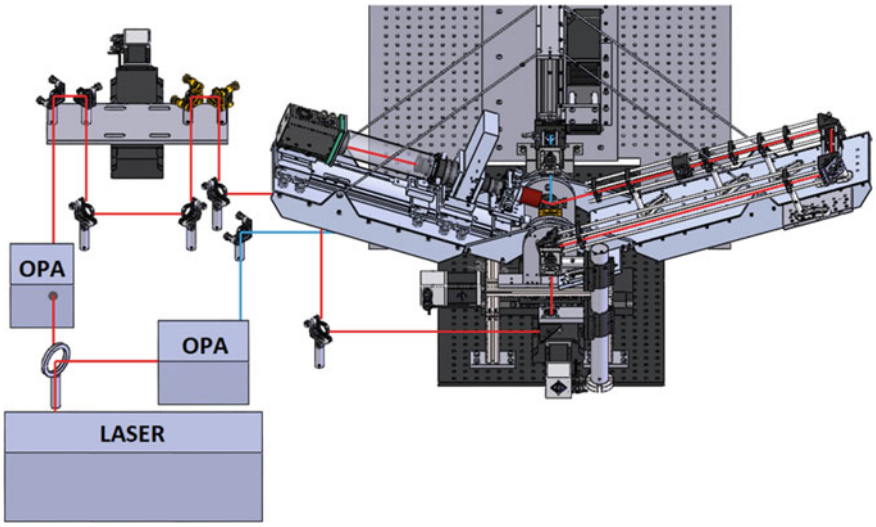

Fig. 17.14 Principle set-up of a temporal and spectral resolved imaging ellipsometer. Radiation of an ultra-fast laser source is converted for the pump as well for the probe radiation by an OPA in deliberate wavelengths. The pump radiation (red beam) is temporally delayed, and then coupled into the ellipsometer together with the probe radiation (blue beam)

of the pump is delayed by a **mechanical delay line** up to about 4 ns in respect to the probe radiation.

The **pump radiation** is directed perpendicular to the surface and focused either by a focusing lens or by reflective optics on the surface, see Fig. 17.15. This radiation induces a modification of the physical properties of the investigated matter.

The probe radiation is linearly polarized and rotated by polarizing tube (P) usually to $\varphi = 45°$, see Fig. 17.4. Using a telescope the probe radiation is imaged onto the surface, thereby illuminating possibly homogeneous, meaning that the intensity distribution on the CCD should be nearly constant on the complete CCD area. A part of the radiation is reflected specularly on the surface and collimated by a microscope objective (O), see Fig. 17.15. The collimation is important, as the polarizing optics in the following are very sensitive on deviations from parallel illumination. A band-pass filter (BPF) blocks diffusely reflected pump radiation and most of the optical emissions from the plasma, and a motorized rotating compensator (C) is varied in its rotation angle κ per image taken. The probe radiation passes an analyzer (A) and is imaged by a tube lens (T) onto the CCD chip (CCD).

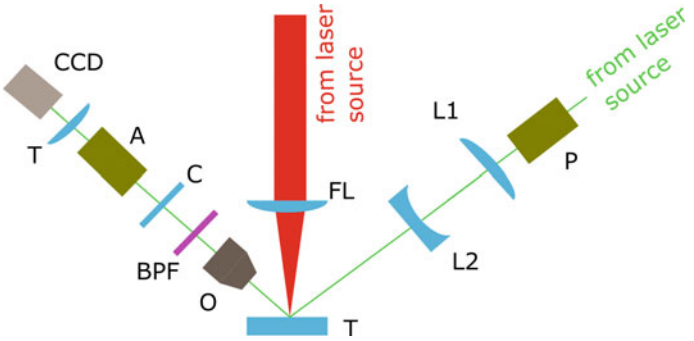

Fig. 17.15 Schematic set-up of the imaging ellipsometer used for time resolved investigations: pump radiation (red) is focused by a lens (FL) onto the target surface (T). The probe radiation (green) is prepared by a polarizing optics (p) and imaged on the surface of the target by the telescope optics (L1 and L2). The reflected radiation is collimated by the microscope objective (O), passes through the compensator (C), analysator and a tube lens and is finally imaged on a CCD

17.8.2 Examples

Irradiating thin gold films with ultra-fast laser radiation at $\lambda = 800$ nm and $t_p = 35$ fs can induce thermophysical modifications of the metal. Here in this example, the fluence was chose below the ablation threshold at $H = 0.5$ J cm^2, meaning that only melting is temporary induced.

The complex refractive index was determined using an effective medium, and plotting the cross-section of the refractive index n, the extinction coefficient κ, the components of the complex dielectric function as function of time, the dynamics of the excitation gets visible, see Fig. 17.16 [11].

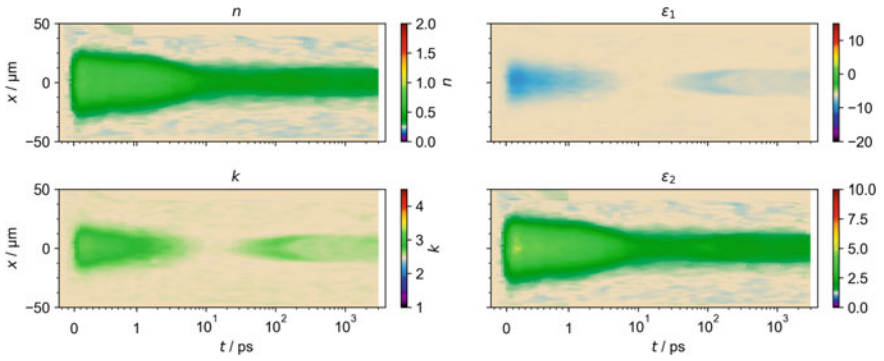

Fig. 17.16 Thin gold film excited by one ultra-fast laser pulse ($\lambda = 800$ nm, $t_p = 35$ fs, $H = 0.5$ J/cm^2). The complex refractive index $\tilde{n} = n + i\kappa$, as well complex dielectric function $\tilde{\epsilon} = \tilde{\epsilon}_1 + i\tilde{\epsilon}_2$ are determined and plotted its cross sections as function of time using the probe radiation at $\lambda = 550$ nm and $t_p \approx 50$ fs [11]

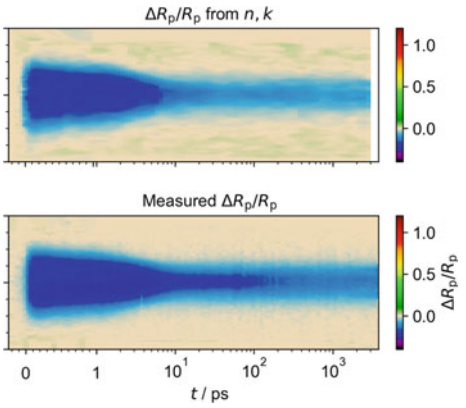

Fig. 17.17 Thin gold film excited by one ultra-fast laser pulse ($\lambda = 800$ nm, $t_p = 35$ fs, $H = 0.5$ J/cm^2). The relative reflectance change is determined by calculation using the measured complex refractive index from Fig. 17.16 (top), and by direct measurement using time resolved reflectometry, see Chap. 16 [11]

The relative reflectance change $\Delta R/R$ was determined, on the one hand measured directly as described in Chap. 16, and on the other hand, using the measured complex refractive index by ellipsometry, the evaluating the Fresnel equations calculating relative reflectance change, see Fig. 17.17. The comparison of the reflectance changes demonstrates that both methods agree very well.

Also, one accounts that more information can be extracted from the complex refractive index than from the relative reflectance measurements, as the refractive index n features no minimum, but the extinction coefficient does. The extinction coefficient κ expresses the amount of absorbed energy and correlates well with the dynamics of the electron system. The constriction of the width of the interaction zone thereby depicts the cooling of the electron system thermalizing at about 10 ps with the phonon system. The subsequent increase in the extinction coefficient for times larger than 10 ps can be attributed to the heating of the metal (phonon system), and changes in the topology by expansion of the surface.

References

1. T. Pflug, Untersuchungen zur ultraschnellen Ellipsometrie von Laserprozessen. Master thesis, University of Applied Sciences, Mittweida, 2017
2. T. Pflug, Strong field excitation of electrons into localized states of fused silica. Ph.D. thesis, Technische Universität Chemnitz, 2022
3. T. Pflug, J. Wang, M. Olbrich, M. Frank, A. Horn, Case study on the dynamics ultrafast laser heating and ablation of gold thin films by ultrafast pump-probe reflectometry and ellipsometry. Appl. Phys. A **124**(2), S.190 (2018) Laserprozessen
4. H. Fujiwara, *Spectroscopic Ellipsometry: Principles and Applications* (Wiley, Chichester, 2009)
5. C. Cobet, *Die dielektrische Funktion verschiedener SiC-Modifikationen im Spektralbereich von 1,5–30 eV* (Technische Universität Berlin, Berlin, 1999)
6. D. Meschede, *Optik, Licht und Laser* (Vieweg+Teubner Verlag / GWV Fachverlage GmbH Wiesbaden, Wiesbaden, 2008)

7. F.L. Pedrotti, L.S. Pedrotti, W. Bausch, H. Schmidt, *Optik für Ingenieure: Grundlagen* (Springer, Berlin, 2008)
8. S. Rapp, M. Kaiser, M. Schmidt, H.P. Huber, Opt. Express **24**, 17572 (2016)
9. https://accurion.com/
10. T. Pflug, A. Anand, S. Busse, M. Olbrich, U.S. Schubert, H. Hoppe, A. Horn, Spatial conductivity distribution in thin PEDOT:PSS films after laser microannealing. ACS Appl. Electron. Mater. **3**(6), 2825–2831 (2021)
11. T. Pflug, J. Wang, M. Olbrich, M. Frank, A. Horn, Case study on the dynamics of ultrafast laser heating and ablation of gold thin films by ultrafast pump-probe reflectometry and ellipsometry. Appl. Phys. A **124**, 116 (2018)

Chapter 18
Nomarski Microscopy

Abstract The ability to detect changes in matter featuring no optical contrast by measuring changes in transmittivity is given using the coherence property or radiation. In this chapter Nomarski microscopy is presented, featuring a qualitative metrology tool to determine phase changes in matter. Coupled with pump and probe techniques, ultra-fast laser-induced modifications in the volume of dielectrics are described.

18.1 Principle of Nomarski Microscopy

Transmitted light Nomarski microscopy,[1] was developed about 40 years ago at the Carl Zeiss company as a microscopy method for observing organic substances. Biological objects are called **phase objects**, because of the different refractive indices of cellular components, such as the nucleus, mitochondria, and cell wall, causing a phase change in the electromagnetic radiation used for illumination, but featuring negligible absorption. Normal light transmitting microscopy methods without staining agents fail for transparent objects with small contrast, e.g. dielectrics.

Nomarski microscopy uses optically broadband radiation, e.g. radiation of a halogen lamp. The radiation is linearly polarized by a polarization filter, separated in a compensator given by a Wollaston prism into two beams, which are perpendicular polarized to each other and spatially displaced, see Fig. 18.1. This offset of the beams represents only a few micrometer. Afterwards, the two beams are collimated by a condenser, undergo a phase shift in the substrate containing phase-changing elements, and are reunited with the objective and an adjustable Wollaston prism. Due to the spatial offset, the beams of linearly polarized radiation experience a different phase change at different locations. The bundles interfere not before they are reunited, because the polarization orientations of the two beams at the substrate location is orthogonal oriented, not allowing any interference. In order interference takes place, the spatial offset of the beams must not exceed the coherence length of the

[1] Also called DIC microscopy: differential interference contrast.

© Springer Nature Switzerland AG 2022

A. Horn, *The Physics of Laser Radiation–Matter Interaction*,
https://doi.org/10.1007/978-3-031-15862-9_18

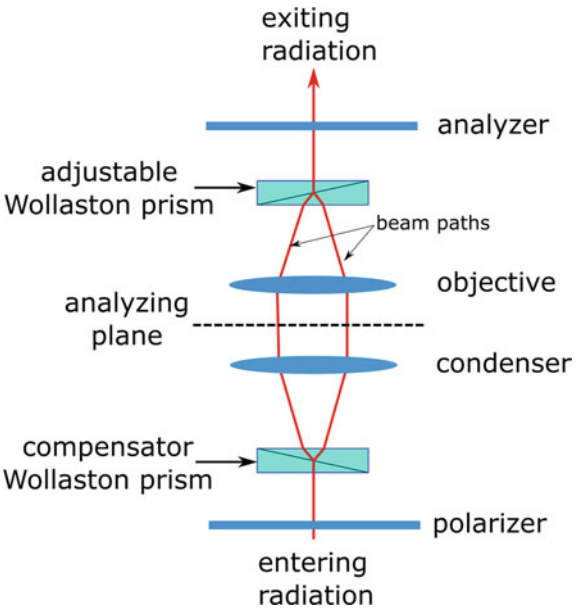

Fig. 18.1 Schematic description of the Nomarski microscope

used radiation. For this reason, the maximum offset is approximately as large as the coherence length of the radiation used.

In order for the extent of the contrast change in the image to remain close to the resolution limit of a microscope (approximately equal to the wavelength used), the coherence length must not be significantly greater than the wavelength. Therefore, a broadband light source is used for Nomarski microscopy, since, for example, thermally generated optical radiation has a spatial coherence length of a few micrometer. A step-wise change of the refractive index in one spatial dimension in the substrate results in a localized increase and decrease of intensity in the Nomarski image, according to the derivative of the refractive index, see Fig. 18.2. Changes of refractive index in phase objects are reproduced by Nomarski microscopy by an increased contrast in the image.

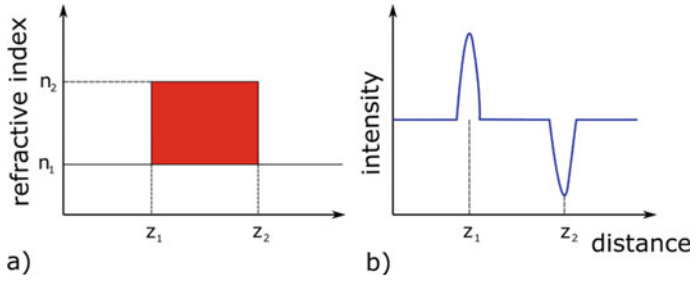

Fig. 18.2 Principle of Nomarski-Microscopy: **a** region with a change in refractive index, and **b** Nomarski image

18.2 Time-Resolved Nomarski Microscopy

The time-resolved Nomarski microscopy is an indirect measurement method and uses pulsed laser radiation, see setup-description in Fig. 18.3. By using ultra-fast laser radiation with a pulse duration in the femtosecond range, a white-light continuum is generated by self-phase modulation, see Sect. 8.4.7, which represents a spectrally broadened radiation with small pulse duration ($t_{p,WLC} \leq 3.5$ ps). Because of the small pulse duration of the individual spectral components of the white-light continuum ($t_p \leq 100$ fs), the coherence length $l_{coh} \approx 30$ µm, and is of the same order of magnitude as the non-coherent light sources used in conventional Nomarski microscopy. The white light continuum features a linear polarization, as the initial laser radiation. For the detection of a Nomarski image, a color-CCD camera with a large number of pixels is used (Arc4000c, Baumer Optronic, 1300 × 1000 pixels^2). By CCD photography, spectral changes of the white-light continuum, which are caused by interference or stimulated amplification, can be observed [1].

The filaments in the generated white-light continuum are detected by CCD photography as spot patterns, see exemplary Fig. 12.13 in Sect. 12.6.2. These images are difficult to analyze, because of the chaotically changing position of the filaments per pulse. For this reason, the Nomarski images are post-processed with a high-pass filter (analysis radius 5 pixels, see Fig. 12.14). This image processing homogenizes the image background, making the background more uniform. Unfortunately, by this

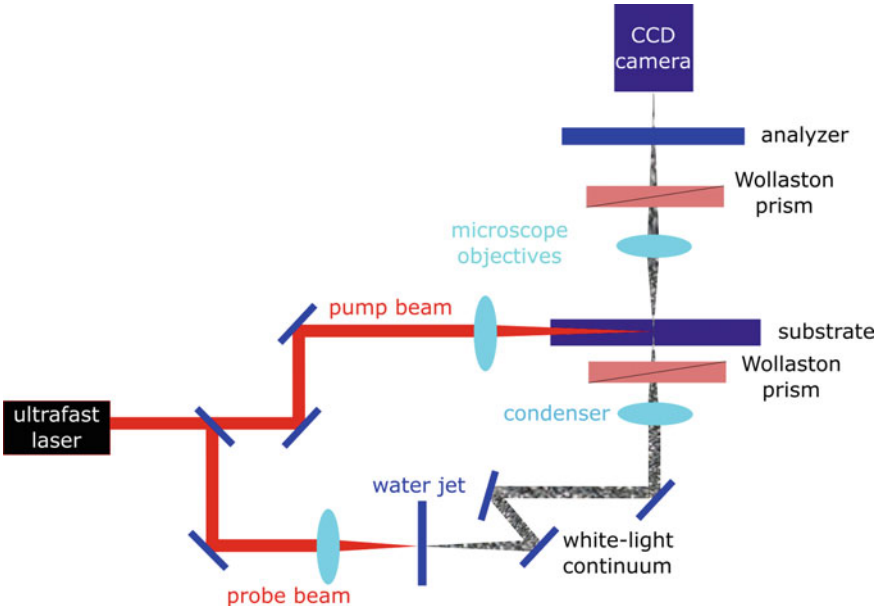

Fig. 18.3 Schematic description of the time-resolved Nomarski microscopy

Fig. 18.4 Temporal dynamics of BK7 glass excited by ultra-fast laser radiation and detected by time-resolved Nomarski microscopy ($\lambda = 810$ nm, $t_p = 3$ ps, $I = 241$ TW/cm^2)

filtering the detection of transmission changes in the image is suppressed. Nomarski photography is generally not suitable for the observation of absorption processes, since phase changes are represented as high-contrast brightness jumps. Nevertheless, strong absorption can be observed at large excitation intensities during the first 100 ps, given in the example of Fig. 12.13.

18.3 Examples

Exciting different dielectrics, like glasses or crystals, being transparent for the radiation at small intensities, results by excitation with ultra-fast laser radiation in nonlinear absorption, generation of quasi-free electrons, refractive index change, filamentation and formation of mechanical stress, see Fig. 12.14. Last one is visualized by Nomarski microscopy very well, see Fig. 18.4. The strong laser-induced heating of the glass induces an intense, but very short expansion of the interaction volume, inducing a sound wave, when the rupture of the material by cracking starts. The semi-spherical sound wave features a geometry being as long as the heated interaction volume, and being spherically formed into the direction to the laser source. Detecting the position of the sound wave as function of the delay time enables to determine the propagation velocity of the sound wave, e.g. for laser-excited BK7 glass using picosecond laser radiation, a sound velocity of about 4 km/s is detected [1].

Reference

1. A. Horn, Zeitaufgelöste Analyse der Wechselwirkung von ultrakurz gepulster Laserstrahlung mit Dielektrika. Ph.D. Thesis RWTH Aachen, 2003, ISBN 3-8322-2068-2

Chapter 19
White-Light Interferometry

Abstract In this section a brief introduction into the principles of interferometry are given. The focus of this section is then moved to specific processes observed with ultra-fast laser radiation in combination with the coherence properties of this radiation. Optical interferometry is a well renowned technique to determine differences in optical thickness and thus refractive index. Phase detection by phase-contrast or monochromatic interferometry with ultra-fast laser radiation is sporadically used in research. For time-resolved applications it has many shortcomings, such as failing in the distinct determination of optical path differences larger than $\lambda/2$. White-light interferometry uses spectral broad illumination that offers unambiguous interference patterns.

19.1 Principle of Mach-Zehnder Interferometry

The Mach-Zehnder interferometer is a further development of the Jamin interferometer firstly developed in 1892. The principle of this interferometer is the "round the square" system, see Fig. 19.1 [1]. The radiation from the source (L) is divided by the beam splitter (T1) in two separated beams, each reflected by the mirrors S1 and S2 and re-combined by the second beam splitter (T2). Thereby the radiation of both beams can interfere.

One beam represents the measurement beam, and the other represents the reference beam. The separation length of the two beams is predefined and is an advantage compared to the spatially limited Jamin interferometer.

19.2 White-Light Interferometry

Optical interferometry is a well renowned technique to determine differences in optical thickness and thus refractive index. Phase detection by phase contrast or monochromatic interferometry with ultra short laser pulses is sporadically used in research. For time-resolved applications it has many shortcomings such as failing

© Springer Nature Switzerland AG 2022

A. Horn, *The Physics of Laser Radiation–Matter Interaction*,
https://doi.org/10.1007/978-3-031-15862-9_19

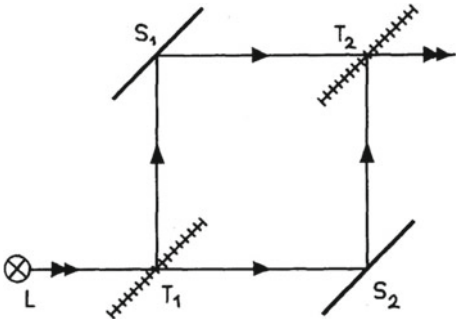

Fig. 19.1 Principle of a Mach-Zehnder interferometer

in the distinct determination of optical path differences larger than $\lambda/2$. White-light interferometry uses broad spectrum illumination that offers unambiguous interference patterns. A commercially available micro-interferometer based on the Horn-design was built in 1960 by Leitz, see Fig. 19.2, but has not been developed further for time-resolved applications.

Interferometry using poly-chromatic radiation features fringes in the interferometer being colored, see also Fig. 19.5. The measurement of the optical retardation is achieved by measuring the displacement of the fringes at each color (or using monochromatic radiation). The optical retardation is thereby calculated by

$$\Gamma_{\text{opt}} = (n_0 - n_{\text{m}})d$$

with n_0 the refractive index of the object, n_{m} the refractive index of the surrounding medium, and d the thickness of the object. With given distance between neighbor fringes z, the value of the fringe displacement y and the wavelength λ, see Fig. 19.2

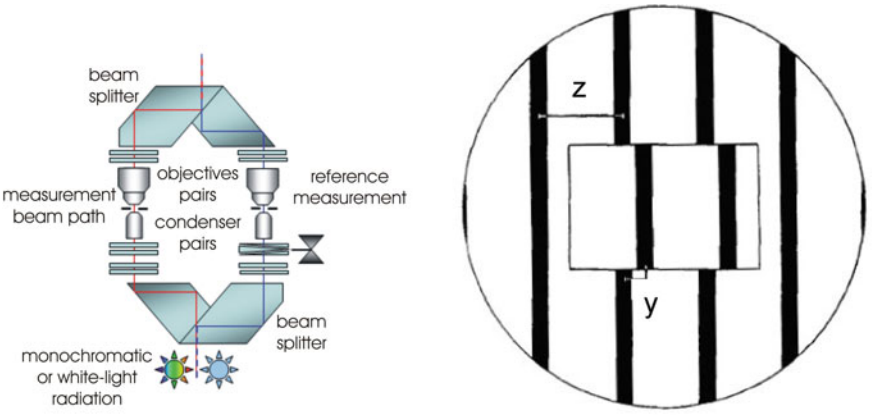

Fig. 19.2 Principle of the Leitz interferometer (left) and reconstruction of the fringe displacement (right)

right, the refractive index of an object can be calculated using the last equation with

$$\Gamma_{\text{opt}} = \frac{\lambda y}{z}.$$

The width of the fringes depends on the interpenetration angle between the beams of the two arms of the interferometer. At an interpenetration angle of 0°, the object is detected with a homogeneous background.

An optical retardation induced by a phase object is now detected using polychromatic radiation, allowing to distinguish different colors.

19.3 Pump-Probe White-Light Interferometry

In order to gain the ability to conduct interferometric pump-probe analysis, a Mach-Zehnder interferometer set-up is conceived, see Fig. 19.3. Like with any amplitude-splitting interferometer, large spatial separations between the interferometer arms are achievable, and offers enough space to shape and guide the interferometer beam paths to fit the demands of different pump-probe set-ups. A beam-splitter (BS 1) is used to divide the amplitude of a laser radiation into an observation and a reference beam. One beam acts as a reference, while the other passes through the object of interest, where its phase gets shifted according to the sample's diffractive and refractive properties.

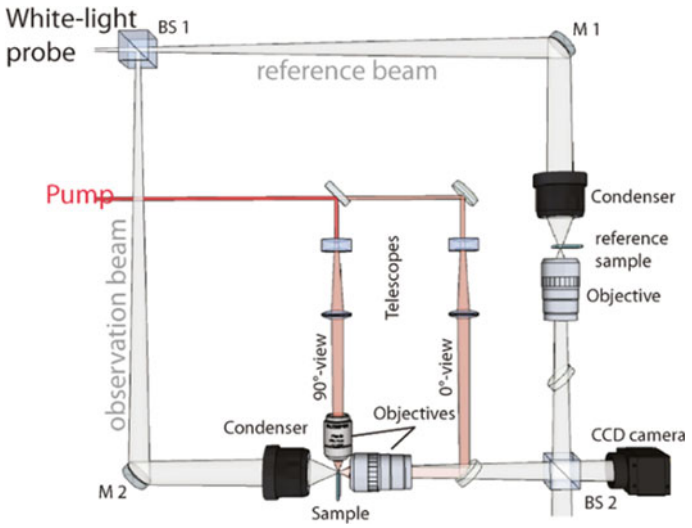

Fig. 19.3 Pump-probe ultra-fast white-light interference microscopy set-up. Two approaches for pumping are given in red, one by coaxial, the other by orthogonal pumping [1]

In order to visualize the phase change as an interferogram, the two beams have to be precisely superimposed and realigned via another beam-splitter (BS 2), and detected by a color CCD camera. A small and controlled misalignment of one arm, using one mirror (M 2), leads to an easily interpretable pattern of intensity fringes. In the undisturbed case, meaning reference and probe beam do not undergo any phase alteration while being split apart, the intensity fringes will be evenly spaced and parallel, as seen in Fig. 19.5 left.

The difference between ordinary Mach-Zehnder interferometry and a Mach-Zehnder interference microscopy basically is that the beam path includes two sets of microscope imaging systems, each consisting of a condenser and an objective, one for the reference and one for the observation arm, see Fig. 19.3. Mach-Zehnder interference microscopy requires two sets of microscope objectives and condensers that are matched as good as possible in terms of phase-distortion.

Here two alignments between the pump and the probe beam are accessible, coaxial with an observation angle of $\alpha = 0°$, and lateral alignment with an observation angle of $\alpha = 90°$ respectively. Coaxial alignment is realized via the interferometer objective as pump and probe objective at the same time and lateral alignment by using an additional objective for pumping. In order to take advantage of the benefits of both, white-light interferometry and time-resolved pump-probe measurements, a suitable super-continuum source (SC) is used, see next section.

19.4 Super-Continuum Source

Pump-probe experiments in the femtosecond regime require temporally constrained probe pulses in order to capture any dynamics on an image. To observe ultra-fast laser-induced phenomena via white-light interferometry, a broadband light source is needed that emits radiation with short pulses ($t_p \ll 1$ ns) at an intensity large enough to sufficiently expose a CCD camera chip. Focusing femtosecond laser radiation in dielectrics generates a white-light continuum, i.e. a super-continuum, possessing a high degree of spatial coherence.

In order to get a bright ultra-fast white-light source, femtosecond laser radiation is directed through an array of 127 hexagonally shaped converging micro lenses, $f = 18$ mm, $NA \approx 0.008$, forming an array of focuses accordingly, see Fig. 19.4 [1]. When focused into a nonlinear medium, such as a sapphire rod, each of the focuses will lead to self-focusing, see Sect. 8.4.7, and cause filamentation with one filament only, and a super-continuum generation of its own, see Sect. 13.5.2. Since the pulse energy is split between all micro lenses, the respective pulse energy per focus is decreased accordingly, allowing a large spatial coherence.

The separated broadband emissions overlap at the exit of the sapphire cylinder, since the spatial separation of each filament is the same as the micro-lens pitch (300 μm). Using single-shot imaging results in sufficiently exposed interferograms, see Fig. 19.5 left. The pulse-to-pulse repeatability of the interference pattern indicates a large degree of spatial coherence, even though the micro-lens array and thus the

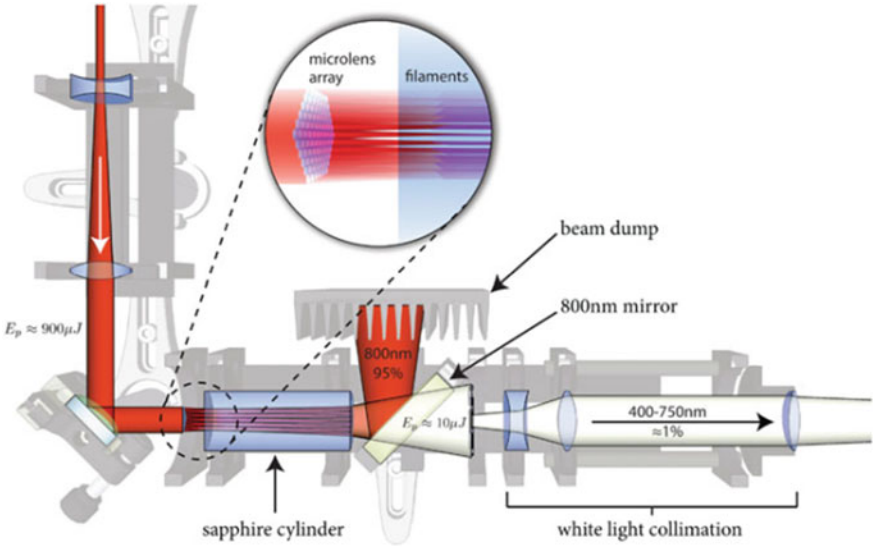

Fig. 19.4 Set-up for a high-brightness ultra-fast white-light/super-continuum generator using micro-lens array [1]

array of focuses is evenly spread over several millimeters. Cross-correlation is used to determine the pulse duration of the white-light generated by the SC source. The total pulse duration of the broadband emission is determined to approximately 10 ps for the used 50 mm long sapphire cylinder.

Fig. 19.5 Straight vertical fringes have been adjusted (left). In this case the optical path difference (OPD) is zero at the center maximum, white light is observed. In case a phase change is give, the fringes get curved (right)

19.5 Interferogram Analysis

Interferograms are images that contain intensity distributions (fringes) due to constructive and destructive interference. The fringe pattern represents the phase difference distribution of the probe and reference arm to analyze the **degree and spatial distribution of the phase change**. A common procedure is the phase-shifting algorithm. Thereby four interferograms are captured sequentially in time at a path length difference of $\lambda/4$ and allows for the unambiguous relative phase determination of each pixel.

Single interferograms cannot be analyzed by this technique. In case of a pump-probe interferometry, only one interferogram can be obtained at a time, since it is not possible to readjust the set-up before the affected area has changed its appearance and phase properties. When limited to one interferogram, the phase information has to be determined by the fringe-position and -shape. A 2D Fourier-transform approach cannot be used to reconstruct the phase in this case, because it is only applicable for radiation with large coherence lengths since a large number of fringe orders is needed for the evaluation. Two approaches are discussed in the following:

The first approach is a method to calculate **quantitative phase changes** from interferograms, given by **measuring the fringe displacements**. The procedure can be been implemented into a MATLAB® program for quick phase analysis of batches of interferograms. For all interference measurements, the interferometer is set up to produce measurably equidistant and straight fringes before any measurement, see Fig. 19.5, left. This fringe configuration then represents a homogeneous optical path length distribution. Any modification of the refractive index (Δn) with thickness d along the beam path then varies the optical path length

$$\mathrm{OPL} = n \cdot d = \int n(s)ds$$

accordingly. This gives the optical path difference

$$\begin{aligned} \mathrm{OPD} &= \mathrm{OPL}_2 - \mathrm{OPL}_1 \\ &= \Delta n \cdot d \\ &= \int \Delta n(s)ds. \end{aligned}$$

As a result, the fringe pattern, or interference order at the position x will resemble the original pattern at $x+$ OPD, see Fig. 19.5 right. The fringe elongation x is defined as the perpendicular distance of a fringe segment of an interferogram to the respective fringe segment of the undisturbed case, where OPD $= 0$ across the image, see Fig. 19.5 right. The undisturbed fringe can be derived from the interferogram itself. Since the interferometer is aligned to produce straight fringes, and any modifications causing an OPD are limited to the inner part of the interferograms, a linear interpo-

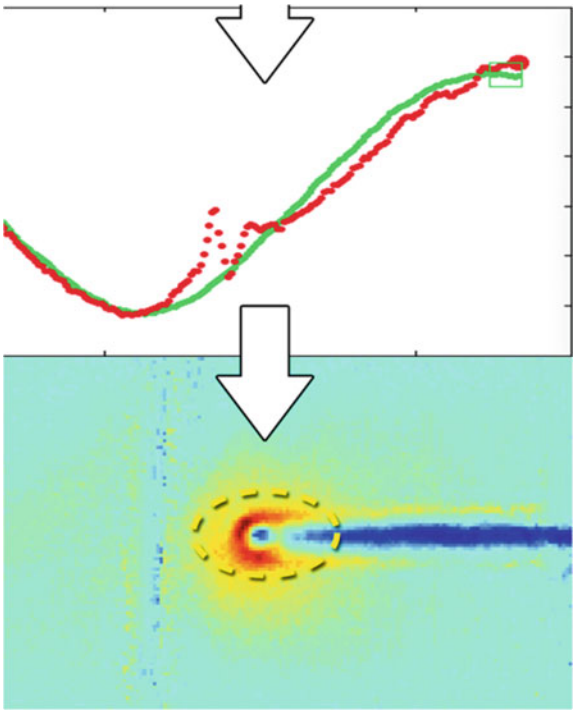

Fig. 19.6 Intensity distribution of interferogram and undisturbed image (top). Final image after pixelwise phase algorithm (bottom)

lation between the top and bottom pixels generates the undisturbed baseline for this fringe. For every fringe this method provides displacement values along its path.

A second approach to determine the phase change is to compare each row of pixels of the interferogram with the analog row of a generated undisturbed image. For example two comparative rows of an interferogram are evaluated resulting in intensity distribution with a red line representing the measurement interferogram and a green line representing the respective undisturbed image, see Fig. 19.6 top. The algorithm compares the intensity values of both rows. The gradient of the intensity of the surrounding points is evaluated in order to calculate possible fringe elongations via intensity comparison throughout the row resulting in a final image, see Fig. 19.6 bottom.

19.6 Examples

A coaxial pump alignment is used to induce melt-tracks in BK7 glass using high-repetitive ultra-fast laser radiation with the sample being moved perpendicularly through the focus area, see Fig. 19.6 bottom. As pump laser radiation an ultra-

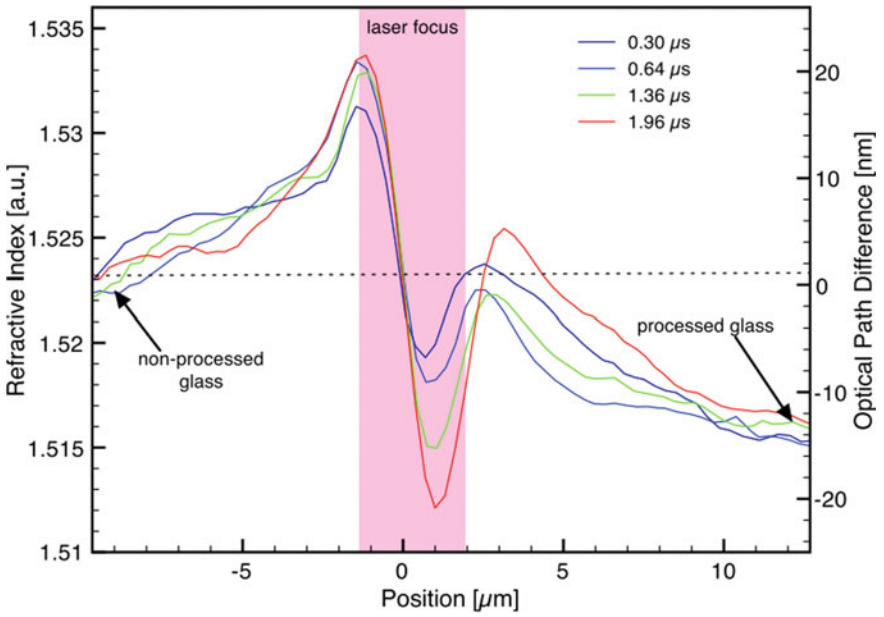

Fig. 19.7 BK7 glass heated and melted using ultra-fast laser radiation. Transient spatially-resolved refractive index and OPD changes co-axially detected along a melt track for different delay times τ, see also Fig. 19.6 bottom

fast laser source was used (IMRA FCPA µ-Jewel D-1000) with a pulse duration $t_p = 500$ fs and a spectral bandwidth of $\Delta\lambda \approx 2$ nm. The repetition rate of the radiation was adjusted to $f_p = 200$ kHz, the translation speed to $v = 26$ µm/s, and the average output power to $P_{av} = 135$ mW. To investigate the temporal changes of the OPD, interferograms were taken at four delays τ with all laser parameters kept constant, see Fig. 19.7. The highlighted area at position $x = 0$ indicates the effective interaction area of the laser focus. The decrease of the OPD and the refractive index there can be attributed to the generation of free electrons by non-linear excitation of the glass. Right of the focus area a region with an relatively increased OPD is detected. The increase is caused by compressed and molten glass, which was heated after electronic relaxation. Further to the right the OPD decreases for all delays until reaching a constant level, which indicates that heat has dissipated. The unprocessed glass is optically thicker than the processed one, which causes a positive OPD and a refractive index change. On the left border of the diagram the glass is not affected yet.

A plasma plume after single-pulse ablation of aluminum is detected using the lateral alignment for the pump source, see Fig. 19.3. Therefore, ultra-fast laser radiation (Thales CONCERTO) at $f_p = 1$ Hz, $\lambda = 800$ nm, and $E_p = 150$ µJ is focused on the metal surface using a 20× microscope objective (NA = 0.3). The phase distribution of an ablation plume is detected $\tau = 4.6$ ns after irradiation, revealing two

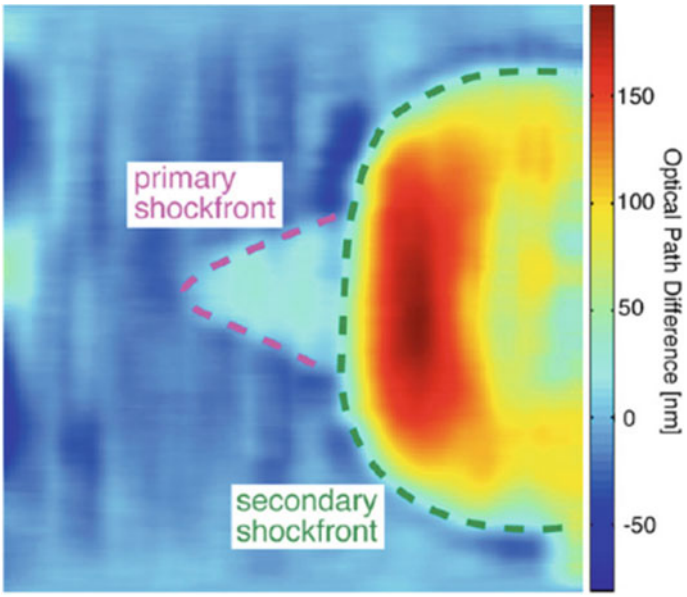

Fig. 19.8 Calculated phase distribution 4.6 ns after single-pulse ablation of aluminum ($f_p = 1$ Hz, $\lambda = 800$ nm, and $E_p = 150$ μJ)

shock fronts, one spherical formed given by the ablated material, Fig. 19.8. The second shock front results from the interaction of the ultra-fast laser radiation with the ambient air, changing by non-linear processes also the optical density.

19.7 Conclusion

Time-resolved Mach-Zehnder micro-interferometry has the advantage of using ultra-fast laser radiation to posses a larger spatial coherence and, by using a white-light continuum, to having unequivocal dependence on the measured phase, also for values $> \pi$. The temporal resolution should be about the pulse duration of the fundamental ultra-fast laser radiation, even when the spectral components are displaced by chirping. Also, used at the fundamental wavelength or SHG of the ultra-fast laser radiation, this pump and probe technique is a very precise tool for space and time-resolved phase measurements, without the drawback of the ambiguity of multiple-π phase values.

Reference

1. A. Horn, D. Wortmann, A. Brand, I. Mingareev, Development of a time-resolved white-light interference microscope for optical phase measurements during fs-laser material processing. Appl. Phys. A **101**, 231–235 (2010)

Bibliography

1. https://physics.stackexchange.com
2. X.Y. Wang, D.M. Riffe, Y. Lee, M.C. Downer, Time-resolved electron-temperature measurement in a highly excited gold target using femtosecond thermionic emission. Phys. Rev. B Condens. Matter **50**(11), 8016–8019 (1994)
3. A. Staudte, Subfemtosecond electron dynamics of H_2 in strong fields. Dissertation, Johann Wolfgang Goethe Universitaet, Frankfurt am Main, 2005
4. https://sl.wikipedia.org/wiki/Parametri%C4%8Dno_oja%C4%8Devanje#/media/Slika:Optical_parametric_oscillation.png
5. https://en.wikipedia.org/wiki/Two-photon_absorption#/media/File:Two_photons_excited_fluorescence_energy_levels.png
6. https://www.spektrum.de/lexikon/physik/above-threshold-ionisation/79
7. https://en.wikipedia.org/wiki/Phase_diagram

© Springer Nature Switzerland AG 2022

A. Horn, *The Physics of Laser Radiation–Matter Interaction*,
https://doi.org/10.1007/978-3-031-15862-9

Index

A
Ab-initio calculations, 258
Above-threshold ionization, 129
Absolute permittivity, 146
Absorption, 117, 277
  bound-free, 118
  coefficient, 246
  edges, 121
  free-free, 118
  linear, 144
  multi-photon, 116
  non-linear, 145
  resonant, 120
  resonant excitation, 114
  simultaneous, 116, 125
Accurion, 383
Acousto-optical
  modulators, 49
  programmable dispersive filter, 47
Acousto-Optical Modulators (AOM), 50
Adiabatic expansion, 346
Albert Einstein, 120
Alkaline
  earth metals, 262
  metal, 260, 327
Amorphous
  material, 273
  matter, 285
Ampère's circuital law, 10
Amplification
  parametric, 206
Angle
  deviation, 110
  scattering, 110
Angular
  frequency, 15
    effective, 218
  momentum
    quantized, 102
Anisotrope permittivity, 190
Anisotropic properties, 158
Anode, 65
  geometry, 65
Anomalous dispersion, 156
Anticipated wave, 164
Anti-Stokes scattering, 119
Atomic
  emission spectroscopy, 115
  number, 255
Attenuation coefficient, **135**
Avalanche ionization, 118, 299, 309, 311
Average
  avalanche coefficient, 309
  collision frequency, 292
  emitted power for oscillating charge, 64
  energy flux, 74
  power, 216

B
Backwards scattered radiation, 161
Ballistic electron, 118, 318
  mean free path length, 319
Band
  formation
    electronic, **255**
  gap, 257, 260, 266
    energy, 304
    energy effective, 304
    materials, 255
    wide, 281
  structure plot, 272, 283
  theory, 285
    crystals, 255

© Springer Nature Switzerland AG 2022

A. Horn, *The Physics of Laser Radiation–Matter Interaction*,
https://doi.org/10.1007/978-3-031-15862-9

Barn, 112
Berreman algorithm, 383
Bethe–Bloch equation, 67
Binding energy, 129
Binodal, 345, 351
  decomposition, 346
Birefringence, 158
Birefringent crystal, 47, 190, 202
BK7, 293
Black-body, 75
  hollow
    one-dimensional, 76
    three-dimensional, 79
  radiation, **75**
Bloch
  electrons, 270
  function, 270
Bohr's
  model, 102
  postulate, 102, 104
  radius, 103
  velocity, 103
Boltzmann constant, 76, 326
Born approximation
  non-relativistic, 122
Borosilicate glass, 293
Bose-Einstein
  distribution function, 79
  statistics, 79, 334
Boson, 9, 79, 327
Boundary, 167
  condition, 225, 337
    electromagnetic fields, 170
Bragg
  regime, 50
  relation, 270
Bremsstrahlung, 51, 65, 88
Brewster
  angle, 74, 176, **181**
Brillouin
  scattering, 120
  wave number vector, 270
  zone, 270
    first, 270
Brownian movement, 326

C
Capacitor, 20
Capacity, 145
Carl Zeiss, 391
Catastrophic self-focusing, 217
Cavitation
  bubbles, 350
  front, 352
Central
  frequency, 39
  wavelength, 39
Centrosymmetric force, 192
Channeling, **312**
Characteristic
  equation, 99
  length for electrons, 330
Charge density
  dipole, 70
  electron, 56
Chemical potential, 237
  for metals, 240
  metals, 241
  semiconductors, 243, 265
Chemical reaction, 52
Cherenkov radiation, 51
Chirp, 40
  positive, 41
Chirped Pulse Amplification (CPA), 209
Classical radius
  electron, 110
  hydrogen atom, 103
Clausius-Clapeyron equation, 344
Cluster
  atoms, 256
Co-existence regime, 347
Coherence, 37
  length, 202, 391
  spatial, 38
  temporal, 38
Coherent
  scattering, **136**
Coherent imaging
  Mach-Zehnder micro-interferometry
    characterization, 405
Cold electron, 240
Collision
  frequency
    electron-electron, 251
  time
    electron-electron, 251
Color-centers, 246
Complex
  optical transfer function, 44
  ratio, 372
  refractive index, 152
Compression wave, 353
Compton
  edge, 131
  scattering, **130**
    total cross section, 131
Condensation, 343
  temperature, 343
Condition of electrical neutrality, 267

Conduction band, **259**, 262, 272
Conductors, 260, 278
Conservation
  law for charges, 11
  momentum, 206
Continuity condition
  electric field, 168
  magnetic field, 168
Continuity equation, 11, 349
  electric and magnetic fields, 168
Continuum spectrum, 88
Copper, 260
  phthalocyanine, 158
  total cross section, 132
Corona
  underdense, 88
Coulomb force, 6, 20, 54
Critical
  angle for total reflection, **181**
  point, 344
  power self-focusing, 216
Cross-section, **109**
  differential, 110
  electron-electron scattering, 319
  ionization
    N-photon, 125
  overall, 135
  Thomson, 111, 113
  three-photon absorption, 308
  total, 111
    photo-effect, 121
  two-photon absorption, 307
Crown glass, 157
Crystal, 223
Crystal orientation, 158
Current density, 57
  time-dependent, 70
Cut-off frequency, 334
Cycle-averaged quiver energy, 122
Cylindrical symmetry, 337

D
d'Alembert
  equation, 19, 58
    generalized, 59
    inhomogeneous, 19
  operator, 19
Damping coefficient, 95, 96
  free electron, 97
  weakly-bounded electron, 106
Dawson integral, 126, 128, 304
de Broglie
  wave length, 9
Debye
  frequency, 334
  law, 335
  model, 335
  temperature, 335
Defects, 246, 289, 293
  electron, 267
  states, 296
Defocusing, 312
Degeneracy, 80
  energy, 227
Degenerated four-wave mixing, 212
Degeneration, 227
Delay line
  mechanical, 387
Delta distribution, 56–58
Densification wave, 353
Density
  tissues, 67
Density of states, **229**, 230, 234
  bottom band edge, 257
  top band edge, 257
De-phasing, 39, 115
  time, 39
DIC, 391
Dielectrics, 143, 260, 278
  excitation, **281**
  excited, 117, 292
  excited-state, 286
  function, 151, 157
    free electrons, 247
  non-magnetic, 177
  relaxation, 282
Difference-frequency mixing, 203
Differential
  area, 63
  cross section, 110
    coherent and incoherent scattering, 138
    many scatterer, 137
  interference contrast, 391
  power, 63, 74
    per solid angle, 74
Dipole
  classes, 147
  dielectric, 147
  directional radiation characteristics, 74
  dynamic, 147
  emission, 77
  far field, 72
  field, 72
  moment

electric, 70
induced, 149
static, 70
temporal-dependent, 70
time-dependent, 96
near field, 72
number density, 149
oscillating
total emitted averaged power, 74
radiation, 73
static, 147
Direct
electron transition, 289
recombination, 289
Directional dose rate, 88
Directional radiation characteristics
accelerated particle, 63
angular dependence, 63
dipole, 74
synchrotron, 68
Discrete wavelength, 225
Disordered matter, 273, 285
partially, 275
Dispersion
anomalous, 156
first-order, 45
group delay, 45
normal, 156
second-order, 45
third-order, 46
Dispersion relation, 152
electron, 226
electron plasma, 250
hollow body, 79
phonon, 334
radiation, 30
Displacement field, 149
Distribution
delta, 57
Distribution theory, 56
Dose
rates, 88
directional, 88
X-ray, 88
Double-pulses, 88
Drude–Lorentz model, 254
Drude model, 292
free electron gas, 247
Duane–Hunt law, 65
Dulong-Petit law, 326, 336

E
Effective
density of state, 238
electron mass, 273
medium, 379
Einstein
coefficient, 53
notation, 211
sum convention, 191
Elastic scattering, 143, 171, 246
electromagnetic radiation, 101
Electric
dipole, 75
time-dependent, 65
energy density
capacitor, 24
field strength
potentials, 18
flux, 148
polarizability, 108
polarization, 147
susceptibility, 147
Electric and magnetic fields
moved charged particle, 61
oscillating dipole, 70
Electromagnetic
energy density, 26, 31
field
inhomogeneous, 123
force, 5
radiation, 145
spectrum, 75
Electron
ballistic, 318
binding energy, 127
cold, 240
diffusion, 318
gas, **246**
photo-ejected, 120
plasma, 250
scattering
inelastic, 280
seed, 287
semiconductors, 264
system, 318
valence, 101
velocity
characteristic, 330
weakly-bounded, 101
Electron density, 233, 238
metal, 241
overall, 236
semiconductors, 266
semiconductors, 243
Electron dispersion relation, 226

Electronic
band formation, **255**
excitation energy, 245
Electron mass
effective, 273
thermal effective, 328
Electron-phonon
coupling
parameter, 332
time, 332
coupling factor, 325
relaxation time, 292
scattering, 282, 291
Electron radius
classical, 110
Electron scattering frequency, 332
Electrostatic
approach, 20
energy
capacitor, 23
Ellipsometric
equation, 373
parameters, 292, 376
Ellipsometry, **369**
imaging, 383
rotating-analyzer, 373
rotating-analyzer with compensator, 373
rotating-compensator, 373
spectroscopic, 158
Elliptical integral, 304
Ellipticity, 370, 373
Emission
gamma radiation, 52
spontaneous, 52, 53
stimulated, 52
x-rays, 87
Emissivity, 87
Emitted power
per solid angle, 100
bounded electron, 108
time-averaged, 97
Energy
bands, 256
conservation, 171, 206, 279
boundaries, 180
flux
averaged, 74
gap, 257
per mode, 79
photon, 78
splitting, 271
Energy bands, 257
Energy density
per mode, 78
spectral, 78, 81
Energy distribution
electron
semiconductor, 265
holes, 267
Energy levels, 255
discrete, 255
quantized, 102
quasi-continuum, 257
Energy transitions
continuous, 51
discrete, 51
Ensemble, 77
Enthalpy
condensation, 343
melting, 344, 347
specific, 326
vaporization, 343, 344, 347
Entry, 259
Equation of motion
bounded electron, 107
electron, 54
free electron, 98
Equilibrium process, 343
Evanescent wave, **185**, 187, 252, 254
Excitation, 297
dielectrics, **281**
probability, 39
processes, 52
semiconductor, **281**
Excited
transition metal, 289
Excited-state transitions, **286**
Extended states, 272, 285
External
force, 98
photo-effect, 120
photoelectric effect, 120
External photo-effect, 120
Extinction coefficient, 152, 246
vanishing, 177

F

Far field, 61
dipole, 72
Fermi
edge, 241
energy, 227
function, 238
gas, 240, 247
level, 284

number, 227
quantum number, 227
sphere, 230, 231
statistics, 327
tail, 242
velocity, 232
wave number, 232
Fermi–Dirac
distribution, 234, 237, 238, 327
metals, 241
semiconductors, 243
statistics, 237
Fermions, 224, 237, 240, 327
Fermi's Golden rule, 53
Feynman diagram, 6
Filamentation, 296, 314, 395, 400
Filters
interference, 362
narrow-band, 362
First-order dispersion, 45
Fluence, 36
Fluorescence, 296
Force
centro-symmetric, 192
non-centro-symmetric, 192
Form factor, 137
Forward scattered radiation, 161
Fourier
coefficients, 374
decomposition, 41
plane, 48
transformation, 41
inverse, 41
Fourier's law, 321
Four-wave mixing, **211**, 296
degenerated, 212
Fraunhofer absorption lines, 115
Free carrier absorption, 117, 246
Free-electron, 120
gas, 223, **247**, 257, 289
Free-free
electrons, 278
generation, 88
Fresnel
equations, 372, 375, 377
complex refractive index, 177
first, 172
fourth, 176
second, 173
third, 175
Friction force, 95
Frictionless elastic fluids, 349
Fringes, 398, 402
Full Width at Half Maximum (FWHM), 153

G
Gamma radiation emission, 52
Gauge transformation, 19
Gaussian fundamental mode, 337
Gauß
law, 10, 147
magnetism, 11
theorem, 21
General Euler equations, 349
Generalized Lorentz force, 6
Glass, 273
Gold, 260
Gradient-index lens, 215
Gravitational force, 6
Graviton, 7
Green
equation
charge and current distributions, 59
generalized, 59
functions, 19
generalized , 60
Group
delay, 45
dispersion, 45
instantaneous, 42
velocity, 34, 250
dispersion, 45
electron plasma, 251

H
Hamiltonian, 224
Hardening of X-rays, 88
Harmonic oscillation, 196
Heat capacity
electron system, 325
free electron, 328
molar, 326
electrons, 327
solid, 326
phonon, 335
phonon system, 334
specific, 326
at constant volume, 326
volumetric, 338
Heat conduction
one-dimensional, 320
Heat conductivity, 321
Heat equation, 320, 337
derivation, **320**

for the electron system, 324
for the phonon system, 324
homogeneous, 324
one-dimensional , 323
phonon system, 333
three-dimensional, 323
Heat flow, 321
coupling electron-phonon, 325
from the surface, 322
local, 321
within solid, 321
Heating
isochoric, 352
metals, **324**
Heat transfer coefficient, 321
Heat transport, 320
Heaviside function, 58, 260
Heisenbergs uncertainty principle, 102
Hermitian, 41
Heterogeneous
boiling, 346
High-energy free electrons, 299
Hole, 264, 267, 281
semiconductors, 264
Homogeneous
boiling, 346
Hot electron gas, 293
Hyperfine structure constant, 103

I
Ideal
absorption, 75
body, 75
emission, 75
semiconductor, 266, 267
Idler, 206
Imaging ellipsometry, 383
Impact ionization, 88, 118, 299, 308
Incoherent scattering, 138
Indirect
electron transitions, 289
recombination, 289
Inelastic
electron scattering, 280
Inelastic scattering, 144
Influence, 20, 147
Inhomogeneous
d'Alembert equations, 19
electromagnetic field, 123
Instantaneous angular frequency, 40
Insulator, 260, 262, 278
Integral description
Maxwell equations, 12
Intensity
electromagnetic radiation
vacuum, 33
matter, 178
second harmonic, 201
third harmonics, 213
Intensity distribution
Gaussian
spatial, 35
temporal, 35
Interaction volume, 318
Interband
absorption, 279
excitation, 264, 277, 279, 288, 298, 303
transition threshold, 282
Interband Transition Threshold (ITT), 282
Interface, 167
Interference, 136
Interferograms, 402
Interferometer
Jamin, 397
Mach-Zehnder, **397**
Interferometry
white-light, **397**
Internal
photo-effect, 120
reflection, 182, **185**
Internal energy
molar, 326
phonon system, 334
specific, 326
Intraband
excitation, 118, 277, **283**, 286, 291
transitions, 288
Inverse bremsstrahlung, 88, **117**, 246, 279, 283, 286, 291, 298
Inverse Fourier transformation, 41
Ionization, 297
above-threshold, 129
atom, 120
energy, 124, 125, 127
K-shell, 122
multi-photon, 124, **125**
n-photon, 125
rate
multi-photon ionization, 125
tunnel ionization, 124
tunnel, **124**
IR radiation, 128
Isentropic expansion, 351, 352
Isochoric heating, 351, 352
Isotropic media, 190

J
Jones transfer matrices, 375

K
Keldysh
parameter, 126, 298
atoms, 126, 127
crystals, **300**
dielectric, 301
tunnel time, 126
Kennedy model, 309
Kerr
coefficient, 214
effect, **213**, 214, 218, 296, 312
-Lens mode-locking, 215
Kinetic
energy of electrons, 245
gas theory, 336
Kramers' opacity law, 118
Kronig-Penney model, 270
K-shell ionization, 122
K-space, 230

L
Lambert–Beer's law, 136, 246, 318, 322
Laplace
operator, 215
Laser, 52
radiation, **35**, 278
tailored, 88
Laser-Induced Periodical Surface Structures (LIPSS), 254
Lateral scattered radiation, 162
Law of reflection, 171
Liénard-Wiechert
potentials, 59
Liénard-Wiechert potentials, 60
Linear
absorption, 144, 298, 299
excitation, 297
magnetization, 150
optics, 143, **167**, 278
polarization, 149
density, 196
Liquid
gas mixture, 353
phase, 343
Liquid-gas boundary, 344
Liu plot, 37
Localized
states, 275, 285
transient, 296
Long-range order, 273, 285
Lorentz
force, 102
gauge, 59
gauge transformation, 19
model, **151**, 292

M
Mach-Zehnder interferometer, **397**
Magnetic
energy density, 25
field strength, 150
induction, 150
susceptibility, 150
Magnetization, 150
linear, 150
Mass attenuation coefficient, 136
Material equation, 149
MATHEMATICA®, 337
Matlab®, 337, 402
Matter
amorphous, 285
disordered, 285
non-crystalline, 273
Max Planck, 78
Maxwell
equations, **9**, 17, 33, 147
matter, 150
vacuum, **9**
Maxwell–Boltzmann
distribution, 88, 265, 267
statistics, 244
Maxwell–Faraday
equation, 9
Maxwell–Faraday equation, 10
Mean
free path
electrons, 330
length of ballistic electron, 319
scattering time
electrons, 330
Measurement method
direct, 359
indirect, 359
Mechanical stress, 395
Melting, 344
temperature, 344
Metals, 144, **239**, 260, 278
Meta-stable
liquid phase, 351
phases, 351
state, 278, **289**

Micro-cracks, 68
Mixing
difference-frequency, 203
sum-frequency, 203
Mößbauer effect, 113
Mobility gap, 276, 286
Mode
density, 77
spectral, 80
distance, 77
frequency, 77
number, 77, 80
frequency, 80
wave number, 80
vector, 80
vibrational and rotational, 119
wavelength, 77
Model
one-temperature, 339
Molecular changes, 296
Møller scattering, 6
Molybdenum, 347
Momentum
conservation, 206
equation, 350
photon, 9
Monochromatic radiation, 34
Multi-channel plate, 359
Multi-photon
absorption, 116
excitation, 297, 300, 303
ionization, 124, **125**, 128, 300
order, 304
scattering, 116
Multi-pulses, 88

N
Nanofilm EP4, 383
Near field
description, 61
dipole, 72
Newton rings, 365
Nomarski, 293
microscopy, **391**
time-resolved, 393
Non-centrosymmetric force, 192
Non-crystalline matter, 273, 285
Non-depleted Pump Approximation (NDP), 207
Non-depleting pumping, 212
Non-equilibrium
process, 343
state, 278
Non-linear
absorption, 145, **297**, 298, 395
excitation, 297
force, 123
ionization, 288
optics, 145, 192
photo-excitation, **300**, 304
photo ionization, **124**
polarizability, 199
polarization density, 191, 196, 197
Non-radiative recombination, 289
Non-resonant process, 117
Non-reversible interaction, 143
Normal dispersion, 156
N-photon ionization, 125
cross-section, 125
Nuclear forces, 5
Nucleation, 346, 350
cavitation bubbles, 350
Number density
dipoles, 149
Number of states
overall, 232
Numerical approach, **337**

O
Occupation density, 78
Ohms resistance, 26
One-temperature model, 339
Opacity, 118
OP-CPA, 209
Optical
parametric
amplification, 192, 208
amplifier, 385
chirped pulse amplification, 209
generation, 208
oscillation, 208
path
difference, 402
length, 402
properties
metals, **291**
rectification, 196
retardation, 398
systems, 278
Optical Parametric Amplification (OPA), 192, 208, 385
Optical Parametric Generation (OPG), 208
Optical Parametric Oscillation (OPO), 208
degenerate, 208

Optical penetration depth, 186
Optics
non-linear, 192
Order
long-range, 273
short-range, 273
Orthogonality relations, 15
Oscillator strength, 156
many atoms, 156
Overall
emitted power, 63
energy, 233

P
Pair production, **132**
total cross section, 132
Parametric amplification, 206
Pauli principle, 224, 237, 244, 256, 257, 260
Period, 15
Permanent
refractive index change, 296
Permittivity
absolute, 146
anisotrope, 190
relative, 146
vacuum, 146
Perpendicular, 169
Perturbation
approximation, 194
theory, 194, 210
Phase, 39
boundary, 346
change, 379
coexistence, 345
diagram, 344
temperature-density, 351
explosion, 347, 353, 364
interface, 346
meta-stable, 346
mismatch, 199, 202
object, 391
shift, 173
space, 229
time-dependent, 218
velocity, 33, 165
electron plasma, 250
Phase-shifting algorithm, 402
Phonons, 120, 245, 282, 291, 319, 334
dispersion
spectroscopy, 336
optical and acoustical, 120
system, 319
Photo
-effect
external, 120
internal, 120
elastic effect, 49
-electric effect, 120
excitation, 120
ionization, **120**
linear, 298
multi-photon probability, 125
-voltaic effect, 120
Photo-electrons, 129
Photo-electron spectroscopy, 131
Photo ionization, 298
Photometry, 178, 246
Photon, **8**, 120
back-scattering, 131
energy, 8, 78
Compton-scattered photon, 130
Phthalocyanine blue, 158
Planar wave, 28
Planck
constant, 79, 120
law, 81
Plane of incidence, 169
Plane wave, 76
Plasma, 344
density
critical, 88
frequency, 88, 152
laser-generated, 118
mirror, 250
state, 320, 344
Platinum, 262
Poderomotive
energy, 123
Poincaré-sphere, 371
Poisson equation, 18
Polarizability
electric, 100
non-linear, 199
Polarization, 149, 370
degree, 370
density
linear, 190, 196
non-linear, 191, 196, 197
electric, 147
ellipse, 370
linear, 149
state, 78, 370
surface charge density, 148
Polarons, 188
Polymer, 273

Polymethylmethacrylate (PMMA), 158, 301
Ponderomotive
energy, **122**, 126, 304
force, **122**, 123
Potential
energy
atomic oscillator, 76
scalar, 17
vector, 17
Power
average, 216
distribution, 36
Poynting
theorem, 27
integral form, 28
vector, 27, 32, 109
charged particle in far field, 61
dipole far field, 73
temporal-averaged, 73
P-polarized radiation, **174**
Principal equation
linear optics, 159, 190
non-linear optics, 191
Probability
integral, 126, 128, 304, 305
multi-photon photo ionization, 125
Probe
pulse, 360
radiation, 387
Programmable pulse shaping, 47
Pulse, 251
burst, 88
duration, 286
energy, 35
shaping
programmable, 47
spectral, 47
Pump, 206
pulse, 360
radiation, 387
Pump-probe
metrology, **360**
white-light interferometry, **399**
Python™, 337

Q
Quantized, 53
energy states, 226
photons, 128
Quantized momentum, 229
Quantum Electrodynamics (QED), 9, 52
Quantum number, 225
main, 103
vector, 228
Quantum tunneling, 124
Quartz, 202
Quasi-free electrons, 278
gas, **251**
generation, 395

R
Radiation
Cherenkov, 51
force, **95**, 97, 105
dissipative, 98
oscillation period, 126
power
emitted, 96
p-polarized, **174**
s-polarized, **168**
thermal, 51
Radiative
decay rate, 53
recombination, 289
Raman scattering, **119**
Rarefaction wave, 352
Rate equation, 53
Ray, 162
Rayleigh-Jeans
law, 82
model, 78
Rayleigh scattering, 112
Total cross-section, 112
Reciprocal lattice
distance, 270
vector, 270
Recombination, **289**
center, 276
decay time, 289
direct, 289
indirect, 289
non-radiative, 289
radiative, 289
Reduced
photon energy, 121, 131
Reduced band structure plot, 280
Reflectance, **178**, 361
metals, 252
specular, 362
Reflection
coefficient
perpendicular, 180
p-polarization, 175
s-polarization, 172

coefficients, 372, 377
internal, 182
law, 171
Reflectometry
space- and time-resolved, 362
time-resolved, **361**, 362
Refraction
Snell's law, 171
Refractive index, 145, **153**
change, 395
complex, 152, 176, 245, 371
free electron gas, 248
frequency-dependent, 44
spatially modulated, 218
weak damping, 155
Relative
permeability, 150, 152
permittivity, 146
velocity, 68
Relativistic
factor, 60
particle, 68
Resonance
absorption, 88
fluorescence spectroscopy, 113
Resonant
absorption, 120
scattering
total cross-section, 113
Resonant excitation
absorption, 114
Rest mass
electron, 132
Retarded
time, 57
wave, 164
Reversible interaction, 143
Ripple, 38, 254
Rydberg energy, 115

S
Safety
work, 88
Saturation vapor pressure, 344
Scalar
potential, **17**
Scattered radiation
backwards, 161
forward, 161
lateral, 162
Scattering, 67
coherent, **136**
Compton, **130**
electron-phonon, 282, 291
incoherent, 138
multi-photon, 116
Rayleigh, 112
Thomson, 113
totally inelastic, 114
Schrödinger equation, 224, 270
Second
harmonic
field strength, 200
generation, 196, **200**
intensity, 201
radiation, 192
Second Harmonic Generation (SHG), 192, 196, **200**
Second-order
dispersion, 45
processes, **192**
Seed electrons, 287
Self-focusing, **215**, 216, 312, 400
catastrophic, **217**
critical power, 216, 217
Self-phase modulation, 208, **218**, 299, 393
Self-trapped
electrons, 300
excitons, 278, 289, 293
Self-Trapped Excitons (STE), 278, 289
Sellmeier, 382
Semiconductor, **242**, 264, 278
excitation, **281**
excited-state, 288
ideal, 266, 267
Semi-metal, 262
Separation ansatz, 79
Shock wave, 352
Short-range order, 273, 285
Signal, 206
Silver, 260
Simultaneous absorption, 116
Slow Varying Envelope Approximation (SVEA), 198
Snell's law, 252
refraction, 171
Solar
atmosphere, 115
spectrum, 115
Soleil Babinet compensator, 47
Solid angle, 63
Solidification, 344
temperature, 343
Sommerfeld parameter
experimental, 328

theroretical, 328
Spallation, 347, 351, 353, 364
Spatial
chirp, 44
light modulator, 48
Specific heat capacity, 325
Speckle-like intensity, 314
Spectral
amplitude, 42
energy density, 75, 78, 81
mode density, 80
phase, 42
pulse shaping, 47
transfer function, 44
Spectroscopic ellipsometry, 158
Speed of light, 33, 145, 250
matter, 152, 164
vacuum, 10
Speed of sound, 336
Sphere equation, 80
Spherical waves, 73
Spinodal, 346, 351
decomposition, 347
s-polarized radiation, **168**
Spontaneous emission, **52**, 115, 116
Standing wave, 76, 270
State
extended, 285
ground, 255
highest occupied, 256
localized, 285
non-equilibrium, 278
Statistics
Maxwell–Boltzmann , 244
Stefan–Boltzmann
constant, 83
law, 83
Step function, 260
Stimulated emission, 52
Stokes
parameters, 370
scattering, 119
vector
normalized, 370
Storage ring, 68
Straight propagation, 160
Strong nuclear force, 5
Sum-frequency mixing, 203
Super-continuum, 218
source, **400**
Supercritical fluid, 352
Super-heated liquid, 346
Surface
charge, 20, 21
densities, 148
density effective, 148
density polarization, 148
heating source, 337
plasmons, 38
Susceptibility
electric, 147
linear, 190
magnetic, 150
non-linear, 190
Synchrotron, 68
energy distribution, 68
radiation, 68

T
Tauc plot, 276
TEM_{00} mode, 35
TEM mode, 337
Temperature
degeneracy, 240
Temperature dependence
heat capacity, 325
Temporal coherence, 38
Tensor, 158
Thermal
conductivity, 252
electron system, 332
free electrons, 330
phonons, 336
diffusivity, 337
equilibrium, 76
radiation, 51
relaxation, 282
Thermalization, 285, 348
Thermalize, 289
Thermodynamic equilibrium, 75
Thermo-mechanical stress, 344
Thermophysical parameters
metals, 338
Thinning wave, 353
Third-Harmonic Generation (THG), **212**, 212
Third-order
dispersion, 43, 46
processes, **209**
Thomson
cross-section, 111, 113, 122
scattering, 113
Three-photon absorption, **307**
THz-radiation, 196
Time-bandwidth product, 39

Time-dependent
phase, 218
Total
cross-section, 111
Compton scattering, 131
pair production, 132
photo-effect, 121
Rayleigh scattering, 112
resonant scattering, 113
derivative, 349
emitted averaged power
oscillating dipole, 74
inelastic scattering, 114
Transient refractive index change, 296
Transitions
excited-state, **286**
Transmission coefficient
p-polarization, 176
s-polarization, 173
Transmittance, **178**, 178
Transparent materials, 297
Transversal wave, 17
Tungsten, 262
Tunnel
effect, 187
excitation, 297, 300, 301
ionization, **124**, 127, 300
time, 127
Two-phase system, 343
Two-photon absorption, **306**
constant, 307
Two-temperature model, **318**

U
Ultra-fast laser radiation, 39
Ultraviolet catastrophe, 78
Under-cooled gas, 346
Universal gas constant, 326
Urbach
energy, 276
tail, 275, 276

V
Vacancy state, 281
Vacuum permittivity, 146
Valence band, **259**, 260, 272
van-der-Waals force, 7
Vaporization, 344
Vector
reciprocal lattice, 270
Vector potential, **17**
Velocity
phase, 33
quantized, 229
Vibronic modes, 119
Virial theorem, 326
Virtual photons, 6
Volumetric heat capacity, 338

W
Wave
guide, 76
number
Fermi, 232
vector, 15, 228
Wave equation
electric field strength, 13
hollow body
one-dimension, 76
magnetic flux density field, 13
Wavelength
discrete, 225
Weak nuclear force, 5
White-light
continuum, 218, 393
interference microscope
Horn, 398
interferometry, **397**
pump-probe, **399**
Wien's
displacement law, 83
law, 82
Wollaston prism, 391
Work, 20
function, 121

X
Xenon, 130
X-ray, 65, 164
Brownian , 65
laser-generated, **87**
photon flux, 88
photon spectra, 88
radiation
soft, 113
spectrum, 67, 87

Z
Zinc, 262